12-2012

A Search for WIMP Dark Matter using an Optimized Chi-square Technique on the Final Data from the Cryogenic Dark Matter Search Experiment (CDMS II).

Manungu Joseph Kiveni
Syracuse University

Recommended Citation

Kiveni, Manungu Joseph, "A Search for WIMP Dark Matter using an Optimized Chi-square Technique on the Final Data from the Cryogenic Dark Matter Search Experiment (CDMS II)." (2012). *Physics - Dissertations*. 129.
https://surface.syr.edu/phy_etd/129

Abstract

During the last two decades, cosmology has become a precision observational science thanks (in part) to the incredible number of experiments performed to better understand the composition of the universe. The large amount of data accumulated strongly indicates that the bulk of the universe's matter is in the form of non-baryonic matter that does not interact electromagnetically. Combined evidence from the dynamics of galaxies and galaxy clusters confirms that most of the mass in the universe is not composed of any known form of matter. Measurements of the cosmic microwave background, big bang nucleosynthesis and many other experiments indicate that $\sim 80\%$ of the matter in the universe is dark, non-relativistic and cold. The dark matter resides in the halos surrounding galaxies, galaxy clusters and other large-scale structures.

Weakly Interacting Massive Particles (WIMPs) are well motivated class of dark matter candidates that arise naturally in supersymmetric extensions to the Standard Model of particles physics, and can be produced as non-relativistic thermal relics in the early universe with about the right density to account for the missing mass.

The Cryogenic Dark Matter Search (CDMS) experiment seeks to directly detect the keV-scale energy deposited by WIMPs in the galactic halo when they scatter from nuclei in the crystalline detectors made of germanium and silicon. These detectors, called Z-sensitive Ionization and Phonon detectors (ZIPs) are operated at ~ 45 mK and simultaneously measure the ionization and the (athermal) phonons produced by particle interactions. The ratio of ionization and phonon energies allows discrimination of a low rate of nuclear recoils (expected for WIMPs) from an overwhelming rate of electron recoils (expected for most backgrounds). Phonon-pulse shape and timing enables further suppression of lower-rate interactions at the detector surfaces.

This dissertation describes the results of a WIMP search using CDMS II data sets accumulated at the Soudan Underground Laboratory in Minnesota. Results from the original analysis of these data were published in 2009; two events were observed in the signal region with an expected leakage of 0.9 events. Further investigation revealed an issue with the ionization-pulse reconstruction algorithm leading to a software upgrade and a subsequent reanalysis of the data. As part of the reanalysis, I performed an advanced discrimination technique to better distinguish (potential) signal events from backgrounds using a 5-dimensional chi-square method. This data-analysis technique combines the event information recorded for each WIMP-search event to derive a background-discrimination parameter capable of reducing the expected background to less than one event, while maintaining high efficiency for signal events. Furthermore, optimizing the cut positions of this 5-dimensional chi-square parameter for the 14 viable germanium detectors yields an improved expected sensitivity to WIMP interactions relative to previous CDMS results. This dissertation describes my improved (and optimized) discrimination technique and the results obtained from a blind application to the reanalyzed CDMS II WIMP-search data.

This analysis achieved the best expected sensitivity of the three techniques developed for the reanalysis and so was chosen as the primary timing analysis whose limit will be quoted in a on-going publication paper which is currently in preparation. For this analysis, a total raw exposure of 612.17 kg-days are analyzed for this work. No candidate events was observed, and a corresponding upper limit on the WIMP-nucleon scattering cross section

as a function of WIMP mass is defined. These data set a 90% upper limit on spin-independent WIMP-nucleon elastic-scattering cross section of 3.19×10^{-44} cm^2 for a WIMP mass of 60 GeV/c^2. Combining this result with all previous CDMS II data gives an upper limit of 1.96×10^{-44} cm^2 for a WIMP of mass 60 GeV/c^2 (a factor of 2 better than the original analysis).

At the moment this analysis is being written, the WIMP-search results obtained with the reanalyzed CDMS II data occupies the second most stringent limits on WIMP-nucleon scattering, after XENON100, excluding previously unexplored parameter space. Interesting parameter space is excluded for WIMP-nucleon cross section as function of WIMP masse under standard assumptions, the parameter space favored by interpretations of other experiments's data as low-mass WIMP signals due to an excess of low energy events and annual modulation is partially excluded for DAMA/LIBRA and CoGeNT.

A Search for WIMP Dark Matter using an Optimized Chi-square Technique on the Final Data from the Cryogenic Dark Matter Search Experiment (CDMS II).

By

Manungu Kiveni, Joseph

B.S. Degree in Physics (University of Kinshasa), Kinshasa, Democratic Rep. of Congo 2004
Diploma Program in Theoretical High Energy Physics (International Center for Theoretical Physics, Trieste), Italy 2005
M.S. Degree in Physics (Syracuse University), Syracuse, May 2009

Dissertation

Submitted in partial fulfillment of the requirements for the

Degree of Doctor of Philosophy

in

Physics

in the Graduate School of Syracuse University

December 2012

Acknowledgments

First and foremost, I would like to take this opportunity express my gratitude to all who have left good and profound impression and to those who have positively impacted my life for they role models and leaderships, and Richard W. Schnee, my advisor, is one among them. All my gratitude and thaks to advisor Richard W. Schnee for his constant encouragements, supports and patience. Richard W. Schnee is an extremely insightful scientist and a very patient advisor, knowledgeable in his field of research. Richard has taught me the value of taking time to reason critically, the need to take time to consider the right approach to solve a problem, the need to figure out ways to check whether the results found makes sense or not. "There are many ways to do something wrong, and so almost every study that everyone does has at least one error in it on the first try, but a good physicist has to be able to perform checks that the work is all consistent and makes sense", Richard Schnee told me one day. During my 5 years of Ph.D. work under Richard W. Schnee's guidance, I have learned all these values and acquired necessary skills needed in order to do research. I am so tankful for that.

I am greatly indebted to my friends and collaborators of the Cryogenic Dark Matter Search (CDMS) at Syracuse University and the Cryogenic Dark Matter Search collaboration as whole. I would like to thank Dr. Mark Kos, Richard Schnee's post doc. Dr. M. Kos was extremely helpful to all graduate students with no or little grasp of research in experimental physics. Mark had always set time to discuss with me some aspects of the cryogenic dark matter search and shared with me his knowledge and insight on how statistics is applied in experimental physics; I am so grateful to you. I wish you all the best in your new job.

I am also extremely indebted and grateful to Dr. Raymond Bunker who was really valuable to me during the timing of the writing of my dissertation. Dr. R. Bunker was almost instrumental to reading and correcting the first versions of many of my chapters and giving valuable feedbacks. Dr. Raymond Bunker is always ready and available to help and I was so lucky to have you around me during the crucial moment of my putting this dissertation together.

My thanks are also in order to other graduate students in the group, Boqian Wang, Yu Chen and Michael Bowles for your readiness to help at any time. Thanks as well to the many loyal and hardworking undergraduates who have been part of the CDMS group at Syracuse University, many of whom have also been instrumental in the proofreading of my posters and abstracts few days and hours before the deadline. Particular thanks to Ian Ruchlin who is now a graduate student at Rochester Institute of Technology (R.I.T.), Tom Goldstein, Dan Jardin and Matthew Voelker. Let me extend my thanks and gratitude to all other undergraduate students in the group whom I have forgotten the names; you all have been good guys and left a profound impression in me for your kindness and friendship. Special thanks goes to Eric West, a graduate of Physics from Syracuse University, who accepted to read my thesis although his extremely busy schedule.

The CDMS collaboration has been a wonderful group to work with and to be a part of. I appreciate working with all of you, but let me single out just a few with whom I've greatly enjoyed working closely during the combined runs 125 to 128, run called c58, I had the privilege to work with: Jodi Cooley(analysis coordinator), Zeesh Ahmed, Lauren Hsu, Dave Moore, Sebastian Arenberg, Tobias Bruch, Oleg Kamaev, Durdana Balakishiyeva, Scott Hertel, Scott Fallows, Kevin Mc Carthy and Mark Kos as well. During the run R130, I was privileged enough to work with: Angie Reisetter (analysis coordinator), Lauren Hsue, Mark Kos, Joel Sander, Kunj Prassad, Scott Fallows and Jiangie Zang. Here I am addressing a special thanks to Angie Reisetter and to Joel Sander for the time spend to teach me the technique of χ^2 for surface events discriminations during the workshop meeting at the university of minnesota, knowledge that I later on used to develop an energy-independent and dependent χ^2 for characterization and understanding of surface events discrimination for the mZIP detector (1 inch thick detectors the CDMS II collaboration has designed). The advance technique presented in this dissertation all started from the lessons I learned from them.

Finally, during the re-analysis of the c58 data, I interacted with Anthony Villano (analysis coordinator), Daniele Speller, Arun aryan, Tommy Hofer, Jianjie Zang, Kris Koch. Thanks to Rupak Mahapatra, Prisca Cushman and Richard Schnee for their constance guidance during the c58 reanalysis, for keeping an eye in our studies and making sure that we produce meaningful, and not erroneous, results.

I will not put an end to this page without recognizing the many help and tutorials I have received from many other CDMS collaborators. My recognition goes to Jeff Filippini, Walter Ogburn, Matt Pyle, Bruno Serfas, Jong Hee and Jeter Hall. Thanks to Matt Fritts and David Moore for the insightful and encouraging private discussions. Thanks to Adam Anderson who has helped in reading many of the chapters of my dissertation in instantaneous manner.

Many thanks to Bernard Sadoulet and Steve Yellin for their insights into my optimized timing cuts analysis and for always keeping analyzers honest. Special Dan Bauer, Blas Cabrera Jim Beaty and Dennis Seitz for their constant guiding presences for Soudan shifters, whether physically or virtually.

My everlasting gratitude to my parents and my siblings, without your love, supports and encouragements, I would have not gotten here. Finally my warn thanks and love to my wife Tatiana and to my children Tiffany Diane and Christopher, for keeping late nights with me, without your supports and encouragement, I would have not made it. This dissertation marks the end of my graduate school, and yet sets the clock back for a start of a glorious exploration that we all are going to discover in days to come.

Contents

List of Tables

List of Figures

Chapter 1

Introduction to Modern Cosmology

1.1 Introduction

This dissertation will describe a search for the constituents of one of the most mystifying particle for which the evidence of its existence came to knowledge mostly through the observation [1, 2, 3, 4]. This particle has thus far been brought to existence by some theories such as the theory of elementary particles, the physics beyond the standard model of particle physics and with the existence of extra dimensions. This mystified particle , coined dark matter, is referred to a particular type of matter which does not clump under the influence of gravitational force and whose existence is inferred solely from the effects of its gravity. Dark matter may be baryonic (i.e. built from the protons, neutrons, and electrons of ordinary atomic matter) or non-baryonic in nature, but the vast majority of it appears to be the latter. The details of this search will be described in chapters 4 to 8. In this chapter, however, I give a very brief introduction of the foundation of modern cosmology theory which gives a very simple justification to the existence of dark matter. The attempt to answer the question ”why has something invisible has become an accepted part of modern astrophysics?” will become clearer as we move along this dissertation.

A complete discussion of the foundation of cosmology would take us far afield from the main topic of this dissertation. So, I will recall only some of the common terminologies. For more details, I invite the readers to look at modern textbooks on the cosmological theory [6, 7, 8, 9, 10, 11, 12, 24, 13, 14].

Cosmology is a subset of astronomy which is trying to answer some of the grandest questions of the universe: how the universe was born, what is the age of the universe, how and when the universe is going to end. In addition to these questions, cosmology is also trying to answer the question of ”what the universe is made of”.

The development of cosmology has no doubt contributed some of the most important scientific triumphs of the twentieth century. Going from mere theoretical predictions (the big bang theory, inflationary model of the universe, dark matter and dark energy) to the experimental discovery of the accelerated expansion of the universe in 1998 by measurement of the luminosity of very distant supernovae [15, 16, 17]. Cosmology is currently a highly active and a growing field, spurred by the influx of a variety of precision measurements and a number of new and proposed experiments that are trying to answer some fundamental questions regarding the truth about the universe in which we are living. This dissertation is going to focus, as I mentioned before, on one of the mysterious components of the universe, the dark matter. However at the time of the writing of this dissertation there is a separate experimental group whose aim is to understand the dark energy which amounts to 73% of the energy-budget of the universe. The Dark Energy Survey (DES) aims to probe the dynamics of the expansion of the universe and the growth of large scale structure using a 4-meter Victor M. Blanco Telescope located at Cerro Tololo Inter-American Observatory (CTIO) in Chile, and the main innovation of that project consists in the development of a new and hyper sensitive camera, called DECam [18].

In the beginning, cosmology hardly existed as a scientific discipline, but now the Hot Big Bang cosmology stands as the accepted description of the Universe as a whole. Telescopes such as the Hubble Space Telescope are capable of seeing light from galaxies so distant that it has been travelling towards us for most of the lifetime of the universe. The cosmic microwave background, a fossil relic of a time when the Universe was both denser and hotter, is routinely detected and its properties examined. The expansion of our universe is presently an established fact with the discovery of Supernova type Ia. Supernovae are extremely luminous and cause a burst of radiation that briefly outshines an entire galaxy (such as our galaxy, the Milky way). Because their higher intensity of luminosity is constant, they are called standard candle [19, 20, 21, 22, 23].

The standard model of cosmology has emerged over the last several years in which some cosmological parameters like Ω_m, Ω_Λ and H_0 have been measured to within an accuracy of 10%. The precision of these measurements comes from testing the consistency of the various methods by which the physical universe is described with the emergence of a well constrained Dark Matter hypothesis. Dark Matter is one example and Dark Energy, the driving force behind the accelerated expansion of the universe, is another.

In this chapter, I will discuss the theoretical and the experimental basis of the standard model of cosmology and introduce the dark matter problem that is going to be the central topic of the subsequent chapters.

1.2 Cosmology's Biggest Ideas

The ancient Greeks, in a model further developed by Ptolemy (the Alexandrian), believed that the Earth was at the center of the cosmos (geocentric). According to this model, the earth would be circled by the Moon, the Sun and the planets, and then the stars would be further away. A complex combination of circular motions, Ptolemy's Epicycles, was devised in order to explain the motions of the planets, especially the phenomenon of retrograde motion where planets appear to temporarily reverse their direction of motion. It was not until the early 1500 that Copernicus stated forcefully the view, initiated nearly two thousand years before by Aristarchus, that one should regard the Earth, and the other planets, as going around the Sun (heliocentric). By ensuring that the planets moved at different speeds, retrograde motion could easily be explained by this theory.

The cornerstone of modem cosmology is the belief that the place in which we occupy in the universe is in no way special and that the universe looks the same everywhere. This is known as **the cosmological principle**. With this principle in mind, our very own galaxy (the Milky Way), located in a disk shaped assembly, must not considered to be at center of the universe. Observations of the disk shaped assembly by Hubble space telescope show however that the Milky Way is at 2/3 off from the center of the disk.

The cosmological principle is the basis of Big Bang Cosmology. The Big Bang is the best description we have of our universe and is a picture of our universe as an evolving entity, which was very different in the past as compared to the present. Originally, the Big Bang theory was forced to compete with a rival theory, the steady state universe, which stipulates that the universe does not evolve but rather has looked the same forever with new material being created to fill the gaps as the universe is expanding. However, the experimental observations we have nowadays are so strongly in support of the Big Bang theory that the steady state theory is almost never considered as an alternative theory that is able to explain the reality of the universe around us.

1.3 Observational facts

Astronomers have very often had to rely on the visible part of the spectrum in order to study or observe distant objects in the universe. One of the great astronomical achievements of the twentieth century was the exploitation of the full electromagnetic spectrum for astronomical measurements. We now have been able to design instruments capable of making observations in all bands of spectrum including radio waves, microwaves, infrared, visible, ultraviolet, X-rays and gamma rays, which all correspond to light waves of different (increasing) frequency. We have even entered a phase where we can go beyond our galaxy and receive information of light originated from sources extremely distant from the earth. A remarkable feature of observations of a nearby supernova in 1987 was that it was also seen through detection of neutrinos, which are extraordinarily weakly interacting type of elementary particle normally associated with radioactive decay (also known as beta decay). Very high energy cosmic rays, consisting of highly-relativistic elementary particles, are now routinely detected, though there is no clear understanding of their astronomical origin. Currently the Laser Interferometer Gravitational Wave Observatory (LIGO) collaboration is seeking for detection of gravitational waves and ultimately to using them to observe astronomical events such as colliding stars. Gravitational waves are ripples in space-time itself, these are waves produced when giant astronomical objects (such as stars) collides in the universe. Such collisions will create a huge perturbation in space-time, thus creating ripples or waves propagating at the speed of light in the fabric of space time. The next advanced generation of gravitational waves detection will be pursued by the Laser Interferometry Space Antenna (LISA), a joint project between the United States apace agency NASA and European Space Agency (ESA).

To probe distant parts of the universe astronomers have used to ground base telescopes and air-born (or space base) telescopes relying on visible light of the electromagnetic spectrum. In most case, light observed by astronomers come from:

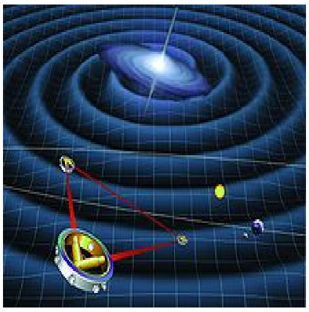

Figure 1.1: Propagation of gravitational waves shown as ripples of space-time. Gravitational waves are minute distortions of spacetime that are predicted by Einstein's theory of general relativity. The existence of gravitational radiation is also a prediction of general relativity. Gravitational waves are perturbations in the curvature of spacetime caused by accelerated masses (NASA illustration of LISA, figure source: www.lisa.jpl.nasa.gov/index.html).

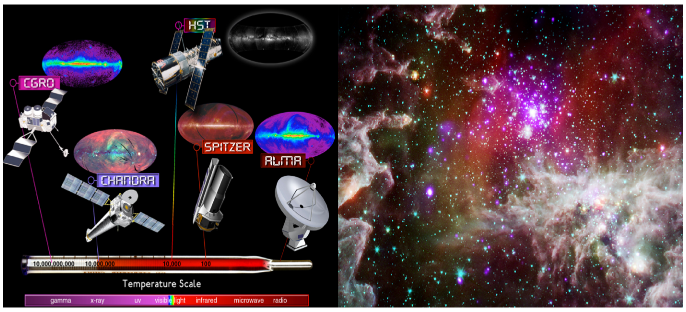

Figure 1.2: Electromagnetic spectrum (left) with different space-base satellites probing different parts of the electromagnetic spectrum; shown in the right a picture of star forming cloud. To see the universe in full, astronomers have to get creative; they combine multiple photos taken by different cameras to make one colorful picture. For example, in this beautiful new picture of a star-forming cloud (right), the space telescope called Chandra only captured the purple regions. Meanwhile, another space telescope called Spitzer saw things a bit differently when it observed the same cloud - everything shown here other than the purple bits. But why don't these two telescopes see the star-forming cloud in the same way? The answer lies in the type of light that the telescopes are designed to observe. Our eyes can only see visible light. But there are many other types of light that can be detected by special telescopes, such as infrared, ultraviolet and X-ray. The Spitzer telescope detects infrared light. Spitzer is perfect for observing dusty star-forming regions, as infrared light can travel through the dust. The Chandra telescope, however, can't see infrared light. Instead, Chandra can detect the X-ray light that is given off by gas when it is heated to incredibly high temperatures by hot, young stars. Although the two telescopes give a different tale about what they see, they are both revealing the truth.

Stars: The main source of visible light in the universe. This light comes from one nuclear fusion within stars. The sun is a typical star, with a mass of about $2{\times}10^{30}$ kilograms also referred to as solar mass, indicated by $M_\odot$ and used as a convenient unit for measuring masses. The sun is the closest star located 1 light year away from the earth.

Galaxies: The solar system lies some way off-center in a giant disk structure called the Milky Way galaxy. It contains approximately one hundred thousand million (10^{11}) stars, with masses ranging from about a tenth of the solar mass $M_\odot$ to tens of times larger. It consists of a central bulge plus a disk of radius 12.5 kiloparsccs (1 pc = 3.261 light years) and a thickness of only about 0.3 kpc. We are located in the disk about 8 kpc from the center.

Local group: The Milky Way galaxy resides within a small concentrated group of galaxies known as the local group. The nearest galaxy is a small irregular galaxy known as the Large Magellanic Cloud (LMC), which is 50 kpc away from the sun. The nearest galaxy of similar size to our own is the Andromeda Galaxy, at a distance of 770 kpc. The Milky Way is one of the largest galaxies in the local group. A typical galaxy group occupies a volume of a $\sim$ 1 Mpc^3 (Mpc or megaparsec is often used in astronomy as a unit for measuring distances; it is roughly the separation between neighboring galaxies. 1 Mpc = 3.086$\times$10^{22} meters).

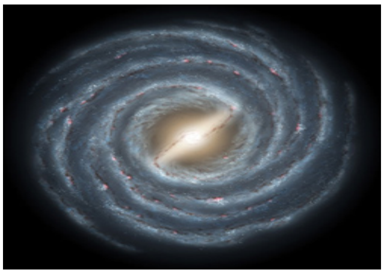

Figure 1.3: Milky way galaxy as imaged by the Hubble Space Telescope. The milky way is home to at least 200 billion stars and their planets with mass between $750\times10^9 M_\odot$ and $1\times10^{12} M_\odot$ ($M_\odot$ is one solar mass), and a diameter of 10^5 light years (light would take 10^5 years to travel from one side to another). Investigations of the hydrogen clouds contained within the Milky Way show that this galaxy is a spiral galaxy. There are many types of galaxy and they are usually categorized by their shape as elliptical, irregular or spiral. Our galaxy has a disk form when viewed from the side, which is 10^5 light years across and 1-2 light years thick, in the center of the disk lies a thin layer of gas and dust. The galaxy has a spiral shape when viewed from above. It also contains a central bulge or nucleus where a large black hole may be contained. The sun lies in the spiral arm named orion (figure source: www.nasa.gov).

Clusters of galaxies (and superclusters): Surveying larger regions of the universe on a very large scale of 100 Mpc leads to the observation of a variety of large-scale structures. Galaxies can also be grouped in galaxy clusters and one obvious example is the coma cluster, 100 Mpc from our very own galaxy. Galaxy clusters are the largest gravitationally-bound objects in the universe. They can group into a large number of cluster occupying a very large portion of the universe and they are called superclusters. Superclusters are believed to be joined by filaments and walls of galaxies and between them there is what is called "foamlike" structure lying in a very large voids as large as 50 Mpc across. Figure (1.3) illustrates the optical telescope image of the coma cluster. Each point like light in this image represent a distinct galaxy; the coma cluster contains approximately 10^3 galaxies.

Large-scale smoothness: At very large distance scales, hundreds of megaparsecs or more, the universe starts to appear smooth. Recent, extremely large, galaxy surveys, the 2dF galaxy redshift survey and the Sloan Digital Sky Survey (SDSS) [99, 100, 101, 102] have surveyed large volumes around $\sim$100 times the size of the the Center for Astronomy (CfA) survey [103], each containing hundreds of thousands of galaxies. Such surveys do not find any huge structures on scales greater than those seen in CfA survey.

Large scale structures such as galaxy superclusters and voids are believed to likely be the biggest structures given

Figure 1.4: The Sloan Digital Sky Survey/Spitzer Space Telescope image of the Coma Cluster in ultraviolet and visible light (figure source: NASA/JPL-Caltech/GSFC/SDSS).

the current stage of observation of stuff in the present universe. At these large scales, the universe indeed becomes smooth. Although smoothness of matter distribution was the bedrock assumption in modern cosmology, it is only recently that it has been possible to provide convincing observational evidence. Astronomical observations for most cases of the scientific history rely on visible light and have provided to us a good picture of what is around us (present and past-day universe). However, many other wavebands make vital contributions to our understanding of the universe, Figure(1.2), and below, let's review some of them very briefly:

Microwave band: Accidentally discovered in 1965 by Penzias and Wilson [104] when working with the horn antenna at Bell Laboratory, this waveband is by far the most important band. Their discovery lead to the understanding that the Earth is filled with microwave radiations, with a black-body spectrum. This discovery was one of the most powerful pieces of information in support of the Big Bang theory, around which cosmology is now based. Other results from experimental observations by the FIRAS (Far Infra Red Absolute Spectrometer) experiment on board the COBE (Cosmic Background Explorer) [105, 106] satellite have confirmed that the radiation is extremely close to the black-body form at a temperature $(2.730 \pm 0.001)\,\mathrm{K}$.

Radio wave band: This has been powerfully used in astronomy as a way of gaining high-resolution maps of very distant galaxies by mapping in the radio part of the spectrum. Many of the farthest galaxies known today were detected by exploiting this band of the electromagnetic spectrum [107, 108, 109].

Infrared band: This region of the spectrum is best for studying the regions of the universe close to our galactic plane where obscuration by dust is strongest. Infra red is an excellent way of seeing young galaxies in which star formation is at an early stage. Using only optical light means the brightest galaxies could be observed, so IRAS (Infra Red Astronomical Satellite) was successful in observing dimmer galaxies by exploiting the infrared spectrum [110, 111].

X-rays: In between galaxies lies gas so hot that it emits X-rays that can only be seen in the X-ray part of the electromagnetic spectrum. These hot gases, corresponding to a temperature of tens of millions of Kelvin were thought to be the remnants of the formation of the galaxies, which failed to collapse to form stars. X-rays are considered as vital as galaxies themselves and are tremendously useful in astronomy to see things that cannot be seen otherwise.

In the subsequent sections of this chapter, I am now going to lay down the foundation of the standard model of modern cosmology, also referred to as ΛCDM cosmology which justifies the need of the two most mysterious energy-matter components of the universe: dark energy and dark matter. As a recall, ΛCDM stands for dark energy (Λ) cold dark matter. I will discuss about dark matter in its entirety all along in this dissertation. As for dark energy, I will briefly describe it since its scope is beyond the limits of this dissertation.

1.4 The foundation of modern cosmology

There are many textbooks on cosmology that students can be referred to in order build a solid understanding of standard cosmology [112, 113, 114, 115, 116]. There are also many advanced textbooks on cosmology with advanced topics such string theory and so on [6, 7, 8, 118, 119, 120, 121, 122, 123, 124, 125, 126]. To avoid confusion, this dissertation will be based on the currently accepted cosmological model that can be found in many standard cosmology textbooks, in particular in [5, 6, 7, 8]. To begin, we will invoke the assumptions which the whole standard model of cosmology is based upon:

Homogeneity and isotropy: Homogeneity is the statement that the universe looks the same at each point, while isotropy states that the universe looks the same in all directions. This is supported by the previously mentioned cosmological principle and a result of this is that the universe appears smooth at very large scale.

The Equivalence Principle: it is assumed that the laws of physics as expressed within special relativity hold in all local inertial frames.

General relativity gives an excellent description of gravitational physics and is considered as the correct setting for discussing cosmological models. An important idea introduced in physics with the advent of general relativity is the concept of **the metric of space-time**, which describes the physical distance between two different points. This metric is also important both for correctly interpreting the geometry of the universe and to fully understand ideas of luminosities and distances in cosmology.

In general relativity we are interested in the distance between points in $4D$ space-time, and we must also allow for the possibility that space-time might be warped (curved). The general expression of a metric is then written as:

$$ds^2 = \sum_{\mu\nu} g_{\mu\nu} dx^\mu dx^\nu, \tag{1.1}$$

where $g_{\mu\nu}$ is the space-time metric (tensor), μ and ν are indices taking the values 0,...,3. In the compact notation of the equation (1.1), x_0 represents the time coordinate and x_1, x_2 and x_3 are the three spatial coordinates. In general, the metric can be a function of the coordinates (indeed, to describe a curved space-time there must be some such dependence), and the distances are written in infinitesimal notation because once space-time is curved it only makes sense to give the distance to nearby points.

Einstein′s formulation of general relativity marked the beginning of modern cosmology by establishing an irrefutable framework which led to a deep understanding of the dynamic evolution of spacetime, matter, and radiation [27]. With the advent of the theory of general relativity, the fundamental ingredients of the cosmological model have been postulated in the following terms: A) Einsteins equation relates the geometry of the universe with its matter and energy content; B) the metric is the measure of distances in curved spacetime and is needed to describe the symmetries of the model; and C) The equation of state specifies the physical properties of the models matter and energy content.

A large number of cosmological models have been constructed according to this recipe though many of them did not withstand the test of time and they have been systematically eliminated as consistent theories given the observational facts we have accumulated.

In cosmology, the metric describing the universe must obey the cosmological principle, i.e the universe must look the same everywhere. This requires that the spatial part of the metric has a constant curvature and this metric is called **the Friedman Robertson Walker (FRW) metric**, given by

$$ds^2 = -c^2dt^2 + a^2(t)\left[\frac{dr^2}{1-kr^2} + r^2\left(d\theta^2 + \sin^2\theta \cdot d\phi^2\right)\right], \tag{1.2}$$

where $a(t)$ is the scale factor characterizing the size of the universe. This is the quantity which expands (dilates) as time goes on. Just to mention, the expansion of the universe is based on observational evidence that everything in the universe seems to be moving away from everything else. The farther the object is the faster the object is receding. Edwin Hubble measured the velocities of some celestial objects by looking at their redshift, which is basically the Doppler effect applied to light waves. Galaxies as with any other atomic material, have a set of absorption and emission lines identifiable in their spectra, whose characteristic frequencies are well known. If a galaxy is moving towards us, the light waves get crowded together, raising the frequency, and this phenomenon is called **blueshift** because blue light is at the high-frequency end of the visible spectrum. But if the galaxy is receding i.e moving away from us, its characteristic lines move towards the red end of the spectrum and the effect is known as a **redshift**. I must call to the reader's attention that the metric described in equation (1.2) describes a universe with no expansion since the cosmological constant Λ is set to be zero. I will, later in this chapter, discuss the general case, which takes into account the cosmological constant that explains the observations experimentalist physicists have made during the last two decades.

Observing whether a galaxy is blueshifting or redshifting was a technique used to measure the galaxy's velocity by Vesto Slipher (1912). Edwin Hubble used the same technique which led to this extraordinary discovery that almost all galaxies are receding from us. Given the emitted and observed wavelengths λ_{obs} and λ_{em}, the redshift

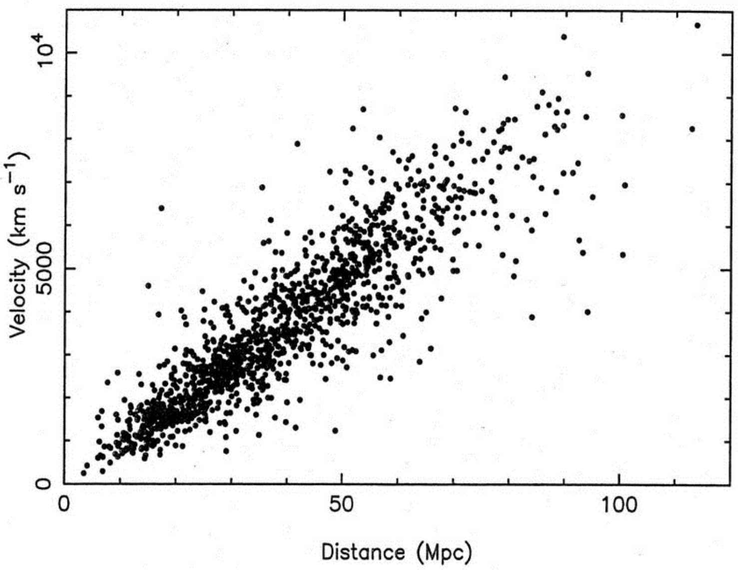

Figure 1.5: velocity vs estimated distance for a set of 1355 galaxies. A straight line relationship between the velocity and the distance is the best fit and implies the Hubble's law. The considerable scatter of data point is due to the uncertainties and the random motions of the galaxies, however the best fit line accurately describes the Hubble's law ($v = H_0 \cdot d$) and gives an accurate estimate of the hubble constant H_0. Figure from [25].

z, can be determined as

$$z = \frac{\lambda_{obs} - \lambda_{em}}{\lambda_{em}}. \tag{1.3}$$

If a nearby object is receding at a speed $v << c^{[1]}$, then its redshift can be calculated using the following formula

$$z = \frac{v}{c}. \tag{1.4}$$

From the observation of the data collected by Hubble and based on Figure(1.5), Hubble concluded that the recessional velocity is proportional to the distance, and that the constant of proportionality is in cosmology referred to as **the Hubble Constant**.

$$\vec{v} = H_0 \cdot \vec{d}. \tag{1.5}$$

The equation (1.5) is know as **the Hubble's Law**. The Hubble′s constant H_0 is commonly expressed in the units of $100\,\mathrm{km{\cdot}s^{-1}}$ $\mathrm{Mpc^{-1}}$, ie

$$H_0 = 100 \cdot h \quad \mathrm{km \cdot s^{-1} \cdot Mpc^{-1}}, \tag{1.6}$$

---

[1] For velocities closer to the speed of light, the redshift formula mentioned in equation (1.4) takes the following form as shown in special theory of relativity: $z = \sqrt{\frac{1+v/c}{1-v/c}} - 1$

where h is the hubble parameter characterizing the uncertainty on the present the value of H_0 (h=0.72±0.08).

1.4.1 Einstein's Equation

To consider the evolution in time of the scale factor, $a(t)$ in equation (1.2), we exploit the theory of gravitation in which the Einstein′s field equations into play. The field equations of Einstein are described by the formula:

$$\mathcal{R}_{\mu\nu} - \frac{1}{2}g_{\mu\nu}\mathcal{R} = \frac{8\pi\mathcal{G}}{c^4}\mathcal{T}_{\mu\nu}. \tag{1.7}$$

The tensor $\mathcal{T}_{\mu\nu}$ is the energy-momentum tensor of the matter which is present, $\mathcal{R}_{\mu\nu}$ and R are the Ricci tensor and the Ricci scalar, respectively, both representing the curvature of space-time. The Ricci scalar $\mathcal{R}$ (1.9), is obtained through contraction of the Riemann curvature tensor $R^{\mu\nu}$ [30]. The tensor $g_{\mu\nu}$ is the metric tensor in which the properties of space-time are imprinted. The left-hand side of the Einstein equation describes the evolution of the metric $g_{\mu\nu}$ and therefore space-time itself; $\mathcal{G}$ is the Newton′s constant. There is, for the sake of generality, an additional term in the right hand side of the equation (1.7) which is generally noted as $\Lambda g_{\mu\nu}$ which I have purposely omitted here, but will be discussed in a later section. Λ is a constant term known as the cosmological constant. As it will be discussed in more detail later, the cosmological constant is an accepted ingredient of Standard Cosmology although it was added by Einstein himself into the equation (1.7) in order to define a static universe. Historically, this term is also known as Einstein's biggest blunder. The fabric of space-time evolves according to the energy content on the righthand side (1.7), therefore the right-hand side of Equation (1.7) can be thought of as a collection of source terms. The Ricci tensor $\mathcal{R}_{\mu\nu}$ and Ricci scalar are defined by the following formula [30, 31]:

$$\mathcal{R}_{\beta\alpha} = \partial_\rho\Gamma^\rho_{\beta\alpha} - \partial_\beta\Gamma^\rho_{\rho\alpha} + \Gamma^\rho_{\rho\lambda}\Gamma^\lambda_{\beta\alpha} - \Gamma^\rho_{\beta\lambda}\Gamma^\lambda_{\rho\alpha}, \tag{1.8}$$

$$\mathcal{R} = g_{\mu\nu}\mathcal{R}_{\mu\nu}, \tag{1.9}$$

with $\Gamma^\lambda_{\mu\nu}$, the christoffel symbol. To solve the equation (1.7), one needs to know the contribution to the energy-momentum from every constituent of the universe. It is therefore assumed that if there is no viscosity or heat flow, and assuming that the universe behaves as a perfect fluid, then the energy-momentum tensor is given by:

$$\mathcal{T}_{\mu\nu} = diag(-\rho c^2, p, p, p); \tag{1.10}$$

with ρ and p are the mass density and the pressure respectively. These two quantities are, in cosmology, related by the equation of state $\omega = \frac{p}{\rho c^2}$. Thus, for different stages of the universe (radiation dominated era, matter dominated era and present), ω will have different values. We will make use of this equation later when we solve the Einstein's equation (1.7).

Using the Friedman Robertson Walker metric (1.2) [32, 33, 34] and the mathematical formulas (1.7) to (1.10), one can show that the temporal and spatial components of the equations (1.7) are:

$$\left(\frac{\dot{a}}{a}\right)^2 = \frac{8\pi\mathcal{G}}{3}\rho - \frac{kc^2}{a^2}, \tag{1.11}$$

and

$$2\frac{\ddot{a}}{a} + \left(\frac{\dot{a}}{a}\right)^2 = -\frac{8\pi\mathcal{G}\cdot p}{c^2} - \frac{kc^2}{a^2}. \tag{1.12}$$

Subtracting (1.11) from (1.12), one obtains the acceleration equation

$$\frac{\ddot{a}}{a} = -\frac{4\pi\mathcal{G}}{3}\left(\rho - \frac{3p}{c^2}\right). \tag{1.13}$$

The equation (1.11) is generally referred to as the Friedmann equation despite in a different form from what Friedmann originally published [33, 34].

From the equation (1.13), it can be noticed that if the material has any pressure, this increases the gravitational force, and so further decelerates the expansion although there are no forces associated with pressure in an isotropic universe, as there are no pressure gradients. A decelerated expansion of the universe was something that physicists have well expected to happen due to the attraction of the gravitational forces, but observational evidence from the supernova in 1998 [15, 16] has unravelled a mystery that the expansion of the universe, rather than slowing down (decelerate) is exponentially speeding up. I will revisit this discovery later when I will have fully described the modern cosmological model with non vanishing cosmological constant (also referred to as dark energy). Λ as supported by the Lambda- Cold Dark Matter model of the Big Bang cosmology and known as standard model of cosmology due to its agreement with the observation [28, 29]. The acceleration equation does not feature the constant k which appears in the Friedmann equation $-$ it cancelled out in the derivation, but keep in mind that this constant k describes the space-time curvature as it will be made clearer later.

Up to this point, we are still not in a position to solve the equations [(1.11) to (1.13)], unless we know what the pressure p and the density ρ are. By specifying the pressure, we are therefore speculating as to what kind of material our cosmological model of the universe is (what kind of matter the universe is filled with). In cosmology, it is usually assumed that there is a unique pressure associated with each density, so that $p = p(\rho)$ (**this relationship is known as the equation of state**).

1.4.2 Fluid Equation

Fluid equation in the theory general relativity describes the energy-momentum conservation which is generally written as

$$\nabla_\mu \mathcal{T}^\mu_\nu \equiv \mathcal{T}^\mu_{\nu;\mu} = 0, \tag{1.14}$$

with $\nabla_\mu \mathcal{T}^\mu_\nu$ (also written in a compact as $\mathcal{T}^\mu_{\nu;\mu}$) is a covariant derivative defined as : $V^a_{b;c} \equiv \partial_c V^a_b + \Gamma^a_{dc}\cdot V^d_b - \Gamma^d_{bc}\cdot V^a_d$. The Einstein summation convention is assumed to apply in equation (1.14) for repeated indices. Writing out the covariant derivative using the Christoffel symbols, equation (1.14) becomes:

$$\partial_\mu \mathcal{T}^\mu_\nu + \Gamma^\alpha_{\alpha\mu}\mathcal{T}^\alpha_\nu - \Gamma^\alpha_{\nu\mu}\mathcal{T}^\mu_\alpha = 0. \tag{1.15}$$

Using the **FRW** metric defined by the equation (1.2), one can compute all the Christoffel symbols and plugging them into the equation (1.15), one obtains the fluid equation:

$$\dot\rho + \frac{3\dot a}{a}\left(\rho + \frac{p}{c^2}\right) = 0. \tag{1.16}$$

Note: The fluid equation (1.16) conserve the energy of the universe's fluid as it expands.

1.5 Expansion and Redshift in the Modern Cosmological

1.5.1 Expansion

The expansion of the universe is related to the scale factor a(t). In fact, modern cosmology explains the Hubble's discovery of recession velocity to be proportional to the distance using the Friedman equation (1.11). If one were to scale the distance $\vec{x}$ by a time dependent constant factor $a(t)$ and obtain a new variable $\vec{r} = a \cdot \vec{x}$, the velocity $\vec{v}$ mathematically defined as the first derivative of the distance with respect to time which is $\dot{\vec{r}}$, can as well be written in the following form

$$\vec{v} = \frac{\dot{\vec{r}}}{\vec{r}} \cdot \dot{\vec{r}} = \frac{\dot a}{a} \cdot \vec{r}, \tag{1.17}$$

leading to Hubble's law [recall Fig(1.5)]: $\vec{v} = H \cdot \vec{r}$, where the hubble constant H is then defined as

$$H = \frac{\dot a}{a}. \tag{1.18}$$

The Hubble constant is not constant in cosmology. Given the evolution or expansion of the universe, there is no obvious reason why the Hubble$'$s should be constant. To see the variation , it is convenient to combine equation (1.11) with (1.18) to obtain:

$$H^2 = \frac{8\pi\mathcal{G}}{3}\rho - \frac{kc^2}{a^2}. \tag{1.19}$$

With an evolving density ρ which takes different values at different times during the evolution of the universe. It is therefore clear that the Hubble constant thus evolves with time as well. The equation (1.19) is also another form of the equation (1.11), the FRW$'$s equation.

1.5.2 Redshift

This concept of redshift was quite clearly elucidated already in the previous section (1.4). Below, I am going to once again invoke the Doppler-Effect and derive the redshift in terms of the scale factor. According to Hubble's law $d\vec{v} = \frac{\dot{a}}{a}\vec{r}$. For two nearby points, the change of wavelength $d\lambda = \lambda_r - \lambda_e$; according to Doppler law, is given by $\frac{d\lambda}{\lambda} = \frac{dv}{c}$. Using the time difference between the emission and reception dt=$\frac{d\vec{r}}{c}$, we obtain that

$$\frac{d\lambda}{\lambda} = \frac{\dot{a}}{a} \cdot \frac{dr}{c} = \frac{\dot{a}}{a} \cdot dt = \frac{da}{a}. \tag{1.20}$$

Integrating (1.20), we obtain that

$$\lambda \propto a. \tag{1.21}$$

The wavelength λ in equation (1.21) is instantaneous and therefore has different values at different times. If we are given the wavelength at the beginning of the universe and the wavelength at the present time, the beauty of the equation (1.21) is that it will tell us whether the universe has expanded or contracted and by how much exactly. To derive the redshift, we use the formula (1.3) which finally leads to:

$$1 + z = \frac{\lambda_r}{\lambda_e} = \frac{a(t_r)}{a(t_e)} \tag{1.22}$$

1.6 Solution of The Einstein's equations

The best theory for a full and complete description (as accepted today) of the universe is given to us by the Big Bang theory. In this theory it is believed that the universe originated from an enormous exploding fire extremely hot which ejected debris in every direction of space-time. At this stage the universe existed in the form of plasma and only radiation was the dominant component. A complete description of the universe's evolution is given by the Big Bang Nucleo-synthesis (B.B.N.) and structure formation theories [127, 128].

The cosmology theory states that radiation dominated the universe at very early time. Then matter started to dominate as the universe expanded down and light chemical elements started to form and fuse together to form the basic constituents of matters that surround us today. We now believe that there is another component which is the most dominant compared to matter and it is called dark energy. So far we have two known forms of matters:

Matter: any type of material which exerts negligible pressure, $p = 0$.

Radiation: radiation in physical cosmology is referred to as particles moving at the speed of light. Their kinetic energy leads to a pressure force, the radiation pressure, which using the standard theory of radiation, can be shown to be

$$p = \frac{\rho \cdot c^2}{3}. \tag{1.23}$$

1.6.1 Solution of the Einstein's equations: case $k = 0$

To solve the equations (1.11) and (1.16), I will constrain my derivation to a particular case for illustration by setting the curvature k to 0. In fact $k = 0$ is referred to as the curvature for a flat universe. Also, I want to make a full use of the equation of state

$$\omega = \frac{p}{\rho c^2} \tag{1.24}$$

So $\omega = 0$ will correspond to matter and $\omega = \frac{1}{3}$ will correspond to radiation dominated era according to radiation equation of state, Equation(1.23). We shall see later that $\omega = -1$ will correspond to dark energy. Using the equation of state (1.24) and the particular case of zero curvature, the equations (1.11) and (1.16) becomes:

$$\begin{cases} \left(\frac{\dot{a}}{a}\right)^2 = \frac{8\pi\mathcal{G}}{3}\rho; \\ \dot{\rho} + 3\rho\left(1+\omega\right)\frac{\dot{a}}{a} = 0. \end{cases} \tag{1.25}$$

Solving (1.25b), we obtain:

$$\rho \simeq a^{-3(1+\omega)}. \tag{1.26}$$

The above relation relates the density of the universe ρ with the equations of state w which is typically expressed as the dimensionless ratio of pressure (p) to energy density (ρ): $w \simeq \frac{p}{\rho}$. The equation (1.26) demonstrates that the energy density evolves as a function of the scale factor and w, from which we can deduce that

$$\begin{cases} \rho = \frac{\rho_0}{a^3} \quad \text{(matter)}; \\ \rho = \frac{\rho_0}{a^4} \quad \text{(radiation)}. \end{cases} \tag{1.27}$$

where the following conditions: $a = 1$, $t = 0$ and $\rho = \rho_0$ at the present time were applied as boundary conditions.

For nonrelativistic matter such as baryons in stars and gas, ($w = 0$) and $\rho \sim a^{-3}$, leading to the z^3 dependence (matter contribution Λ_M); the density of matter dilutes during the expansion of the universe. If the amount of matter is considered to be constant, its density should scale according to the volume. The equation of state for ultra-relativistic matter, photons (radiation) and neutrinos is $w = 1/3$ leading to $\rho \sim a^{-4}$, thus Ω_R evolves with an extra factor of z as radiation contribution. Radiation not only dilutes proportional to the volume expansion, but its wavelength redshifts as well. The two terms Ω_M and Ω_R, with other terms namely Ω_Λ and Ω_k (representing contribution from the dark energy and the curvature of the space-time) are combined together in the Friedman Robertson Walker equation. According to [35]:

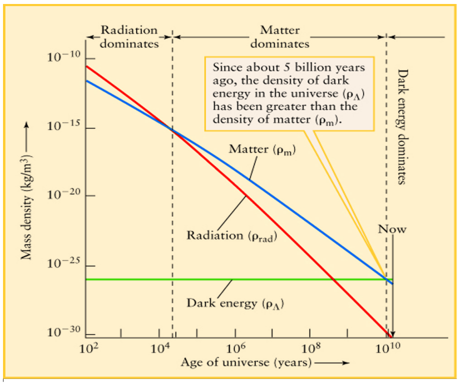

Since about 5 billion years ago, the density of dark energy in the universe (ρ_Λ) has been greater than the density of matter (ρ_m).

Figure 1.6: Mass density as function of the age of the universe. The dark energy component, assumed constant, existed during the early universe, however its magnitude was small compared to the density due to matter and radiation. Dark energy started to dominate much later, its magnitude is $\sim 10^4$ times larger than that of normal matter. The dark-energy density is assumed to be constant, with an equation of state defined by $w = -1$ [47]. Figure from [26].

$$H^2(z) = H_0^2 \left[\Omega_\Lambda + \Omega_k(1+z)^2 + \Omega_M(1+z)^3 + \Omega_R(1+z)^4\right]; \tag{1.28}$$

where H_0 is the hubble constant at the present time. To obtain the time dependence relation of the scale factor $a(t)$, one need to combine the density $\rho = \rho(a)$ and Friedman equation. Therefore substituting (1.26) in the equation (1.25a) and integrating, it follows that

$$a(t) = \left(\frac{t}{t_0}\right)^{\frac{2}{3(1+\omega)}}; \tag{1.29}$$

with the constant t_0 given by

$$t_0 = \frac{2}{3(1+\omega)}\left(\frac{3}{8\pi\mathcal{G}}\right)^{1/2}. \tag{1.30}$$

Given the scale factor a(t) as I derived it in the equation (1.29), we can the calculate the Hubble's constant H as a function of time.

$$H = \frac{2}{3(1+\omega)t}. \tag{1.31}$$

The equation (1.27) shows that the universe's density dilutes more quickly as the expansion is going on during the radiation dominated era than during the matter dominated era. Contrary to Hubble's expansion, Table (1.1) shows that the expansion rate is slower now than it was during the very early moments after the big bang. This assessment is what physicists have believed until the discovery of the accelerated expansion of the universe from the supernova type Ia.

The evolution of the universe is determined by an imbalanced of forces between the momentum of expansion and the pull of gravity. The current rate of expansion is measured by the Hubble Constant, while the strength of gravity depends on the density and pressure of the matter in the universe. If the pressure of the matter is low,

Table 1.1: summary table of density, scale factor and the hubble's constant for radiation and matter dominated universe.

	radiation dominated era ($\omega = \frac{1}{3}$)	matter dominated era ($\omega = 0$)
$\rho(t)$	$\rho_0\,(t_0/t)^2$	$\rho_0\,(t_0/t)^2$
a(t)	$(t_0/t)^{1/2}$	$(t_0/t)^{2/3}$
H(t)	$1/2t$	$2/3t$

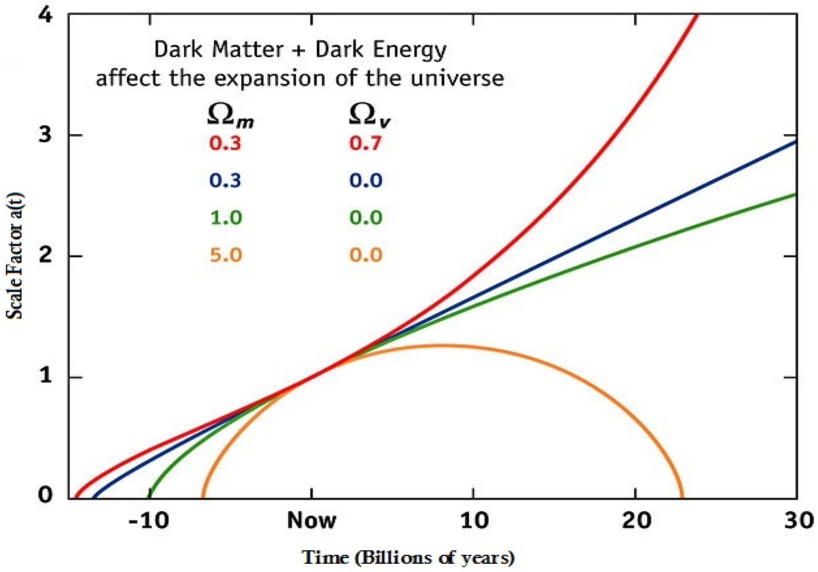

Figure 1.7: Evolutions for the Universe, corresponding to three different curvatures. For $k = 0$ (flat geometry) the expansion rate will approach zero in the infinite future. The case $k < 0$ (hyperbolic geometry) the universe is doomed to expand forever; this case is consider as a runaway universe. In the spherical geometry ($k > 0$) however the universe will collapse back to its initial singularity and re-birth again instantaneously leading to a series of big bangs - big crunches. This is an oscillating universe which is (maybe) far from what we are seeing now with observation. We must note that during the early phases of the expansion, it is observationally difficult to say with accuracy the geometry or the actual path the universe will follow. The above conclusions are true only in a universe without the cosmological constant Λ. If there was no cosmological constant, open and flat Universes would expand forever, while closed Universe will end in big crunch. In a such situation, the geometry would have determined the future fate. However, once Universe become cosmological constant dominated it will exponential expand forever with a positive acceleration unless dark energy decay somehow in another form of matter.

as is the case with most forms of matter we know of, then the fate of the universe is governed by the density. If the density of the universe is less than the critical density, then the universe will expand forever, like the green or blue curves in the graph shown in Figure (1.7). Gravity might slow the expansion rate down over time, but for densities below the critical density, there is not enough gravitational pull from the material to ever stop or reverse the outward expansion. This is also known as the Big Chill or Big Freeze because the universe will slowly cool as it expands until eventually it is unable to sustain any life. If, however, the density of the universe is greater than the critical density, then gravity will eventually win and the universe will collapse back on itself, this is the so called Big Crunch, like the graph's orange curve, Figure(1.7). In such case, there is sufficient mass in the universe to slow the expansion and to bring it completely to a stop, then eventually reverse it.

Table (1.1) only summarizes few of the cosmological parameters for two different stages of the universe: the radiation dominated era and matter dominated era. However, there is another phase whose significance and importance prevail over the two precedent phases at much later times (at present universe's time for example); this is dark energy whose equation of state is characterized by $w = -1$. Although I have reserved a section in this chapter discussing the mathematics governing the existence of dark energy, I am taking the liberty to include it the discussion relative to the evolution of density of the universe throughout time. After the Big bang, the universe started to expand. As it expanded, the density of matter also started to change. At this early time, the expansion of the universe is dominated by Ω_R term (universe is radiation dominated), which specifies what component has the largest contribution to the total density. At the present time, according to the accepted cosmological model, the universe is dark energy dominated, designated by Ω_Λ. Ordinary matter dominance Ω_M existed significantly in between these two aforementioned phases and its contribution is now less important compared to the Ω_Λ term. To summarize, the density of different types of matter changes differently as the universe expands.

Ordinary matter: Its density changes because the volume of the universe changes, while no new matter is created. $\rho_m \sim 1/V \sim 1/a^3$; where $a = a(t)$ is the distance scale between galaxies. Exploiting (1.22) and (1.27), in terms of the redshift, the matter density is therefore given by:

$$\rho(t)_M = \rho(t_0)_M \left(\frac{a(t_0)}{a(t)}\right)^3 = (1+z)^3. \tag{1.32}$$

Radiation: made of particles such as photons, its number density changes $\sim 1/V$ and that the photon wavelength is redshifted, so energy of individual photon also changes as $E \sim (1+z) \sim 1/a$. Therefore the energy density (expressed as mass density) of radiation evolves as

$$\rho(t)_R = \rho(t_0)_R \left(\frac{a(t_0)}{a(t)}\right)^3 \times \frac{a(t_0)}{a(t)} = (1+z)^4. \tag{1.33}$$

Dark energy: whose density does not change at all, that's why it is called the cosmological constant.

$$\rho(t)_\Lambda = K, \tag{1.34}$$

with K, a constant. So, combining the equations (1.32), (1.33) and (1.34) into the Friedman equation, one can derive without difficulty the Hubble constant redshift dependence relationship mentioned in (1.28).

To end this section, let me discuss the significance of the concept of redshift in cosmology and astronomy. Redshift is is way to look back in time. In cosmology the light signals that were produced and emitted far back in the past can be observed today by astronomers. The earlier the light signal was emitted, the more it is redshifted by the time it reaches us. Thus, the redshift z of the source is the measure how far in the past the light was emitted. Therefore higher z means further away in the past the source is, and $z = 0$ represent the present moment (the light is emitted right here, and took no time to travel (wavelength did not change at all). $z = \infty$ at the start of Big Bang, when we consider $t = 0$, however the relation between redshift and time depends on how exactly the expansion of the Universe proceeded.

1.6.2 Solution of the Einstein's equations: case k≠0

The solution of the equation (1.11) for the general case of $k \neq 0$ is mathematically a bit more involving that the simple case I have discussed above. However with a bit of trickery and ansatz, one can work out the solution for the most general case that many textbooks in cosmology and general relativity usually leave aside. Below, I am going to illustrate only the case for which $k > 0$. With this derivation done, the case $k < 0$ will no longer be a mystery any more (the case $k = 0$ has already been discussed in the previous section).

Before delving into the details, I am going to make one additional simplification. I will assume than the universe is matter dominate (though recent evidence clearly indicates a dark energy dominated era), which implies that $\omega = 0$ and therefore the matter density will dilute as the universe expands according to $\rho \sim 1/a^3$ [see the general formula, Equation(1.26)]. With these simplifications, the equation governing the evolution of the scale factor $a(t)$ becomes:

$$\dot{a} = \frac{da}{dt} = \sqrt{\frac{8\pi G}{3a} - k}. \tag{1.35}$$

The solution of the above equation can be found by using a brute force method, i.e by integrating after doing the variable separation, but the result is a very long and nasty expression that you will certainly never find in any textbook. There is however an elegant way to get around this, it is by invoking the chain rule. Since $\frac{da}{dt} = \frac{da}{d\theta} \cdot \frac{d\theta}{dt}$, we can make a change of variable such that the right hand side of the equation (1.35) becomes a function of the new variable θ introduced in the chain rule. Such functions may be some trigonometric functions ($\sin(\theta)$, $\cos(\theta)$, etc). Let me make such a change of variable now by defining

$$\frac{8\pi G}{3a} = \frac{k}{\sin^2(\theta/2)}. \tag{1.36}$$

The choice of the angle $\theta/2$ will be made clear in the subsequent derivation. We can always chose any angle, say ϕ, but we will have to define $\phi/2 = \theta$ to get the result (1.37). The equation(1.36) which solves to

$$a(\theta) = \frac{4\pi G}{3k}\left(1 - \cos(\theta)\right). \tag{1.37}$$

Recalling that

$$\frac{da}{dt} = \frac{da}{d\theta} \cdot \frac{d\theta}{dt} = \sqrt{k} \cdot \tan(\theta/2). \tag{1.38}$$

It is now simple matter to show that

$$t(\theta) = \frac{4\pi G}{3k^{3/2}} \left(\theta - \sin(\theta)\right). \tag{1.39}$$

So, for a universe with the curvature $k > 0$, the equations (1.37) and (1.39) define the parametric solutions of such universe. The geometry associated with this universe is spherical while $k = 0$ is associate a flat geometry also called a flat universe (Euclidian geometry).

Following the same footsteps as in the above, we can show that for a universe with negative curvature, its parametric solutions are given by:

$$\begin{cases} a(\theta) = \frac{4\pi G}{3k}(\cosh(\theta) - 1); \\ t(\theta) = \frac{8\pi G}{3k^{3/2}}(\sinh(\theta) - \theta). \end{cases} \tag{1.40}$$

Table 1.2: summary table of possible geometries in the universe.

curvature	geometry	type of the universe
$k > 0$	spherical	Closed
$k = 0$	flat	Flat
$k < 0$	hyperbolic	Open

1.7 The density parameter Ω_0 and the critical density ρ_c

For a given value of H in the equation (1.19), there is a special value of the density ρ which would be required in order to make the geometry of the universe flat, i.e. $k = 0$. The critical density ρ_c is defined as the density for which the curvature of space-time is null. From (1.19), it implies that

$$\rho_c = \frac{3H^2}{8\pi\mathcal{G}}. \tag{1.41}$$

Consequently, the density of the universe, a very useful quantity in cosmology, is defined relative to the critical density. This dimensionless quantity is known as the density parameter Ω (or abundance), and it is defined by

$$\Omega(t) = \frac{\rho}{\rho_c}. \tag{1.42}$$

The present value of the density parameter is denoted Ω_0. With this new notation, the Friedmann equation (1.19) becomes (in units where $\hbar = c = 1$):

$$H^2 = \frac{8\pi\mathcal{G}}{3}\rho_c\Omega - \frac{k}{a^2} = H^2\Omega - \frac{k}{a^2}, \tag{1.43}$$

which can finally be written as

$$\Omega + \Omega_k = 1, \tag{1.44}$$

with

$$\Omega_k = -\frac{k}{a^2H^2}. \tag{1.45}$$

From the equation (1.44) for a special case of a flat universe (for which the curvature $k = 0$), the density $\Omega = 1$ for all time. This is true regardless of any type of matter in the universe and it is often referred to in cosmology as **the critical-density universe**.

The equation (1.45) is in a very instructive form since it allows us to draw the following conclusions regarding the relationship between the Universes energy content and its spatial curvature: i)if the energy density exceeds the critical density ($\Omega > 1$), the spatial curvature is closed because k is strictly positive $k > 0$; ii)if the energy density equals the critical density ($\Omega = 0$), the Universe is flat because $k = 0$; and 3)if the energy density is less than the critical density ($\Omega < 1$), the spatial curvature is open because k is strictly negative $k < 0$.

1.8 The deceleration

We know that the universe is expanding and that the Hubble's parameter which characterizes the expansion rate, is changing with time. A way to quantify the change in the rate of the expansion is known as the deceleration parameter. The deceleration parameter is defined as the Taylor expansion of the scale factor $a(t)$. Considering only terms up to second order, the Taylor expansion of $a(t)$ will be:

$$a(t) = a(t_0) + a(t_0)\cdot(t-t_0) + \ddot{a}(t_0)\cdot(t-t_0)^2 + \cdots . \tag{1.46}$$

Dividing (1.46) by $a(t_0)$:

$$\frac{a(t)}{a(t_0)} = 1 + \frac{\dot{a}(t_0)}{a(t_0)}\cdot(t-t_0) + \frac{\ddot{a}(t_0)}{a(t_0)}\cdot(t-t_0)^2 + \cdots . \tag{1.47}$$

This expression is commonly written as:

$$\frac{a(t)}{a(t_0)} = 1 + \frac{\dot{a}(t_0)}{a(t_0)}\cdot(t-t_0) - \frac{q_0}{2}H^2\cdot(t-t_0)^2 + \cdots . \tag{1.48}$$

Where the deceleration parameter q_0 can be inferred to be defined as:

$$q_0 = -\frac{\ddot{a}(t_0)}{a(t_0)\cdot H_0^2}. \tag{1.49}$$

For illustration, consider a matter dominated universe (i.e. the pressure $p = 0$), the acceleration equation (1.13) can be combined with (1.42) to give a deceleration parameter of

$$q_0 = \frac{4\pi\mathcal{G}}{3}\rho\frac{3}{8\pi G\rho_c} = \frac{1}{2}\Omega_0. \tag{1.50}$$

So in the case illustrated above, an accurate measurement of q_0 would immediately tell us about Ω_0 . Conversely, if we know the properties of the matter in the universe, then the deceleration parameter q_0 can immediately be inferred. The two parameters, H_0 and Ω_0, are sufficient to describe all the possibilities. However, we don't know everything about the material in the universe, so q_0 can provide a way of looking at the universe. It can in principle be measured directly by making observations of objects at very large distances, such as distant galaxies, because the deceleration governs how large the universe would be at very early times.

1.9 Cosmological Framework of Modern Cosmology in the presence of dark energy ($\Lambda \neq 0$)

1.9.1 Introducing dark energy, Λ

The cosmological constant Λ has been introduced by Albert Einstein himself in order to have a full description of a static universe. Because gravitational attraction pulls matter together, Einstein introduced another term, a fudge factor, in his general relativity field equations (1.7) to act against the force of gravity so that the overall exerted forces destroy each other. This new force, which has the nature of opposing the attractive gravitational force, is **repulsive**. The fudge factor Λ, called the cosmological constant, is mathematically allowed and permitted by the theory of general relativity. However it was later found not be physically well motivated because none of the solutions birthed from this modification of the equation (1.7) correspond to a static universe, with a constant scale factor, have ever been found or observed today. Introduction of Λ in the equations (1.7) led to a more general form of Einstein's field equations given by:

$$\mathcal{R}_{\mu\nu} - \frac{1}{2} g_{\mu\nu} \mathcal{R} = 8\pi \mathcal{G} \mathcal{T}_{\mu\nu} + \Lambda g_{\mu\nu}, \tag{1.51}$$

which leads the modified **Friedman Equations**:

$$H^2 = \frac{8\pi\mathcal{G}}{3}\rho - \frac{k}{a^2} + \frac{\Lambda}{3}, \tag{1.52}$$

and

$$\frac{\ddot{a}}{a} = -\frac{4\pi\mathcal{G}}{3}\left(\rho - \frac{3p}{c^2}\right) + \frac{\Lambda}{3}. \tag{1.53}$$

If, at some stage in the history of the universe, the cosmological constant is positive and large enough to dominate over the energy density and curvature terms in (1.52), then the Friedmann equation has the solution

$$a(t) = e^{\sqrt{\frac{\Lambda}{3}} \cdot t}. \tag{1.54}$$

implying an exponential expansion of the universe. This kind of expansion is believed to happen at extremely late times in the expansion history of the universe. In fact, this prediction has been experimentally explored since 1998 with the discovery of the accelerated expansion of the universe.

For a positive cosmological constant there will a positive contribution to the acceleration $\ddot{a}$ as one can see from the equation (1.53), therefore acting effectively as a repulsive force. However, if the cosmological constant is sufficiently large, it can overcome the gravitational attraction represented by the first term and lead to an accelerating universe. Restricting the equation (1.52) for a flat geometry, one can define the density Ω_Λ, associated with the cosmological constant, as

$$\Omega_\Lambda = \frac{\Lambda}{3H^2}, \tag{1.55}$$

therefore, generalizing (1.44) to

$$\Omega + \Omega_k + \Omega_\Lambda = 1. \tag{1.56}$$

So, for $k = 0$,

$$\Omega + \Omega_\Lambda = 1. \tag{1.57}$$

The equation (1.56), or in particular the equation (1.57), is of extreme importance in cosmology. Tremendous experimental effort is currently undergoing trying to measure with accuracy the contribution of each individual term of this equation. The geometry of the universe can be told with exactitude once one knows the total sum contribution from Ω and Ω_Λ.

Table 1.3: geometries of the universe inferred from the contribution of the densities of the matter and the cosmological constant.

geometry	geometry	curvature (k)
open universe	$\Omega + \Omega_\Lambda < 1$	$k < 0$
flat universe	$\Omega + \Omega_\Lambda = 1$	$k = 0$
closed universe	$\Omega + \Omega_\Lambda > 1$	$k > 0$

1.9.2 Fluid dynamics of Λ

The cosmological Λ is often described in cosmology as a fluid with a pressure p_Λ and a density ρ_Λ.

$$\rho_\Lambda = \rho_c \cdot \Omega_\Lambda = \frac{3H^2}{8\pi\mathcal{G}} \cdot \frac{\Lambda}{3H^2} = \frac{\Lambda}{8\pi G}. \tag{1.58}$$

Modifying the Friedman equation (1.52) to

$$H^2 = \frac{8\pi\mathcal{G}}{3}\left(\rho + \rho_\Lambda\right) - \frac{k}{a^2}. \tag{1.59}$$

The pressure p_Λ can be obtained by introducing the following change $\rho \to \rho + \rho_\Lambda$ and $p \to p + p_\Lambda$ into the acceleration equation. Keeping in mind that ρ and ρ_Λ are independent variables, so by separation of variables, one finds that

$$\dot{\rho}_\Lambda + \frac{3\dot{a}}{a}\left(\rho_\Lambda + \frac{p_\Lambda}{c^2}\right) = 0. \tag{1.60}$$

Since ρ_Λ is constant, the pressure p_Λ must be

$$p_\Lambda = -\rho_\Lambda c^2. \tag{1.61}$$

This last result clearly show that the cosmological constant has a negative effective pressure which means that, work done on the cosmological constant fluid, allows its energy density to remain constant even though the volume of the universe is increasing.

The cosmological constant Λ has many implications to the way we should view the universe. For example, it is no longer necessarily true that a closed universe ($k > 0$) will collapse back to its initial point, nor that an open universe will expand forever. In fact, if the cosmological constant is large enough, there need not even be a Big Bang, with the universe instead beginning in a collapsing phase, followed by a bounce at finite size under the influence of the cosmological constant (though such models are ruled out by observations). It is also possible to have a prolonged phase where the universe remains almost static, known as **loitering** by arranging parameters so that the universe closely approaches the unstable Einstein static model of a universe [39, 40, 41], see Figure(1.8).

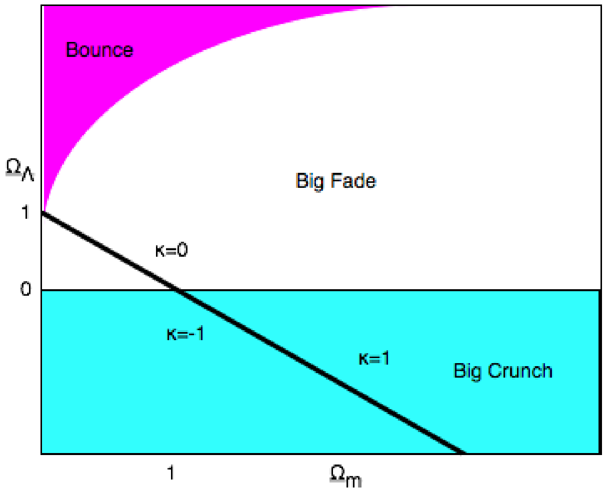

Figure 1.8: Dark Energy density Ω_Λ as function of matter density Ω_M for different situations including hypothetical ones such as the bounce universe, also referred to as loitering. By adjusting the cosmological parameters, we can get different universe's generic behavior: (i) the Big Crunch, (ii) the Big Fade (exponentially expanding), (iii) the Big Fade (critical matter universe), (iv) the Big Bounce (contracting phase, followed by exponentially expanding phase; there is no Big Bang in this situation as universe's starting point), and (v) the loitering (realized by adjusting Ω_M so that universe almost crunches and then the dark energy starts to dominate and win over the matter density. Figure from [39].

Bounce cosmology is ruled out by the existence of high-redshift phenomena such as high-redshift quasars known with $z = 4.89$ imposing a restriction on $\Omega_M < 0.01$. This is quite unlikely favored on direct observational grounds, and is also incompatible with the successful predictions of the theory of big bang nucleosynthesis. Thermalization of the microwave background at $z > 103$ implies $\Omega_M < 2 \times 10^{-9}$, which is impossible [38].

The deceleration parameter q_0 for a universe with all the types of matter (radiation, normal matter and cosmological constant Λ or dark energy) can be generalized to the following form:

$$q_0 = \frac{1}{2}\sum_j (1 + 3\omega_j), \tag{1.62}$$

with $\omega_j \cdot \rho_j = p_j$, the equation of state. So, for a universe with only normal matter ($\omega = 0$) and cosmological constant ($\omega = -1$), we get the following important relation

$$q_0 = \frac{1}{2}\Omega_0 - \Omega_\Lambda. \tag{1.63}$$

Measuring the terms of the equation (1.63) has been at the center of two major experimental group during the last decade: The Supernova Cosmology Project (SCP) and High−z Supernova Search Team. The universe will be accelerated if $q_0 > 0$, implying that $\Omega_\Lambda > \frac{\Omega_0}{2}$. If, in addition, we assume a flat and pressureless universe, as is the case for the universe at this present time, the above equation can set a strong bound on the cosmological parameter Λ for a decelerated and accelerated universe. Since $\Omega_\Lambda = 1 - \Omega_0$, there will be acceleration if the deceleration parameter $q_0 = \frac{3}{2}\Omega_0 - 1 > 0$. So the universe will be accelerated if $\Omega_\Lambda > \frac{1}{3}$. This value is far less than the observed value of $\Omega_\Lambda \simeq 0.70$, meaning that the universe is in an accelerated phase.

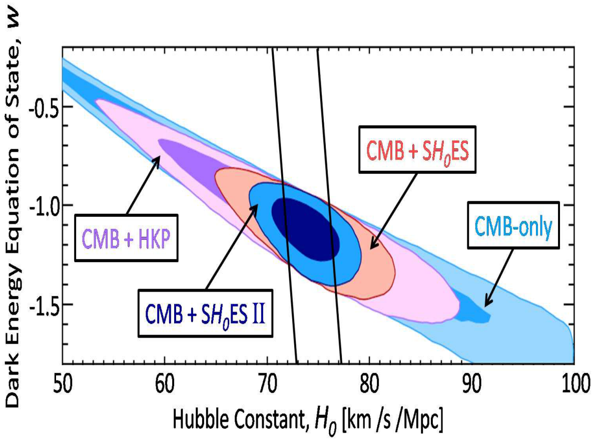

Figure 1.9: Combined measurement of the cosmological constants equation of state w and the present day value of the Hubble parameter H_0. WMAP 7-year analysis of the cosmic microwave background data provides a degenerate constraint (outermost contours) that is improved by the measurement of H_0 (nearly vertical solid lines), 73.82.4 kms^{-1}Mpc^{-1}, by the SH0ES II program, resulting in the two innermost contours and corresponding to $w = -1.08 \pm 0.10$ [43, 44]. Also shown are similar contours derived from the previous SH0ES result [45] and the Hubble Key Project (HKP) [46]. The 68.3% and 95.4% confidence-level regions are given for each combination as similarly colored inner and outer contours, respectively. Figure from [43].

The deceleration parameter q_0 is a measurable parameter which determines the linear combination of the density components Ω_0 and Ω_m. By measuring the luminosity for very distant supernova type Ia as a function of the redshift (up to the redshift of $z \sim 1$), one obtains $\Omega_m \approx 0.25$. There exist, however, other techniques based on large structure formation or the weak gravitational lensing effect that are directly sensitive to Ω_m. The 2dF galaxy redshift survey has estimated a value of $\Omega_m \cdot h = 0.20 \pm 0.01$ [59].

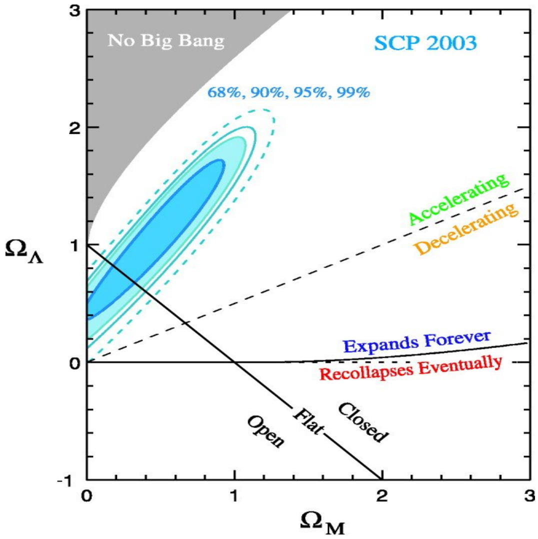

Figure 1.10: Models of the universe as identified by their location in the plane showing the densities of matter $\Omega_M = \rho_M/\rho_c$ and $\Omega_\Lambda = \rho_\Lambda/\rho_c$ with ρ_M and ρ_Λ, are matter density and dark energy density respectively, ρ_c is the critical density.This figure indicates the main results from different experimental groups. The colored light blue contours represents 1σ, 1.7σ, 2σ and 3σ confident regions from measurements of type Ia Supernova (SNe). Figure from [16].

Dark energy will affect the overall evolution of the universe only if it represents a significant fraction of the universe′s content. In fact, supernovae data as well as many other observations indicate that the current amount of dark energy in the universe is 2.7 times the amount of matter ($\Omega_\Lambda = 2.7 \times \Omega_M$). This means that the universe is made of $\Omega_M = 0.27$ of matter and $\Omega_\Lambda = 0.73$ of dark energy. From the conclusions drawn by this observation, it is not a hard exercise to figure out the fraction of dark matter in the universe. From the rotation curves of galaxies, 85% of matter must consist of dark matter, implying that ordinary matter amounts to $\Omega_m = 0.04$ and the dark matter has a fraction of $\Omega_\chi = 0.23$.

1.10 Age of the Universe

One of the important questions of our time that cosmology has answered with great accuracy is the answer to the question **how old is our universe?**. As studied so far, one would define the age of the universe as the time since the big bang to the very present moment, so given the Hubble's law, this time is naively nothing but the inverse of the Hubble's constant H_0 at the present moment. Since $H_0 = 100h\text{kms}^{-1}\text{Mpc}^{-1}$, this implies a universe age of about $t_0 = H_0^{-1} = 9.77h^{-1} \times 10^9$ years. What happens if we try to do better with our theoretical estimates? Although the precise cosmological model describing our universe is uncertain, we are pretty sure that it has been matter dominated, i.e. dominated by some form of pressureless material for some considerable time, and so we can use the matter-dominated evolution to calculate the age. For such a universe, Table (1.1) gives a

Hubble's constant $H(t) = \frac{2}{3t}$, thus implying the age of the universe of about

$$t_0 = \frac{2}{3} H_0^{-1} = 6.51 h^{-1} \times 10^9 yrs \tag{1.64}$$

Deriving the formula for the universe's age is tricky. For a spatially-flat cosmology with a cosmological constant there are two equivalent (and equally unpleasant) forms. By writing the Friedman equation in the form $\dot{a}^2 = H_0^2[\Omega_0 a^{-1} + (1-\Omega_0)a^2]$, given $t_0 = \int_0^{t_0} dt$, one obtains:

$$t_0 = \frac{2}{3}\frac{1}{\sqrt{1-\Omega_0}} \ln\left[\frac{1+\sqrt{1-\Omega_0}}{\sqrt{\Omega_0}}\right] = \frac{2}{3}\frac{1}{\sqrt{1-\Omega_0}} \sinh^{-1}\left[\sqrt{\frac{1-\Omega_0}{\Omega_0}}\right] \tag{1.65}$$

The "break-even" point where $t_0 = H_0^{-1}$ is at $\Omega_0 = 0.26$, close to the value preferred by observation. With the values of $\Omega_0 \simeq 0.3$ and $h \simeq 0.72$ we get an age of about fourteen billion years which sits comfortably with the estimated age of the universe.

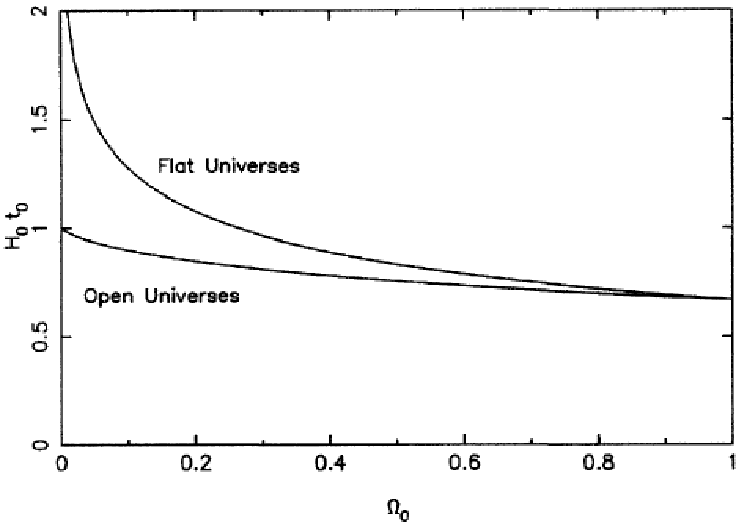

Figure 1.11: Universe's predicted ages as fractions of the Hubble time H_0^{-1} as function of abundance Ω_0, for open universes and for universes with a flat geometry plus a cosmological constant. The prediction $H_0 t_0 = 2/3$ for critical density models is at the right-hand edge. Figure from [24].

1.11 Distances in Cosmology

1.11.1 Luminosity and Luminosity Distances

A very common tool used to measure distances in cosmology is known as the distance modulus noted as μ. In astronomy, distances are very often quoted in terms of the distance modulus rather than in term of the units of distance that we are all familiar with. The distance modulus is defined as the difference between the absolute and the apparent magnitudes of a given celestial object. It is important to recall that the absolute magnitude (M) is the is the measure of a celestial object's intrinsic brightness; this magnitude is absolute and does not change. The apparent magnitude (m) is the magnitude that the object appears at a given distance from the observer. The absolute magnitude is equal to the apparent magnitude of the object if it were 32.6 light years (10 parsecs) away from Earth. The absolute magnitude M is defined by

$$M = -2.5 \cdot \log_{10}(L) + C_1 \tag{1.66}$$

with C_1 a constant and L is the luminosity. The flux luminosity (F) is related to the luminosity distance (d_L)by the relation

$$F = \frac{L}{4\pi d_L^2} \tag{1.67}$$

Given the flux F, one can determine the apparent luminosity m by exploiting the following relation

$$m = -2.5 \cdot \log_{10}(F) + C_2 = M + 5 \cdot \log_{10}(d_L) + C \tag{1.68}$$

Therefore, the distance modulus μ

$$\mu = m - M = 5 \cdot \log_{10}(d_L) + C \tag{1.69}$$

The constant C is determined by the requiring that at a typical distance (d_L) of 10 parsecs that both the absolute and apparent magnitudes to be equal, which leads to C=-5, so

$$\mu = m - M = 5 \cdot (\log_{10}(d_L) - 1) \tag{1.70}$$

1.11.2 The Tully-Fisher Relation

Another method to measure the distance is through the observation of the width of galactic absorption lines. These lines are red-shifted or blue shifted depending on whether the galaxy is receding from us or moving towards us. A superior method for estimating galactic luminosities from rotational velocities is to use the Tully-Fisher Relation (TFR) [51].

The Tully-Fisher relation is used for spiral galaxies and makes use of a relation between the speed v at which the galaxy spins and the luminosity L (observed flux) of a galaxy. Specifically the relation of L is proportional to v^4. The speed v_c at which the galaxy spins can be determined spectroscopically [for example, narrow emission lines will be broadened due to the Doppler effect emission from the approaching side of the galaxy and blue-shifted (relative to the line centroid), emission from the receding side of the galaxy are red-shifted (relative to the line centroid)], but the observed flux or luminosity L of a galaxy can be determined photometrically by simply integrating the surface brightness to determine the total flux or luminosity from the galaxy. The Tully-Fisher relation is a great method for estimating galactic luminosities from rotational velocities. Literature about this

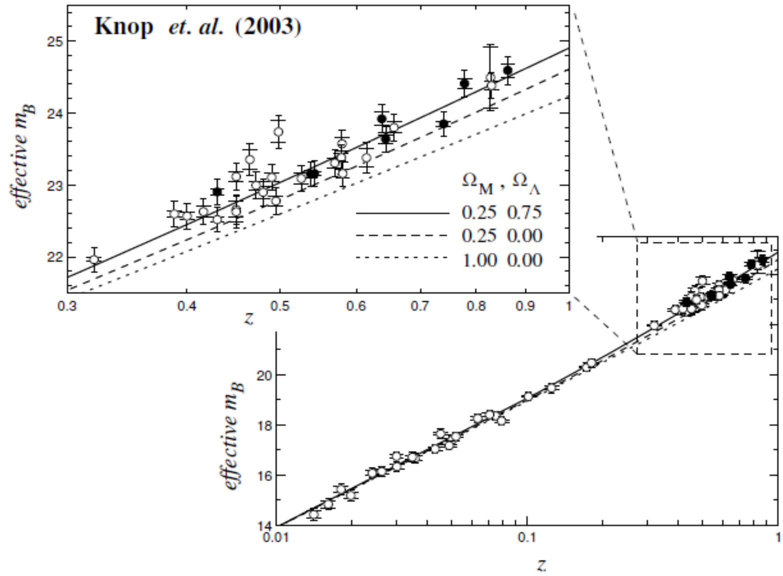

Figure 1.12: Hubble diagram of the effective distance modulus μ vs the logarithm of the redshift. Filled circles represents supernova observed by Hubble Space Telescope (HST). The large error bar include the 0.17 magnitude intrinsic dispersion in addition to the measured uncertainties. Figure from [167].

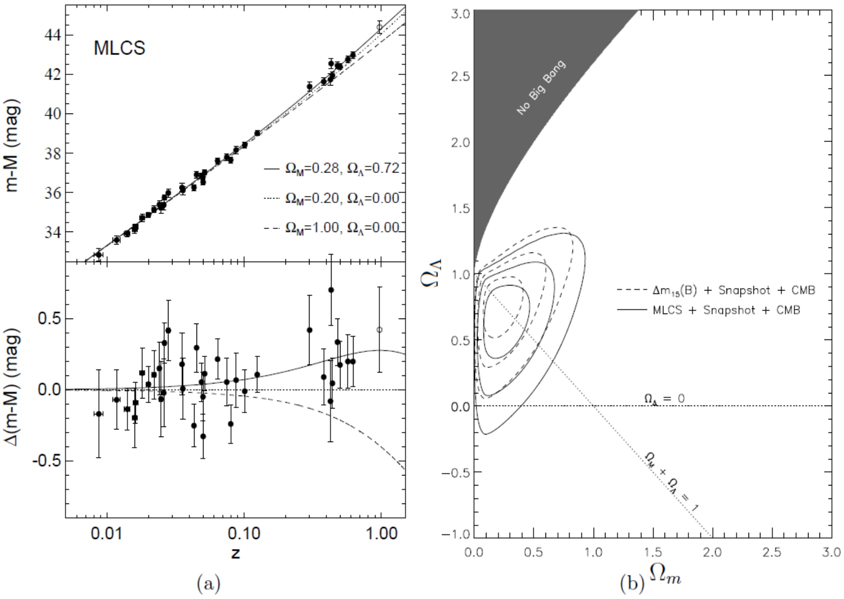

(a)

(b)

Figure 1.13: Determination of m with Type Ia supernovae data. Measuring the luminosity of standard candles (Type Ia supernovae) as a function of redshift (a) results in a constraint on $\frac{1}{2}\Omega_m - \Omega_\Lambda$. Applying the constraint of $\Omega_m - \Omega_\Lambda = 1$, based on CMB data, yields a value for m of Ω_m of ~ 0.28. Figures taken from [8].

relation was refers to the tight correlation between the value of a disc galaxy's rotational velocity (where its rotation curve is flat) and global parameters such as its total baryonic mass, stellar mass or luminosity. Tully and Fisher originally observed a relationship between luminosity (in terms of absolute magnitude) and rotational velocity v_c.

To grasp an understanding on how v_c relates to a galaxy's dark halo, let's consider the simplest possible dark halo model, a spherically symmetric isothermal sphere of ideal gas (see [18] for a detailed discussion). For the purposes of this discussion, whether the gas particles are dark baryons or nonbaryonic dark matter is irrelevant. An isothermal velocity distribution is isotropic. It has a velocity dispersion σ that is independent of radius and relates the gas pressure to its density

$$p = \rho(r)\sigma^2. \tag{1.71}$$

The hydrostatic equilibrium requires the pressure force to balance the gravitational force (per unit volume), such that

$$-\frac{dp}{dr} = -\sigma^2\frac{d\rho}{dr} = \frac{G_N M(r)}{r^2}\cdot\rho(r) \tag{1.72}$$

where $M(r)$ is obtained by integrating $\rho(r)$ over a sphere with radius r. The solution to Equation 1.72 is nontrivial and generally requires a numerical rather than analytic approach. However, at large radii the density approaches $\rho(r) \sim r^{-2}$. Substituting this form into Equation 1.72, an expression for the total mass as a function of radius can be found

$$M(r) = \frac{2\sigma^2 r}{G_N} \tag{1.73}$$

Comparing this to the galactic rotation curve, the flatness (as we'll see in chapter 2) can be related to an isothermal dark halos velocity dispersion

$$v_c = \sqrt{2}\sigma \tag{1.74}$$

The Tully-Fisher relation between luminosity and v_c directly relates a galaxy's luminosity to a fundamental property of its dark halo. The dark halos velocity dispersion is larger for more luminous galaxies reflecting the gravitational influence of a larger dark halo. Disc galaxies with larger dark halos have deeper gravitational wells that are (apparently) more effective at causing visible matter to collapse into luminosity-producing star forming regions.

The I-band luminosity Tully-Fisher Relation (TFR) for a sample of $\sim$ 100 disc-dominated galaxies selected from the SDSS 2002 main galaxy catalog [132] is shown in Figure(1.14). The best-fit TFR relation is [187]

$$L_I = 1.8\left(\frac{v_{2.2}}{149.6Kms^{-1}}\right)^{2.6} \times 10^{10} L_\odot \tag{1.75}$$

with $v_{2.2}$ is the rotational velocity at 2.2 times the disc-scale length and can be considered equivalent to v_c. Substituting $v_{2.2} = v_\odot = 220\pm20$ kms^{-1} into Equation (1.75) yields a prediction for the Milky Ways total luminosity

$$L_{MilkyWay} = 5 \times 10^{10} L_\odot \tag{1.76}$$

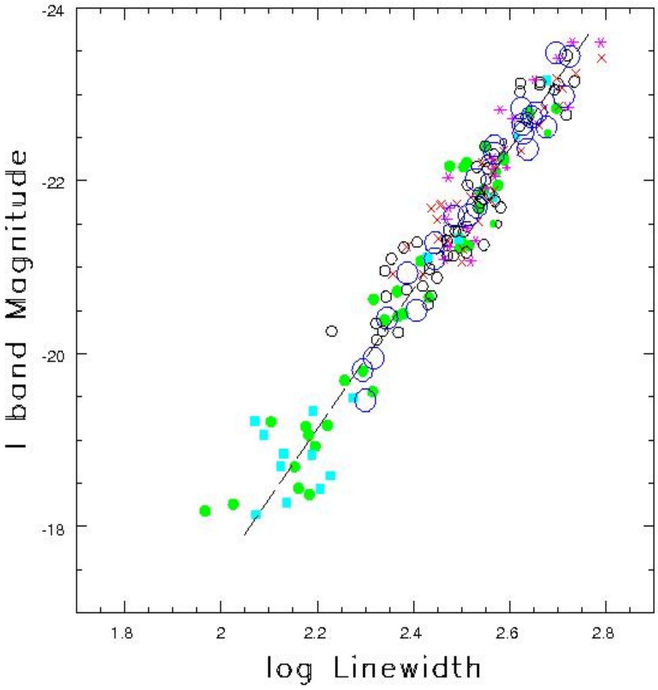

Figure 1.14: The Tully-Fisher Relation plotted in absolute magnitudes in the I band centered at 820 nm vs. the logarithm of the Doppler width of the 21 cm radio line (in km/s) corrected for inclination. The amplitude of the linewidth is approximately twice the maximum rotation velocity since the linewidth includes components of the motion toward and away from the viewer. The small symbols of various shapes and colors represent galaxies drawn from 5 separate clusters of galaxies and the large open symbols represent nearby galaxies with accurate, independently-known distances. The straight line is a regression to the data with errors in linewidth. The 5 cluster sample defines the slope and the galaxies with independently-known distances define the zero point. Figure from www.scholarpedia.org/article/Tully−Fisher_relation.

Chapter 2

Dark Matter Problem

2.1 Dark matter existence

The previous chapter of this dissertation has thus far shed light about the big bang theory which is considered to be the best theory we have so far that can explain the evolution of the universe. During the last couple decades or so, the concordance cosmology ΛCDM has emerged as the standard model of the big bang cosmology and attempted to explain the existence of large scale structures of galaxies and galaxy clusters, the accelerated expansion of the universe by observing light emitted from very distant supernovae (also referred to as standard candles), the temperature anisotropy in the cosmic microwave background (CMB) and the nucleosynthesis which led to the formation of very light elements during the early universe.

The modern concordance model of cosmology, known as ΛCDM cosmology or Λ cold dark matter, describes a universe (with a total matter $\Omega \simeq 1$) strongly dominated today by contributions Ω_m and Ω_Λ. The term cold indicates that the bulk of the universe's matter was non-relativistic during the formation of large-scale structure. It is worth noting that in this ΛCDM model, Λ represents the cosmological constant (the simplest form of vacuum energy also know as dark energy).

This standard model of cosmology draws a clear picture of the evolution of the universe. The universe started and expanded from a singularity called the big bang, an explosion which took place 13.7 billions years ago. During its expansion, the universe underwent phases of radiation dominance (during the early moment after the big bang), matter dominance (some times after the universe has cooled enough) and it is now believed to be dominated by dark energy which is some sort of anti-gravity; dark energy is the force associated with negative pressure, it repels matters away from each other rather than pulling them together as gravity does.

The left pane of Figure (2.1) shows a pie chart of the universe's content budget as it stands today and at z$\simeq$1100, deduced from a variety of cosmological observations. The two largest energy and matter components are labelled 'dark'. This is because they seem invisible; they have eluded detection via conventional observation.

We infer their abundances from various cosmological observations as shown in the right pane of Figure (2.1), but we have absolutely no understanding of the nature of these components.

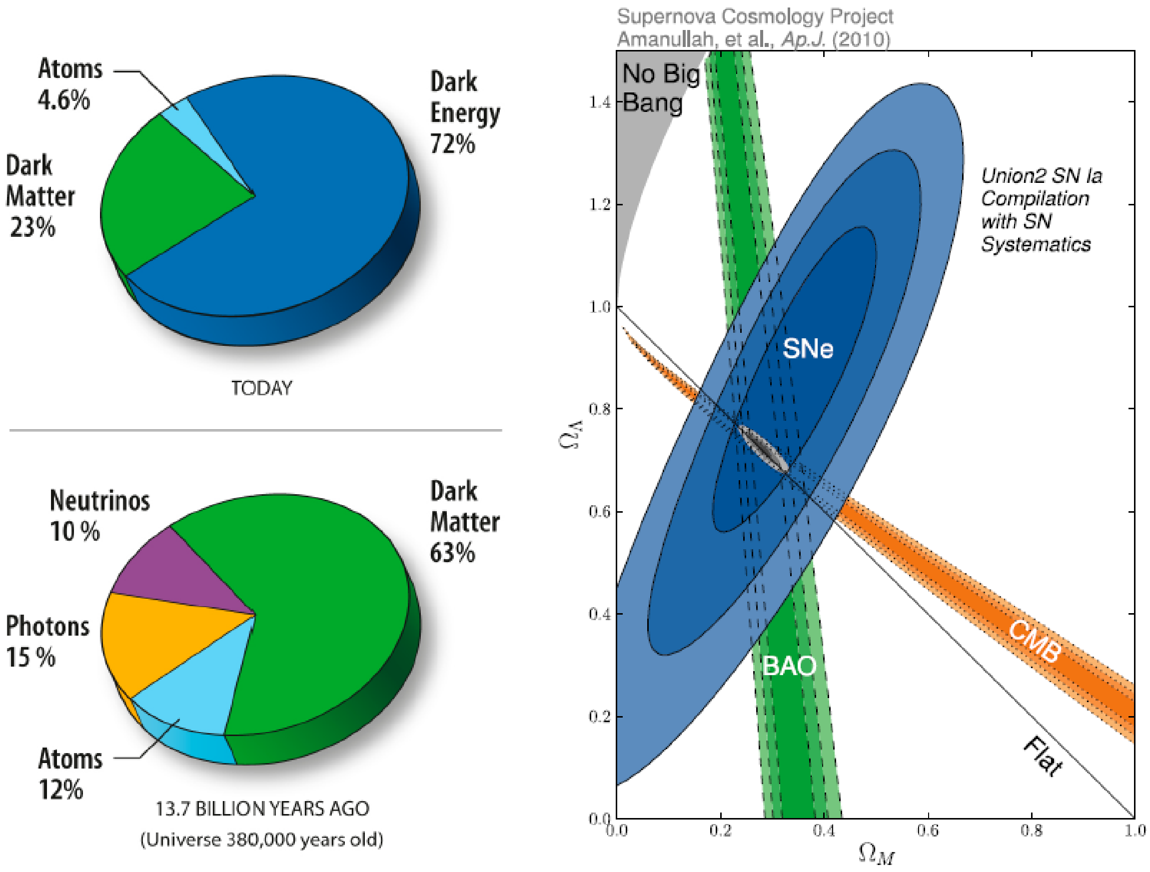

Figure 2.1: The Universe's matter budget (also referred to as the pie chart) as portioned by the concordance cosmology ΛCDM. On the left it is shown the universe's content budget show at a redshift of about z ≈0.4 (top left plot) and at the redshift z ≈ 1200 (bottom left plot). The universe today is dominated by dark energy (Λ) whereas it was dominated by matter when the universe was at a redshift of z ≈ 1200 with contributions from neutrinos, photons and baryons. In the right plot, it is shown the abundance of dark energy (Ω_Λ) as function of the abundance of the matter (Ω_M) as obtained from the Baryon Acoustic Oscillation (BAO), Cosmic Microwave Background (CMB) and from Type Ia Supernovae (SNe). Contours regions show 1σ, 2σ and 3σ confidence regions. Figures from [129, 130].

Three different and separate observations all converging toward the same findings that the geometry associated to the universe is flat. These observations clearly indicate that most of the matter contents of the universe is completely alien to us, they are invisible and so far undetected as shown in the left panel plots in Figure (2.1). The dark matter abundance is believed to be approximately $\Omega_m = 0.24$ and that of dark matter $\Omega_\Lambda = 0.72$, leaving only a small fraction of the baryonic matter corresponding to an abundance of $\Omega_b = 0.04$. Recall that the abundance is defined as the density of a given state normalized by the critical energy density, required to make the universe flat.

Before the concordance cosmology emerged, we knew about dark matter only through the observations. Dark matter existence came to our knowledge for the first time through observations made in the Coma galaxy cluster in 1933 by Fritz Zwicky followed by the rotation speeds of galaxies carried out by Vera Rubin (1970).

Since then, more pieces of evidence which support the existence of dark matter and dark energy come from observations such as studying the gravitational effects of dark matter at various scales: galaxies, clusters etc. More accurate measurements was also made using the CMB anisotropy and complete surveys of galaxies and clusters. With the success of the Big Bang nucleosynthesis and the observations made using the supernovae Ia studies, we were able to narrow down with great accuracy the estimates of the various parameters of the Standard Model of Cosmology, including Ω_Λ, Ω_m and Ω_b.

In the subsequent paragraphs of this chapter I will discuss briefly the evidences for dark matter from the rotational galaxies. I will explore dark matter interplay during the early moments of the universe following the big bang and then talk about some candidates for dark matter. Finally, I will introduce the Weakly Interacting Massive Particles and give reasons why this particular class of particles is considered to be favorable candidates for dark matter.

2.1.1 Rotation curves of galaxies

The first and the most compelling argument for the existence of dark matter on galactic scales is provided by the rotation curves of spiral galaxies. The visible structure of spiral galaxies is dominated by a luminous disk of stars that rotates about its axis.

The first hint of dark matter came in 1933 when Fritz Zwicky and Walter Baade measured the velocities of galaxies in the Coma Cluster. From the observed dynamics, they calculated the cluster mass. The velocity distributions yielded an astonishing result that the galaxies were moving in the gravitational potential of a total mass about 160 times greater than expected based on the luminous matter in the cluster. From these observations, Zwicky postulated the existence of an unseen component of the cluster that contributed most of the mass, and called it **dark matter**. An independent observation was carried out in 1970, when Vera Rubin and Kent Ford published their results on the rotation curve for the Andromeda Galaxy M31. As seen by Fritz Zwicky, the orbital velocities of objects in the galaxy were much faster than expected, revealing a much larger mass than indicated by the luminosity of the galaxy. In addition, the rotation curves were found to rise in the inner region, but to flatten near the edge of the disk and remain nearly constant out to high radius, Figure (2.2).

The dynamics of spiral galaxies is an important avenue for understanding the nature of dark matter. Vera Rubin and Ford used Hα and other spectral lines to study individual ionized atomic hydrogen (H II) clouds in the Andromeda galaxy [131, 132]. By measuring the Doppler shift of spectral features such as the electronic and hyperfine spectral lines of neutral and ionized atomic hydrogen it is possible to determine the distribution of mass at the center of the bulge, through the disk, and in the outer halo [133]. Other techniques used in these observations are various optical lines, 21 cm radio, CO rotational transitions, maser lines and the proper motion (for stars near the center of the Milky Way galaxy).

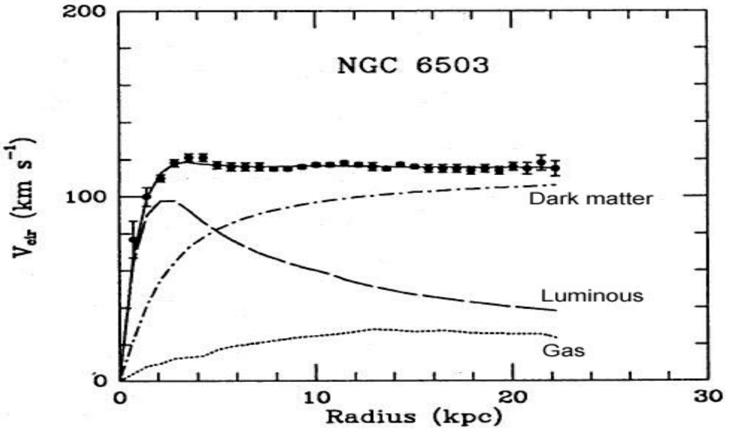

Figure 2.2: Rotational speed of the galaxy NGC 6503 as function of the galactic radius shown in black data points overlaid with a solid black line representing the fit to the data. The solid line is the theoretical rotation curve and the dots with error bars the measured object speed. Also shown are the contributions made to the curve by gas (dotted curve), luminous matter (dashed curve) and dark matter (dashed dotted curve). Figure from www.astro-photography.net/Dark-Matter.html.

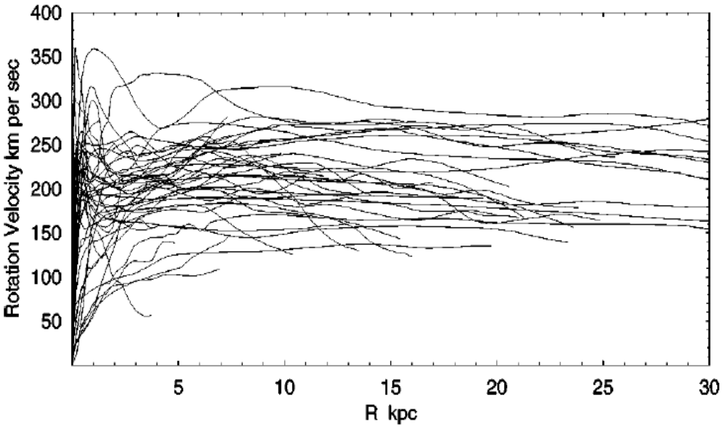

Figure 2.3: Rotational curves of several spiral galaxies. Figure from [133].

One remarkable feature of these curves which can be observed from Figures (2.2 and 2.3) is that they are flat or nearly flat between 1 and 2 optical radii and show little sign of falling off, but it is straightforward to calculate the mass profile needed to produce a flat rotation curve. Requiring that the gravitational and centripetal forces for a particle in a circular orbit of radius r to equal, one gets:

$$m\frac{v^2}{r} = G \cdot \frac{m \cdot M(r)}{r^2}, \tag{2.1}$$

where $v(r)$ is the observed rotation curve and $M(r)$ is the mass enclosed in a sphere of radius r. If the matter distribution in these galaxies is dominated by visible matter, then the rotational speed of objects beyond the visible disc of spiral galaxies should fall off as $\sim 1/\sqrt{r}$. However, observed results show that rotation curves are flat at large radii, implying $M(r) \propto r$ [133]. To explain this observation, it requires to postulate an addition of an invisible halo of matter to the mass profiles of galaxies. This invisible halo of matter extends beyond the visible component; this invisible halo, is generally attributed to dark matter. Assuming a spherically symmetric halo component, then $M(r) \propto r$ can be produced if the volume mass density of the spherical component obeys a density profile of the form $\rho \propto 1/r^2$ at large r. The density profile is provided by an isothermal halo by assuming a system of particles interacting gravitationally and in thermal equilibrium at some temperature temperature. In the phase-space, its distribution function is

$$f(\vec{r},\vec{v}) = \frac{\rho_0}{\left(\frac{2\pi k_B T}{m}\right)^{3/2}} \cdot e^{-\frac{\frac{1}{2}mv^2 + m\Phi(\vec{r})}{k_B T}}, \tag{2.2}$$

where ρ_0 is the density at the center of the disk and $\Phi(\vec{r})$ is the gravitational potential. As one can notice, the equation (2.2) is nothing else but a thermal Boltzmann distribution with the total energy $E = \frac{1}{2}mv^2 + m\Phi(\vec{r})$ and the velocity dispersion $\sigma^2 = \frac{k_B T}{m}$. Given the nonlinear dependence of the phase-space distribution through the potential $\Phi(\vec{r})$, it becomes extremely difficult to solve for the density distribution. The authors in [134] used the assumption that the density distribution is softened so that it flattens at small radii where ρ_0 becomes finite and that the density distribution can be approximated to the following the form

$$\rho(r) \propto \frac{1}{1 + (\frac{r}{a})^2}. \tag{2.3}$$

The total mass in this profile (2.3) grows arbitrarily large out to unlimited radius. For this reasons, we need an alternative profile. So the commonly used form, designed to match simulations of structure formation in dark matter-dominated galaxies, is the Navarro-Frenk-White profile [135]

$$\rho(r) = \frac{\rho_0}{\frac{r}{a}\left(1 + \frac{r}{a}\right)^2}. \tag{2.4}$$

The above profile approximates $1/r^2$ at intermediate radius and has a somewhat cuspy central behavior. At large radius, it falls of as $1/r^3$ and gives a total mass that is logarithmically divergent; this is an example of a cored inner profile with constant density at the center. This distinction between the two asymptotic behaviors of the above profiles has serious implications for dark matter detection since both models have divergent total mass, therefore some sort of truncation is needed to keep the total halo mass finite.

2.1.2 Galaxy clusters and galactic dynamics

Galaxy clusters are the largest bound structures in the universe, containing not only visible galaxies, but also a much larger mass of hot gas called intracluster medium (ICM) and the dark matter. The fact that the cluster are bound for a very long time, their dynamics can be described by the virial theorem which can be used to relate the kinetic and potential energies by the following formula:

$$\frac{1}{2}\langle m\rangle\langle v^2\rangle = G\frac{M}{2\langle r\rangle}\langle m\rangle, \tag{2.5}$$

where $\langle v^2\rangle >= \sigma^2$ is the velocity dispersion of the galaxies, $\langle m\rangle$ is the velocity-squared-weighted mean galaxy mass, and $\langle r\rangle$ is the virial radius, defined circularly as the radius inside of which the assumption of virialization holds. M is the cluster virial mass, the mass inside the virial radius.

From the virial theorem, F. Zwixky found a startling result that the gravitational mass was higher than expected based on the luminosity of the galaxies (by a factor of 400). This discrepancy is usually expressed as a mass-to-light ratio ($\frac{M}{L}$) normalized to 1 for the mass and luminosity of the sun, with M the total mass inferred from gravitational dynamics using the virial theorem, and L the luminosity from the visible light emitted by the cluster galaxies. A study of 29 clusters from the ESO Nearby Abell Cluster Survey (ENACS) found an average value of $\frac{M}{L} = 454h\frac{M_\odot}{L_\odot}$ [136, 137] (where h is the Hubble parameter in units of 100 km/s/Mpc). The results obtained are compatible with cuspy profiles like Navaro Frank White (NFW) as well as cored profiles like the isothermal spherical halo. Figure (2.4) shows the velocity dispersions from the data (averaged over clusters), compared with selected halo profiles.

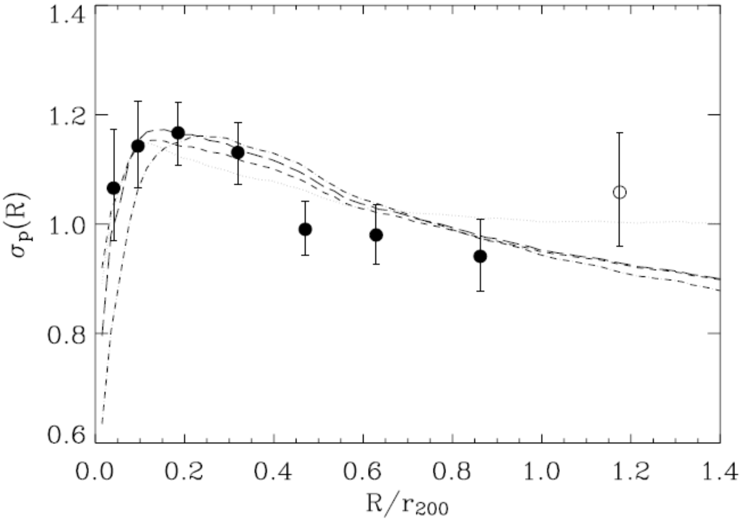

Figure 2.4: Cluster velocity dispersions from the ESO Nearby Abell Cluster Survey [139]. Circles with error bars are from early-type galaxies (last data point not used). The curves represent several halo models: isothermal (dotted), NFW (long dashes), M99 (short dashes), and Burkert (dot-dash). The cluster radius is normalized to r200, the radius at which the cluster density is 200 times greater than the cosmological critical density and the velocity dispersion is normalized to the global value for each cluster considered as a whole. Figure from [318].

2.1.3 Optical light and gravitational lensing

Gravitational lensing has been used as a way to probe cluster masses by observing the light deflection field of background galaxies and other objects, generated by a cluster in the foreground [138]. Strong gravitational lensing produces arcs called Einstein rings and multiple images from background objects, but weak lensing gives a slight distortion to the shapes of distant galaxies. Since most galaxies are not intrinsically spherical, the lensing effect can only be detected statistically, using a large number of galaxies.

In the weak-field and low-velocity limit of general relativity, the refractive index of a gravitational lens is directly proportional to its gravitational field

$$n(x) = 1 + \frac{2}{c^2}\Phi(x) \tag{2.6}$$

Therefore, the lensed images enable the determination of the true mass density including that of dark matter. Lensed images (rings and arcs) have been used to estimate a mass-to-light ratio of the order of 80 to 180 in solar units, depending upon the portion of the cluster considered in these analysis although lensing distortions can sometimes be difficult to identify in a strong gravitational regime [140, 141]. In the weak field limit (weak lensing), the authors in [142], performed an analysis of 130,000 galaxy clusters and groups identified in the Sloan Digital Sky Survey and they find general agreement with virial cluster masses and with the overall ΛCDM cosmology, suggesting a total matter density (with respect to the critical density) of $\Omega_m \approx 0.2 - 0.3$.

Figure 2.5: Hubble Space Telescope image of the cluster Abell 2218, showing a presence of the prominent arcs from strong gravitational lensing. Image from the Space Telescope Science Institute.

2.1.4 Bullet clusters

The Bullet cluster is actually two separate and distinctive galaxy clusters which have recently collided. As they passed through each other, the gas in each cluster interacted, producing a drag force similar to air resistance, and slowed down. This is how normal matter should and does behave. However, the bulk's matter or cold dark matter interacts with gravity only, and so the dark matter in the clusters is able to move ahead of the gas, producing the shape of the Bullet seen today. D. Clowe and al. in [143] have reconstructed the distribution of hot gas and of total mass in this system. Figure (2.6) show the lensing mass contours overlaid on the optical and X-ray images of the structure. The stark segregation between total matter (traced by lensing) and the smaller proportion of baryonic matter, traced by the X-ray gas as shown in the left panel of Figure (2.6), is completely consistent with the dark matter model: the collisionless dark matter halos (as well as the galaxies themselves) have passed through one another essentially unchanged, while the two populations of hot gas have been shocked by interactions during the collision and remain between the two colliding structures.

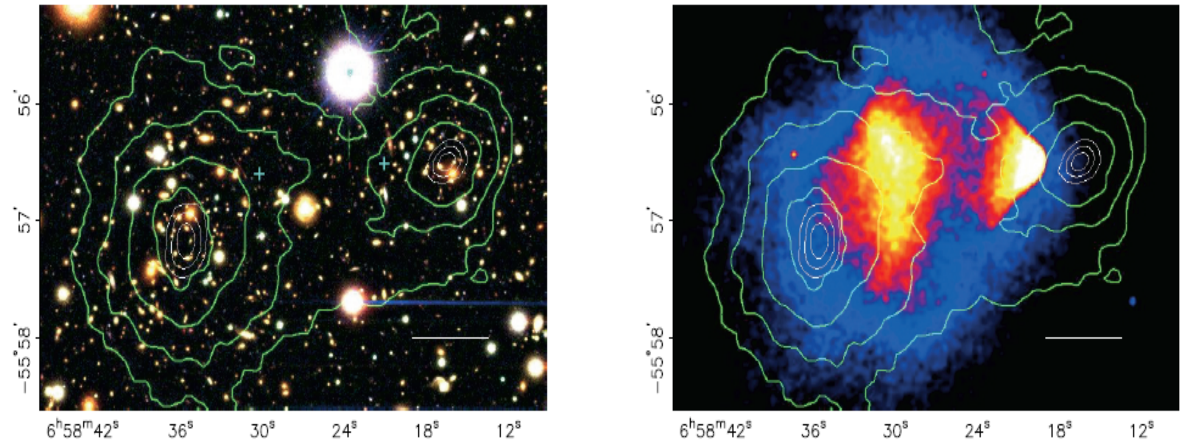

Figure 2.6: Optical image of the bullet cluster with the weak lensing overlaid indicating the contours of mass densities from Hubble Space Telescope (left) and the X-ray image of the bullet cluster from Chandra X-ray observatory. Figures from [143].

2.1.5 Elliptical Galaxies

The existence of dark matter can also be inferred using elliptical galaxies. An elliptical galaxy is viewed as a gas of stars in thermal equilibrium. They are anisotropic, exhibiting triaxial ellipsoidal shapes. The elliptical galaxies appear to be in gravitational-thermal equilibrium (they are neither collapsing nor expanding).

Elliptical galaxies are placed in the categories E0 to E7 [1] depending on their degree of ellipticity. They have a uniform luminosity and are similar to the bulge in a spiral galaxy, but with no disk. The stars are old and there is no gas present. Ellipticals are usually found in the high density field, at the center of clusters and possess halos of ionized, X-ray-emitting gas arising scattering and thermal bremsstrahlung.

The gravitational-thermal equilibrium is linked by a relation between the gas density distribution $\rho_g(r)$, the total mass $M(r)$ enclosed up to a distance r, and the observed X-ray temperature T which can be derived under

---

[1] Elliptical galaxies are denoted by the letter E. They are also given a number from 0 to 7. An E0 galaxy looks like a circle. An E7 galaxy is very long and thin. Astronomers have specific mathematical definitions for each number, but these definitions are beyond the scope of this dissertation. Elliptical galaxies have a large range of sizes. The largest elliptical galaxies can be over a million light-years in diameter. The smallest "dwarf elliptical" galaxies are less than one-tenth the size of the Milky Way. Elliptical galaxies have very little gas and dust. Since stars form from gas, little star formation occurs in elliptical galaxies. Most of their stars are old and red. With some practice, one can learn to visually tell what type of elliptical galaxy one is observing. For details, I refer the reader to the following web site: http://cas.sdss.org/dr5/en/proj/basic/galaxies/ellipticals.asp

the assumption of hydrostatic equilibrium:

$$\frac{dp_g(r)}{dr} = -G\frac{M(r)\cdot\rho_g(r)}{r^2}. \tag{2.7}$$

The ideal gas law provides the relationship between the pressure and temperature of the gas: $p_g = \rho_g k_B T/\mu m_p$, where m_p is the proton mass and μ is the average atomic mass of the ions in the gas, transforming the equation (2.7) to the following form:

$$\frac{d}{dr}\left(\frac{\rho_g(r)k_B T}{\mu m_p}\right) = -G\frac{M(r)\cdot\rho_g(r)}{r^2}. \tag{2.8}$$

The whole system made of stars and the gas (no dark matter taken into account) can be virialized and so would move in the same gravitational well, and would, therefore, have the same velocity dispersion given by

$$\sigma^2 = k_B T/\mu m_p, \tag{2.9}$$

and the goal was to check if the stellar velocity dispersion σ and the gas temperature follow Equation(2.9). Davis and White [144] have performed such study on a sample of 30 elliptical galaxies and have observed $T \propto \sigma^{1.45}$ rather than $T \propto \sigma^2$. More detailed study [145] in terms of

$$\beta_{spec} = \frac{k_B T}{\mu m_p \sigma^2}. \tag{2.10}$$

revealed for different stellar and dark halo models that, without the presence of dark halo, β_{spec} is never less that 0.75. The typical observed value is $\beta_{spec} \approx 1/2$, this implies that the stars have $\sim 1/2$ the velocity dispersion they should have, concluding that dark matter is very common in elliptical galaxies.

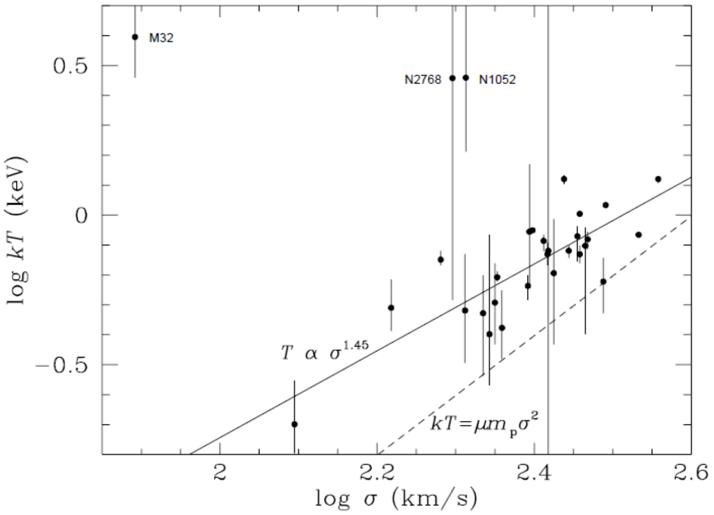

Figure 2.7: The logarithm of the X-ray temperature vs. the logarithm stellar velocity dispersion σ. for a set of X-ray-emitting elliptical galaxies. The solid line indicates the best fit exponent, 1.45, and the dashed line indicates the expectation for $T \propto \sigma^2$. Figure from [144].

2.1.6 Intracluster medium and X-ray emission

The hot intracluster gas can also be used as a probe of dark matter, gas falling into a cluster's gravitational well is pressure heated to temperatures of $10^6 - 10^8$ K as it falls into the center of the cluster's gravitational well, and emits X-rays by thermal bremsstrahlung; the emission spectrum depends on the depth of that well. Therefore, observations of the X-rays from the intracluster medium (ICM)[2] can reveal not only the mass of the ICM, but also the dark matter mass and its distribution. Like elliptical galaxies, clusters are permeated by x-ray emitting ionized gas that can be used to trace their gravitational potentials. The methodology for estimating cluster mass from x-ray temperature is essentially the same as was described in the previous section (2.1.5). Assuming the gas is in hydrostatic equilibrium, the mass profile can be derived from equation (2.8) by modelling the gas density according the β-model given in Equation (2.10). However, due to the relative size of clusters compared to galaxies, the angular resolution available with current x-ray observatories makes it possible to characterize the radial dependence of the temperature in far greater detail than is possible for elliptical galaxies and such a dependence can be precisely measured. For details, I will refer the reader to the followings publications: [52, 53, 54, 55, 56, 57, 58, 59].

2.2 Cosmic Microwave Background

The Cosmic Microwave Background (CMB) is the universe's primordial relic blackbody radiation, last emitted (scattered) from the surface of last scattering when the universe became transparent approximately 400,000 years after the Big Bang. Superimposed on its blackbody spectrum at 2.73 K, the CMB has anisotropy in temperature [146] and polarization [147] at the $\sim 10\,\mu K$ and $\sim 0.1\,\mu K$ levels, respectively. The predicted anisotropies are very sensitive to a wide range of cosmological parameters and accurate measurements of the CMB anisotropies provide excellent constraints on cosmological parameters.

The Cosmic Microwave Background (CMB) radiation is the oldest light in the universe that can be observed today even on Earth. The early universe was so hot that it was opaque due to the strong coupling between photons and baryons. Tiny density perturbations, on the order of 10^{-5}, created potential wells. Since baryons and photons were strongly coupled, there was a competition between gravity and radiation pressure around these wells which caused oscillations that are generally referred to as acoustic oscillations. These oscillations continued until the universe expanded and cooled sufficiently so that the photons were no longer coupled to baryons. This point is known as surface of last scattering. The acoustic oscillations created temperature fluctuations in the CMB, Figure (2.8), which were frozen at last scattering. Measuring the resulting CMB temperature power spectrum, Figure (2.9), gives information about the dark energy, dark matter, and baryonic matter densities in the universe. The relative amounts of dark and baryonic matter affect the amplitudes and positions of the power

---

[2] In astronomy, the intracluster medium (ICM) is the superheated plasma present at the center of a galaxy cluster. This is gas heated to temperatures of between roughly 10 and 100 megakelvins and consisting mainly of ionised hydrogen and helium, containing most of the baryonic material in the cluster. The ICM strongly emits X-ray radiation

spectrum peaks because they have strong effects on the acoustic oscillations; baryons increase the oscillations while dark matter reduces them. This occurs because dark matter interacts gravitationally but would not have been coupled to the photons.

The fundamental measurement in microwave background is the temperature of the microwave background seen in a given direction on the sky, $T(\theta, \phi)^{[3]}$ usually expressed in terms of the dimensionless temperature anisotropy and the mean temperature $\overline{T}$.

$$\frac{\Delta T}{T} = \frac{T(\theta, \phi) - \overline{T}}{\overline{T}} \tag{2.11}$$

The expression (2.11) is usually written as an expansion of spherical harmonics similar to Fourier series for surfaces or sphere.

$$\frac{\Delta T}{T} = \sum_{l=1}^{\infty} \sum_{m=-l}^{l} a_{lm} Y_l^m(\theta, \phi) \tag{2.12}$$

The coefficients a_{lm} tell us the size of the irregularities (anisotropies) on different scales. As with the galaxy distribution, to compare with theory we are interested only in the statistical properties of these coefficients, quantified by the radiation angular power spectrum, now known universally by the notation C_l. The angular power spectrum (C_l), for a given multipole moment, is given by an average over the moments and is defined by

$$C_l = \langle |a_{lm}|^2 \rangle = \frac{1}{2l+1} \sum_{m=-l}^{m=l} |a_{lm}|^2 \tag{2.13}$$

with the angled brackets being the statistical average, as known in statistical mechanics. Care needs to be taken when making comparisons with theory and observation due to the cosmic variance which limits the observer's ability to see the region up to the horizon, so there is a difference between our region of the Universe as compared to the average region of the universe. Moreover, the power spectrum is usually plotted as a function of the multipole l in terms of the squared temperature anisotropy, i.e.

$$(\Delta T_l)^2 = \frac{l(l+1)}{2\pi} C_l \tag{2.14}$$

The spectrum can be understood as the amount of power stored in small and large scale fluctuations in the microwave background temperature, where low multipole moments represent large angular scales (for example $l < 100$ will correspond to $\theta \geq 2°$) and high multipole moments represent relatively small angular scales ($l > 1000$ corresponds to $\theta \leq 2°$). Since these temperature differences represent fluctuations in the temperature of the surface of last scattering, they correspond to the matter-density fluctuations in the early Universe that eventually evolved into the structures we see today. The first two thousand multipole moments in the shape of the curve of the power spectrun, Figure (2.9), is primarily due to three effects: the Sachs-Wolfe effect [77], acoustic oscillations, and Silk damping [78, 79].

The flat power spectrum for the first hundred multipole moments corresponds to gravitational fluctuations

---

[3] The radiation is also predicted to have a small level of polarization and this was first detected in 2002 by the DASI experiment. Polarization can be described similarly to temperature and is likely to become an increasingly important observational measurement.

on scales larger than the cosmic horizon and reflect the nature of the earliest gravitational perturbations. These perturbations cause slight gravitational redshifts and blueshifts to the CMB photons at the surface of last scattering due to matter overdensities and underdensities, resulting in a weak CMB anisotropy for $l < 100$ generally referred to as the Sachs-Wolfe (SW) effect [77] , i.e. photons from the CMB are gravitationally redshifted, causing the CMB spectrum to appear uneven. This effect is the predominant source of fluctuations in the CMB for angular scales above about ten degrees. The power spectrum's shape for $l < 100$ has sensitivity to a cosmological parameter; the spectral index of density perturbations, n_s. In general, if $n_s \sim 1$, the initial perturbations will result in a CMB power spectrum that is amost constant for large angular scales (scale-invariant). This generally happens for $10 < l < 100$ and is referred to as the Sachs-Wolfe plateau. For multipoles corresponding to $l \leq 10$, there is a substantial contribution to the power spectrum caused by the integrated Sachs-Wolfe (ISW) effect. At the largest scales there is a bit of extra power in the CMB anisotropy due to gravitational redshifting and blueshifting of the CMB photons as they travel from the surface of last scattering to the Earth. The ISW effect is caused by gravitational redshift; it occurs between the surface of last scattering and the Earth, and it is not considered to be part of the primordial CMB. The ISW effect occurs when the universe is dominated in its energy density by something that is different than matter. For example if the universe is dominated by radiation, or by dark energy, their energy potentials will change the energy of photons passing through this (potential) well. In other words, the photon may have more or less energy when exiting the well than the energy it had when it was falling into these kinds of potentials. There are two contributions to the ISW effect. The **early-time ISW effect** occurs immediately after the (non-integrated) SachsWolfe effect produces the primordial CMB, as photons course through density fluctuations while there is still enough radiation around to affect the expansion of the universe. The second contributions to ISW effect is called the **late-time ISW effect**, Although it is physically the same, is usually lumped in with the primordial CMB, since the matter fluctuations that cause it and are in practice undetectable.

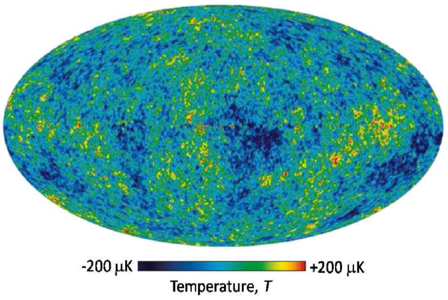

Figure 2.8: The Wilkinson Microwave Anisotropy Probe (WMAP) 5-year data all-sky map of the cosmic microwave background primary anisotropy. The red and blue spots indicates regions of space with extremely hot and cold temperature (relative to this scale), other colors are regions of space with temperatures in between, with a precision of 10^{-5}. A Mollweide equal-area projection is used to display the entire sky in galactic coordinates, with temperature differences given in units of thermodynamic temperature. The most recent primary anisotropy maps from the 7-year data release tend to be published in the form of differences relative to this map. The differences are consistent with pixel noise, slight calibration errors and an expected change in the Earth$'$s dipole signature. Figure from [49].

The most prominent feature in the cosmic microwave background is the $l = 1$ perturbation, known as the dipole. It corresponds to a pattern which is hot in one direction and cold in the opposite direction, with a smooth transition between them. Although the dipole $l = 1$ is interesting, it does not however tell us about the properties intrinsic to the microwave background, and so the dipole is studied separately and $l = 2$ is the smallest value considered.

The microwave background's temperature fluctuations record inhomogeneities in the photon-baryon fluid at the era of last-scattering. These inhomogeneities can be seen as an acoustic waves in the photon-baryon fluid of the last-scattering surface, and the densities of baryonic and non-baryonic matter have strong effects upon these oscillations: baryons tended to gravitationally collapse and form overdensities, whereas the photon pressure countered these overdensities, causing oscillations (dark matter reduces the driving effect of those oscillations upon the gravitational potential).

The angular power spectrum of the anisotropies is thus a sensitive probe of cosmological parameters, encoded in the positions and heights of the various spectral peaks. When combined with other cosmological measurements, current CMB data provides precise confirmation of the modern cosmological model, Figure (2.1.b).

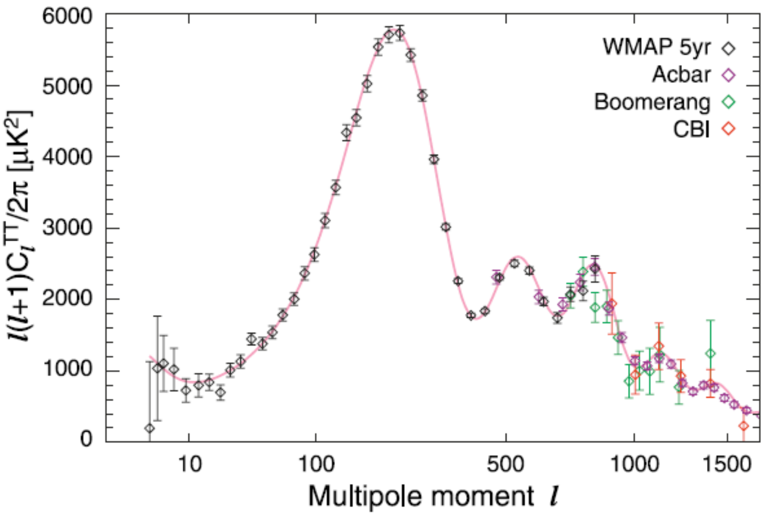

Figure 2.9: Temperature power spectrum of primary CMB anisotropies, as estimated from the WMAP 5-year data and an assortment of observations at small angular scales. The red curve indicates the prediction of the best-fit ΛCDM cosmological model. Figure from [148].

The structure of the peaks in the power spectrum, Figure (2.9), at $l \sim 100$ is due to acoustic oscillations in the baryon-photon fluid prior to recombination. Acoustic oscillations are normally thought of as a competition between the tendency for baryonic matter to clump as it falls into the gravitation well caused by the initial gravitational potential (perturbations) and the tendency for the radiation pressure of the tightly coupled photon background to oppose the clumping. After recombination, the photon background decoupled and the phases of the acoustic oscillations froze out, resulting in the pattern of harmonic peaks we see in the CMB power spectrum until today.

The acoustic peaks in the power spectrum are in general sensitive to certain parameters of the modern cosmology: for example, the position of the peaks of the angular spectrum is sensitive to Ω_k, so sensitive to the curvature of spacetime k. The peaks amplitudes relative to the Sachs-Wolfe plateau provide a way to determine the re-ionization optical depth τ. The CMB anisotropy for angular scales $\theta \preceq 1^\circ$ cause a diminution of the acoustic peak′s amplitudes by a factor of $e^{-2\tau}$ relative to the Sachs-Wolfe plateau after the reionization (at a redshif of $z < z_{reion}$). Finally, the acoustic peaks at higher and higher multipol has a damped behavior, especially at $l \sim 2000$. This is a direct consequence of the nonzero time scale over which recombination occurs and is called Silk damping [76].

During the last two decades or so, many experiments (ground and space based) set goals to measure the CMB anisotropy and polarization modes. Among these experiments, we can name ground-based telescopes such as VIPER [61] and TOCO [62], interferometers such as CBI [63] and DASI [64], as well as balloonborn instruments (MAXIMA [65] and BOOMERANG [66]). All these different experimental groups have started running almost at the same, however, only the satellite-born Wilkinson Microwave Anisotropy Probe (WMAP) [67] has provided a detailed all-sky map of the anisotropy with which the Standard Cosmology can be comprehensively tested. papers by the WMAP collaboration that explore the collection, processing and implications of their 7-year CMB data in far greater detail [68, 69, 70, 71, 72, 73].

The best fit curve in Figure (2.9) takes into account many effects in order to give to get the shape which follow the tredn of the data. In fact, the model used in WMAP is called the minimal ΛCDM model. The minimal ΛCDM model is a six-parameter model for which the geometry of the Universe is assumed to be flat (i.e. $k = 0$), the dark-energy $\Omega_\Lambda \neq 0$ (who equation of state is $w = -1$) and Ω_M, the nonbaryonic and cold dark-matter (CDM) component Ω_{CDM} or Ω_χ in addition to a baryonic component Ω_b.

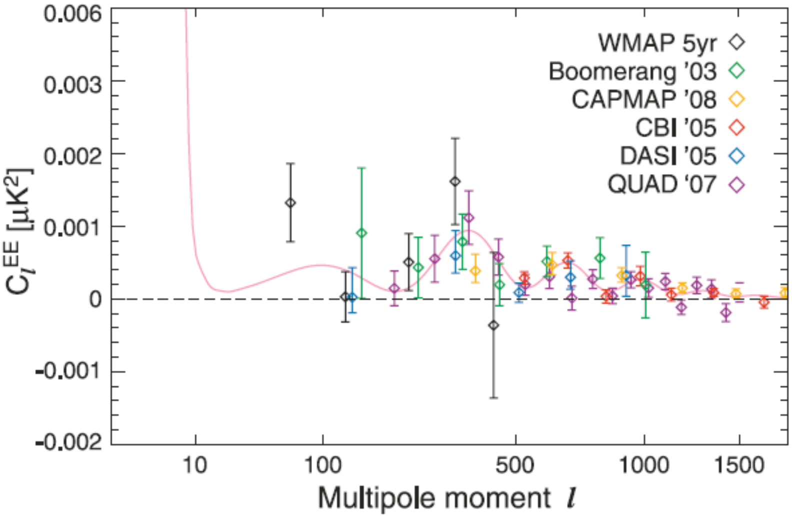

Figure 2.10: E-mode polarization (EE) power spectrum of primary CMB anisotropies, as estimated from the WMAP 5-year data and an assortment of other observations. The curve indicates the prediction of the best-fit ΛCDM cosmology. Figure from [148].

Remark: The WMAP data are measured in the frequency band and converted to an all-sky map using a technique called Mollweide equal-area projection [4] in the galactic coordinates, with the temperature differences given in units of CMB thermodynamic temperature [74, 75, 76]. At this stage, the maps not only include the primordial-temperature differences from the surface of last scattering (primary anisotropy), but also include features due to diffuse galactic emission, point sources such as planets and nearby galaxies, and a large dipole signature caused by the motion of the Earth relative to the cosmic rest frame. The reason the maps are recorded at five different frequencies is to remove these foreground features. The technique for extracting the primary anisotropy is described in [76] and results in a single map like the one shown in Figure (2.8).

2.3 Big Bang Nucleosynthesis

The previous paragraphs, as demonstrated by the concordance cosmology ΛCDM and many other observations, have sufficiently shed light on the nature of the universe's contents. It is proven that most of the matter in the universe is dark in some sort of substances called dark matter and dark energy. These two components are weird and are subjects of active physics research. The normal matter, matter that we can see and touch, matter which can be detected by means of electromagnetic interaction, amounts to a small fraction, about $\sim 4\%$ only that is characterized as baryonic matter.

During the early universe, the whole universe was in radiation dominance phase. Everything that existed was completely ionized. To understand how matter came to form, one needs to turn to the study of the abundances of light elements, the theory behind the big bang nucleosynthesis and the structures formation of the universe. Below, I am going to briefly discuss these important topics in order to grasp an understanding of how the big bang nucleosynthesis (BBN) provides strong evidence for existence of the non-baryonic dark matter.

To study nature on its largest scales, we turn to observations related to the early universe. The Big Bang Nucleosynthesis (BBN) model predicts the abundances of the light elements produced in the early stages of the Universe, moments after the bing bang occurred (with a time scale of $1 - 180$ seconds). This model sets strong constraints on the density of the baryonic matter in the universe noted as Ω_b. During the very early times when the Universe was less than 1 second old and the temperatures > 1 MeV, the weak interactions such as

$$n + \nu_e \leftrightarrow p + e, \tag{2.15}$$

were in equilibrium (of neutrons and protons). The neutron to proton ratio is thus maintained at the equilibrium value set by the two particle$'$s mass difference [8]:

$$\frac{n}{p} = e^{-\Delta m/T}, \tag{2.16}$$

---

[4] The Mollweide projection is a type of coordinate transformation commonly used for maps of the globe or the sky. It accurately represents area while tending to distort angles and shapes. For CMB anisotropy maps, the galactic plane runs horizontally through the middle of the map.

where $\Delta m = m_n - m_p$ is the neutron and proton mass difference. As the Universe expands and cools at $T \sim 3$ MeV neutrinos decouple, halting the above reaction. The weak interactions interconverting neutrons and protons freeze out, and the n/p ratio is given the equilibrium value (which took place before freeze-out) by $\sim 1/6$. At this time, the reactions producing light nuclei are still in equilibrium with the reactions of photo-dissociation of the same nuclei. For example, for deuterium: $n + p \rightarrow D + \gamma$ as the Universe cools and expands further, the temperature of photons becomes low enough that the dissociation reactions halt. The protons and neutrons then proceed to form deuterium and the light nuclei, until all neutrons are used up. About 20% of the neutrons decay prior to being incorporated in the nuclei. Roughly 100 seconds after the Big Bang (at the temperature of about 0.03 MeV), the abundances of the light nuclei D, ^{3}H; ^{3}He; ^{4}He; ^{7}Li and ^{7}Be are set. The heavier nuclei are not formed because of the large Coulomb barrier to the necessary reactions. Deuterium is the most powerful of these baryometers. Deuterium is a delicate nucleus, easily destroyed within stars and therefore no longer created in the modern universe. Since the deuterium abundance is sensitive to $\eta = n_b/n_\gamma$, the baryon-to-photon ratio, and decreases with time, any measurement of deuterium yields a direct upper limit on η. Current deuterium measurements from quasar absorption lines [30] indicate $\eta \approx 5.5$ [29], implying a modern baryon density of $\Omega_b \approx 0.04$, implying that ordinary, baryonic matter thus cannot constitute more than a small fraction of the universe's total matter density, so dark matter must therefore be non-baryonic in nature.

Two cosmological parameters are of critical importance in determining the natural abundances of the light elements: the expansion rate (relative to the rate of the weak interaction which sets the abundance remained at the freeze-out when neutron-proton equilibrium is established at the freeze-out temperature T_f: the ratio n/p and the final number of neutrons available to form elements of $A > 1$). The other important parameter is the baryon density ρ_b which affects the relative abundances of the elements: if ρ_b is larger, the nucleosynthesis starts earlier and more nucleons end up in the stable element. Generally, the baryon-to-photon ratio η is often used instead of ρ_b, and the photon density η_γ is obtained from the CMB measurement. Figure (2.11) shows the evolution of the light-element abundances as the Universe cooled, as predicted by the BBN model.

In general, one sets the task to measure the abundances of light nuclei in the universe, and from them infer the density of baryons ρ_b (or, equivalently, Ω_b). The ratio of abundances of two elements is measured (one of which is usually hydrogen, whose density is usually the easiest to measure). The major difficulty, however, lies in estimating the departures from the primordial abundances. The most reliable primordial abundance measurement is believed to be the that of deuterium D, Figure (2.12). The measurement is made using low metalicity absorption line systems in the spectra of high-redshift quasars. The gas in these systems is in the outer regions of galaxies or in the intergalactic medium, and it is not related to the quasars. The low metalicity of the absorption system is required as it implies that no significant amount of D was destroyed in stars. A high redshift is required as the Universe was then too young for the low-mass stars to eject large amounts of gas. However, complications arise if the absorption by D is contaminated by the absorption by H, so careful selection of the absorption system is required and D/H ratio ([150, 151, 152, 153]), has been estimated to be $\Omega_b h^2 = 0 : 019 \pm 0 : 0012$ (at 68% C.L.).

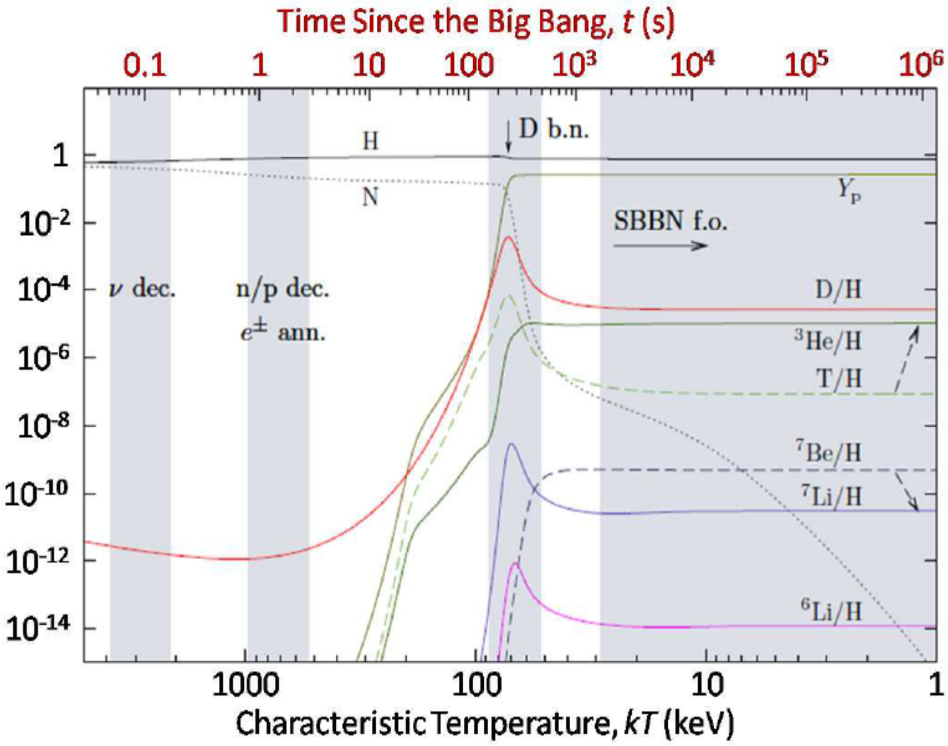

Figure 2.11: Evolution of light-element abundances as function of characteristic temperature (bottom x-axis) and as function of time (top). The blue bands indicate significant stages in Big Bang nucleosynthesis: neutrino decoupling, freeze-out of the neutron-to-proton ratio, the deuteron bottleneck, and freeze-out of the light-element abundances. The proton (H) and neutron (N) abundances are given relative to the total number of baryons, and Y_p denotes the ^4He mass fraction. Figure taken from [149].

The abundance of ^{4}He is measured using the emission spectra of the ionized gas surrounding hot young stars, such as in blue compact galaxies. These stars are chosen as they provide the least stellar contamination. The observed ^{4}He mass fraction is plotted against the abundance of O (or N) in the gas, and then extrapolated to zero O (or N), yielding the mass fraction of baryons which is in ^{4}He, $Y_p \approx 0.24$ [154, 155]. The dependence of the ^{4}He abundance on ρ_b is weaker than the dependence of D. Therefore, the deuterium abundance measurement is more constraining on ρ_b and Ω_b.

The measurement of the abundance of ^{7}Li is more difficult, but it is made in the old halo stars, formed from gas with low iron abundance. There is a plateau called the Spite-plateau where stars show approximately constant ^{7}Li/H $\approx 1.6\ \times 10^{-10}$, which is close to primordial. Finally, the abundance of ^{3}He is the most difficult to estimate, because stars are expected to both make and destroy it. The abundance of ^{3}He in the Galactic H II regions was measured, ^{3}He/H $\approx (1.6 \pm 0.5) \times 10^{-5}$, but it is not clear how this value relates to the primordial one [156].

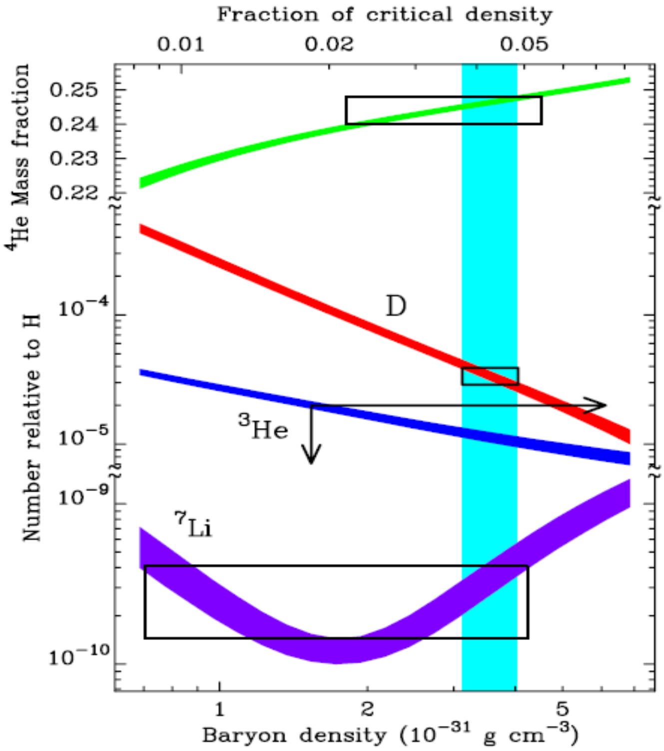

Figure 2.12: Expected abundances (calculated in the standard BBN) for the light elements are shown as gray bands. The rectangles show the 95% confidence intervals for the measurements cited in the text. The deuterium measurement is the most constraining on the only free parameter of the model, ρ_b. Figure taken from [149].

2.4 Supernovae Type Ia

Supernova Type Ia is considered as a sub-category of supernovae which results from the violent explosion of a white dwarf star (the remnant of a star that has completed its normal life cycle and has ceased nuclear fusion) of binary systems in which a white dwarf accretes mass from a nearby star until it crosses the Chandrasekhar limit of $\sim 1.44\mathcal{M}_{\odot}$ [157].

The Chandrasekhar limit is defined as the maximum mass of a stable white dwarf star. White dwarfs, unlike main sequence stars, resist gravitational collapse primarily through electron degeneracy pressure, rather than thermal pressure. The Chandrasekhar limit is the mass above which electron degeneracy pressure in the star's core is insufficient to balance the star's own gravitational self-attraction. Therefore, white dwarfs with masses greater than the Chandrasekhar limit will eventually undergo further gravitational collapse, evolving into a different type of stellar remnants, such as a neutron stars or black holes. However, stellar object with masses under the Chandrasekhar limit will remain stable as white dwarfs. If the star′s mass approaches the limit $1.44\mathcal{M}_{\odot}$ (the Chandrasekhar limit), the electron degeneracy pressure that prevents a white dwarf from collapsing further can no longer balance the star's inward gravitational self-attraction, the white dwarf will eventually collapse, initiating a brief but extremely intense period of burst during which its core material undergo a runaway fusion reaction that generates enough energy to completely unbind the star. Since the accretion mechanism causes the build up of a consistent amount of stellar material before the $1.44\mathcal{M}_{\odot}$ limit is reached, the peak light output or luminosity of the subsequent explosion is highly uniform from one SNe Ia to the next. This is what makes this class of supernovae (SNe Ia) an excellent standard candles which can be used to test the Universes distance versus redshift relation [158]. Therefore, measurement of the redshift of a SNe Ia, along with the observed flux, can be used to constrain the cosmological parameters. The argument is as follows: for an object of luminosity L and redshift z, the flux observed by a detector is given by

$$F = \frac{L}{4\pi d_H^2 (1+z)^2}, \tag{2.17}$$

with d_H, the proper distance between the object and the detector at the present time. If there is no expansion, $z = 0$ and the equation reduces to the familiar, intuitive, form that we are used to in Euclidian geometry. One factor of $(1+z)^{-1}$ in the above equation comes from the decrease in energy due to the red-shifting of each individual photon that travels the distance d_H, and the other comes from the fact that the photons are more spread out in time when they arrive at the detector than they were when they were emitted by the object (this spreading is also due to the expansion). The luminosity distance can also be written as $d_L = d_H(1+z)$, in order to express the flux in a simpler form $F = \frac{L}{4\pi d_L^2}$, with d_L the luminosity distance which depends on the redshift and is defined by:

$$d_L(z) = \sqrt{\frac{L}{4\pi F}} = (1+z) r(z), \tag{2.18}$$

with $r(z)$, the comoving distance to an object at redshift z and is function of the curvature parameter k_c defined as:

$$r(z) = \int_0^z \frac{dx}{H(x)}. \tag{2.19}$$

if $k = 0$, and

$$r(z) = \frac{1}{\sqrt{|k|}} G\left(\sqrt{|k|} \int_0^z \frac{dx}{H(x)}\right). \tag{2.20}$$

if $k \neq 0$ with $G(x) = \sin(x)$ if $k = 1$ and $G(x) = \sinh(x)$ if $k = -1$ [159].

Focussing ourselves now for the case of a universe with a flat geometry, i.e the curvature of the spacetime k is null, one can use the equation (1.28), from the chapter $\mathcal{I}$, to re-write (2.18) in the following form

$$d_L(z) = \frac{(1+z)}{H_0} \int_0^z \frac{dz'}{\sqrt{\Omega_\Lambda + \Omega_m (1+z')^3 + \Omega_R (1+z')^4}}. \tag{2.21}$$

in which $\Omega_k = \frac{k^2}{a^2 H^2}$ has no contribution in the denominator of the equation (2.21) for the simple fact that $k = 0$. The equation (2.21) is of extreme importance in cosmology because it tells us that the relationship between flux and redshift for a collection of standard candles with known intrinsic luminosities (such as Type Ia Supernovae) is sensitive to a number of cosmological parameters. Hence, measuring the flux of these given standard candles and their redshifts directly probes the allowed values of H_0, Ω_m and Ω_Λ (although these parameters cannot be estimated independently, for example Ω_m and Ω_Λ are related to each through the constrained equation $\Omega_m + \Omega_\Lambda = 1$). Moreover, if one considers the ratios of d_L for different objects, the dependence on H_0 can be removed, and therefore Ω_m and Ω_Λ can then be deduced.

The equation (2.21) encodes the Hubble's law of the expansion of the universe. As the author in [50] has shown, for low z objects ($z \ll 1$ and $\Omega_R \ll 1$), the integral performed on the leading terms in Z, yield the following result:

$$d_L(z) \approx \frac{z(1+z)}{H_0} \tag{2.22}$$

which can be recognized as Hubble's law in which the comoving distance is directly proportional to redshift: $r(z) = \frac{z}{H_0}$ [160], and therefore for low z nearby Type Ia Supernovae ($z \ll 0.1$) the relationship between distance and redshift is thus sensitive to the Hubble constant H_0 [44, 45]. The measurement of the Hubble constant H_0 using low-z standard candles was the Hubble Space Telescopes key project. The SH0ES program used several hundred Cepheid variable stars[5] to calibrate nearby SNe Ia luminosities and estimate $H_0 = 73.8 \pm 2.4$ kms^{-1}Mpc^{-1} [46].

Two experimental groups have searched for and observed the SNe Ia at various redshifts: the Supernova Cosmology Project (SCP) [161] and the High-z Supernova Search Team (HZT) [162]. The Supernova Cosmology Project has observed 42 supernovae at redshifts between 0.18 and 0.83. The two groups corrected the observed light curves for the stretch factor (relativistic time dilation) by fitting the template light curves from a low-redshift calibration set. This procedure further improved the uniformity of the supernovae. Finally, they fitted Ω_m and Ω_Λ to the flux redshift relation (using the apparent magnitudes, rather than flux, to avoid the H_0 dependence) and obtained the following values $\Omega_m = 0.28^{+0.10}_{-0.09}$ (stat) $^{+0.05}_{-0.04}$ (syst) (for a flat Universe) [161].

The High-z Supernova Search Team observed 16 high-redshift Type Ia Supernovae. They performed similar analysis, but they applied a multi-wavelength correction method to remove the time-dilation effect. Their result is consistent with the one from the Supernova Cosmology Project: $\Omega_m = 0.28 \pm 0.10$ (stat) (for a flat universe) [160]. In a separate run, the High-z Supernova Search Team observed has observed 8 more SNe Ia with an extended redshift from 0.3 to 1.2. They combine these observations with the previously observed SNe Ia from both SCP and HZT (and others). The data was fitted to the various cosmological models and they obtain $\Omega_\Lambda - \Omega_m = 0.35 \pm 0.14$ [163]. Under the assuming of a flat Universe and the equation of state $w = -1$, their analysis yields $\Omega_m = 0.28 \pm 0.05$. There are however systematics issue which arise when combining data sets from different team's observations to form a high statistics sample over a broad range of redshifts. There have been several efforts to compile SNe Ia data into self-consistent and systematic-free catalogs suitable for measuring

---

[5] Cepheid variables are very bright, pulsating stars whose luminosity varies periodically with time; they are categorized into several subclasses according to their masses, metallicities, and evolutionary histories. Classical (Type II) Cepheids are massive stars (low mass stars) that pulsate with a periodicity ranging between days and months. Their intrinsic luminosities can be reliably measured based on their pulsation periods, making them excellent standard candles for measuring cosmic distances out to a few tens of megaparsecs. Hubble's discovery in 1929 that the universe is expanding was based on Cepheids.

cosmological parameters (for details, I refer the readers to the following papers: [164, 165, 166, 167, 168, 169]). The most recent and comprehensive review is the Union2.1 compilation [170].

The distance modulus, μ_0 is defined as the difference between the apparent m_{mag} and absolute magnitudes M of a given object defined by 1.70. In terms of the redshift, the distance modulus can be written as:

$$\mu_0(z) = m_{mag} - M = 5\left[\log_{10}(r(z)(1+z)) - 1\right], \tag{2.23}$$

which is referred to as the Hubble diagram. Figure (2.13) shows the distance modulus as function of the redshift for several experimental results for Type Ia Supernovae based on Hubble diagram. The best-fit minimal ΛCDM cosmological model for a flat geometry and constant dark energy (with the equation of state $w = -1$) yields the best-fit values for the total amount of matter and dark energy in the universe given by: $\Omega_M \approx 0.29^{+0.043}_{-0.040}$ and $\Omega_\Lambda \approx 0.71^{+0.040}_{-0.043}$ at 1σ confidence intervals and includes both statistical and systematic uncertainties [170].

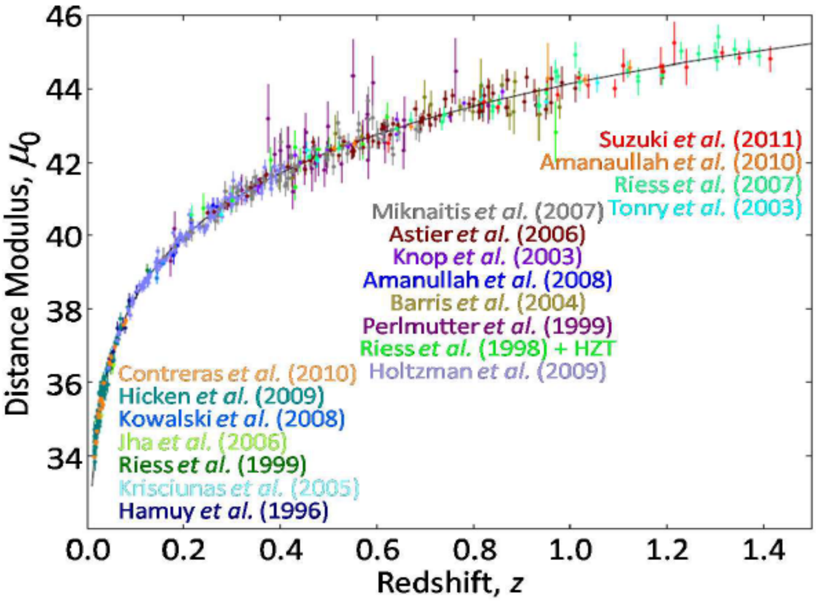

Figure 2.13: Distance modulus versus redshift for the Union2.1 Type Ia supernovae compilation. The curve represents the best-fit minimal ΛCDM cosmological model and is consistent with the ΛCDM fit to the CMB power spectrum. Figure from [170].

The observation of Type Ia Supernovae also suggests an eternally expanding universe that is accelerated by energy in the vacuum Ω_Λ. Although these data do not provide independent constraints on Ω_m and Ω_Λ to high precision without ancillary assumptions or inclusion of a supernova with uncertain classification, specific cosmological scenarios can still be tested without these requirements. In terms of the redshift, the decceleration parameter can be written as

$$q_0(z) = -\frac{\ddot{a}/a}{H^2(z)} = -\left(1 - \frac{d^{-1}H(z)}{dt}\right). \tag{2.24}$$

In terms of the Hubble parameter $H = \dot{a}/a$, the deceleration $q(t) = -(\ddot{a}/a)(\dot{a}/a)^{-2}$ and jerk parameters $q(t) = (\dddot{a}/a)(\dot{a}/a)^{-3}$ (all dimensionless), the Taylor expansion of for the luminosity distance (in Euclidean space) is given by

$$d_L(z) = \frac{z}{H_0}\left[1 + \frac{1}{2}(1-q_0)z - \frac{1}{6}(1 - q_0 - 3q_0^2 + j_0)z^2 + ...\right]. \tag{2.25}$$

Although related, the jerk j_0 parameter as defined here is not precisely equivalent to dq/dz parameter, providing an alternative parametrization. The SNe Ia data constrain the j_0 parameter to the positive domain at the 92% to 95% confidence level. That is, the expansion history over the range of the SNe Ia data is equally well described by recent acceleration and a constant jerk. Models with discrete values of j_0 are shown in Figure (2.15) [17]. In summary, they find a strong evidence for a change in the sign of cosmic acceleration at the present time, i.e the expansion of the universe is not all slowing down as intuitively one would expect, but rather speeding up (exponentially speeding up). This finding will have a profound impact for the future of the universe; gravity and the matter density (Ω_m) will continue to weaken more and more while the dark energy (Ω_Λ) is expected to continue to dominate rest of matter-density contributions. In the very far future of the universe, gravitationally bound systems such as our very planet own, will be completely separated from any other celestial objects; and even the sun will be far away from earth. As a result of this, the fate of the universe will be cold, meaning the existence of will be impossible.

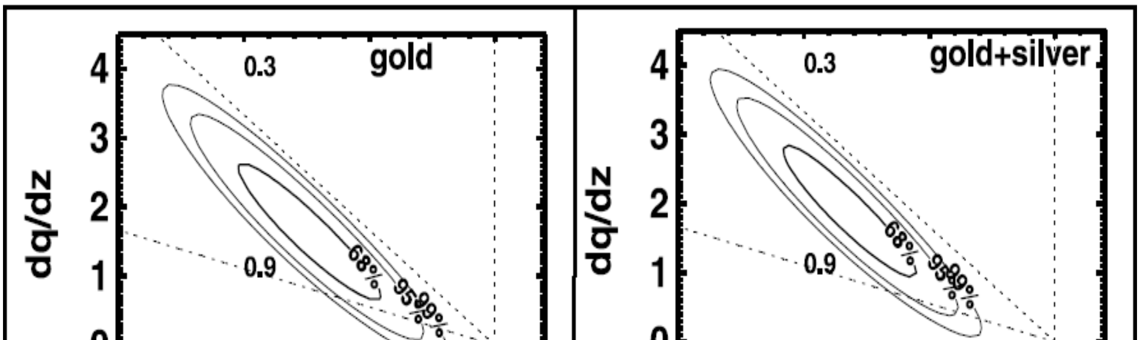

Figure 2.14: Joint confidence intervals for a two-parameter model of the universe's expansion history with $q(z) = q_0 + dq/dz$ from SNe Ia. The left shows the constraints derived from the gold sample; the right includes both gold and silver samples. For either set, the data favor the quadrant with recent acceleration ($q_0 < 0$) and past deceleration ($dq/dz > 0$) with high confidence. Lines of fixed transition redshift $[q(z_t) = 0]$ are shown. Figure from [17].

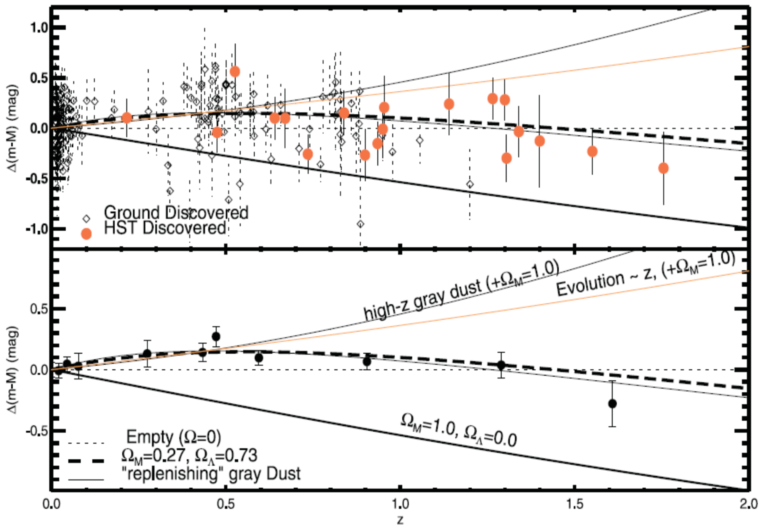

Figure 2.15: Kinematic SNe Ia residual Hubble diagram. Top is the SNe Ia from ground-based discoveries in the gold sample are shown as diamonds and HST-discovered SNe Ia are shown as filled symbols. Bottom, the weighted averages in fixed redshift bins are given for illustrative purposes only. Data and kinematic models of the expansion history are shown relative to an eternally coasting model, $q(z) = 0$. Models representing specific kinematic scenarios such as constant acceleration are illustrated. Figure from [17].

2.5 Baryon Acoustic Oscillations (BAO)

Baryon acoustic oscillations (BAO) relate to the clustering of nearby galaxies caused by gravitational perturbations in the early Universe. These perturbations (baryon over-densities and under-densities causing baryon − photon oscillations) are observed in the CMB power spectrum as peaks and are referred to as the the acoustic peaks. To get a real sense of these acoustics, imagine an overdense region of the primordial plasma, overdensity gravitationally attracts matter towards it, the heat of photon-matter interactions creates a large amount of outward pressure. These counteracting forces of gravity and pressure create oscillations, analogous to sound waves created in air by pressure differences. Consider a single wave originating from this overdense region in the center of the plasma. This region contains dark matter, baryons and photons. The pressure results in a spherical sound wave of both baryons and photons moving with a speed slightly over half the speed of light outwards from the overdensity. The dark matter only interacts gravitationally and so it stays at the center of the sound wave, the origin of the overdensity. Before decoupling, the photons and baryons move outwards together. After decoupling the photons are no longer interacting with the baryonic matter so they diffuse away. This relieves the pressure on the system, leaving a shell of baryonic matter at a fixed radius. This radius is often referred to as the sound horizon (characterized by a speed c_s). Without the photo-baryon pressure driving the system outwards, the only remaining force on the baryons is gravitational. Therefore, the baryons and dark matter (still at the center of the perturbation) form a configuration which includes overdensities of matter both at the original site of the anisotropy and in a shell at the sound horizon. The ripples in the density of space continue to attract matter and eventually galaxies in a similar pattern, therefore one would expect to see a greater number of galaxies separated by the sound horizon than by nearby length scales. This particular configuration of matter occurred at each anisotropy in the early universe, and therefore the universe is not composed of one sound ripple, but many overlapping ripples. As an analogy, imagine dropping many stones into a pond and watching the resulting wave patterns in the water. It is not possible to observe this preferred separation of galaxies on the sound horizon scale by eye, but one can measure this signal statistically by looking at the separations of large numbers of galaxies.

The baryon acoustic oscillation (BAO) scale is set by the size of the sound horizon at recombination defined by

$$S_{BAO} = \int_{z_{rec}}^{\infty} \frac{c_s}{H(z)} dz \tag{2.26}$$

with c_s, the speed of sound at the horizon (sound horizon). Assuming that dark energy is negligible during the early universe ($\Lambda \ll 0$), one can write the Hublle's parameter $H(z)$ as

$$H(z) = H_0(1+z)\sqrt{\Omega_M(1+z)}\sqrt{1+\frac{1+z}{1+z_{eq}}} \tag{2.27}$$

with $z_{eq} = \Omega_M/\Omega_R$ is the redshift at time the matter and radiation contributions becomes equal. Combining the equations (2.26) and (2.27), one finds that the BAO scale is then given by:

$$S_{BAO} \approx \frac{2}{H_0\sqrt{3\Omega_M z_{eq} R_{eq}}} \ln\left[\frac{\sqrt{1+R_{rec}}+\sqrt{R_{eq}+R_{rec}}}{1+\sqrt{R_{eq}}}\right] \tag{2.28}$$

with R_{rec} and R_{eq} are the baryon-to-photon density ratios at recombination and matter-radiation equality, respectively [171]. Plugging in the known and accepted values into the equation (2.28), one finds that $S_{BAO} \approx 146$ Mpc, however the true value is believed to be around 153 Mpc because immediately after recombination the momentum of the baryons causes the acoustic waves to continue to expand for a short time up to the redshift $z_d \simeq 1052$ (from CMB) at which the acoustic waves attend their maximum size (baryon-drag epoch).

Quite recently, the authors in [172] derived improved BAO-based constraints by combining a number of galaxies from the 2dFGRS catalog and an updated SDSS catalog. They presented the data in terms of the residual power spectrum of galaxy density fluctuations in overlapping redshift slices which showed clear signs of the ∼153 Mpc BAO scale in the clustering of nearby galaxies and are consistent with a significant nonbaryonic contribution to Ω_M. Their results compares favorably to the ΛCDM cosmological model for which $h = 0.72$, $\Omega_b = 0.043$ and $\Omega_M = 0.25$.

2.6 Structure formation

Another important argument for the existence of non-baryonic dark matter comes from modern observations of more recent large inhomogeneity (anisotropies).Observations such as the cosmic microwave background indicates

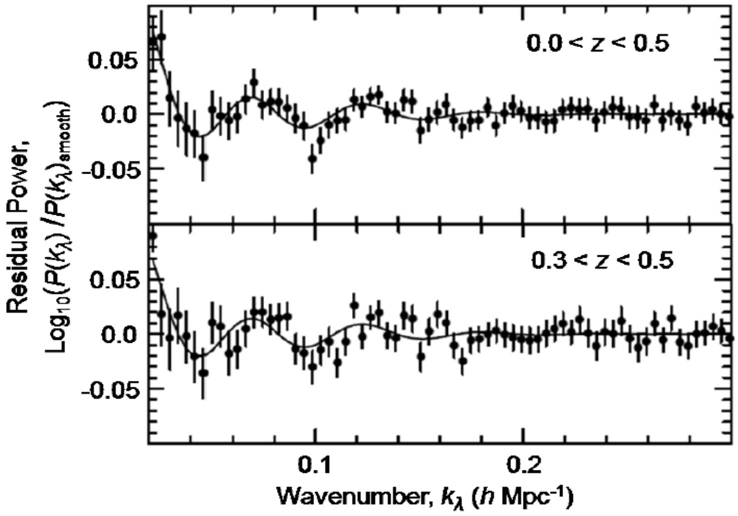

Figure 2.16: Residual power spectrum of density fluctuations in the spatial redshift distribution of nearby galaxies compared to the power spectrum as function of the wavenumber for a ΛCDM cosmological model with $h = 0.72$, $\Omega_b = 0.043$ and $\Omega_M = 0.25$. The smooth component of the ΛCDM model has been divided out to make the modulation due to the characteristic scale of baryon acoustic oscillations more apparent. The upper panel shows the residuals for ~900,000 galaxies with redshifts between 0 and 0.5 selected from the Sloan Digital Sky Survey and Two-degree Field Galaxy Redshift Survey [131] catalogs, while the lower panel shows the residuals for an ~70,000 galaxy subsets with redshifts between 0.3 and 0.5, [173]. Figure from [172].

the presence of anisotropies of the order of 10^{-5} level. At the early universe, photons and baryons were tightly coupled leading to baryon inhomogeneity when the universe was only a few hundred thousand years old (with a redshift $z \approx 1000$). As the universe expanded by a factor of ≈ 1000 since then, a wealth of galaxies and galaxy clusters then began to form (this took place at a redshifts of at least $z \approx 7.6$.

Our best guess at how the galaxies and large scale structure formation is envisioned from slight density enhancements that were present in the very early universe. During the first few millions years after the big bang, the universe expanded and gradually the stronger gravity of enhanced density pulled matter together which, after a long period of time, became the construction sites for many large structures that we see today in the universe. So, while density fluctuations at shorter scales remain frozen until matter-radiation equality ($z \approx 3000$), they are free to grow afterwards. This is not true however for baryonic matter which continues to oscillate in a photon-baryon fluid until decoupling. Baryonic over-densities can grow only after $z \approx 1100$. Thus, the over-densities from baryonic matter alone are insufficient to seed large-scale structure formation in the time span that we start observing galaxies unless a component of dark matter is allowed to grow in over-density between the matter and radiation. After decoupling, baryonic matter is attracted by these pre-existing over-densities, leading to a start of structure formation on the correct time scale. Furthermore, this imposes the requirement that dark matter must be cold i.e. be non-relativistic at the time of matter-radiation equality in order not to skew the structure formation process. This problem is quantitatively handled by defining the fluctuation in the matter density as follow:

$$\delta(\vec{x}) = \frac{\rho(\vec{x}) - \overline{\rho}}{\overline{\rho}}, \tag{2.29}$$

where $\overline{\rho}$ is the average matter density and $\rho(\vec{x})$ is the matter density at position $\vec{x}$. Given the density fluctuation as put in evidence by the equation (2.29), one can then calculate the auto-correlation function $\xi(\delta(\vec{x}))$ given by

$$\xi(\delta(\vec{x})) = \langle \delta\left(\vec{x}\right) \cdot \delta\left(\vec{x} + \delta\left(\vec{x}\right)\right)\rangle \tag{2.30}$$

where the average is taken over all $\vec{x}$ and $\overline{\rho}(t)$ is the universe's mean energy density at time t. In practice, it is convenient to consider the statistical distribution of the density contrast at different length scales, given by the power spectrum $P(\vec{k})$ which is defined as the Fourier transform of the auto-correlation function and is given by:

$$P(\vec{k}) = |\delta(\vec{k})|^2 = \frac{4\pi}{k} \int \xi(x) \sin(kx) d^3x \tag{2.31}$$

The growth of fluctuations can be calculated by solving the equations for the evolution of a fluid in an expanding universe which is classically modelled as perfect fluid and solved using the Euler equations which are described in more detail in PhD dissertations of Sunil Golwala and Vuk Mandic [175, 176]. The solution of the density fluctuation includes the effects of gravity and of pressure of any electromagnetically interacting, relativistic component. The relativistic component provides the photon's pressure. The case of relativistic, weakly interacting matter is also considered. At high redshift, perturbations are small and the equations can be linearized. It is necessary to work in comoving coordinates so that it is possible to track a given mode as the universe expands. Linearity allows independent treatment of different Fourier modes. One finds a second-order differential equation, modified by the expansion of the universe. In the absence of expansion and of fluid pressure, the solutions are exponential growth and decay: overdensities grow exponentially.

The introduction of pressure provides a restoring force against collapse. Energy can stream out of overdensities if the wavelength of the mode is smaller than the timescale of collapse and the sound speed (c_s), of order the speed of light for relativistic matter. In an expanding universe, the exponential forms are modified to power laws. In addition, calculation of the growth for super-horizon-scale perturbations requires a full general-relativistic formulation which we do not intend to tackle in this dissertation given the limited scope of this work. Below we briefly discuss the main findings of the Euler equation for the density fluctuation of the universe: for small density contrasts $\delta \ll 1$ we can solve for the evolution of $\delta(\vec{k})$ using linear perturbation theory leading to a decouples from one epoch to another until $\delta \approx 1$; however propagation to later epochs requires numerical computation and simulations. The main epoch obtained from the Euler equations in various regimes are:

(i). Radiation: considered as a regime during which the photon pressure prevented the perturbations in the photon-baryon fluid from growing significantly. Characterized by $p = \rho/3$, the photon-baryon fluid underwent acoustic oscillations during this period, which lasted until the baryons decouple from the photon field at the epoch of last scattering also referred to as non transparent and non opaque surface of last scattering ($z \approx 1000$).

(ii). Matter: in this era the universe was pressureless.

(iii). Dark Matter: this era began to grow as soon as the universe became matter-dominated. The photon-baryon fluid continued to oscillate until the baryons decoupled. After decoupling, the baryons falls into the existing potential wells of the dark matter perturbations. In the standard model of the growth of density fluctuations, it is assumed that all relativistic matter is strongly interacting. If this does not hold, then relativistic matter can stream away from overdensities, carrying away energy, without being stopped by interactions with other particles. This phenomenon is called **free streaming**. Free streaming does not fit the observations, however pure cold dark matter is more compatible with observations and is therefore considered as a good alternative explaining the growth of structure formation in the universe, thus cold dark matter has acted as the seed leading the large scale structures that we see today around us.

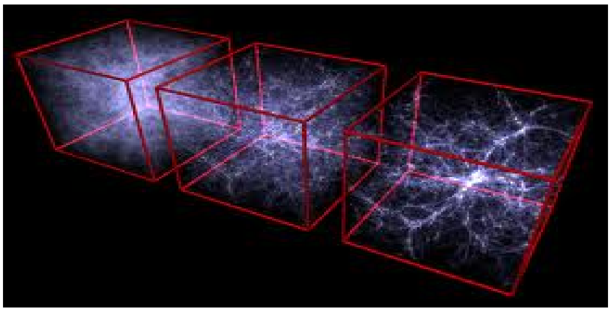

Figure 2.17: Computer simulation of structure forming process. In this simulation, small fluctuations in density in the far left box collapse into large structures on the right in this computer simulation of the universe. Large structures formed as small density fluctuations in the early universe collapsed under the influence of gravity. Here, we see three different stages of structure formation in a computer simulation starting on the left with 10^9 particles almost uniformly distributed in space. The center box shows an intermediate stage in the evolution of the universe, and the rightmost box shows the universe at the present time, with filaments and clusters of galaxies strung out in space; the law of gravity is the only physics applied in this simulation.

One interesting and convincing way to learn about dark matter through large scale structures is to compare the density perturbations seen today (at redshift much less than 1) with those seen in the CMB and estimate if there was sufficient time for gravitational collapse to produce the observed universe's structure that we see today. Perturbations seen in the CMB, at redshift of $z \approx 1000$, are of the order of $\sim 10^{-5}$ as predicted by the CMB. For a matter dominated universe, where $\Omega_b = 1$, perturbations would grow with time (or with redshift z) as $1/1+z$. Based on this reasoning, the density perturbations today would be $\sim 10^{-2}$. However this value is smaller than the observed fluctuations in the universe today. Therefore this model does not allow enough time to produce the present universe. This argument can also be used to estimate the amplitude of the CMB density perturbations based on the structure seen today. Assuming that galaxies and quasars form when the perturbations are larger $\delta > 1$, the fact that there are quasars at a redshift of $z = 6$ predict CMB temperature fluctuations of $\sim 10^{-3}$. However this is larger than the observed CMB temperature fluctuations. Non-baryonic dark matter, on the other hand, allows the observed large scale structure to form from the initial perturbations measured in the CMB.

Comparing numerical simulations of structure growth with the observed large scale structure gives additional information about the dark matter properties. In particular these comparisons show that relativistic or hot dark matter produces less structure than seen today while non-relativistic or cold dark matter with an energy density $\approx 23\%$ creates approximately the structure seen today.

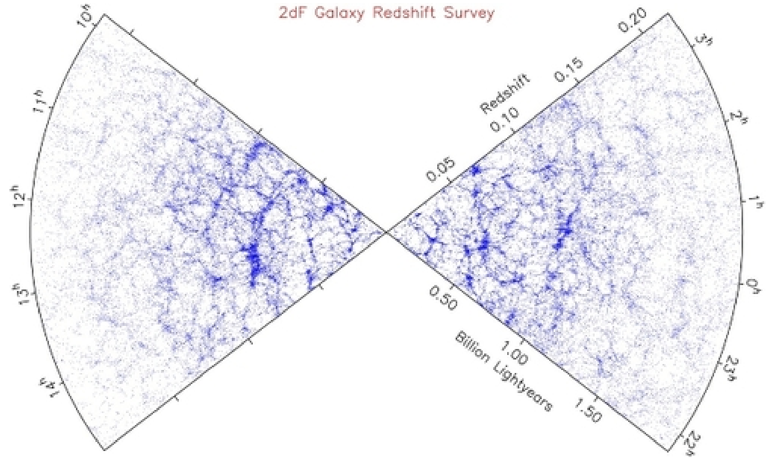

Figure 2.18: Map of the galaxy distribution as a function of redshift, as projected from the 2dF Galaxy Redshift Survey, showing the universe's current large scale structure. Figure taken from [59].

2.7 Cosmic Concordance and Quintessence.

The most widely studied cosmological models at the present time are variants of the Cold Dark Matter (CDM) paradigm within which adiabatic perturbations in a dominant CDM species grow due to gravitational instability from quantum fluctuations imprinted during an inflationary era. The bulk of the evidence today strongly favors models within which $\Omega_m < 1$ and any hot component is significantly disfavored.

None of the experimental observations that we know today is able to constrain all the physical parameters of the standard model of cosmology (ΛCDM). The SNe Ia data is most sensitive to the properties of the dark energy, CMB anisotropy power spectrum constrains some cosmological parameters under the assumption of a flat universe with a non zero component of dark energy. To constrain additional cosmological parameters, several data from several experiments were combined and produced constraints which are not only more precise, but also serve as consistency checks of the individual results from the separate experiments.

Several ΛCDM-sensitive experiments were considered and combined to get additional constrain on the astrophysical cosmological parameters. Among these experiments, there are: (i) The CMB anisotropy power spectrum derived from the WMAP 7-year data, (ii) The compilation of Type Ia supernovae, (iii) The Baryon-Acoustic Oscillation (from 2dFGRS and SDSS) and (iv) The SH0ES II program estimate of the present-day value of the Hubble parameter derived from Cepheid-calibrated nearby SNe Ia. The results obtained by combining the data from all these observations yields two to three times precise results than individual experiments. This analysis yields $\Omega_m = 0.271 \pm 0.014$ and $\Omega_\Lambda = 0.729 \pm 0.014$, and combining the CMB, BAO and H_0 results also yielded improved estimates of the baryon and cold dark-matter densities: $\Omega_b = 0.0458 \pm 0.0016$ and $\Omega_\chi = 0.229 \pm 0.015$. Furthermore, the hypothesis that the geometry of the universe is not flat and that the equation of state inconsistent with $w = -1$ were examined. The results found are entirely consistent with the minimal ΛCDM model and yield $\Omega_k = 0.002 \pm 0.005$ and $w = -1.013^{+0.068}_{-0.073}$, respectively

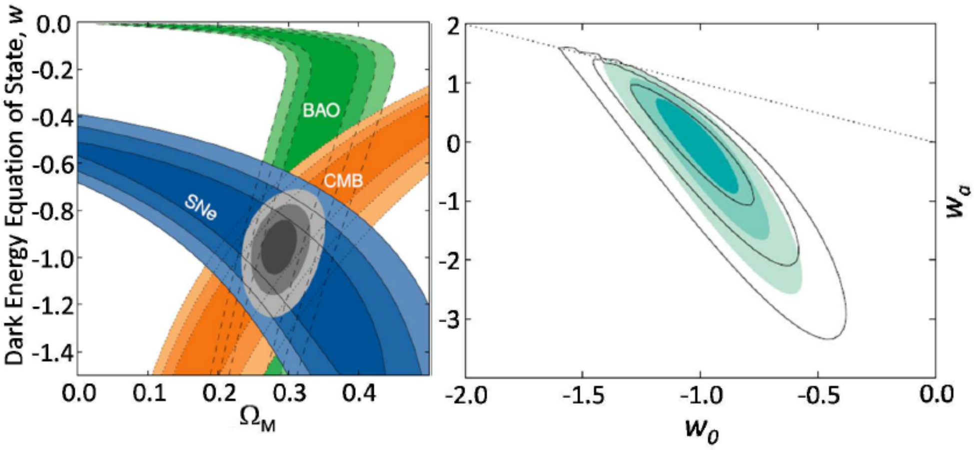

Figure 2.19: The equation of state w as function of the total matter density Ω_M for the combined cosmological constraints based on cosmic microwave background (CMB, orange) [76], Type Ia supernovae (SNe, blue) [110], and baryon acoustic oscillations (BAO, green) [118] data. In the right is shown w_a versus w_0 for the combined constraints based on cosmic microwave background, Type Ia supernovae, baryon acoustic oscillations, and H_0 [25] data, with (solid black contours) and without (shaded contours) SNe Ia systematic errors. The region above the dotted line ($w_0+w_a > 0$) violates early matter dominated. The contours represent, from big to small, the 99.7%, 95.4% and 68.3% confidence regions. Figure taken [60].

2.8 Dark matter Candidates: Baryonic and Non-Baryonic

The standard model of cosmology also known as the concordance cosmology or ΛCDM, together with many other observations (such as CMB, BAO, SNe, WMAP, etc.) have convincingly painted, with high accuracy, a clear picture of what the energy-mass budget of the universe is and concluding that visible matter (i.e. matter made of stars, gas, galaxies, galaxy clusters, etc.) amount to only 4.6% of the visible matter (baryonic matter) in the universe as shown in Fig (2.1) in the top left panel. In the pie chart shown in Fig (2.1) however, there is a large amount of matter which cannot be accounted as baryonic; they are termed as “dark”. Dark matter is believed to be a particle which makes up a 23% of matter in the universe and it is believed to be non-baryonic due to the fact that it interact weakly or event not with normal or baryonic matter.

In the literature, there is a whole zoo of elementary particles proposed in order to accommodate the dark matter. To be a candidate for dark matter, any proposed particle must satisfy the following criteria:

1. The nature of Dark matter must predominantly be non-baryonic as supported by evidence from BBN (big

bang nucleosynthesis) and CMB (cosmic microwave background).

2. Dark matter must be weakly interacting as evidenced by the limits on self-interaction from astrophysical observations (e.g. the Bullet cluster) and direct terrestrial searches.
3. Dark matter must be cold and non-relativistic throughout the formation of large scale structures. Relativistic dark matter particles (light neutrinos) and streaming would disrupt the hierarchical formation of large-scale structure. In this circumstance, the universe would have been less clumpy than it is today.
4. Finally Dark matter must be stable (compared to the present age of the universe).

Numerous candidates have been proposed classified as hot and cold dark matter (also referred to as thermal relics produced in thermal equilibrium and non thermal relics). Among these candidate, there are: neutrinos, heavy neutrinos, axions, MACHOs, neutralinos (or WIMPs), wimpzillas and some exotic particles such as Q-balls, etc. Below I give a brief description of some of the more prominent candidates.

2.8.1 Light and Heavy Neutrinos

Neutrino oscillation phenomenon showed that neutrinos do have mass and. If lepton number violation occurs in the leptonic sector, neutrinos can oscillation from one species to another. The oscillation term is thus function of the mixing angle θ and the mass difference squared Δm^2. The standard model of particle physics accommodate the existence of three leptons: electron (e), muon (μ) and tau (τ), each associated with its own neutrino ν. Similar the quark sector, the leptonic sector has three lepton generations: $\binom{e}{\nu_e}$, $\binom{\mu}{\nu_\mu}$ and $\binom{\tau}{\nu_\tau}$.

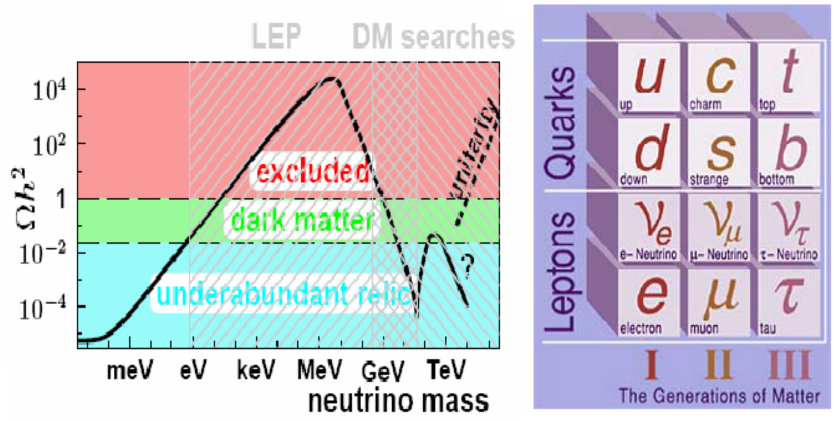

Figure 2.20: Neutrinos as dark matter. Relic density of a thermal Dirac neutrino with standard-model interactions, together with current constraints from cosmology, accelerators (LEP), and dark matter searches (left); the green belt indicates the region where possible neutrino dark matter can be observed. The right plot is the Standard model of particle physics families showing the three generations for quarks and leptons. Figure taken from Dennis Just talk on non baryonic dark matter at Arizona University.

Motivated by LSND results [80] and by many phenomenology of neutrinos cosmology [82] (and references therein), a fourth generation (sterile neutrino), much heavy than any other neutrino in the three first generation, has been proposed and emerged as a dark matter candidate [83]. Light neutrinos, with masses of a few eV to tens of eV, are disfavored as the dominant weakly interacting dark matter because they damp density fluctuations on scales smaller than the horizon size at radiation-matter equality. However, a small admixture of neutrinos may reduce the power on small scales to the level required by observation. Neutrinos belong to the class of hot relics, i.e. particles that are relativistic when they fall out of thermal equilibrium with the rest of the universe. This process is called **freeze-out**. The general criterion for freeze-out to occur is that the annihilation rate (per particle) of the particle species, which maintains equilibrium with other particle species, falls below the universe expansion rate characterized by the hubble constant: $\Gamma_A < H$, with the annihilation rate given by

$$\Gamma_A = n\langle\sigma_A v\rangle \tag{2.32}$$

where n is the particle density, σ_A is the annihilation cross section, and v is the relative velocity of two particles. The neutrinos, the interaction cross section is given by the weak interaction:

$$\sigma_A = G_F^2 E_\nu^2. \tag{2.33}$$

The number density of neutrinos in equilibrium (at freeze-out) is calculated by evoking Fermi-Dirac statistics. It is given by:

$$n = \frac{3\zeta(3)}{2\pi^2}\left(\frac{k_B T_\nu}{\hbar c}\right)^3. \tag{2.34}$$

The hot relics abundance at the freeze-out, however, is function of the their number density and it is given by

$$\Omega = \frac{8\pi G}{3H_0^2} n_\nu m_\nu. \tag{2.35}$$

Combining the equations (2.32) through (2.35), and assuming an equilibrium temperature of $T_\nu = 1.95$ K (i.e. gives $n_\nu = 113$ cm^{-3}) [81], one obtains:

$$\Omega = 0.011\left(\frac{m_\nu}{1\text{eV}}\right)h^{-2}; \tag{2.36}$$

which leads to a bound of neutrino mass given by

$$m_\nu = 91\Omega \cdot h^2\,\text{eV}^2. \tag{2.37}$$

Setting $\Omega = 1$, the above equation yields a neutrino mass much larger than a 1 eV which is ruled out by structure-formation arguments.

Light neutrinos are ruled out as prominent dark matter candidates due to the fact they are not cold and their mass is so small to account for the total mass needed for dark matter, however heavy Dirac neutrinos are viable dark matter candidates in the mass range from 40 GeV to a few TeV. Some special mechanisms however such as resonance annihilation or coannihilation are required if the neutrino mass is below 700 GeV. Such kind of signal might be expected in direct detection experiments in the near future especially in the mass range relevant for searches at the International Large Collider (I.L.C.) [177]. Although their discovery could just be in the corner and they could be a tiny part of dark matter halo, however they cannot solve the dark matter problem.

2.8.2 Axions

As mentioned in the previous section, the standard model of particle physics does not contain a particle that qualifies as dark matter. However, extensions to the standard model do provide viable particle candidates for dark matter. The axion, also known as the pseudo-Nambu-Goldstone boson, was proposed by Peccei- Quinn as a solution to the strong CP violation in the QCD sector [179, 180, 181, 182]. In the early universe, cold axion populations arise from vacuum realignment [183] and string and wall decay [184]. Which mechanisms contribute depends on whether the Peccei-Quinn symmetry breaks before or after inflation. These cold axions were never in thermal equilibrium with the rest of the universe and could provide the missing dark matter.

The strong CP problem arises from the non-Abelian nature of the QCD gauge symmetry (or color symmetry). Non-Abelian gauge potentials have disjoint sectors that cannot be transformed continuously into one another. Each of these vacuum configurations can be labelled by an integer, the topological winding number. Quantum tunnelling occurs between vacua. Consequently, the gauge invariant QCD vacuum state is a superposition of these states, i.e.,

$$|\theta\rangle = \sum_n e^{-in\theta}|n\rangle. \tag{2.38}$$

The angle, θ, is a parameter which describes the QCD vacuum state, $|\theta\rangle$. In the massless quark limit, QCD possesses a classical chiral symmetry. However, this symmetry is not present in the full quantum theory due to the Adler-Bell-Jackiw anomaly [185]. In the full quantum theory, including quark masses, the physics of QCD remains unchanged under the following transformations of the quark fields, q_i, quark masses, m_i, and vacuum parameter, θ: $q_i \to e^{i\alpha_i\gamma_5/2}q_i$, $m_i \to e^{-i\alpha_i}m_i$ and $\theta \to \theta - \sum_i \alpha_i$, with α_i the phases and γ_5 is the usual product of gamma matrices. This is not a symmetry of QCD due to the change in θ. These transformations can be used to move phases between the quark masses and θ. The quantity $\overline{\theta} \to \theta - arg(detM)$ is invariant and thus observable, unlike θ, M is the quark mass mixing matrix.

The presence of θ in QCD violates the discrete symmetries P and CP. However, CP violation has not been observed in QCD. However, an electric dipole moment for the neutron is the most easily observed consequence of QCD, or strong, CP violation. The presence of θ results in a neutron electric dipole moment of [186].

$$|d_n| \approx 10^{-16}\overline{\theta}\, e(\mathrm{cm}), \tag{2.39}$$

with e, the electric charge. The current experimental limit is

$$|d_n| < 6.3 \times 10^{-26}\, e(\mathrm{cm}). \tag{2.40}$$

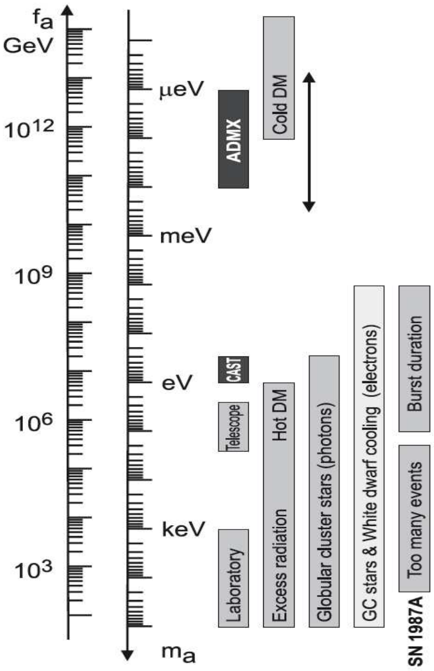

Figure 2.21: Constraints on the PQ-scale f_a and corresponding m_a from astrophysics, cosmology and laboratory experiments. The light grey regions are most model-dependent. Figure from [187].

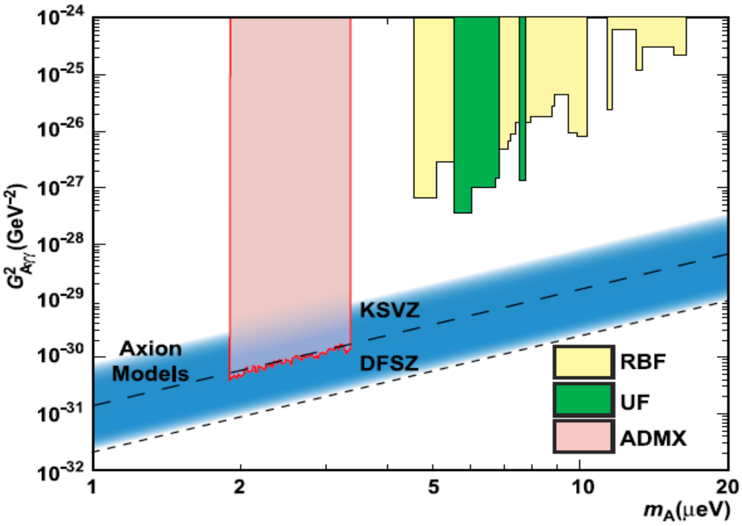

Figure 2.22: Current exclusion limits on the axion-photon-photon coupling from leading experiments in the region of axion dark matter candidates. The blue band indicates the approximate range of model-dependence for this coupling. The dashed and dotted lines indicate two common axion benchmark models. Figure from [188].

with $|\bar{\theta}| \preceq 10^{-9}$. There is no natural reason to expect $\bar{\theta}$ to be this small. CP violation occurs in the standard model by allowing the quark masses to be complex and thus the natural value of θ is expected to be of order one. This is the strong CP problem, i.e. the question of why the angle θ should be nearly zero, despite the presence of CP violation in the standard model. The Peccei-Quinn (PQ) solution [179, 180] to this problem results in an

axion [181, 182]. While other solutions to the strong CP problem have been proposed, the presence of the axion in the PQ solution has finally emerged and was proposed as a dark matter candidate. Axions satisfy the two criteria necessary for cold dark matter:
(i) a non-relativistic population of axions could be present in our universe in sufficient quantities to provide the required dark matter energy density and,
(ii) they are effectively collisionless, i.e., the only significant long-range interactions are gravitational.

Axions particles are characterized by a coupling constant f_a with units of energy, and its mass, by allowing the spontaneous symmetry breakdown to occur in the QCD lagrangian, is given by

$$m_a \simeq 6 \times 10^{-6} \left(\frac{10^{12}\text{GeV}}{f_a} \right), \tag{2.41}$$

and their abundance given by:

$$\Omega_a h^2 \simeq \left(\frac{f_a}{10^{12}\text{GeV}} \right)^{7/6} \tag{2.42}$$

implies an axion mass of the order of $10\,\mu$eV can constitute the universe's dark matter. These lighter axions are cosmologically excluded. Furthermore axions are produced non-thermally and are non-relativistic cold dark matter despite their very low masses. It is believed that axions are created by two mechanisms: vacuum realignment and cosmic string emissions.
(1) Vacuum realignment: in this mechanism a potential is generated and the axion field rolls towards the minimum and oscillates around it. The oscillation is what we see as axion emission.
(2) Cosmic string emissions: cosmic strings are topological defects in the space time created during phase changes (transitions). Above the phase transition the axion is massless and the zero momentum mode contributes nothing to the energy density, so the value of the field can be any constant from 0 to f_a without affecting the physics. Causality arguments imply that it is $\vartheta(f_a)$. At the phase transition instanton phenomena give mass to the axion field and it begins to undergo spatially homogeneous coherent oscillations about zero, with frequency m_a. These oscillations are what we consider as axions [193], see Fig (2.25).

The most relevant searches for axion dark matter are based on the Primakoff process ($L_{a\gamma\gamma} = g_{a\gamma\gamma} a \tilde{E} \cdot \tilde{B}$), with $g_{a\gamma\gamma}$ the Primakoff coupling [189]. In these processes, the axions are converted to photons within a strong magnetic field. Such experiments attempt to detect the excess of photons in resonant microwave cavities within strong magnetic fields [190]. The leading experiment at μeV masses is ADMX [191], which has already started probing cosmologically-interesting axion masses.

2.8.3 Massive Compact Halo Objects (MACHOs)

The Massive Compact Halo Objects (MACHOs) were one of the most popular candidates proposed to solve the dark matter problem. MACHO is a generic name for dark, compact and massive objects populating the halo of our galaxy. Such objects could, for example, be brown dwarfs - gravitationally collapsed objects of sub-stellar

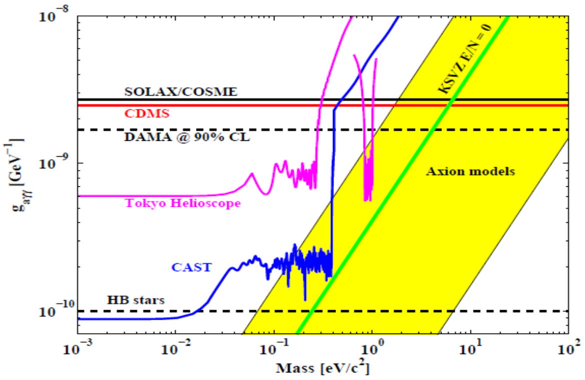

Figure 2.23: Comparison of the 95% C.L. upper limit on $g_{a\gamma\gamma}$ as function of mass obtained by CDMS collaboration (red/solid) with other crystal search experiments (SOLAX/COSME in black/solid) and DAMA (upper black/dashed) and helioscopes (Tokyo heslioscope (magenta/solid) and CAST (blue/-solid). Figure from [192].

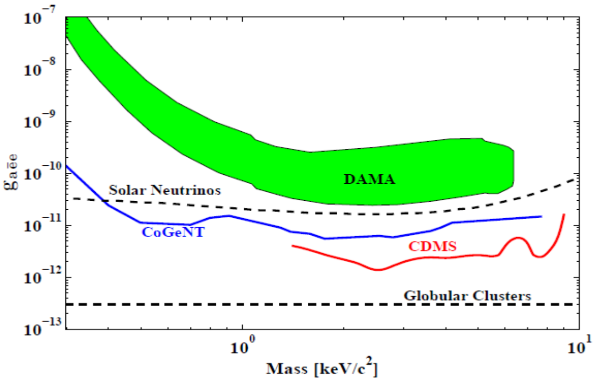

Figure 2.24: The allowed region (green/filled) from a Galactic axion interpretation of the annual modulation signature observed by the DAMA experiment. The 90% C.L. upper limits on the g_{aee} coupling constant from the CDMS collaboration (red/solid) and the CoGeNT experiment (blue/solid) completely rule out the DAMA allowed region. Figure from [192].

mass that could not reach high enough pressure in the core to start fusing hydrogen. Hence the mass of such objects is bounded from above ($< 0.08 M_\odot$) by this requirement. Another possibility is Jupiter-like objects, with mass $\sim 10^{-3} M_\odot$ and black holes, which may have been formed by the collapsing of baryonic matter.

Given that these objects are dark, one way to search for them is gravitational lensing. In particular, one can observe temporary brightening of a star due to a MACHO passing near the line-of-sight between the observer and the star. Since the probability of such events is very small, millions of stars have to be monitored on a daily basis, in order to make the search plausible. The duration of such microlensing event is determined by the lens mass m, distance x, transverse velocity v, and by the distance L to the source star [60].

Two experiments, MACHO [61] and EROS [62] searched for these objects by making nightly observations towards the Large and the Small Magellanic Clouds. Over a 5.7-year period, MACHO observed 13-17 events (depending on the classification) toward the large magellanic cloud (LMC) of typical duration $\sim$ 100 days, and one towards the small magellanic cloud (SMC) (also observed by EROS). The rate was larger than the expected

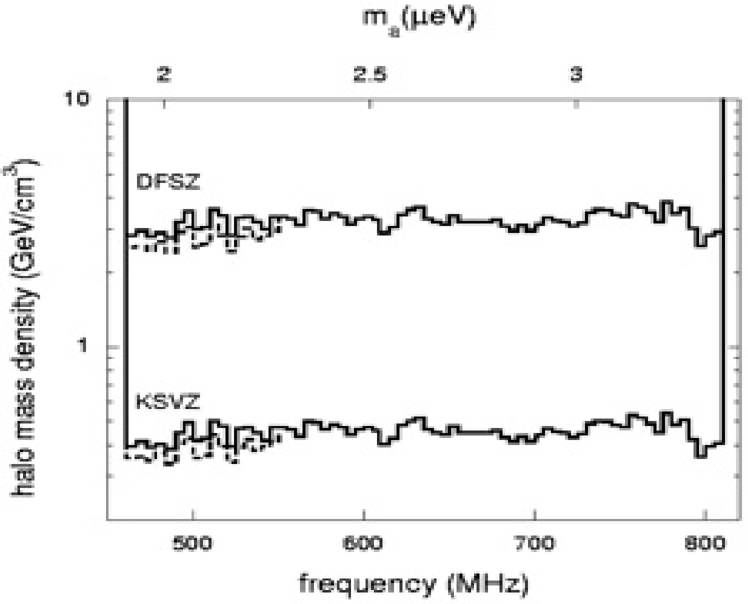

Figure 2.25: Experimental constraints on the density of axions in the galactic halo near the Sun as a function of the axion mass (upper scale) and cavity frequency (lower scale). The regions above the curves marked 'DFSZ' and 'KSVZ' are excluded from the respective axion models. The currently accepted value for the local dark halo density is 0.45 GeV/cm^3, which is approximately the extension of the excluded region for the KSVZ axion. Figure from [84].

background of 2-4 events due to known stellar populations, but not enough to account for a significant fraction of the halo. The absence of short-duration events ($\sim$ 20 days) implies that less than 20% of the halo can be in the form of MACHOs of mass between $10^{-4}M_\odot$ and $10^{-2}M_\odot$. Furthermore, from the observed rate of events, the MACHO team determined that an all-MACHO halo is ruled out at 95% confidence, in the same mass range [61]. Based on the 4 observed events towards the small magellanic cloud (SMC), the EROS team placed similar constraint: $< 25\%$ of the halo is in the form of MACHOs in the mass range $2 \times 10^{-7}M_\odot$ to $1 \times M_\odot$, at 95% confidence [85].

2.8.4 Black holes

A generic class of black holes produced in the very early universe, before nucleosynthesis, known as primordial black holes have been also considered as plausible candidates for dark matter. When primordial black holes are created, they accrete essentially all of the mass within their horizons. This relates their mass and their time of production [196]:

$$M(t) \approx 10^{15} \left(\frac{t}{10^{-23}\mathrm{s}}\right) g. \tag{2.43}$$

Baryon segregation occurs at approximately 1 minute before nucleosynthesis. With this time scale, the primordial black holes may have masses no larger than $10^6 M_\odot$. Detection of very low mass primordial black holes is possible by their Hawking radiation. The mechanism for generation of Hawking radiation can be described

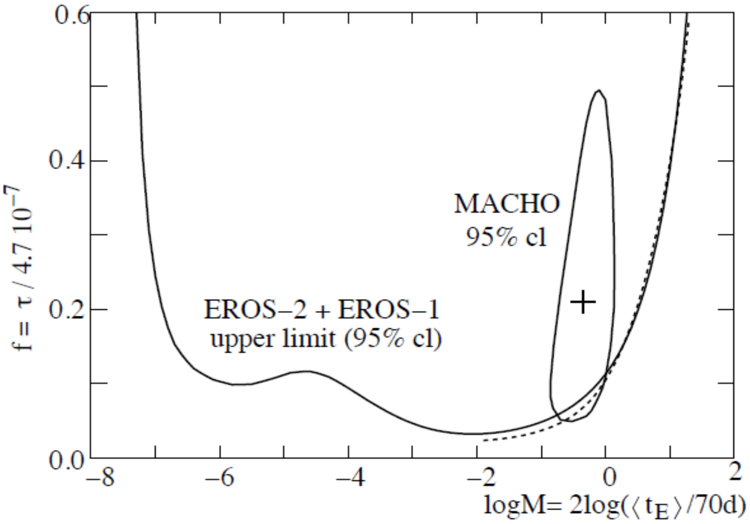

Figure 2.26: 95% confidence upper limits on the MACHOs halo mass fraction as a function of $log_{10}M_{MACHO}/M_{\odot}$ from the EROS-1 and EROS-2 experiments. The closed contour represents the 2000 signal claim of the MACHO collaboration. Figure from [86].

as follows. Virtual particle-antiparticle pairs pop in and out of existence all the time. If such an event occurs near the horizon of the black hole and one of the particles crosses through the black hole horizon, the pair cannot annihilate. Thus, the remaining particle becomes real. To conserve energy, the black hole must lose the energy required to create the particle. Effectively, the black hole emits elementary particles. The emission spectrum is a blackbody spectrum. The temperature of the blackbody and the mass loss rate are related to the mass of the black hole by [196]:

$$\frac{M(t)}{dt} = -5 \times 10^{-27} \frac{f(M)}{M^2} \mathrm{gs}^{-1}, \tag{2.44}$$

where the function $f(M)$ is related to the number of particle species light enough to be emitted by the black hole. The MACHO exclusion results disallow a significant component of black holes in the mass range 10^{-4} to $0.03M_{\odot}$ in the galactic halo.

2.8.5 Supersymmetric dark matter candidates

Supersymmetry (SUSY) is a well-motivated and presently the most-favored extension to the Standard Model of particle physics. It's a theory that relates fermions and bosons. SUSY is motivated by the desire to find a unifying theory. This theory is renormalizable as shown by Gerad Tooft and that the fundamental forces (electromagnetic, weak and strong) unifies around 10^{18} GeV. Supersymmetry predicts the existence of, yet to discovered, superpartners for every known particles called sparicles. Sparticles and particles do not have the same mass; their spins differs by 1/2. In order for SUSY to work and in order for the particles introduced in SUSY to have mass, the internal symmetry of the system must be spontaneously broken. This is exacttly what happens in the standard model where the spontaneous symmetry is broken in order for the gauge bosons ($W^{\pm}s$ and Z) to acquire mass via the higgs mechanism.

SUSY is believed to describe nature and provide elegant solution to the quadratic divergences (hierarchy problem) and coupling unification that the standard model of particle alone is not able to explain without evoking an arbitrary cut-off or an excessive fine tuning. However SUSY has lots of free parameters. The minimal supersymmetric standard model (MSSM) has 106 parameters that need to be fixed. The MSSM, which have less number of parameter as opposed to SUSY, was originally proposed to stabilize the weak scale, solving the hierarchy problem, i.e. the Higgs boson mass of the Standard Model is unstable up to some quantum corrections and the theory predicts that weak scale should be much weaker than what is observed to be. In the MSSM, the Higgs boson has a fermionic superpartner, the Higgsino, that has the same mass as the Higgs if supersymmetry were an exact symmetry. Because fermion masses are radiatively stable, the Higgs mass inherits this stability. However, in MSSM one needs to indroduce a Higgs doublet for the theory to work.

To reduce the number of parameters in SUSY, the constrained Minimal Supersymmetric Standard Model (cMSSM) was introduced. The cMSSM is the most widely discussed extension of the Standard Model of particle physics. Despite its relative simplicity, this model has the advantage of capturing some key phenomenological features of Supersymmetry (SUSY), while making definite predictions for the properties of the the lightest neutralino χ_1^0 (or χ) as a linear superposition of the superpartners of the neutral Gauge bosons and the neutral Higgses, which is by far the most popular Dark Matter (DM) candidate [194, 195].

Particle	Spin	Superparticle	Spin
Electron	1/2	Selectron	0
Muon	1/2	Smuon	0
Tau	1/2	Stau	0
Neutrino	1/2	Sneutrino	0
Quarks	1/2	Squarks	0
Fermions		Bosons	

Particle	Spin	Superparticle	Spin
Graviton	2	Gravitino	3/2
Photon	1	Photino	1/2
Gluon	1	Gluino	1/2
W-bosons (+/-)	1	Wino	1/2
Z-boson	1	Zino	1/2
Higgs	0	Higgsino	1/2
Bosons		Fermions	

Table 2.1: Standrad particles with their superpartner. Every fermion has a boson superpartner and vice versa. Their spin is obtained by subtraction 1/2 to the fermionic of bosonic spin and taking its absolute value to get the superpartner spin.

In the context of this dissertation, one important connection to SUSY is its implication for weakly interacting massive particles (WIMPs). The lightest new particle predicted by SUSY is an ideal candidate for dark matter. This new particle is called neutralino or a WIMP. WIMPs produced in thermal equilibrium in the early universe (thermal WIMPs) are particularly interesting. Their cosmological density is naturally of the right order of magnitude when their interaction cross section is of the order of the weak cross section, and so can be detected in the laboratory.

In the early Universe, annihilation reactions that convert WIMPs into standard model particles were initially in equilibrium with their opposite reactions. As the universe expanded, and the temperature became smaller than

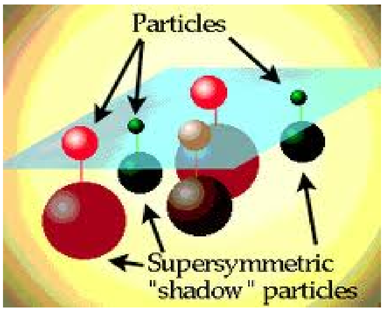

Figure 2.27: Supersymmetric partners of the standard model of particle physics illustrated as mirror particles. Figure courtesy of Dan Hooper (http://home.fnal.gov/ dhooper/supersymmetry.gif).

the WIMP mass, the gas of WIMPs, still in equilibrium, diluted faster than the gas of standard model particles. This occurred because the equilibrium number density of non-relativistic particles is suppressed by a Boltzmann factor $e^{-M_\chi c^2/k_B T}$ with respect to the number density of relativistic particles. After a while, WIMPs became so rare that the WIMP annihilation reactions could no longer occur (freeze-out), and from then on the number density of WIMPs decreased inversely with volume (or in other words, the number of WIMPs per comoving volume remained constant). Decoupling occur approximately when the WIMP annihilation rate $\Gamma_{\chi\chi} = \langle \sigma_{\chi\chi} v \rangle n$ becomes smaller than the universe expansion rate H ($\sigma_{\chi\chi}$ is the WIMP annihilation cross section, v is the relative velocity of the annihilating WIMPs, n is the WIMP number density, and the angle brackets denote an average over the WIMP velocity distribution). The number density, at the freeze-out, is given by:

$$n_\chi^{(eq)}(T) \approx g \left(\frac{M_\chi k_B T}{2\pi \hbar^2} \right). \tag{2.45}$$

More accurate calculations require numerical solutions of the Boltzmann equation in an expanding universe

$$\frac{dn_\chi}{dt} + 3Hn_\chi = -\langle \sigma_{\chi\chi} v \rangle \left[n_\chi^2 - n_\chi (eq)^2 \right]. \tag{2.46}$$

To find WIMPs relic density, it must be reminded that the decoupling of non-relativistic particles occur when $m > T$. If $T > m$, WIMPs annihilation occur and if $T < m$, there will be creation, which is however suppressed by the Boltzman factor $e^{m/t}$. During the expansion, the WIMP density changes as

$$n \sim \frac{1}{a^3}, \tag{2.47}$$

which implies

$$\frac{dn}{dt} = -3\frac{\dot{a}}{a} n = -3Hn. \tag{2.48}$$

At the freeze-out temperature, $\frac{dn}{dt} = 0$, and using Friedmann's equation to find the expansion rate H, the relevant relic density can be approximated to [117][6]

$$\Omega_\chi h^2 \simeq \frac{3\times 10^{-27}}{\langle\sigma_{\chi\chi}v\rangle} cm^3 s^{-1}, \tag{2.49}$$

with $\langle\sigma v\rangle$ the thermally averaged annihilation cross section times the relative velocity; $3Hn$ is the dilution term due to expansion. An important property of this equation is that smaller annihilation cross sections correspond to larger relic densities. This can be understood from the fact that WIMPs with stronger interactions remain in chemical equilibrium for a longer time, and hence decouple when the universe is colder, therefore their density is further suppressed by a smaller Boltzmann factor.

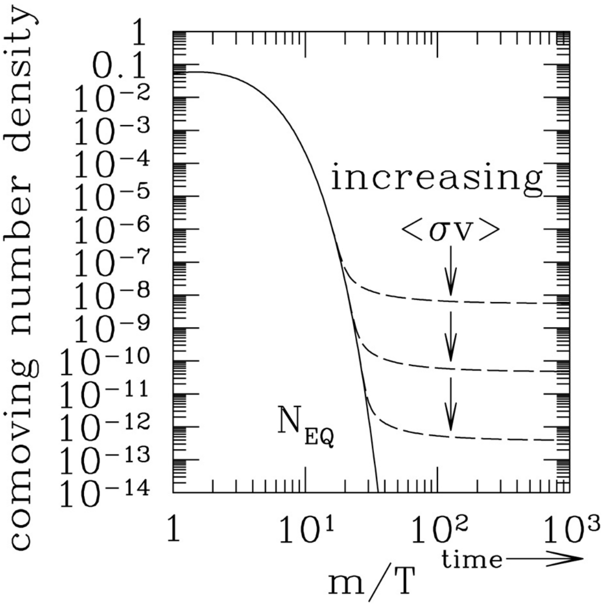

Figure 2.28: Evolution of a typical WIMP number density in the early universe. The number of WIMPs in a volume expanding with the universe (comoving density) first decreases exponentially due the Boltzmann factor $e^{-M_\chi/T}$ and then freezes out to a constant value when the WIMP annihilation reactions cannot maintain chemical equilibrium between WIMPs and standard model particles. As shown in the figure, WIMPs with larger annihilation cross section end up with smaller densities. Figure from Jodi Cooley's talk at TAUP.

2.8.6 Exotic Dark Matter Candidates

In addition to the candidates described above, a number of other possibilities have been proposed to explain the apparent need for dark matter. Each of them represents physics beyond the Standard Model of particle physics. Let' review some of these below.

---

[6] The numerical solution of the Boltzman equation was first attempted by Lee-Weinberg (1977) and by Stephen Wolfram (1979).

SuperWIMPs

The basic idea is as follows, consider models with high-scale supersymmetry-breaking (supergravity models) and R-parity[7]. If the lightest supersymmetric particle (LSP) is the neutralino, with mass and interaction cross section set by the weak scale M_{weak} ∼100 GeV − 1 TeV, such models are well-known to provide an excellent dark matter candidate, which naturally freezes out with the desired relic density [198, 199]. This scenario relies on the (often implicit) assumption that the gravitino is heavier than the lightest standard model superpartner. However, even in simple and constrained supergravity models, such as minimal supergravity [200, 201, 202, 203], the gravitino mass is known only to be of the order of M_{weak} and is otherwise unspecified. Given this uncertainty, assume that the LSP is not a standard model superpartner, but the gravitino. The lightest standard model superpartner is then the next-lightest supersymmetric particle (NLSP). If the universe is reheated to a temperature below $\sim 10^{10}$ GeV after inflation [204], the number of gravitinos is negligible after reheating. Then, because the gravitino couples only gravitationally with all interactions suppressed by the Planck scale $M_{Pl} \simeq 1.2 \times 10^{19}$ GeV, it plays no role in the thermodynamics of the early universe. The NLSP therefore freezes out as usual; if it is weakly-interacting, its relic density will again be near the desired value. The WIMP decays to the LSP, converting much of its energy density to gravitinos. Gravitino LSPs therefore form a significant relic component of our universe, with a relic abundance naturally in the desired range near $\Omega_M \simeq 0.23$ [205].

Models with weak-scale extra dimensions also provide a similar dark matter particle in the form of Kaluza-Klein gravitons [197], with Kaluza-Klein gauge bosons or leptons playing the role of WIMP [206]. As such dark matter candidates naturally preserve the WIMP relic abundance, but have interactions that are weaker than weak, we refer to the whole class of such particles as superWIMPs.

WIMPZillas and Q-Balls

This class of particles, also called super heavy relics (or super heavy dark matter) were proposed as a generic class for dark matter candidates. WIMPZillas are extremely massive WIMPs ($M \sim 10^{13}\,\mathrm{GeV/c^2}$), but very low in density. WIMPZillas are produced gravitationally at the end of the inflation as result of the expansion of the

---

[7] R-parity is a concept in particle physics, which arise mainly in theory such as the supersymmetric extension of the Standard Model. In this theory, baryon number and lepton number are no longer conserved by all of the renormalizable couplings in the theory. Since baryon number and lepton number conservation have been tested very precisely, these couplings need to be very small in order not to be in conflict with experimental data. R-parity is a symmetry acting on the Minimal Supersymmetric Standard Model (MSSM) fields that forbids these couplings and can be defined as:

$$R = (-1)^{3(B-L)+2s},$$

where s is the particle's spin,B is the baryon number, and L is the lepton number [87, 88, 89]. All Standard Model particles have R-parity of 1 while supersymmetric particles have R-parity -1. As possible origins of R-parity, a very attractive way to motivate R-parity is with a B-L continuous gauge symmetry which is spontaneously broken at a scale inaccessible to current experiments. A continuous forbids renormalizable terms which violate B and L [90, 91, 92, 93]. If is only broken by scalar vacuum expectation values (or other order parameters) that carry even integer values of $3(B-L)$, then there exist an exactly conserved discrete remnant subgroup at our scale which has the desired properties [94, 95]. This phenomenon can arise as an automatic symmetry in SO(10) grand unified theories. This natural occurrence of R-parity is possible because, in SO(10), the Standard Model fermions arise from the 16-dimensional spinor representation, while the Higgs arises from a 10 dimensional vector representation. In order to make the coupling of the group SO(10) invariant, one must have an even number of spinor fields (i.e. there is a spinor parity). After GUT symmetry breaking, this spinor parity descends into R-parity so long as no spinor fields were used to break the GUT symmetry [96, 97].

universe. These particles can carry electric charge and color and are as well proposed as source of ultra high energy cosmic rays.

Q-Balls instead, are solitons that come from SUSY and a wide range of particles physics models. They can satisfy dark matter constraint over a wide range of mass and possibly decay into neutrralinos. It is believed that Q-Balls interact with ordinary matter, so experiments such as ANTARES, IceCube and Super-K, may be able to detect them in the future.

Q-Balls might have been produced in the early universe by three mechanisms: phase transitions, solitosynthesis (which is analogous to nucleosynthesis), i.e. once the universe drops below some critical temperature, Q-Balls can minimize the energy and the free energy of the system and rapid coalescence can occur. The third mechanism that produce Q-Balls is the fragmentation of the scalar condensate at the end of inflation. At the end of inflation, scalar fields rolling down a potential can encounter instabilities or oscillations which can produce particles that we call Q-Ball. Although Q-Balls interaction with matter solves the cold dark matter problem, however there are few serious issues that this class of particles faces; the central cusp problem is the well known one.

It is also worth mention that other and more exotic dark matter candidates were proposed: D-particles, Axinos (supersymmetric partner of the axions) and Mirror Matter [207]. These particles are less interesting than the ones I have briefly discussed and given the scope of this work, I do not intend discuss them in detail.

2.8.7 Modified Gravity (MOND)

Modified Newtonian Dynamics (MOND) is a theory that modifies Newton's force law to explain observations that most astronomers interpret as evidence for dark matter (flat rotation curves). However the observations of Bullet Cluster has offered the best evidence against MOND and MOND-like theories and some of the best evidence for dark matter [208].

Milgrom, in 1983, proposed a modification of Newtonian dynamics (MOND) in order to explain observations that the scientific community believed was an indication of the presence of a weakly interacting massive particles or dark matter. Milgrom formulated MOND and described how it would explain various observational laws [208].

One way to modify Newtonian dynamics would be to modify Newton's gravitational force law such that it matches these rotation curves. To lessen the dependence on distance of the gravitational force for large radii is what Milgrom suggested that may be the strength of the gravitational force change as the distance increase. Above a certain distance r_0, gravity may have a different dependence than what we normally know and proposed the following modification:

$$F_g = \frac{GMm}{r^2} f(r/r_0), \tag{2.50}$$

with $f(r/r_0) = 1$ if $r \ll r_0$ and $f(r/r_0) = r/r_0$ if $r \gg r_0$ (r_0 is the minimal distance where the Newtonian gravitation field starts to behave unusually). According to this theory, Newton's second law of dynamics will be equally modified and can be written as

$$\vec{F} = m\vec{a}\mu(a/a_0), \tag{2.51}$$

where with $\mu(a/a_0) = 1$ if $a \ll a_0$ and $\mu(a/a_0) = a/a_0$ if $a \gg a_0$. The true gravitational acceleration $\vec{g}$ relates to the Newtonian gravitation acceleration $\vec{g}_n$ by

$$\vec{g}_n = \vec{g}\mu(g/a_0). \tag{2.52}$$

The above aforementioned equations (2.50) through (2.52) were used by MOND to explain the Tully-Fisher Law - that a galaxy's mass M and its its rotational velocity V are related by $M \propto V^{\alpha}$ in K-band luminosity. From Equation (2.52), one can see that in the low acceleration regime $g = \sqrt{g_n a_0}$. Setting $g = V^2/r$ yields

$$V^4 = GMa_0 \tag{2.53}$$

which reproduced the Tully-Fisher law. By taking the logarithm of the equation (2.53), one can derive the following relation

$$\log(L) = 4\log(V) - \log(Ga_0) - \log(M/L) \tag{2.54}$$

Taking the last term of the above equation to be $log(< M/L >)$, with $< M/L >$ the average mass-to-light ratio of the galaxy. So, given the mass-to-light ratio curve as function of the B-V color, one can use the equation (2.54), to determine the acceleration scale a_0 that differentiates MONDian dynamics from Newtonian dynamics. With an acceleration scale, estimate to be $a_0 \sim 10^{-8}$ cms^{-2}. Realizing that $a_0 \sim cH_0$ within a factor of 5-6, Milgrom speculated that MOND may have applications in cosmology.

Although MOND was succesful in fitting the flat rotation curves, MONDian force (Equation (2.51)) does not obey linear momentum conservation, which is a big theoretical obstacle. Recently, Bekenstein, in 2004 [98], formulated the Tensor-Vector-Scalar (TeVeS) theory of gravity, in which he effectively invented a theory of general relativity that obeys MOND's requirements which can be useful when comparing MOND cosmology to that of the Cold Dark Matter (CDM) models, but MOND has still lots of caveats in order to be accepted as an alternative explanation of flat rotation curves. MOND does not reproduce the whole spectrum of observation that GR is able to do. The observation of the bullet cluster is one solid ground that sufficient to rule out MONDian theory.

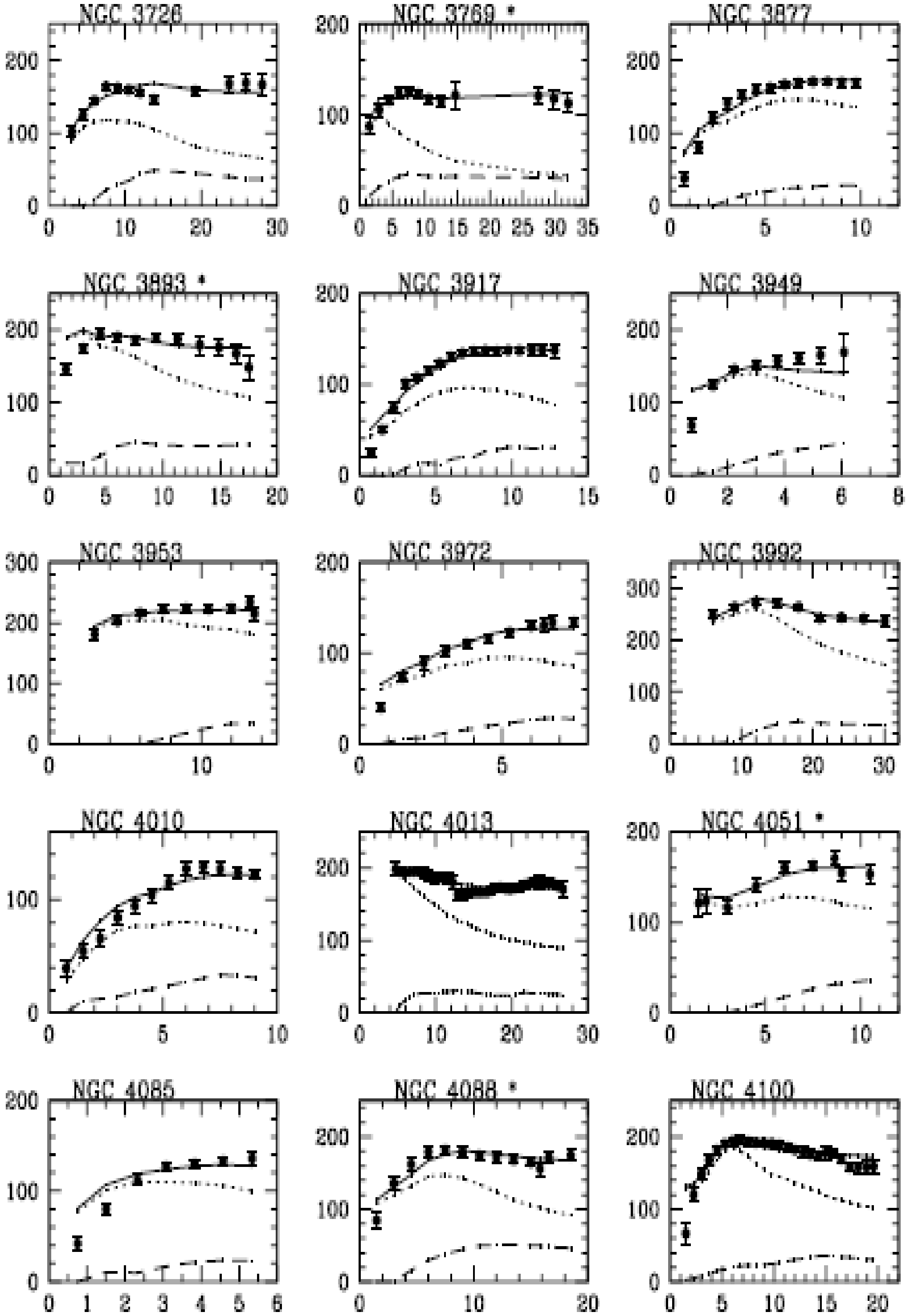

Figure 2.29: With only the M/L ratio as a free parameter, MOND fitted well a variety of galactic rotation curves, such as those of these Ursa Major spiral galaxies at 15.5 Mpc. Figure from ([208]).

Chapter 3

WIMP Signatures and Detections

3.1 Introduction

Weakly interacting massive particles (WIMPs) are a well motivated class of non-baryonic dark matter in the universe and within our very own galaxy, the milky way. Astrophysical evidence provides strong constraints on dark matter, but they do not provide answers to some questions such as the exact mass of dark matter is, its spin and cross section on a known target nucleus, etc. Observations of dark matter interactions can provide answers to some of these questions.

WIMPs can be detected either directly by scattering off nuclei whose recoil can be measured, or indirectly by observing the annihilation products of WIMPS in the cosmos. In indirect detection, the idea is that if WIMPs are abundant in space, they may scatter and annihilate each other producing secondary products such as gamma rays, cosmic rays and particles such as neutrinos. One can therefore devise an experiment to observe these annihilation products. I have reserved an entire section in this chapter to discuss in some detail the techniques and status of indirect dark matter searches.

In a direct dark matter search, WIMPs interact with nuclei by weak interactions and produce nuclear recoils. In this approach, experimentalists measure the amount of energy deposited in the crystal by a dark matter interaction. The information on the WIMP kinetic energy distribution can then be obtained from the distribution of the energy deposited.

The cryogenic dark matter search (CDMS), and many other experiments searching for dark matter by a direct detection, measures the energy deposited for nuclear recoils induced by WIMP interactions. The experiments also measure recoils produced by the backgrounds (such as gamma rays) which are far more dominant than the rate expected for dark matter interactions.

In this chapter, I cover some of the basics of direct and indirect detection of weakly interacting massive particles (WIMPs). Section (3.2) will describe the physics of the direct search: the expected WIMP flux, WIMP elastic scattering, spin-independent and dependent scattering cross-section and the expected WIMP rate. Section (3.4), however, introduces the grounds for an indirect dark matter search which measure a wide range of annihilation signatures. Indirect detection experimental signatures are discussed in section (3.5) while direct search of dark matter discussion is done under the section (3.6). Some useful techniques and strategies for suppressing the backgrounds which dominate the weak expected signal from nuclear recoils are discussed as well in this last section.

3.2 WIMP Detection

The effort for detecting dark matter which is believed to pervade the universe is currently on-going around the world. This broad experimental program tasked specifically for searching for and characterizing the dark matter is of an utmost importance. In this section, I am going to review some of the techniques employed in the effort to detect WIMP dark matter.

Direct detection experiments attempt to observe the recoil from the elastic scattering of dark matter particles interacting with nuclei in a detector. Indirect detection experiments are designed to observe and identify the annihilation products of WIMPs, such as gamma-rays, neutrinos, cosmic rays, and emission at radio/microwave wavelengths. Alternatively, one could potentially produce and observe dark matter particles in collider experiments, such as at the Large Hadron Collider (LHC). These detection techniques are therefore generally grouped into one of three categories: **direct production at a particle collider**; **indirect detection of WIMP-annihilation products** and **direct detection of WIMPs interacting with terrestrial matter**. The direct detection schemes are based on WIMP scattering off the nuclei on terrestrial detectors and give off a nuclear recoil which can be measured by means of various techniques discussed in section (3.6.2). However, as for indirect detection methods, the WIMP annihilation rate scales as the square of the WIMP density. Therefore, the most luminous sources are expected to be near the Galactic center of dark matter sub-halos, where the dark matter density peaks [212, 213, 214, 215, 216, 217]. In addition, the Sun and Earth capture WIMPs and may be seen as sources of WIMP annihilation [218, 219, 220, 221, 222]. In all cases, the annihilation rate is sensitive to the dark matter's phase space structure. Finally, WIMPs can also be be produced in collider experiments (such as Large Hadron Collider at CERN) with sufficient energy reach.

It is quite remarkable to note that each of these approaches has their advantages and disadvantages. Moreover, it is interesting to note that all these strategies for detecting dark matter particles have reached, or are about to reach the level of sensitivity that has long been anticipated to be required to observe most postulated varieties of WIMPs.

3.3 Direct Detection

3.3.1 WIMP Flux

The halo profile for the milky way predicts a dark matter density of $\rho_0 \approx 0.3$ GeV/cm^3. Assuming a WIMP mass of $M_\chi = 100$ GeV/c^2, one expects a flux of

$$\Phi = \frac{\rho_0 v_0}{M_\chi} \approx 7 \times 10^4 \,\mathrm{cm}^{-2}\mathrm{s}^{-1}. \tag{3.1}$$

For CDMS detectors which have an area of $\sim 45\,\mathrm{cm}^2$, there will be $\sim 3.2 \times 10^6$ WIMPs per second crossing the detector. There is an abundance of particles to be detected, if the cross-sections are high enough. The possibility of directly detecting certain dark matter candidates was suggested by Goodman and Witten, who pointed out the importance of coherent interactions between dark matter particles and nuclei [209].

3.3.2 WIMP elastic scattering

Relic WIMPs have weak-scale cross-sections for annihilating to standard model particles. They may also be expected to have weak-scale cross-sections for elastic scattering on standard model particles (cross section of the order of 10^{-27} cm^2). The form and magnitude of these interactions depends on the precise model considered. Even within the constrained minimally supersymmetric standard model or cMSSM, there are many adjustable parameters that affect the cross-sections. However, we can write a general framework for WIMP-nucleon scattering, with two classes of interactions:

1. spin-independent interactions which couple to the entire nucleus; and
2. spin-dependent interactions which couple to unpaired spins.

WIMPs are bound within the galactic halo and they travel at typical galactic velocities in the solar neighborhood, velocities of about ~ 250 km/s $\sim 10^{-3}c$. A WIMP with mass M = 100 GeV/c^2 will possess a kinetic energy of $E_\chi = \frac{1}{2} M_\chi v^2 \approx 50$ keV. In an elastic collision with a stationary target of mass M_T, the recoil energy E_R is given by:

$$E_R = \frac{2M_T M_\chi}{(M_T + M_\chi)^2} E_\chi \cdot (1 - \cos(\theta)) = \frac{1}{2} r \cdot E_\chi \cdot (1 - \cos(\theta)) \tag{3.2}$$

with $r = \frac{4M_T M_\chi}{(M_T+M_\chi)^2}$ the kinematical factor. The mean kinetic energy of the recoiling target is obtain by averaging over every possible recoil scattering angle θ:

$$\overline{E}_R = \frac{2M_T M_\chi}{(M_T + M_\chi)^2} E_\chi \tag{3.3}$$

and the maximum recoil energy will be twice the energy given in the equation 3.3. For a germanium target (Ge) of atomic mass 72.61 a.m.u. (where a.m.u. stands for atomic mass unit, 1 a.m.u = 0.93146 GeV/c^2), $M_T c^2 \approx 67$

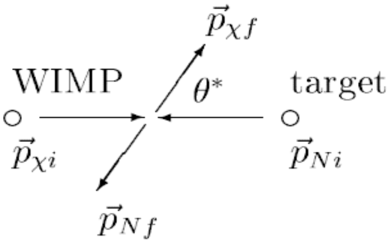

Figure 3.1: Illustration of WIMP scattering in the center of mass frame. Incoming WIMPs, with an initial momentum $\vec{p}_{\chi^i}$, scatter off a target nucleus at rest. In the center of mass frame, the target's momentum is $\vec{p}_{N^i} = -\vec{p}_{\chi^i}$. After scattering, each of these particles recoils in different direction deflected by an angle θ^*, the scattering angle. $\vec{p}_{\chi^f}$ and $\vec{p}_{N^f}$ the WIMP and target final momenta. Figure from [339].

GeV. Furthermore, assuming an elastic collision between a 100 GeV/c^2 galactic WIMP and a Ge nucleus, one will expect the nucleus to recoil with typical kinetic energy of $\sim$ 25 keV. This energy deposition is detectable in a variety of low-threshold particle detectors.

Let us now consider a WIMP-electron collision. Following the same reasoning as above, one expects the electron to recoil with an energy less than 1 eV of kinetic energy. This energy is not enough to ionize a single charge carrier. So, direct detection efforts therefore focus upon WIMP-induced nuclear recoils.

A 100 GeV/c^2 galactic WIMP has a de Broglie wavelength of $\lambda = \frac{h}{M_\chi v}$ which is about $\approx$ 12 fm corresponding to the diameter of a large atomic nucleus. Therefore, an incident WIMP will interact coherently with an entire atomic nucleus rather than scattering off of single nucleons. Such a large wavelength means that WIMPs will see the nucleus at this scale of resolution and cannot resolve individual nucleons). The cross section calculations must account for constructive or destructive interference among the individual WIMP-nucleon scattering amplitudes.

WIMP-nucleon scattering amplitude takes different forms depending on the WIMP's spin and the symmetries of its couplings. The possible interaction symmetries described by the standard model of particle physics are scalar, pseudoscalar, vector, axial-vector, tensor, or pseudotensor. It is, however, demonstrated by Kurylov and Kamionkowski [210], that only scalar and axial-vector terms survive in the extreme non-relativistic limit; the remaining terms are either suppressed by large factors or can be absorbed into these two. In this limit, the general interaction Lagrangian becomes

$$\mathcal{L}_{\chi N} = 4\chi^\dagger\chi\left(f_p\eta_p^\dagger\eta_p + f_n\eta_n^\dagger\eta_n\right) + 16\sqrt{2}G_F\chi^\dagger\frac{\vec{\sigma}}{2}\chi\left(a_p\eta_p^\dagger\frac{\vec{\sigma}}{2}\eta_p + a_n\eta_n^\dagger\frac{\vec{\sigma}}{2}\eta_n\right) \tag{3.4}$$

where χ is the WIMP wavefunction, a_p and a_n are the proton and neutron Weyl spinors, $\vec{\sigma}$ is the spin operator (Pauli spin matrices), and G_F is the Fermi constant ($G_F = \frac{g^2}{4\sqrt{2}M_W^2}(\hbar c)^3$) , g is the electro-weak (weak interaction) coupling constant and M_W is the W-boson mass). The WIMP-nucleon interaction is characterized by five parameters: the WIMP mass M_χ, the spin-independent (SI) couplings f_p and f_n, and the spin-dependent (SD) couplings a_p and a_n.

In the subsequent sections I will describe these two particular classes of interactions (spin-dependent and spin-independent WIMP-nucleon interaction cross sections). I will as well discuss the WIMP event rates for nuclei of interest used as target materials in direct dark matter detection experiments.

3.3.3 Spin-Independent Scattering

To calculate the WIMP-nucleus elastic-scattering cross section, we follow the standard review on the subject by Lewin and Smith [211]. In the case of spin-independent interactions, the procedure is fairly straightforward. The spin-independent interaction is very simple, with an effective WIMP-nucleon interaction

$$\mathcal{L}_{\chi-n}(\vec{x}) = f_n\overline{\chi}(\vec{x})\chi(\vec{x})\overline{n}(\vec{x})n(\vec{x}) \tag{3.5}$$

where $\chi(\vec{x})$ is the neutralino (or simply a WIMP, weakly interacting massive particle) and $n(\vec{x})$ is the nucleon wavefunctions. In minimal supersymmetry, the couplings of WIMPs to neutrons and protons are the same and take a common value f_n [174, 175, 176]. The nucleus can be approximated as a collection of nucleons with overlapping wavefunctions, so an effective WIMP-nucleus interaction may be written in the following form

$$\mathcal{L}_{\chi-n}(\vec{x}) = f_n\overline{\chi}(\vec{x})\chi(\vec{x})\sum_{k=1}^{A}\overline{n}_k(\vec{x})n_k(\vec{x}) \tag{3.6}$$

The differential cross section is easily calculated using Fermi's Golden rules:

$$\frac{d\sigma}{dq^2} = \frac{1}{\pi v^2}|\mathcal{M}(\vec{q})|^2 \tag{3.7}$$

The factor $1/(\pi v^2)$ arises from the final-state density of states and the standard Golden Rule $2\pi/h$ factor. $\mathcal{M}(\vec{q})$ is the scattering matrix element characterizing the transition from the final to the initial states. In the context of this computation, the matrix elements $M(\vec{q})$ characterize the transition from a nucleus at rest to a nucleus with momentum $\vec{q}$. The scattering matrix element $M(\vec{q})$ is obtained by integrating the interaction-Lagrangian density (3.7) over the whole space

$$\mathcal{M}(\vec{q}) = f_n\sum_{k=1}^{A}\int d^3x|n_k(\vec{x})|^2e^{i\vec{q}\cdot\vec{x}} \tag{3.8}$$

The quantity $|n_k(\vec{x})|^2$ is the probability of the k^{th} nucleon being at $\vec{x}$. The probability of any nucleon being at $\vec{x}$ is the sum over all nucleons given above. The A- dependence is factored out, leaving the probability $\rho(\vec{x})$ of a given nucleon being at $\vec{x}$ averaged over all nucleons. Therefore, the scattering matrix becomes:

$$\mathcal{M}(\vec{q}) = f_nA\int d^3x\rho(\vec{x})e^{i\vec{q}\cdot\vec{x}} = f_nAF(\vec{q}) \tag{3.9}$$

where $F(\vec{q})$ is the Fourier transform of $\rho(\vec{x})$, called the form factor which is a measure of the scattering amplitude of a wave by an isolated atom. The form factor expresses the dependence of the interaction on the shape of the nucleus, given by the density $\rho(\vec{x})$.

If we assume for now that the WIMP-proton and WIMP-nucleon couplings, f_p and f_n, may be different, a complete calculation from [239] and references therein show that

$$\mathcal{M}(\vec{q}) = [f_p Z + (A - Z) f_n] \cdot F(\vec{q}) \tag{3.10}$$

As the transfer momentum $\vec{q}$ rises, the nuclear structure becomes important, with the exact dependence encoded in $F(\vec{q})$. There are several commonly used models of $F(\vec{q})$. We adopt the form factor of Lewin and Smith [211]; this is the Helm form factor defined by

$$F(qr_n) = \frac{3j_1(qr_n)}{qr_n} e^{-(qs)^2/2} \tag{3.11}$$

where $j_1(q) = \frac{\sin(qr_n) - qr_n \cos(qr_n)}{(qr_n)^2}$ is a spherical Bessel function and $\vec{q}$ is the momentum transfer. Given a nuclear recoil energy E_R and a given target mass A, the momentum transfer is given by: $q = \sqrt{2M_T E_R}$ as

$$q = \sqrt{2 \cdot 0.932(GeV/c^2) \cdot A \cdot E_R(keV)} \tag{3.12}$$

The parameter r_n is defined as

$$r_n = \sqrt{c^2 - 5s^2 + \frac{7}{3}\pi^2 a^2} \tag{3.13}$$

with $s = 0.9$ fm, $a = 0.53$ fm and $c = (1.23A^{1/3} - 0.60)$ fm. The effective nuclear radius r_n can be approximately found by fitting muon scattering data to a Fermi distribution. The form factor (3.11) is taken as a good fit to the lepton-nucleus scattering data down to $A \approx 10$. The value of r_n (3.13) and other aforementioned quantities have been chosen to make the equation (3.11) approximately equal to the Fourier transform of the Woods-Saxon formula, which is a two-parameter Fermi distribution giving the spatial distribution of charges in the nucleus. Therefore the form factor $F(q)$ amounts to a fit of a fit. More sophisticated approaches are based on electron elastic scattering data rather than model-dependent parameterizations. Lewin & Smith formula has been found to be an acceptably close match and has been adopted as a working standard by most direct-detection experiments. Combining the equation (3.7) and (3.10), we obtain the differential spin-independent scattering cross-section:

$$\frac{d\sigma}{d|\mathbf{q}|} = \frac{1}{\pi v^2} [f_p Z + (A - Z) f_n]^2 \cdot |F(\vec{q})|^2 \tag{3.14}$$

where A and Z are the atomic mass and atomic number of the target material, v is the WIMP velocity, q is the transferred momentum. $F(q)$ is the form factor that accounts for the momentum distribution of nucleons in the target. The couplings f_p and f_n to protons and neutrons are typically similar, and depend on the scattering processes available to a given type of WIMP. The cross-section does not scale linearly with the size of the nucleus, but quadratically. This arises because the neutralino can interact coherently with the entire nucleus rather than with a single nucleon, as long as the momentum transferred is not too large. The coherence in scattering happens when the momentum transfer q corresponds to a wavelength much larger than the nucleus size, so the scattering

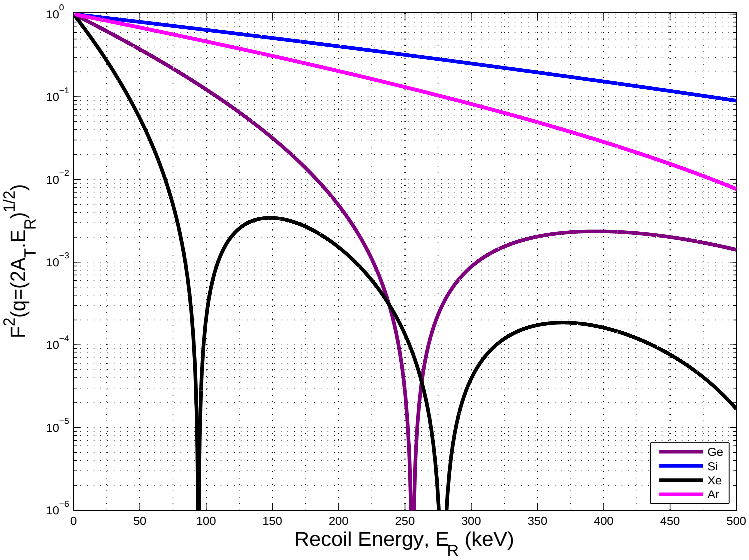

Figure 3.2: Helm nuclear form factor as function of nuclear recoil energy for four different target materials: germanium (Ge), silicon (Si), xenon (Xe) and argon (Ar). Germanium and Silicon are the two target used in CDMS experiment; Xenon and Argon are used in other dark search experiments such as Xenon10 (Xe100) and MiniClean. The minima in Ge and Xe curves are resonances caused by destructive interference of scattering amplitudes when the WIMP wavelength becomes comparable to the size to the size of the nucleus.

is fully coherent.

The energy dependence of the differential WIMP-nucleon cross section can be written in terms of σ_{0WN} which is independent of the momentum transfer and the form factor $F^2(q)$, i.e.

$$\frac{d\sigma}{d|\mathbf{q}|} = \frac{\sigma_{0WN}}{4\mu_A^2 v^2} F^2(q) \tag{3.15}$$

with

$$\sigma_{0WN} = \frac{4\mu_A^2}{\pi}[f_p Z + (A - Z) f_n]^2 \tag{3.16}$$

where v, in equation (3.15), is the velocity of the WIMP in the lab frame, and $\mu_A = \frac{M_\chi M_T}{M_\chi + M_T}$ is the WIMP-nucleus reduced mass in terms of the WIMP mass M_χ and the mass M_T of a target nucleus of atomic mass A. Supersymmetric models predict that the coupling constants f_p and f_n are identical, reducing the cross section (3.16) to

$$\sigma_{0WN} = \frac{4\mu_A^2}{\pi} f_n^2 A^2 \tag{3.17}$$

This effect is called coherent enhancement and it can be enormous for scalar interactions compared to axial vector interactions (or spin-dependent) as we will see shortly. Assuming a germanium target, $A_{Ge}^2 \approx 5000$, so a WIMP target built of heavy nuclei is vastly more sensitive to WIMP interactions than one composed of lighter nuclei. For real collisions with non-zero momentum transfer, the various WIMP-nucleon scattering amplitudes will not interfere perfectly constructively and the actual cross section will be somewhat less than that in equation (3.15). This reduction is embedded in as a multiplicative effect coming from the nuclear form factor $F^2(q)$, the normalized Fourier transform of the nuclear density distribution with the following bound: $0 < F^2(q) < 1$.

The dependence of this cross section on the target material in (3.17) may be factored out by rewriting this result as

$$\sigma_{0WN} = \sigma_{SI}\frac{\mu_A^2}{\mu_n^2}A^2 \tag{3.18}$$

where μ_n is the reduced mass of the WIMP-nucleon system. The spin-independent cross section of a WIMP on a single nucleon thus becomes:

$$\sigma_{SI} = \frac{4\mu_n^2 f_n^2}{\pi} \tag{3.19}$$

Figure (3.2) shows the form factor as a function of the transfer momentum for several target nuclide. Note the periodic deep troughs in $F^2(q)$, which corresponds to the momentum transfers yielding completely destructive interference across the nucleus. These dips in sensitivity occur at lower momentum transfers for heavier target nuclei, somehow counteracting their A^2 sensitivity enhancement over light nuclide. A target made of a heavy nuclide, such as Xe, must run at a low detector threshold to see the same event rate as a comparable mass of Ge. The event rate of a light nuclide (Si or Ar) experiment varies comparatively little with threshold.

3.3.4 Spin-Dependent Scattering

The spin-dependent cross section is the most complicated to derive. Following the recipes given by G. Jungman, M. Kamionkowski and K. Griest [237] , the spin-dependent differential cross section can be be written as

$$\frac{d\sigma_{SD}}{dq^2} = \frac{8}{\pi v^2}G_F^2\Lambda^2 J(J+1)F_S^2(q) \tag{3.20}$$

with Λ a coefficient that depends both on particle physics on the particular assumption for the distribution of the nuclear spin J among the nucleons (if the interaction is through Z exchange, the particle-physics piece of Λ is 1 while the nuclear-spin piece is nontrivial; if the interaction is via exchange of a different particle, such as a squark, Λ may also contain correction factors due to different couplings and propagators). $F_S^2(q)$ is the spin-dependent form factor which depends on the transfer momentum q.

The parameter Λ is calculated using the single-particle shell model. All nucleons are assumed to be paired into spin singlets except for possibly one unpaired proton and one unpaired neutron. It is assumed that the total spin J of the nucleus is given by the spin and orbital angular momenta of these unpaired nucleons, and the interaction is assumed to be mediated by virtue of a Z-boson exchange so Λ contains only spin factors.

If we consider the case of a single unpaired nucleon, so that only one nucleon's spin $\vec{S}$ and angular momentum $\vec{L}$ which determine the nucleon's total angular momentum $\vec{J} = \vec{L} + \vec{S}$. The nuclear Hamiltonian depends on the square of the total angular momentum $J^2 = (\vec{L}^2 + \vec{S}^2)^2$. The projection of $\vec{S}$ along $\vec{J}$ is given by $\vec{S} \cdot \vec{J} = \frac{1}{2}(\vec{J}^2 - \vec{L}^2 + \vec{S}^2)$ and commutes with the Hamiltonian. The expectation value $\langle \vec{S} \cdot \vec{J} \rangle$ is nonzero, whereas the expectation values of the other projections of $\vec{S}$ vanish. It is therefore this projection to which the WIMP spin may couple. Thus, the WIMP-nucleus spin-dependent coupling satisfies the following relation

$$\Lambda = \left[\frac{\vec{J}.\vec{S}}{J^2}\right]^2 \tag{3.21}$$

which can be expanded to

$$\Lambda = \left[\frac{J(J+1) - L(L+1) + \frac{3}{4}}{2J(J+1)}\right]^2 \tag{3.22}$$

According to [237], the above formula can be generalized to the following form

$$\Lambda = \frac{1}{J}\left[a_p \langle S_P \rangle + a_n \langle S_n \rangle\right] \tag{3.23}$$

with a_p and a_n the proton and neutron spin-dependent coupling constants to WIMPs. Authors in the reference [237] combined the equations (3.20) and (3.23) to obtain a more generally known expression given by:

$$\frac{d\sigma_{SD}}{dq^2} = \frac{8(J+1)}{\pi v^2} G_F^2 \mu_A^2 \left[a_p < S_P > + a_n < S_n >\right]^2 \tag{3.24}$$

with $\mu_A = \frac{M_\chi M_A}{M_\chi + M_A}$ is the WIMP-nucleus reduced mass.

In the non-relativistic limit, axial-vector couplings (characterized by coefficients a_p and a_n) give amplitudes proportional to the inner product of the WIMP and nucleon spins. Since the interaction amplitude switches signs when the nucleon spin is flipped, a WIMP's spin-dependent interaction amplitudes with two nucleons of opposite spin will interfere destructively in the zero-momentum-transfer limit. Nucleons align into spin singlet pairings within nuclei, so spin-dependent cross sections are dominated by unpaired nucleons and vanish entirely for spinless nuclides. This leads to very different constraints on experimental design: experiments targeting spin-dependent interactions generally use light odd-proton or odd-neutron nuclides to maximize the nuclear spin per unit mass, rather than the heavy nuclides preferred for spin-independent sensitive detectors. At vanishing momentum transfer, the WIMP-nucleon spin-dependent interaction cross section is [237]:

$$\sigma_{SD}^0 = \frac{32(J+1)}{\pi J} G_F^2 \mu_A^2 \left[a_p \langle S_P \rangle + a_n \langle S_n \rangle\right]^2 \tag{3.25}$$

The spin expectation values $\langle S_p(S_n) \rangle = \langle N | S_p(S_n) | N \rangle$ (N is the nucleon wavefunction) is obtained from detailed nuclear structure calculations [240, 241]. These calculations also show that an odd-neutron nucleus may have a small but non-zero $\langle S_p \rangle$ (or vice versa) due to polarization effects within the nucleus. For free nucleons $\langle S_p \rangle = \langle S_n \rangle = \frac{1}{2}$. Table 1 from [238, 239] lists values of $\langle S_p \rangle$ and $\langle S_n \rangle$ for materials commonly used for dark matter searches.

For the extreme case of a spin-dependent WIMP that interacts solely with protons (neutrons), the form factor should depend on the distribution of proton (neutron) spin in the nucleus. The distributions of proton

Table 3.1: Values of the atomic number Z, the total nuclear spin J and the expectation values of the proton and neutron spins within the nucleus S_p and S_n for various nuclei with odd numbers of protons or neutrons, leading to the relative sensitivities to spin-dependent interactions [238, 239].

Nucleus	Z	odd Nuclide	J	$\langle S_p\rangle$	$\langle S_n\rangle$	$\frac{4\langle S_p\rangle^2 J(J+1)}{3J}$	$\frac{4\langle S_n\rangle^2 J(J+1)}{3J}$
^{19}F	9	p	1/2	0.477	-0.004	9.1×10^{-1}	6.4×10^{-5}
^{23}Na	11	p	3/2	0.248	0.020	1.3×10^{-1}	8.9×10^{-4}
^{27}Al	13	p	5/2	-0.343	0.030	2.2×10^{-1}	1.7×10^{-3}
^{29}Si	14	n	1/2	-0.002	0.130	1.6×10^{-5}	6.8×10^{-2}
^{35}Cl	17	p	3/2	-0.083	0.004	1.5×10^{-2}	3.6×10^{-5}
^{39}K	19	p	3/2	-0.180	0.050	7.2×10^{-2}	5.6×10^{-3}
^{73}Ge	32	n	9/2	-0.030	0.378	1.5×10^{-3}	2.3×10^{-1}
^{93}Nb	41	p	9/2	-0.460	0.080	3.4×10^{-1}	1.0×10^{-2}
^{125}Te	52	n	1/2	0.001	0.287	4.0×10^{-6}	3.3×10^{-1}
^{127}I	53	p	5/2	0.309	0.075	1.8×10^{-1}	1.0×10^{-2}
^{129}Xe	54	n	1/2	0.028	0.359	3.1×10^{-3}	5.2×10^{-1}
^{131}Xe	54	n	3/2	-0.009	-0.004	1.8×10^{-4}	1.2×10^{-1}

and neutron spin may be very different in a given nucleus, and so finite momentum effects may be very model-dependent. The preferred way to write the spin-dependent WIMP-nucleus differential cross section is in the following form [242]

$$\sigma^0_{SD} = \frac{8G_F^2}{(2J+1)v^2} S(q) \tag{3.26}$$

where $S(q)$ is the spin dependent structure function which encompasses the effects of finite momentum transfer, as well as values for the neutron and proton spin expectations. There is no universal form for $S(q)$; it is usually calculated separately for each nuclide using nuclear structure models [240, 241].

$$S(q) = a_0^2 S_{00}(q) + a_0 a_1 S_{01}(q) + a_1^2 S_{11}(q) \tag{3.27}$$

with $a_0 = a_p + a_n$ and $a_0 = a_p - a_n$. The functions $S_{ij}(q)$ describe the distribution of spins within the target nucleus, analogously to $F(q)$ in the spin-independent case. There is however no general rules regarding spin-dependent WIMP-nucleus cross sections except that one should use odd-p, odd-n, or odd-p/odd-n nuclei in order to maximize the unpaired nucleon spins.

In many models, spin-dependent WIMP-nucleon interaction cross section is extremely small (due to no coherence) than its analogous spin-independent cross section. As shown in Table 3.1, nuclei with even numbers of protons have nearly no net proton spin and essentially no sensitivity to spin-dependent interactions on protons, and nuclei with even numbers of neutrons similarly have almost no sensitivity to spin-dependent interactions on neutrons. Experiments thus quote limits of the spin-dependent WIMP- proton cross section (σ_{SDp}) separately to spin-dependent WIMP- neutron cross section (σ_{SDn}).

The current direct detection techniques are orders of magnitude away from being sensitive to MSSM WIMPs via spin-dependent interactions.

Note: Natural-germanium detectors used in CDMS are composed primarily of spin-0 isotopes, with only a 7% contribution from ^{73}Ge.

3.3.5 WIMP Rates and Spectra

To get a quantitative intuition of the event rate one expects to observe in dark matter searches, let us begin by assuming for the moment that the WIMP-nucleon scattering cross section is indeed $\sigma \approx 1$ pb (10^{-36} cm^2). Then a 100 GeV/c^2 WIMP would produce a few scatters per day in a kilogram of hydrogen target mass. This is a sufficiently rare rate which requires a carefully built low-background experiment. In this section, I provide a quantitative argument for the expected WIMP-scatter rate and details of the nature of WIMP-nucleon couplings.

For a given WIMP model, it is possible to make some specific assumptions and construct general arguments for rates of interaction of WIMPs in terrestrial detectors and the recoil energy spectra one would expect in such detectors as described by Lewin and Smith [211]. Assuming that the WIMP velocity distribution is Maxwellian, in phase-space such a velocity distribution is given by:

$$f(\vec{v}, \vec{v}_E) = e^{-(v+v_E)^2/v_0^2} \tag{3.28}$$

where $\vec{v}$ is the velocity with respect to the target, $\vec{v}_E$ is the Earth's velocity with respect to the dark matter halo, and v_0 is a characteristic velocity, usually set to the galactic rotation velocity; it is also the most probable WIMP velocity with respect to the Earth. The most probable WIMP velocity is set to $v_0 \simeq 220$ km/s in the vicinity of the Sun while the Earth's velocity, normally defined by $v_E \simeq 244 + 15\cos(2\pi t)$ km/s, where t is the time measured in years since the maximum velocity near June 2^{nd} and the minimum near December 2^{nd} [211]. This sinusoidal functional form approximately captures the motion of the earth relative to the Sun as the solar system orbits the Milky Way.

Now, let us consider a target nucleus with atomic mass M_T measured in atomic mass units (amu). The event rate per unit mass is then given by

$$dR = \frac{N_A}{M_T}\sigma \cdot v \cdot dn \tag{3.29}$$

whit N_A denotes Avogardo's number, σ the WIMP-nucleus cross section, v the velocity of the WIMP impacting on the nucleus and dn is the differential particle density given by

$$dn = \frac{n_0}{k} f(\vec{v}, \vec{v}_E) d^3v \tag{3.30}$$

k is the normalization constant and n_0 is the dark matter particle mean density given by $n_0 = \frac{\rho_\chi}{M_\chi}$ for a WIMP with mass M_χ and local density ρ_χ. The normalization constant, denoted by k, in equation (3.30) is defined such that

$$\int_0^{v_{esc}} dn = n_0 \tag{3.31}$$

where v_{esc} is the escape velocity which is numerically defined by the Rave survey to be $v_{esc} = 545\,\mathrm{km\,s^{-1}}$ [243]. Inserting equation (3.30) into the integral (3.31) over the velocity distribution $f(\vec{v}, \vec{v}_E)$, the normalization constant k takes the following form:

$$k = \int_0^{2\pi} d\phi \int_{-1}^{1} d(\cos\theta) \int_0^{v_{esc}} f(\vec{v}, \vec{v}_E) d^3v \tag{3.32}$$

For a distribution truncated at $|v + v_E| = v_{esc}$, the constant k would be given by

$$k = k_0 \cdot \left[erf(\frac{v_{esc}}{v_0}) - \frac{2}{\sqrt{\pi}} \cdot \frac{v_{esc}}{v_0} \cdot e^{v_{esc}^2/v_0^2} \right] \tag{3.33}$$

where erf is the error function defined by:

$$erf(x) = \frac{2}{\sqrt{\pi}} \int_0^x e^{-t^2} dt \tag{3.34}$$

satisfying the limit erf(x)⟶ 1 when x⟶ ∞. k_0 is the value of the same normalization constant in the simplest case when $v_{esc} = \infty$:

$$k_0 = (\pi v_0^2)^{3/2}. \tag{3.35}$$

It is appropriate to define R_0 as the event rate per unit mass for $v_E = 0$, $v_{esc} = \infty$ and with the zero momentum transfer cross section σ_0,

$$R_0 = \frac{2}{\sqrt{\pi}} \cdot \frac{N_A}{M_T} \cdot \frac{\rho_\chi}{M_\chi} \cdot \sigma_0 \cdot v_0 \tag{3.36}$$

so that the equation (3.29) can be written as

$$dR = R_0 \cdot \frac{k_0}{k} \cdot \frac{1}{2\pi v_0^4} \cdot v f(v, v_E) d^3v \tag{3.37}$$

If one plugs in known numerical values into the equation (3.36), the total WIMP rate thus becomes

$$R_0 = \frac{375}{M_\chi(\mathrm{GeV.c^{-2}})} \cdot \frac{\sigma_{0WN}}{1(\mathrm{pb})} \cdot \frac{\rho_\chi}{0.3(\mathrm{GeV.c^{-3}})} \mathrm{events.(kg.days)^{-1}} \tag{3.38}$$

Equation (3.38) is extremely useful because it predicts the number of events expected in 1 kg.days of exposure. To make this a bit clear, let's illustrate this using the following example. Assuming a 25 GeV/c^2 - WIMP with a WIMP-nucleon cross section σ_{0WN}1 pb, and considering the WIMP density $\rho_\chi = 0.3$ GeVcm^{-3}, the equation (3.38) yield an event rate of $R_0 = 12$ events/kg.days; thus for 1 kg.days of exposure, one expects to observe 12 WIMP events.

The recoil energy of a nucleus struck by a dark matter particle with a kinetic energy $E = \frac{1}{2}M_\chi v^2$ scattered at an angle θ in the center of mass frame is given by the equation (3.2). Assuming isotropic scattering, so that the recoils are uniformly distributed in E$_R$, over the range $0 \leq E_R \leq E \cdot r$, the differential energy-recoil spectrum can be derived by averaging over the incident energy spectrum. According to Figure (3.3)

$$\frac{dR(E_R)}{dE_R} = \int_{E_{min}}^{E_{max}} \frac{dR(E_i)}{E_i r}. \tag{3.39}$$

The maximum initial WIMP energy may be taken as infinity as an initial approximation, however for the sake of generality, I will not do it here. The maximum energy may be computed based upon the Galactic escape velocity, v_{esc}, *i.e.* $E_{max} = \frac{1}{2}M_\chi v_{esc}^2$. To cause a recoil of energy E_R, the minimum initial WIMP energy $E_{min} = \frac{E_R}{r}$ (for head-on scattering, with $\theta = \pi$), and the minimum WIMP velocity $v_{min} = \sqrt{\frac{2E_{min}}{M_\chi}} = \sqrt{\frac{2E_R}{rM_\chi}}$. Therefore the differential rate becomes:

$$\frac{dR(E_R)}{dE_R} = \frac{1}{E_0 r}\int_{v_{min}}^{v_{max}} \frac{v_0^2}{v^2} dR(v) = \frac{R_0}{E_0 r} \cdot \frac{k_0}{k} \cdot \frac{1}{2\pi v_0^2}\int_{v_{min}}^{v_{max}} \frac{1}{v} f(v, v_E) d^3v \tag{3.40}$$

Before quoting the expression for the fully general differential spectrum, it is instructive to consider the case for which $v_E = 0$ and $v_{esc} = \infty$. But before I do, I wanted to draw the reader's attention to the fact that in case of non a zero momentum transfer, the form factor $F(q)$ must be taken into account as it comes from the total integrated cross section momentum-independent σ_0. In such a case, expression (3.40) takes the following form:

$$\frac{dR(E_R)}{dE_R} = \frac{R_0}{E_0 r} \cdot \frac{k_0}{k} \cdot \frac{1}{2\pi v_0^2} F^2(q) \int_{v_{min}}^{v_{max}} \frac{1}{v} f(v, v_E) d^3v \tag{3.41}$$

where $F(q)$ is the same form factor discussed in length in the previous paragraphs ($q = \sqrt{2M_T E_R}$). In the limits where $v_E = 0$ and $v_{esc} = \infty$, the integral in (3.41) is isotropic in v can be evaluated without any difficulty. Therefore, on obtains the following result:

$$\frac{dR(E_R)}{dE_R} = \frac{R_0}{E_0 r} e^{-E_R/E_0 r} F^2(q) \tag{3.42}$$

This limiting case provides some useful insight into the expected WIMP signal without having to resort to numerical calculations. As expected, the differential spectrum as a function of nuclear-recoil energy is essentially a falling exponential. The ability to detect small energy depositions is therefore critical to the sensitivity of a direct-detection experiment; scattering events with the lowest recoil energies are expected to be the most numerous. While a realistic form factor, WIMP-Earth velocity and Galactic escape velocity are important considerations, they (generally) cause only minor modifications to this exponential behavior.

Considering now the limits where $v_E \neq 0$ and $v_{esc} \neq \infty$, the integral (3.41) can be evaluated over the velocity distribution. Under the assumption that $F^2(q) = 1$, the differential recoil rate can be written as [211]:

$$\frac{dR}{dE_R} = \begin{cases} 0 & \text{if } v_{esc} + v_E < v_{min} \\ \frac{R_0 \cdot k_0}{E_0 \cdot r \cdot k} \left\{ \frac{\sqrt{\pi} v_0}{4 v_E} \left[erf(\frac{v_{min}+v_E}{v_0}) - erf(\frac{v_{min}-v_E}{v_0}) \right] - e^{-v_{esc}^2/v_0^2} \right\} & \text{if } 0 < v_{min} < v_{esc} - v_E \\ \frac{R_0 \cdot k_0}{E_0 \cdot r \cdot k} \left\{ \frac{\sqrt{\pi} v_0}{4 v_E} \left[erf(\frac{v_{esc}}{v_0}) - erf(\frac{v_{min}-v_E}{v_0}) \right] - \frac{v_{esc}+v_E-v_{min}}{2 v_E} e^{-v_{esc}^2/v_0^2} \right\} & \text{if } v_{esc} - v_E < v_{min} < v_{esc} + v_E, \end{cases} \tag{3.43}$$

3.4 Indirect Detection

WIMPs can also be detected indirectly, by observation of their annihilation products in the atmosphere. These WIMP-annihilation signatures can be observed in regions of high dark matter density. WIMP-annihilation rates scale as the square of the WIMP number density, i.e

$$\Gamma_{\chi\chi \to X} \sim \rho_\chi^2 \tag{3.44}$$

so the most luminous sources are expected to be near the Galactic center or the center of dark matter sub-halos, where the dark matter density peaks, characterized by a radius R_c, called the halo galactocentric radius. In addition, the Sun and Earth capture WIMPs and may be seen as sources of WIMP annihilation [218, 219, 220,

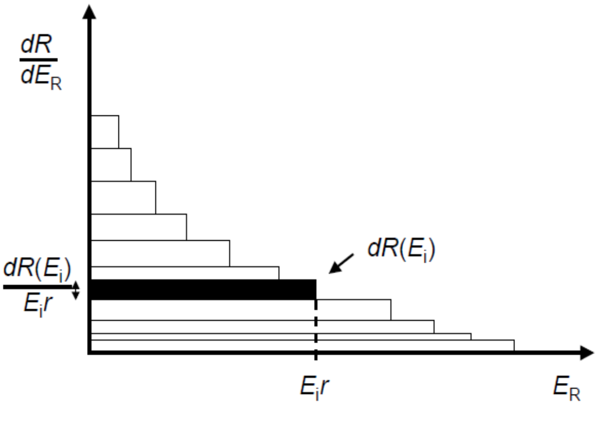

Figure 3.3: Plot showing schematically how contributions to the differential rate dR/dE_R for different values of the initial WIMP energy E_i add. The total differential rate dR/dER of WIMPs with initial energy E_i is defined to be $dR(E_i)$. For a WIMP initial energy E_i, the recoil energy E_R is uniformly distributed between 0 to $E_i r$, so $dR(E_i)$ contributes equally to the rates of all recoils between 0 to $E_i \cdot r$, as depicted by the shaded area in the figure. The contribution to the differential rate at a given recoil energy (the height of the shaded area in the figure) is simply the area divided by the length, or $dR(E_i)/(E_i r)$. The total differential rate can then be found by summing all the boxes. Figure from [239].

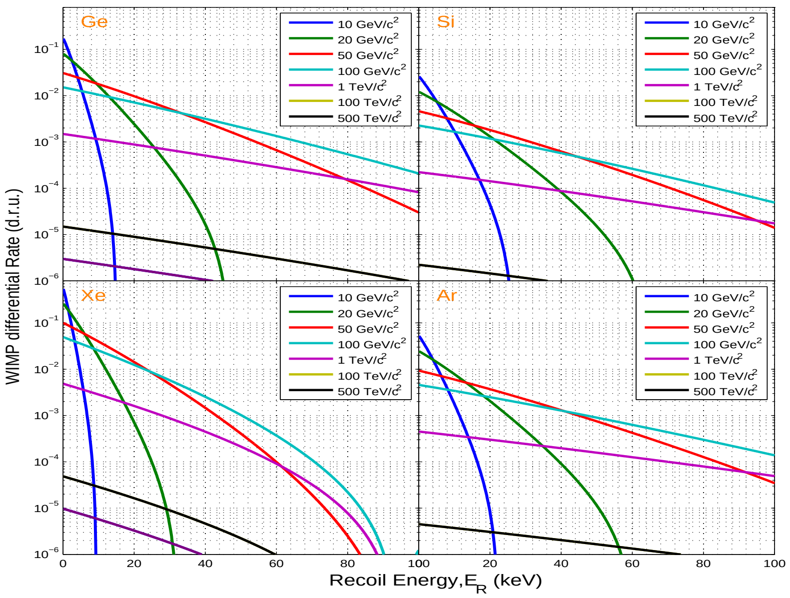

Figure 3.4: WIMP differential rate as function of recoil energy (in keV) plotted for different target material and different WIMP masses (M_χ) from 10 GeV/c^2 to 500 TeV/c^2. The most probable WIMP velocity used in these plots is v_0=220 km/s and the galactic escape velocity is the most recent value of v_{esc} = 545 km/s (as recommended by RAVE survey). The spectra of low-mass WIMPs are softer and they have a cut off at lower energy due to the finite Galactic escape velocity. The spectra of WIMPs heavier than the target nucleus are nearly identical; their rate is 10 times larger for a 100 GeV/c^2 WIMP than for a 1 TeV/c^2 WIMP. High-mass spectra deviate from straight lines due to non-unity form factor F^2. Due to the soft spectra for lower mass WIMPs, these WIMPs produce recoils that are difficult to observe. High-mass WIMPs produces recoils that are easier to detect and have cutoff energies so high as to usually be negligible. The cutoff energy, however, is significant for low-mass WIMPs as it can be noticed in this plot. Experiments will have no sensitivity at all to WIMPs of low enough masses due to the cutoff. Caution should be exerted when drawing conclusions that may be sensitive to the the number of WIMPs with velocities at or near the assumed cutoff energy.

221, 222]. In most cases, the annihilation rate is sensitive to the dark matter's phase space structure. The pair annihilation of weakly interacting massive particles (WIMPs) in the halo is predicted to be an important source of non-thermal particles, including a significant fraction as photons covering a broad multiwavelength spectrum of emission (Bergstrom 2000; Colafrancesco et al. 2006). Despite the fact that galaxy clusters are located at much further distances than the dwarf spheroidal galaxies around the Milky Way, the higher annihilation luminosity of clusters make them comparably good targets for indirect detection of dark matter.

The total annihilation cross section required to produce the WIMP relic density is well known, although highly model-dependent. To calculate the expected rates, the model requires some astrophysical assumptions. These astrophysical assumptions need to be clearly made for parameters that are not well known experimentally. One of these assumptions is the shape of galactic dark matter halo profiles and their clumpiness which can lead to vast differences in WIMP-density assumptions which can as well lead to orders of magnitude in uncertainty on expected rates of annihilation products. Furthermore, if we assume that there exist a WIMP density sufficient to cause a detectable annihilation signal, one difficulty which arises more often is the possibility of unknown rates of the astrophysical background processes which are not associated with dark matter. Therefore, it is difficult to know with certainty that an indirect signal is truly due to WIMP annihilations if one is not able to clearly identify and quantity contributions arising from astrophysical backgrounds. As a result, although an incontrovertible indirect dark-matter signal has still to be uncovered, data from indirect measurements have caused great excitement and controversy within the community. The detectable products of WIMP annihilation depend on several factors: if the WIMP source is too far away, the solid angle subtended by the flux of annihilation products will be too small to be detectable above backgrounds, so nearby sources for which the WIMP density is expected to be large offer the best chance.

In general, indirect dark matter searches seek to detect dark matter annihilation products in anti-matter, gamma rays, neutrinos, etc. The viable place to look for these annihilation products is the galactic center, the Milky way halo, individual dark matter substructures, satellite galaxies, Earth and the Sun. Below in this section, I provide a brief review of the theoretical considerations and then I will briefly describe the experimental signatures of a few of the common indirect search techniques up to date in the field.

3.4.1 Gamma Ray Flux

The flux of gamma rays from WIMP dark matter annihilation in clusters of galaxies is possibly large enough to be detected by current γ-ray telescopes. Also standard astrophysical scenarios have been proposed for γ-ray emission, in particular, collisions of intergalactic cosmic rays and target nuclei from the intracluster medium. Despite these predictions, no significant γ-ray emission has been observed in local clusters by indirect WIMP search experiments such as High Energy Stereoscopic System (H.E.S.S). The expected energy-differential gamma ray flux from dark matter annihilations at an observation direction θ with respect to the galactic center is given by the following equation:

$$\frac{d\Phi_\gamma(E_\gamma, \Delta\Omega)}{dE_\gamma} = \frac{\langle\sigma v\rangle}{8\pi M_\chi^2} \frac{dN_\gamma}{dE_\gamma} \times J(\Delta\Omega) d\Omega \tag{3.45}$$

where $\langle\sigma v\rangle$ is the velocity-weighted annihilation cross-section, M_χ the mass of the dark matter particle and $\frac{dN_\gamma}{dE_\gamma}$ the gamma (photon) spectrum per annihilation. The factor $J(\Delta\Omega)$ defined by

$$J(\Delta\Omega) = \frac{1}{\Delta\Omega} \int_{(\Omega)} d\Omega \int_{los} dl \rho^2(r(l)) \tag{3.46}$$

reflects the dark matter density distribution inside the observing cone subtended by a solid angle $\Delta\Omega$. The annihilation luminosity scales with the squared dark matter density ρ^2, which is conveniently parameterized as a function of the radial distance r from the center of the astrophysical object under consideration. This luminosity is integrated along the line of sight and within an angular region $\Delta\Omega$, whose optimal value depends on the dark matter profile of the target and the angular resolution of the instrument. If dark matter particles produce annihilation to charged final states, internal bremsstrahlung processes can contribute significantly to the high-energy end of the gamma ray spectrum. This effect of the continuous spectrum of secondary gamma rays (from pion decay for example) has to be added to the total spectrum. The magnitude of this effect depends on the intrinsic properties of the dark matter particle.

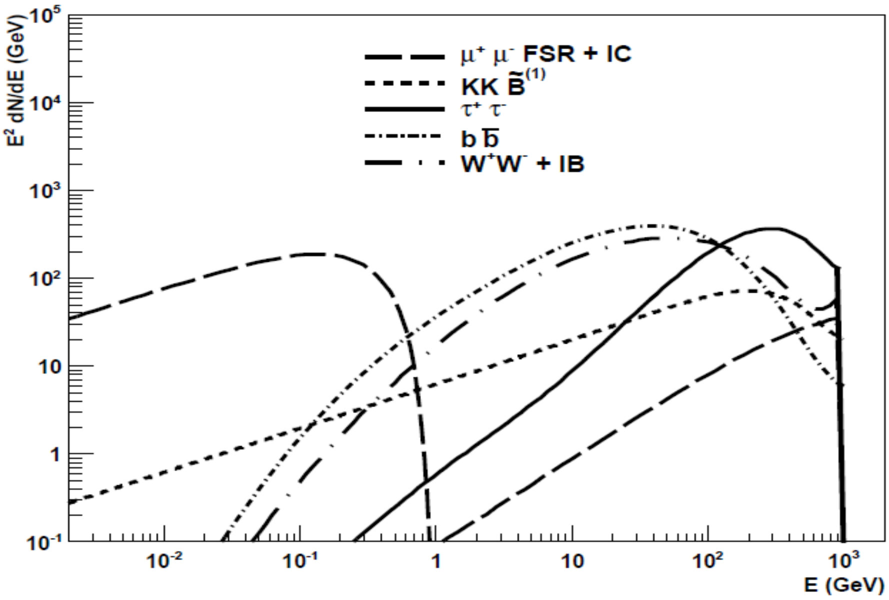

Figure 3.5: gamma spectra for 1 TeV dark matter particles self-annihilating in different channels. Spectra from dark matter annihilating purely into $b\bar{b}$ (dot-dashed line, quarks), $\tau^+\tau^-$. (black solid line) and W^+W^- (long-dashed dotted line) are shown. The latter shows the effect of Internal Bremsstrahlung (IB) occurring for the W^+W^- channel. The γ-ray spectrum from the annihilation of $\widetilde{B}^{(1)}$ hyper gauge boson pairs arising in Kaluza-Klein (KK) models with universal extra dimensions is also plotted (dotted line). The long dashed line show the photon spectra from final-state radiation (FSR) and the inverse Compton (IC) scattering contribution in the case of dark matter particles annihilating into muon pairs. Figure taken from [252].

3.4.2 Proton - Antiproton Flux

Proton, antiprotons and positrons are a small but not negligible components of the cosmic radiation. They are (can be) produced in the interactions between cosmic-ray nuclei and interstellar matter. Detailed measurements of the cosmic-ray antiproton energy spectrum therefore provide important information concerning the origin and propagation of cosmic-rays. Exotic sources of primary antiprotons such as the annihilation of dark matter particles [254, 255, 256] and the evaporation of primordial black holes [257, 258] can also be probed. The energy spectrum of secondary antiprotons has a distinct peak around 2 GeV and rapidly decreases towards lower energies due to the kinematic constraints on the antiproton production. At higher energies the spectrum is slightly steeper than that of the parent protons [259], which results in a slight decrease of the antiproton-to-proton flux ratio. The antiproton flux is given by

$$\Phi_{\overline{p}}(E) =< \sigma v > \sum_f \frac{dN_f}{dE} B_f \frac{\rho_\chi^2}{M_\chi^2} C_{prop}(E) \tag{3.47}$$

where $C_{prop}(E)$ is a term taking into account the physics related to the antiproton propagation. Figure (3.6) shows the antiproton energy spectrum and Figure (3.7) shows the antiproton-to proton flux ratio measured by PAMELA along with other recent experimental data [254, 256] and theoretical calculations assuming pure secondary production of antiprotons during the propagation of cosmic rays in the galaxy. The curves were calculated for solar minimum, which is appropriate for the PAMELA data taking period, using the force field approximation [267, 268, 269].

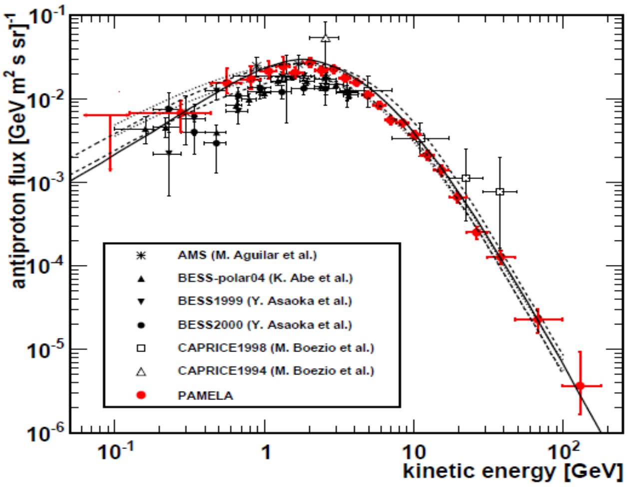

Figure 3.6: The antiproton energy spectrum compared with contemporary measurements and theoretical calculations for a pure secondary production of antiprotons during the propagation of cosmic rays in the galaxy [261, 262]. The dotted and dashed lines indicate the upper and lower limits calculated by Donato et al. [263] for different diffusion models, including uncertainties on propagation parameters and antiproton production cross-sections, respectively. The solid line shows the calculation by Ptuskin et al. [264] for the case of a Plain Diffusion model. Figure taken from [253].

3.4.3 Neutrinos Capture in the Sun and Muon Neutrino Flux

WIMPs can be gravitationally trapped inside the Sun and Earth, if their final WIMP states have velocities below the escape velocity. The annihilation rates in the Sun and Earth have been estimated using the Standard Halo Model (SHM), which is modelled as a smooth, spherically symmetric density component with a gaussian velocity distribution. However, some recent simulations show deviations from the standard due to density fluctuations on scales of the order of $\sim$ 100 pc scales, density fluctuations due to the presence of substructure which comprise a $\sim$ 0.5% variation of the mass of the solar circle leading to a small deviation of the velocity distribution from gaussian [270, 271]. The indirect detection signal from the Earth and Sun rarely deviate significantly from the SHM prediction because the annihilation rate is sensitive to the phase space density averaged over long timescales. As a result, indirect detection by annihilation in the Earth and Sun is only sensitive to the local dark matter.

WIMP annihilation produces a wide range of final state products, of which the produced muon neutrinos can escape and reach terrestrial detectors. On Earth, these muon neutrinos produce muons in charged current

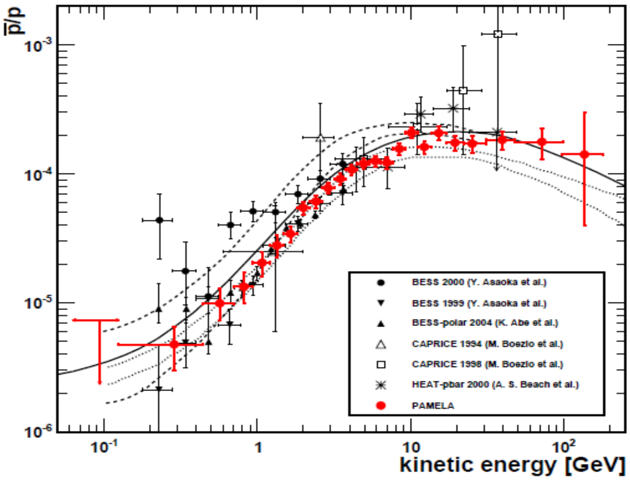

Figure 3.7: The antiproton-to-proton flux ratio compared with contemporary measurements and theoretical calculations for a pure secondary production of antiprotons during the propagation of cosmic rays in the galaxy [261, 265]. The dashed lines show the upper and lower limits calculated by Simon et al. [259] for the Leaky Box Model, while the dotted lines show the limits from Donato et al. [266] for a Diffusion Reacceleration with Convection model. The solid line shows the calculation by Ptuskin et al. [264] for the case of a Plain Diffusion model. Figure taken from [253].

interactions with nuclei: $\nu_\mu + N \to \mu^- + X$. Muons produced can be detected by their Cerenkov radiation in large water or ice-based neutrino telescopes. So far, neutrino telescopes have found no evidence for high-energy neutrinos of astrophysical origin above the detected atmospheric neutrino background. The most sensitive bounds on high-energy neutrinos from the Sun and Earth come from Super-Kamiokande [272], AMANDA [273] and IceCube [274].

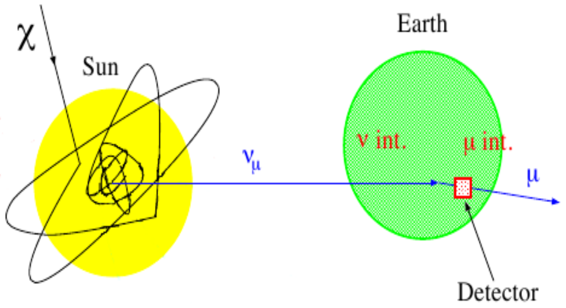

Figure 3.8: Illustration of neutrino capture in the sun and neutrino production from the sun and propagation in the atmosphere to the earth where it can be detected. During neutrino propagation from the production point to the detection point, another phenomenon normally occur, called neutrino oscillation which allows a given flavor of neutrino to transform into another flavor.

Defining the velocity distribution $f(u)$ such that $\int f(u)d^3u = \rho/M_\chi$, the capture rate $\frac{dC_x}{dV}$ from a nuclear species x per unit volume shell is usually defined by [275]:

$$\frac{dC_x}{dV} = \int_0^{u_{max}} du \int d\Omega_\zeta f(u) u \zeta^2 \sigma_x n_x \tag{3.48}$$

where σ_x and n_x are the cross section and the density of the species under consideration respectively, and ζ is the shell velocity which is related to the velocity at infinity u and the escape velocity v_{esc} by the relationship $\zeta = \sqrt{u^2 + v_{esc}^2}$. Since u, as physical observable, cannot possibly be infinity, the upper limit is usually used; it is given by: $u_{max} = 2\frac{\sqrt{M_\chi \cdot m_x}}{M_\chi - m_x} v_{esc}$, where m_x is the mass of the nuclear species x, [276]. The rate at which neutrinos annihilate however can be estimated using the Boltzman equation which is given by:

$$\frac{d\Gamma_A}{dV} =< \sigma_A v >_0 n_\chi^2 \tag{3.49}$$

where $< \sigma_A v >_0$ is the velocity averaged annihilation cross section in the limit of non-relativistic velocities, and n_χ is the number density of WIMPs in the body. If WIMPs quickly thermalize with nuclei in the body once captured, the number density of WIMPs in that body can be described by

$$n_\chi(t, x) = N_\chi(t) \tilde{n}_\chi(t, x) \tag{3.50}$$

with $\int \tilde{n}_\chi d^3x = 1$, and the number $N_\chi(t)$ of WIMPs in the body is given by the solution to $\frac{N_x(t)}{dt} = C - 2\Gamma_A$, where the total capture rate is $C = \sum_i C_i$ [277, 278]. The factor of 2 in equation (3.50) reflects the fact that two WIMPs destroy each other for self-annihilating particles. Assuming that the total capture rate C is constant with time, the annihilation rate is given by:

$$N_x(t) = \frac{C}{2} \tanh^2(t/\tau) \tag{3.51}$$

with τ, the integration constant given by:

$$\tau = \left(2C < \sigma v >_0 \int d^3x \tilde{n}_\chi^2(x)\right)^{1/2} \tag{3.52}$$

Physically speaking, the integration constant τ is the time scale required to reach equilibrium between capture and annihilation, I should then write $\tau = \tau_{eq}$; saturation is reached when $t/\tau_{eq} \ll 1$. For spin-independent interactions for example, the capture rate is 9 to 10 times greater for the Sun than for the Earth, while C_A is about three orders of magnitude smaller, implying that the equilibrium timescale is orders of magnitude shorter in the Sun than in the Earth [277].

Muon neutrinos produced in the sun travel almost at the speed of light and reach the earth with a flux given by:

$$\Phi_\odot^{\nu_{mu}}(E) = \frac{\Gamma}{4\pi d^2} \sum_f \frac{dN_f}{dE} e^{-E/E_0} \tag{3.53}$$

where $E_0 = 150$ GeV, d is the distance between the sun and the earth, f is the decay channel, dN_f/dE is the corresponding energy spectrum and e^{-E/E_0} is the depletion factor of the spectrum caused by scattering with the solar medium [276].

3.4.4 WIMPs Production at Particles Colliders

If WIMPs are really part of the physics beyond standard model of particle physics such as supersymmetry or other proposed extensions of the Standard Model, then they might be within the reach of collider physics, such as the Large Hadron Collider (LHC) at CERN, in the next few years or within the reach of the proposed International Linear Collider (ILC) [244].

Although the attempts to produce and detect new particles that lie outside the Standard Model of particle physics have grown into a colossal, multi-national effort, the technique is generally quite simple. Particles such as electrons and protons (and their antiparticles) are accelerated to near the speed of light ($\beta = 0.95$ or even more) and smashed together. If the center-of-mass energy of the collision is sufficiently large, the particles will scatter inelastically, converting a fraction of the initial-state momentum into the rest masses of heavier particles. In the case of particle colliders, the collision points are surrounded by highly segmented detectors capable of tracking the electrically charged collision products. Large magnetic fields applied near the collision point cause charged particles to leave curved tracks, allowing identification of their masses and other properties such as their charge by examining their curvature in the presence of the magnetic field. Calorimeters are usually interspersed with the trackers to detect photons and neutral hadrons (e.g., light mesons such as the π_0, η and ρ). The heaviest particles tend to be the most transient, typically decaying (almost immediately) to lighter particles whose tracks must be reconstructed in order to deduce the properties of the parent. Modern particle detectors are designed specifically to track heavy particles that might travel only a few millimeters from the collision point before decaying, while also tracking longer lived decay products that might travel many meters. Minimum ionizing particles such as muons, in particular, can penetrate many kilometers through dense materials. Muons are the primary reason for the tremendous size of modern detectors.

Several of the Standard Model's fundamental particles were detected in the laboratory using the method described above (for example, the weak boson force carriers Z and $W^{\pm}$, and third-generation of quarks (top and bottom)). With the advancement in particle-acceleration technology over the last several decades, larger center-of-mass energies have become available for the production of heavier and heavier states, a direct consequence of Einstein's famous formula $E = mc^2$. To push collision energies to ever higher levels in the pursuit of new, heavy states is often referred to as the **energy frontier**. Although center-of-mass energies at the level of TeV are now possible, no particles with masses greater than the top quark have yet been discovered ($m_t = 172$ GeV/c^2) [246].

In collider experiments, the evidence for WIMPs would come though the observation of missing energy and momentum in particle collisions, because their scattering cross sections are too small to be directly detected. This signal is easily reconstructed in linear lepton colliders through various decay channels where the collision energy and momentum are precisely known. It is much harder in hadron colliders where the collisions are those of

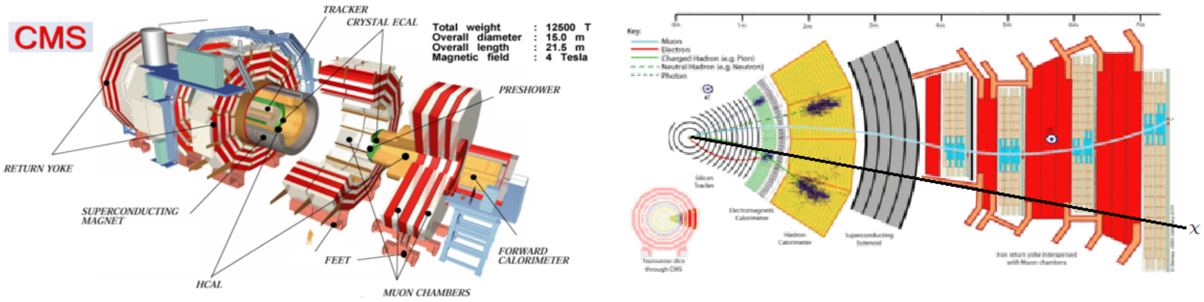

Figure 3.9: CMS cross-sectional schematic view (right) of the Compact Muon Solenoid (CMS) detector at the Large Hadron Collider (LHC). The collision point for the Large Hadron Collider's twin proton beams is surrounded (from left to right of the same right plot) by a silicon tracker, an electromagnetic calorimeter (ECAL), a hadronic calorimeter (HCAL), a superconducting solenoid that generates a 4T magnetic field within the silicon tracker (perpendicular to the plane of the page), and a series of muon chambers interspersed with iron slabs that act as the return yoke for the magnetic field. A variety of particle interactions are depicted, demonstrating the intended utility for each detector segment. However, particles such neutralinos (or WIMPs denoted by χ) would escape the detector without interacting with any of the detector elements. The left panel show the view of the whole detectors as it is disassembled. Figures taken and adapted from [245].

composite particles and the exact longitudinal energy and momenta of individual quarks are not known. Thus, at hadron colliders, the properties of new particles with small interaction cross sections must be inferred statistically from the missing transverse momentum of a large number of collisions. Many Standard-Model extensions predict new colored particles with mass similar to what is expected for WIMPs. Such particles would be produced in abundance at the LHC if their mass is below ~ 2 TeV/c^2 [245]. These would decay to leats stable particles or LSPs (potentially WIMP dark matter) and partons (i.e. quarks and gluons), producing a characteristic signature of hard jets and missing transverse momentum. Different model-dependent limits have been set by various colliders [247].

The most probable neutralino production channels at the LHC are indirect, i.e neutralinos which are created through the production and subsequent decay of heavier, colored sparticles (such as quarks superparteners, for instance squark-squark, squark-gluino and gluino-gluino pair production are some of these colored particles). If R-parity is conserved, each sparticle created will eventually decay into an LSP. Assuming the neutralino is the LSP, pair produced squarks and gluinos will decay into a pair of neutralinos as well as some number of quarks and gluons. The colored particles immediately pull other colored particles out of the vacuum so as to create color-neutral hadrons, a violent process that results in hadronic-particle **jets**. The event signature is therefore two or more jets and missing energy. Furthermore, since the jets are decay products of presumably heavy sparticles, the total jet energy is expected to be (on average) larger than for SM backgrounds [226, 227, 228].

For the CMSSM, the constraint on the neutralino mass is set using model-dependent limits obtained by various experiments as shown in Figure (3.10). However, without a gaugino mass unification assumption, this limit does not apply. Searches for charginos and neutralinos with D0 and CDF at the Tevatron have excluded some parameter space in the CMSSM with ~ 4.98 fb^{-1} of integrated luminosity, without the observation of

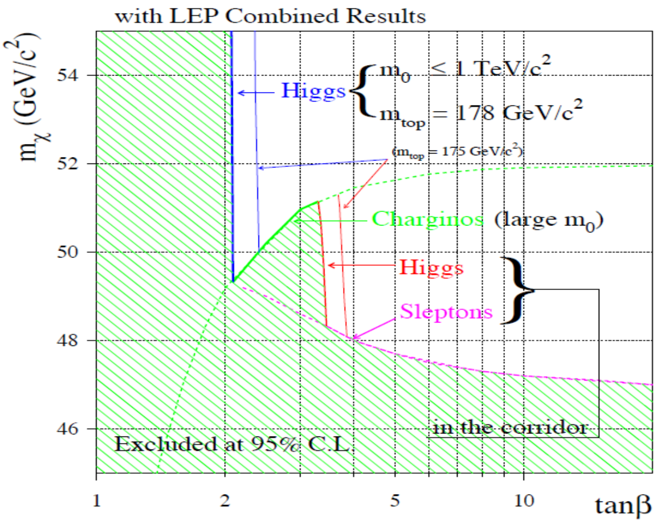

Figure 3.10: Mass limit of the SUSY lightest stable particle (LEP or neutralino χ) as function the cMSSM parameter $\tan\beta$, from searches at LEP for charginos, sleptons, and neutral Higgs bosons. It's worth to note that $\tan\beta = \frac{v_1}{v_2}$, with v_1 and v_2 are the vacuum expectation value (vev) of the the Higgs doublet field. The green hatched region is excluded by a combination of constraints from different channels marked by the various colored solid lines. Figure taken from [247].

events above background [248, 249]. Current constraints on CMSSM in the $m_{1/2}$ vs m_0 plane from CMS with $\sim$ 35 fb^{-1} of integrated luminosity are shown in Figure (3.10), no significant evidence for SUSY or WIMPs is seen yet.

One of the major difficulties at colliders has to do with production rates. Heavy particles near the energy frontier are not created as often as collections of lighter particles. Despite TeV-scale collision energies, the majority of the tracks recorded at colliders are due to well known standard model particles, called SM backgrounds. Consequently, to increase the likelihood of creating a heavy state, colliders experiments must operate at high luminosityas many particle collisions per second as can be managedwhich in turn requires advanced hardware and software capable of handling large data rates. Detection of WIMPs at a collider is complicated by their long lifetimes and weak-scale interaction rates. As indicated in Figure (3.9), for instance, if a neutralino were produced in a collision it would escape the detector without depositing energy in any of the detector elements. Fortunately, since neutrinos behave in the same manner, a method for searching for missing energy has been developed specifically to search for long-lived and/or or stable particles capable of escaping direct detection. In the case of neutralino production, if R-parity is conserved, at least two neutralinos will escape and at least $2\,\mathrm{mc}^2$ of the initial-state energy will be missing in the whole particle energies detected. One must exercise caution to avoid confusion with missing energy due to neutrinos. Normally events with lepton tracks are commonly excluded from neutralino searches because they are often the result of weak decays with final-state neutrinos. Further complication arises when attempting to detect light neutralinos since each detector element has a finite energy resolution. When the corresponding energy variances are summed over all of an event's detectable decay

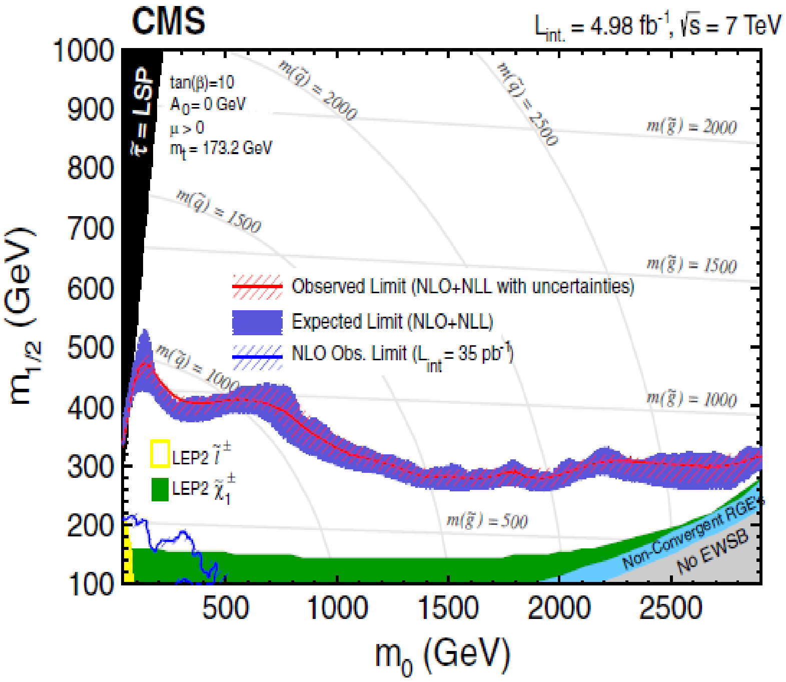

Figure 3.11: CMS constraints on cMSSM parameter $m_{1/2}$ as function of m_0 for $\tan\beta = 3$, $A_0 = 0$ and sign$(\mu) > 0$. The exclusion region, below the red curve, in the cMSSM corresponds to the observed upper limits on the number of events from NP. The central observed curve, which includes experimental uncertainties, is obtained using high pT leptons with $HT > 450$ GeV and $E_T^{miss} > 120$ GeV. The hatched region corresponds to the theoretical uncertainties on the cross section, whereas the shaded region shows the experimental errors with $\pm 1\sigma$ variation. Figure taken from [236].

products, they can conspire to produce an under-measurement that mimics missing energy. With the energies available at modern facilities like the LHC, mis-measuring a few hundred GeV is difficult. Despite this fact, finite-resolution effects can easily lead to a false missing energy of several GeV [229, 230, 231].

Several event selections are applied in these analysis, but one of the most important event selection employs a variable called α_T that has been shown to be an effective discriminator against the SM multi-jet background in searches for SUSY [224, 225]. The discriminator α_T is most easily understood in the context of di-jet events [232, 233], in which there are exactly two jets:

$$\alpha_T = E_T^{j2}/M_T \tag{3.54}$$

where E_T^{j2} is the transverse energy of the least energetic of the two jets, and M_T is the transverse mass of the di-jet event [223]. For perfectly back-to-back di-jet events with perfectly measured jet energies, $\alpha_T = 0.5$. Mis-measured jet energies will tend to yield $\alpha_T < 0.5$. while events with true missing energy can have $\alpha_T > 0.5$. For events with more than two jets, two pseudo-jets are formed by clustering the jets into two groups such that the difference between the pseudo-jets transverse energies is minimized [234, 235, 236].

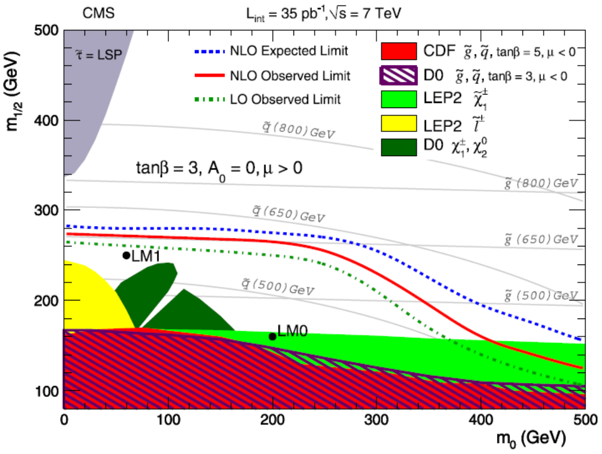

Figure 3.12: CMS constraints on cMSSM in the $m_{1/2}$ vs m_0 plane for $\tan\beta = 3$, $A_0 = 0$ and sign(μ); colored regions indicate the parameters space already ruled out by other experiments. CMS's measured exclusion contours at 95% CL are plotted in dot-dashed green and solid red for leading-order and next-to-leading-order cross sections obtained from simulation. The dashed blue curve indicates the expected limit. Area below the curves is excluded. Also plotted are contours of constant squark and gluino masses. This analysis was carried out with the data taken with an integrated luminosity of 35 pb^{-1} and total center of mass energy of 7 TeV. Figure taken from [50].

3.4.5 Theoretical Considerations for Indirect Detections

WIMPs indirect techniques are based on the measurements of the annihilation products. Two WIMPs colliding could annihilate to produce gamma rays or particle-antiparticle pairs. This could produce a significant number of gamma rays, antiprotons or positrons in the galactic halo. The detection of such a signal is not a conclusive evidence for dark matter, as the production of gamma rays from other sources are not fully understood [250, 251]. However, tremendous efforts have been made and continue to be made in understanding the flux produced by many products that results from WIMPs-annihilation. Below, I am going to cover the theoretical ground of some of them, although I do not intend to cover extensively these topics in this dissertation. Readers will be referred to indicated publications for more technical details which are certainly overlooked in my descriptions below.

3.5 Indirect Detection Experimental Signatures

As introduced in the section (3.4), WIMPs can be searched indirectly by measuring their annihilation products. The final decay products can be antimatter (such positron $e^+$and anti-proton $\bar{p}$), gamma radiation, neutrinos, etc. Experimental groups such as PAMELA and Fermi-LAT searches for cosmic sources of WIMP events (antimatter, gamma rays radiation, etc.) whereas the experiment such as IceCube seek to detect high energy neutrino mainly produced in the Sun. Below, I am going to briefly discuss three of these experiment. For details, I refer the reader to the references given hereafter and references therein.

3.5.1 PAMELA

The Payload for Antimatter Matter Exploration and Light-nuclei Astrophysics (PAMELA) experiment is a spaceborn experiment launched in 2006 onboard a 6 foot satellite. PAMELA is an indirect dark matter experiment which seeks to measure anti-protons $\bar{p}$ (proton anti-particle). PAMELA experiment has detected a larger number of positrons than expected. These extra positrons could be produced by dark matter annihilation, but may also come from pulsars. No excess of anti-protons has been observed [279, 280].

Experimental Setup and Description

The principal components of the PAMELA detector comprised a Time of Flight system(TOF), scintillator (3×2), a Spectrometer, a magnet and a tracking system, the neutron detector and the calorimeter.

1. **The Time-of-Flight** The time of flight System triggers the measurements based on a defined trigger logic hard coded and implemented with the data acquisition system, it also detects ionization dE/dx produced by charged particles flying through the detector and gives a rough estimate of the particle's direction.
2. **Spectrometer** The spectrometer measures the rigidity parameter (momentum/charge) and deflection of incoming particles. Charged particles are deflected by the presence of a magnet
3. **The magnet** The PAMELA detector contains a 0.43 T permanent magnet and a tracking system of 6 evenly spaced silicon detectors. The permanent magnet is required to distinguish between the tracks of protons and anti-protons.
4. **The tracking system** The tracking system, together with the time of flight system, measures ionization losses and infers the absolute charge (Z). The charge of particles is well determined by the PAMELA detector at least up to $Z = 8$ (Oxygen).
5. **Neutron detector** The neutron detector comprises 36 proportional counters made of ^{3}He arranged in two layers and surrounded by a polyethylene moderator (of 9 cm thick). The polyethylene moderator is used as neutron stopper by continuously reducing the neutron speed until it eventually stops.
6. **Calorimeter** The calorimeter has the role to select the positron e^+ and the antiproton $\bar{p}$ from the proton and electron background. Designed as 16.3 radiation lengths deep, the calorimeter completely contains the electromagnetic (EM) shower of an $e^\pm$ whereas the proton will cause a hadronic shower, where hadronisation products like neutrons may leave the calorimeter and enabling PAMELA to distinguish between e^+ and p or e^- and $\bar{p}$.

PAMELA backgrounds are classified into two types: the spillover and misidentification of like-charged particles. The spillover such as proton in antiproton sample or positron in electron sample, is due to to incorrect determination of charge's sign, however they can be eliminated by imposing strict selection criteria on quality of the fitted tracks. Misidentification of like-charged particles are backgrounds caused by electrons in antipro-

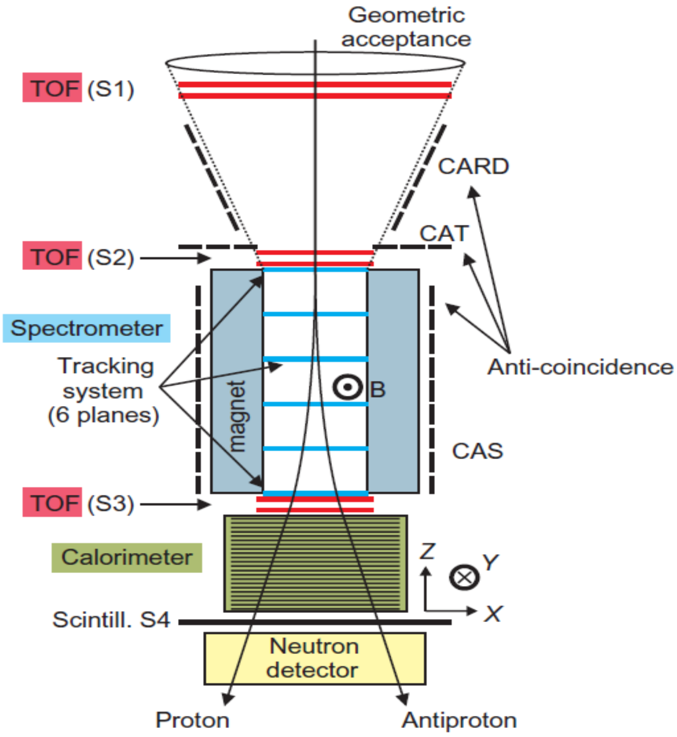

Figure 3.13: Schematic overview of the PAMELA apparatus. The detector is approximately 1.3 m high, has a mass of 470 kg and an average power consumption of 355 W. A WIMP particle will zip through this detector in a straight line trajectory without interacting, however charged particles, such as electrons, protons and their antiparticles will deposit energy in the PAMELA calorimeter due to ionization energy losses (dE/dx). Further, the 0.43 T magnet creates a magnetic field (lines inside the spectrometer cavity and oriented along the y-direction) sufficient enough to deflect these particles, giving PAMELA the ability to distinguish a positively charged and negatively charged particle. PAMELA's ability to identify the aforementioned particles allowing the experiment to measure antiproton-to-proton faction. Figure taken from [280].

ton samples or positrons in proton samples. Due to electron-hadron separation performance since leptons cause electromagnetic showers in the calorimeter, positrons in antiproton samples can be identified with high accuracy

From PAMELA results, it has been noticed that the $\bar{p}/p$ ratio agrees with models, however the $e^+/(e^-+e^+)$-ratio does not agree with models, but rather increases with energy. Many possible explanations have been found to explain PAMELA's results, among them one often evokes pulsars which produce the e^+ excess. The other explanation is that the increase in the $e^+/(e^- + e^+)$-ratio is due to WIMP annihilation. If this is true, then the PAMELA excess of the $e^+/(e^- + e^+)$-ratio is an uncontroversial hint of the observation (existence) of WIMPs by an indirect detection [279, 280].

3.5.2 Fermi Large Area Telescope (LAT)

Fermi Large Area Telescope (LAT) is a satellite-borne gamma-ray detector launched on 2008. The Large Area Telescope (LAT) is the main instrument on board and the satellite also hosts a Gamma-ray Burst Monitor

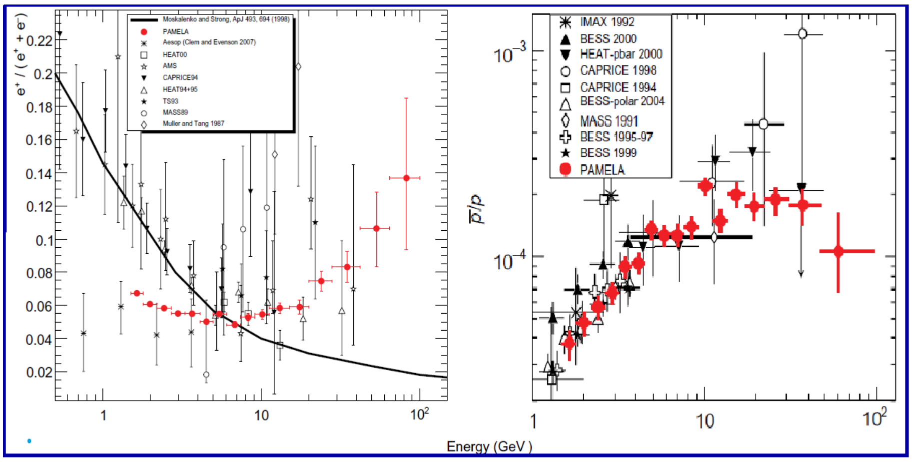

Figure 3.14: $e^+/(e^+ + e^-)$ and $\bar{p}/p$ ratio obtained by PAMELA. The plot of the left show the positron fraction measured by the PAMELA experiment compared with other recent experimental data (references [35]−[43] of [280]). On right is shown the PAMELA antiproton-to-proton flux ratio compared with previous measurements (references [27]−[33] of [280]). Figure adapted from [280].

(GBM). The LAT is a modular, consisting of a 4×4 array of identical towers. Each 40×40 cm^2 tower is composed of a tracker, a calorimeter, and a data acquisition module. The tracker array is covered by a segmented anti-coincidence shield (ACD). The tracking detector consists of 18 2D layers of silicon strip detectors interleaved with 16 layers of tungsten foils. Each calorimeter module has 96 CsI(Tl) crystals, arranged in an 8 layer hodoscopic configuration with a total depth of 8.6 radiation lengths, giving both longitudinal and transverse information about the energy deposition pattern. The calorimeter's depth and segmentation enable the high-energy reach of the LAT and contribute significantly to background rejection. The ACD is the LAT's first line of defense against the charged cosmic ray background. It consists of 89 different size plastic scintillator tiles and 9 ribbons with wave-length shifting fiber readout. The segmentation is necessary to suppress self-veto effects caused by secondary particles emanating from the calorimeter showers of high energy gamma-rays.

Fermi LAT faces one major difficulty in their experiment. Their goal is to measure high energy gamma rays, however highly energetic gamma rays cannot be deflected (reflected or refracted) in the presence of the electric field. To overcome this obstacle, the solution is to turn gammas into an $e^- - e^+$ pair by letting the gamma-ray to pass through the tracker until it hits one of the conversion foils, where it produces an $e^- - e^+$ pairs. The $e^- - e^+$ will cause electromagnetic showers inside the calorimeter and deposit energy by ionization energy loss dE/dx [281, 282, 283, 284].

3.5.3 IceCube

Relic neutralinos in the galactic halo may become gravitationally trapped in the Sun and accumulate in its center, where they can annihilate each other, producing standard model particles. These particles may decay, creating neutrinos which can escape and reach the Earth. The IceCube detector records Cherenkov light in the ice

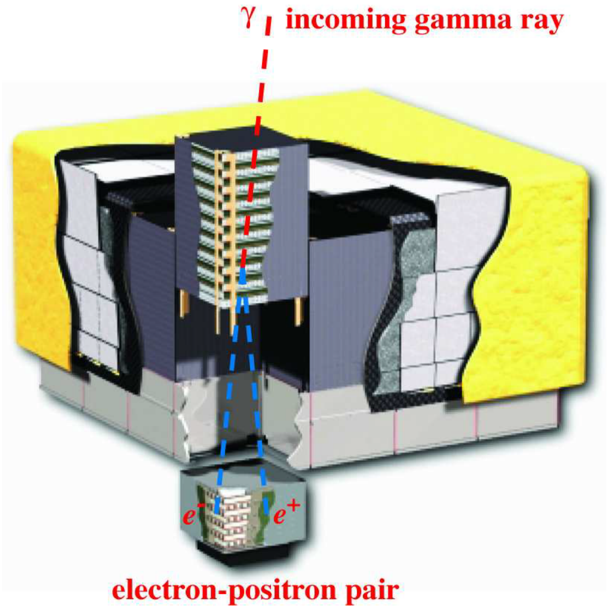

Figure 3.15: Schematic diagram of the Large Area Telescope. The telescope's dimensions are 1.8 m × 1.8 m × 0.72 m. The power required and the mass are 650 W and 2,789 kg, respectively. Figure from [282].

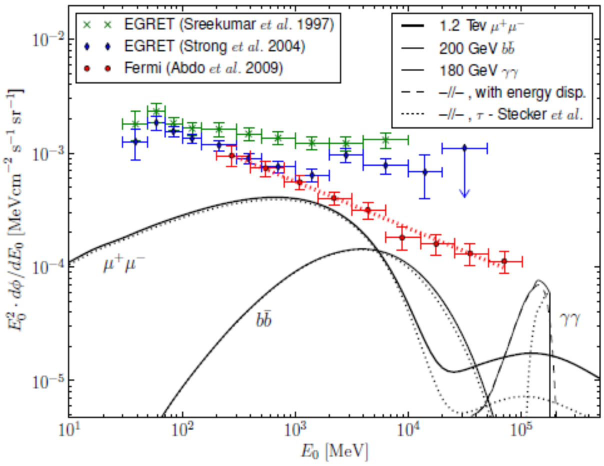

Figure 3.16: Measurements of the IGRB by Fermi-LAT and EGRET, together with three types of gamma-ray spectra induced by Dark Matter (DM). The overall normalization of the DM spectra are given by assuming the MSII-Sub1 Δ^2 model, and for this visualization the cross sections $< \sigma v_i > =$ $5{\times}10^{-25}$ cm^3 s^{-1} (for b$\bar{b}$), $1.2{\times}10^{-23}$ cm^{3}s^{-1} ($\mu\mu$) and $2.5{\times}10^{-26}$ cm^{3}s^{-1} ($\gamma\gamma$). The solid lines are with the Gilmore et al. absorption model applied, and the dotted lines with the Stecker et al. absorption. The plot also show the line spectra convoluted with the energy resolution of the Fermi-LAT experiment (dashed line). The dotted line passing through the Fermi data points is a power law with the spectral index of -2.41. Figures from [284].

from relativistic charged particles created in neutrino interactions [285]. Once cosmic (or atmospheric) neutrinos reaches the ice, they interact weakly through deep inelastic scattering with the ice's nucleons N via charged and neutral current interactions:

$$\begin{cases} \nu_L + N \to L + X & \text{charged current} \\ \\ \nu_L + N \to \nu_L + X & \text{neutral current} \end{cases} \tag{3.55}$$

where L refers to leptons (electrons, muons and taus).

The detector consists of an array of 22 vertical strings with 60 Digital Optical Modules (DOMs) each, deployed in the clear Antarctic ice at the South Pole at depths between 1450 m and 2450 m below the ice surface. The vertical spacing between DOMs is 17 m and the horizontal distance between strings is 125 m. Each DOM consists of a pressurized glass sphere containing a 25 cm photomultiplier tube (PMT) and a digitizer board. The PMT waveforms are stored when nearest or next-to-nearest DOMs fire within 1 μs. The trigger selects time windows when eight DOMs produce waveforms within 5 μs. The reconstructed first photon arrival times are used to determine the muon direction. The background in the search for neutrinos from the sun comes from air showers created by cosmic ray interactions in the atmosphere. The showers cause downward going atmospheric muon events, triggering at several hundred of Hz, as well as atmospheric muon neutrino events triggered at a few mHz. When the Sun is below the horizon, the neutrino signal can be distinguished from the atmospheric muon background by selecting events with upward-going reconstructed muon tracks [285, 286, 287, 288].

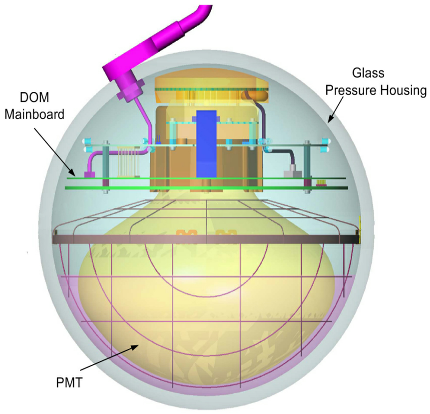

Figure 3.17: IceCube Digital Optical Module (DOM) designed to optically detect neutrinos passing through the IceCube detector. Figure from [285].

Many sources of visible muon traces exist. Secondary particles mostly originate from the interaction of cosmic rays with the atmosphere such as secondary hadronic decays after interaction with the atmosphere from pions $\pi^{\pm}$ and muons $\mu^{\pm}$:

$$\begin{cases} p + p \to \pi^{\pm} + X & \text{, and} \\ \\ \pi^{\pm} \to \mu^{\pm} + \nu_{\mu}^{\pm} \end{cases} \tag{3.56}$$

IceCube mainly detects three kinds of particles: (1) atmospheric muons which comprise a major part of the background, (2) atmospheric neutrinos which represent another source of irreducible isotropic background, and (3) signal neutrinos originating from sun or earth's center which is exactly what IceCube is looking for.

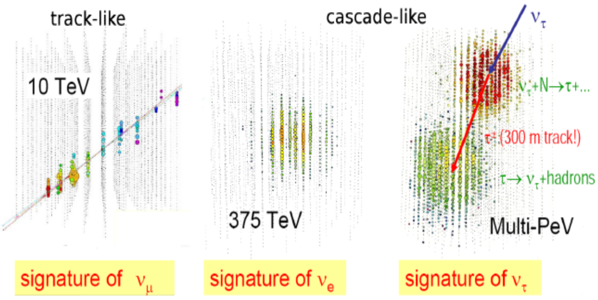

Figure 3.18: Particles tracks in IceCube detector. μ_ν produce μ, which typically have track-like signatures, μ_e produce e, which immediately produces electromagnetic (EM) showers (or cascades) and particles such as ν_τ produce τ, which typically produce two showers. Based the track linearity, IceCube can select mainly events with muon neutrinos track-like. Figure from [285].

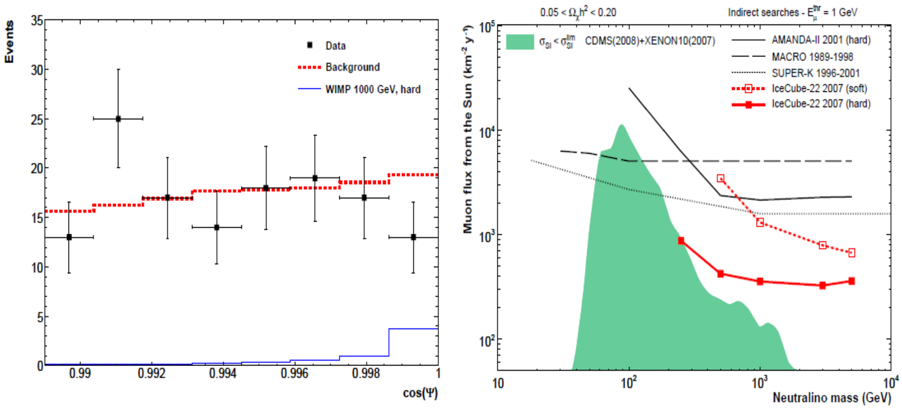

Figure 3.19: Shown on left is the cosine of the angle between the reconstructed track and the direction of the Sun, Ψ, for data (squares) with one standard deviation error bars, and the atmospheric background expectation from atmospheric muons and neutrinos (dashed line). A simulated signal is also shown ($m_{\chi 1^0}$ = 1000 GeV, hard spectrum) scaled to μ_s = 6.8 events. The Upper limit at the 90% confidence level on the muon flux from neutralino annihilations in the Sun for the soft ($b\bar{b}$) and hard (W^+W^-) annihilation channels, adjusted for systematic effects, as a function of neutralino mass is shown on the right plot. The shaded area represents MSSM models not disfavored by direct searches. Figures from [284].

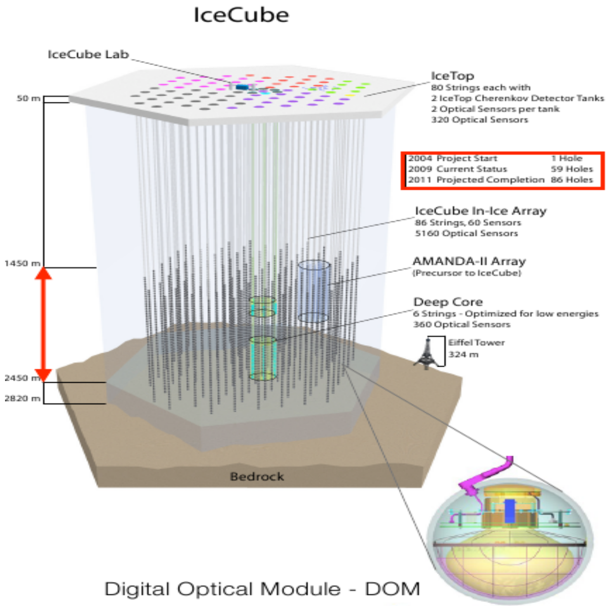

Figure 3.20: Schematic of the IceCube detector. IceCube is a particle detector at the South Pole that records the interactions of a nearly massless sub-atomic particle called the neutrino. IceCube searches for neutrinos from astrophysical sources: events like exploding stars, gamma ray bursts, and other phenomena (involving black holes and neutron stars). The IceCube telescope is a powerful tool for the search of dark matter. Figure from [287].

3.6 Direct Search of Dark Matter

In a direct detection experiment, the reach potential of the experiment is mainly determined by the target material which determines the detection channels of an interaction. In general, direct dark matter experiments measure the nuclear recoils produced by a dark matter particle (WIMP) when scattering off the nuclei in the detector's target material. There exist various techniques that are exploited by different direct dark matter experiment, however, to date there are three main technologies used in direct detection experiments: solid state detectors, noble liquid detectors, and threshold (phase transition) detectors.

Direct detection experiments use event-by-event discrimination techniques to identify nuclear recoils from WIMP interactions (or neutrons) which is buried in a far larger rate of electron recoils from radioactive decays and cosmogenic processes. The discrimination is accomplished by measuring two or more distinct channels for each event and taking their ratio as a particle identification parameter. The most common of such channels are phonons or (heat, temperature change in the detector caused by the energy deposited by the interaction), ionization (due to energy loss), and scintillation light (due to photo-emission). The choice of detection channels carries tradeoffs in readout technology and experimental resolution. A sufficiently accurate discrimination can reduce an experiment's background rate enough, to maintain operation near the zero-background regime, even at very large WIMP-search exposures.

Direct detection of WIMP interaction, as many rare event searches, requires an efficient discrimination be-

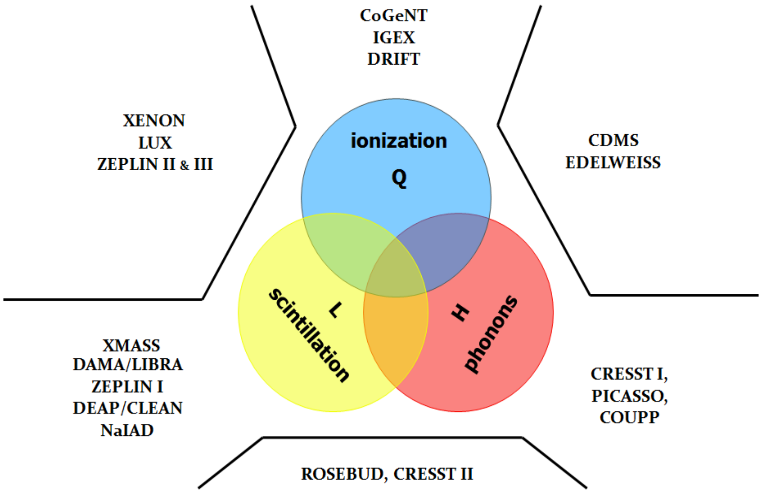

Figure 3.21: Schematic of direct detection techniques. As shown, most of direct detection experiments measure the phonons, ionization and the scintillation produced by the interacting particle with the detector. The ratio of these quantities, when plotted against the recoil (ionization) energy can be used as discriminator and so as a particle identification. Figure from Blas Cabrera's talk at Princeton.

tween background interactions and event candidates. This implies having a rigorous control of the background for any direct detection experiment, regardless of which detection technology it utilizes.

3.6.1 Backgrounds

A 60 GeV/c^2– 100 GeV/c^2 WIMP mass will normally produce a recoil energy of $\sim \mathcal{O}(10)$ keV or less. In this low-energy regime backgrounds from natural radioactivity and cosmic rays are dominant. Direct WIMP detection experiments are thus low-background experiments, requiring superior protection from background events and must possess the ability to identify a spectrum of $\sim \mathcal{O}(10)$ keV nuclear recoils occurring at a very low rate.

For direct WIMP search experiment using a detector's total target mass M (kg) and acquire data for a livetime T (days), one defines the exposure as the product of the total target mass with the livetime; exposure $= MT$ (kg-days). For an exposure MT, the experiment will expect to observe B background events which are indistinguishable from WIMP interactions. There are three general sensitivity classes in which the experiment can be operated, depending on the observed (estimated) number of the expected background events B:

1. **Background-free experiment:** If the expected number of backgrounds B $\simeq$ 0, then any observed event candidates are evidence for WIMPs. However, if zero event candidate is observed, the experiment can set a 90% confidence level Poisson upper limit on the WIMP interaction rate (or sensitivity) of $R = \frac{N90(B)}{MT}$ events per kilogram-day, and the experiment's sensitivity improves as the exposure MT increases. $N90(B)$ is the 90% confidence level Poisson upper limit, defined by

$$N90(B) = \begin{cases} 2.3026 & \text{if } B = 0 \\ \\ (B + 1.07)\left[1 + \frac{1.28}{\sqrt{B+1.07}}\right] & \text{if } B \neq 0. \end{cases} \tag{3.57}$$

with the case $B =\neq 0$ not being a Poisson definition, nonetheless, it is a good approximation.

2. **Background subtraction:** If the expected number of background B is non-negligible and if it can be well characterized using the calibration data, and if the background energy spectrum can be well characterized with negligible systematic errors, then one can subtract the background rate from the observed count rate. In such a situation, the experiment is thus searching for an excess of events above the known background. The accuracy of such a subtraction is limited by Poisson statistics giving an error on the subtraction of $\sigma_B = \sqrt{B}$. As the exposure increases, the background also grows proportionally to the exposure, i.e. $B \approx MT$ and thus $\sigma_B \approx \sqrt{MT}$. The number of excess candidate events needed to claim a detection scales as σ_B, so the experiments sensitivity grows only as $\sqrt{MT}$.

3. **Background limited:** If the experiment has completely no control, little or no knowledge of its backgrounds, and its systematic uncertainties on the expected backgrounds, then the experiment's sensitivity will ultimately be limited. The systematical errors on the background count generally grow in proportion to B, while the statistical uncertainty will grow as $\sqrt{B}$. Such an experiment cannot distinguish WIMP event candidates and the background, and therefore cannot claim detection since the background has a higher excess of events on top of what cannot also be accounted with certainty as WIMP events. No increased exposure will enhance the sensitivity of the experiment until improvements are made in background levels or background rejection. For these reasons, it is most desirable for direct search experiments to operate as close to the background-free regime as possible.

3.6.2 Direct detection technologies

Most of the direct dark matter searches measure one or two of the three physical quantities namely phonons, ionizations and scintillation light produced by the interacting particle as pictorially shown in Figure (3.21). At the time of the writing of this dissertation, there are three main technologies used in direct detection experiments: solid state detectors, noble liquid detectors and threshold (phase transition) detectors.

1. **Solid-state detectors**

   Solid-state detectors possess by far a superior energy resolution compared to any other detector technologies. This class of detectors also has a powerful discrimination against electron recoils. The Cryogenic Dark Matter Search (CDMS) experiment is currently the leading experiment in this category. Below, I briefly touch upon some of the direct dark matter experiment in this category. CDMS is excluded in this discussion since the remaining chapters of this dissertation will completely be devoted to CDMS experiment.

(a) **DAMA/LIBRA**

The DAMA/LIBRA collaboration employs an array of low-background NaI(Tl) scintillator crystals at the Gran Sasso Laboratory in Italy. Interactions in the crystals are identified by their scintillation light alone. The scintillation yield of a nuclear recoil is reduced compared to that of an electron recoil of similar energy by a quenching factor $Q_{Na} = 0.3$ for Na recoils and $Q_I = 0.009$ for I recoils [289]. The approach used by DAMA/LIBRA collaboration is a bit different compared to what other direct experiments are doing. Rather than achieving background rejection by measuring the nuclear recoils produced by WIMPs when scattering off the nucleus, DAMA/LIBRA experiment rather searches for a modulation signature, generally referred to as annual modulation.

The annual modulation is caused by the revolution of the Earth around the Sun as the solar system tracks its path through the Milky Way. This leads to a modulation in the Earth's velocity with respect to the galactic frame and hence a detectable modulation of WIMP flux throughout the year. The detection of modulation-based evidence of WIMPs typically requires a very large sample of WIMP recoils, and extremely well characterized and stable backgrounds.

Based on the data collected over a period of 13 annual cycles, the DAMA/LIBRA collaboration reports evidence of an annual modulation with a statistical significance of 8.9σ. The variation of their rate is consistent with a sinusoid peaking at May 16 ± 7 days at energies between 2 and 4 keV, May 22 ± 7 days between 2 and 5 keV, and May 26 ± 7 days between 2 and 6 keV, consistent with that predicted for dark matter with a roughly Maxwellian velocity distribution.

Although DAMA/LIBRA's strategy of looking for an annual modulation in their rate can be successfully used to separate a dark matter signal from many possible backgrounds, one might worry about sources of background which could also exhibit seasonal variation. For example, the underground muon flux is known to modulate as a result of temperature variations in the stratosphere (although with a later phase and lower rate than is observed by DAMA/LIBRA [290]). Observed variations in the radon-induced background rate are also out-of-phase with the signal reported by DAMA/LIBRA. To date, no background has been identified with a phase, spectrum and rate compatible with DAMA/LIBRA's signal [293, 294, 295].

(b) **EDELWEIS**

The EDELWEISS collaboration uses semiconductor crystals (germanium crystals) operated at cryogenic temperatures in the search for dark matter interactions. The detection channels are ionization and phonon detection. The phonon detection is based on the measurement of the near-equilibrium temperature change of the entire crystal substrate.

Currently the EDELWEISS collaboration is using a new detector technology which uses an interleaved charge electrode design [293, 296, 297]. This new detector design allow the EDELWEISS collaboration to demonstrate a powerful discrimination of the main background events in semi-conductor crystals.

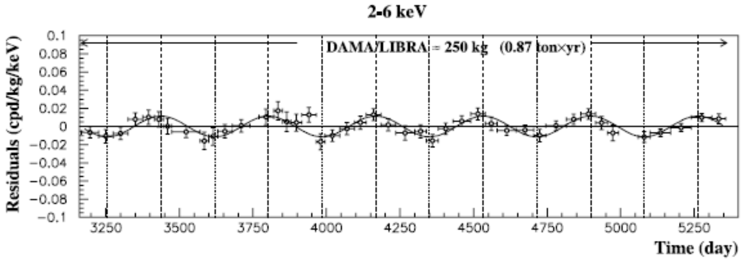

Figure 3.22: DAMA/LIBRA events rate in the 2−6 keV energy range. The solid curve over the data is the best fit sinusoidal curve with a fixed phase and period to match the expected dark matter modulation signal. Figure from [295].

This new technology is currently adopted by the CDMS collaboration (although they attempted to develop such kind of detector in past [296], but never pursued it further) and it is certainly going to become the leading technology in the ionization readout of solid-state detectors in future experiments.

(c) **CREST**

The CREST (CRESST-II) experiment (Cryogenic Rare Event Search with Superconducting Thermometers) is located at LNGS in Italy. The experiment uses cryogenic detector modules which consist of scintillating $CaWO_4$ crystals operated as bolometers (sensitive to phonons) and a nearby but separate cryogenic light detector (a silicon wafer with a tungsten thermometer). Simultaneous detection in both the phonon channel and the light channel (scintillation) allows for efficient discrimination between electronic, α-particle and nuclear recoils, because of substantial differences in light yield. In addition to this, the crystal together with the light detector are completely surrounded by scintillating and reflecting foil. This is critical for discrimination of ^{210}Po decays, which occur on the inner surface of the reflective housing or on the crystal surface. When the recoiling ^{206}Pb enters the crystal, potentially generating a WIMP−like background event, the escaping 5.3MeV α particle reaches the foil and generates enough light to veto the event.

The CRESST detector is instrumented with two thermometers to detect the thermal phonon signal and the scintillation light from a particle impact in the cryogenic substrate. The phonon signal is measured directly as a temperature rise of the crystal, while the scintillation light is detected by the temperature rise of a light-absorbing silicon wafer. CREST collaboration has set limits on the spin-independent WIMP-nucleon cross section at the 5×10^{-43} cm^2 level and is proceeding with a larger experimental installation to improve their sensitivity to WIMP-nucleon interactions [299].

(d) **CoGeNT**

The CoGeNT Experiment has used a single, 440-gram, high-purity germanium crystal (HPG) cooled to liquid nitrogen temperatures. The CoGeNT detector has the advantage of a very low energy threshold (∼0.5 keV), which allows it to search for nuclear recoil events due to dark matter particles of relatively low mass (>5 GeV/c^2). In addition to a low-background configuration, the detector is capable of distinguishing and rejecting background events from the surface through measurement of the risetime of the detector's signals. The CoGeNT detector senses only ionization charge and places limits on the mass and interaction cross-section of dark matter particles by excluding any candidate mass and cross-section pair that would result in a signal above the background of the detector.

Recently the CoGeNT collaboration has developed a p-type point contact (PPC) germanium detectors. PPCs display an unprecedented combination of target mass and reduced electronic noise, resulting in an enhanced sensitivity to low-energy rare events with every promising applications in astroparticle and neutrino physics expected from this technology [300].

2. **Noble liquid/gas detectors**

Liquid noble detectors are large tanks of liquified noble gases observed by photomultiplier tubes. Nobel liquids are excellent scintillators, with light yields approaching that of NaI(Tl) and long attenuation lengths. Noble liquid detectors (or noble gases) also have great promise for WIMP detection. They have the advantage of relatively easy scaling to larger masses which is an important factor in a dark matter search. However, these experiments must overcome significant challenges of maintaining discrimination to low energies, which is difficult since there are relatively few light quanta (typically $5-10$ phot-electron per keV) collected. High purity levels ($\sim 10^{-9}$ impurities) must be achieved in order to prevent absorption of the scintillation light or attachment of drifting electrons. Another barrier to overcome is the irreducible radioactive backgrounds such as ^{85}Kr in Xe or especially ^{39}Ar in liquid Ar (which produces 1 decay per second per kg of natural Ar).

To date, there exist two types of noble detectors: single-phase (liquid), which detect only the primary (S_1) light signal, and dual-phase time-projection chambers (TPC), which employ a large electric field to drift ionization electrons upwards out of the liquid and into a region where the noble is in its gas phase, where electrons produce a large secondary (S_2) light signal by electroluminescence that is proportional to the amount of ionization. The ratio of the secondary light to the primary scintillation (S_2/S_1) provides additional discrimination with typical background leakage $10^{-2} - 10^{-3}$ at 50% acceptance (see [239] and references therein).

The relative high boiling point of liquid noble gases make the cryogenic requirements far simpler than those needed for the phonon readout in cryogenic solid-state detectors. Nuclear and electron recoils are distinguished in two distinct ways:

2.1. Nuclear and electron recoils produce a different amount of ionization and scintillation in the liquid. The primary scintillation can be measured directly with phototubes, while the charge carriers can be drifted and extracted into a gas volume where they cause secondary proportional scintillation. Such a dual-phase detector thus observes two scintillation pulses for each interaction. The amplitudes of the two light signals identify the energy and recoil type of each interaction, while the time delay between them can be used to measure the event's position along the drift axis.

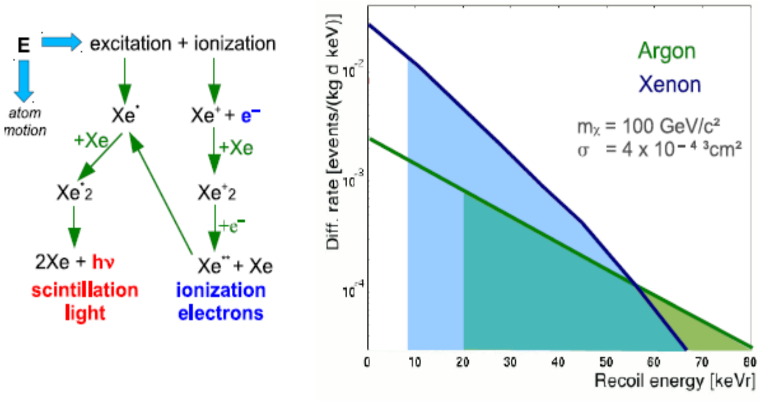

Figure 3.23: Left, is a diagram of the processes leading to primary scintillation (S_1) light in a liquid noble detector (Xe), and (if the detector is dual-phase) to secondary (S_2) light proportional to the amount of ionization. Recoils dissipate energy as atomic motion, excitation, and ionization. Both excitation and ionization result in excited dimers, Xe_2^*, in either a longer-lived triplet state or a shorter-lived singlet. Particle interactions excite and ionize the target (Xe in this example, but Ar works exactly the same way). Excited atoms Xe* combine with a neutral atom and form an excimer state Xe$_2^*$ which decays under the emission of scintillation light. If ionization electrons are not removed from the interaction site (by an electric field in a TPC), they eventually recombine and also produce scintillation light. Therefore, the light and the charge signal are anti-correlated. The right plot show the expected nuclear recoil spectra from interactions of a 100 GeV/c^2 WIMP with LXe and LAr, assuming a cross-section of $\sigma = 10^{-43}$ cm^2. The expected rate is higher in LXe at low energies, but the form factor suppressed at higher energies, which is not the case for LAr. A low detection threshold is therefore necessary if LXe is used. Experimentally achieved thresholds are indicated by the colored areas. Figure from [291].

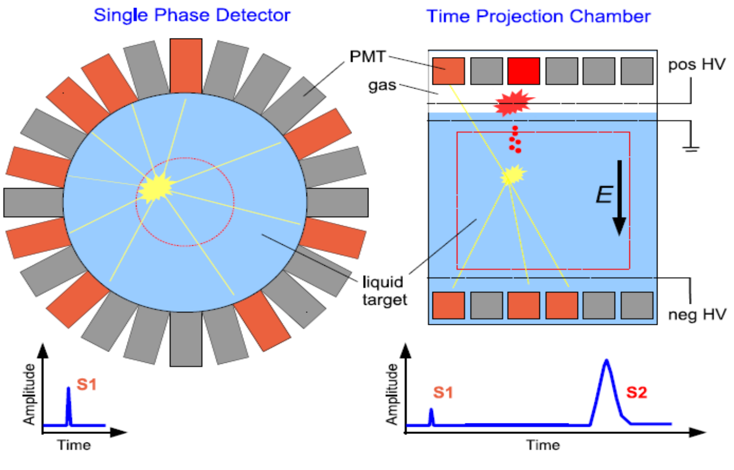

Figure 3.24: The two detector concepts currently used for dark matter detectors based on liquid noble gases. (Left) Single phase detectors are essentially a large volume of a noble liquid which is viewed by many photosensors, usually PMTs, in order to detect the scintillation light S1. (Right) In a double phase detector the S1 signal is also detected by photosensors, but the ionization charge signal is measured as well since the detector is operated as a time projection chamber (TPC). An electric field across the target volume removes the ionization electrons from the interaction site and drifts them towards the gas phase on top of the liquid. The electrons are extracted into the gas and generate proportional scintillation light S2, which is registered time-delayed by the drift time. Figure from [291].

2.2. The pulse shape of the primary scintillation signal can be used as a basis of discrimination between electron and nuclear recoils. Each noble liquid has two scintillation time constants (τ_1 and τ_3), corresponding to the de-excitation of singlet and triplet excimer states. Nuclear recoils populate the singlet state preferentially. Since $\tau_1 < 3\tau_3$, the tail of the primary scintillation pulse can be used as a discriminator if the time difference between τ_1 and τ_3 is large enough to be recognized by the readout channel. In addition the pulse shape has to be well reconstructed even at low energies, thus requiring a reasonable number of primary scintillation photons at the experiment recoil energy threshold [291]. Below are some of the current dark matter experiments using noble liquid/gas technology:

(a) **Dark matter experiments using liquid Xe**

Liquid xenon is one of the most most promising of the noble liquid targets. It possess the largest light yield, no long lived radioisotopes and the scintillation light does not require a wavelength-shift in order to be detected. Due to its large atomic mass, a Xe target give a large cross section for spin-independent interactions. Dark matter searches with liquid Xe is not well suited for pulse shape discrimination, due to its extremely short scintillation times (τ_1 = 2.2 ns and τ_3 = 21 ns).

Nowadays, there are two direct dark matter experiments using a Xe target in a dual-phase detector: XENON10 [301] and the ZEPLIN [302] collaborations. XENON10 experiment employs a 15-kg detector (they have observed 10 candidate events which were all consistent with backgrounds in a 136 kg-day exposure [301]). The ZEPLIN experiment however uses a 12 kg detector (and had reported 7 candidate events also consistent with backgrounds in a 127.8 kg-day exposure [302]).

To increase their sensitivity to WIMP-nucleon interactions, several other experiments are scaling up the mass of their target material [304]). LUX experiment, located at the 4850 ft of the Homestake mine, makes use of an active water shield as part of the new design to help neutron rejection, however they still use the same detector technology as the XENON100 experiment. The XMASS collaboration is another dark matter experiment that uses liquid Xe as target material. They have built an 800 kg single-phase detector, focusing on the self-shielding and good position reconstruction to eliminate backgrounds [305].

The XENON collaboration is already working on the next phase, XENON1T, which aims to explore cross sections down to 2×10^{-47} cm^2 by 2017, after two years of data taking with a TPC of 1 ton LXe fiducial mass. XENON1T will be also installed at LNGS, inside a water shield of ∼10 m diameter which is operated as a Cherenkov muon veto and will suppress ambient gamma radiation and neutrons similar to the LUX experiment.

(b) **Dark matter experiments using liquid Argon**

Among these experiments, we have:

DEAP-3600 is a large a single-phase detector using 3.6 tons of LAr, with about 1000 kg being used as WIMP target. The LAr will be contained inside an acrylic vessel installed in a cryostat which itself is inside a water shield. Construction of the experiment is ongoing at SNOLAB (Canada) and the first filling is expected around the end of 2013. The science goal is to reach the 10^{-46} cm^2 level after 3 years of operation. The large light collection in the single-phase setup will allow for a very good rejection of electronic recoil background via pulse-shape discrimination. A small prototype, the MiniCLEAN, experiment is currently installed right next to DEAP-3600, with 150 kg LAr fiducial mass (500 kg total). The experiment is designed such that it can also be operated with liquid neon (LNe). Initially, this has been proposed in order to detect low energy neutrinos from the sun and from supernovae. MiniCLEAN is expected to run from end of 2012 to early 2013 [306, 307, 308].

ArDM is a double-phase LAr detector which has been installed and commissioned at CERN and is currently being moved underground to the Canfranc laboratory (Spain). ArDM uses a large target mass of 850 kg of LAr in a TPC of 120 cm height and 80 cm diameter. The collaboration has developed novel ways to deal with the technical challenges of multi-ton LAr/LXe detectors. The high voltage to bias the TPC is generated next to the field cage in a Greinacher circuit and ArDM's final goal is to detect the charge signal with sub-mm precision in large micro-machined charge amplification detectors (large electron multipliers, LEMs) [309].

DarkSide is a double-phase TPC which will use LAr as a WIMP target. The goal for the next years is to build and operate DarkSide-50 with about 50 kg target mass. It will be located at LNGS (Italy), inside the the Borexino counting test facility (CTF), a large water tank which is currently being refurbished for this purpose. Inside the water shield, DarkSide will be surrounded by a spherical boron-loaded liquid scintillator neutron veto and it will use Ar which is depleted in ^{39}Ar by a factor ∼100. Commissioning is scheduled for end of 2012, and two years of data taking is necessary to reach the final sensitivity around 10^{-45} cm^2 [310].

3. **Threshold detectors**

The bubble chamber concept that was extensively used in elementary particles physics in the 1960s to identify tracks of particles, has created a renewed attention in physics and in particular in the field of direct detection of dark matter. Detectors invented for direct detection experiments, by using similar idea to bubble chamber, are called **threshold or phase transitions detectors**.

The phase transition detectors are based on the principle that an abrupt transition makes an effective detector. If a liquid is superheated to a metastable state above its boiling point, the energy deposited by a particle interaction can cause a very localized evaporation of the liquid. This boiling will only occur if enough energy deposited in a small enough volume, i.e. the particle track must have an energy loss (dE/dx) greater than a certain threshold. By tuning this threshold, phase transition detectors can be rendered insensitive to electromagnetic interactions while still remaining sensitive to nuclear recoils.

Threshold detector technology uses a superheated liquid (in the bulk or as droplets within a matrix). By tuning thermodynamic parameters (e.g. temperature and pressure), the detector may be made insensitive to the low energy density deposited by a minimum-ionizing electron recoil. Only a dense energy deposition, such as from a nuclear recoil, will provide enough energy to cause nucleation (smaller depositions resulting to sub-critical bubbles that are squashed to nothing by their surface pressure). The attraction of these detectors is that they could allow inexpensive scaling to very large masses with a broad range of materials and without need of cryogens or photon shielding.

COUPP and **PICASSO** experiments uses a CF_3I target in a phase transition. These detectors, as most of the phase transition detectors, measures only the count rate above threshold. To acquire information about the energy spectrum of the interaction data, a range of different energy thresholds must be acquired, since it is in general not possible to determine the energy deposited by the creation of a bubble [311].

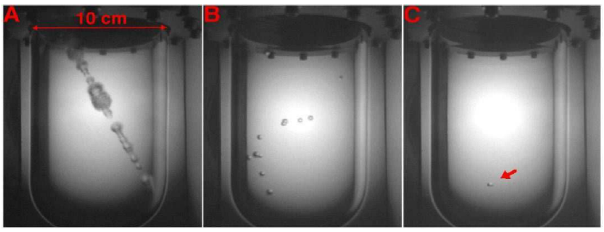

Figure 3.25: Images of three different types of particle interactions in the COUPP bubble chamber: (A) cosmic ray event, (B) neutron multiple-scatter event, and (C) neutron single-scatter event. Figure from [311].

Chapter 4

CDMS II Detector Technology: ZIPs.

4.1 Introduction to ZIP and mZIP Detectors

Direct detection of dark matter presents enormous technical challenges. In order to be able to detect the dark matter signal, an effective search for WIMPs requires sensitivity to an extremely small signal rates at low energies (of the order of ∼10 keV or lower) while distinguishes the signal from the backgrounds. A competitive WIMP search experiment must be able to identify a certain number (handful) of WIMP-induced scattering events amongst a far larger population of background interactions.

The Cryogenic Dark Matter Search (CDMS) experiment employs low temperature germanium (Ge) and silicon (Si) detectors to detect WIMPs via their elastic scattering off target nuclei. Dark matter particles, such as WIMPs, can only interact with nuclei. Scattering events inducing nuclear recoils are tagged in most direct dark matter searches as indication of WIMP interaction. Every single interaction in the semiconductor crystals creates two distinct signals: the ionization signal from electron-hole pairs and the excitation of the lattice in the crystal. The motion of the drifted charged particles produces phonons (propagation of particles in a crystal medium). Ionizations and the athermal phonons are generally produced and recorded by the CDMS ZIP detectors used in the CDMS-II experiment.

Coherent elastic scattering of dark matter WIMPs with the nucleus is the physical process by which WIMPs interact with the crystal. However, at the time of the writing of this dissertation, there has been a different proposal of WIMPs interaction mechanism: the inelastic scattering between dark matter and electrons. This mechanism is now being promoted due to the fact that there is more energy available in inelastic processes which by far is more convenient to probe lower mass scales. Few possible inelastic processes considered under this model are: electron ionization, electronic excitation and finally molecular dissociation [313, 314].

The CDMS II experiment uses Z-sensitive Ionization and Phonon ZIP detectors, made of germanium (Ge) or silicon (Si). The experiment is installed at the Soudan mine (northern Minnesota) and operated at 40 millikelvin. The charge and phonon energy from a particle interaction measured in these detectors, provides an excellent discrimination between electron recoils and WIMP-like nuclear recoils. Events occurring close to the surfaces (dead layer) of solid-state detectors usually mimic nuclear recoils, but the phonon timing information obtained from the shape of phonons pulses in ZIPs allow the experiment to reject these backgrounds as well, thus enabling CDMS to maintain high sensitivity in WIMP searches.

4.2 ZIP detectors

ZIP detectors are cylindrical crystal of Ge and Si. The collaboration has fabricated 30 of these detectors among which 19 of them were made of Ge and 11 were made of Si. The substrate, made of p-type[1] or n-type[2], is 1 cm thick and 3 inches in diameter. The outer edge of the crystal has five flats, as shown in Figure (4.1), in order to facilitate alignment and handling: two major flats at the north and south positions, separated by 7.22 cm; two minor flats at east and west, separated by 7.55 cm; and a small fifth flat at the northwest, with a distance of 3.77 cm to the center). The exact position of the fifth flat indicates the orientation of the crystal axis, Figure (4.2) [318].

The substrate material used to make the ZIP detectors are prepared with low impurity and dislocation concentrations ($\sim 10^{11}$ impurities/cm^3 and less than 5000 dislocations/cm^2 for Ge) to ensure good charge transport. The cylinder axis of each detector is oriented along a $\langle 100 \rangle$ crystal axis (centered at 45°) and $\langle 111 \rangle$ (centered at 30°) [315].

The 30 ZIP detectors of the CDMS-II experiment consisted of 5 tower shown in Figure (4.3). A tower is a stack of 6 ZIPs vertically arranged. These ZIP detectors are adjacent to other detectors and separated by 2.2 mm with no intervening material. The collaboration has decided to operate detectors in such close proximity because it has the advantage that events due to backgrounds will often deposit energy in more than one detector. WIMP interactions, however, are expected to be so localized and infrequent that multiple-scatter events can be safely rejected without loss of signal efficiency .

One of the most important features of a ZIP detector is its ability to discriminate electron recoils from nuclear recoils. When an interaction occurs in a ZIP detector, the energy imparted to the crystal is deposited as a spectrum of high-frequency athermal phonons (called primary phonons). These are localized lattice vibrations which quickly downgrade in frequency as they travel toward the surfaces of the detector. Along the path of the

---

[1] A p-type semiconductor is obtained by carrying out a process of doping by adding a certain type of atoms (acceptors, positively charge) to the semiconductor in order to increase the number of free charge carriers (holes). When the doping material is added, it takes away weakly bound outer electrons from the semiconductor atoms. This type of doping agent is also known as an acceptor material and the vacancy left behind by the electron is called hole. The purpose of p-type doping is to create an abundance of holes

[2] A n-type semiconductor is a type of extrinsic semiconductor where the dopant atoms (donors) are capable of providing extra conduction electrons to the host and create an excess of negative electron charge carriers.

recoiling electron or nucleus, electron-hole pairs are created as well. The energy required to produce an electron-hole pair is 3 eV(3.82 eV) for Ge(Si). To avoid recombination of these particles, an electric field is applied across the crystal in order to drift the electrons and holes to opposite sides towards the surface electrodes where they can be measured.

For a given recoil energy from an interaction, the ratio of the ionization and phonon measurement is characteristically smaller for a nuclear recoil than for an electron recoil. This ratio is used as a particle identification parameter and constitutes the basis of the ZIP discrimination technology.

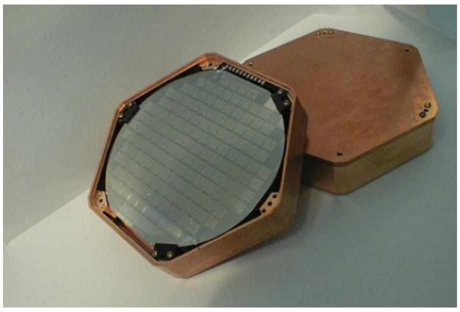

Figure 4.1: View of the CDMS-II Z-sensitive Ionization Phonons detector. The top view is photolithographically patterned by Transition-Edge Sensors (TESs) for phonon signal readout while the bottom side is patterned by Field Effect Transistors (FETs) to readout the charge ionization signal. Figure fron [317].

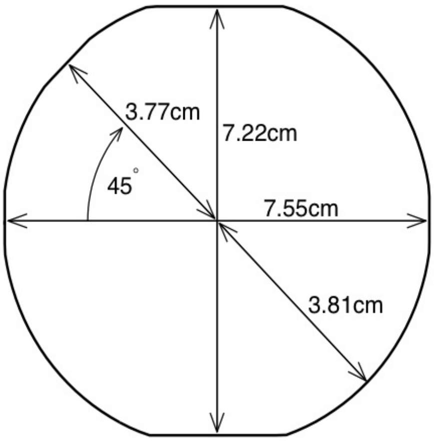

Figure 4.2: Geometry of a ZIP detector substrate as seen from the top, showing all flats. The major flats are at north and south, and the minor flats are at east and west. The small fifth flat is at 45^o north of the west position, indicating a $\langle 100 \rangle$ crystal axis. Figure from [318].

The signal readout of CDMS-II ZIP detector is made possible using its two faces (sides). The top side is used for phonon signal measurement while the bottom side is used for charge signal measurement, Figure (4.4). Each of the two detector faces is photolithographically patterned with sensor wiring. The bottom face is divided into two concentric ionization electrodes: an inner electrode (Qinner) covering ∼85% of the detector surface and an outer ring 3 mm in width (Qouter). The top face of each detector is occupied by four phonon sensors, each

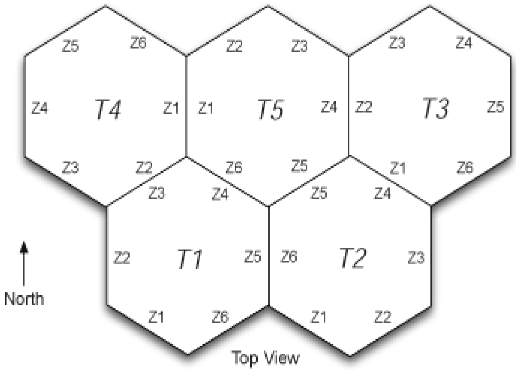

The following shows detector stack placement:

	T1	T2	T3	T4	T5
Z1	G6	S14	S17	S12	G7
Z2	G11	S28	G25	G37	G36
Z3	G8	G13	S30	S10	S29
Z4	S3	S25	G33	G35	G26
Z5	G9	G31	G32	G34	G39
Z6	S1	S26	G29	G38	G24

Figure 4.3: CDMS-II Soudan five Tower configuration. The top panel show the Tower/Detectors orientations. The bottom panel show the sideview of the detector stack placement. Table (4.1) gives the type of the substrate that were used in fabrication for each of the detectors shown above. Figure courtesy by Kyle Sundqvist [320].

composed of a total of 1036 tungsten transition-edge sensors (TESs) wired in parallel and fed by an array of aluminum quasiparticle traps.

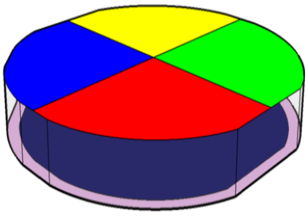

Figure 4.4: Schematic sensor configuration of a ZIP detector, showing four phonon sensor quadrants on the top face and two concentric charge electrodes on the bottom.

4.3 Ionization Signal

Free electrons and holes can be generated by the lifting of electrons from the valence band into the conduction band, thus creating equal numbers of electrons and holes. This can be accomplished by various mechanisms such as thermal agitation, optical excitation and ionization by penetrating charged particles that have to supply the necessary energy [322].

At low temperatures all valence electrons remain bound in their respective (tetrahedral) lattice. At higher

Table 4.1: List of CDMS-II detectors names, material used as substrates, thicknesses and masses. The difference between boule A, boue B and boule C is not only the doping type, but also the impurities and concentrations. Boule A has an impurity of 9.5×10^{10} (and a concentration of 10^{11} per cc), Boule B has an impurity of 2.7×10^{11} (and a concentration of 4.7×10^{11} per cm^3) while Boule C has an impurity of 8.5×10^{10} (and a concentration of 1.9×10^{11} per cc). Table from [321].

Detector Name	Material	Thickness (cm)	Mass (g)
T1Z1	Ge (n-type boule A)	9.65±0.05	230.5
T1Z2	Ge (n-type boule A)	9.53±0.23	227.6
T1Z3	Ge (n-type boule A)	9.18±0.05	219.3
T1Z4	Si (n-type boule A)	10.00±0.05	104.6
T1Z5	Ge (n-type boule A)	9.18±0.05	219.3
T1Z6	Si (n-type boule A)	10.00±0.05	104.6
T2Z1	Si (n-type boule A)	9.70±0.05	101.4
T2Z2	Si (n-type boule B)	10.00±0.05	140.6
T2Z3	Ge (n-type boule A)	9.18±0.05	219.3
T2Z4	Si (n-type boule B)	10.00±0.05	104.6
T2Z5	Ge (n-type boule B)	10.00±0.05	238.9
T2Z6	Si (n-type boule B)	10.00±0.05	104.6
T3Z1	Si (n-type boule b)	10.00±0.05	104.6
T3Z2	Ge (n-type boule B)	9.68±0.05	231.2
T3Z3	Si (n-type boule A)	10.00±0.05	104.6
T3Z4	Ge (p-type boule C)	10.00±0.05	238.9
T3Z5	Ge (p-type boule C)	10.00±0.05	238.9
T3Z6	Ge (n-type boule B)	9.70±0.05	231.7
T4Z1	Si (p-type boule A)	9.70±0.05	101.4
T4Z2	Ge (n-type boule A)	10.00±0.05	238.9
T4Z3	Si (n-type boule A)	9.70±0.05	101.4
T4Z4	Ge (p-type boule C)	9.82±0.23	234.6
T4Z5	Ge (p-type boule C)	9.71±0.05	231.9
T4Z6	Ge (p-type boule C)	10.00±0.05	238.9
T5Z1	Ge (n-type boule A)	9.40±0.23	224.5
T5Z2	Ge (p-type boule C)	9.61±0.23	229.5
T5Z3	Si (n-type boule b)	9.70±0.05	101.4
T5Z4	Ge (n-type boule B)	9.40±0.05	224.5
T5Z5	Ge (p-type boule C)	9.83±0.05	234.8
T5Z6	Ge (n-type boule B)	9.36±0.05	223.6

temperatures thermal vibrations may break the covalent bond and a valence electron may become a free electron, leaving behind a free place called hole. Both the electron and the hole (to be filled by a neighboring electron) are available for conduction as illustrated in Figure (4.5).

In crystal detectors, particle interactions in a semiconductor crystal can liberate some electrons (in their bound states) if they have sufficiently enough deposited energy to do so. These liberated electrons called primary electrons may have sufficiently high momentum to liberate other electrons from their bound states to the conduction band, producing a cascade of charge carriers as the energy of the primaries is dissipated into the crystal. This process leads to the production of lower-momentum electrons and holes in the vicinity of the particle track; this is the ionization process characterized by a loss of energy (dE/dx) of the particle as it moves.

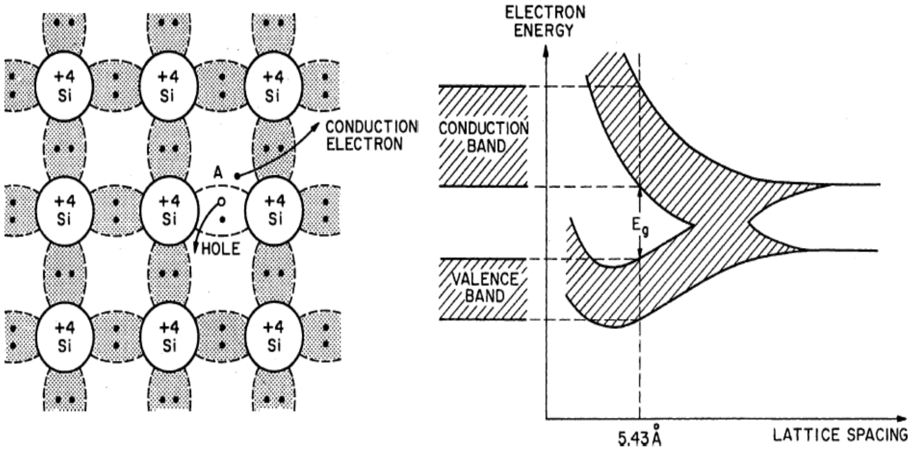

Figure 4.5: Left: Schematic bond representation of a single crystal with one broken bond in the center. Right: Energy levels of silicon atoms arranged in a diamond structure, as a function of lattice spacing. Figure from [323].

When a particle interaction supplies the energy needed to free electrons to the conduction band, a current proportional to the number of electron-hole pairs flows across the crystal. For a given recoil energy, the intensity of the current depends on the amount of energy it takes to produce an electron-hole pair, and whether it was an electron or nuclear recoil. For a semiconductor, the band gap is temperature dependent, and is well approximated by the Varshni relation [324]

$$E_g(T) = E_g(0) - \frac{\alpha}{T+\beta}T^2 \tag{4.1}$$

where $E_g(0)$, α and β are constants which depend on the type of semiconductor. For Ge (Si) semiconductors, these constants are given in the Table (4.2)

Table 4.2: Parameters $E_g(0)$, α and β of the Varshni equation for the temperature dependence band gap energy. Table from [324].

Semiconductor	$E_g(0)$/eV	α (10^{-4} eV K^{-1})	β (K)
Si	1.170 ± 0.001	4.730 ± 0.25	636 ± 50
Ge	0.7437 ± 0.001	4.774 ± 0.30	235 ± 40

so, for CDMS ZIP-detectors, since they are operated at $\sim$ 50mK, the band gap energy is approximately equal to E_0 (i.e. $E_g(T=0) \simeq E_0$).

The partition of energy in Ge (Si) semiconductor crystal is characterized by a quantum noted by ϵ which is equal to the average incident energy required to create (produce) one electron-hole pair. Though the band gap E_g of Ge (Si) is 0.734 eV (1.12 eV) at 0 K, the average deposited energy required to generate an electron-hole pair is substantially greater because some of the energy is shed as optical and acoustic phonons. For Ge (Si) substrates, $\epsilon = 3.0$ (3.8) eV at mK temperatures [327, 328, 329]. The number of electron-hole pairs created (by an electron recoil) is simply the ratio of the recoil energy to ϵ:

$$N_Q = \frac{E_R}{\epsilon} \tag{4.2}$$

For scatters off of nuclei, as experienced by neutrons or WIMPs, ionization is smaller by a factor of ∼3. This quenching factor for nuclear recoils is energy dependent and different for silicon and germanium targets as explained in detail in the Lindhard papers [330, 331].

4.3.1 Charge Transport

Charge transport is the physical process during which a charged particle (electron or hole) produced in a given location A has to be moved (transported) to another location B. In general, such a physical process requires the intervention of an electric field to drift the electron or hole from one location to another. However, if an electric field is present, due to the anisotropic nature[3] of the crystal material, the charge carriers will be accelerated in between random collisions in a direction determined by the electric field, and the net average drift velocity is given by

$$\vec{v} = \mu \vec{\mathcal{E}} \tag{4.3}$$

where $\vec{v}$, is the net (average) drift velocity, μ is the electron (hole) mobility and $\vec{\mathcal{E}}$ is the applied electric field.

Transport is strongly anisotropic, as discovered by Sasaki and Shibuya [332]. In particular, conduction of electrons occurs in band minima at the edges of the Brillouin zone, along the $\langle 111 \rangle$ direction in Ge and the $\langle 100 \rangle$ direction in Si. Surprisingly, this results in larger mobility in $\langle 100 \rangle$ in Ge and $\langle 111 \rangle$ in Si. In the case of holes, the band minima are all in the center of the Brillouin zone with larger mobility along $\langle 100 \rangle$ in both cases. These results, however, go to temperatures no lower than 8 K in most cases, and are affected by both phonon emission and scattering on thermal phonons.

4.3.2 Charge Readout

The CDMS-II ZIP-detector ionization channels are two electrodes (one is annular and the other is circular) deposited onto the bottom surface of each detector. One circular inner electrode (called Q-inner and noted by QI) covers most of the physical area (85%). The inner electrode is encircled by a thin annular electrode (Q-outer or QO). Both electrodes, Q-inner and Q-outer, are used to define the fiducial volume based on the partition of charge between the two electrodes.

Furthermore, the Q-outer electrode serves as a guard ring to reject events that may suffer from degraded ionization signals. The outer sections (including the side walls) are more exposed to background radiation. Background particles resulting from decays of radio-contaminants on the copper surfaces of the tower's mechanical

---

[3] In any material (anisotropic or not, carriers are accelerated in the direction determined by the $\vec{E}$-field which is dependent on the mobility μ too.

support structure are more likely to be incident upon these outer sections. The Q-outer electrode grants a level of protection against such events, while the Q-inner electrode is used to identify interactions occurring in the central part of the crystal, the fiducial volume.

The ionization measurement is accomplished by grounding the phonon side while a biasing the ionization electrodes at a bias voltage of -3 V, causing liberated holes and electrons to drift to opposite sides. A charge equal to eN_Q accumulates on the feedback capacitor shown in Figure (4.6) through the action of a charge amplifier. The build-up and subsequent decay (charge builds up over a few μs rise time and decays over $\sim$100 μs) of charge on the feedback capacitor results in an ionization pulse. As the charges drift across the crystal, image charges are induced on the metallized top and bottom surfaces. According to Ramo's theorem, the charge induced is equal to the charge drifted, so that the integrated current flowing to either surface is a measurement of the ionization produced by the initial interaction, discussed more fully in Section (5.1) of the Walter R. Ogburn's dissertation [318]. The relatively quick response of the ZIP ionization measurement makes the ionization-pulse start time the most accurate indicator of when a scattering event occurred. Independent Q-inner and Q-outer signals are digitized for each event. An optimal-filter template fit measures the pulse height (and start time) of each digitized signal and determine the exact energy deposited for each channel.

The ZIP ionization channels are biased through a large resistance, and capacitively coupled to a Field Effect Transistor (FET) amplifier to ensure that the electrodes are well coupled to the readout for fast pulses. The charge bias is coupled to the detector by a large bias resistor $R_b = 40$ kΩ , which does not dissipate much charge over the time scale of the pulse. Each electrode is connected to a coupling capacitor $C_c = 300$ pF, which passes the fast charge pulse, but keeps the bias and readout circuit relatively floating. Charge collected across the detector crystal quickly transfers to the feedback capacitor C_{fb}, producing a voltage spike V_{out}. This pulse decays as the capacitor drains through the feedback resistor R_{fb}, producing an exponential falling edge of the voltage pulse. The fall-time $\tau_f = 40$ μs of the pulse is determined by the $R_{fb} = 40$ MΩ and $C_{fb} = 1$ pF. The feedback capacitor is in parallel with a feedback resistor of 40 kΩ , which slowly dissipates the charge. The combination of feedback resistor and capacitor acts as a high-pass filter with time constant $\sim$40 μs. The ionization pulses therefore have a very fast rise, with rise time set by the amplifier response and the anti-aliasing filter in the RTF boards, and a fall time set by $R_{fb} \cdot C_{fb}$ (of about $\sim$40 μs). A fraction of the charge signal is lost in the capacitive coupling where the charge induced at the feedback capacitor is less than the induced image charge. The stray (parasitic) capacitance C_s incorporates several different components: relative capacitance of QI and QO, capacitance to neighboring detectors and the detector housing [318].

The transimpedance (complex impedance) of this system is given by [317]

$$A(\omega) = \frac{R_{bf}}{1 + j\omega R_{bf} C_{bf}}, \tag{4.4}$$

where $\omega = 2\pi f$ is the frequency of the fourier analogous of the time dependent input signal.

Although the CDMS read out set up is a low-noise transimpedance, the FET amplifier contributes a to

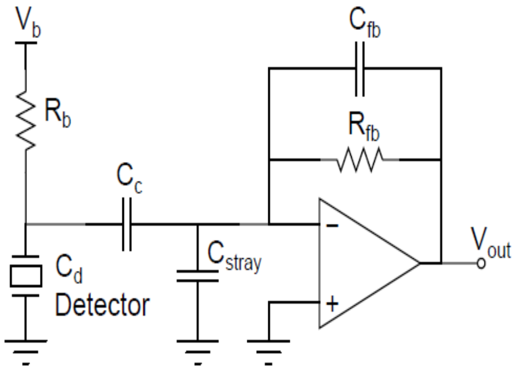

Figure 4.6: Ionization readout electronics. The ZIP detector has capacitance $C_d \sim 50$ pF, and is coupled to the amplifier through a coupling capacitor $C_c = 300$ pF. As an image charge is induced on the detector surface, the same charge appears at the feedback capacitor $C_{fb} \sim 1$ pF. The FET amplifier adjusts the output voltage to keep the potential difference between its two inputs to zero. The charge stored fades away through the feedback resistor $R_{fb} = 40$ kΩ. There are also stray capacitances $C_{stray} \sim 100\,$pF. The detector is biased with a voltage V_b, through a bias resistor R_b =40 kΩ. Figure from [318].

substantial amount of noise in the overall charge signals. The voltage noise in this system comes primarily from the amplifier's first-stage JFET and from the feedback and bias resistors. Other sources of noise include the current noise from the JFET, detector leakage current and microphonic effects from the wiring.

In practice, there is also a very large contribution from pickup of ambient noise, which has been reduced by the use of an radio-frequency shielded experimental enclosure and a careful grounding scheme. An expression for the total output voltage noise as a function of frequency has been derived [317]:

$$e_0^2(f) = |A(f)|^2 \left\{ i_{FET}^2 + i_d^2 + i_u^2 + \frac{4k_B T(R_{fb} + R_f)}{R_{fb} R_f} + e_{FET}^2 \left[(2\pi f)^2 (C_d + C_{fb} + C_s)^2 + \left(\frac{1}{R_{fb}} + \frac{1}{R_b} \right)^2 \right] \right\} \tag{4.5}$$

where e_{FET} represents the FET noise contribution and i_{FET} the current noise contributions from the FET input. The noise contributions from the detector leakage is denoted in above expression by i_d and any microphonic noise on the detector and its wiring is i_u.

4.4 Phonon Signal

When an interaction occurs in the ZIP detector, charged particles (electrons and holes) are first produced. Due to the electric field created by the biasing voltage across the two faces of the detector, these charged particles drift to opposite sides. Phonons (athermal phonons) are generated as result of drifting charged particles in the crystal. Phonons are generated through several distinct processes with very different energy spectra and transport properties. The initially displaced nucleus or electrons shed their kinetic energy in the form of primary phonons at the interaction site [340].

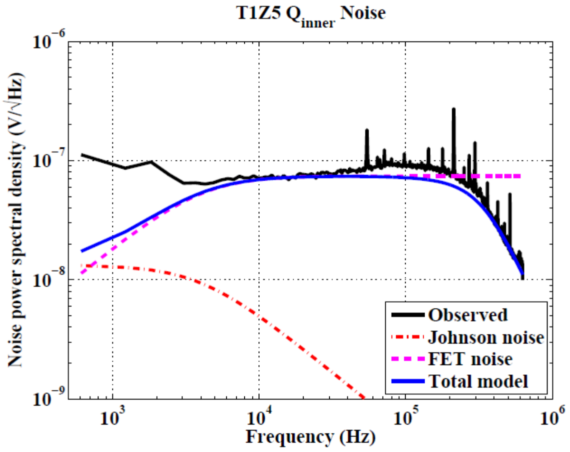

Figure 4.7: Measured ionization noise spectrum in the Q-inner charge ionization electrode for T1Z5 overlaid with model predictions (equation 4.5). The noise spectrum is rolled off at high frequencies by a low pass filter. The total contribution from the Jonhson and FET noise well match the shape of the measured charge noise at high frequency. Figure from [315].

Phonons are measured before the detector goes back to thermal equilibrium. These out-of-equilibrium phonons are often called **athermal-phonons**. The phonon signal does not only possess the information about the energy deposited by the particle interaction, it also retains a tremendous amount of information about the interaction type and location. This additional information which is lost in an equilibrium detector is a vital contribution to the background rejection and event reconstruction of CDMS-II ZIP detectors [341].

The ZIP phonon read out technology used in the CDMS experiment is called Quasiparticle-trap-assisted Electrothermal-Feedback Transition-edge sensors (or simply QETs). Detailed descriptions of the CDMs-II QETs can be found in a number of papers and CDMS theses [335, 336, 337, 338, 339, 340, 341].

4.4.1 Phonon Generation

The phonons generated by a particle interaction originate from three distinct mechanisms: primary phonons, recombination phonons and Luke phonons.

Primary Phonons

When a particle interacts in a ZIP detector, nuclear or electron recoils are produced. This initially displaced nucleus or electron deposits it kinetic energy as phonons at the interaction site as it relaxes back to equilibrium. A recoil energy E_R deposits a certain amount of energy to the primary phonons:

$$E_{prim} = E_R - N_Q E_g, \tag{4.6}$$

where N_Q is the number of generated electron-hole pairs and E_g is the energy band gap of the crystal or the Fermi energy. The primary phonons carry information about the position, timing and the energy characteristics of the particle event that are important for particle identification.

Recombination Phonons

Once the charged particles (electrons and holes)are generated and if there is not enough energy (external) to drift them apart or if the applied external $\vec{\mathcal{E}}$ field produce an energy $E_{\vec{\mathcal{E}}} \ll E_g$, the produced electrons and holes will eventually recombine. Recombination is the process where the charge carriers restore energy to the phonon system by relaxing back to the Fermi level. The recombination phonons have a total energy

$$E_{relax} = N_Q E_g. \tag{4.7}$$

Luke Phonons

Luke phonons (also commonly referred to as Neganov-Trofimov-Luke phonons) are emitted when charge carriers travel at the speed of sound in the crystal (analogous to Cerenkov radiation). The energy dissipated to the crystal as phonons radiate is the mechanism proposed by Neganov, Trofimov and by Luke [342, 343]. This phonon radiation contributes additional energy to the crystal beyond that in the initial interaction. This energy contribution is equal to the fields work on each charge and is defined by:

$$E_{Luke} = \sum_i^{2N_Q} q_i \int_{path} \vec{E} \cdot d\vec{x}, \tag{4.8}$$

where the sum is over each charge i (there are N_Q electrons and N_Q holes, so a total of $2N_Q$ charged particles) and the integral over the path taken by that charge. If the electric field is uniform and the charge carrier has elementary charge e the integral can take the following form:

$$E_{Luke} = eV_b \sum_i \frac{d_i}{a}, \tag{4.9}$$

where V_b is the applied bias voltage, a is the thickness of the crystal and d_i is the distance travelled by charge carrier i. If the detector always has complete charge collection, equation (4.9) takes the following form:

$$E_{Luke} = eV_b N_Q. \tag{4.10}$$

Since it takes an energy ϵ, 3 eV (3.83 eV), to produce an electron-hole pair in Ge (Si), the measured ionization energy in the ZIP detectors is then given by $E_Q = N_Q \epsilon$, leading to the Luke contribution to the phonon signal

$$E_{Luke} = \frac{eV_b}{\epsilon} E_Q \tag{4.11}$$

The above relation remains true for the case of incomplete charge collection although derived form a full (complete) charge collection. Incomplete charge collection is caused by trapping charges that occur before they reach the surface due to impurity in the crystal. This formula remains true for both case because the measured charge signal is proportional to the number of charges and the Ramo potential that they drift through. When some charges get trapped in the crystal, the loss in the ionization signal is in the same proportion as the loss to Luke phonons. The total phonon energy is given by: $E_P = E_{prim} + E_{Luke}$, we obtain:

$$E_P = E_R + \frac{eV_b}{\epsilon} E_Q \tag{4.12}$$

4.4.2 Phonon Propagation

There are four main processes contributing to the phonon propagation across a semiconductor crystal: phonon-carrier scattering, phonon-phonon scattering, phonon-impurity scattering and anharmonic phonon decay [344, 345]. Phonon-carrier and phonon-phonon scattering are essentially negligible at milikelvin and sub-milikelvin temperatures, since there are no free carriers or phonons outside of the initial phonon ball. The athermal phonons however are subject to two types of scattering, both of which become stronger with increasing phonon frequency: isotopic scattering and anharmonic decay [346].

The isotropic scattering is a Rayleigh scattering on isotopic impurities, with a ν^4 frequency dependence. It is a form of elastic scattering. For silicon and germanium, isotope scattering is independent of direction and phonon mode with a scattering time given by [347]:

$$\tau^{-1} = A_0 \nu^4 \tag{4.13}$$

with

$$A_0 \simeq ca^3 \left(\frac{\Delta m}{\bar{m}}\right)^2 \frac{(2\pi)^4}{4\pi v^3} \tag{4.14}$$

a constant characteristic of the crystal. In the formula (4.14), c is the impurity concentrations, a is the lattice spacing and $\Delta m/\bar{m}$ is the fractional mass difference; and v is the sound speed in the crystal. Reported values of A_0 are listed in the Table (4.4 [346, 348].

Table 4.3: Reported numerical values of the constant A_0 for the phonon isotope scattering for Silicon and Germanium semiconductors [346, 348].

Semiconductor	A_0 (s^3)
Si	2.43×10^{-42}
Ge	3.67×10^{-41}

The Anharmonic decay occurs when a higher-energy phonon splits into two lower-energy phonons. The frequency dependence is ν^5. This scattering process occurs primarily for longitudinal acoustic phonon modes, rather than slow or fast transverse modes. The rates for transverse phonons are very anisotropic, and can approach the rates for longitudinal phonons only in certain directions. The rates for longitudinal acoustic phonons at low temperatures (3 K) and 1 THz are 1.2310^5 s^{-1} and 1.6210^6 s^{-1} in Si and Ge [349, 350].

Since the two processes described above are strongly frequency-dependent, the mean free path of low-frequency phonons is much longer than that of their higher-frequency brethren. The vast majority of primary phonons are generated at multi-THz frequencies and therefore have mean free paths of the order of mm.

The anharmonic decay quickly reduces to a **bottleneck** frequency near 1.6 THz at which isotope scattering begins to dominate. After a few μs of quasi-diffusive propagation, these phonons decay sufficiently to bring their mean free path above the crystal dimension. At this point, these phonons becomes ballistic and propagate the detector surface without significant scattering [317].

Since only phonons that reach the detector surface are detected, the observed phonon signals in ZIP detectors are dominated by these ballistic phonons. Primary phonon detection is thus delayed by various processes: isotropic and anharmonic decays, quasi-diffusion followed by ballistic propagation. Recombination phonons are generated at energies of a few tenths of an electron volt but down-convert rapidly through interaction with the metal films (aluminum) at the detector surface [315, 318].

4.4.3 Phonon Readout

One of the important features and an extreme success of the ZIP athermal phonon measurement is its spectacular particle identification ability. This success is made possible through the use of phonon pulse shape information. The CDMS-II experiment uses the Transition Edge Sensors (TESs) aided by a quasi-particle trap assisted for phonon measurements. The top face of each ZIP detector is patterned with four phonon channels forming four quadrants, denoted by A, B, C and D. Each channel contains arrays of transition edge sensors, amounting to 1036 TESs per channel. Each superconducting tungsten (W) transition-edge sensor is 1 μm in width, fed by a set of 350 μm-long aluminum (Al) collector fins. The TES serves as a sensitive thermometer and the fins act as a reservoir, concentrating phonon energy from a wide area onto the tiny TES. Each TES and its surrounding fins are together referred to as a QET standing for quasiparticle-trap-assisted electrothermal-feedback transition-edge sensors. The structure of the ZIP-detector's QET consists of ten $\sim 380 \times 60$ $\mu\mathrm{m}^2$ Al collector fins attached to a ~ 250 $\mu\mathrm{m}^2$ W transition-edge sensor as illustrated in Figure 4.9. For Ge (Si) ZIP detectors, 28 of these QET structures are arranged in a 7×4 (6×4) array to form a $5 \times 5\,\mathrm{mm}^2$ QET cell [50].

Each TES is configured to detect phonons as the superconducting tungsten (W) resistance change due to the increase of the substrate temperature. To make the TES extremely sensitive to extremely small temperatures increase, every TES is kept at the transition temperature or transition point (T_c), temperature at which the tungsten becomes superconducting. If these phonons have at least twice the superconducting gap energy in Al ($2\Delta = 0.36$ meV) they can break a Cooper pair in the Al fins to generate quasiparticles. This minimum energy is much greater than the typical thermal energy $k_B T = 3.4\,\mu\mathrm{eV}$ of thermal phonons at 40 mK (therefore, only energetic phonons far from equilibrium can create quasiparticles). Once Cooper pairs are broken, electrons are freed and become quasi-particles. The quasi-particles can diffuse through the Al fins, until they reach the end near the TES. The minimum quasiparticle energy in the W TES $2\Delta = 25\ \mu$eV is much lower than that in the fins. A quasiparticle that diffuses to the TES edge can thus enter the W, but quickly loses enough energy to prevent its return to the Al fins; it is trapped. The quasiparticle energy in the Al fins is thus collected in the W TES. The phonon energy from a wide area is concentrated into a TES of low heat capacity, producing a much larger temperature change than would be achieved with the TES alone. The transition edge sensor is essentially a very sensitive thermometer. By maintaining a piece of tungsten at its critical (transition) temperature, Tc, a small change in the W temperature causes a large change in its resistance, as shown in Figure (4.10).

The measurement of the phonon signal in the ZIP-detectors starts when a ballistic phonon interacts with one of the many Al collector fins photolithographically coated onto the top side of each detector. The 300 nm-thick Al films are held well below their superconducting transition ($T_c \approx 1.2$ K) where the electrons are coupled into pairs of electrons called Cooper pairs.

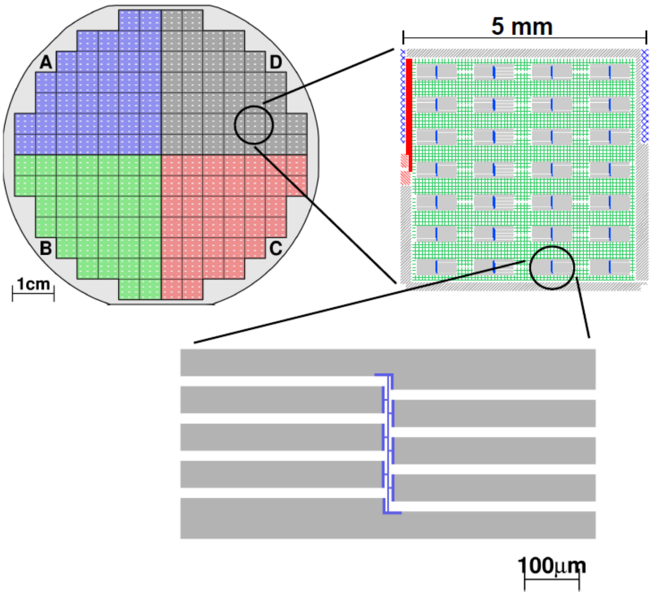

Figure 4.8: Schematic layout of the ZIP detector phonon sensors. Top left: Layout of the phonon side, illustrating the four sensor quadrants each consisting of 37 5mm×5mm dies. Top right: One of the 37 photolithography dies. Each die consists of 28 individual QETs. Bottom: A single QET, showing the 1 μm-wide W TES connected to Al collector fins. Figure from [316].

As mentioned in the previous paragraph, once cooper pairs are broken and quasi-particles are free, quasi-particles are the produced and they can quasidiffuse into the W region where the energy gap is smaller than the Al fin, in this region, the quasi-particles are trapped and cannot diffuse back into Al fins. Therefore the quasiparticles become trapped by the smaller tungsten (W) energy gap. Unable to return to the Al collector fin, the quasiparticles continue to a W-only region that is held at its superconducting transition point where, finally, the quasiparticles transfer their energy to the W films electron system, causing an increase in temperature that increases the W films resistance. This whole process is helped by quasiparticle trap-assisted electrothermal feedback. The change in resistance can be measured by biasing the W and monitoring the flow of current with a low-noise readout circuit.

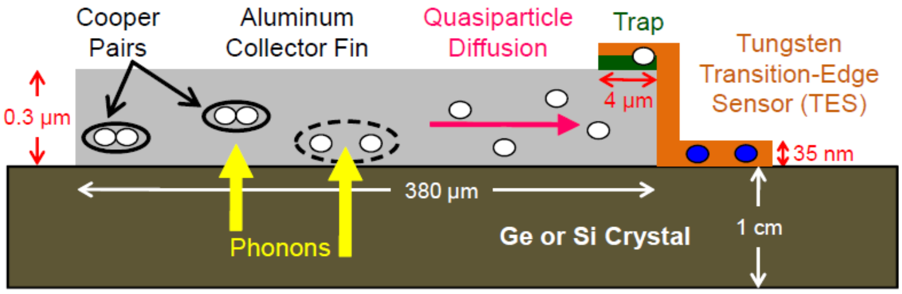

Figure 4.9: Quasiparticle trap-assisted transition-edge sensor (QET): ballistic phonons resulting from a particle interaction in the Ge or Si substrate travel to the surface of the detector where they encounter an aluminum collector fin. The Al is held below its superconducting transition such that many of its electrons are coupled into Cooper pairs. Phonons can dissipate their energy by breaking these Cooper pairs into quasiparticles, which may diffuse toward an Al-W transition region where they become trapped. The W film is held at its superconducting transition such that the change in temperature due to the quasiparticles causes a corresponding increase in the tungsten's resistance. Figure from [50].

The CDMS-II ZIP detector QET design was the result of a quasiparticle-collection optimization, described in greater detail in Tarek Saab's Ph.D. thesis [339]. This design of the QETs yields a quasiparticle-collection efficiency of nearly 25%. Previous ZIP detectors had nearly all the phonon side covered by Al collector fins. Such a configuration is non-optimal because the average distance a quasiparticle has to diffuse before encountering an Al-W transition region is a factor of ∼3.5 larger than the quasiparticle diffusion length (∼180 μm) [50, 362]. Since quasiparticles are likely to travel more than 1−2 diffusion lengths ($l_{diff} \sim \sqrt{\mathcal{D}\tau_{qp}}$, with $\mathcal{D}$ the diffusivity and τ_{qp}, the quasi-particle lifetime) before recombining back into Cooper pairs, the original design suffered from a quasiparticle collection inefficiency of ∼ 95%. The signal-to-noise ratio (S/N) in the phonon channel is critically dependent on the number of collected quasiparticles per keV of deposited energy. Such a design had limited sensitivity to the small energy depositions expected from WIMP-nucleus interactions. As the CDMS collaboration is attempting to increase their detector's sensitivity by 2 orders of magnitude in a second generation direct search dark matter experiment, new and improved QET design was proposed and tested. The next generation device, the interleaved ZIP or iZIP, which has significantly improved fiducialization performance. Unlike in the CDMS II design, both sides of the iZIPs are instrumented with high impedance charge electrodes and thus both the number of electrons and holes produced during the event interaction are measured separately which leads to a significant improvement of the radial fiducial volume. In addition to what is said, the number of phonon channels has been increased from 4 to 8 from and phonon sensors are now interleaved on both sides of the detector leading to superior z-fiducial volume definition. The channel geometry was redesigned so that there is now a circular outer phonon channel on both sides of the detector for significant improvement radial fiducial volume control through the partitioning of energy and pulse shape in the phonon channels. A complete description of the optimized generation CDMS detector device can be found in PhD dissertation of Matt Pyle [364].

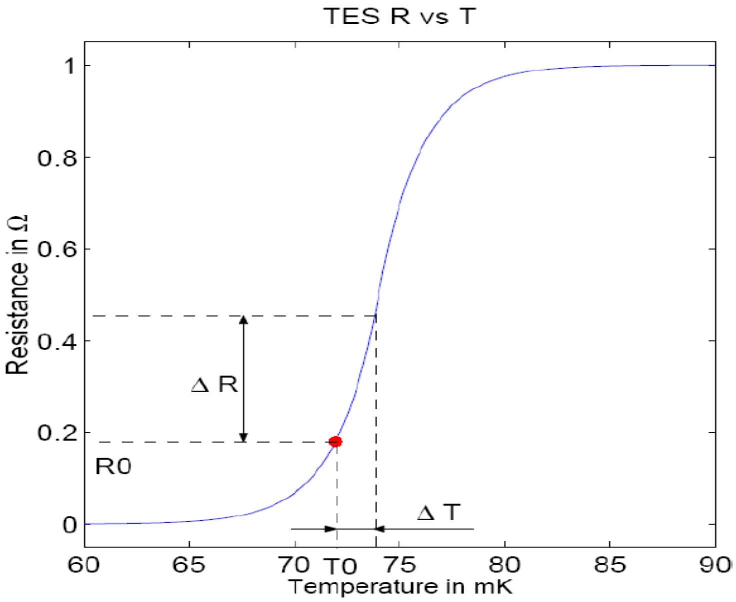

Figure 4.10: Transition edge sensor's resistance $R(T)$ as function of the temperature. The resistance is zero in the superconducting state (lower temperature) and higher in the normal state (at higher temperature). For CDMS purposes, the tungsten TES is kept exactly at the transition temperature T_c via a negative electrothermal feedback. The value of T_c and the transition width are characteristics of the W films used for the ZIPs. Figure from [407].

4.4.4 Electro Thermal Feedback

Another very important feature of the ZIP-detector phonon measurement is the use of ElectroThermal Feedback (ETF). A small change in temperature caused by quasiparticles transfer their energy to the electrons in a W TES. The transferred energy is measured as a change in resistance as shown in Figure (4.10). The largest change in resistance (for a given rise in temperature) occurs at the superconducting transition.

The Si or Ge substrates of the ZIP detectors are normally maintained at an operating temperature of about 40 mK, about half of the tungsten transition temperature. The sensor temperature is maintained within its superconducting to normal transition via the Joule heating associated with the voltage bias. The intrinsic stability of the voltage bias is due to negative electrothermal feedback (ETF), whereby an increase in sensor temperature and thus an increase in sensor resistance causes a decrease in Joule heating ($P = V^2/R$), and similarly a decrease in sensor temperature causes an increase in Joule heating, thus leading to a stable situation. A current bias however will result in power dissipated to the substrate proportional to applied current ($P = RI^2$), thus if the current increases and the resistance increases, the joule heating will increase as well resulting in a runaway situation where the sensor can never return to the equilibrium. The negative electrothermal feedback is the only biasing mode which will guarantee the sensor to switch back to the optimal operating point.

Figure (4.11) illustrates schematically the thermal circuit that the TES forms with its surroundings. The electron-phonon thermal conductivity and the conductivity between the substrate and the crystal are sufficiently large such that the thermal link between the phonons in the W and the bath (refrigerator) is strong. Consequently,

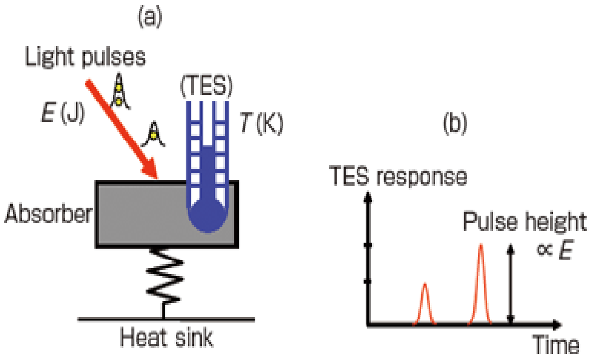

Figure 4.11: Right: Thermal schematic of an electrothermal feedback (ETF) TES illustrating the various thermal sources, sinks, and impedances. The thermal bath between the W phonons and the heat sink must be sufficiently low for the phonons to be at the refrigerator temperature. Left: show the TES response signals to light pulses.

the W phonons and the detector substrate are at the refrigerator's base temperature. If the temperature of the W electron system is higher than the base temperature then it will experience cooling. For the power flow to the heat bath, we assume a power-law dependence, which can be written as

$$P_{bath} = \kappa(T^n - T^n_{bath}), \tag{4.15}$$

where $n = 5$ is the thermal conductance exponent, and the pre-factor $\kappa = G/nT^{n-1}$, where the differential thermal conductance $G = \frac{dP_{bath}}{dT}$.

The response of the TES is governed by two coupled differential equations describing the electrical and thermal circuits. Each differential equation governs the evolution of a state variable: the electrical equation determines the current I, and the thermal equation determines the temperature T. Ignoring noise terms for the present, the thermal differential equation is

$$C_v \frac{dT}{dt} = -P_{bath} + P_J + P; \tag{4.16}$$

where C_v is the heat capacity (of both the TES and any absorber), T is the temperature of the TES (the state variable), P_{bath} is the power owing from the TES to the heat bath, P_J is the Joule power dissipation and P is the signal power. The other differential equation which govern the evolution the TES response is the electrical differential equation, given by

$$L\frac{dI}{dt} = V - IR_L - IR(T; I); \tag{4.17}$$

where L is the inductance, V is the Thevenin-equivalent bias voltage, I is the electrical current through the TES (the state variable) and $R(T; I)$ is the electrical resistance of the TES, which is generally a function of both temperature and current.

In order to keep the TES at its $T = T_c$ as required for optimal operating conditions, the net power flow must equal zero. This is accomplished by applying a voltage bias across the TES which, through joule heating, allows the TES to maintain an equilibrium temperature at T_c. The equilibrium point achieved in this manner is stable, and underlies the mechanism by which the TESs measure energy; this is the negative electrothermal feedback. The power balance equation can be expressed as

$$P_{etf} = \frac{dE}{dt} = \frac{dE}{dT_e} \cdot \frac{dT_e}{dt} = C_v \frac{dT_e}{dt} = \frac{V_b^2}{R(T_e)} - \kappa(T_e^n - T_{sub}^n) \tag{4.18}$$

where C_V is the heat capacity and V_b is the applied bias voltage. Assuming a δ-function energy deposition response from the TES, an extremely small temperature excursion (ΔT_e) from the equilibrium point will yield, at first order, the following time dependent change in the temperature

$$C_v \frac{d\Delta T_e}{dt} = -\frac{V_b^2}{R_0^2} \frac{dR}{dT_e} \Delta T_e - \kappa \Delta T_e \tag{4.19}$$

which solves as

$$\Delta T_e = \Delta T_0 \cdot e^{-t/\tau_{ETF}} \tag{4.20}$$

where $\Delta T_0 = E/C_v$ and the electrothermal feedback time constant is given by

$$\tau_{ETF} = \frac{\tau_0}{1 + \frac{\alpha}{n}(1 - \frac{T_{bath}^n}{T_0^n})} \tag{4.21}$$

where $\tau_0 = \frac{C_V}{\kappa}$ is the intrinsic thermal decay time and T_0 is the equilibrium temperature of the TES electron system. Usually, one define a unitless parameter $\alpha = \frac{d \ln R}{d \ln T}$ as measure of the slope of the resistance curve at the superconducting transition. The bigger the value of the α is, the more sensitive the TEs will be. The reduction of Joule heating on the time scale of τ_{ETF}, measured to be ~40 μs, which means that the energy deposited in the TES is measured before much can escape into crystal.

4.4.5 SQUID Readout and TES biasing circuit

Array of Superconducting Quantum Interference Devices (SQUIDs) inductively coupled to the TES biasing circuit provides the current-sensing element required for low-noise, high-bandwidth amplification of QET signals. A SQUID is a very sensitive magnetometer used to measure extremely subtle magnetic fields (5×10^{-18} T), based on superconducting loops containing Josephson junctions [50].

Current flowing through the TES induces magnetic flux in the SQUID which results in a voltage change across its terminals. This change in voltage drives an amplifier which feeds a current back into the feedback coil in order to cancel the change in magnetic flux through the SQUID. An input to feedback coil ratio of 10:1, and a feedback resistor $R_{feedback} = 1$ kΩ; convert the TES current into an output voltage given by $V_{out} = 10 \times I_{TES} \times 1\text{k}\Omega$. The CDMS SQUIDs are characterized by a modulation depth of 5 mV, flux quantum of 25 μA, and a nominal noise performance of 2 pA/ $\sqrt{Hz}$ (both referenced to the input coil). A more complete description of the SQUID characteristics and details can be found in [351]. The bias resistor R_{bias} and bias current I_{bias} provide the TES bias voltage. $R_{bias} = 20$ mΩ provides a stiff voltage source for TES resistances above ∼200 mΩ.

SQUID characteristics

The SQUIDs used by the CDMS collaboration possess the following characteristics:

1. **Turns ratio**

   The CDMS SQUIDs are designed with an input coil and a feedback coil characterized by inductances L_i and L_f respectively. The ratio of the number of turns in the input coil to the number of turns in the feedback coil is referred to as the turns ratio. It is designed to be 10 for an optimal operation [176, 407].

2. **Current-per-Φ_0**

   This is the current in the input or feedback coils corresponding to one quantum of flux in the SQUID. It is 25 μA in the input coil or 250 μA in the feedback coil.

3. **V-Φ curve**

   The V-Φ curve is given by the variation of the voltage across the SQUID caused by changing the flux through the SQUID. The maximum peak-to-peak amplitude of the V−Φ curve is also referred to as the modulation depth (typically equal to 5 mV).

4. **Responsivity**

   The responsivity is a very important characteristic of the SQUIDs is. The responsivity $r = \frac{dV_{sq}}{dI}$ is defined as the change in voltage across the SQUID for a given change in current (either in the input or in the feedback coil). This can also be estimated from the slope of the V−Φ curve. The responsivity is important for two reasons: (i)the input noise of the amplifier (used to amplify the SQUID voltage) is amplified by the factor R_f/r, where R_f is the feedback resistance. A very large responsivity reduces the impact of the amplifier noise and increases the signal-to-noise ratio. (ii) the open-loop gain of the amplifier (which includes responsivity as one of the gain factors) sets the bandwidth of the amplifier chain in the closed loop mode. The amplifier is designed to give ∼2 MHz bandwidth for $r = 1000\ \Omega$ referred to input (for the NIST SQUIDs, responsivity of 500 - 1000 is normally referred to input and noted as RTI) but this value varies for different values of responsivity [407].

5. **SQUIDs resonances**

   The resonances appear as distortions of the V−Φ curve and they tend to increase the SQUID noise significantly, so it is desirable to avoid them. The SQUID resonances are well known and have been studied, [356]. There are two types of resonances that appear in the SQUIDs used by the CDMS experiment. First of all, there is a feedback-type resonance. In this case, the current through the tunnel junctions capacitively couples to the coils, which then feeds back inductively into the SQUID. On one slope of the V−Φ, the two effects will cancel each other out. On the other slope, however, the feedback will be positive and a resonance will be created; this kind of resonance can appear only on one slope of the V−Φ curve. Second, there is a junction-type resonance. In this case, the bias of the SQUID introduces a voltage drop across the SQUID, which is, in turn, related to the frequency of the currents flowing through the SQUID loops, so changing the SQUID bias changes this frequency. If the frequency matches the natural frequency of the system, a resonance appears. Hence, this kind of resonance appears only at a particular, usually relatively large, SQUID bias voltage. Both types of resonances can be avoided by applying relatively low SQUID bias and by locking the SQUID on the side of the V$-\Phi$ which has no feedback-type resonances [176, 356].

Noise

The actual SQUID circuitry used in the CDMS experiment is extremely more complex. It has the ability to modify the amount of magnetic flux trapped in the SQUID array (see, for example, Sae Woo Nam's Ph.D. thesis [352]). The particular dc-SQUIDs used by CDMS are described in detail in [353, 354]. During normal operations, the combined noise performance of the phonon measurement (including the QET and biasing circuit) tends to vary from $\sim$10$-$20 pA/ $\sqrt{Hz}$ (depending on detector stability). The phonon-signal noise resolution is comparable to the ionization resolution at the 1σ level [50, 315].

The noise performance of the phonon channel is set by fluctuations in the system due mainly to the following dissipative components: the TES's electrical resistance, the shunt resistor, keep the electron-phonon conductance g_{e-ph} within the TES and by the noise current of the SQUID array. The Johnson noise of the shunt resistor is the dominant contribution to the current noise in the input coil: $i_{sh} = \frac{\sqrt{4k_B T_{sh} R_{sh}}}{R_{TES}} \approx 15$ pA/$\sqrt{Hz}$. It is worth mentioning that the electrical response of the TES circuit such as its complex impedance can be used to probe the electrothermal characteristics of the TES itself. A rigorous derivation of the the contributions to the readout circuit noise, arising from the Johnson electrical noise of the TES, bias, and parasitic resistors are given by [339]. The largest sources of noise in ZIP phonon channels are the Johnson noise of the TES and other resistive elements in the QET circuit, and the phonon noise in the TES. Johnson noise is caused by the thermal fluctuations of charge carriers in a resistor at finite temperature. For an ordinary resistor, the Johnson noise can be considered a voltage noise per unit bandwidth $v_n = \sqrt{4k_B TR}$ in series with the resistor, or equivalently, as a current noise per unit bandwidth $i_n = \sqrt{\frac{4k_B T}{R}}$ in parallel with the resistor (T is the temperature in Kelvin, R is the resistance and k_B is the Boltzman constant). A modified circuitry of the CDMS phonon amplifier is oftentimes used for derivation of the full expression of the noise contribution. Using the symbols used in the Figure (4.13), the expression of the noise at the input coil resulting from the Johnson noise of the parasitic resistance and the bias and shunt resistors is given by the following expression:

$$\begin{aligned} i_R^2(\omega) = \frac{4k_B T_p}{R_p}\left(\frac{R_p}{R_p + R_s + R_{sh}}\right)^2 + \frac{4k_B T_{sh}}{R_{sh}}\left(\frac{R_{sh}}{R_p + R_s + R_{sh}}\right)^2 \\ + \frac{4k_B T_b}{R_b}\left(\frac{R_b}{R_p + R_s + R_{sh}}\right)^2 \end{aligned} \tag{4.22}$$

assuming that $R_{sh} \ll R_b$. This expression can further be simplified using the fact that the bias resistor is very

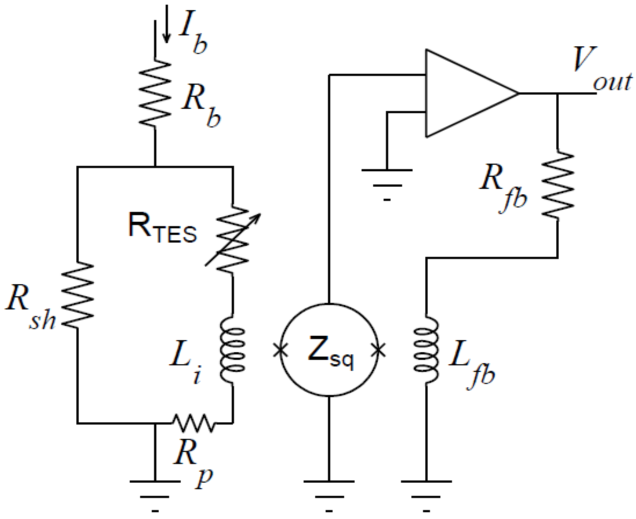

Figure 4.12: schematic of the CDMS phonon amplifier for the CDMS-II circuit. The transition edge resistance (TES) $R_{TES} \simeq 200$ mΩ is biased voltage since it is placed in parallel with the shunt resistor. The bias condition creates stable, negative electrothermal feedback. The current source is provided by a large resistor $R_b = 1\,\text{k}\Omega$ at room temperature, There is a small parasitic resistance R_p of few mΩ. The feedback resistor $R_{fb} = 1\,\text{k}\Omega$ converts the current signal to a voltage. The input coil $L_i = 250\,\text{nH}$ couples the TES current to the SQUID. The integrated amplifier adjusts its output voltage in order to cancel the flux through the SQUID, resulting in an amplification given by the turn ratio of the input and feedback coils, $L_i/L_{fb} = 10$. Figure adapted from [318].

large compared to the other resistances, i.e. $R_b \gg R_s + R_p + R_{sh}$:

$$i_R^2(\omega) = \frac{4k_B}{(R_{sh} + R_s + R_p)^2}\left(T_pR_p + T_{sh}R_{sh} + T_b\frac{R_{sh}^2}{R_b}\right)^2. \tag{4.23}$$

Table (4.4) illustrate the approximate values of the resistances and temperature contributing to the Jonhson noise. For a voltage-biased TES, the noise expression was derived by Kent Irwin [355] and it is given by

$$i_{TES} = \frac{4k_BT}{R_0}\frac{(n/\alpha)^2 + (\omega\tau_{etf})^2}{1 + (\omega\tau_{etf})^2} + \frac{4k_BT}{R_0}\frac{n/\alpha}{1 + (\omega\tau_{etf})^2}, \tag{4.24}$$

where the first term is the Johnson noise, and the second term is the phonon noise (i.e. thermal fluctuations in the thermal link between the tungsten electron system and the substrate). The total current noise at the input coil is the sum of the noise contributions given by the equations (4.23) and (4.24). The entire expression is rolled off at high frequencies by the self-inductance of the input coil, with a time constant L/R_s. The action of the R-L circuit is a single-pole low-pass filter, with a gain given by

$$G_L^2(\omega) = \frac{(\omega L)^2}{R_s^2 + (\omega L)^2}. \tag{4.25}$$

The current noise in the input coil of the SQUID is rolled off by the L/R (time constant) filter on the input side of the SQUID where $L = 0.25$ μH is the self-inductance of the input coil and R is the combined

Table 4.4: Contribution of various resistances to the noise in the phonon channel. The total noise including the SQUID noise contribution is about ∼2 pA/ $\sqrt{Hz}$. Table from [339].

	R(mΩ)	T(mK)	Noise pA/$\sqrt{Hz}$
R_{sh}	4	4000	4.2
R_b	20	600	3.6
R_s	∼200	∼80	4.2

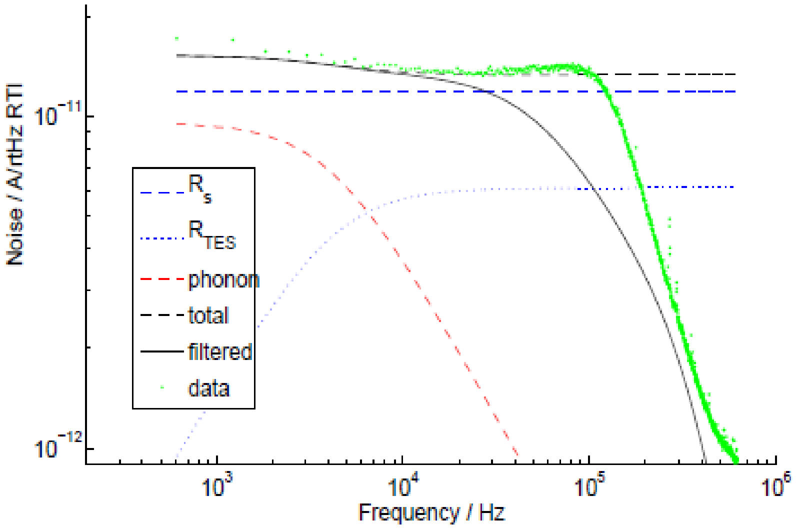

Figure 4.13: The predicted and observed noise in a ZIP detector phonon channel. The noise was measured during SQUET testing, or in the case of R_s, as inferred using saturating pulses from muon events. The discrepancy at around 100 kHz indicates an unexpected resonant behavior of the SQUID amplifier, which extends the bandwidth beyond the L/R cutoff. The bandwidth of the system is set by the amplifier; the −3 dB point is at ∼160 kHz. Figure from [318].

resistance on the input side, dominated by R_s in the usual mode of operation. The signal-noise ratio is optimal for $R_s = 100 - 200$ mΩ, resulting in a frequency-dependent current noise in the input coil. The power spectrum density PSD has a −3 dB point in the frequency range of $65 - 130$ kHz, after which it has $\sim 1/f$. There is another noise component which is frequency independent in the output and it is composed of the amplifier noise and the digitizer noise. It contributes ∼5 pA$\sqrt{Hz}$ or less, depending on the digitizer. The total output noise is dominated by the amplifier and digitizer noise components at frequencies much above 140 kHz; however, at these frequencies, the signal-to-noise ratio is typically negligible already for most phonon pulses for which the shape of the noise spectrum is experimentally confirmed.

The intrinsic rise time and delay of a phonon pulse are modified by the bandwidth of the QET circuit and the SQUID amplifier. The current through the QET is inductively coupled to the SQUID, giving an intrinsic L/R. Additionally, the RTF board includes a 8-pole antialiasing filter immediately before the signal is digitized. This filter acts as a second-order Butterworth filter at 335 kHz. The actual bandwidth of the readout circuit is immensely affected by resonant behavior in the SQUID amplifier, so that the minimum rise time is typically faster than L/R, still slower than the frequency of the antialiasing filter.

Falling Edge

When particles such as gammas or WIMPs (neutrons) interact with the phonons sensors of the ZIP-detectors, they deposit energy. This deposited energy is quickly absorbed by the transition edge sensors (as results of change of the substrate resistance from the superconducting state to normal as the temperature increased). The energy is quickly deposited into a TES, it must cool back to its equilibrium temperature by shedding heat into the substrate. The power dissipated from the TES is approximately constant. In equilibrium, it exactly balances Joule heating. When the TES warms up, the Joule heating is greatly reduced, so that the TES cools due to the effect of negative electrothermal feedback (ETF). The thermal time constant of the TES is set by $\tau_0 = C/g$ [355]:

$$\tau_0 = \frac{\tau_0}{1 + \alpha/n} \tag{4.26}$$

However, it is observed that the falling edges of pulses created by particle interactions have much longer fall times which presumably indicates that the arrival of the energy at the TES is not instantaneous. There are long tails, either because some phonons continue to be absorbed in the aluminum fins at late times, or because some quasiparticles are trapped in the aluminum for a certain amount of times before they can be released and make it to the W-TES.

To estimate the ETF time, which however is unaffected by the long tails in energy arrival, we have resorting to using noise glitch events. By averaging over many of these noise glitch traces and fitting exponentials to the falling tails, the true ETF time of each sensor is determined.

4.5 T_c Tuning and $I_b - I_s$ characteristics

The superconducting to normal resistive transition in a W thin-film provides the best fast response thermal sensor. These are called superconducting transition-edge sensors (TES). CDMS collaboration developed a SQUID-based voltage-bias readout scheme which takes advantage of negative electrothermal feedback (ETF). The W films possess two crystalline phases: α and β phases. The α phase has a $T_c \sim 15\,\text{mK}$ while the β phase has $T_c \sim 1\,\text{K}$ (0.2 $\Omega\mu$m and 1 $\Omega\mu$m of resistivity respectively). The W films produced by the CDMS collaboration are predominantly α phase (catalyzed by O_2 as found by using gas trace analysis in W- sputtering). The T_c values vary between different depositions, but tend to lie in the range of 100 to 150 mK. In addition, the W films exhibit a T_c variation, on the order of 20 to 40 mK, across the surface of an individual detector [318].

The transition temperature T_c of the TESs depends on the thickness and phase mixture of the tungsten films. Although α-W has a low T_c, the long-range structure of β-W allows it to superconduct at higher temperatures, up to 4 K. Tungsten TESs operated at ~100 mK must therefore have a mixture of the two phases which requires careful control of the metallization process and wafer preparation for which the recipe was developed at Stanford

[357, 358].

A T_c gradient across the surface of a detector causes, in addition to varying noise contributions, a variation in pulse shape, as a function of position. This results in a position dependent systematic uncertainty in the energy measurement as well as a degradation in the ability to perform particle identification based on pulse shape. If the intrinsic properties of the films often vary across the crystal, there will be a T_c gradient across the phonon sensors of the ZIP-detectors. In order to reduce the effect of the T_c variations a method of tuning the W T_c was developed [359]. The mechanism behind the tuning lies in the dependence of the critical temperature on the concentration of magnetic impurities (dopants) in the film [360, 361].

After each detector is fabricated, it is cooled below 50 mK in one of CDMS test facilities: University of California at Berkeley, University of Minnesota and Queens University in Canada. The fabrication facilities are University of Stanford, CA and the University of Texas A&M. Each quadrant is characterized by measuring its $I_b - I_s$ characteristics measured as the variation of sensor current as a function of bias current at a fixed substrate temperature. This is equivalent to measuring the sensor resistance as a function of bias current.

IV curves

IV measurement is an important tool in characterizing the parameters and performance of a TES. It provides a diagnostic for understanding the the behavior and parameters of a TES as well as extracting its R vs. T dependence. $I - V$ and $I_b - I_s$ measurements are useful in determining the width of the superconducting transition as well as the variation of sensor current as a function of bias current at a fixed substrate temperature; his is equivalent to measuring the sensor resistance as a function of bias current.

To describe the behavior of a TES, there usually are three distinct regimes: normal, biased, and superconducting. Each regime is determined by the voltage bias applied to the TES [362].

1. **Normal**

   In such s regime, the current through the substrate (I_s), is extremely large, the W will revert to its normal state with a resistance of $\sim 1\,\Omega$. The bias current I_b will create a voltage across the branch of the TES so that the current flowing throug the substrate (the TES) is such that $I_b\,R_b = R(R_{TES}, L_i)\,I_s$ since the normal state resistance is much larger than R_{bias} and R_{sh}, so the whole current applied will pass through the TES, with I_s the TES current and $R(R_{TES}, L_i)$ is the impedance on the branch which is approximately given by $R(R_{TES}, L_i) \approx R_{TES}\left(1 + \frac{1}{2}\left(2\pi f \frac{L_i}{R_{TES}}\right)^2\right)$. Given that the ratio $L_i/R_{TES} \ll 1$, the current through the substrate will be governed by the following equation

   $$I_s = \frac{R_{bias}}{R_{TES}} I_b \tag{4.27}$$

2. **Biased**

   In the biased regime, the Joule heating generated in the W TES equals the power lost to the cold substrate due to negative electrothermal feedback. The temperature dependence of the power dissipated by the TES into the substrate is given by 4.15. Given the fact that the superconducting transition is few mK wide, it is a good approximation that the power dissipation is constant throughout the transition.

$$P = \frac{V_b^2}{R} \tag{4.28}$$

3. **Superconducting**

   If the bias current becomes extremely small such that R_{TES} becomes comparable to R_{bias}, the TES will cease to be voltage biased and will become current biased. In such a case, Joule heating will decrease with the bias current and the TES will quickly cool (snap) becoming fully superconducting. In this state one would expect I_s to be equal to I_b, however, due to small parasitic resistances, I_s will be slightly smaller but linearly dependent on I_b.

$$I_s = \frac{R_{bias}}{R_{TES} + R_{para} + R_{bias}} I_b \tag{4.29}$$

The TES will remain superconducting as the sensor current is increased, until I_s exceeds the critical current (I_c), at which point the sensor quickly becomes normal.

TES Phase Separation

One phenomenon which can impact the performance of the TES and affect the shape of the IV curve, is phase separation. It refers to a superconducting - normal phase separation in which a portion of the TES is normal (resistive) while the remainder is fully superconducting. This effect is often times swept under the rug when we talk about TES. We have always assumed that the entire length of the TES is at the same temperature and in the same phase. A possible mechanism behind phase separation in a TES is the balance of heat flow along the TES with that of heat flow into the substrate. The general idea is that the equilibrium power balance between Joule heating (at a given I_b and a T_c) can be satisfied by having a fraction of the TES being normal, with $T > T_c$. Detailed necessary criteria for phase stability and consequently the solution of the heat flow equations along the TES are described in [339, 352]. It is believed phase separation is still present in the currently fabricated CDMS detector; however its effect is minor and not worrisome. However, with the advent of the interdigitated detectors (commonly referred to as iZIPs), it was observed that the phonon fall times becomes longer than usual. The falltimes are longer in the iZIPs designs than in our previous designs (CDMS II ZIP-detectors and SuperCDMS Mercedes Designs or mZIPs). It therefore becomes imperative to check whether the unusual phonon fall times are due to an increased of TES local saturation (due to ion implantation) if the phase separation is at play [363].

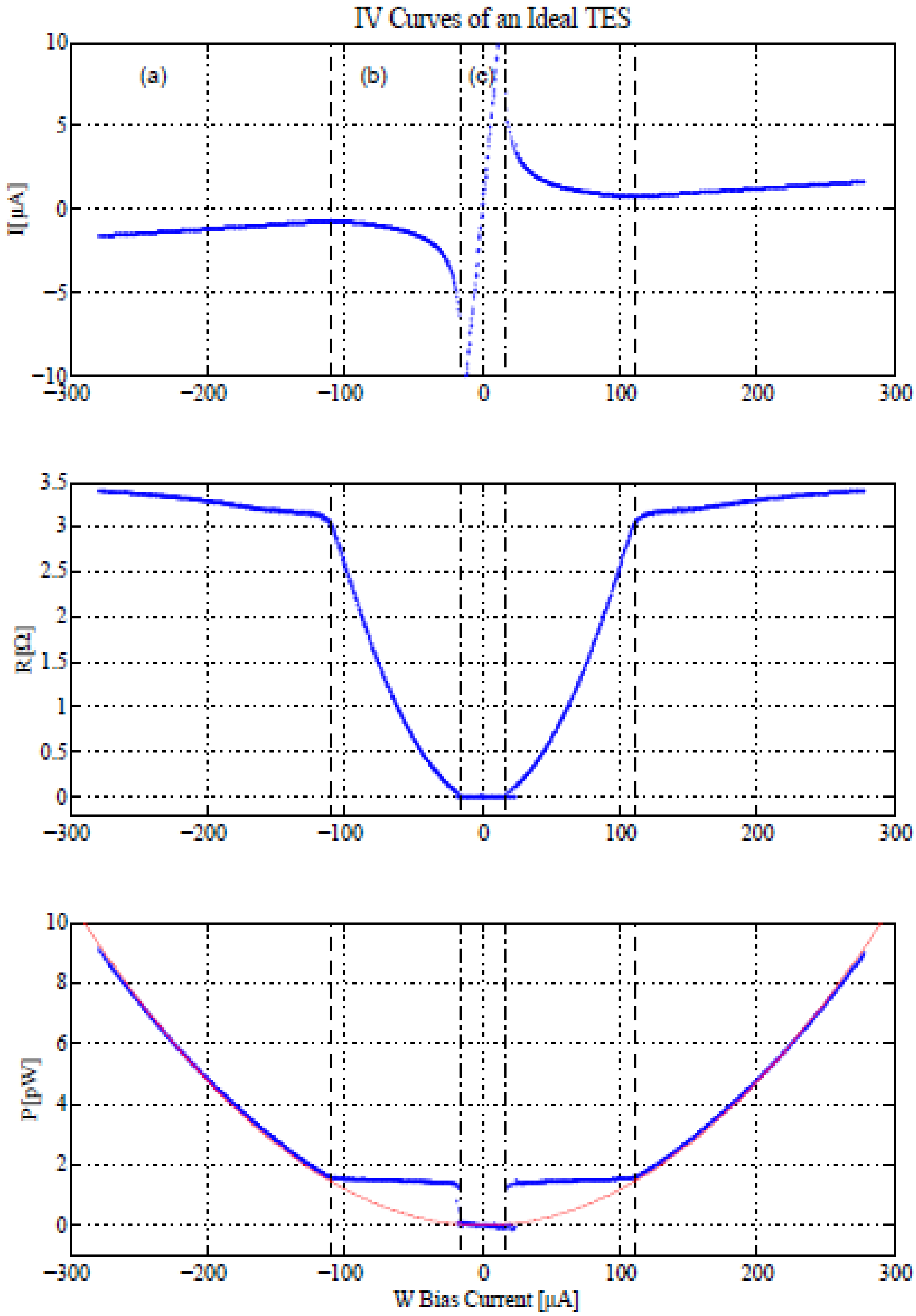

Figure 4.14: The current bias through the parallel circuit (proportional to the sensor voltage bias) in Fig 1a versus (a) the current through the W sensor, (b) the resistance of the W film, and (c) the power dissipated in the sensor. [362].

Chapter 5

CDMS–II Experiment at Soudan: An underground Laboratory

5.1 Introduction

Searches for rare events such as dark matter require the experiment to run in a place where backgrounds can be reduced or mitigated as much as possible. In a shallow experimental site, hadronic component of cosmic rays [365], which constitutes background for dark matter search, can be stopped by making use of shields. During the CDMS-I experiment housed at the shallow site at Stanford University, it was noticed that a high flux of muons (∼6 kHz) passed through the veto shield [315]. Most of the neutrons produced by muons were vetoed, but occasionally, a muon interacted in the walls (rocks) of the cavern to produce an external neutron that passed through the shield and interacted with the detectors. These external neutrons constitute an irreducible background for dark matter experiment because they cannot be distinguished from WIMP scatters on an event-by-event basis. Moreover, they can be statistically subtracted, since some of them scatter in multiple detectors, and they produce more frequent above-threshold events in Si than in Ge. Background substraction, however, demands the experimenter to have a very good understanding and characterization of the experimental backgrounds in order to subtract them from any signal excess that presumably can become a WIMP signal.

The interaction of energetic cosmic-ray induced muons with the cavern rock and materials of the experimental setup can generate neutrons at MeV energies which can produce keV nuclear recoils in the detectors. The neutrons generated through spallation (muon-induced nuclear disintegration) or various secondary processes within muon-induced hadronic and electromagnetic showers. At Soudan underground facility, at depth of 2090 m.w.e, corresponding to the rock overburden at the experimental site the muon flux is reduced by a factor of $\sim 5 \times 10^4$ with respect to the surface flux. Nonetheless the remaining muon flux ($<$ 1 muon per minute interacts in the experiments veto shield) produces a possible neutron background which must be contained.

Most WIMP searches use a series of active and passive shields. In addition to this shielding, the experiment is brought deep underground in order to reduce the flux of cosmic ray muons, Figure 5.1.

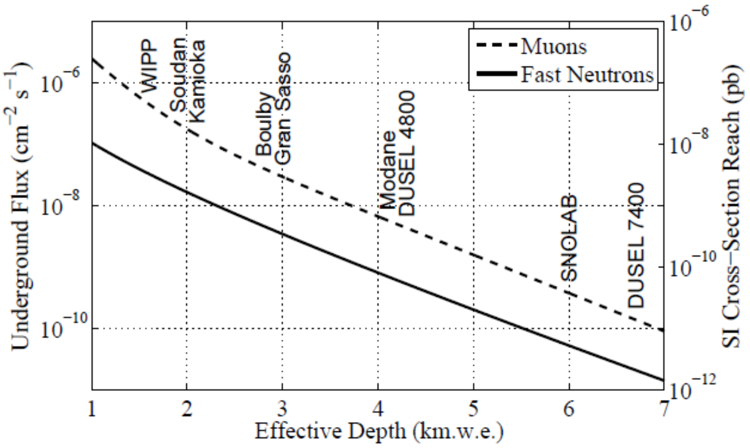

Figure 5.1: Flux of muons (dashes) and muon-induced neutrons (solid) as functions of depth underground, measured in terms of the equivalent thickness of water in km below a flat surface that is needed to provide equal shielding. Effective depths of primary underground facilities for dark matter experiments are listed. Neutron background resulting from a given fast neutron flux is highly dependent on the experimental setup and materials, the curve of neutron flux (still solid) referred to the right-hand axis shows the limit on sensitivity due to neutron backgrounds. Figure from [366].

5.2 Soudan Laboratory

The CDMS-II experiment is located at the Soudan mine in northern Minnesota. The mine was exploited for iron by U.S. Steel until its closure in 1962 when it was handed over to the state Department of Natural Resources which partnered with the University of Minnesota to make part of the mine available to physics experiments as the Soudan Underground Laboratory. The CDMS-II experiment laboratory is in Level 27 (the same level as the MINOS neutrino oscillation experiment), the deepest level of the mine at 2341 feet (714 m) below the surface, corresponding to an effective depth of 2090 mwe (meter water equivalent) [317]. Figure (5.2) show the Soudan's headframe mine. An elevator runs twice daily (morning around 7:30am and evening at 5:30) am in order to take people down and up.

The great depth of the Soudan site makes it extremely attractive to many forms of low-background experiments particularly searches for rare events. Its depth reduces the cosmic-ray muon flux by a factor of ∼50,000 from its value at the surface. This reduction in muons is accompanied by a corresponding reduction in muon-induced particle showers, particularly the neutrons generated in such showers. Since neutron-induced nuclear recoils cannot be distinguished from their WIMP-induced counterparts, direct detection experiments at great depth have much lower background rates (and hence greater sensitivities) than similar experiments conducted at the surface. As an example, the sensitivity of the first CDMS-II run at Soudan in 2003 was an order of magnitude

Figure 5.2: Entrance to the headframe of the Soudan Underground Laboratory.

greater than that of CDMS-I last run at Stanford Underground Facility (17 m.w.e.) in 2001 [315].

Muons are the most numerous energetic charged particles at sea level. A charged particle cannot avoid losing energy by ionization. As it passes through matter the charged particle interacts with the electric fields and typically knocks loose some of the loosely bound outer electrons. A muon interacts very little with matter except by ionization. Because of this, muons can travel large distances and commonly reach the ground. However, they lose energy proportional to the amount of matter they traverse. The energy loss is proportional to the density (g/cm^3) times the path length (cm) [370].

Muons lose energy at a fairly constant rate of about 2 $MeV/g/cm^2$. Since the vertical depth of the atmosphere is about 1000 g/cm^2, muons will lose about 2 GeV due to ionization before reaching the ground. The mean energy of muons at sea level is still 4 GeV. Therefore the mean energy at creation is probably about 6 GeV. The atmosphere is low dense (tenuous) at higher altitudes that even at $15,000\,\mathrm{m}$ it is still only 175 g/cm^2 deep. Typically, it is about here that most muons are generated. Muons arrive at sea level with an average flux of about 1 $muon/cm^2/min$. This is about half of the typical total natural radiation background [372].

If muons are generated within a cone-shaped shower, with all particles staying within a certain angle θ (usually about 1 degree) of the primary particle's path, the flux should be corrected by the cone cross-section by multiplying it by a factor equal to $1/\cos(\theta)$ [373].

5.3 CDMS-II Facility at Soudan

The Soudan 2 cavern was excavated in order to accomodate the special infrastructures needed to support CDMS II experiment [317]. The detectors are housed in a cold enclosure called the icebox connected to a dilution refrigerator by a cold stem (c-stem) and to a front-end electronics system by an electronics stem (e-stem). All of these sit in a class-10000 clean room with receiver filter shielding to provide a low-electrical-noise environment.

The cryogenic control systems developed by the cryogenics dark matter search (CDMS) collaborator allow

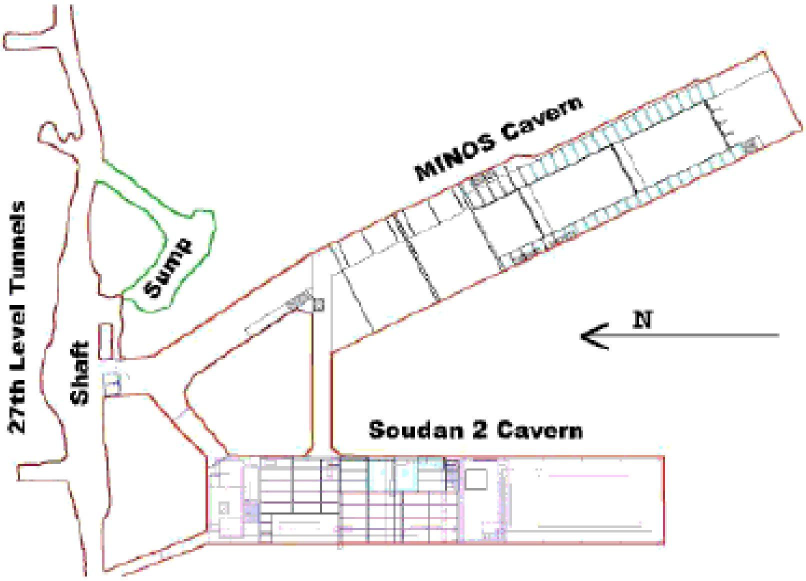

Figure 5.3: Schematic layout of the 27^{th} level of the Soudan Underground Laboratory. The CDMS-II experiment is located and installed in the Soudan 2 Cavern [317].

the experiment to run in a stable a stable low-noise, low-background mode within the access constraints of the underground laboratory at Soudan. However, cryogenic systems demand a wide array of specialized support equipment which also presents a certain number of challenges. To maintain the experiment at low temperature (millikelvin), the cryogenic systems require equipment such as pumps, plumbing, thermometry, electronic control systems, etc. This equipment is housed on a cryopad, as shown in Figure 5.4, which is adjacent to the RF clean room. However much of this equipment produces electrical noise and microphonics which can be picked up in the signal measured by our data acquisition system (DAQ) and if care is not taken, one may be fooled by it. To reduce the noise production, the equipment used needs to be isolated from the detector electronics as much possible.

In addition to the required isolation of the equipment, a careful choice of low-activity materials has to be made since most traditional low-temperature and high-vacuum equipment (components) are generally not made of radioactive free materials. For example, a dilution refrigerator is built primarily of steel, generally with an unacceptable level of uranium, thorium, and ^{60}Co contamination. Therefore, the CDMS-II experiment must carefully choose the kind of equipment and materials to use in order for radioactive background level requirement to be met. Due to the limited access to the underground laboratory at Soudan, physicists have access from 7:30 a.m. to 5:30 p.m. Monday to Friday in order to be able to continue data taking and cryogenic operations during the time that no human has access underground, the whole system (cryogenic control and data taking) is automated by implementation of monitoring softwares to supervise and and control the experiment in order to keep the fridge operating without human intervention. This implementation made it possible for the shifter experts to remotely monitor and control the run from a surface control room. The automated control system has operated nearly perfectly at Soudan during the 5 CDMS-II runs.

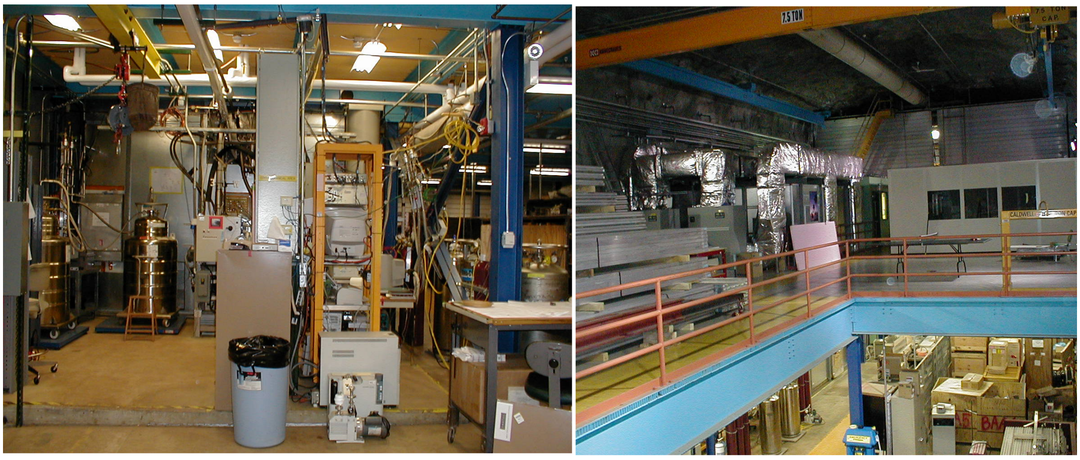

Figure 5.4: Left: CDMS-II cryogenics workspace: the cryopad, adjacent to the CDMS clean room at Soudan. It's in this place that the dilution refrigerator, the monitoring computers, the intelligent gas handling systems (IGH) as well as the nitrogen dewars and helium dewars needed for the cryogenics are located. Right: Soudan 2 cavern taken from the mezzanine level. The RF room is visible on the far front left, and the CDMS-II office space on the back front .

5.4 Cryogenics

The CDMS experiment achieves its low base temperature (~ 50 mK) required for the operation of the ZIP-detectors by cooling all the towers housed inside a cold compartment called **the icebox**. The base temperature is achieved by using a 400S ^{3}He-^{4}He dilution refrigerator, from Oxford Instruments, which delivers a cooling power of 400 μW at 100 mK and a base temperature below 10 mK with no external load.

Since the fridge is made of steel which is not radio-pure and contains some residues of Uranium, Thorium and ^{60}Co, it is mounted outside the shielding on top of set of structures connecting various temperature stages to the icebox. The thermal coupling to the dilution refrigerator is provided by a set of concentric copper pipes, called the **cold stem or c-stem**, which couple each of the fridge's temperature stages to the concentric low-activity copper cans of the icebox. The dilution refrigerator is supported by vacuum pumps, plumbing, and cryogens (liquid helium and nitrogen) located on the cryopad. Opposite to the c-stem we have the E-stem (electron stem) which carries the detector stripline wiring from the icebox to the E-box. The E-box is a box-shaped structure which connects the striplines to external cabling through an array of vacuum-sealed connectors (called D-connectors) [315].

To maintain the purity of the ^{3}He$-$^{4}He gas mixture in our cryogenic system, the gas is circulated through a series of regularly cleaned cold traps. The loop is controlled and monitored by an instrument unit referred to as the Intelligent Gas Handling (IGH) system which is also operated remotely by a RS-232 serial port running virtual instruments LabVIEW software to communicate with the DAQ (Data Acquisition) System. The IGH computer is equipped with remote desktop software that allows it to be accessible from the surface building Users divert the mixture into or out of the storage keg and the circulation pumps, as well as turn on (off) the pump on the 1K pot to prevent damage in runaway situations. The IGH also controls the heaters on the mixing chamber, still and helium bath (although they are unused during ordinary running). The IGH also allows monitoring, but not control, of fridge temperatures and cryogen levels. The cryogenic real-time monitoring status is published to the internal web page: trending plots and long-term historical.

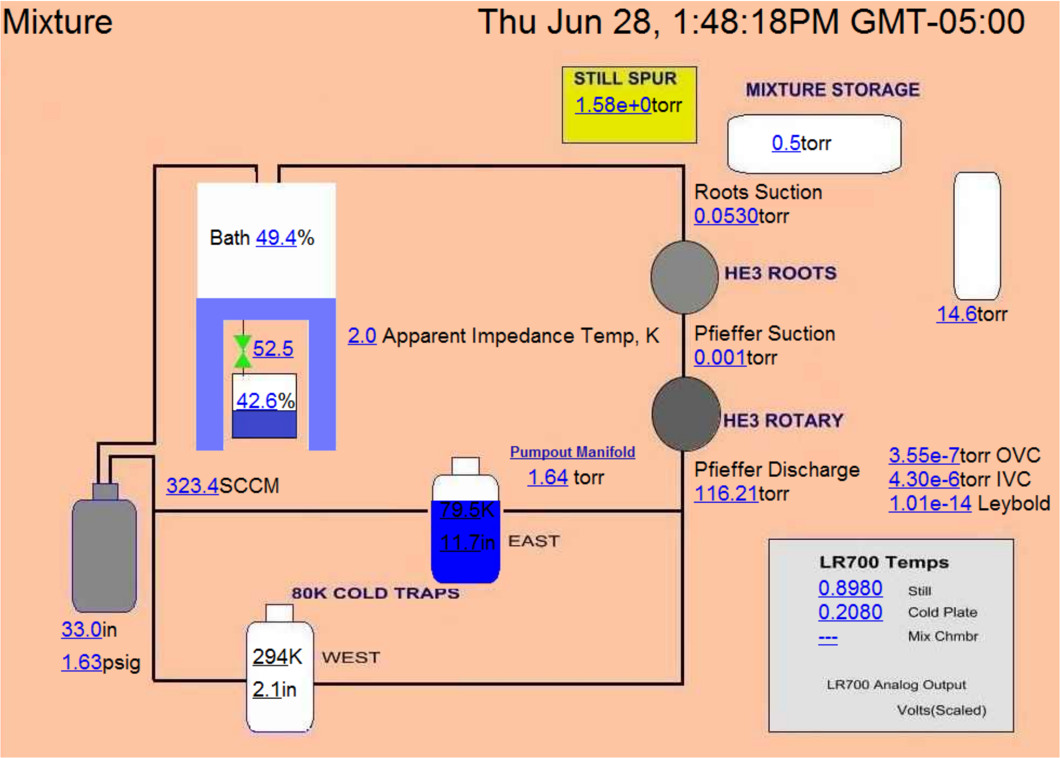

Figure 5.5: View of CDMS-II gas mixture circulation. The gas is regularly circulated through a loop in order to clean up the cold traps. The loops are controlled and monitored by an instrument called the Intelligent Gas Handler (IGH)

.

The circulation of the ^{3}He-^{4}He mixture is driven by a Pfieffer rotary pump and a Roots blower connected in series, Figure (5.5). Before entering the fridge the mixture is circulated through a series of three cold traps to clean it of impurities: a liquid nitrogen cold trap on the cryopad, an external liquid helium cold trap on the cryopad, and an internal liquid helium trap within the helium bath of the refrigerator itself. All three of these traps are cleaned regularly during normal operation, generally on a monthly interval. An Oxford Instruments IGH unit controls and monitors the ^{3}He-^{4}He circulation loop. The IGH regularly reports pressures, valve settings, and cryogen levels to a dedicated Macintosh computer, which publishes this information to a web site for remote monitoring [318].

A Moore APACS automated industrial control system, located on the cryopad with the IGH and the mac computer control housing the virtual instrument LabView codes, monitors and directs the numerous aspects of cryogenic operations, such as the refrigerator's daily refilling of liquid helium and nitrogen baths. Refills occur automatically at a user predefined time each day, but can be manually initiated if necessary. The automated APACS system keeps the helium and nitrogen reservoirs and the cold trap dewars full and adjusts a needle valve to control the filling rate of the 1 K pot as needed (needle valve adjustment can also be done manually by the shifter when it is required to do so) rendering our dilution refrigerator system capable of running over weekends with no human intervention, and to reach a safe state if anything unexpected should happen overnight. APACS also regularly records temperatures, pressures, flow rates and other quantities; this provides a complete historical record of the cryogenic operations that can be accessed anywhere over the Internet through custom java graphical user interfaces (GUIs).

The CDMS-II APACS was implemented with the ability to communicate with the DAQ in the situations when the former needs to take some action while the latter is running and taking data. For instance, before starting a cryogen transfer, APACS notifies the DAQ and waits until the later stopes the data taking. After the transfer has finished, APACS signals the DAQ that it is safe to start taking data again and the DAQ will then automatically resume taking the data. This level of automation and intercommunication between the APACS and the DAQ makes our system able to run without risk of acquiring noisy data that could result from microphone and elevation of the temperature due to the transfer.

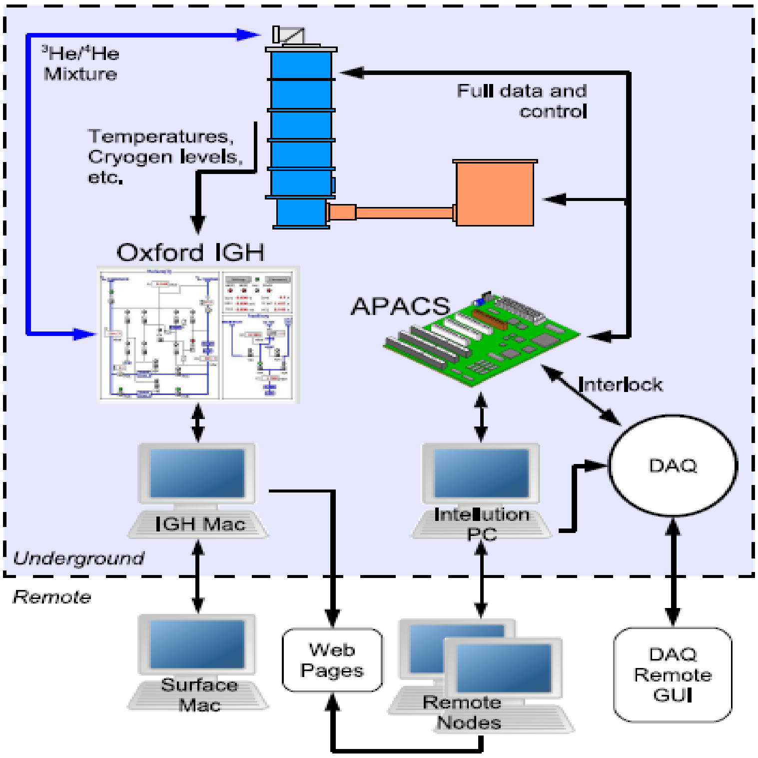

Figure 5.6: CDMS-II cryogenic control system at the Soudan Underground Lab. Components inside the dashed box are physically inside the mine. The remote Intellution nodes are the primary means of remote control, with the surface IGH Mac for controlling mixture circulation. Figure from [318].

Immediately after successful installation of the CDMS experiment at Soudan, the collaboration increased the number of ZIP detectors from 6 (as during the CDMS-I experiment at Stanford underground Facility) to 30 (at Soudan mine) detectors, stacked in 5 towers. Given the number of (additional) towers (each containing 6 ZIP detectors), the detector temperature quickly rose from the transition temperature ($T_c \sim 45\,\mathrm{mK}$) to $\sim 4\,\mathrm{K}$ due to extra heat load. This extra heat was mostly dumped out by radiation from the additional FETs and conduction through striplines. Our thermal modeling showed that the heat leakage through the towers was sufficient enough raise the detectors above the super conducting transition temperatures, rendering many phonon readout channels inoperable. As a remedy, a Gifford-McMahon cryocooler was added as a second refrigeration system. The cryocooler was mounted on the E-Stem, driven by an external compressor outside the clean room. Helium gas is driven to the head at high pressure (∼20 atmospheres) and compression and expansion of the piston providing us the cooling power needed to maintain the experiment at low base temperature. This cooling unit has two cooling stages, cooling both the 77 K and the 4 K stages of the E-stem, intercepting the heat load from the striplines to prevent large temperature excursion (or temperature gradient) across the 4 K layer. The cryocooler is connected to the E-Stem through flexible copper couplings designed to maintain excellent thermal conductivity and limit the transmission of mechanical vibration.

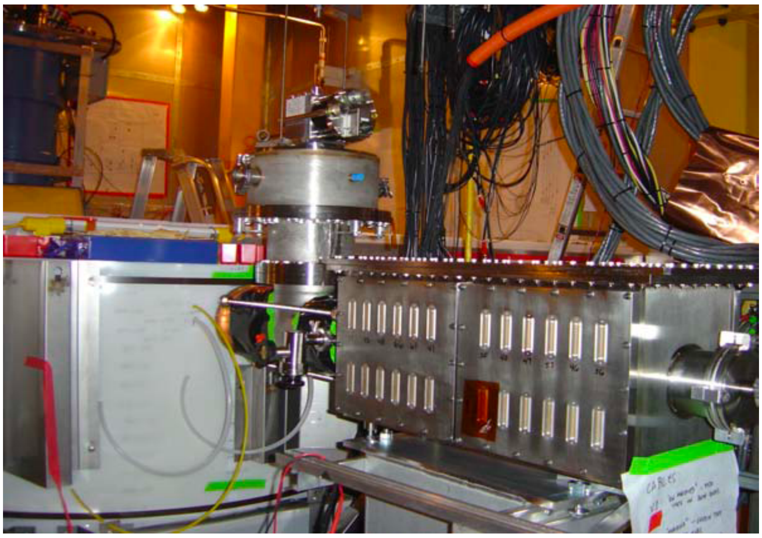

Figure 5.7: CDMS II shield, E-stem and E-box (left to right), with detector cables unplugged to the bulkhead. The double cylinder attached vertically to the E-stem is the cryocooler head, which normally is connected to He flow lines. Structures bellow are used to aid in vibration isolation along the E-stem. Figure from [315].

5.5 Shieldings

To reduce the background rate, the CDMS-II icebox is surrounded by several layers of shielding. The CDMS setup consists of an active shielding component to suppress residual cosmic-ray interactions and a passive component to shield against natural radioactivity. Due to the fact that radioactivities induces low charge yield events (betas or surface events) are extremely problematic, it is desirable that the detectors are exposed only to radioactive backgrounds from inserted (calibration) sources as well as radioactivity from the immediate surrounding materials and the detectors themselves.

5.5.1 Passive shield

The CDMS-II passive shielding consists of an outer layer of polyethylene, two layers of lead and an inner layer of polyethylene. The purpose of passive shielding is to moderate the gamma-ray and neutron backgrounds. This is achieved at the Soudan Underground Laboratory site by a use of tightly packed layers of lead and polyethylene. The outer polyethylene layer is composed of one inch thick slabs that are designed to stick around the outer lead layer. The outer poly layer (∼40 cm thick on the sides and ∼40.6 cm thick at the top and bottom) serves to moderate incident low-energy neutrons sufficiently to prevent nuclear recoils above the detector energy threshold.

Several holes in the outer lead and polyethylene shields allowed access to the interior of the apparatus. Additionally, there was a small hole with a removable plug in the south side of the outer lead shield, allowing exposure of the detectors to gamma and neutron calibration sources (^{133}Ba for gammas and ^{252}Cf for neutrons). To reduce the ambient gamma flux from radioactivity outside of the experimental apparatus, a lead shield is used and it is composed of inner and outer layers of lead surrounding the detector's cylindrical walls. The outer layer consisting of low-activity lead has a thickness $\sim 17.8\,$cm on the top, bottom and the sides. The inner lead layer with a thickness of 4.4 cm on the top, bottom and the sides is composed of ancient lead from a French ship. ^{210}Pb, the naturally occurring radioactive lead isotope with the longest half-life of 22.3 years, is no longer present in the ancient lead. The ancient lead is used to attenuate gamma backgrounds due to radioactive isotopes in the outer lead.

The inner layer of polyethylene shielding is inside the inner ancient lead and provides an additional neutron moderation. The inner poly (10 cm thick on the side, 7.6 cm thick on the top, and 10.2 cm thick at the bottom) also suppresses the cosmic-ray induced neutrons in the lead. The ordering of the passive shielding was determined by Monte Carlo simulations to be optimal in terms of suppression of neutron background. Inside the inner polyethylene layer, a can of muon-metal surrounding the detectors is inserted in order to reduce the external magnetic field that might affect the performance of parts of the cold electronics due to noise that could eventually be produced by the magnetic flux in the vicinity of the detectors. If this noise is not reduced, it would be mimicked with the phonon and charge readout channels. The purpose of the mu-metal is to further reduce the effect of the earth's magnetic field (by a factor of ∼10 to 100) on the SQUIDs, Figure (5.10).

Although the ZIP detectors are are kept under vacuum, the air radon level in the Underground Laboratory at Soudan air is relatively high: ∼700 Bq/m^3. Although there is adequate shielding from air outside the shield, any substantial amount of air inside the shield will increase the gamma background rate significantly. Therefore, we were forced to purge continuously with dry nitrogen any mine air between the outer copper can and the mu-metal

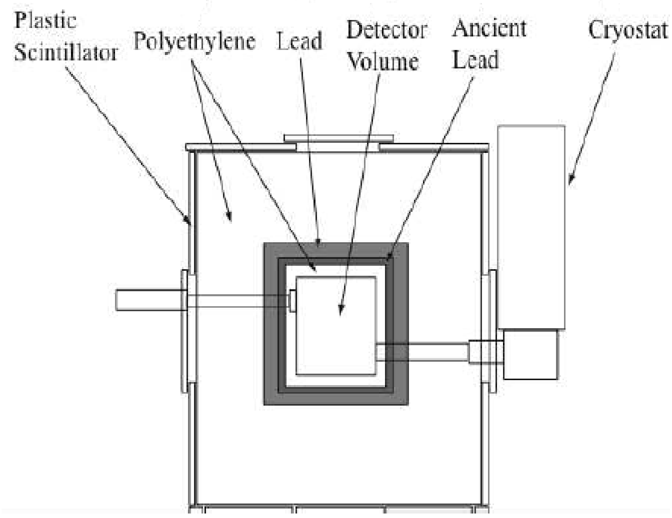

Figure 5.8: CDMS-II shielding configuration. From the inside to the outside, the detectors were surrounded by an inner polyethylene shield, an ancient-lead (taken from a sunk french ship), a copper cryostat (Icebox), an outer polyethylene shield, an outer lead shield, and a plastic-scintillator muon veto. The Icebox connected to the dilution refrigerator via a cold stem (C-stem) that penetrated through the northern side of the outer shielding layers. Also shown is the region of the outer lead shield which gives access to the interior. Figure from [315].

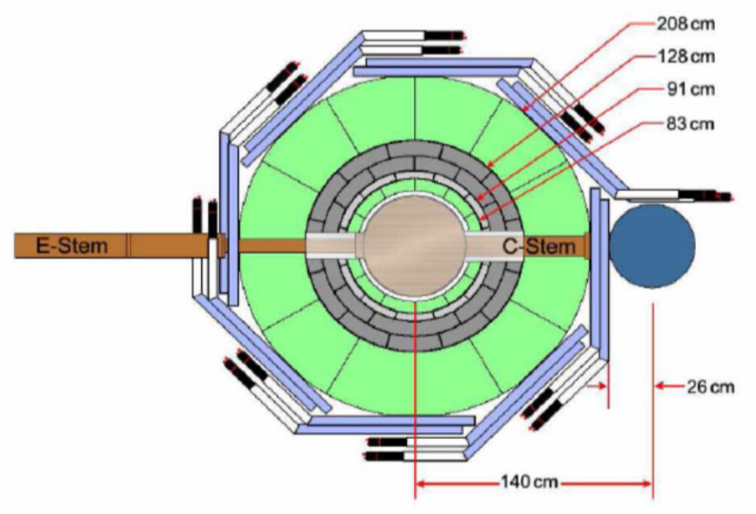

Figure 5.9: Top view of the active veto and passive shielding. From the outside to the inside the figures show the veto panels (light blue) which enclose the outer polyethylene shield (green), the outer low radioactive lead shielding (gray), the inner ancient lead shield (light gray), the inner polyethylene shield (green) and finally the mu-metal shield (light metal colored). The E-stem and C- stem (brown) pass between the veto panels and the passive shielding and connect to the mu-metal shield. The C-stem connects to the dilution refrigerator (dark blue) providing the thermal contact between the cold layers and the fridge. Figure from [317].

shield.

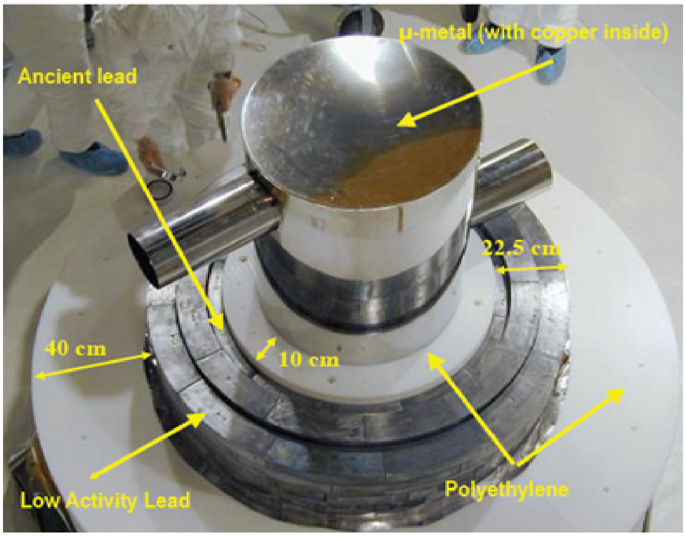

Figure 5.10: View of the CDMS-II packed layer of passive shield: the lead and poly. The lead is used as shield for gamma background resulting from radioactivity, the polyethylene is however used for moderation for neutrons produced by fission decay and from (α,n) interactions resulting from Uranium/Thorium decay chain. The mu-metal is a thin shell of aluminum that surrounds the inner-most copper can of the icebox. It's purpose is to reduce the effect of the earth's magnetic field (by a factor of $\sim$10 to 100) on the SQUIDs. Figure from Jodi Sekula's talk at TAUP.

5.5.2 Active shield: muon scintillator veto

The purpose of the active muon veto system, made of plastic scintillator, is to reject the muon flux that is not stopped by the rock overburden. Since muons could interact with nuclei in the passive shielding and produce neutrons whose interaction with the ZIP detectors gives the same type of signature as a WIMP-induced recoil.

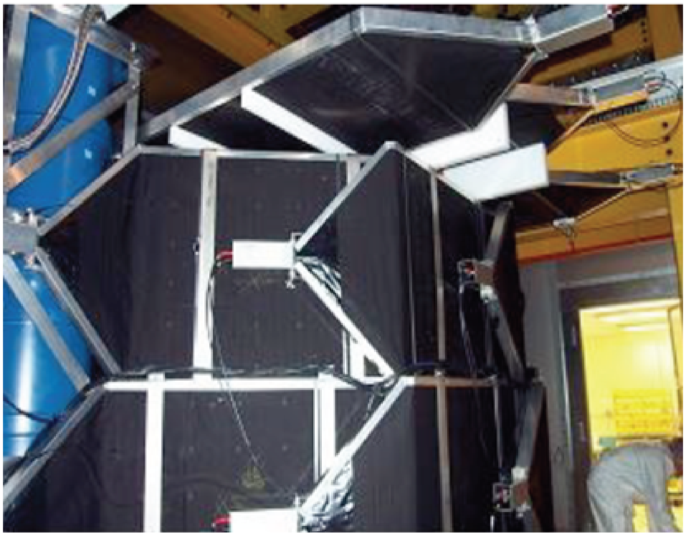

Figure 5.11: View of the CDMS-II active shield. The black panels in this picture are the muon veto made of plastic scintillator covering all the sides of the passive shield. The icebox housing the ZIP-detectors and the cold hardware is at the center.

The CDMS-II muon veto consists of 40 plastic scintillator panels (BICRON BC-408) surrounding the inner passive shielding. The panels are arranged in a way that adjacent panels have a slight overlap to cover the whole experimental setup. Acrylic light guides direct the scintillation photons in the panels to the attached photo multiplier tubes or PMTs (Hamamatsu R329-02). The scintillator panel and light guide are wrapped in mylar foil for light isolation. The veto system also includes a source of blue light, transported to each panel with an optical fiber. Periodic pulsing of the blue light source (between data acquisition runs) allows calibration checks of the PMTs. Details about the architecture and design of the veto can be found in Ray Bunker's PhD dissertation [50].

Since a minimum ionizing muon typically deposits 2 $\mathrm{MeV/g/cm^2}$, muons deposit approximately 10 MeV in the 5 cm thick veto panels which have a density of 1.03 g $\mathrm{cm^{-3}}$. A muon passing through our scintillator generates approximately 100 pC of collected charge (after amplification) and the veto efficiency is $99.9616\pm^{0.0035}_{0.0036}\%$ (or $99.9225\pm^{0.0060}_{0.0062}\%$ depending on the rejection threshold chosen) [317, 374].

5.6 Cold hardware

The CDMS-II icebox contains the cold hardware necessary to operate the experiment at a low base temperature. The whole assembly, Figure (5.12), is mounted by a fixture designed to minimize the heat conducted and radiated into the cold stages, allowing the FETs to operate with suitably low noise. The cold hardware components are constructed with low radioativity materials namely kapton and a low-activity custom solder. Each tower of the CDMS-II detectors contains a stack of 6 detectors hanging in the middle of the icebox can. Their electrical connection is through an electronic board that we referred to as detector interface board (DIB) and side coax board. Above the stack is a heatsinking assembly (known as the tower), and above the tower sit the cold hardware electronics, the field effect transistor (FET) and superconducting quantum interference device (SQUID) boards both together forming the SQUET board, Figure (5.12).

5.6.1 Detector housing

Every single ZIP detector is mounted in a hexagonal copper housing, and supported with three cirlex[1] clamps on the top face and three on the bottom face. The ZIP detector housing is open at the top and bottom, as shown in Figure (5.13), with a vacuum gap of 2 mm between detectors to allow particles to multiply scatter in several detectors. Such events are easily be tagged and rejected by a multiplicity cut during the analysis.

Each detector is connected to the readout electronics through a small DIB situated on one edge of its housing. The DIB feeds into the end of a side coax and couples the detector through ten Aluminum wire-bond connections. The DIB also houses two infrared LEDs for clearing trapped charges in the detectors. The LED shines on the phonon face of its own detector and the charge face of the neighboring detector. The LED flashes periodically in

---

[1] A circlex is a substrate that helps block the IR radiation because it is capable of absorbing IR [175].

order to maintain the charge collection over a certain period of time. The length of time over which the charge stability is still acceptable is normally determined by a study done with the calibration data. The charge stability study is referred as **neutralization**, which I will describe in bit more detail in the section (7.3.4).

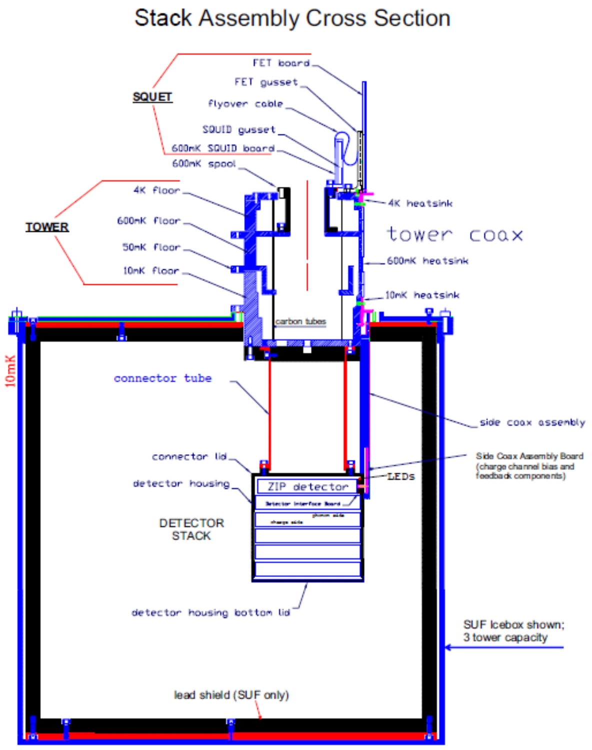

Figure 5.12: Overview of cold hardware, detector stack, and icebox can. The configuration shown is for the Stanford icebox. At Soudan the inner lead shield is absent, and the towers are placed closer to the edge of the can (with one exactly in the center). Figure from [375].

5.6.2 Tower

A Tower is a hexagonal copper structure that supports the detector stack and connects it electrically to the SQUET (**SQUID+FET**) cards. The Tower consists of four copper stages, each made of material heat-sunk to one of the icebox cans consisting of four thermally isolated sections separated and supported by graphite cylinders, which supports the four stages, holding them separated without excessive heat conduction. Each face of the tower carries the bias and signal wires of one detector, connecting the side coax at the base temperature stage to the SQUET card mounted at 4K. The wires are heat-sunk to three of the temperature stages (base, still, and 4K) and held under tension in vacuum channels along the tower faces to limit their sensitivity to mechanical vibration.

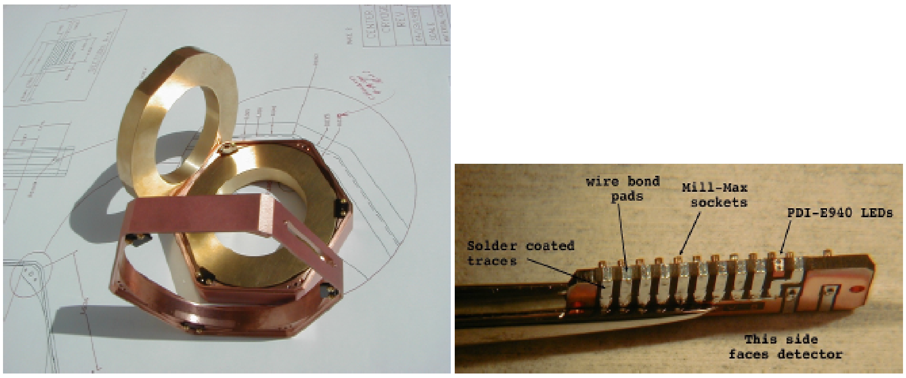

Figure 5.13: ZIP housings pictured with metallic placeholders of the mass (Ge) and outer shape of ZIPs. Right: Detector Interface Board. Figure from [375].

5.6.3 SQUETs

A SQUET (Figure 5.14) is a combination of two electronic circuit boards that houses the SQUID arrays for phonon signal amplification and the first-stage FETs for charge signal amplification for the channels of a single detector. The FETs are supported on a Kapton membrane within a copper gusset on the primary card. This enables the FETs to self-heat to ∼140K for nominal operation, while still being mounted to the 4K stage. The SQUID card is heat sunk to an extension of the still layer of the tower to improve SQUID performance and reduce the Johnson noise of the shunt resistors. The two cards are joined by a flexible cable composed of twisted-pair superconducting niobium wires sandwiched between layers of Kapton tape. The SQUID and FET cards are connected by a flyover cable, each tower contains one SQUET card sitting on the top of the tower. The SQUET cards reside at the 4K stage at the top of the tower. The wires connecting the SQUETs and the side coaxes reside in vacuum coax channels, are tensioned to reduce microphonic noise, and are heat-sunk along the way to reduce thermal load on the side coaxes at base temperature.

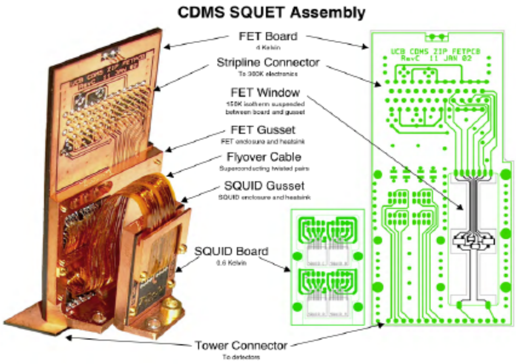

Figure 5.14: Left: is the SQUET circuit board layout. Right: show the SQUET card, a combination of both the SQUID and FET cards. Figure from [375].

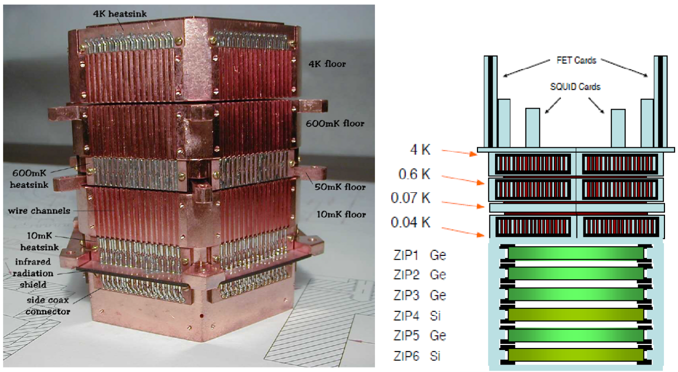

Figure 5.15: Left: CDMS II tower, consisting of four isolated metal stages, and stretched wires on the sides to provide connections between SQUET cards on top and the side coax mill-max connectors on the bottom. Right: The cross-sectional view of the stack (composed of 6 ZIP-detectors) inside the icebox can. Dennis Seitz.

5.6.4 Side coax

CDMS-II Detectors are normally electrically connected to the base temperature stage of their tower by a custom connector card called a side coax (Figure 5.16). A side coax also houses the coupling capacitors (C_c) and bias and feedback resistors (R_f) for the charge channels of a detector, to minimize Johnson noise. Side coaxes for CDMS-II were made in six different lengths to reach each of the detector's positions in the stack.

Figure 5.16: CDMS side coax used in the ZIP detectors. Figure from [375].

5.6.5 Stripline

The signal created by particle interactions is carried to the electronic box through the cables called striplines (Figure 5.17), which are flexible, 2.5 cm wide, 3 m long made of copper-kapton to limit heat flow between the room temperature and the 4K stage. These cables are heat-sunk at $4]textK$ and $77]textK$, and pass through a copper radiation shield as they proceed through the electronics stem and into the breakout box. The cold end of a stripline attaches to a SQUET card, and the warm end attaches to a vacuum D connector in the E-stem breakout box. The striplines are flexible enough to turn over a radius of a few inches, but cannot easily cross over each other. Therefore, it is necessary to arrange them with the correct lengths to reach their target SQUET cards with no crossings. This arrangement is fixed before the striplines are inserted, as the striplines are clamped into the thermal intercepts and a gamma radiation intercept before the entire bundle is pulled through the electronics stem.

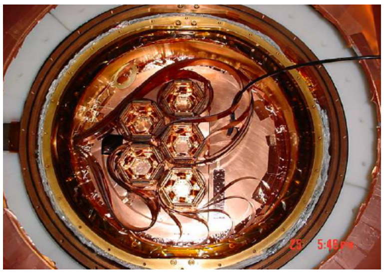

Figure 5.17: CDMS-II tower configuration of the Soudan icebox, showing the SQUETs and their respective striplines winding around and exiting the icebox through the e-stem. Stripline cables are made of copper-kapton to limit the heat flow between the the room temperature and the cold hardware.

5.7 Warm electronics

The CDMS warm electronics is located in the RF room at room temperature. The electronics are used for the readout of the signals from the detectors and recording of the data; they are placed outside of the experimental clean room, to allow easy access to the different components and most importantly to control the experiment. Some of the many of these warm electronics are visited below.

5.7.1 Front End Boards (FEBs)

Signals coming from the E-box pass through cables to a rack of front-end boards (FEBs) in the RF room (there is one front-end board for each detector). Each FEB is a custom-made circuit board carrying the amplifiers and other components of the ionization and phonon readout circuits: FET and SQUID boards. The FEBs also contain circuits to control biasing of the detectors, cold amplifiers, LEDs flashes for neutralization, etc. Signals are brought to them from the e-box by 50-wire cables with detachable connectors. The processed signals are then sent to the electronics room for triggering and digitization. The FEBs are operated from the electronics room by a fiber-optic-linked GPIB controller. A fiber-optic GPIB extender connects the GPIB Interface Box to the data-acquisition computers, electrically isolating the front-end digital control [177].

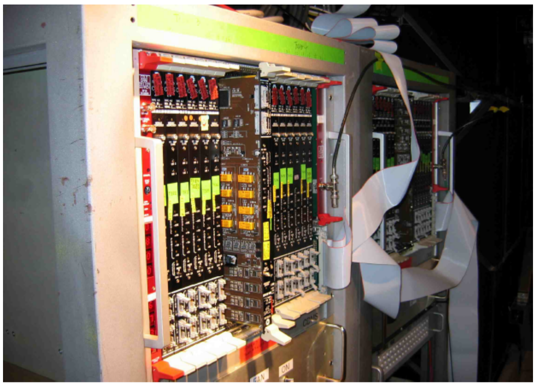

Figure 5.18: CDMS-II frond-end boards in the electronic room.

5.7.2 Receiver Trigger Filter Boards (RTFs)

Once the phonon and charge signals from the FEB are amplified, they are sent through the RF-room (electronic room) according to the logic implemented in receiver trigger-filter (RTF) board in the electronics room. The RTF board conditions the FEB signals for digitization by baseline adjustment and applying a 336 kHz 2-pole Butterworth anti-aliasing filter. A Butterworth filter has a frequency response which is maximally flat in the passband (below a pre-determined cut-off frequency), and decays (rolls off towards) to zero at the frequencies above the cut-off. The filtered signals are then used to generate five types of triggers for the digitizers which are hard-coded in a Trigger Logic Board (TLB); the TLB is responsible for generating the experimental trigger from a configurable pattern of low- and high-level phonon and ionization hits whenever certain programmable conditions are satisfied. The primary trigger, Plo, is issued when a comparator (from a Lecroy NIM crate) determines that the sum of the four phonon pulses exceeds a pre-defined threshold set in software and dictated by the TLB, generally 3-4mV. Phi is similar but has a larger threshold ($\sim$500 mV), while Pwhisper has a lower threshold and it's intended for tagging multiply-scattered events. Similarly for the charge ionization signals, we define Qlo and Qhi which are similar to Plo and Phi that uses the summed charge signal to generate triggers. Although all these threshold are defined, the CDMS trigger logic is entirely based on Plo. We set our trigger threshold in TLB such that the DAQ trigger whenever the energy deposited exceed the already pre-defined Plo threshold.

5.8 Veto Triggers

Similar to the phonon and charge signals, the veto signals are transported from the veto panels to the electronics room (RF room) where their triggers are conditioned and controlled by LeCroy discriminators which compares the PMT pulse heights to a software pre-defined threshold and issue triggers for veto panels whose signal exceeds threshold. Scintillation light from particle interactions in each of the veto pannel counters are detected with two photomultiplier tubes (PMTs) optically coupled to bars of wavelength shifter. The PMT signals are conditioned by stretching them from $\sim$ns scales to $\sim \mu$s scales by a special filter network before being sent to the DAQ hardware. A $\sim$30 mV discriminator converts the analog veto signals to logical pulses that are continuously monitored by a history-buffer unit. The resulting record of muon-veto hits is recorded to an event record whenever a ZIP-detector causes an experimental trigger. The veto signals are also connected to a variety of other electronics that do not contribute directly to ZIP-detector event records. These are used to monitor each counters event rate as a function of time, control each PMT's bias voltage, and diagnose and tune the PMT gains [50, 318].

5.9 Data Acquisition Hardware

Upon an interaction, a global trigger is issued to record the event and veto traces to disk whenever any of the following conditions is satisfied:

- the Plo trigger for any ZIP is issued by an RTF board;
- The LeCroy discriminators issue triggers for two or more veto panels, and finally;
- the DAQ software issues a random trigger for purposes of monitoring the noise level.

During the ^{252}Cf calibration run or during a WIMP-search run, when a global trigger is received, digitized traces from the phonon and charge channels of all ZIPs as well as the 40 traces from the veto panels are recorded to disk. However, during ^{133}Ba-calibration run which is selective readout, only digitized traces from the phonon and charge channels of ZIPs that had Plo triggers are recorded (the veto traces are not recorded during the selective readout in the ^{133}Ba-calibration run).

Immediately after the issuance of a global trigger, the six readout channels of each ZIP detector are recorded by an array of 14-bit Struck SIS 3301 analog-digital converters and written to a disk located at the Soudan mine. Later on, an automated perl script copies the data to a Stanford University disk. The digitizers operate at a 100 MHz sampling rate, but 80-sample sequences are internally averaged to yield an output rate of 1.25 MHz with a corresponding reduction in digitizer noise. Each digitizer records a 2048-sample (1.6 ms) trace. The trigger itself occurs in the 512^{th} bin, so each trace includes 409 μs preceding the trigger. Photomultiplier signals from the 40 scintillator veto panels are processed by an analogous set of boards. The raw veto signals are extremely short in duration ($\sim$ 10 s of ns); these signals are reshaped by a pulse-stretching filter network before digitization. The reshaped veto pulses are recorded by an array of 12-bit Joerger VTR812 ADCs, each acquiring 1024 samples at 5 MHz. A set of comparators also issues trigger signals from the veto shield; these are fed to the TLB for evaluation of global triggers. All of the above trigger signals (phonon, charge and veto) are also recorded by a set of Struck SIS 2400 time-to-digital convertors (TDC's). These boards record the time stamps of each trigger in a circular buffer with 1 μs resolution. A portion of this trigger history buffer is recorded along with each event written to disk, giving a record of the several triggers immediately preceding and following the global trigger.

Finally, a **slow DAQ** monitors all ZIP and veto channels, recording signal offsets and mean trigger rates once every minute. The former monitor the evidence and track loss of SQUID flux lock point [2], and the latter helps monitoring of changes in detector noise.

---

[2] The phonon DC offsets, the difference between the raw phonon trace's baseline and zero, are a measure of the SQUID and TES stability. If the offset is greater than the value of one flux quanta, approximately 0.2 V, it indicates that the SQUID has likely lost its stable lock point compromising the SQUID noise performance and possibly the phonon time measurement (due to lower bandwidth). These DC offsets are measured and recorded for each detector channel every minute. During each data set the offset for each detector channel is averaged. If at any point during the data set a detector channels DC offset is greater than 0.2 V, the data set is paused and all of the SQUIDs are relocked to restore stable SQUID operation.

5.10 Data acquisition software

The CDMS-II DAQ software has two components: the DAQ servers, which run in the mine and the DAQ GUI, which can be used anywhere; the two software packages are detailed in the doctoral dissertation of Joel Sander [429].

The CDMS-II DAQ is controlled by a custom-written software package of programs in Java and C++ and run on a small cluster of computers in the electronics room. Different components of the DAQ are controlled by dedicated pieces run on their own servers, but with great flexibility in adding or removing components. This is facilitated by the CORBA network messaging framework and Java Remote Method Invocation for communication between modules.

All the different modules have user interfaces for control by the operator, however the main interface is called the RunControl which enables the control and monitoring of the experiment's runs. The RunControl is a Java cross-platform network application that can control the entire experiment over the internet. The DAQ has a limited locations from which users can access the RunControl and monitor the progress of the experiment in the mine. These locations are: the surface building at Soudan, and a few other super users located anywhere, especially at Fermilab, Texas A&M and University of Evanville where some of our DAQ experts are.

The DAQ GUI allows users to see the DAQ state, monitoring information, and trending cryogenic data. Users in this observer mode cannot control anything, beyond posting messages that are visible to all users. The DAQ GUI can also be run in a trusted mode from a few locations in the mine and at the surface. This allows runs to be started and stopped, and all run configurations to be changed. Operators taking shifts at Soudan can fully control the experiment through the GUI, which communicates with the servers using Java remote method invocation (RMI) and CORBA protocols. The DAQ also controls the automated routine operations which require little or no operator intervention. Data taking is automatically stopped before a cryogen transfer begins, using the signal received from APACs, and resume the data taking after the end of the transfer. The detectors and DAQ hardware are configured at the start of each run using stored settings. LED flashes are also performed periodically, in order to maintain good neutralization and ensure full charge collection.

There is a deadtime of about ∼50 ms required for the DAQ for acquiring traces from the digitizers and storing them after a global trigger, allowing a maximum event rate of 20 Hz, far lower than the ∼0.3 Hz background rate during WIMP-search running. In selective-readout mode for ^{133}Ba calibration, this deadtime falls to ∼15 ms, enabling event rates as high as 70 Hz.

5.11 Data processing

The CDMS raw event data is acquired by a LabView software implemented and serviced by our automated data acquisition system (DAQ). The acquired data are first stored to local disks in the mine and as each raw event file is completed, a set of perl scripts compresses the file and writes a copy of the compressed file to a digital backup tape located in the mine and at the surface facilities. There is another script that transfers the the raw data over the internet to Fermilab for complete data processing on the FermiGrid cluster in order to generate reduced datasets that the users can analyze for WIMP search. Separately, another automated perl script monitors the disk space in the mine to less than 90% full. If the disk reached 90%, the script will automatically transfer the data to FermiLab and Stanford cluster and will automatically empty out the disk space for the new data to be saved.

Most of the reprocessing tasks starts when the data is transferred at Fermilab. The raw data undergo several stages of data processing on Fermilab'ss computing cluster before it becomes available for analysis. The first stage for the CDMS raw data processing consist of generating detector's quantities which contains information relative to the trigger settings, event traces, veto activity, etc. These quantities are converted into reduced quantities (RQs) which still are non-physical and not calibrated.

In the history of the CDMS experiment, the data processing pipe line was previously entirely a MATLAB reprocessing package called DarkPipe which was used for data processing until the last CDMS Soudan runs (called c58). This package was completely re-written in favor of a streamlined, C++ package called BatRoot, the CDMS Soudan data processing pipeline is shown in Figure (5.19). BatRoot combined all the old algorithms with new time-domain fitting routines from an alternate pipeline called PipeFitter. The advantage of the new package was its modularity in adding new experimental algorithms, and its ability to produce RQs in ROOT Ntuple format, a better standard ROOT (or C++) format for handling large datasets than the MATLAB's data format.

After the production of the RQs, the second step in the data processing is the calibration of the charge and phonon RQs. The calibration of the RQs results in physically meaningful quantities called relative RQs (RRQs). The energy calibration coefficients are calculated first for charge and then later for phonons. These calibrations are used by BatCalib in order to produce the physical meaningful quantities (RRQs) needed for next level in the data processing. The position dependence removal normally intervene at this stage using our position correction scheme to generate the final physical quantities that are most important for the WIMP search analysis.

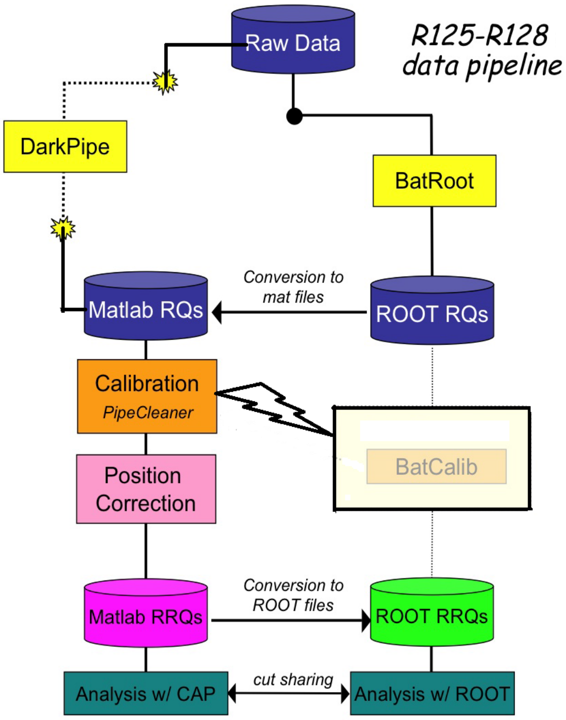

Figure 5.19: Last CDMS-II Soudan's run data processing pipeline. The Darkpipe processing package, a MATLAB based software was replaced by the BatROOT, a streamline C++ software developed at the end of the CDMS-II experiment. Figure adapted from [316].

Chapter 6

Position Reconstruction and Energy Calibration.

6.1 Introduction

The energy response of ZIP detectors is determined in-situ by using radioactive calibration sources. These calibration sources are used to determine the amount of energy deposited in a ZIP detector as well as the position of the event, i.e. the location where the interaction took place. For energy calibration, ^{133}Ba source is used, which is a gamma source with strong lines at 275, 303, 356 and 384 keV. For WIMP-like interactions, a ^{252}Cf-neutron source is used. The calibration sources are inserted into the experimental setup, outside the icebox copper cans, using two feedthroughs along the c-stem and the e-stem. In addition to the energy calibration, the detector response shows a position dependence with event location caused by the geometrical properties of the crystals. For a uniform response of the detectors, these position dependencies have to be corrected.

During the calibration, the spectral lines from the ^{133}Ba are used to calibrate ionization energy (E_Q) in Ge ZIP detectors. These lines do not show up at all in Si-ZIP detectors because the gammas rarely deposit their full energy in one single detector. To calibrate the Si-ZIP detectors, we instead use shared events (energy) between two neigboring Si detectors. If a 356-keV gamma distributes its energy between a Si detector and an adjacent Ge detector, the sum of the energy deposited in these two separate detectors should add up to the full 356 keV. This is the trick to which we have resorted in order to calibration energy in the Si detectors. Each of the Ba lines of the ZIP detectors for Ge and Si (under consideration of an adjacent Ge detector) are visible as a diagonal line with slope of -1 in a scatter plot showing the energy in each detector. We normally adjust the calibration in the Si detector to correctly place the shared energy line. The peaks are also visible in the phonon spectrum for Ge detectors, but with coarser resolution at high energy. Therefore, the ionization energy is calibrated first, and then the calibration to the phonon energy response (E_P) is handled by setting the ionization yield[1] to one for gamma scatters as illustrated in Figure (6.1).

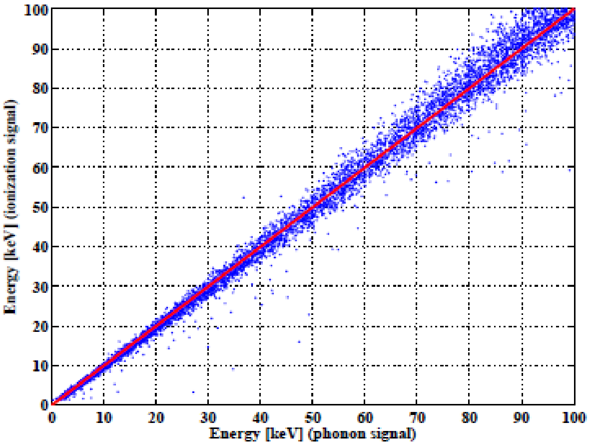

Figure 6.1: The calibrated charge energy as function of the total calibrated phonon energy. Notice that the ratio of the ionization energy to the phonon energy, i.e. the yield, is exactly equal to 1 for events laying at center of the band (electron recoil band). This is the normalization we impose to the ^{133}Ba calibration events; all gammas will have a yield 1. As for nuclear recoil events, events caused by neutron illumination using ^{252}Cf and WIMPS-induced recoil events will have a yield of about $\approx 1/3$. This is why the yield quantity can be used a good discriminator parameter.

6.2 Charge reconstruction: optimal filtering

The CDMS-II data processing package converts each event's digitized ionization traces into more physical quantities: energy, start time, etc which are used for later analysis. The major reconstruction algorithm used for the ionization channels is based on an optimal filtering. Optimal filtering is the technique we use to estimate the energy that an event deposits in the ZIP detector after an interaction. This algorithm is described in its entirety in Appendix A of Jeff Filippini and in Appendix B of Sunil Golwala's dissertations [175, 315]. In this chapter, I am going to very briefly describe how this algorithm works.

The tool used for charge-reconstruction in the CDMS processing package is optimal filtering. The optimal filtering technique takes advantage of the characteristics of ZIP ionization signals. Each pulse from a ZIP detector is of essentially fixed shape, with time constants determined by the electrothermal time constant, and the noise is assumed to be (predominantly) gaussian in nature which makes it ideal candidate for optimal filtering which is done by transforming the timing domain to a frequency-domain and fit the fixed template to the observed trace, accounting for variations in the noise power spectrum with frequency. More sophisticated versions of this algorithm were recently developed by Matt Pyle [376, 377, 378] and it is implemented for SuperCDMS data taken with the interleaved ZIP detectors (iZIPs).

---

[1] The ionization yield is a dimensionless quantity defined as the ratio between the ionization energy to the phonon energy for a given event, i.e. yield = $\frac{E_Q}{E_P}$. This quantity is used for particle identification in the ZIP detectors.

The charge reconstruction optimal filtering requires two ionization pulses QI and QO, and two crosstalk pulses QIx and QOx between the inner and outer ionization electrodes as shown in Figure (6.2). Two ionization pulses *SI* and *SO*, one for each ionization electrode, are formed using four template traces which represent the pulse shapes of the two ionization channels and the crosstalk between them (see Equation 6.6), and fitted simultaneously to a set of templates in order to determine the charge deposited in each channel. The crosstalk between the two ionization electrodes is due to the mutual capacitance between them [315]. The portion of the ionization pulse due to crosstalk is not identical in shape to that of the primary pulse. This poses a slight problem for optimal filtering since the exact pulse shapes for any given event depend on the ratio of QI and QO signals, and this ratio is not known before hand. To account for tiny variations between channels, we generate the templates by averaging the ionization traces from a selection of well-chosen events from each detector. From this well-chosen template, we compute the χ^2 using the optimal filter algorithm in order to determine the goodness of the fit parameters (the pulse amplitude and the start time).

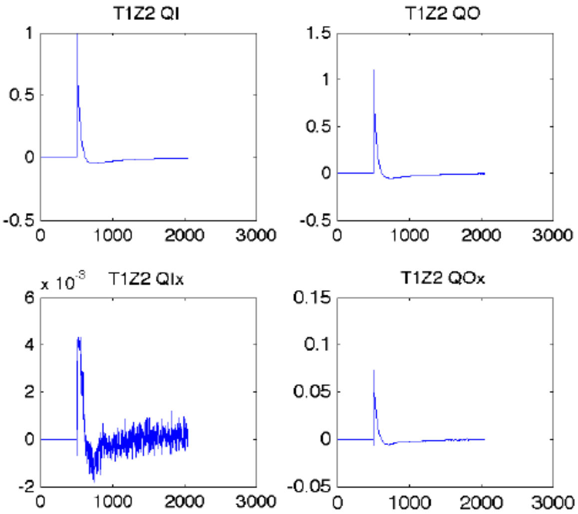

Figure 6.2: Illustration of the optimal filter templates for the T1Z2 charge channels using c34 data. The QI and QO templates represent the pulses generated in these channels by events from the Q-inner and Q-outer electrodes, QIx and QOx are the crosstalk signals observed in QI and QO channels. Figure from [315].

Charge start time t_0:

The charge start time t_0 is computed for every charge inner ionization signal (QI). This computation, done on event by event basis, is accomplished via the use of the optimal filtering technique which takes into account the noise power spectrum density and properly determines the fit parameters (such as the start time t_0 and the amplitudes) that we use for later analysis. Our processing software requires all ionization pulses to occur within a search window of [-100 +10]μs for Ge ([-50 +10]μs for Si) around the global trigger time. This condition must be satisfied for all normally-triggered events, but events can occasionally fall outside this window at high trigger rates. Also, cross-detector pileup is problematic because the pulses of the second particle event may occur outside of the optimal filter search window. To determine the start time, we can thus shift the template from $t = 0$ to $t = t_0$ time offset, then apply the FFT to the resulting signal, producing a χ^2 given by:

$$\chi^2(a, t_0) = \sum_n \frac{|\widetilde{S}_n - ae^{-2\pi i t_0 f_n}\widetilde{A}_n|^2}{J_n} \tag{6.1}$$

We need to minimize the above χ^2 to find the best estimates $\widehat{a}$ and $\widehat{t_0}$. The optimal amplitude estimator can be derived similarly to (6.21):

$$\widehat{a}(t_0) = \frac{\sum_n e^{2\pi i t_0 f_n} \frac{\widetilde{A}_n^* \cdot \widetilde{S}_n}{J_n}}{\sum_n \frac{|\widetilde{A}_n|^2}{J_n}} \tag{6.2}$$

The value of t_0 can similarly be found by minimizing the χ^2 (6.1), i.e. $\frac{\partial \chi^2(a,t_0)}{\partial t_0} = 0$, therefore solving the equation

$$-2a \sum_n 2\pi i f_n e^{2\pi i t_0 f_n} \frac{\widetilde{A}_n^* \cdot \widetilde{S}_n}{J_n} = 0 \tag{6.3}$$

which is a nonlinear equation which has no analytical solution. To circumvent this difficulty, we take the derivative of equation (6.2) to find:

$$\frac{\partial \widehat{a}}{\partial t_0} = \frac{\sum_n 2\pi i f_n e^{2\pi i t_0 f_n} \frac{\widetilde{A}_n^* \cdot \widetilde{S}_n}{J_n}}{\sum_n \frac{|\widetilde{A}_n|^2}{J_n}} \tag{6.4}$$

The above equation shows that the value of t_0 which extremizes $\chi^2(a, t_0)$ is the value which extremizes $\widehat{a}(t_0)$. The second derivatives indicate that these are minimum of χ^2 and a maximum of $\widehat{a}$. The best-fit value of $\widehat{t_0}$ is indeed the value which maximizes the amplitude estimate $\widehat{a}(t_0)$.

6.3 Charge Calibration

The calibration of charge ionization energy in the ZIP detector is accomplished using the 356 keV line of the ^{133}Ba calibration source. The calibrated quantities are labelled as qi and qo respectively for the two electrodes. Prior to calibration, a correction to crosstalk between the two ionization channels and a position dependence are performed. Such dependencies are removed in order to avoid skewing the charge amplitude and start times estimate to obtain from the optimal filter algorithm. Section (6.3.1) discusses the crosstalk removal while section (6.3.2) will shift the discussion to the position dependence.

6.3.1 Crosstalk Correction

A correction between the two ionization channels due to the capacitive crosstalk is applied to generate qi and qo. Given QI, QO, QIx and QOx, and the two noise power spectral density (PSD) from the inner and outer electrodes obtained from the 500 randoms taken at the beginning of each run, it is possible to construct the inner and outer charge signal SI and SO such that

$$\overrightarrow{S} = M \cdot \overrightarrow{a} + \overrightarrow{n} \tag{6.5}$$

where $\vec{a}$ is a vector amplitude whose estimate $\widehat{a}$ is determined for a given template $A(t)$, signal $S(t)$ and noise spectrum $n(f)$ using the optimal filter, so the noise PSD is then defined as $J(f) = |n(f)|^2$. To reconstruct the two amplitudes aI and aO simultaneously, given these four templates and two noise spectra, JO and JI, equation (6.5) can be conveniently written in the form of a matrix expression:

$$\begin{pmatrix} SI \\ SO \end{pmatrix} = \begin{pmatrix} QI & QIx \\ QOx & QO \end{pmatrix} \times \begin{pmatrix} aI \\ aO \end{pmatrix} + \begin{pmatrix} nI \\ nO \end{pmatrix} \tag{6.6}$$

To determine the best estimate amplitude $\widehat{a} = \begin{pmatrix} aI \\ aO \end{pmatrix}$ for the inner and outer channel which properly account for the crosstalk between them, one can construct a χ^2 function which depends on $\begin{pmatrix} aI \\ aO \end{pmatrix}$:

$$\chi^2(aI, aO) = \sum_n \left[\frac{|\widetilde{SI} - (aI\widetilde{QI} + aO\widetilde{QIx})|^2}{JI} + (I \leftrightarrow O) \right] \tag{6.7}$$

where the second term in the above equation is exactly similar to the first term with inner quantities referred by the index I replaced by outer ones, i.e those with index O, and vice versa. By minimizing the χ^2 (6.7) with respect to the amplitudes a_I and a_O, one finds:

$$\begin{pmatrix} \widehat{a}_I \\ \widehat{a}_O \end{pmatrix} = P^{-1} \times \begin{pmatrix} \sum_n Re\left(\frac{\widetilde{QI}^*}{JI} \widetilde{SI}^* + \frac{\widetilde{QOx}^*}{JO} \widetilde{SO}^* \right) \\ \sum_n Re\left(\frac{\widetilde{QO}^*}{JO} \widetilde{SO}^* + \frac{\widetilde{QIx}^*}{JI} \widetilde{SI}^* \right) \end{pmatrix} \tag{6.8}$$

where P is a 2×2 non singular matrix whose complete expression is derived from the χ^2 minimization, i.e. $\frac{\partial \chi^2}{\partial aI} = 0$ and $\frac{\partial \chi^2}{\partial aO} = 0$ (see appendix A of [315] for detailed expression of P).

6.3.2 Energy and Position Dependence Correction

As described in the section (6.3), the ionization channels of each detector are calibrated using spectral lines from ^{133}Ba sources. The most visible line Ge detectors is the is a 356-keV line. Before the ionization energy can be calibrated to a physical meaningful energy deposition, a correction due to a position dependence of the ionization signal has to be applied. This position dependence is only of importance for the inner electrode due to the fact the outer electrode is dominantly used as a veto electrode which does not directly affect the result of any analysis based on events in the fiducial volume. There is $\sim$ 5% of charge collection across the crystal which show a dependence of the ionization amplitude of the 356 keV of ^{133}Ba line as a function of the event position, defined by the delay quantities xdel and ydel (see Equations (6.14)and (6.15) under the section (6.5.2)). By correcting for such position dependencies, we see significant improvement in the ionization resolution at high energies. The flowchart shown in Figure (6.3) illustrates the steps in the crosstalk removal procedure.

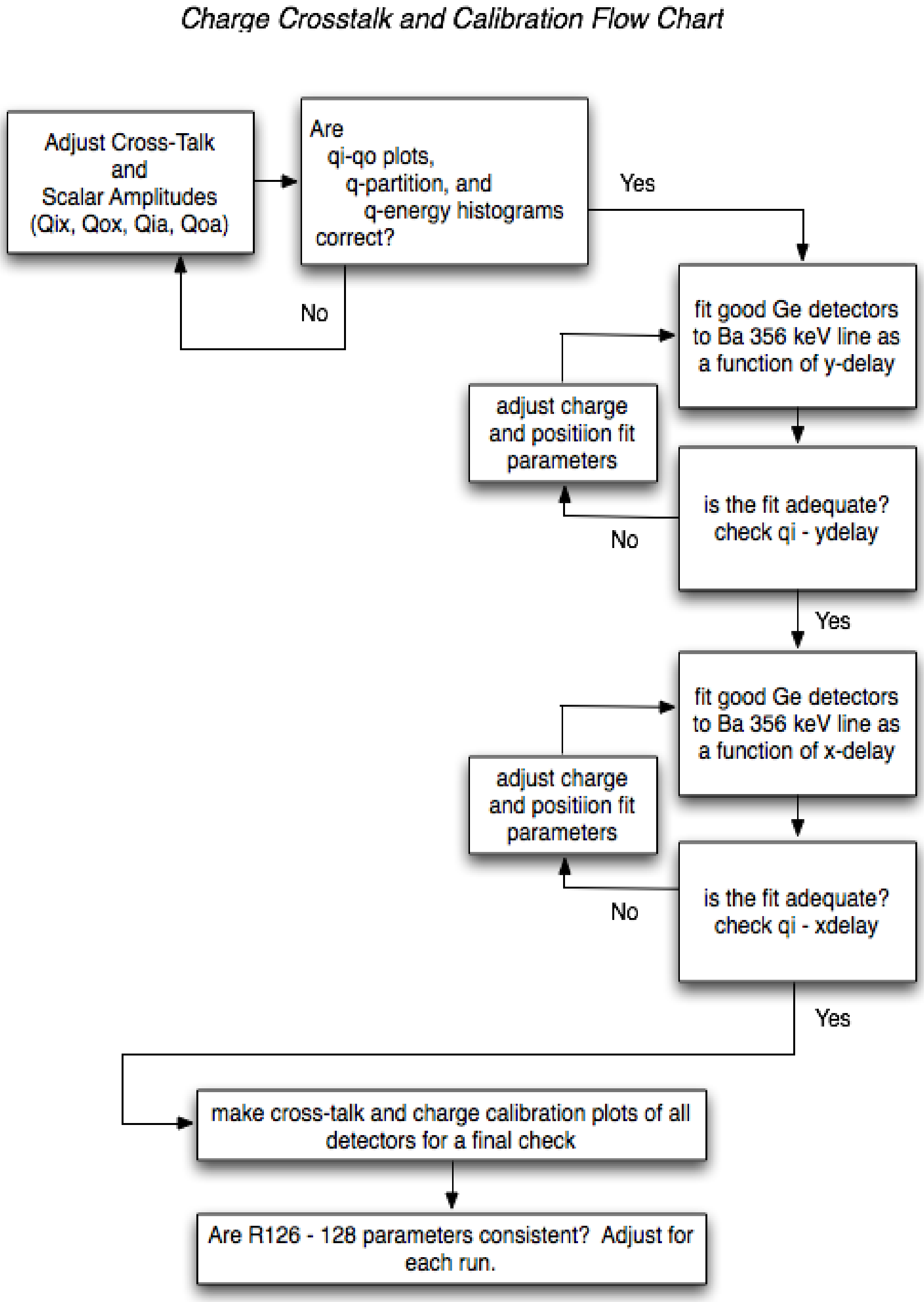

Figure 6.3: Flow chart of the crosstalk correction procedure. Figure courtesy of Kyle Sundqvist [379].

Y-dependence

It is observed that the position dependence in the CDMS-II ZIP-detector is more pronounced in the y-direction of the crystals than in the x-direction. Such a strong position dependence in the y-direction is not understood quantitatively, but it is conjectured that this may result from the TES ion implantation or neutralization effects due to varying distance from the LED flashes. Due to the strong position dependence in the y-direction, we first correct for such dependence before removing any position dependence in the x-direction.

The ionization correction removal is performed by selecting events which are located around the 356 keV line ($\pm 2\sigma$ from the mean of the 356 spike-centroid). We correct qi (qo) using polynomials fitted to the centroid of the 356 keV line as functions of xdel and ydel. In practice, we primarily correct the charge ionization in the y-direction, i.e remove any position dependence in QI (QO) from the y-delay. The correction factor is determined by taking the ratio of the polynomial value to a straight line. Each measured charge event is then multiplied by this correction factor to correct for the position dependence.

The dependence in the y-direction is corrected for by cutting in energy around the 356 keV of the Ba line and splitting the range in delay into 10 bins. We then project onto the QI axis and fit to a gaussian to the line. The means of these gaussian fits, and their errors, were fitted with a 5 (4) parameter polynomial as shown in Figure(6.4), however in a few cases a 4-term polynomial was used, when the 5-term polynomial appeared to overfit. Figure (6.5) show the position dependence in the y-direction using the energy qi (QIOFvolts) as a function of the y-delay (ydel). The left plot in this figure shows this dependence before any correction is applied, and the right plot pictures what the left plot becomes after correcting for position dependence. The red horizontal straight line on the left plot shows the 356 keV line of the ^{133}Ba source. This line is clearly flat after removing the dependence in position while, as one can observe in the left plot, it wasn't prior to the correction.

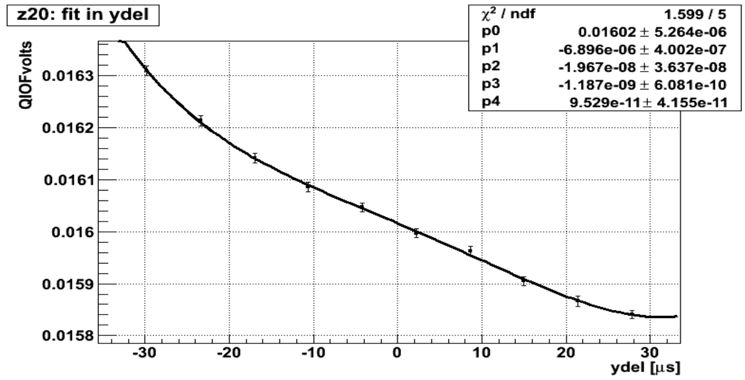

Figure 6.4: Fitted 4-parameter polynomial of the 356 keV line as function of the y-del for T4Z2 (R130). Figure courtesy of Scott Fallows [388].

X-dependence

After correcting for in the y-dependence (in the y-direction), the same procedure is applied to the events as a function of the x-direction where the position dependence is not as strong as it is in the y-direction. We believe that the position dependence is strong in ydel because of the y-dependence of TES ion implantation or neutralization effects due to varying distance from the LEDs. Similarly to the y-dependence, the dependence in the x-direction was corrected by also cutting in energy around the 356 keV of the Ba line and splitting the range

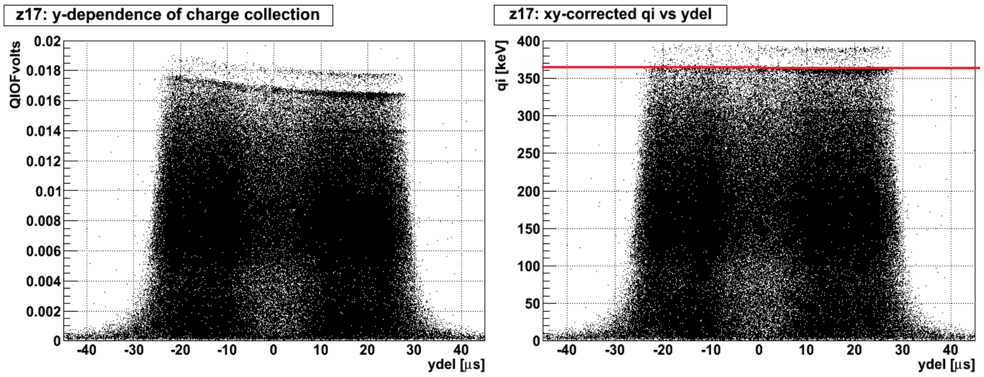

Figure 6.5: Charge ionization position dependence correction in the y-direction (y-del) for T3Z5(Ge). Red lines in this figure show the fitted contour of the 356 keV ^{133}Ba line, both before and after polynomial correction. Figure courtesy of Scott Fallows [388].

in delay into 10 bins and then project onto the QI axis and fit the line to a gaussian. The means of these gaussian fits, and their errors, were fitted with a 4-parameter polynomial as shown in Figure(6.6). Figure (6.7) shows the x-dependence before and after the correction. As one can see from the left plots of Figures (6.5) and (6.7), the y-dependence is indeed stronger compared to the x-dependence.

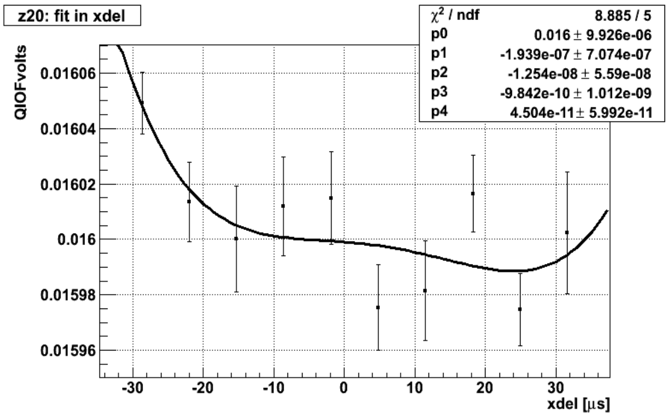

Figure 6.6: Fitted 4-parameter polynomial of the 356 keV line as function of xdel for T4Z2 (R130). Figure courtesy Scott Fallows [388].

Note

For Silicon ZIP detectors, due to the fact that ^{133}Ba lines are not always visible, we calibrated the inner electrode using 356 keV events shared with neighboring detectors. This calibration procedure is successful if the neighboring detector is germanium, at the exception of T2Z1, which is the only silicon detector without a neighboring germanium detector. In the absence of a charge line, the calibrations of the inner and outer electrode are assumed to be equal and no charge position correction is performed [315].

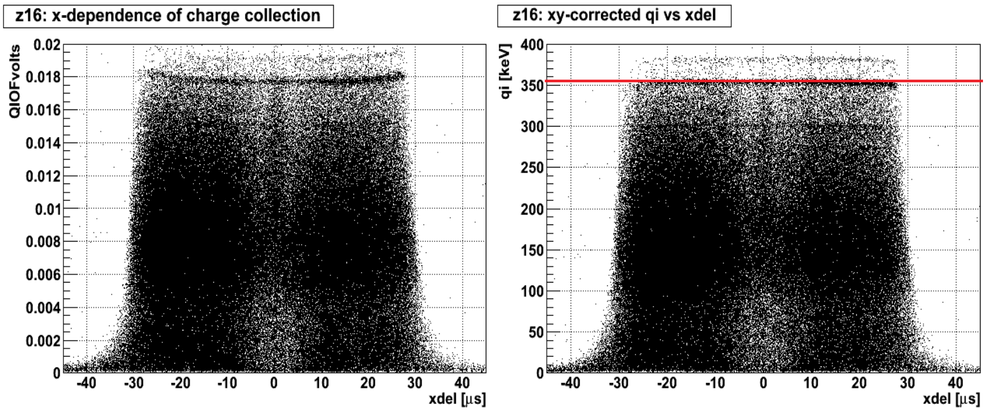

Figure 6.7: Charge ionization position dependence correction in the x-direction (xdel) for T3Z5(Ge). Red lines in this figure show the fitted contour of the 356 keV ^{133}Ba line, both before and after polynomial correction. Figure courtesy Scott Fallows [388].

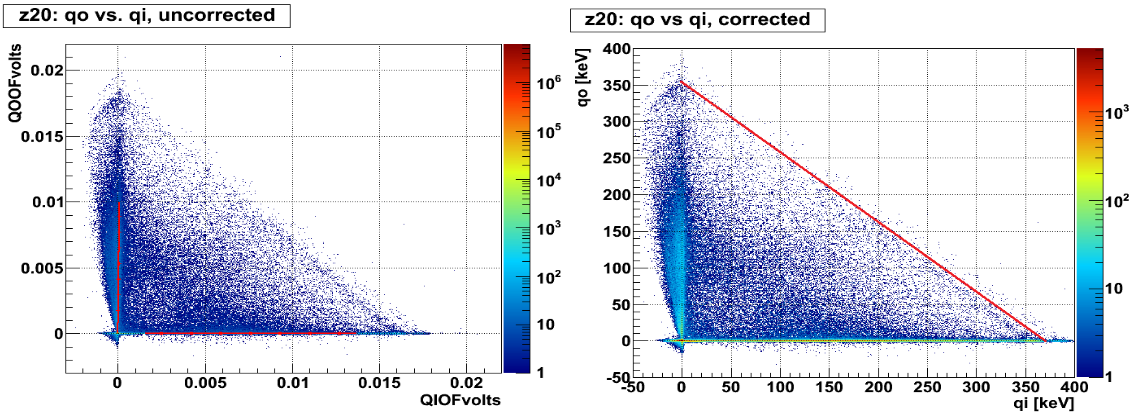

Figure 6.8: Scatter plot of the qo (QOOFvolts) as function of the qi (QIOFvolts) before and after calibration for ^{133}Ba events in T4Z2 (R130). The red line indicates qi + qo = 356 keV [379].

6.4 Phonon reconstruction

Phonon pulse reconstruction is more complex and more difficult than charge reconstruction due to variations in pulse shape with amplitude, position and type of recoiling events. Preliminary estimates of phonon energy are made using a fixed-pulse-shape optimal filter. This technique provides preliminary energy estimates with lowest measurement noise with some systematic errors. Below, I am going to discuss basic principle of phonon energy measurement in CDMS analysis using the optimal filter. Toward the end of this section, phonon calibration procedure will discussed. This discussion is build on a past analysis that I worked on during one of the past CDMS runs.

6.4.1 Relative phonon calibration

Before discussing the phonon calibration in this section, it is important to introduce some of the phonon and charge quantities which will be used in the subsequent discussion that we are going to delve into below. Once an interaction occurs in the ZIP detectors, both phonon sensors and charge ionization electrodes measure and record four signals for the phonon and two signals for the charge. The 4 phonon signals are labelled as pk (with k representing a phonon channel: $k = \{a, b, c, d\}$) while the ionization signal is noted by qt (where t indicates the inner electrode or the outer electrode: $t = \{i, o\}$). The total phonon energy pt is obtained by summing all the phonon contribution, i.e. $pt = pa + pb + pc + pd$. Similarly the total charge energy is given by $qsum = qi + qi$.

The phonon energies (pa, pb, pc, and pd) are calibrated using the charge energies, particularly $qsum$, which are calibrated beforehand. The first step in the phonon calibration is to find absolute coefficients that minimize chi-squared between the uncalibrated phonon energies and the calibrated charge energies. Secondly, one finds the relative coefficients that are iteratively adjusted, so that the peaks of the phonon fraction distributions (pa/pt, etc.) are aligned for each detector as shown in Figure (6.9) [390]. The partition plots (also called box plots), as illustrated in Figure (6.10) for a representative detector in R130, are shown for each detector in order to assess the quality of the calibration. The more squares these plots look, the better the calibration is. To make the phonon response more uniform across the detector, the four sensor amplitudes are scaled by four gain factors chosen to minimize the width of the ionization yield band. After applying these relative gains, the phonon energy is calibrated with reference to the ionization signal ($qsum$). The summed phonon amplitude is multiplied by an overall gain factor chosen to ensure ionization yields near unity at low energies. Although we usually calibrate our phonon pulse height to estimate recoil energy, based on discrete lines seen in the charge spectrum ($qsum$). Walter Ogburn pointed out that it is also possible to convert our signals to units of power. The integral of a pulse is then the total energy deficit in Joule heating, which (in the strong electrothermal feedback regime) is equal to the total energy deposited in the TES. The absolute calibration then shows what fraction of the recoil energy of an event is deposited in working TESs.

Both the optimal filtering phonon quantities and the phonon integral quantities are calibrated. As a reminder, the optimal filter algorithm gives the best estimate for both charge and phonon energy by calculating their respective pulse amplitudes. The integral gives a better estimate at high energy where noise does not have as much of an effect to the signal as it does in a low energy region.

6.4.2 Some thoughts about phonon calibration

During the run R130, Mark Kos, a postdoc with the CDMS collaboration at Syracuse University, proposed another way for calibrating the phonon energies. The charge ionization qi (for the inner electrode) and qo (for the outer electrode) are calibrated using the 356 keV line in the ^{133}Ba calibration, and since this line is also visible in the summed phonon energy, one can devise a way of calibration energy by finding the coefficient α, β, γ and δ such that

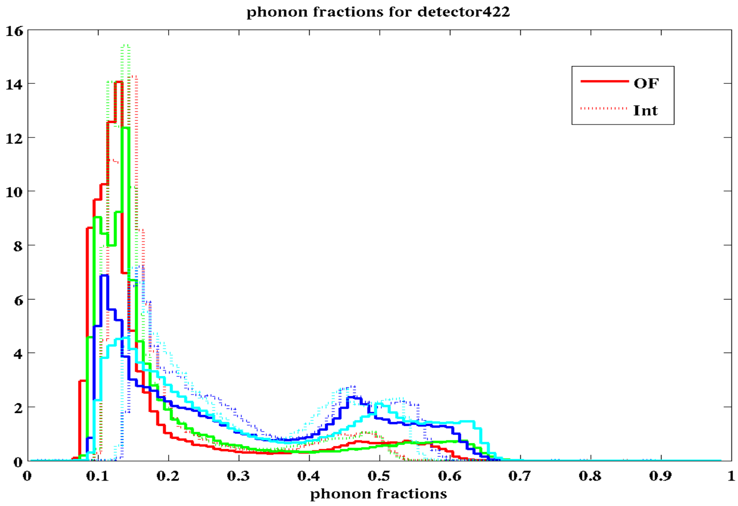

Figure 6.9: Histogram of the phonon fraction for the optimal filtering quantities and the integral phonon quantities for T3Z2 - R130.

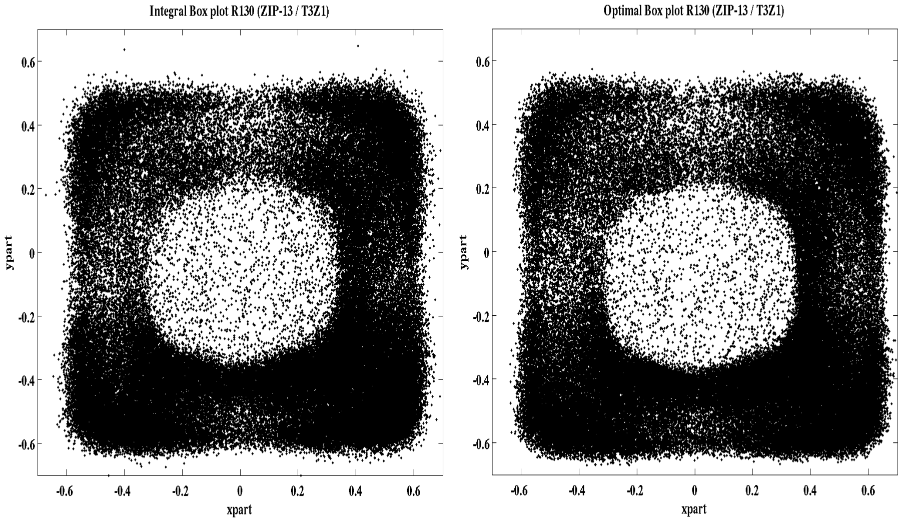

Figure 6.10: The partition plot (also referred to as the box plot) generated after phonon calibration for the optimal filtering quantities and the integral phonon quantities for T4Z4 - R130. A square box plot is an indication that the phonons energy are well calibrated.

$$\alpha \cdot p_a + \beta \cdot p_b + \gamma \cdot p_c + \delta \cdot p_d = 356 \tag{6.9}$$

By resealing the coefficients α, β, γ and δ to $\alpha' \to \alpha/356$, $\beta' \to \beta/356$, $\gamma' \to \gamma/356$ and $\delta' \to \delta/356$, the equation 6.9 becomes equivalent to

$$\alpha' \cdot p_a + \beta' \cdot p_b + \gamma' \cdot p_c + \delta' \cdot p_d = 1 \tag{6.10}$$

which is nothing else, but the sum of the phonon fraction

$$f_k = \frac{p_k}{p_a + p_b + p_c + p_d} \tag{6.11}$$

obeying the same constraint as (6.10), i.e $\sum_{k=1}^{4} f_k = 1$ with $k = \{a, b, c, d\}$.

6.5 Position Reconstruction

The segmentation of the phonon sensors of CDMS-II ZIP detectors into four quadrants provides a very rich stream of information and a way for reconstructing the position of the events in the plane parallel to the detector's top and bottom surfaces (xy position). In practice, the (x,y) position of an event can be measured from differences in either phonon-signal start times or pulse heights. Since the quasiparticle-assisted TESs respond quickly to athermal phonons, with rise times on the order of tens of microseconds and since the sound speed in the crystal is about 5 mm/μs in Ge (8 mm/μs in Si), the shapes and start times of the phonon pulses contain information about the types of phonons absorbed and the distances they travelled before reaching the sensors.

6.5.1 x-y position from energy partitioning

The first position reconstruction of events in the CDMS-II ZIP-detectors comes from the partition of phonon energy among the four phonon quadrants. The x-y position, whose coordinate is denoted (xppart,yppart), is defined as:

$$xppart = \frac{p_c + p_d - p_a - p_b}{pt} \tag{6.12}$$

and

$$yppart = \frac{p_a + p_d - p_b - p_c}{pt} \tag{6.13}$$

with $pt = p_a + p_b + p_c + p_d$, the sum of the four phonon energy from the four channels.

Due to its characteristically square shape, the plot of the partition coordinates is referred to as **the box plot**. The partition coordinate is a good estimator of position near the center of the detector, however, as you go farther out it begins to exhibit some pathologies: events closer to the outer edge of the detector (i.e. events in the outer ionization electrode) with the larger physical radius, do not have the largest values of $r_{ppart} = \sqrt{xppart^2 + yppart^2}$ $\left(\theta_{ppart} = \tan^{-1}(\frac{yppart}{xppart})\right)$, the equivalent polar coordinate), but instead **fold back** to smaller values. Second, the density of points is very high at the outer edge of the plot, representing a second pathology called **pile-up**, where r_{ppart} is not very sensitive to changes in the physical radius. The foldback and pile-up are clearly visible in the partition plot shown in Figure (6.11), where the outer-electrode events (orange) occur closer to the center of the plot than many inner-electrode events [46, 318].

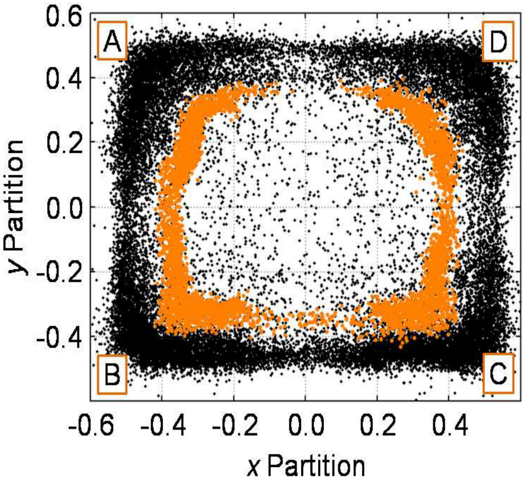

Figure 6.11: CDMS-II ZIP detector xy position reconstruction using partition coordinates (box plot). Each data point corresponds to an electron recoil induced by a uniformly illuminating ^{133}Ba gamma-ray source (dark-black dots). Events with more significant Q-outer than -inner signals (light-orange dots) correspond to events occurring near the edge of the detector. However they appear at smaller partition radius than expected due to a position dependent phonon response.

6.5.2 x-y position from the phonon delays relative to the charge

The start-time delay for each phonon signal relative to the start time of the prompt charge (Q-inner) signal also provides a good estimator for event positions in the ZIP detectors. The x-delay and the y-delay coordinates are defined as the difference between the shortest such time (among the four phonon channels) and the start-time delay for the horizontally (vertically) adjacent channel. We use a start time defined by the point at which the pulse in each quadrant reaches 20% of its peak value, PXr20 ($X = \{A, B, C, D\}$). The two coordinates are defined by

$$xdel = \begin{cases} PAr20 - PDr20 & \text{if the interaction occurs in quadrants A or D.} \\ \\ PBr20 - PCr20 & \text{if the interaction occurs in quadrants B or C.} \end{cases} \tag{6.14}$$

$$ydel = \begin{cases} PBr20 - PAr20 & \text{if the interaction occurs in quadrants A or B.} \\ \\ PCr20 - PDr20 & \text{if the interaction occurs in quadrants C or D.} \end{cases} \tag{6.15}$$

with $r20$, the 20% phonon rise time. The x and y delay coordinates (in μs) is negative if the shortest start-time delay occurs in channels A or B (B or C), and positive otherwise. Figure (6.12) show the delay plot using the delay coordinate x delay and y-delay. In this coordinate system once again the fold back and pile-up pathology observed with the partition coordinate show up again in the delay plot. The outer-electrode events (orange) occur closer to the center of the plot than many inner-electrode events [46, 318].

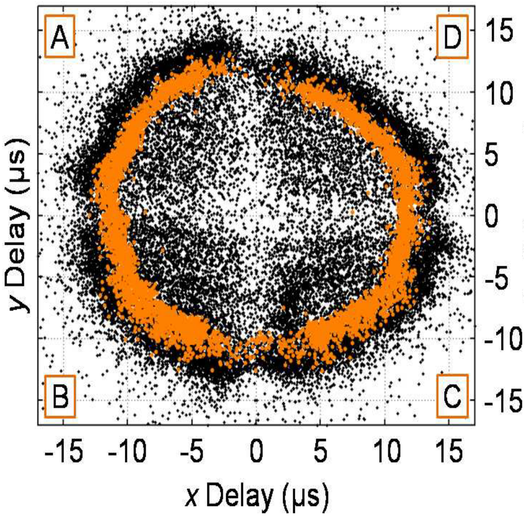

Figure 6.12: CDMS-II ZIP detector xy position reconstruction using delay coordinates (delay plot). Each data point corresponds to an electron recoil induced by a uniformly illuminating ^{133}Ba gamma-ray source (dark-black dots). Events with more significant Q-outer than -inner signals (light-orange dots) correspond to events occurring near the edge of the detector. However they appear at smaller than expected partition and delay radius due to a position dependent phonon response.

Like the partition coordinates, the delay coordinate has a very clean response near the center of the detector. As you go further out, it begins to pile up and fold back somewhat at large delay radius $\left(r_{del} = \sqrt{xdel^2 + ydel^2}\right)$. There is a clear difference in the delay plot caused by the choice of crystal substrate. For instance, the delay plots in Si are much smaller than those in Ge because of the faster sound speed in Si [318]. The physical outer edge of the crystal actually corresponds to the inner edge of the ring of QO events. This radial degeneracy is unfortunately generic to ZIP detector position estimators, because of decreased resolution far from the quadrant boundaries, and because of increased reflection from the outer detector edge. Fortunately, delay and partition do not undergo foldback at exactly the same physical radius, so one can be used to break the degeneracy of the others.

6.5.3 Radial Degeneracy

The first attempt to reconstruct the event position in the ZIP detectors comes from the delay and partition quantities. However, the delay and partition radius exhibit a pathology that we have called fold back: events of low and high radius can have degenerate reconstructed radii. Fortunately, the x-y position reconstruction technique can be combined to break this degeneracy since the location of the degeneracy is different for the partition plot than in the delay parameters. The combination of the x and y partition coordinates with delay radius produces a three-dimensional plot that is commonly referred to as the **phonon position manifold** shown in Figure (6.13). The projection of any event in the manifold onto the partition radius and delay radius plane is a shrimp-shaped plot, where the true radius of an event can thus be estimated by walking along the shrimp.

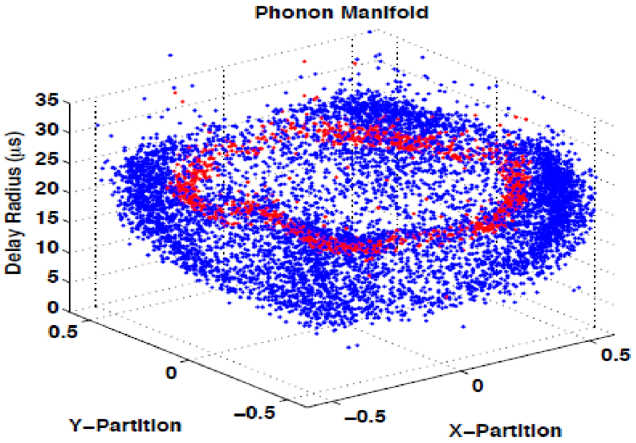

Figure 6.13: The manifold plot showing the x-y reconstruction degeneracies broken by combining information from both the partition and delay information. Events occurring under the Q-inner electrode (blue) are distinguished from those occurring under the Q-outer electrode (red), highlighting the degeneracy. Figure from [316].

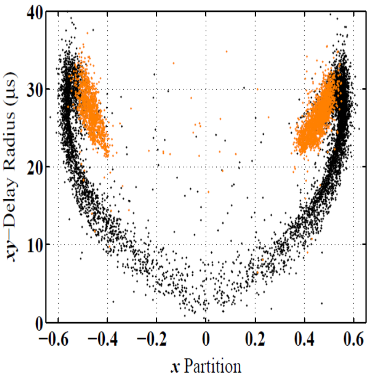

Figure 6.14: The delay radius as a function of the x-partition parameter for a restricted range of y-partition values (-0.25 to 0.25), demonstrating how the degeneracy in the xy-position reconstruction can be broken. Each data point corresponds to an electron recoil from a ^{60}Co gamma-ray calibration. Events occurring under the Q-inner electrode (black) are distinguished from those occurring under the Q-outer electrode (orange), highlighting the degeneracy of the delay and partition parameters when not used in conjunction [50].

6.6 Position Correction

After the calibration of the phonon energy, a small population of surface events (non-gaussian tail of timing) constitute a class of outliers that cannot be discriminated without further correction. These outlier events extend to low yield and slow timing in the Ba calibration data and thus pollute the nuclear recoil band where any WIMP signal should lie. The degeneracy shown in Figure (6.13) in xy-position reconstruction is caused by (and is one example of) position (and energy) dependence [395]. The projection of the manifold into a 2D plane as shown for example in Figure (6.14) shows that one can use the x-partition and xy-delay radius for a restricted values of y-partition in order to break the degeneracy at high radii. These degeneracies introduce mis-corrections of timing parameters, which generally become slower at large detector radii. The timing parameters we use for event discrimination have some energy and position dependence. In order to make the cuts simple, we have to correct for that, otherwise we are obliged to form energy and position dependent cuts.

6.6.1 Energy measurement

The phonon energy deposited by a particle in a ZIP detector is estimated by measuring the height of the resulting pulses from the four phonon channels. For every event in a detector, the pulse height is estimated in first-tier data processing using a fixed-template optimal filter for each quadrant [316]. The template pulse uses a two-exponential functional form, $A(t) = A_0 \times (1 - e^{-t/\tau_1}) \times e^{-t/\tau_2}$, where τ_1 and τ_2 are characteristic risetimes and falltimes, estimated from several good pulses.

To estimate the phonon energy, we can also fit the phonon pulses to functional forms in the time-domain [315, 381]. However, such fits have convergence problems and other systematic issues, leading to degraded energy resolution compared to the estime found using optimal filter algorithm [382, 383, 384, 385].

Another possible way to estimate the event energy is to compute the area of the raw pulse by integrating the pulse after the fitting. However, the optimal filter estimate has better resolution than the integral estimate because it is able to suitably de-weight noisy low-frequency components of the acquired traces. With increasing energy, the integral estimate improves as the signal-to-noise increases, whereas the optimal-filter estimate starts to suffer from systematic errors because of mismatches in true pulse shape and template shape [386]. The optimal filter gives better estimates at low energy since optimal filtering takes into account the noise and de-weights them accordingly. The integral estimates are better at high energy. However care must be taken for saturated pulses because the integral quantities may not be accurate since the pulse shape is truncated due to saturation. In such a situation, the estimate obtained using the optimal filter may be more accurate than the integral one because the optimal filter fits the pulse shape using a two-exponential functional form as described at the beginning of this section.

In summary, the CDMS-II collaboration has relied to two methods for estimating phonon pulse energy: (i) the simple amplitude estimators (and the phonon integral) and (ii) the optimal filter amplitude estimator. These techniques are discussed in more detail in [315]. In the past, the integral quantities have been used as a cross-checked to the estimates obtained using the optimal filter and I am not going to pursue its discussion further in this dissertation. Below, I briefly describe how one can crudely estimate a pulse energy by measuring its height. After that I will switch the discussion to a far more sophisticated method to which we have always resorted to using and which gives better energy estimates, especially at low energy: the optimal filter.

Simple amplitude estimators

A very simple way to estimate the energy of an event from its phonon pulse is to take the peak value of the signal trace. This method assumes that the pulse $A(t)$ decay quickly as $t \rightarrow \infty$. Assuming that the pulse in the time domaine is given by

$$S(t) = a \times A(t), \tag{6.16}$$

the amplitude, $\widehat{a}$, representing the energy estimate, is the given by

$$\widehat{a} = \frac{max(S_k)}{max(A_k)}. \tag{6.17}$$

The above estimator, however, is quite poor because it assumes no prior knowledge about noise spectrum and the pulse shape. Since, in practice, the measured signal will be polluted (mimicked) with noise n(t), the most general expression of (6.16) should then be

$$S(t) = a \times A(t) + n(t). \tag{6.18}$$

A better way to determine the amplitude $\widehat{a}$ is to perform a time-domain fit and minimize the χ^2 between template and model which yield the following result:

$$\widehat{a} = \frac{\sum_k \frac{S_k * A_k}{<n_k^2>}}{\sum_k \frac{|A_k|^2}{<n_k^2>}}, \tag{6.19}$$

where $\langle n_k^2 \rangle$ is the noise variance. Although the estimator (6.19) takes into the account the noise spectrum and the pulse shape of the signal, however this formula gives accurate results if the noise fluctuations are statistically independent in every consecutive time bins. If the noise has a non-trivial power spectrum then noise fluctuations at different times are correlated, the equation(6.19) will no longer be a proper maximum-likelihood estimator. In the frequency domain, all the frequency components are truly independent for gaussian random noise. It is therefore desirable to shift gear into the frequency domain.

Optimal filter amplitude estimators

The optimal filtering algorithm transforms the signal S(t) from the time domain to the frequency domain using Fourier transformation. In light of this, the $\chi^2(a)$ will then written as

$$\chi^2(a) = \sum_n \frac{(\widetilde{S}_n - a\widetilde{A}_n) \times (\widetilde{S}_n - a\widetilde{A}_n)^\dagger}{J_n}, \tag{6.20}$$

which is minimized when

$$\widehat{a} = \frac{\sum_n \frac{\widetilde{A}_n^* \cdot \widetilde{S}_n}{J_n}}{\sum_n \frac{|\widetilde{A}_n|^2}{J_n}}, \tag{6.21}$$

with J_n the power spectral density of the random noise taken at the beginning of every single run.

6.6.2 Energy dependence

The phonon delay and phonon rise-time of the phonon pulses have some energy dependence that makes them become slower as the energy increases, as shown in Figure (6.15). As the energy of an event increases more and more, TESs which are very near the event location, begin to saturate, i.e. the phonon pulse flattens and peaks later in time since the TESs further away from the event location have a significantly retarded response. The net effect is that timing parameters become slower as the event increases in energy. After the energy corrections of the data, this energy dependence is minimized and the pulse shape quantities are nearly independent of the event's energy (see Figure (6.15)).

6.6.3 Position dependence

Phonon pulse shapes vary substantially with position (and even with energy), resulting in amplitude estimates that have significant position dependence and energy nonlinearity which must be corrected for since such dependencies tend to wash out intrinsic discrimination. Figures (6.16) and (6.17) show how position (and energy) dependence limits our ability to efficiently discriminate surface events against what could potentially be a WIMP signal. In order to create a uniform response of the detector which does not depend on the event's location, this dependence must be corrected for. The partition and the delay coordinates defined in sections (6.5.1) and (6.5.2) are not perfect candidates for reconstructing the event location because they both present a fold back pathology that we have already described. As the location of a particle interaction moves radially outward, a larger percentage of phonons are absorbed after bouncing off of the detector's cylindrical wall. This physical process manifests itself by folding back (reflection) the timing and energy radial estimates. It is, however, possible to construct a monotonic event location using a combination of the delays and partition. In particular a 3-dimensional position coordinate using xppart, yppart and the delay radius ($r_{del} = \sqrt{xdel^2 + ydel^2}$) can be used to break most of the degeneracies in the reconstructed position. Figure (6.14) shows the position of events under the central inner electrode and the outer electrode at the edge of the detectors. The fold-back for the individual parameters for events at high radius can clearly be seen and how the chosen position coordinates break this degeneracy.

6.6.4 Phonon correction table

Position and energy-dependencies are reduced by making use of a phonon correction table. This technique was initially developed by Blas Cabrera and Clarence Chang as described in its doctoral dissertation [395]. The basic idea for this technique is to compare the phonon parameter values for each event against a look-up table which describe how the mean values of these parameters vary with the location and energy of the event. By factoring out the bulk trends expressed in the look-up table, one obtains corrected parameters with more uniform response and superior resolutions.

The position correction is described in the doctoral dissertation of Z. Ahmed [316]. The phonon position correction is achieved by first producing a table that is used later for correction. We call this table the phonon correction table or look-up table. The basic principle of this method is to compare each event's phonon parameter values against the look-up table describing how the mean of these parameters vary with event location and energy. The look-up table correction homogenizes the detector's response throughout the entire crystal by comparing an event's parameter to those of its nearest neighbors. The look-up table of correction factors is derived empirically from the large sample of photon events from ^{133}Ba calibration runs. A separate table is defined for each ZIP detector and for each of the four phonon sensors. Each event is located in a five-dimensional manifold defined by four position variables (xppart, yppart, xdel, ydel) and the energy. The addition of phonon energy to the table definition was an innovation introduced by Bruno Serfass during runs 123 and 124. The inclusion of this new coordinate into the correction table achieved superior parameter resolution and avoided the need for a separate correction for energy nonlinearities. The position within the manifold is defined by a metric which can be written the following vectorial form

$$\vec{r} = xppart \cdot \vec{e}_1 + yppart \cdot \vec{e}_2 + \frac{xdel}{L_{del}} \cdot \vec{e}_3 + \frac{ydel}{L_{del}} \cdot \vec{e}_4 + \frac{prg}{L_E} \cdot \vec{e}_5 \tag{6.22}$$

where $(\vec{e}_1, \vec{e}_2, \vec{e}_3, \vec{e}_4, \vec{e}_5)$ represent an orthogonal basis in a 5 dimensional space. L_{del} and L_E are weight factors which take into account the relative importance of partition, delay, and energy quantities in determining the position of an event and its associated nearest neighbors within the manifold. The above metric on this five dimensional parameter space and the weight factors are chosen empirically to achieve good correction performance. The look-up table is thus a mapping between each of the calibration photon events and the mean values of the phonon parameters across a set of nearest neighbors events. The number of nearest neighbors affects the performance of the correction algorithm: a table with too few nearest neighbors is limited by statistical noise, while a table with too many nearest neighbors averages over a too large region in the manifold and misses local trends.

For every single event from low-background or calibration data, the nearest neighbors from the look-up table gammas are computed according to the metric defined above. The lookup table provides a mean value of the quantity to be corrected over a set of neighboring events. Given an event and phonon parameter rq the corrected parameter rqc is defined as

$$rqc = rq \cdot \frac{< rq_{cal} >_{all}}{< rq_{cal} >_{NN}} \tag{6.23}$$

where $< rq_{cal} >_{all}$ is the mean over all calibration events, and $< rq_{cal} >_{NN}$ stands for the mean of the parameter for those events in the nearest neighbor cluster drawn from the look-up table. Figures (6.15) to (6.17) illustrates the results of the position correction removal in the ZIP detectors.

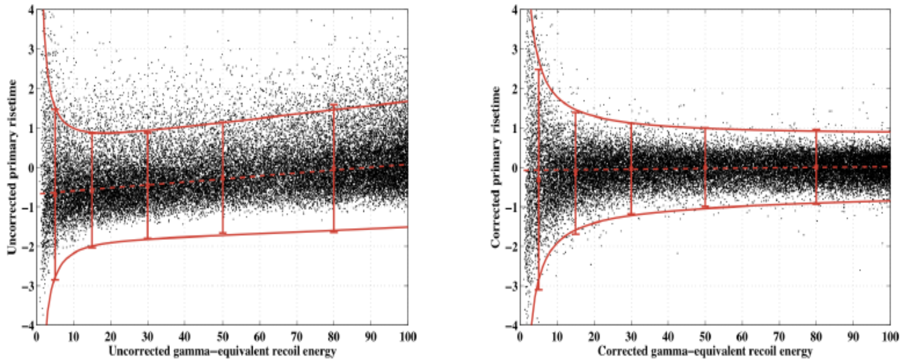

Figure 6.15: Normalized pminrt as function of recoil energy for ^{133} Ba calibration gammas before and after removal of position and energy dependencies. Figure from [316].

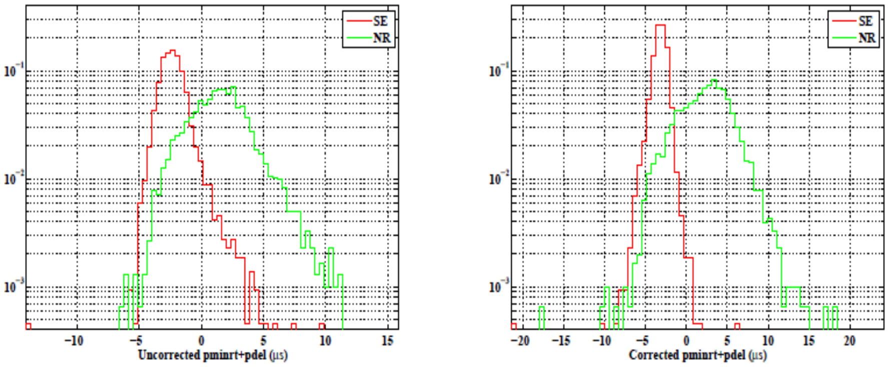

Figure 6.16: Histograms of normalized pminrt+pdel distributions for ^{133}Ba induced surface events (SE) and neutrons from ^{252}Cf (NR) before and after removal of position and energy dependencies.

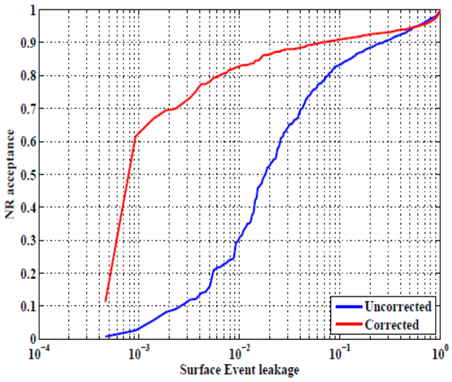

Figure 6.17: Surface-event leakage rate vs. nuclear-recoil acceptance efficiency for ^{133}Ba induced surface events and neutrons from ^{252}Cf. At 60% signal acceptance, the empirically corrected phonon timing provides 20x better rejection of surface events. Figure from [316].

Chapter 7

c58 Reanalysis: CDMS-II Soudan's last runs.

7.1 Introduction

The last CDMS-II science run data was taken during the period of time running from July 2007 to August 2008. The main WIMP-search analysis for the data acquired during this science run started from September 2008 and ended at December 2009. This last CDMS-II WIMP-search analysis resulted in two observed event candidates (in detectors T1Z5 and T3Z4) after the unblinding. All the checks conducted concluded that the analysis could not be interpreted as statistically significant evidence for WIMP interactions, but that neither event could be rejected as signal [425].

Although the two candidate events were recorded under normal running conditions of the experiment without any indication of reduced performance which would have, in principle, resulted in rejection of these events as WIMP candidates, the investigation of the raw data pulses revealed an issue with the ionization pulse reconstruction algorithm. One of the two candidate events suffered from an approximation in the fitting algorithm that yielded an optimal filter start time not being a global minimum of the χ^2, therefore overestimating the phonon delay, Figure (7.1). A start time inferred from the global minimum of the χ^2 would have resulted in the event failing the timing cut.

Given what we learned after all the checks conducted during the post unblinding, it was then decided to improve our software fitting routine and reprocess the entire CDMS-II 2007-2008 data and carry out a separate and independent analysis with the reprocessed data in order to ascertain whether or not the two observed events would still show up inside the signal region and whether other events might move into the signal region. The reprocessing of the last CDMS-II data started in October 2010 and the reprocessed data has been available for more than a year. During the reanalysis, 3 different timing cuts were explored: the traditional (or classical) timing cut used during the CDMS-II previous WIMP search analysis and two other new methods developed during the c58 reanalysis: the neural network and the 5 dimensional χ^2. I was the architect of the 5 dimensional χ^2, a timing cut which was tuned in a way that the total target leakage is exactly the leakage at which the expected sensitivity is optimal.

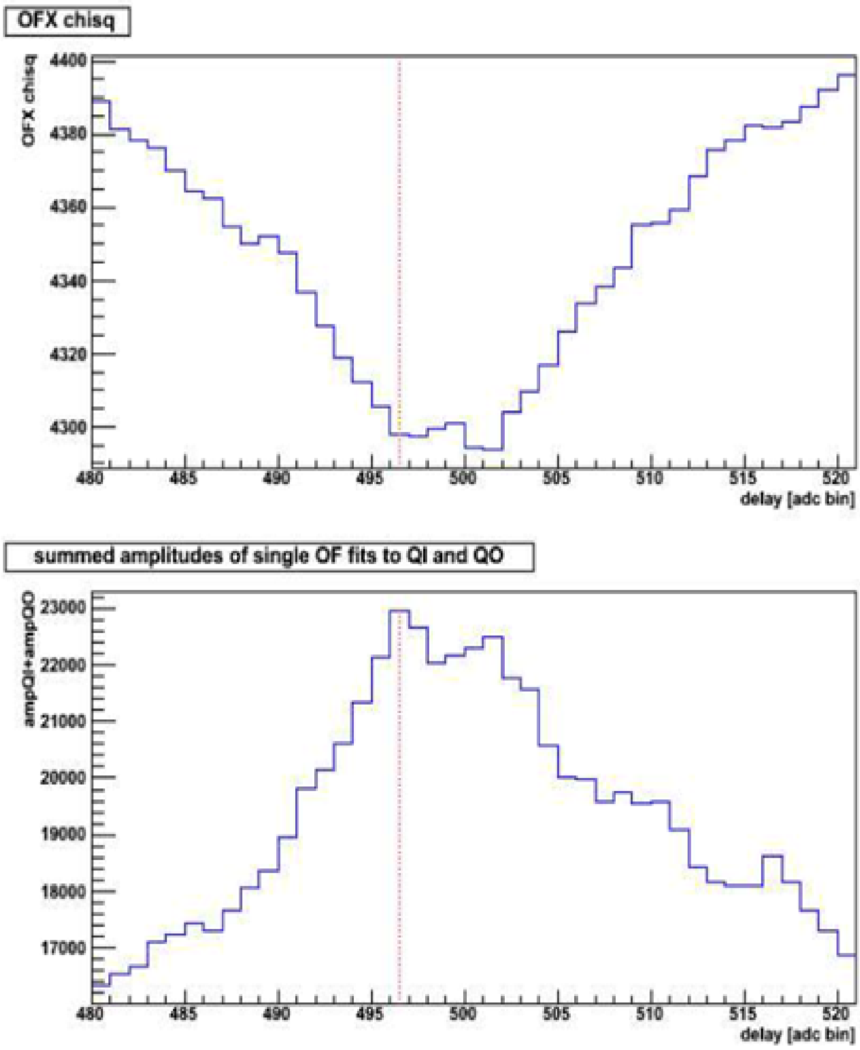

Figure 7.1: Top: Value of the optimal filter fit χ^2 as a function of the start time bin of the ionization pulse. The selected bin from the maximal amplitude algorithm is indicated by the red-dashed line, which is at the global maximum of the summed amplitude; however the global minimum of the χ^2 distribution occurs 5 ADC bins later. Bottom: Amplitude of the summed inner and outer-electrode ionization signal as a function of the start time bin of the ionization pulse. The start time is determined by the bin which maximizes the summed amplitude (marked by the red/dashed line). Figure courtesy of Lauren Hsu.

In this chapter, I will touch upon some of the works I authored during the last CDMS-II WIMP-search analysis and its main analysis streamline compared with the reanalysis for some cuts which needed to be tuned. This chapter is structured as follows: first I discuss, in section (7.2), the blinding procedure used in the CDMS experiment which requires that the signal region (or nuclear recoil band) has to be masked during cuts development. In section (7.3), I discuss cuts related to good time events selection. Section (7.4) discusses the bad detector region cut, section (7.5) describes the reconstruction quality cuts and section (7.6) event-selection cuts are discussed in details. The ionization yield based rejection in section (7.7) while section (7.8) discusses the limitation of the ionization yield based rejection. Section (7.9) talks about the timing and motivates the need for using the timing parameters for surface event rejection. At the end of the chapter, more precisely in section (7.10), I will briefly introduce our traditional-classical-simple timing cuts which uses the timing quantities from the phonon pulse shape to define a discriminator threshold for surface-events rejection. In the next chapter, chapter (8), I will take sufficient time to delve into the details of 5 dimensional χ^2 timing cuts for surface events rejection, a technique in which I played a key role.

7.2 WIMP Search Analysis: A Blind Analysis

The goal of WIMP-search analysis is to develop a series of cuts that will be applied to the WIMP-search data in order to find WIMP candidates. Normally this analysis is done using the calibration data and the entire analysis is blind, i.e. the events which could potentially be WIMP candidates, for example those in the nuclear recoil band, are removed from the WIMP-search data until the cuts are finalized, so the entire analysis is a blind analysis in the sense that no one looks at what is inside the nuclear-recoil band until the cuts are fully defined.

The analysis blindness is assured during the analysis development by removing any potential candidate events from the data by a cut called the blinding cut. The blinding cut represents a simplified and conservative version of the WIMP-search analysis. It is conservative in the sense that it removes more events from the data set than the final selection criteria would. Events satisfying the following criteria are removed from the data set until the final selection criteria have been defined:

- **Single scatters**: This cuts checks whether or not the total phonon recorded is inconsistent with the noise distribution in a single detector only. An event is classified as a single scatter if it shows significant energy deposition in one and only one detector. More specifically, the cut requires that the uncorrected phonon energy be 6σ above the detector's phonon noise mean and should fall below the 4σ upper edge for all other detectors.
- **Energy range**: the energy range cut selects events for which the recoil energy lies in the interval from $5 - 120$ keV. This energy range is not the analysis energy range; the final results are calculated with $10 - 100$ keV energy range with 10 keV considered as the phonon recoil energy threshold.
- **Fiducial volume**: The ionization signal in the outer electrode (Q_{outer}) has to be consistent with the noise distribution of the outer electrode: $|\frac{Q_{inner}-Q_{outer}}{Q_{inner}+Q_{outer}}| < 0.2$, yielding the restriction that the ionization charge in outer electrode must normally have less than 5 keV energy deposited or $|Q_{outer}| < 5$ keV given the nature of the previous condition.

- **Ionization yield**: the ionization yield requires the events to lie within $\pm 3\sigma$ of the nuclear recoil band predefined using the ^{252}Cf data.
- **Veto anti-coincident**: this cut require that there should be no signal in the scintillator veto shield within 50 μs preceding the global trigger of the event.

The blinding cut is normally created using the non-position-corrected quantities; however, after the position correction, few events in the yield vs recoil energy plane can move inside the nuclear recoil band, rendering the whole not blind if nothing is done to mask them. This was noticed during the c58 analysis and also probably during the previous runs. For this reason and in order to stick to the blindness of the analysis, it is required that another blinding mask is developed with the position corrected quantities and apply to the data in order to remove events that could make their way inside the signal region. For the rest of this chapter, I will be discussing some of the many important data selection and data quality cuts which goes into the whole WIMP-search analysis. Some of these cuts were developed during the original c58 analysis and they did not changed if they are phonon based cuts. However, the ones requiring the charge information were re-tuned using the reanalysis c58 data and if need be, I will discuss the main difference between the previous results and the new ones.

7.3 Good times events selection

In order to guarantee the stability of WIMP-search analysis, several cuts are created in order to select events during periods of stable running. This section discusses some of the relevant cuts used during a WIMP-search analysis. Among these cuts, the trigger rate and stability, which looks at the number of events over a period of time is discussed. The Kolmogorov-Smirnov test, which selects events (or data series) which belongs to the same parent is also described in this section. The Helium film, neutralization for the charge stability and neutron activation are all part of the discussion.

7.3.1 Trigger rate and trigger stability

To ensure the quality of the data, we need to make sure that all the data has been acquired under good conditions. Any period of time with excessive trigger rate can be indicative of electronics problems and/or an increased phonon noise. During the c58 analysis, I carried out this analysis of trigger rate in order to investigate whether the event rate for the WIMP-search data was within our accepted trigger rate threshold [396]. Data series with short livetimes and high trigger rate must be removed.

The trigger rate was examined on a series by series basis. Periods with an overall trigger rate > 0.7Hz over at least 100 consecutive non-random events are considered as periods with high trigger rates and completely or partially removed from the analysis. For the partial removal of the data, only the live data that was mostly affected by the high trigger rate was cut out, this was however governed by investigating the empirical cumulative distribution function of the live time for the culprit data series and remove only the fraction of live time where the slope tend to exhibit a curvature. If the slope is the same, the whole series was kept and used for the WIMP-search analysis. The trigger rates were investigated for each data series in every detector separately to cut periods of high trigger rates on a specific detector but keep the data for non affected detectors. Figure (7.2) shows the trigger rate as function of the live time for all the runs, and Figure (7.3) shows the cumulative live time for the runs that were affected by high trigger rates during the c58 analysis. The trigger rate cut is entirely based on the time; a cut on noise might be effective, however, cutting out on times of high rates remove negligible livetime.

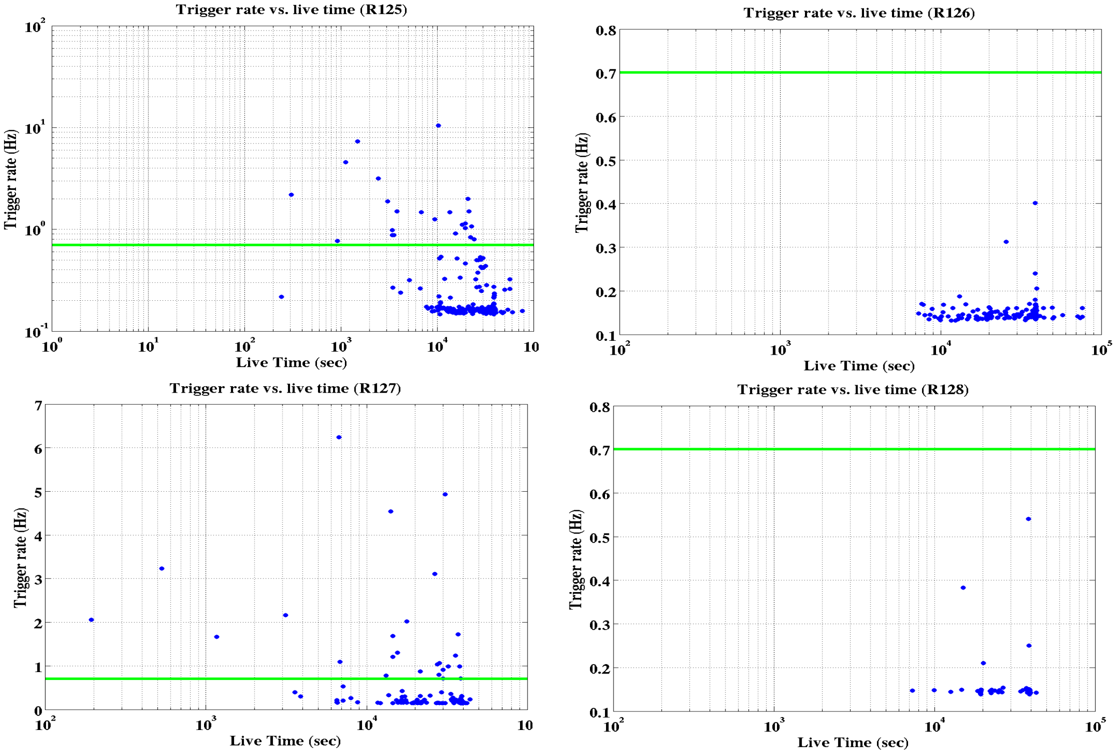

Figure 7.2: Trigger rate (in Hz) as function of the Live time (in sec) for R125-R128. Each dot in these graphs represents a single data series; the green horizontal line shows the trigger rate threshold (0.7Hz). As can be observed, only two low background runs, R125 and R127, experience some high trigger rate. The fraction of livetime removed is 0.048% for R125 and 0.018% for R127.

7.3.2 KS test

The Kolmogorov Smirnov (KS) test determines whether two data sets differ significantly from each other, or whether they consistent with having been drawn from the same parent. The KS-test has the advantage of making no assumption about the distribution of data, i.e. KS test is non-parametric and distribution free [401]. For the KS test, one needs to determine first the cumulative distribution functions (CDF) or the empirical distribution functions of the data sets one is comparing. The KS-test uses the maximum vertical deviation D between the two curves (CDF) as the test statistic. From the statistic D, one can calculate the significance or

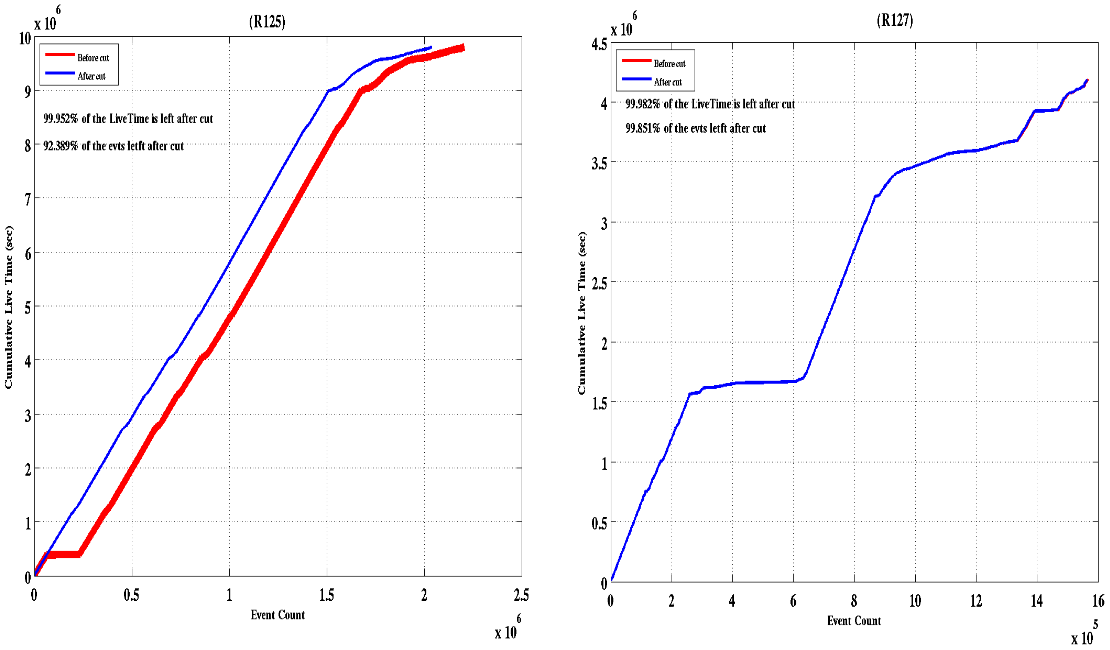

Figure 7.3: Cumulative live time as function of the event count before and after the removal of the period with high trigger rate.

the p-value or the KS probability which is used to tell whether the two distributions are similar or not. So, the KS test compares a 1-dimensional empirical distribution with the cumulative distribution of a reference set and assigns a distance between them called the KS statistic, see Figure (7.4). Under the null hypothesis, both sets are derived from the same parent distribution.

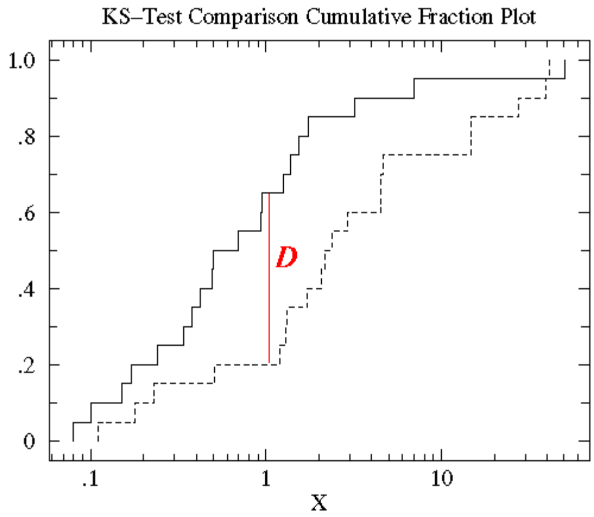

Figure 7.4: Illustration of the comparison of two different data sets, whose the cumulative distribution functions are shown, using the KS test. The test statistics D (red line) is the maximum deviation (distance) between the the two data set. Figure taken from [401].

For the c58 analysis, the KS tests were performed for every data series in a run against a carefully selected golden set of about 30 data series (of the same run) called the template with average livetime [402, 403, 404, 405]. The KS test is usually performed separately for calibration data series and for WIMP-search data using variables such as ionization yield, primary rise-time, primary fall-time, delay radius, partition radius, charge partition distribution and the charge chi-squared representing the goodness-of-fit parameter for the charge optimal filter. For each data series, the 30 data series in the template, the KS statistic values were averaged for each of the seven relative reduced quantities (RRQs) and then assembled into distributions. Data series that had average KS statistic values below 2σ of the mean KS value for any of the tested RRQs was removed by cuts cBadDet_bg_c58 for WIMP-search data and cBadDet_ba_c58 for 133Ba data.

7.3.3 Helium films on the detectors

During the c58 analysis, many detectors exhibited a large increase in trigger rate, especially during the runs R125 and R127 for the following periods of time: December 2007 - January 2008 for R125 and July 2008 - August 2008 for Run 127. The increased trigger rate was caused by events showing only a phonon signal but without the ionization signal. It was believed that this event pathology was caused by the settlement of helium films creeping on to the detectors. If a helium atom hits a detector, a phonon signal is released but no ionization signal, since the helium nucleus does not penetrate deep into the crystal, therefore result to a high rate of events with no or extremely low ionization yield value (<0.1). One sign of these helium films is the increased temperature following the shutdown of the cryocooler. Helium frozen in the E-box can migrate into the icebox and to the detectors.

The high trigger rates caused by the Helium films prevented us from taking good WIMP search data for certain runs as we have learned from the previous high trigger rate analysis. In order to restore a stable WIMP search operation, the phonon triggers of affected detectors had been turned off (using the cut cTrigBurst_c58 cut) for any WIMP search analysis.

To remove the data affected by the Helium films, Mark Kos conducted an analysis study where he flagged out all events with excessive low charge yield [406] . For each of the runs before and after the the Helium film onset the rate of events with yield < 0.1 was determined. A flat line was fitted to the low-yield rate before the onset of He films. Figure (7.5) shows the event rate for yield < 0.1 for runs before and after the He film onset. The red line is 10σ cut above the straight line fit.

7.3.4 Neutralization

In order to maintain good ionization-yield discrimination in the CDMS WIMP-search detectors, charge trapping, which leads to incomplete ionization collection, must be minimized. To reduce bulk trapping by defects and lattice impurities, detectors routinely undergo neutralization, a process during which the detector is grounded and bombarded with energetic particles (process we call baking or flashing when used for short periods of time), see Figure(7.6). These particles create electron-hole pairs in the crystal which diffuse to neutralize ionized

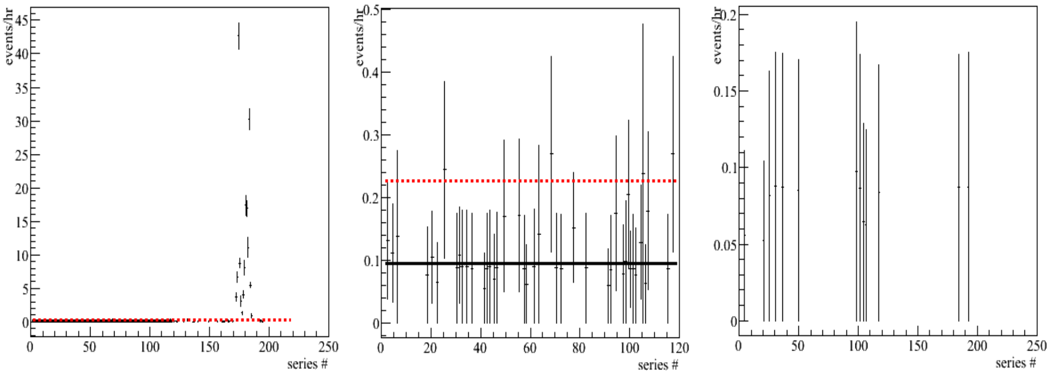

Figure 7.5: Left: the rate of events with yield < 0.1 for runs before and after the He film onset for R125. The plot to the middle shows a zoom in of the fit region, and the right plot shows the event rates with a charge threshold cut applied. Figure courtesy Mar Kos [406].

impurities by releasing trapped charged particles (electrons and holes) by recombination. Neutralizing ionized impurities causes these sites to have a smaller trapping cross-section than if they were charged, therefore reducing bulk trapping in the detector.

There are several methods for generating the energetic particles used to bombard the detector crystals during neutralization. These techniques include the use of LED photons, radiation from radioactive sources, and ambient background radiation. Each of these methods is particularly well suited for certain circumstances and each has its own set of variables to take into consideration. Depending on the testing location, a combination of LED and source neutralization techniques should be used together. A complete and detailed study of neutralization can be found in the doctorate dissertation of Cathy N. Bailey [407], its architect.

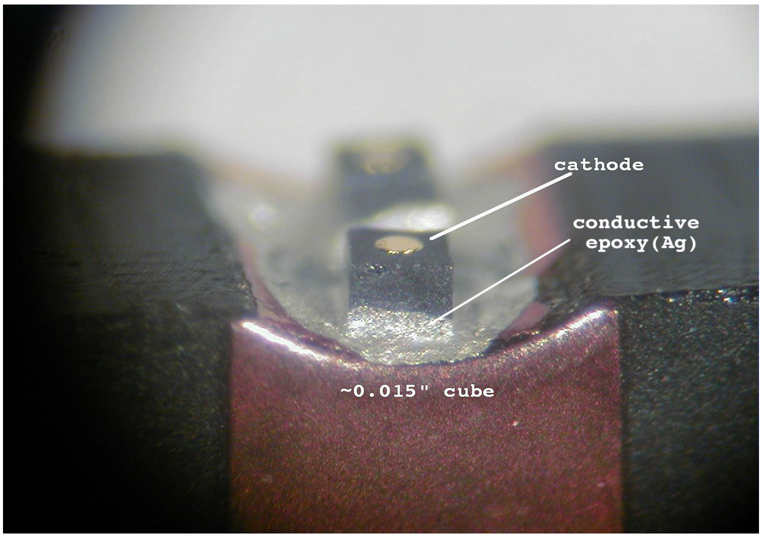

Figure 7.6: Photo of LED mounted in CDMS ZIP detector housing. Figure from [407].

To maintain detector neutralization over long periods of time during WIMP search running there were two LED flashes each day (for more than 30 minutes after every barium calibration data set). One of these LED flashes occurred automatically during the daily cryogen transfers and the other occurred after approximately 11 hours of data taking. The neutralization state of the detectors is monitored off-line for ^{133}Ba calibration and WIMP search data. Any period of time showing a loss in neutralization is in general excluded from the analysis.

The the state of neutralization in the barium calibration data is evaluated by grouping the data series into chunks with 105 events. The fraction of low yield events ($0 <$ yield < 0.8) passing basic quality cuts and their standard deviations based on the confidence intervals from a binomial distribution were calculated for each chunk and for the whole series. The means of the fraction of low yield events over each run and series were calculated under the assumption that the fractions of low yield events follow a normal distribution. For each chunk, the Poisson probability of observing as many low yield events or more in a particular chunk given the mean low yield event fraction was calculated according to the statistical formula below

$$Q = 1 - \sum_{k=0}^{k_{obs}-1} \frac{N^k}{k!} e^{-N}. \tag{7.1}$$

k_{obs} is the number of low yield events in a given chunk and N is the expected number of low yield events given the mean fraction of low yield events over each run. Any series or chunk with a Poisson probability criteria ($Q < 10^{-10}$) or chunks of data with loss of neutralization greater than 2σ above the run mean were rejected, with σ defined by:

$$\sigma = \sqrt{\frac{n}{\sum_{i=1}^{n} \frac{1}{\sigma_i^2}}}, \tag{7.2}$$

where σ_i is the standard deviation of the i^{th} series while n is the number of series.

For the WIMP search data however, due to the lower statistics, it was not possible to subdivide the data series into chunks. For this reason, we monitored the neutralization state within a series. In addition to the two conditions used to reject data series (or even a chunk) with low charge yield in the Ba calibration, for the WIMP-search data, however, another criterion was added. If the low-yield fraction was an outlier located 5σ away from the average standard deviation from all data series, the chunk or the suspected series was removed [408, 409, 410].

7.3.5 Neutron activation

When the ZIP detectors are exposed to neutron calibrations, the copper (precisely ^{64}Cu) from the detector supporting structure is activated. The weak interaction, more precisely the beta decay, is the physical process through which the decay occurs (β^+ and β^-). Betas are not penetrating and since copper possesses a small solid angle to the detector faces, there is no increased surface event rate after neutron calibration. Nonetheless, the gamma rates normally increase by a factor of 6 after the calibrations, potentially increasing ambient gamma induced surface-events during this activated period of time. The bottom panel of Figure (7.8) shows the gamma rate since the last time of the neutron calibration. The data is fitted with decaying exponential plus a constant.

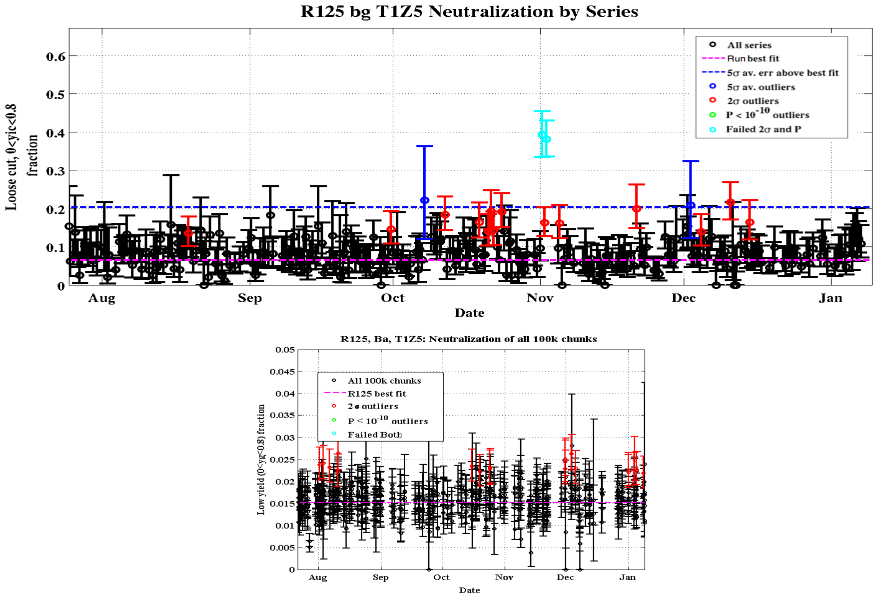

Figure 7.7: Low-yield fraction vs. time for WIMP-search data in T1Z5 for the WIMP-search data (top) and Barium calibration data (bottom) in Run 125. Data series passing cBadNeut_bg_c58 are marked with black points. Data series 2σ above the run mean are marked with red points and are removed. Series that fail the probability condition and the 2σ condition are marked with cyan points and are also removed. The 5σ run-averaged outlier level is marked with a blue dashed line and all series with low-yield fraction above this are removed as well. Figure taken and adapted from [408, 409].

The decay times constant correspond to the ^{64}Cu half-life, thus indicating that the dominant contribution to the increased rate after neutron calibrations is caused by ^{64}Cu. To ensure that no significant contribution from gamma due to the activation is included in the final data set, all data taken within two days after a neutron calibration are not considered in the analysis. It is also worth mentioning that neutron capture on ^{70}Ge produces ^{71}Ge during the neutron calibrations which undergo an internal conversion and produce 1.36 keV X-rays and an Auger-electrons causing 10.36 keV electron recoil events. These lines can be used for detectors energy calibration at low energies, see the two top plots of Figure (7.8).

7.3.6 Disabled triggers

During the runs R125 to R128, some detectors had their Plow triggers inadvertently disabled mostly in run 127. The trigger efficiency as function of energy and as function of time has been re-calculated by taking into account the fact that the plow triggers were disabled in some detectors in this run. A cut, name cPlo_Disabled_c58 were created to remove events recorded in detectors without a plow trigger in R127. A total of 24 series in this run were identified with no plow trigger in one or more detectors, they were removed based on the rate since the rate will drop to zero for detectors which do not trigger [420].

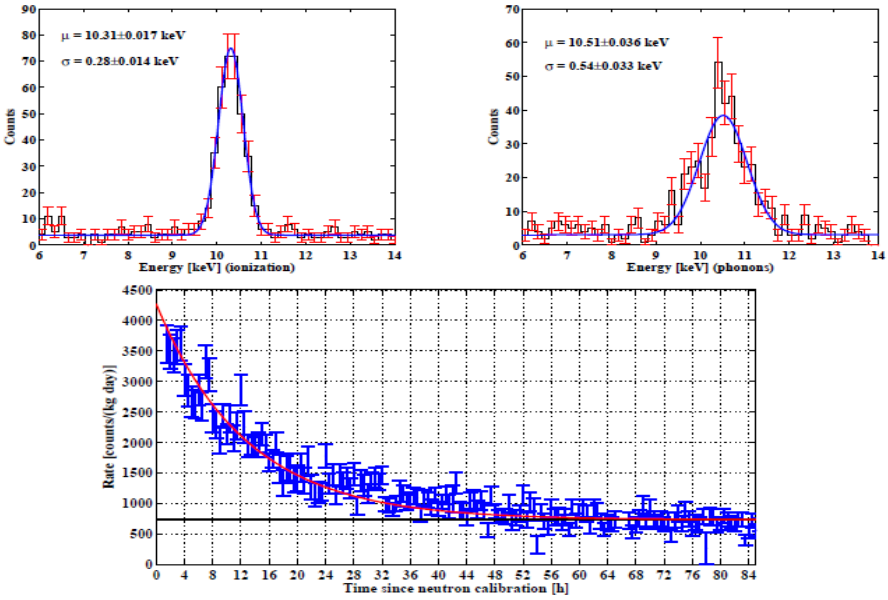

Figure 7.8: Resolution of the 10.36 keV line from ^{71}Ge for the inner ionization electrode signal (top left) and the phonon signal (top right) overlaid with the fit (blue) consisting of the Gaussian with constant background added to it. In the bottom is shown the background rate as function of time since the last neutron calibration (for an energy range from 15 to 200 keV) fitted with an exponential decay component plus a constant (black) and the sum of the two components is shown in red ($\tau = 12.7\,h$, corresponding ^{64}Cu half-life). Figure taken and adapted from [317].

7.4 Bad detector regions

Individual phonon channels in some detectors were malfunctioning or had broken sensors. This pathology was evident in the partition and delay plots.

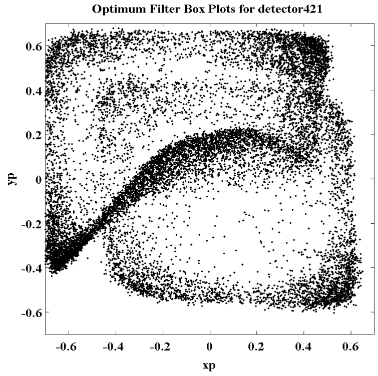

Figure 7.9: Malfunctioning phonon sensor, channel C, for T3Z1 (lazy channel). Figure courtesy Kevin McCarthy.

The ZIP detector T3Z1, for instance, does not have the box shaped plot as normally seen with other detectors. This is because the phonon channel C of this detector is malfunctioning (this phonon channel C is called lazy channel), see Figure (7.9). To remove the data from the malfunctioning channel, a cut called cBadDetRegion was

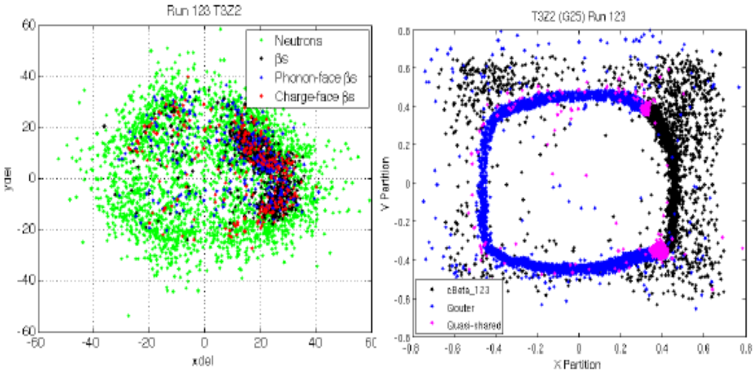

Figure 7.10: Shown in the left is the phonon delay plot for detector T3Z2 where green events are the and the black dots indicate the low yield surface events (phonon-side events in blue and charge-side events in red). Along the positive value of the x-delay, there is an excess in low yield events in the quadrant C and D. The plot in the right illustrates the detector's malfunctioning region causing the excess in low-events. Black indicates inner ionization electrode events, blue indicates outer ionization electrode events, and magenta indicates shared events. Figure taken from [317].

devised in order to ensure that data from the broken phonon channels are excluded. Another pathological issue which was also identified in R123/R124 was seen in T3Z2 which showed a localized anomalous behavior in the charge collection of the outer electrode, producing an excess of events at low ionization yield and slow phonon timing in quadrants C and D. The right graph in Figure (7.10) shows that this population is concentrated in the gap between the inner and the outer ionization electrodes. It is believed that the outer electrode was disconnected or other effects prevented the charge collection on the outer electrode in this region although the malfunctioning charge collection in this particular detector region is not fully understood. To exclude any affected event from the analysis in this detector region, only events with $xdel < 0$ are considered in the analysis, reducing thus this detector's exposure by half.

7.5 Reconstruction Quality Cuts

The reconstruction quality cuts remove events with specific reconstruction pathologies or misfitted traces since such traces may produce faulty energy and timing information which are crucial for the WIMP-search analysis. Some of these cuts are discussed in the rest of this section of this chapter.

7.5.1 Charge χ^2

The quality of charge optimal filter the ionization-pulse reconstruction,is assessed by the use a χ^2 that is calculated on an event-by-event basis. All abnormal events with high χ^2 value are rejected. The upgraded software used to reprocess the c58 data used a charge optimal filter which chooses the delay based on the minimum of the χ^2 instead of the maximum of the summed amplitudes [411].

The χ^2 goodness of fit is used for rejecting events mainly arising due to pile-up of multiple events within a single trace or electronic glitches in the ionization channel with a trigger time sufficiently close (the occurrence of more than one particle hit in a single trace length of $\sim 1640\,\mu$s). This kind of trace cannot be used to correctly estimate energy or timing. Pileups have large optimal filter χ^2 values and can be removed by setting a cut on this parameter, as a function of energy. Although pileups events are very rare at the low trigger rates required for WIMP search data, they are very common in calibration data. The reconstruction of such distorted pulses usually yields faulty results and therefore must be removed from consideration as WIMP candidates and in calibration data for detector characterization.

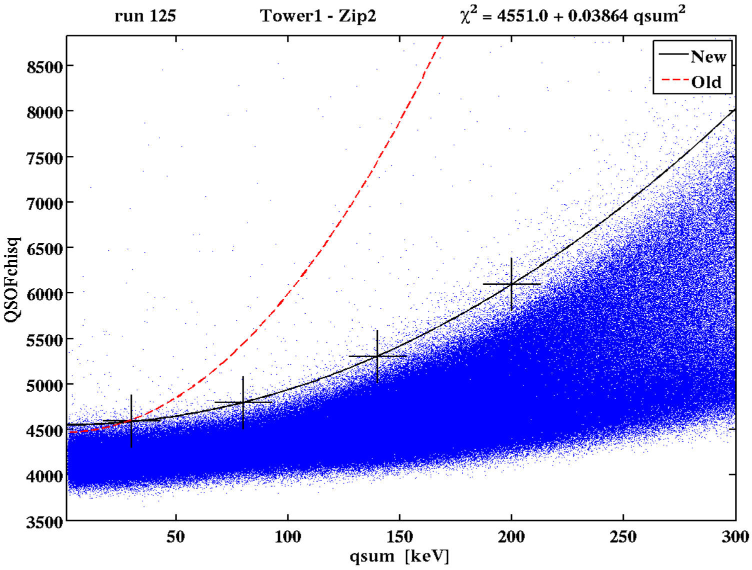

Figure 7.11: The reprocessed ionization charge χ^2 (blue dots) as function of the total charge energy Q_{sum}. The red and the black curves indicate the χ^2 cut cChiSq_c58 before and after the reprocessing. Figure courtesy of Jianjie Zhang.

To define the χ^2 cut cChiSq_c58, for each detector in each run, the χ^2 distributions were binned into four energy intervals as shown in Figure(7.11), the fitted to Gaussians. The 3.5σ deviations from each mean χ^2 value from each of the bins were fit to a quadratic function to provide the energy-dependent cut [412]

$$\chi^2 = A_1 + A_2 \cdot \mathrm{qsum}^2. \tag{7.3}$$

Figure (7.11) shows the χ^2 distribution as a function of the total charge energy qsum. The new χ^2, obtained as a result of the improved reprocessing charge software is shown in black while the old χ^2 is shown in red. Given the position of the cut lines (red and black), one can see that the distribution of the χ^2 QSOFchisq was broader because of the change in the charge optimal filter. The less broad distribution of this χ^2 in much wider energy range is indicative of better reconstructed ionization charge traces.

The distribution of QSOFchisq at lower energy bins is close to Gaussian and identical to the old one. At higher energies, however, QSOFchisq distributions have slower decaying tails at high values of QSOFchisq than a Gaussian distribution, making its distribution to broaden.

7.5.2 Phonon and Charge pre-pulse baseline

I have describe in section (7.5.1) that pileup events are rejected using the χ^2 cut (cChiSq_c58R). Another safety precaution to protect our WIMP-search data sample from pileup events is to cut on the standard deviation of pre-pulse baseline of the phonon traces. This helps to identify traces that may contain residual long phonon tails of events preceding the global trigger. This category of traces need to be discarded before we attempt to determine the energy and timing information. The cut cPstd_c58 rejects phonon-tail pileup events. This cut is engineered by fitting a gaussian to the distribution of the standard deviation of the first 400 μs (stored as RQ PAstd, PBstd, PCstd and PDstd) of all traces of a data series and then rejecting 5σ outliers on a series-by-series basis [415, 416].

The charge pre-pulse baseline cut, cQstd_c58, is implemented in a similar manner as the phonon pre-pulse baseline cut. The purpose of this cut is to reject events with high noise caused by microphonic pickup from cryocooler mechanical vibrations. The cQstd_c58, similar to cPstd_c58, is defined by fitting to gaussians the distribution of QAstd, QBstd, QCstd and QDstd to a gaussian. For the charge pre-pulse baseline for all traces of a data series, a 4σ outlier cut is chosen to remove noise data on a series-by- series basis, QXstd $> 4\sigma$ (with X=$\{i\,,o\}$) are [157, 158].

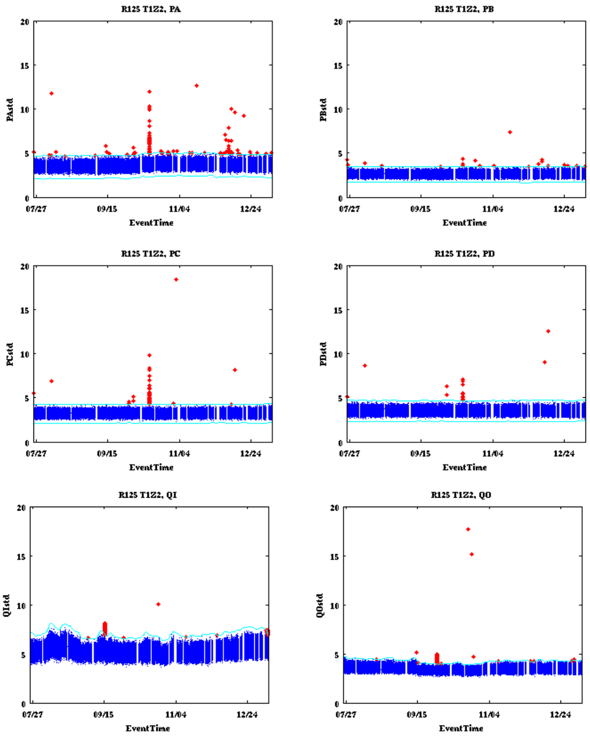

Figure 7.12: Phonon pre-pulse (two top plot) cut cPstd_c58 and charge pre-pulse (bottom) baseline cut cQstd_c58. Shown in blue are the events which pass these cuts and in red, the events rejected by the phonon and charge pre-pulse baseline cuts. Figure taken from [415, 416].

7.5.3 Good phonon and charge start time

To reject pileup events, the CDMS analysis resorts to using the charge χ^2 and the pre-pulse baseline (for both phonon and charge) cuts: cChiSq_c58, cPstd_c58 and cQstd_c58. Another safety line to help rejecting such pathological events which, if not removed, are usually misreconstructed and lead to wrong energy and timing information, is to constrain the WIMP-search data sample to events for which the start time is within the optimal search window and this requirement is enforced by the use of the good pulse start time cut. The CDMS reprocessing package BATROOT only searches for the start time of a Ge ionization pulse within a window of [-50,+100] around the trigger time. The phonon pulse start time is searched in the interval of [-50,+10] μs around the trigger time, which occurs 512 bins ($\sim$400 μs) into the digitized trace. For the Si detectors however, due to the faster phonon response, the search windows are slightly modified to [-25,+10] (for the ionization pulse) and [-25,+100] μs (for the phonon pulse) respectively. If a pulse lies outside this window the optimal filter will select an incorrect start time within the window, resulting in anomalously low amplitudes. Widening this window would worsen the threshold energy, and pulses well outside the window may be truncated and thus not well-reconstructed. The good phonon start times cut, cGoodPStartTime, rejects cross-detector pileup by enforcing that the start time of the primary phonon pulse lies within the optimal filter window for the ionization channels, i.e. that PXr20 (X=$\{A, B, C, D\}$) start time be in the interval of [-50; +10] μs for Ge ([-25; +10] μs for Si).

As the collaboration has moved toward the SuperCDMS phase with detectors, about 2.54 times thicker than the CDMS ZIP detectors, it is worth bring the reader's attention that for such thicker detectors, the optimal filter window, as mentioned in this section here, will no longer be valid. During the run R130, I conducted a study investigating the optimal filter window for the mercedes detectors (mZIPs) which are as thick as the currently deployed CDMS detectors at Soudan, the iZIPs. This study revealed that the phonon optimal filter window needed to be widened for these tick detectors, and that the proposed new optimal filter window was [-80; +10] μs [419]. At the time of the writing of this dissertation, this change has already been implemented with the data acquired using the interdigitated detectors (iZIPs).

7.5.4 Charge Threshold and charge time stability

The charge threshold cut is designed to reject events that are consistent with noise. In order to define the charge threshold cut, we select all the noise blobs (randoms) and plot them in the (qi, q0) plane. In the c58 original analysis and in prior CDMS analyzes, the histograms of the distribution of these noise blobs in terms or qi and qo were uni-modal (one peak) and could then be fitted to a single gaussian function. However, for the c58 reanalysis data, with the implementation of the full chi-square in the optimum filter [411], the noise blobs are now rather bimodal, Figure(7.13).

The noise distributions in the inner charge electrode vs outer charge electrode is shown in Figure (7.14). The noise blob charge energies are circularly distributed around zero (since they are just random noise) and have the form of donut that we commonly call noise donuts.

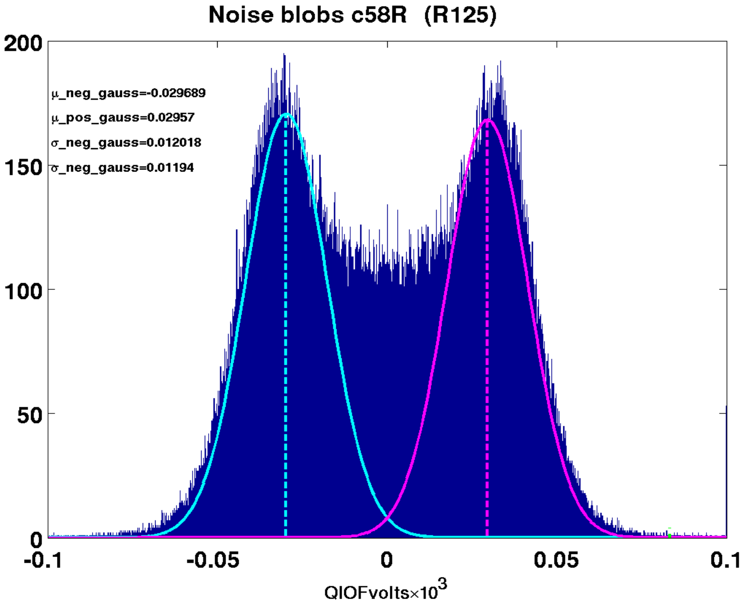

Figure 7.13: Histogram of the charge energy QIOFvolts. The bimodality nature of this distribution is particular to c58 reanalysis data due to the implementation of the full χ^2 in the charge optimal filter.

To define the charge threshold, the noise donuts have been examined series by series. We calculate the series-independent detector thresholds, by fitting the rightmost peak of the inner charge distribution to a partial-Gaussian and set the threshold $4.5\,\sigma$ beyond the mean of the peak. The efficiency of the charge threshold (cQThresh_c58R) and the effect of the effect of the cut on the data are shown in Figure(7.15)

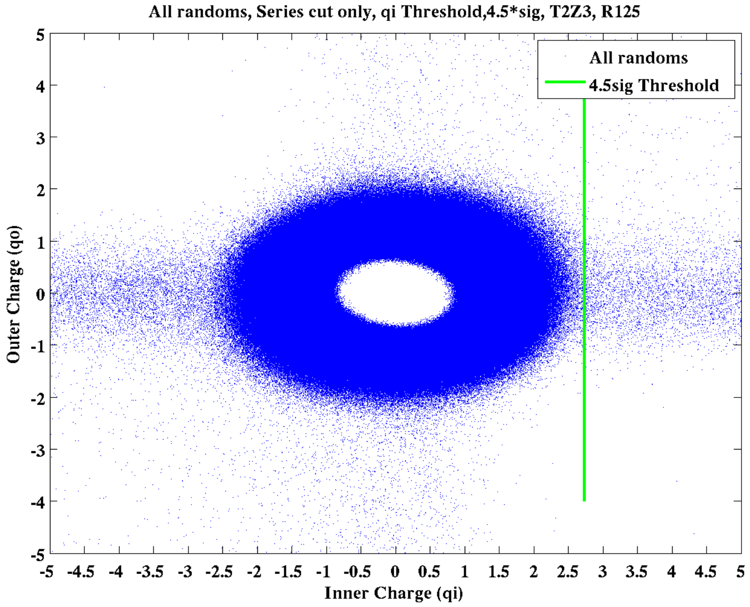

Figure 7.14: Distribution of the noise donut in q-outer vs q-inner. The green vertical line shows the cut (threshold) position which is situated at $4.5\,\sigma$ away from the mean of the q-inner distribution. Figure courtesy of Danielle Speller.

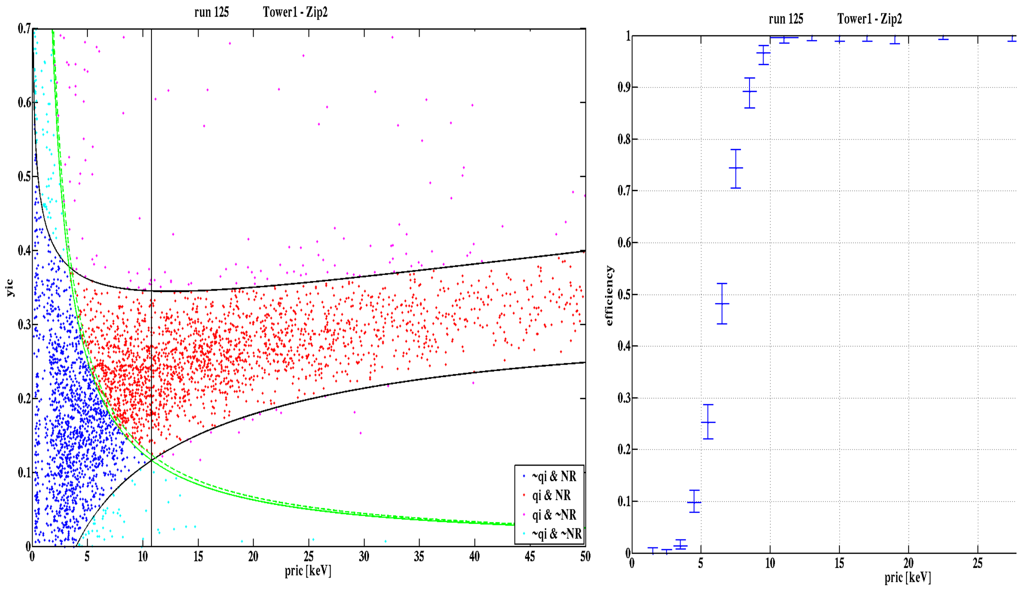

Figure 7.15: Charge threshold effect on the data in the yield vs energy plane (left). Blue events represents the californium (neutron) data satisfying the basic data-quality cuts, but failing the charge-threshold cut (green curve). The red events represents the events passing the data quality-cuts and the charge threshold cut (cQThresh_c58R). The black curves represents the nuclear recoil band and the vertical line is the phonon energy threshold. On the right is the cQThresh_c58R efficiency calculated using the neutron calibration data. Figure courtesy of Danielle Speller.

In addition to the cQThresh_c58R cut efficiency, the noise variations during the course of the runs were also investigated as shown in Figure(7.16). For this purpose, the mean and the standard deviation of the charge noise (the most right peak) for every series independently were calculated. Series removed by cBadDet_Ba_c58 (the KS test) or cStabTuning_c58 (series with stable tunings) are marked with magenta dots. In order to account for noise fluctuations a run-dependent threshold cut was defined in addition to the run-independent cut, the cQThresh_c58R cut. This new cut was also set at 4.5σ above the mean of each noise blob and is computed for every detector and every series independently. The maximum of both thresholds was choosen to set the final cut.

7.6 Event-selection cuts

WIMP-search analysis requires that any WIMP-event satisfies certain event selection based on the event properties and run conditions in order to minimize the expected background in the signal region. These-event selection cuts are discussed below in this section.

7.6.1 Q-inner cut

Events near the outer side wall of the detector suffer from incomplete charge collection due to distortions (fringing) of the electric field configuration. Such events have characteristically low charge yield which droops inside the

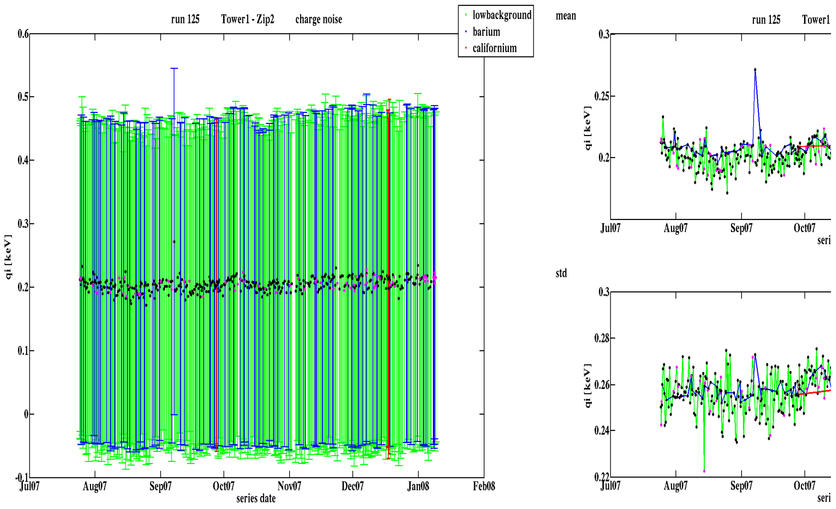

Figure 7.16: Time stability of the charge noise for the reanalysis c58 for both the the neutron and the barium calibration data. Figure courtesy of Danielle Speller.

region of interest and mimicking any event-like signal. To reject these events, the charge fiducial volume cut (cQin_c58) is created by requiring the candidate events to have energy in the outer-charge electrode of each detector consistent with $\pm 2\sigma$ of the series-specific noise for the electrode [166].

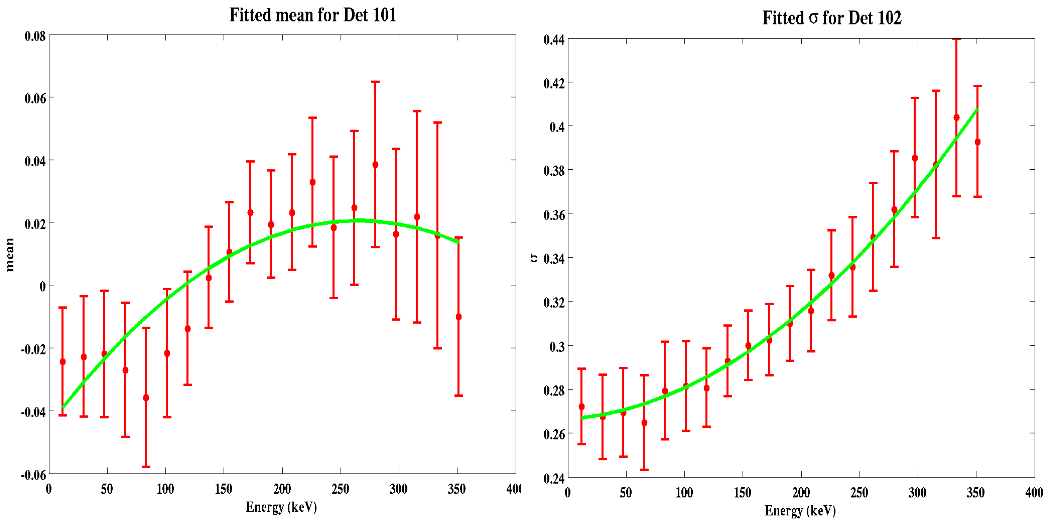

Figure 7.17: Outer ionization electrode (qo) mean and sigma as function of the inner ionization energy (qi). The data shown in red is fitted by a polynomial function. Figure courtesy of Jianjie Zhang.

The outer-charge electrode energy is binned by inner charge energy and fitted to a Gaussian for each of the bins to determine the bin-wise mean and standard deviation. The outer-charge noise band is defined by fitting polynomials to the bin-wise mean and standard deviation. During the c58 analysis, the means of the distributions are fitted to a first order polynomial and the widths to a second order polynomial to define the cut as a function of the inner-electrode ionization signal. Any event that lies $> 2\sigma$ away from the mean is rejected in the analysis as shown in Figure (7.18). However, during the c58 reanalysis, it was observed that both the means and sigmas were fit to a polynomial functional form which fitted the data better.

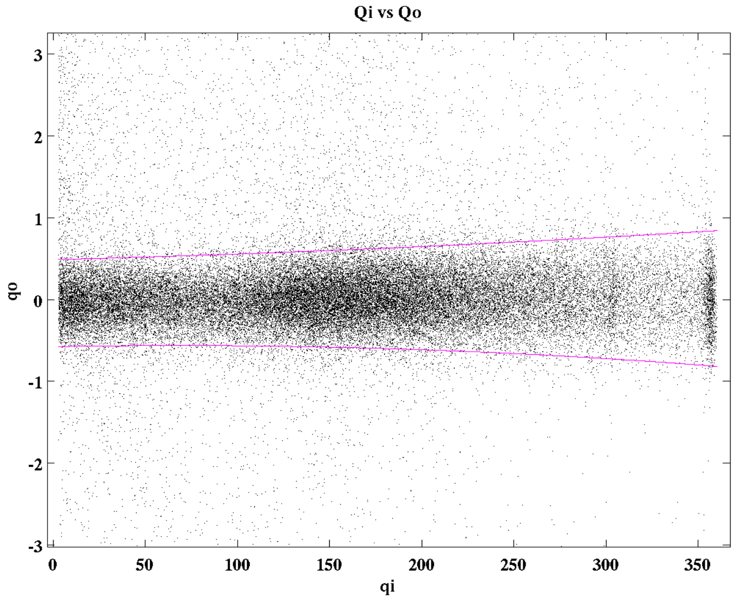

Figure 7.18: Charge-outer energy (qo) as function of Inner-charge energy (qi). The black events represents the calibration data while the magenta lines are the $\pm 2\sigma$ from the q-outer fitted mean. Figure courtesy of Jianjie Zhang.

The efficiency of the fiducial volume cut (cQin_c58R) is calculated using the neutron calibration data by taking the ratio of the number of events passing the preselection cuts and the cQin_c58R to the number of events passing the preselection cuts without the cQin_c58R cut. Given that the inner electrode covers $\sim$ 85% of the detector's volume, the expected cQin_c58R cut efficiency should be around that number. It has been noticed, however, this approach underestimated the efficiency due to the contamination of the nuclear recoil band from the gamma leakage. A corrective approach, formulated by J. Sander and R. Mahapatra [413], was motivated for the following reasons: since we are interested in the passage fraction of nuclear recoils after applying the cQin_c58R fiducial volume cut given that the cut feeds into our overall WIMP search analysis efficiency and given that a simple measure of cQin_c58R efficiency is inaccurate because of contamination of the NR region with gamma leakage. Low-yield gammas in the Q-outer region bias the efficiency to be lower, and low-yield gammas in the Q-inner region bias it higher. Fortunately, one can make an estimate of gamma leakage and subtract it before calculating the efficiency [413]:

1. Define reasonable preselection cuts, and bin data by energy.
2. Define the electron recoil (ER) and nuclear recoil (NR) bands according to the fitted means and sigmas obtained from the calibration data.
3. for evey i ={ear, funnel, qpart>funnel}, see the right plot in Figure(7.19):

- Use the Ba calibration data to compute, bin-wise, the ratio of events in NR to number events between ER and NR.
- Use the neutron calibration data to count the number of {(events between ER and NR) - spill of neutrons above NR} and infer the low-yield count.
- Multiply the neutron low-yield count with the correction ratio to get gamma leakage in NR for each blob i.

4. compute the bin-wise efficiency as follow:

$$\text{Qin\_eff\_bin\_i} = \frac{\sum_i \{\text{cQin(events in NR} - \text{leakage)}\}}{\sum_i \{\text{events in NR} - \text{leakage}\}} \tag{7.4}$$

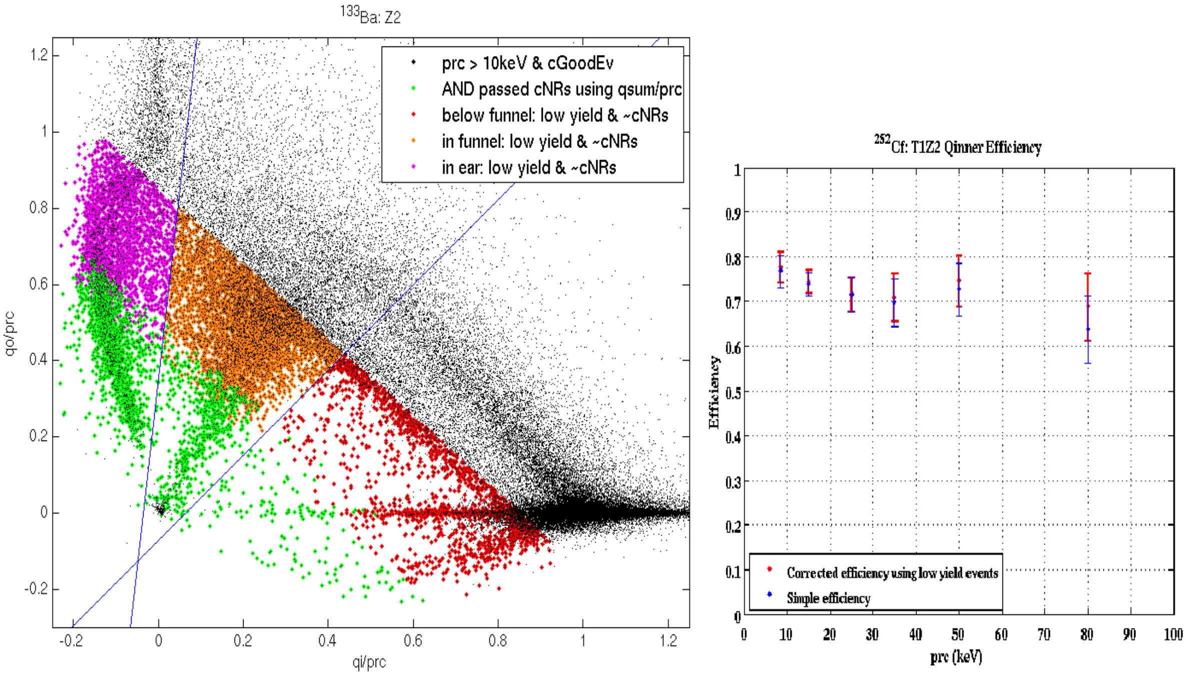

Figure 7.19: On the left is the funnel plot using the yield quantities yi (in the inner ionization ring) and yo (in the outer electrode). The black events represent all the data while the events in red, orange and magenta indicate the yield events in the outer electrode, the bulk and the outer electrode used to correct the cQinner efficiency. On the right is the efficiency of the cQinner cut calculated using the simple and the corrected methods. Figure from [414].

The right plot in Figure(7.19) compares the cQin_c58R cut efficiency as calculated using the simple method and the correction approach formulated in [413]. Ignoring the error bars indicating the uncertainties, the two methods give similar results at low energies. At high energy, there is a clear and distinct increase in efficiency (by 1% to 4% level bin-wise) with the corrected approach. Although the efficiency is not improved by a lot, this method gives an estimate for the cQin_c58R efficiency by removing (correcting by subtracting) for surface events leakage that pollutes the nuclear recoil band.

7.6.2 Singles cut

WIMPs are expected to interact only once in the entire experimental apparatus due to their small and vanishing interaction cross section. Radioactive particles, which make the majority of backgrounds, will typically scatter multiple times. Multiple interactions in different detectors can be used as an excellent way to reject background. Single-scatter events are classified as events that deposit energy above the threshold in only one detector, while the signal recorded in all other detectors is consistent with noise.

The singles cut (cSingle_c58R) is defined in the following way: for every data series, the threshold is determined using the optimal filter for the WIMP-search data and the calibration data. This optimal filter amplitude is determined for random trigger traces for all phonon and charge channels in order to define the noise distributions for every channel. These distributions are fit to Gaussians, and a mean and standard deviation of the noise distributions is then calculated for each channel of every ZIP detector for all data series in all four runs [417].

An event is selected as a single scatter in a detector if the phonon energy of that event is 6σ above the mean of the noise distribution for that detector and series, and the phonon energy in every other detector is within 4σ of the mean of its series-noise distribution. The efficiency of cSingle_c58R was $> 99\%$ for all detectors in all runs except few detectors, where the efficiencies hover around 98%. The efficiency is plotted as a function of data series in Figure(7.20) for detector T1Z2.

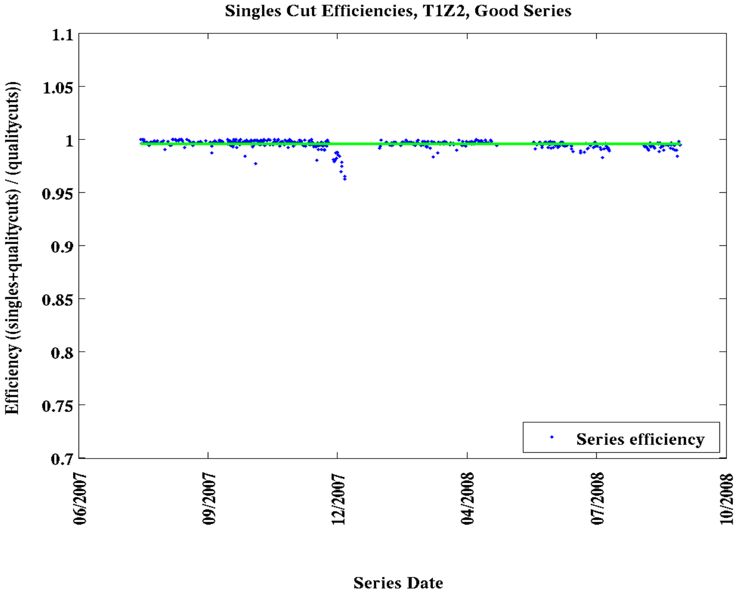

Figure 7.20: The efficiency of the cSingle_c58 as function of time for T1Z2 shown the four runs of the c58 analysis [417].

7.6.3 Veto-anticoincident events

The CDMS experimental setup is surrounded by a plastic scintillator veto whose primary purpose is to protect the experiment from muons that could produce neutrons whose signals are indistinguishable from WIMP interactions.

The veto cut cVTStrict_c58 selects detector events coincident with activity in any of the 40 scintillator panels of the surrounding muon veto counter. The events passing this cut are rejected from consideration as WIMP candidates. An average of one muon per minute is incident on the veto, while the mean veto rate is approximately ∼600 Hz. The primary obstacle to setting this cut is the high trigger rate in the veto counter from ambient gamma rays. The detectors are protected from these events by several layers of shielding and powerful discrimination, but these gammas would lead to a loss of $< 5\%$ in livetime if they were allowed to trigger the veto rejection cut. The amplitude trace of every panel is recorded for every event in a time window of [-180 +25] μs relative to the global trigger. This threshold is set high enough to exclude essentially all gamma events, generally between 30-50 pC [418]. The cut position for one panel is plotted in Figure (7.21), indicating a threshold near the upper edge of the gamma distribution but well below most muons and showers. Any events removed the veto cut must thus satisfy at least one of the two following two conditions:

- The photoelectron signal in at least one scintillator panel lies above a panel specific threshold within the recorded veto trace window.
- A discriminator threshold is exceeded at less than 50 μs before or during the event trigger

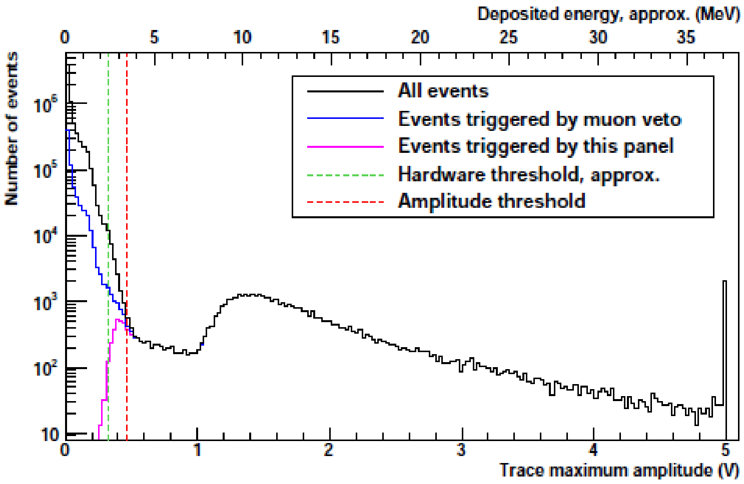

Figure 7.21: Histogram of maximum amplitude of veto traces from a top panel during runs c58. The green vertical dashed line indicates the hardware threshold, and the red vertical dashed line indicates the threshold. The characteristic 10 MeV muon bump is visible. Figure taken from [418].

In Figure (7.21), the bump between 1 & 2 volts is a peak is due to minimum ionizing muons. Muons tend to deposit ∼ 2 MeV per cm of material they pass through and the thickness of CDMS veto panels is 2" (5 cm). Therefore, minimum-ionizing muons will deposit total of ∼ 2 Mev/cm × 5 cm = 10 MeV. The broadness of the peak is primarily caused by variations in path length of the muons in the scintillator. If the muon is incident at a slight angle, it will traverse a greater distance inside the scintillator and thus deposit more energy. Also, the broadness of the peak tells you something about the angular distribution of muons underground (see, e.g., Bob Nelson's undergrad UCSB thesis, [423]). The long tail toward high energy is due to the less common creation of a delta ray (basically a high-energy electron) as the muon passes through the scintillator. The peak at ~ 5 volts is a saturation peak, in this case, it is a saturation of the veto digitizer. Sometimes a broader saturation peak can also be seen and doesn't cut off sharply, which is saturation of the veto amplifier. Below the muon bump, there is an exponential rise in rate due to environmental gammas (the thorium 2.6 MeV end point) starting roughly below the red dashed line (this is in fact the reason for the red dashed line). We normally don't want to veto ZIP events that show gamma-like energy in the veto because those gammas will not make it through the lead shield. Any events with energy greater than gamma energies, however, may be indicative of a muon passing through the shielding since muons can very easily get through the lead, therefore we want to veto such events. Finally, the region below 1 volt but above the red dashed line gets filled in by a combination of muons that clip the edges of the veto panels and by resolution smearing the gamma tail to higher energy [424].

7.7 Ionization Yield

The ZIP detectors have been designed in order to provide a discrimination between nuclear recoils and electron recoils. The discrimination parameter is a dimensionless quantity called **ionization yield** and is defined as the ratio of ionization to recoil energy.

$$y = \frac{E_Q}{E_R} \tag{7.5}$$

with E_Q the calibrated charge ionization energy and E_R, the event's recoil energy. The measured total phonon energy is a sum of the recoil energy (E_R) and the contribution by Neganov-Luke phonons (E_{Luke}); they are related to the recoil energy E_R by the relationship give by Equation (4.12). The phonon, due to Luke contribution is defined by $E_{Luke} = E_R + N_Q e \cdot V_b$ (N_Q is the number of electron-hole pairs created and V_b, the applied bias voltage). Given that $E_Q = \epsilon N_Q$, where $E_{Luke} = \frac{e \cdot V_b}{\epsilon} E_Q$, which remains true even when some charges are trapped before reaching the surface. This true with a single biased electrode. However, with two electrodes, as it is the case for the CDMS experiment, the Ramo potential and the physical potential are not the same. Moreover, if there is enough trapping to produce space charge, then the physical potential may deviate significantly from the Ramo potential. The total phonon energy is given by

$$pt = E_R + \frac{e \cdot V_b}{\epsilon} E_Q, \tag{7.6}$$

from which the recoil energy E_R can be inferred:

$$E_R = pt - \frac{e \cdot V_b}{\epsilon} E_Q. \tag{7.7}$$

Therefore the ionization yield y is

$$y = \frac{E_Q}{pt - \frac{e \cdot V_b}{\epsilon} E_Q}. \tag{7.8}$$

If the charge fiducial volume cut is defined and applied, then events passing the cut have outer-charge electrode signal consistent with noise. For such events, the phonon energy can be written as:

$$pri = pt - \frac{e \cdot V_b}{\epsilon} qi \tag{7.9}$$

with pri the phonon energy and qi is the charge energy in the q-inner electrode. For photons, ionization yield is normalized to 1 due to the definition of E_Q. We define a quantity called photon-equivalent recoil energy, prg, defined only using pt. This quantity has the advantage of being a less noisy estimator of recoil energy for photons than pr: $prg = pt - \frac{e \cdot V_b}{\epsilon} prg$, implying that

$$prg = \frac{pt}{1 + \frac{e \cdot V_b}{\epsilon}}. \tag{7.10}$$

Photon-equivalent yields can also be defined: $yg = \frac{qsum}{prg}$ and $ygi = \frac{qi}{prg}$. These photon-equivalent quantities are useful for phonon-pulse-shape correction, since they are not affected by charge noise. Nonetheless yg and ygi are affected by noise on ionization energies $qsum$ and qi.

Theoretically, nuclear-recoil ionization yield in semiconductors is well described by Lindhard theory [330, 331], in which a material's stopping power is understood in terms of velocity-dependent electronic and nuclear components. Low-velocity nuclear recoils deposit most of their energy through nuclear interactions, while high-velocity electron recoils prefer electronic interactions. Since ionization results from electronic excitations, the ionization yield for nuclear recoils (relative to electron recoils) is smaller. This, of course, is the basis of CDMS electron-recoil discrimination. Lewin and Smith have simplified Lindhard theory to the following set of equations [391]:

$$y(E_R) = \frac{\kappa g(\varepsilon_z)}{1 + \kappa g(\varepsilon_z)} \tag{7.11}$$

$$g(\varepsilon_z) = 3\varepsilon_z^{0.15} + 0.7\varepsilon_z^{0.6} + \varepsilon_z \tag{7.12}$$

$$\kappa = 0.133 Z^{2/3} A^{-1/2} \tag{7.13}$$

and

$$\varepsilon_z = 11.5 E_R Z^{-7/3} \tag{7.14}$$

where E_R is the recoil energy (in keV). A number of neutron-scattering experiments have attempted to test the recoil-energy dependence predicted by these equations. Figure (7.22) shows a compilation of measurements obtained with various Ge detectors compared to the Lindhard-theory prediction. The average ionization yield for a representative Ge ZIP (operated with a -3V bias) is shown as well. The comparison confirms that the ZIP-detector energy scale, as derived from electron recoils, is roughly appropriate for nuclear recoils. A more thorough inspection of the nuclear-recoil energy scale will be discussed in doctorate dissertation of Scott Fallows and this analysis is still on going.

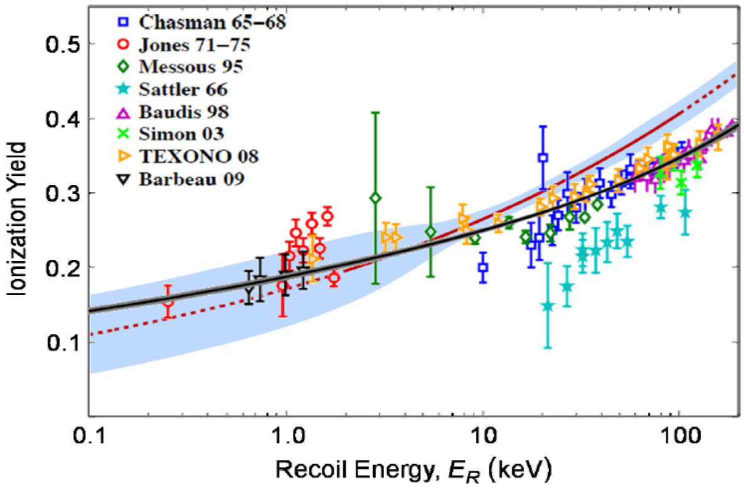

Figure 7.22: Compilation of ionization-yield measurements for neutrons scattering in Ge (data points with error bars) compared to Lindhard theory (black/solid line), and the average ionization yield as measured (between 2 and 100 keV) with a representative Ge ZIP (dark red/solid line). The latter is extrapolated below 2 keV and above 100 keV (dark red/dotted lines) via a power law such that y = 0 at 0 keV. Figure from [50].

The ionization yield is one of the main discriminators between electron and nuclear recoils provided by the ZIPs. To calibrate the ionization yield parameter and define the recoil type populations the ionization yield of electron recoils from ^{133}Ba calibration is calibrated to a value of 1; this is a normalization we impose on a true average for an electron-recoil event. The calibration based on electron recoil events sets the scale for the ionization yield of nuclear recoil (NR) and electron recoil (ER) bands.

7.7.1 Nuclear Recoil Band

The nuclear-recoil (NR) band is defined from ^{252}Cf calibration data as shown in Figure (7.23). As for the electron-recoil band a gaussian distribution function is fitted to the ionization yield distribution in several energy bins. Due to the approximately exponential energy spectrum of nuclear recoils from the calibration runs, logarithmically spaced energy bins are chosen. The functional form fitted to the means of the gaussian in the energy bins as a function of recoil energy is the same as used for the electron recoil band. However the functional form used for the standard deviations is defined differently:

$$\sigma_{ER}(E_R) = \begin{cases} \frac{\beta_1^2 \cdot E_R^{\beta_2} + \beta_3^2}{E_R} + \beta_4 E_R^{\beta_5} & \text{if } E_R \leq E_{cut} \\ \\ \frac{\beta_1^2 \cdot E_R^{\beta_2} + \beta_3^2}{E_R} + \beta_4 E_{cut}^{\beta_5} & \text{if } E_R > E_{cut} \end{cases} \tag{7.15}$$

where the cutoff energies E_{cut} was defined for each individual detector and it was found to be in the 20-40 keV range. The additional terms in the equation (7.15) were deemed necessary for the stability of the band at high energies

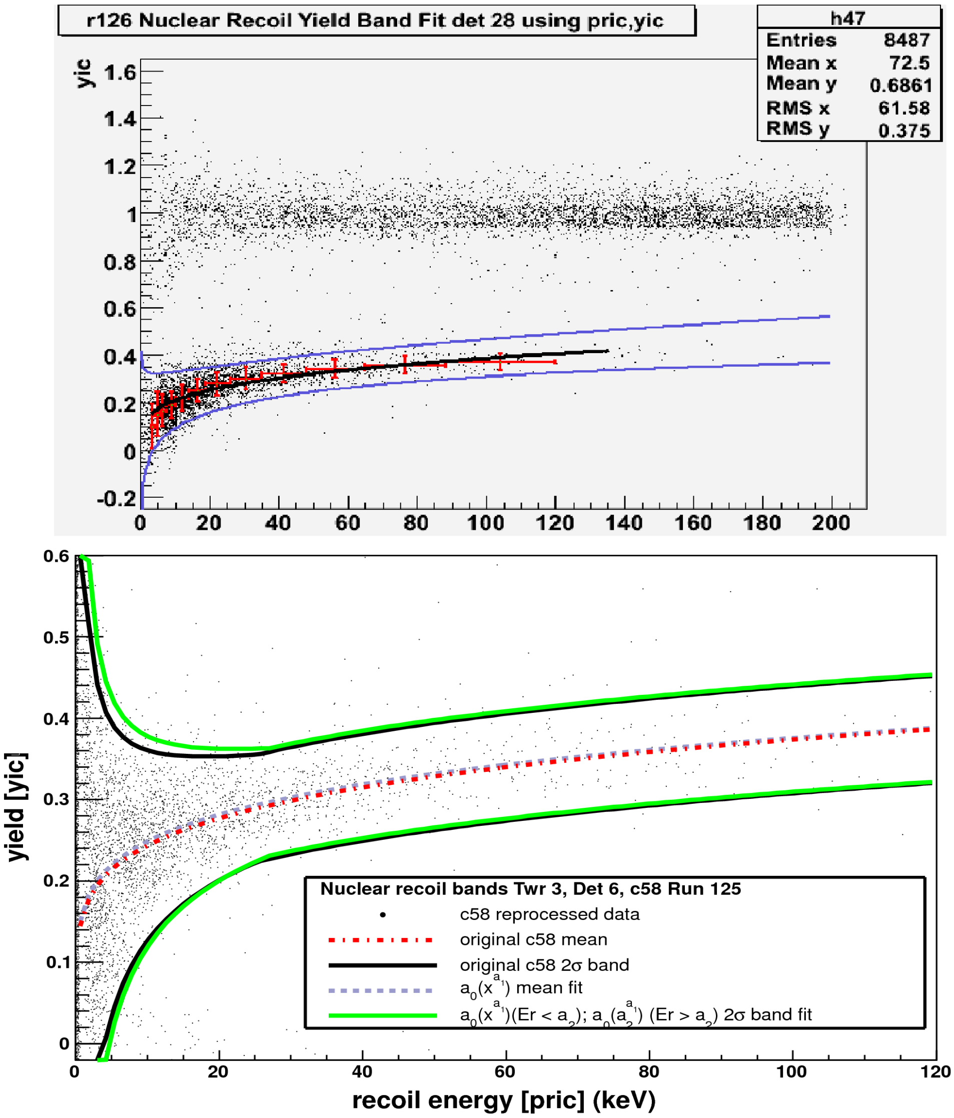

Figure 7.23: Nuclear Recoil (NR) band in the ionization yield vs recoil energy. Top: the centroid and the $\pm 2\sigma$ region of the band are shown by the red error bars data points (fitted with the black line) and the blue curves [392]. Bottom: comparison of the NR bands from the c58 analysis and c58 re-analysis [393].

7.7.2 Electron Recoil Band

The electron-recoil (ER or gamma) band is defined from ^{133}Ba calibrations. The electron-recoil distribution is defined by fitting gaussian distribution functions to the ionization yield distribution in several energy bins. The mean and the edges of the band are the fitted by functional forms that depend on the recoil energy (E_R). The fit is performed in the yic vs pric plane, where yic and pric are the ionization yield and phonon recoil energy subjected to the position correction. During the runs 125-128, the gamma bands were fitted with the following functional forms:

$$\mu_{ER}(E_R) = \alpha_1 \cdot E_R^{\alpha_2} \tag{7.16}$$

and

$$\sigma_{ER}(E_R) = \frac{\beta_1^2 \cdot E_R^{\beta_2} + \beta_3^2}{E_R} \tag{7.17}$$

The coefficients α_k and β_k are determined individually for each detector. Knowing the fitted mean $\mu_{ER}(E_R)$ and fitted sigma $\sigma_{ER}(E_R)$(or standard deviation), it becomes simple to define a selection of electron recoils events in the ionization yield vs. energy plane as shown in Figure (7.24). This $\pm 2\sigma$ region is what we referred to as the **electron-recoil band or simply ER band**. The electron-recoil band widens at lower recoil energies due to fluctuations in noise which become a large fraction of the recoil energy where it becomes small.

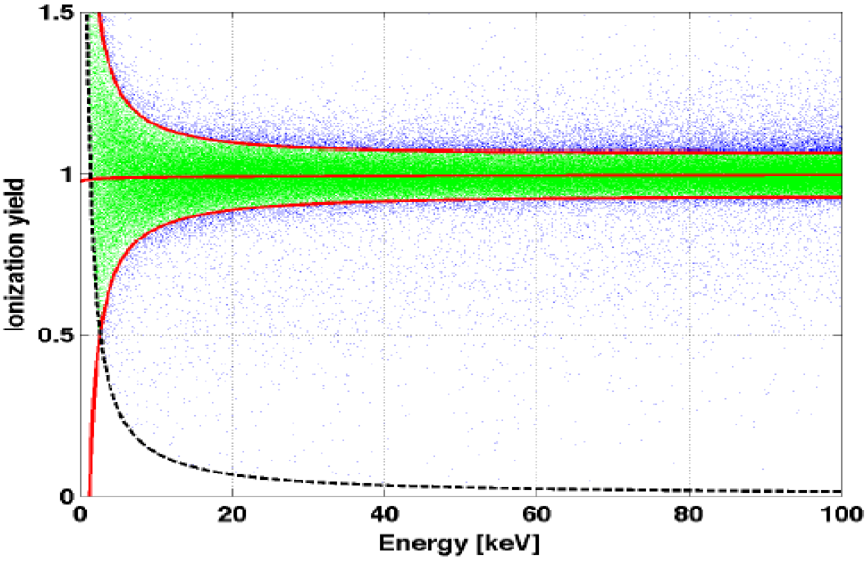

Figure 7.24: Electron- Recoil (ER) band in the ionization yield vs recoil energy. The centroid and the $\pm 2\sigma$ region of the electron-recoil distribution are shown by the red lines. Selected events are shown in green. The dashed black line shows the charge threshold from the ionization signal applied to the ^{133}Ba calibration data shown in the figure.

7.8 Limitation of yield-based discrimination

Figure(7.25) illustrates the illumination of one of the ZIP-detectors to the ^{133}Ba and ^{252}Cf radioactive calibration sources. The gamma band and nuclear recoil band are shown as well to demonstrate how gamma backgrounds can be mitigated from nuclear induced events by rejecting all events inside the ER band. However, outside the

ER band, there still is a lot of events from the ^{133}Ba with low yield, characteristics of nuclear recoil induced events, drooping inside the NR band and therefore mimicking the signal. These events are classified as surface events or beta events. We normally call surface events any low yield event from the ^{133}Ba located 5σ below the mean of the ER band. Surface-events are events with incomplete charge collection. Their occurs not too far from ZIPs detector's surfaces, a region called the dead layer ($\sim 10\,\mu m$ deep) [422].

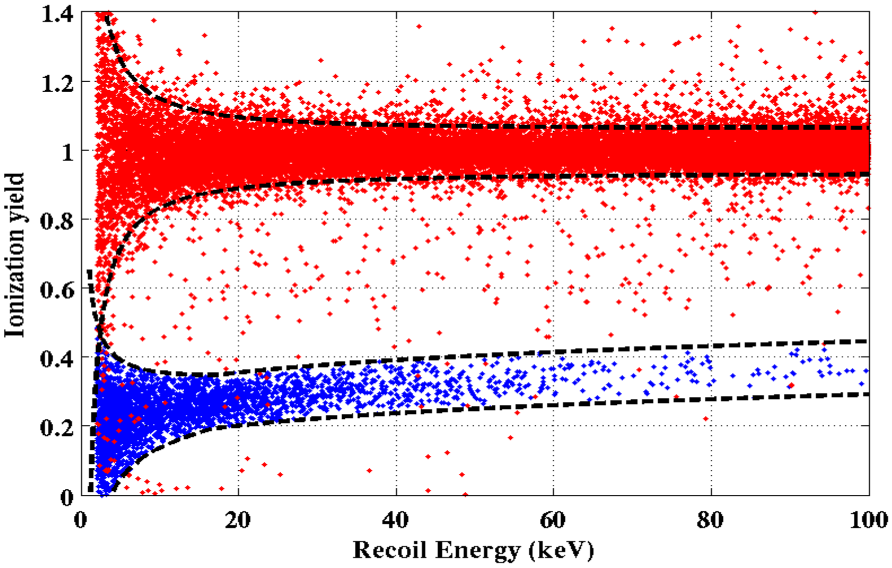

Figure 7.25: Nuclear Recoil (NR) band (blue) and Electron Recoil (ER) band (red). Notice other low yield events from the ^{133}Ba droops inside the NR band which cannot be rejected using the yield based rejection. This class of events are called surface events (or betas). To reject these events we resort to the phonon pulse shape discrimination based on the timing between these events and NR events.

Although the yield based rejection has demonstrated a discrimination level of $> 10^4 : 1$, drooping (low-yield) events cannot be rejected by the ionization yield based rejection. To reject surface-event leakage inside the NR band, we use phonon pulse-shape discrimination (PSD). The standard signal acceptance region in ionization yield is defined by the cut cNR_c58R as a $\pm 2\sigma$ band about the mean ionization yield as a function of recoil energy. This cut is slightly different for each of the runs because of the changes in phonon response and noise variation between all the four cryogenic runs.

As it will be shown and discussed in chapter 8, section (8.6.6), the traditional nuclear recoil band definition of $\pm 2\sigma$ is not quite optimal. A simultaneous optimization aimed at determining the optimal timing cut positions for surface-events rejection and an optimized nuclear recoil band was performed. The optimized nuclear recoil band which maximize the the experiment's expected sensitivity was found to be $[-1.9\,,+1.8]\sigma$ [444]. This is the nuclear recoil cut that was used in the final analysis for the WIMP-search data discussed in chapter 8.

7.9 Phonon Timing

The sensitivity of a ZIP detector to athermal phonons produced by an interaction provides for background rejection using phonon pulse-shape information. The timing from the phonon pulse is intrinsically different for surface events than for nuclear-recoil events. Surface events are normally faster than the bulk nuclear recoils due to their quick down-conversion from the edge effect catalyzed by the Al fin collector coating the surface of the ZIP-detector. As soon as the primary phonon are down-converted, they become ballistic phonons and they propagate at the speeds of sound in the crystal. Since down-conversion for surface events occur much earlier for surface-events than for bulk nuclear recoils, phonons from surface events tend to arrive at the TESs earlier than the phonons from the bulk NR events [319]. Using the phonon pulse shape to reject surface-electron recoils is especially significant, since these events can have reduced ionization collection, leading to misidentification if using the ionization yield alone as discriminator. In this section, the surface event will be introduced and a simple timing cut will be used as an illustration. Although the timing cut is introduced and discussed here, a more sophisticated and optimized timing cut that I have developed during the reanalysis will be the central topic of the next chapter.

Phonon-pulse-shape characteristics help distinguish background surface events from nuclear-recoil signal. Figures of merit for characterizing the pulse shape are constructed during the processing. Phonon pulses are first low-pass filtered using a 50 kHz Butterworth filter [427]. Filters are electronics designed to let pass or suppress (attenuate) signals for certain range of frequencies. There exist various different kind of filter, the most well know are: low passes which passes only low-frequency signals below a certain frequency cutoff called the -3dB frequency; a low-pass filter attenuates (reduces the amplitude of) signals with frequencies higher than the cutoff frequency. The attenuation factor for each frequency varies from filter to filter. Another type of filter is a high-pass filter which is the opposite of a low-pass filter, i.e. it accepts frequency above the cutoff frequency and attenuates signals below the cutoff frequency. A band-pass filter is another type of filter. This filter is a combination of a low-pass and a high-pass. Low-pass filters exist in many different forms. The Butterworth filter is a type of signal processing filter designed to have as flat a frequency response as possible in the passband. It is also referred to as a maximally flat magnitude filter [428]. The gain $G(\omega)$ of an n-order Butterworth low pass filter is given in terms of the transfer function $H(s)$ as

$$G(\omega) = |H(j\omega)|^2 = \frac{G_0^2}{1 + (\frac{\omega}{\omega_c})^{2n}}, \tag{7.18}$$

where n =is the order of filter, ω_c is the cutoff frequency (or the -3dB frequency). G_0 is the DC gain (gain at zero frequency). It can be noticed that as n approaches infinity, the gain becomes a rectangle function and frequencies below ω_c will be passed with gain G_0, while frequencies above ω_c will be suppressed. For smaller values of n, the cutoff will be less sharp.

During the data processing, an an algorithm called the RTFT (Rise Time and Fall Time) walk algorithm walks down the rising edge of the filtered pulse, and records the time corresponding to the first-crossing point in pulse amplitude at some fraction of the pulse height, such as 10%, 20%, 40% and 70% [319]; these quantities are used to create the phonon risetimes. The primary phonon risetime is defined as the time difference between the 40% and the 10% times measured along the slope of the rising edge of the phonon pulse. Similarly, the same algorithm is applied on the falling edge of the pulse to provide the falltimes, but falltimes do not provide surface event discrimination in ZIP detectors and we don't use them for surface events rejection in the main analysis. The risetimes can be compared with the charge-signal start time, from the ionization optimal filter, to provide a phonon-pulse arrival delay.

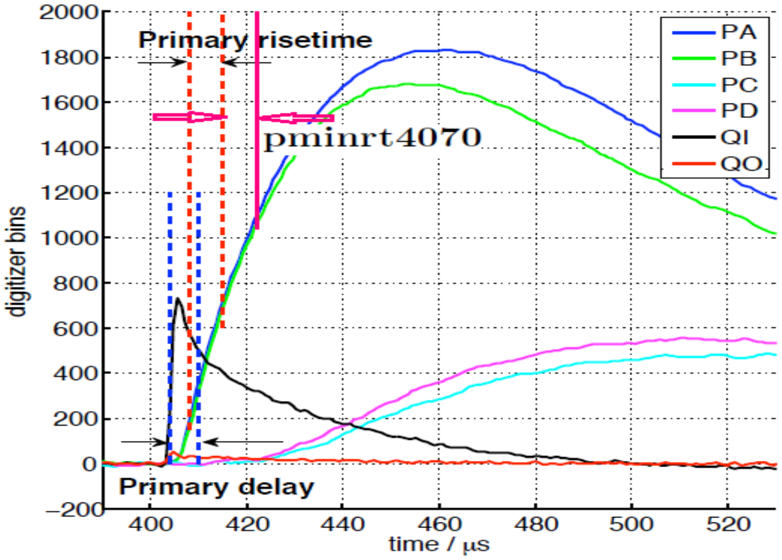

Figure 7.26: Traces from a high-energy event for all four phonon channels and the two charge channels are shown as a function of time. The primary channel A and its 10%-40% risetime is the primary phonon risetime (dashed vertical red lines) and the difference of its 20% risetime and the charge-pulse start time t_0 is the primary phonon delay (dashed vertical blue lines). Figure adapted from [315].

Risetimes and delays are constructed for the primary channel (phonon quadrant with maximum pulse height). These quantities are defined as follows [as shown in Figure (7.27)]:

- **Primary Phonon Risetime**: The phonon risetime is defined as the difference between the 40% and 10% risetimes of the primary phonon pulse, and it is denoted as **pminrt** within the CDMS analysis reduced quantities (RQs). The primary risetime (**pminrt**) is a powerful discriminator between surface events and nuclear recoils.
- **Primary Phonon Delay**: The phonon delay is defined as the difference between the charge signal start time t_0 (computed by the charge optimal filtering) and the 20% risetime of the primary phonon pulse. Denoted by **pdel**, the primary phonon delay is also a powerful discriminator against surface events in WIMP-search running.

The phonon pulses from the four quadrants of every ZIP detector are different for background and signal-like events. The most difficult class of background in our experiment is surface events that result in low charge yield

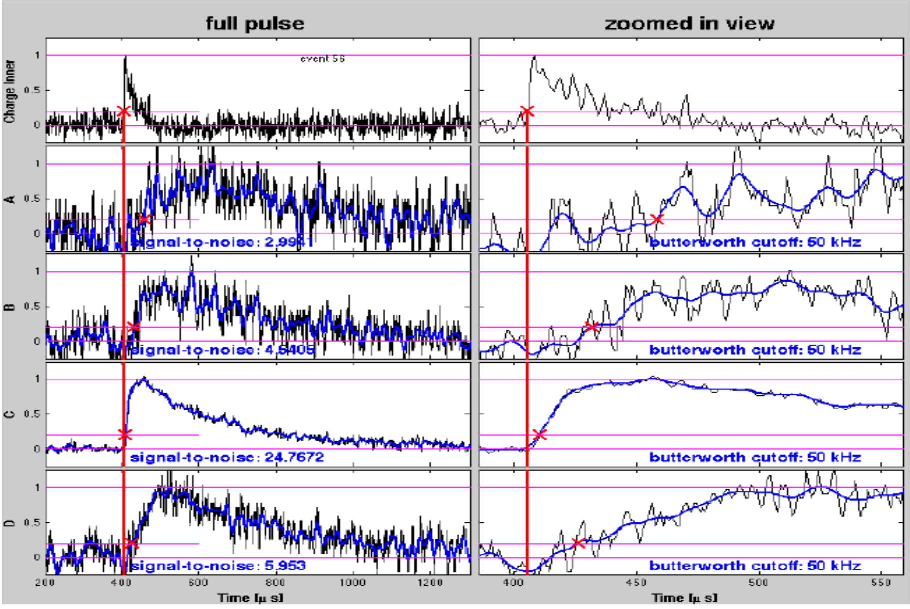

Figure 7.27: RTFT walk algorithm used to extract various timing information from the phonon pulse shape. The top row shows the inner charge trace, and the four lower rows are the four phonon channels. (the right column is simply a zoomed in view of the left) The raw traces are shown in black; the filtered (50kHz cutoff butterworth) traces in blue. For each of the four phonon traces, the red crosses indicate the 20% crossing times, as calculated by passing the filtered trace into RTFT Walk. The same event is shown on both the left and the right (zoomed in on the rising edge). Channel C is the primary phonon channel (well-measured using a 50kHz cutoff), and channel A is the opposite channel (poorly-measured using a 50kHz cutoff). At low energy, the RTFT algorithm suffers from poor signal-to-noise, leading to mis-estimated timing parameters and poor resolution. Figure from [394].

and are thought to be primarily due to ^{210}Pb betas. The timing distributions for surface events and bulk nuclear recoils differs in two aspects: their phonon rise and delay times. Therefore, surface-event rejection parameters are defined to exploit these differences. The 5 timing parameters used in the development of the optimized χ^2 analysis discussed in chapter 8 are described below.

pminrtc

The difference between the rise time at the 40% and the rise time at the 10% amplitude is defined as the primary rise time or **pminrtc**[1].

pminrtCFc

The primary phonon rise time **pminrtCFc** is extracted from the fitted phonon pulse, following application of a constant frequency (of 50 kHz) Butterworth low-pass filter [427]. Then using the 40% and 20% rise time difference, the value of the quantity **pminrtCFc** is determined. It is important to stress the fact the difference between the previous timing quantity **pmirtc** and the **pminrtCFc** discussed here is that **pminrtCFc** is evaluated after

---

[1] The subscript "c" at the end of each parameter's name indicates that the parameter has been position corrected.

applying a Butterworth low-pass filter at constant frequency of 50 kHz while the quantity **pminrtc** is calculated at a variable frequency components. The constant Butterworth frequency was used during during the original c58 analysis. The reason for developing the RD **pminrtc** was the following: when the signal-to-noise of a pulse is low, the walk algorithm finds noise dips rather than the actual crossing points. To avoid this situation, we needed to use a butterworth filter that emphasized on the longer-frequency components in this low-signal-to-noise situation, and a butterworth that allowed all frequency information for the high-signal-to-noise situation. This variable filter was useful in making delay-based position measures (used later for position correction). The RTFT algorithm strategy works well under the followings assumptions: the amplitude of the noise is much smaller than the amplitude of the pulse, and the slope of the rising edge is relatively steep. If either of these two conditions fails, then the rising edge will be non-monotonic, and the walk algorithm will find the first instance of a 20% point at the position of a random downward fluctuation from the noise, rather than at a point more accurately representative of the rising edge timing. As shown in Figure (7.27), one would have to smooth the pulses more, by decreasing the cutoff to the low-pass filter. One draw back here is that the rising edge slope of primary pulses would start to loose its distinctive steep shape if we decrease this low-pass filter for all pulses. This is of a crucial importance to our analysis and we cannot afford to loose such ability. The question that needed to be answered here was to find the highest cutoff frequency for which the rising pulse will be monotonic given the signal-to-noise ratio input. An analysis conducted by Scott Hertel showed that 50 kHz was that cutoff [394].

pminrtCF4070c

In similar fashion we define the pminrt4070c as the difference between the 70% and 40% rise times.

pdelc

The phonon delay time, or **pdel**, is defined as the difference between the charge arrival time and the 20% rise time of the phonon pulse. Phonon pulses from surface events arrive sooner relative to their associated ionization pulses than do phonon pulses from nuclear recoils. The typical time delay for phonons relative to ionization is 2 to 15 μs. Surface events, however, have shorter delays due to quick downconversion from high (slower) to low frequency phonons (faster), caused by interactions with the superconducting aluminum fins at the crystal surfaces.

pdelCFc

In a similar way the delay time pdelCFc is calculated from constant frequency low-pass Butterworth filter, using the difference between the charge arrival time and the 20% rise time of the phonon pulse as illustrated in Figure (7.26).

Note:

The new pulse-specific filter definitions created using a constant frequency Butterworth low-filter work wonderfully well at low-energy. At high energy, the traditional ones still performed better. For this reason, we have decided to combine all of them together in a χ^2 analysis in order to exploit each one's discrimination in the whole energy range of interest in our analysis. The simple timing (or the classical timing) cut analysis used both pminrtCFc and pdelCFc.

7.10 Simple Timing cut

The sum of the primary risetime and primary delay was often used as a key discriminator for surface event rejection during CDMS-II WIMP-search analysis. Several other timing discriminators have been constructed and tested but the two above have provided most surface-event rejection in past WIMP searches [425]. In Chapter 8, I will describe in detail, another timing cut technique we have developed for surface-event rejection using an optimized χ^2 which corrects for the energy dependencies of the elements of the covariance matrix. First, let's illustrate how a simple timing cut can be implemented for surface-events discrimination.

The ultimate goal of a WIMP-search analysis is to be able to distinguish background events and the signal events which will potentially become the WIMP signal. In the CDMS analysis, such a goal is accomplished through the use of the phonon timings which are intrinsically different for surface events and signal events. One simple method that is used to discriminate surface-events electron-recoils is "the simple timing cut" which uses the phonon primary rise and delay times: **pdelCFc** and **pminrtCFc**. Rather than making independent cuts using the reduced quantities **pminrtCFc** and **pdelCFc**, we take advantage of the strong correlation between the two variables and employ principle component analysis (PCA) by making cuts along rotated axes: **pdelc+pminrtc** and **pdelCFc-pminrtCFc**. A lower limit in (**pdelc+pminrtc**) serves as a discrimination cut, positioned to accept nuclear recoils while rejecting surface events. An upper and lower limit in (**pdelCFc-pminrtCFc**) acts as a consistency cut, rejecting events which lie far from the nuclear recoil population. Figure (7.28) illustrates the implementation of such cut showing the distributions of neutrons, bulk gammas and surface events for c58 analysis [425].

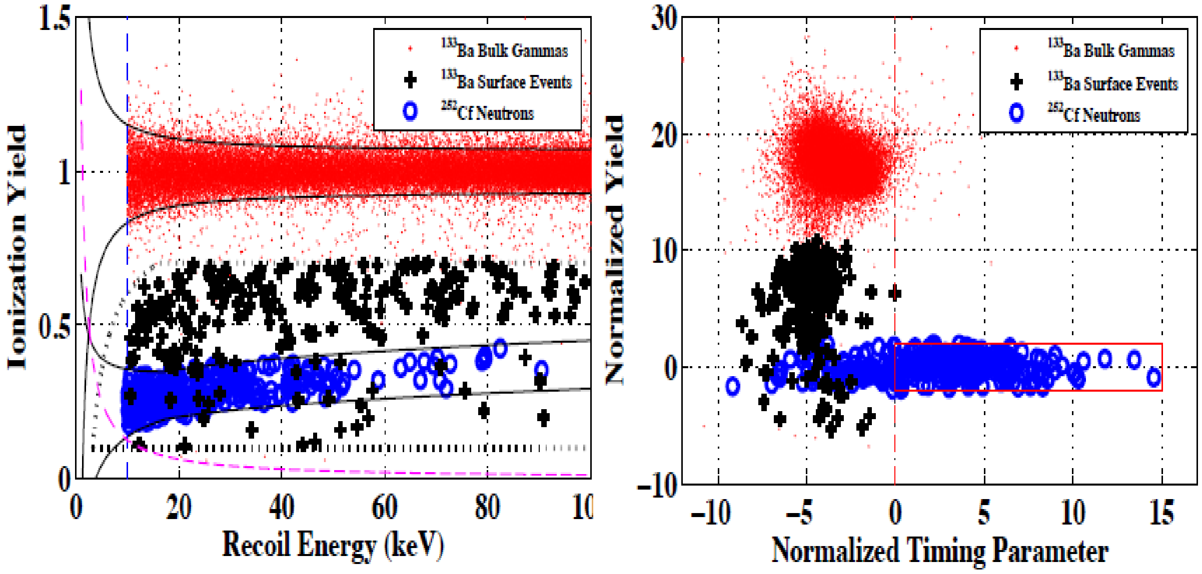

Figure 7.28: Illustration for a typical detector using in situ calibration sources and as the plots indicates: bulk electron recoils (red points), surface electron events (black crosses) and nuclear recoils (blue circles) with recoil energy between 10 and 100 keV. Left: Ionization yield as function of recoil energy. The solid black lines define bands that are $\pm 2\sigma$ from the mean electron and nuclear-recoil yields. The sloping magenta line indicates the ionization energy threshold while the vertical dashed line is the recoil energy analysis threshold. The region enclosed by the black dotted lines defines the sample of events that are used to develop surface-event cuts. Right: Normalized ionization yield (number of standard deviations from mean of nuclear recoil band) versus normalized timing parameter (timing relative to acceptance region) is shown for the same data. Events to the right of the vertical red dashed line pass the surface-event rejection cut for this detector. The solid red box is the WIMP signal region. Figure adapted from [394].

Chapter 8

Optimized 5-dimensional χ^2 timing-cut analysis

8.1 Introduction

One of the primary challenges of a CDMS analysis is to develop techniques that are able to clearly differentiate a WIMP signal from interactions due to radioactive backgrounds which can mimic the expected signal. It's in this spirit that the CDMS experiment uses the timing parameters derived from the phonon pulse to construct an event-by-event discriminator.

In the previous chapter, a few CDMS timing quantities were introduced. These timing quantities are the basis of the 5 dimensional χ^2 timing-cut analysis featured in this thesis. In this chapter, I explore the energy dependence of the χ^2 analysis and expand on the details of how one forms a simple timing cut using the χ^2 technique. Before doing so, it is necessary to lay down the foundation on which this analysis is built on. We structure this chapter as follows: first, we discuss on the construction of a χ^2 and motivate the energy dependence of the mean and the covariance matrix going into the computation of the χ^2. After this discussion, the implementation of a simple timing cut based on the χ^2 will be introduced. Since the goal of this analysis was to optimize the energy-dependent χ^2 timing cut, the expected leakage and the exposure, two important ingredients for this recipe, will be discussed. Finally, a simultaneous optimization of the yield and timing cuts will described in order to implement an energy-dependent cut which is defined in a manner that optimizes the experiment's sensitivity to WIMPs.

It is worth mentioning that the χ^2 timing-cut technique was originally developed by previous CDMS analyzers. For example, χ^2 timing-cut surface-event rejection was the main subject of Joel Sander's doctoral dissertation [429]. Other CDMS collaborators have explored 3 and 4 dimensional χ^2 timing-cut. J. Sander and R. Mahapatra in [430, 431, 432, 433], Jeff Filippini in [434, 435, 437, 438], and Walter Ogburn in [439, 440, 441] have explored energy-independent and an energy-dependent χ^2 cuts, correcting for the energy dependence of the covariance-matrix elements in the latter case. Following these authors footsteps', Kunj Prassad combined timing parameters with phonon energy partition and delay variables, the fractional timing from the primary phonon pulse's rise time, and the total-phonon rise time variables to form a 5-dimensional χ^2 for surface-event rejection in mZIP (mercedes) detectors [442]. Concurently, I developed a 3-dimensional χ^2 cut using three timing variables. Unfortunately, this cut performed poorly; it had too many outliers, necessitating a relatively severe cut that compromised nuclear recoil detection efficiency. Subsequently, I started developing an energy-dependent analysis, correcting for the energy dependence of the covariance-matrix elements, while leaving the timing-parameter means energy independent [443]. This energy-dependent χ^2 cut performed a little better (56% of neutron efficiency) compared to the 5-dimensional energy-independent that Kunj developed (52% of neutron efficiency with the same expected leakage).

The 5-dimensional energy-dependent and sensitivity-optimized χ^2 timing cut described in this chapter evolved further for the c58 reanalysis, building upon the CDMS work that precedes it. This timing-cut differs from the previous works by correcting for the energy dependence of the means (μ) of the variables going into the χ^2 and by tuning the cut to allow a total background-event leakage that optimizes the total sensitivity. This goal is accomplished by incorporating the energy-dependence of the cut-position and simultaneously optimizing the yield and the timing cut. These aspects are implemented for the first time in this analysis. This analysis achieved the best expected sensitivity among all three timing-cut techniques developed for the reanalysis as described in section (8.7). It has also yielded a 2× lower limit than the original c58 analysis.

8.2 χ^2 Analysis

For the sake of developing a timing cut capable of rejecting surface events while maintaining signal efficiency, two event types are needed: one representing the signal (or nuclear recoils) and one representing the background (or surface events). In a CDMS analysis, a ^{252}Cf neutron source is used to acquire nuclear recoils, while a ^{133}Ba gamma-ray source is used to acquire surface events. For simplicity, we refer to signal-like events as a neutrons and surface-events as betas.

With these two events types, a χ^2 must be calculated for two hypotheses: a neutron hypothesis and a beta hypothesis. A χ^2 for the neutron hypothesis is calculated on an event-by-event basis and denoted χ^2_N. Similarly, for the beta hypothesis, χ^2_B is computed.

8.3 Constructing a χ^2 statistic.

The general form of a χ^2 statistic can be written as [426]

$$\chi^2 = \sum_{j,k}(x_j - \mu_j) \cdot (\Sigma)^{-1}_{jk} \cdot (x_k - \mu_k), \tag{8.1}$$

where x represents the observables, μ is the mean of the observables and $(\Sigma)^{-1}$ is the covariance matrix defined as the inverse of the error matrix Σ. In 2 dimensions, the error matrix Σ for the observables x and y is defined as

$$\Sigma = \begin{pmatrix} \sigma_x^2 & cov(x,y) \\ cov(x,y) & \sigma_y^2 \end{pmatrix}, \tag{8.2}$$

with $cov(x,y)$ the correlation term between the variables x and y. The covariance matrix can then be written as

$$(\Sigma)^{-1} = \frac{1}{1-\rho^2} \begin{pmatrix} \frac{1}{\sigma_x^2} & -\frac{\rho}{\sigma_x \sigma_y} \\ -\frac{\rho}{\sigma_x \sigma_y} & \frac{1}{\sigma_y^2} \end{pmatrix}, \tag{8.3}$$

where the parameter ρ is known as the correlation coefficient (for the variables x and y):

$$\rho \equiv \frac{cov(x,y)}{\sigma_x \sigma_y}. \tag{8.4}$$

The correlation coefficient ρ is bounded between -1 and 1, i.e $|\rho| \leq 1$. Not surprisingly, $\rho = 0$ when the variables are uncorrelated, therefore the off-diagonal terms of the matrix (8.2), or (8.3) for the 2-dimensional case,will vanish. In such a situation, the variables x and y are therefore independent.

In the analysis described here, the variables used in the χ^2 are the timing parameters extracted from phonon pulse shapes: the primary rise time and the delay with respect to the ionization pluses. Specifically (and in the jargon of CDMS reduced quantities): **pminrtc**, **pdelc**, **pminrtCFc**, **pdelCFc** and **pminrtCF4070c** parameters described in section (7.9) are used. Figures (8.1) and (8.2) shows the binned energy dependence of the correlation coefficients ρ_{12} and ρ_{24}. Plots for other correlation coefficients are shown in Appendix B. As it can be notice (from these two plots as well the plots for other correlation coefficients shown in Appendix B), the variables are highly correlated for the neutron sample in all detectors and these coefficients are consistent to being constant for the energy range of $10 - 100$ keV corroborating the results Jeff Filippini found during his 3-dimensional energy-dependent χ^2 that used the **pdelc**, **pminrtc** and **pfrac** [435]. The quantity **pfrac** is defined as the fraction of phonon energy deposited in one phonon sensor relative to the total (the sum) of the phonon energy in the 4 phonon sensors (also called quadrants). Since phonon sensors are denoted by p_k; $k = \{a, b, c, \text{and}\, d\}$, the total phonon energy in the 4 quadrants is then given by $pt = \sum_{k=1}^{4} p_k$. Therefore the phonon fraction in each quadrant is $\frac{p_k}{pt}$.

8.4 Correcting for energy dependence

The timing parameters used in this χ^2 analysis possess a strong energy dependence. As the energy decreases, their resolutions (the variance or σ^2) flare out, as shown in Figure (8.4). Since the WIMP rate is expected to be much higher at low energy, it is critical to have the surface-event rejection cut perform well at low energy. If one forms a cut without correcting for these energy dependencies, the cut will perform poorly at low energy, thus making

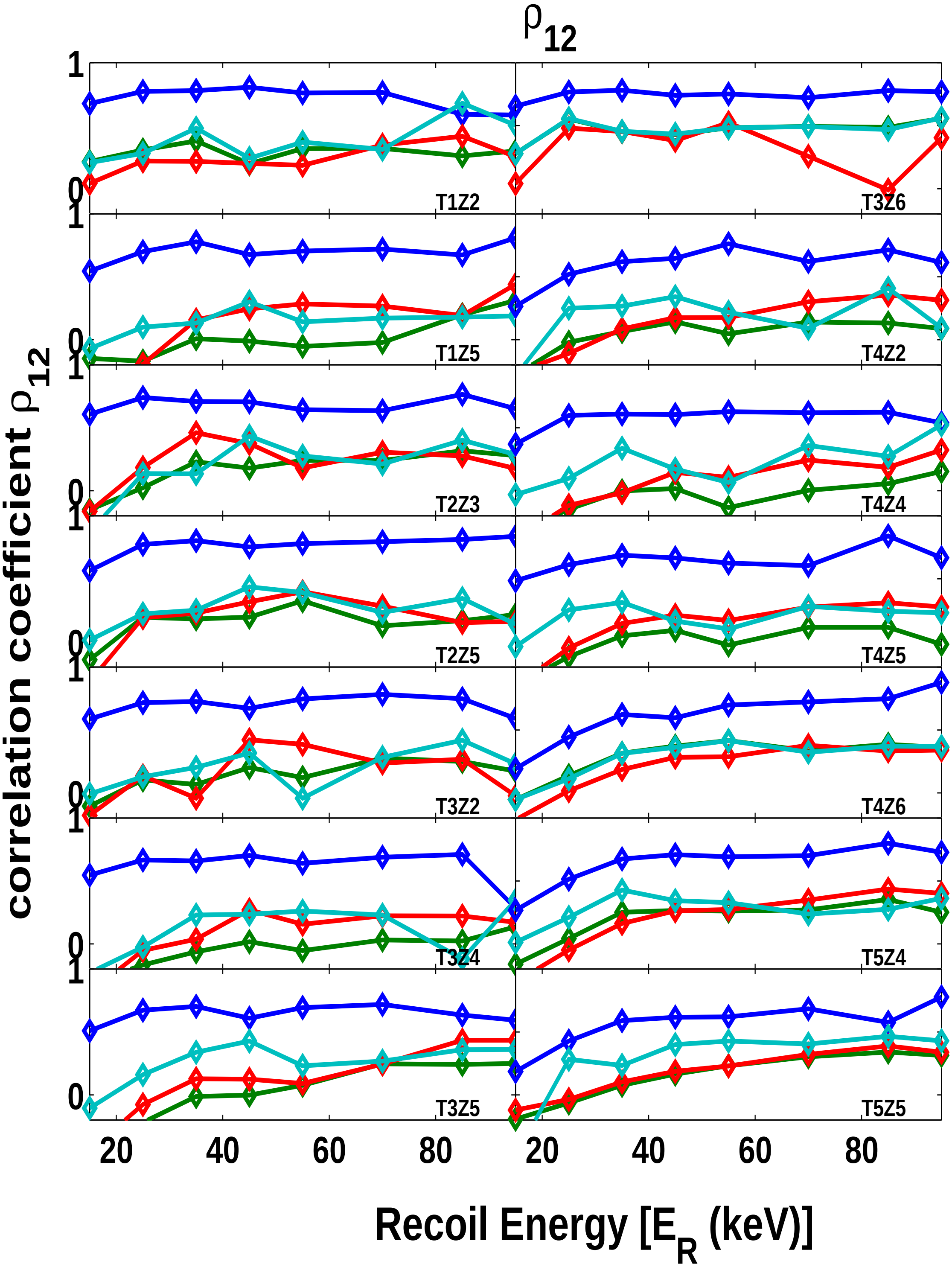

Figure 8.1: The correlation coefficient between the first and the second timing variables (i.e. **pminrtc** and **pdelc**) as function of energy. The blue curve represents the energy dependence of ρ_{12} for the neutron sample while the green, the red and the cyan curves represents the energy dependence for the surface events betas, the phonon and the charge-side events respectively.

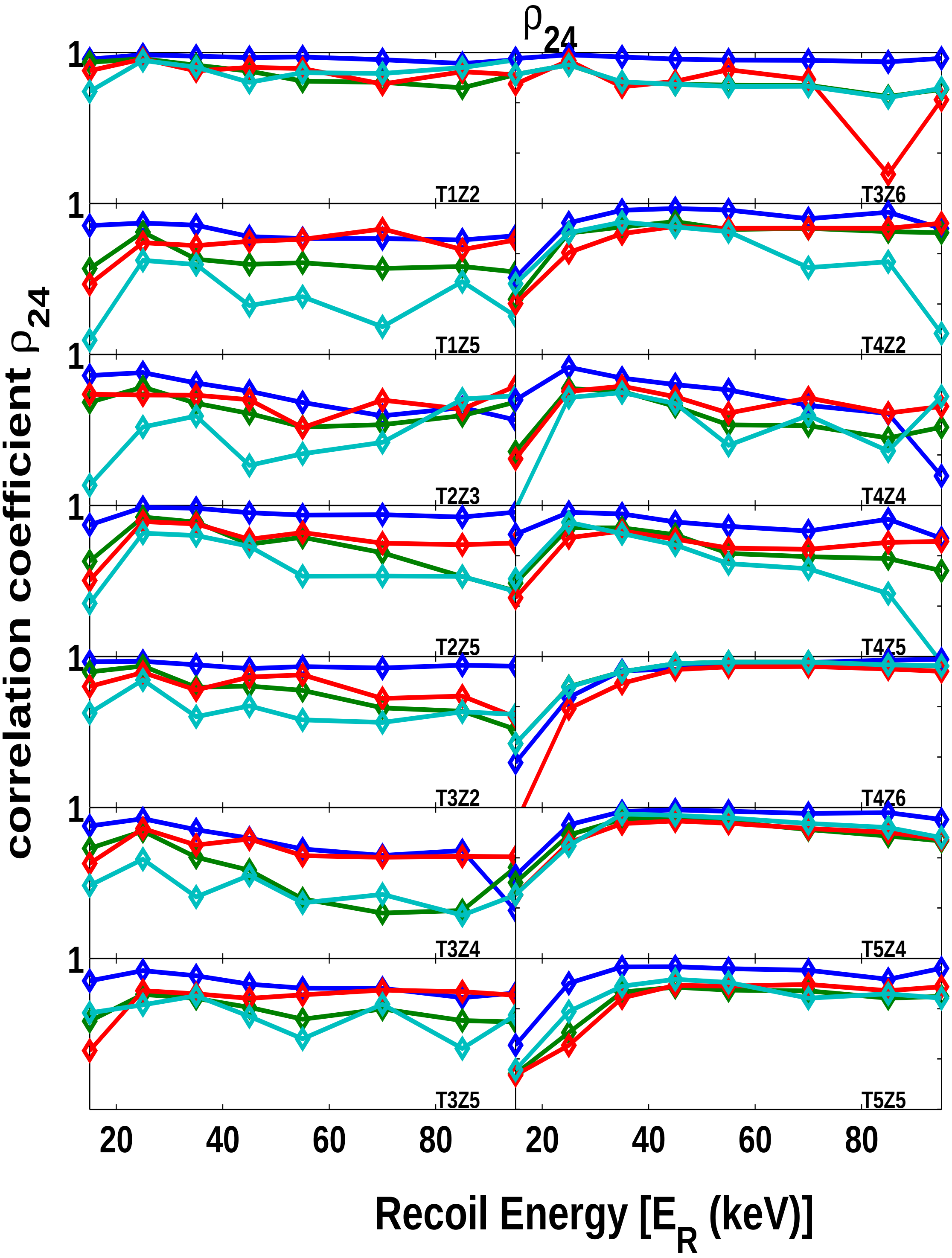

Figure 8.2: The correlation coefficient between the second and the fourth timing variables (i.e. **pdelc** and **pminrtCFc**) as function of energy. The blue curve represents the energy dependence of ρ_{24} for the neutron sample while the green, the red and the cyan curves represents the energy dependence for the surface events betas, the phonon and the charge-side events respectively.

the rejection cut insensitive to distinguishing background from signal in the most important energy regime. The energy-dependent cut which is the subject of this chapter was implemented by incorporating and correcting for the energy dependence of the elements of the covariance matrix and the means of the timing variables used in the χ^2.

For the fits discussed in the subsequent part of this section, the events used were required to pass simple timing-parameter outlier cuts. The outlier cuts were formed by keeping only events within $\pm 3\sigma$ from the mean of the timing distributions for a given event type. Since ZIP detectors have phonon sensors at the top and ionization sensors at the bottom, there is an intrinsic asymmetry that causes phonon and charge-side surface events to have different distributions. Consequently, there are more low-yield events from the phonon-side than from the charge side. For this reason, the energy dependence of the covariance matrix was calculated for side-specific surface-event populations.

8.4.1 Means of the χ^2 variables

The means (μ) of the timing parameters used in the χ^2 were calculated as functions of energy from 10 to 100 keV in five 10-keV bins from 10 to 60 keV and two 20-keV bins from 60 to 100 keV. The following functional form was fit to the bin-wise collection of means to model each parameter's energy dependence. The energy-dependent mean $\mu_\alpha(E)$ of the k^{th} timing variable for sample α was fitted to the binned means using the functional form

$$\mu_{k\alpha}(E) = A_{k\alpha}(1) + A_{k\alpha}(2) \cdot E^2 + A_{k\alpha}(3)\sqrt{E}, \tag{8.5}$$

where $A_{k\alpha}(1)$, $A_{k\alpha}(2)$ and $A_{k\alpha}(3)$ are the fit parameters and depend on event type and detector [444]. The index α refers to event types ($\alpha = \{\text{neutron, phonon-side betas, charge-side betas}\}$) and k refers to the timing variables: $k = \{1, 2, 3, 4, \text{and } 5\}$ taken for the following order {**pminrtc**, **pdelc**, **pminrtCFc**, **pdelc**, and **pminrtCF4070c**}.

The fits were performed for a variety of event types: signal-like using californium neutron events, and background-like events. The background sample is extracted from the Barium calibration to form a data subset that we call the beta sample. The betas are considered as electron recoils with low charge yield or with incomplete charge collection. Charge-side events are selected by requiring that the detector under test and the detector right above it to have a hit (i.e. energy deposited by the interacting event above the noise threshold), but no hit should be observed from the detector below. For phonon-side events, we require that the event deposits energy on the detector under test and the detector underneath, and not on the detector above.

The fit parameters used to model the means of the timing parameters according to equation (8.5) are shown in the tables of Appendix A.

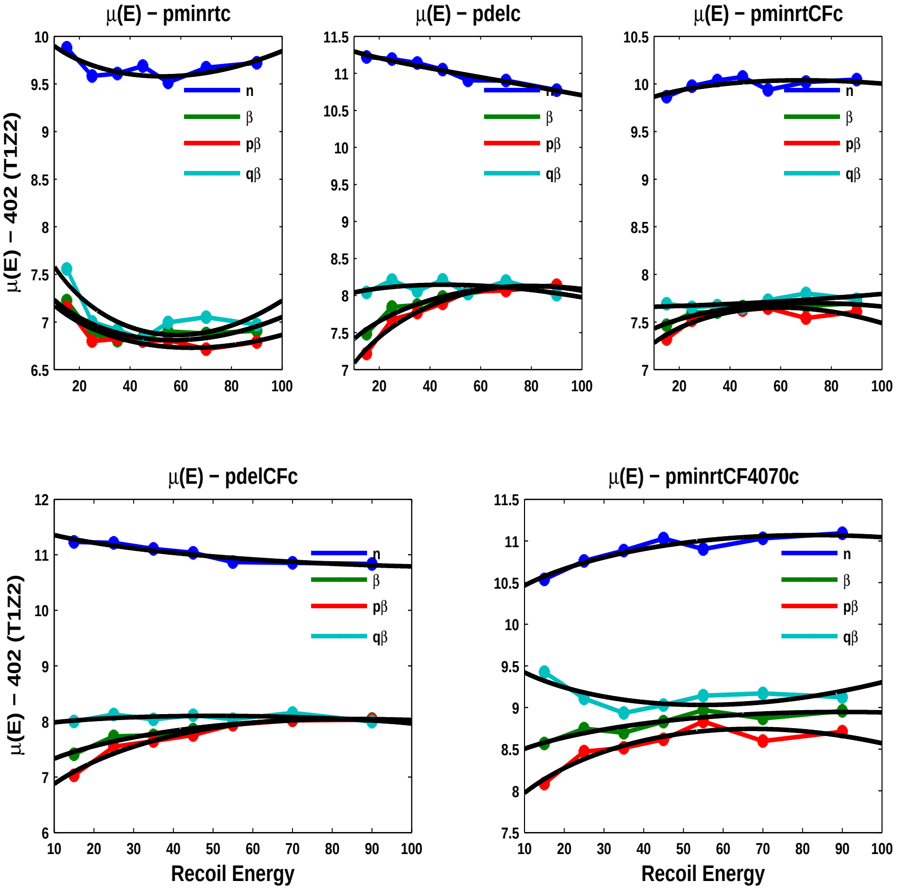

Figure 8.3: Energy dependence of the means of the timing variables used in the χ^2 for T1Z2. In black is shown the fit to the data using the functional form fit in equation (8.5). Different colors indicate different event types: neutron (blue), surface events - betas(green), phonon-side surface events (red) and charge-side surface events (cyan).

8.4.2 The covariance matrix

The elements of the covariance matrix exhibit a strong residual energy dependence. To compensate, the covariance matrix elements were also calculated as functions of energy from 10 to 100 keV (using the same energy bins used for the timing parameter means).

For each detector, the covariance matrix was calculated in every energy bin for each event type (surface events and neutrons). The diagonal elements of the covariance matrix, the variances (σ^2_{kl}), as well as the off-diagonal terms, the correlation terms (cov_{kl}, $k \neq l$), are plotted against recoil energy, Figure (8.4). The energy dependence of the covariance matrix element between the k^{th} and l^{th} timing variables for the α sample, $\sigma^2_{kl\alpha}$, was fitted using the functional form [445]

$$\sigma^2_{kl\alpha}(E) = B_{kl\alpha}(1) + \frac{B_{kl\alpha}(2)}{E^2}. \tag{8.6}$$

where the constants $B_{kl\alpha}(1)$ and $B_{kl\alpha}(2)$ are the fit parameters and depend on the event type α and detector. The parameter $B_{kl\alpha}(2)$ takes into account the noise distribution, which is dominant at low energy, i.e. when

$E \to 0$. $B_{kl\alpha}(1)$, however, is the asymptotic value of the variance at high energy. The fits for the variances and the correlation terms are shown in Figure (8.4) for a representative detector (see appendix B for equivalent plots for other detectors and for tables with the fit parameters).

The χ^2_α for each particle-type is then formed for every event candidate under the approximation that the timing variables are each gaussian distributed, i.e.

$$\chi^2_\alpha(E) = (x - \mu_{k\alpha})^T \cdot \sigma_{kl\alpha}(E)^{-1} \cdot (x - \mu_{l\alpha}). \tag{8.7}$$

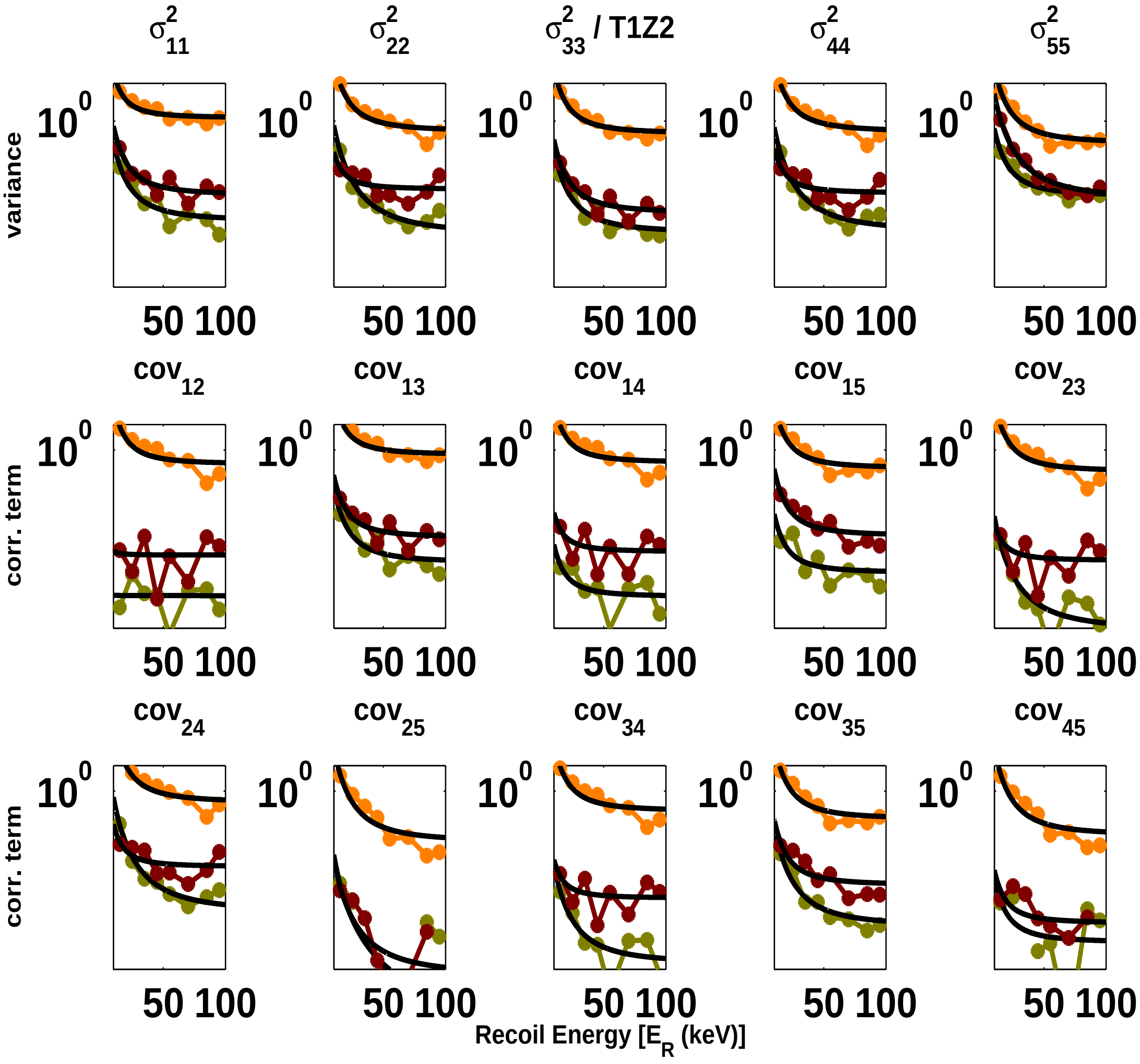

Figure 8.4: Covariance matrix elements binned as function of energy for T1Z2. In black is shown the fits to the data using the functional form in equation 8.6. Different colors indicate events of different type: neutron (blue), surface events - betas(green), phonon-side events (red) and charge-side events (cyan). The numbers $\{1, 2, 3, 4, \text{and}\, 5\}$ refers to the timing variables used in the construction of the χ^2, they must be taken in the following order $\{$**pminrtc**, **pdelc**, **pminrtCFc**, **pdelc**, and **pminrtCF4070c**$\}$.

8.4.3 Method

Given the neutron and beta hypotheses, the χ^2s represent the likelihood for a given event to be neutron-like or beta-like. In order to compute χ^2_N for neutron-like distributions and χ^2_B for the beta-like distributions, the appropriate covariance matrices for these specific classes of events have to determined using well-defined samples of neutron and beta events.

For a preselected sample of neutrons, the means of the 5 timing variables and the covariance matrix were calculated as function of energy. Using the energy-dependent mean and covariance matrix, $\chi^2_N(E)$ can thus be determined. For the the beta distributions however, side (face) events were used to infer the $\chi^2_B(E)$. Using phonon-side and charge-side events, energy-dependent means and covariance matrices were computed to obtain $\chi^2_p(E)$ and $\chi^2_q(E)$. From these, the beta χ^2_B was inferred:

$$\chi^2_B(E) = \min(\chi^2_p(E), \chi^2_q(E)). \tag{8.8}$$

8.4.4 Forming the cut

The final goal is to form a cut which can reject as many surface events as possible. Once χ^2_B and χ^2_N are computed, they are plotted against each other for both neutron and beta event populations. In the 2 dimensional plane as shown in Figure (8.5), one needs two cut types:

- The rejection cut, and
- The consistency cut.

Rejection cut:

The rejection cut is intended to distinguish potential signal events from the expected distribution of surface events. The rejection cut is related to the probability that the event is a nuclear recoil ($\sim e^{-\frac{1}{2}\chi^2_N}$) and to the probability that the event is a surface event ($\sim e^{-\frac{1}{2}\chi^2_B}$). χ^2_N and χ^2_B can also be interpreted as the distance of an event from the mean of the nuclear recoil band, $\mu(E_R)_{NR}$, which exhibit a strong energy dependence as well. In order to form this cut, one can explore two different approaches:

1. **Rejection cut based on a constant χ^2_B:**

   Cutting on a constant χ^2_B requires a definition based only on χ^2_B such that most of the surface events (green dots) are rejected while most of the neutrons (blue dots) are accepted. Such a cut can be accomplished by keeping only events for which

   $$\chi^2_B \geq C. \tag{8.9}$$

   However, there obviously a more intelligent approach that can be taken and this is discussed below.

2. **Rejection cut based on $\chi^2_B - \chi^2_N$:**

To cut on $\chi^2_B - \chi^2_N$, requires very good knowledge of the functional form that defines the relationship between χ^2_B and χ^2_N, which can depend on many factors. The simplest way to derive such a functional form was studied in the past by Joel Sander [429] and Xinjie Qiu [446], who used the ratio of the probability that an event is likely be a surface event to the probability that of an event to likely be a nuclear recoil, i.e:

$$r \approx e^{-\frac{1}{2}(\chi^2_B - \chi^2_N)}. \tag{8.10}$$

It is easy to define a cut by taking the negative logarithm of the above expression. This negative logarithm is referred to as the χ^2 distance (denoted d_{χ^2}).

$$d_{\chi^2} = -2\ln(r) = \chi^2_B - \chi^2_N, \tag{8.11}$$

so, in order to keep more neutron events and reject most of the surface events, the d_{χ^2} must satisfy the following criteria:

$$d_{\chi^2} = \chi^2_B - \chi^2_N \geq \eta. \tag{8.12}$$

where η may be constant or energy-dependent.

Consistency cut:

A potential WIMP signal must have a value of χ^2 that is consistent with nuclear recoils. For this reason, a consistency cut (also referred to as the outlier cut) has to be applied in order to keep as many neutrons as possible while rejecting events at very large values of χ^2_N. Most neutrons pile up at low χ^2_N. Consequently, this analysis is simplified by rejecting large χ^2_N events without losing much detection efficiency. Events are kept if and only if

$$\chi^2_N \leq C_1. \tag{8.13}$$

where C_1 is a hard cut value chosen in such a way that most of the signal is kept. Concurrently, this same cut also helps to reject surface-events outlier events at large χ^2_N values. There is an important reason for the consistency cut to be defined in the way it is written in equation (8.13). This cut is used to protect against shortcomings of the model. Surface-events betas become harder to cut at large χ^2_N. Furthermore, the consistency cut (8.13) is justified since most neutrons are at low χ^2_N, so it makes sense not to use large χ^2_N.

A combination of the cuts (8.13) and (8.9) or a combination of the cuts (8.13) and (8.12) suffice to form a χ^2-based timing cut. However, one figure of merit which goes into the preference between these different approaches is the signal efficiency. Obviously, the cut with higher neutron efficiency will be preferred. A study by Xinjie Qiu [446] using the 2-dimensional Gaussian density of the χ^2 timing cut, demonstrated that neutron efficiency is much higher if one cuts on the difference of χ^2_B and χ^2_N rather than cutting on a constant χ^2_B. Consequently, I use the combination of the cuts (8.13) and (8.12).

8.5 Energy-Independent χ^2 cut

The energy-independent χ^2 timing cut discussed in this section uses the energy-dependent covariance matrix and means in the computation of χ^2_B and χ^2_N. What makes this cut energy-independent is the fact that the two cut types (the consistency and rejection cuts) have not been made energy-dependent.

The consistency cut in this analysis and for the subsequent parts of this chapter was set such that it passes 90% of neutrons. However, the rejection cut for this energy-independent cut is determined on a detector-by-detector basis by requiring that the surface-event leakage fraction, calculated using the beta sample in energy range of $10 - 100$ keV, be of the order of 1 out of 200, i.e. by changing η in bins of 0.1 and requiring a leakage fraction $\leq \frac{1}{200}$. If two different cuts have the same leakage fraction, we select the cut with the largest efficiency. Figure (8.5) shows the implementation of the cut for a representative detector. Table (8.1) shows the neutron efficiency and surface-events passage fraction for all detectors. The energy dependence of the efficiency was explored and Figure (8.6) illustrates it for a representative detector. The functional form used to fit the neutron efficiency data was an error function times a decaying exponential:

$$f(E) = A(1) \cdot [1 + \text{erf}\,(A(2) \cdot (E - A(3)))] \cdot e^{-A(4) \cdot E}. \tag{8.14}$$

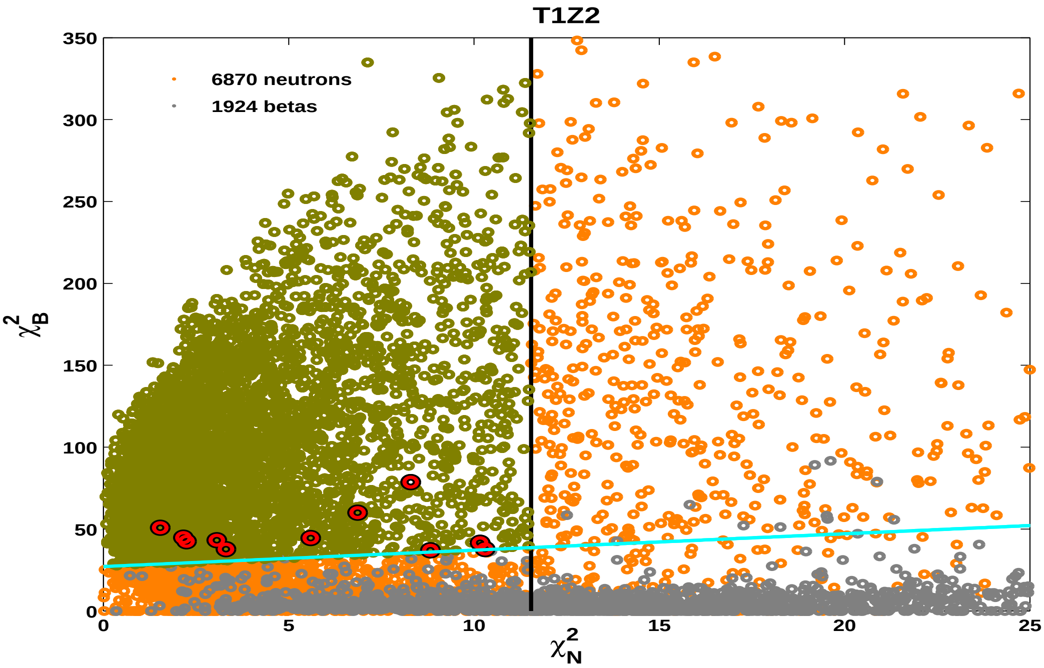

Figure 8.5: χ^2_B as function of χ^2_N with an energy-independent cut implemented. The black vertical line is the consistency cut which is set in such that 90% of neutrons survive. The rejection cut however (cyan), which is energy independent, is defined so that the surface-event leakage fraction is 1:200. The overall neutron efficiency (dark yellow circles) is 68.91%, while the surface leakage fraction (red black circled events) is $\sim 0.49\%$ for this detector.

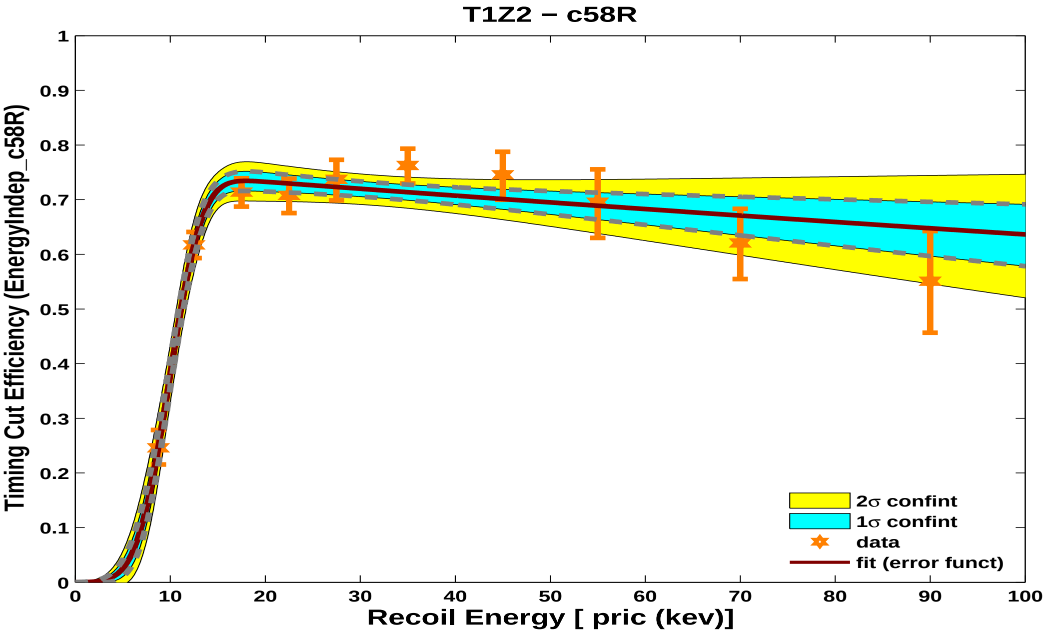

Figure 8.6: Neutron efficiency of the χ^2 energy-independent cut as a function of recoil energy. The solid darker red line is the fit to the data obtained using an error functional form, cyan and yellow regions represents the $\pm 1\sigma$ and $\pm 2\sigma$ confidence intervals, respectively.

As can be noticed from Table (8.1), the neutron efficiency is quite acceptable in most detectors with an average efficiency significantly better than the original c58 result. However, this cut is limited by systematics for the leakage estimate. The leakage estimate obtained with this cut is underestimated since its computation does not take into account the energy spectrum of the background. The energy dependent cut discussed in section (8.6), however, will address this issue. Figure (8.5) shows the distribution of χ^2_B as function of χ^2_N and the (energy-independent) cut positions. The efficiency of the cut as function of energy is shown in Figure (8.6). The error bars shown in orange color represents the data while the dark red curve is the fit to data obtained with the functional form given by Equation (8.14). The cyan and yellow region in Figure (8.6) are the 1σ and 2σ confidence interval. The plots and fits for other detectors are shown in Appendix C.

8.6 Energy-Dependent χ^2 timing cuts

In the previous section, an energy independent cut was developed to establish the χ^2-based timing-cut method. The following two improvements can be implemented in order to improve the rejection of surface events, especially at low energy where leaking events are most likely:

1. **account for the energy dependence of $\chi^2_B - \chi^2_N$:** The energy dependence of the χ^2 difference for the surface events and the signal was completely ignored in setting the energy-independent cut. Figure (8.7) shows that this χ^2 difference does indeed depend on energy. For the detector shown, there are quite a few outliers at low energy with substantially larger values of the χ^2 difference that cannot be rejected with an

Detector Name	Neutron Efficiency(%)	Surface Events Leakage Fraction
T1Z2	68.91	$0.00490 \pm 3.92 \times 10^{-4}$
T1Z5	64.93	$0.00460 \pm 4.14 \times 10^{-4}$
T2Z3	69.58	$0.00486 \pm 4.37 \times 10^{-4}$
T2Z5	59.89	$0.00472 \pm 5.19 \times 10^{-4}$
T3Z2	54.02	$0.00478 \pm 3.34 \times 10^{-4}$
T3Z4	73.60	$0.00487 \pm 3.41 \times 10^{-4}$
T3Z5	73.81	$0.00499 \pm 4.49 \times 10^{-4}$
T3Z6	45.62	$0.00500 \pm 4.25 \times 10^{-4}$
T4Z2	37.89	$0.00481 \pm 4.33 \times 10^{-4}$
T4Z4	66.08	$0.00478 \pm 3.49 \times 10^{-4}$
T4Z5	71.56	$0.00495 \pm 4.46 \times 10^{-4}$
T4Z6	40.05	$0.00473 \pm 5.20 \times 10^{-4}$
T5Z4	24.02	$0.00497 \pm 3.73 \times 10^{-4}$
T5Z5	37.52	$0.00497 \pm 3.74 \times 10^{-4}$

Table 8.1: Neutron Efficiency and Surface events passage fraction for the energy-independent χ^2 cut for the ZIP detectors used during the reanalysis c58R. The neutron passage fraction satisfies both the consistency (set in order to allow 90% of neutrons to pass) and the rejection cuts (tuned for a rejection of 200:1).

energy-independent cut without compromising the signal efficiency at higher energies.

2. **optimize the cut:** The χ^2 timing cut for which the neutron efficiency and leakage passage fraction shown in Table(8.1) was not optimized in any sense. Because all detectors do not have the same performance, an optimized cut could set the cut positions in such a way that the exposure is higher while the surface-event leakage is lower in detectors with stable running periods and good performance. For detectors with less performance however, the cut position will be stricter so that the leaking surface events are minimized. This has the potential to have a strong impact on the overall WIMP-search exposure.

In this section, I develop a χ^2 energy-dependent cut which makes these two improvements. The energy dependence is taken into account by the use of three energy bins: $10-20$ keV, $20-30$ keV and $30-100$ keV. Prior to developing an optimized χ^2 timing cut, two important ingredients need to be determined: the expected leakage and the final signal efficiency for a set of timing cuts weighted by the live time and the expected WIMP spectrum-averaged exposure, or SAE, which depends on WIMP mass as discussed in section (8.6.2). These two quantities have to be calculated for different timing-cut positions. The optimization which will be discussed later will determine the optimal timing cut to use; which should optimize the experimental sensitivity, see section (8.6.4) for more details.

8.6.1 The Expected Leakage

The expected leakage in each energy bin of each detector is calculated according to the recipe developed during the c58 analysis [447], where, for any desired cut position η on a given detector z, the expected WIMP-search nuclear-recoil single-scatter (NRSS) leakage n_z was determined from the scalar product of the expected number

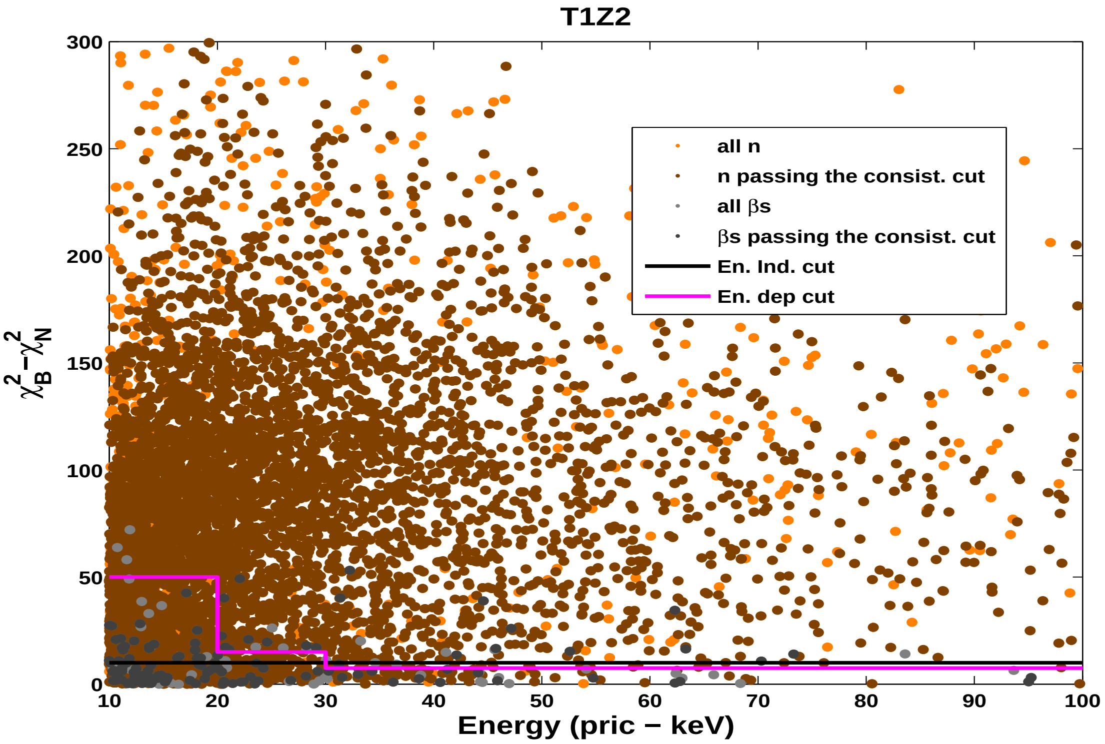

Figure 8.7: Energy-dependence of $\chi^2_B - \chi^2_N$. The black horizontal line is the energy-independent rejection cut while the magenta stair-step line indicates the energy-dependent rejection cut. Notice that the energy-dependent cut rejects a higher fraction of signal and background events at low energy while the energy-independent cut is loose. Orange-cyan events represent neutron and surface events respectively before the consistency cut, while darker orange and darker cyan are the events of the same types that pass the consistency cut (8.13). Plots for other detectors are shown in Appendix D.

of WIMP-search single-scatter events (N_z) in the nuclear-recoil band with the expected leakage fraction ($\frac{L}{B}$), in three energy bins and for both detector's faces, after taking into account the systematic differences between the background energy spectrum in barium data and the leakage spectrum in the WIMP-search data. The barium background leakage fraction was calculated according to

$$\left(\frac{L}{B}\right)_z = \sum_{e,f} (b_{ef})_z \cdot (S_{ef})_z, \tag{8.15}$$

where the subscript z refers to a given ZIP detector. The other subscripts e, f represent specific interaction categories for recoil energy bin e and detector face f. The b_{ef} values are the leakage fractions of surface electron recoils in the various categories expressed as a function of the timing-cut cut position. They are calculated using the barium calibration data as the ratio of events passing the cut position (η) to the total number of calibration events in the energy bin and face of the detector considered, *i.e*:

$$(b_{ef})_z = \frac{(L_{ef})_z}{(B_{ef})_z}, \tag{8.16}$$

where L_{ef} and B_{ef} are the number of leakage events passing the timing cut and the total number of calibration events in the energy bin e and detector face f respectively for the detector under consideration. Finally, the scaling factor S_{ef} is calculated using R123/R124 data and takes into account the systematics difference between the surface-event energy spectrum in Ba calibration data and WIMP-search data. The scaling factor was simply determined as the scaling factor needed to reweigh (multiply) the Barium expected leakage in energy bin and detector's face in order to get the same expected leakage in WIMP-search data. For the exteriors detectors (endcaps), it is not as straightforward to tag phonon vs. charge side events since there is no adjacent detector on the phonon/charge face for top/bottom detectors. For the c58 analysis as well as for the reanalysis, the only endcaps considered are bottom endcaps (T3Z6 and T4Z6). To estimate the scaling factors for these detectors, it was assumed that all single scatters are untagged charge side events, which slightly overestimates the number of charge side events. Howsever, this approach was deemed to be conservative since charge side betas have higher passage fraction than phonon side giving a conservative estimate of the true fraction of phonon side and charge side events for the endcaps. The overall expected leakage for a given cut position is estimated according to the formula

$$n_z(\eta) = N_z \cdot \sum_{e,f} (b_{ef}(\eta))_z \cdot (S_{ef})_z \tag{8.17}$$

where η is the timing cut position and N_z is the number of surface electron recoils with WIMP-like ionization yield (NRSS) expected in c58 for a ZIP detector z.
The value of N_z was calculated using three different methods [447]

1. Measure the number of nuclear recoil single scatters (NRSS) in the unblinded c34 data, and then scale this number by the livetime of c58 to the livetime of c34. This method assumes that the surface-event rate of c34 is the same as the surface-event rate in c58.

2. Measure the ratio of nuclear recoil multiple scatters (NRMS) to NRSS in the unblinded c34 data by counting the NRMS in c58 low background data, and scale this observed number by the ratio computed in c34. Because the blinding cut includes cSingle, the NRMS of c58 can be counted without unblinding the NRSS. This method assumes that the $NRMS : NRSS$ ratio of c34 is the same as that of c58.

3. Measure the ratio of multiple scatters to single scatters outside of the NR band in c58 data by counting the NRMS in c58 low background, and scale according to the MS:SS ratio observed outside of the NR band. This method assumes that the $MS : SS$ ratio outside of the NR band is the same as that in the NR band.

In the computation of the expected leakage, only the values of N_z calculated using Method 1 were used. The outcomes from the other two methods were used as cross checks of the calculated expected leakage. These numbers can be found in chapter 6 of Matt Frits's dissertation [382].

The expected leakage was calculated using the equation (8.17) for the c58 reanalysis data. Because of the small data samples and lack of statistics in Ba calibration data as the timing-cut position becomes tighter, the tails of the surface-event leakage distributions in each energy category are fit to a functional form to allow an extrapolation beyond the data, allowing flexibility to set the timing cut position in regions where the surface-event background statistics are low. In order to get the right shape of the expected leakage, the cut position was changed by units of 2 for $\chi^2_B - \chi^2_N < 50$ and ina step size of 1 for $\chi^2_B - \chi^2_N > 50$ (finer binning might be better, but would compromise the software speed). Figure (8.8) shows the expected leakage as a function of the cut position for a representative detector (see Appendix F for equivalent plots for the other detectors).

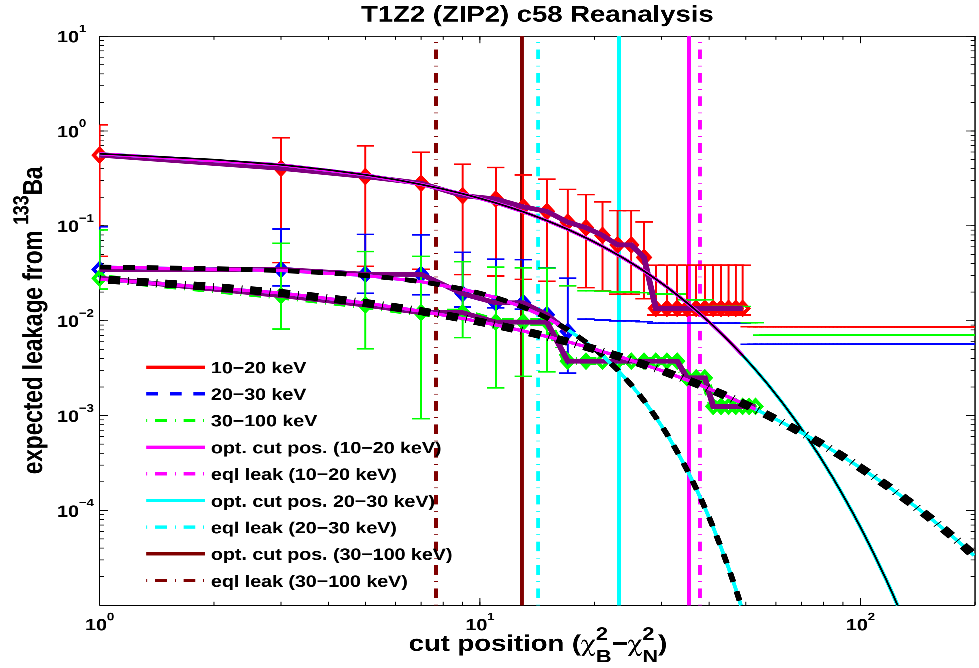

Figure 8.8: The expected leakage as function of cut positions calculated using the ^{133}Ba calibration data for the c58 reanalysis. The black lines represent fits to the data (shown in solid for the red 10-20 keV data, dashed for the blue 20-30 keV data and dotted for green 30-100 keV data). The vertical magenta, cyan and dark red lines represents the optimal cut positions while the dashed magenta, dashed cyan and dashed dark red lines are the cut positions for equal leakage in the three energy bins respectively. Plots for other detectors are shown in Appendix F.

The curves of the expected leakage as a function of cut position ($\chi^2_B - \chi^2_N$) for the three energy bins are stored as a set of points, one for each cut position. As can be seen in figure (8.8) this resolution is sufficient for encoding the shape of the curve. The black lines in figure (8.8) are the fits to the expected leakage computed in the three energy bins. The most interesting regions of the fits are the tails of the distributions where the statistics become extremely small. The fits allow extrapolation of an expected leakage for tighter cut positions. The tails of the leakage distributions were modelled with the functional form

$$f_l(\eta) = a_1 \cdot \log\left(1 + e^{-a_2 \eta^{a_3}}\right), \tag{8.18}$$

with $[a_1, a_2, a_3]$ the fit parameters and $\eta = \chi^2_B - \chi^2_N$ the cut position. The function $f_l(\eta)$ was chosen because it seemed to fit the data well.

8.6.2 Spectrum-Averaged Exposure

The spectrum-averaged exposure was also calculated as a function of cut position $\eta = \chi^2_B - \chi^2_N$, similar to leakage. The exposure is defined as the product of the live time and the nuclear-recoil detection efficiency calculated for ^{252}Cf passing all the data-selection cuts, including the timing cuts (the χ^2 timing cut in this case). Since in general these efficiencies are energy-dependent, the true efficiency is an average weighted by the expected WIMP spectrum. This spectrum depends on the WIMP mass; a 60 GeV/c^2 WIMP was used to generate the expected WIMP spectrum used to weight the efficiency. The following formula was used to compute the spectrum averaged exposure $\mathcal{S}$:

$$\mathcal{S}(\eta) = MT \frac{\int_{q_{min}}^{q_{max}} \frac{dR}{dq} \cdot \epsilon_\eta(q) dq}{\int_{q_{min}}^{q_{max}} \frac{dR}{dq} dq}, \tag{8.19}$$

where $\frac{dR}{dq}$ is the WIMP spectrum (or differential rate), ϵ_η is the energy-dependent analysis efficiency calculated at a given cut position $\eta = \chi^2_B - \chi^2_N$ and q_{min} and q_{max} represent the analysis energy range. $q_{min} = 10\,\text{keV}$ is the recoil-energy threshold and $q_{max} = 100\,\text{keV}$ is the maximum analysis energy. The quantity MT in Equation (8.19) represents the exposure, which is defined as the product of the detector's mass M and the livetime T.

Similarly to the expected leakage, the WIMP spectrum-averaged exposure, shown for a representative detector in Figure (8.9), was also calculated and stored as function of cut position $\eta = \chi^2_B - \chi^2_N$. The tails of the distributions of the exposures were fit using the following functional form:

$$f_S(\eta) = (b_1\eta + b_2) \cdot e^{-b_3\eta^{b_4}}, \tag{8.20}$$

with $[b_1, b_2, b_3, b_4]$ the fit parameters and η is the cut position. This function $f_S(\eta)$ was also chosen because it fitted the data well.

It is important to mention at this point that the three energy bins used in this analysis show that there is more exposure and leakage in the lowest energy bin, i.e. in $10 - 20$ keV, as shown in Figures (8.8) and (8.9). If we chose to set a constant cut position for the three energy bins, the lowest energy bin would dominate both the expected leakage and the signal-exposure. Such a cut will compromise the detection sensitivity.

The optimization scheme developed in this analysis rather chooses different cut positions for the three energy bins. This optimization selects the cut positions by cutting hard, i.e. rejecting more leakage, in bins where the leakage is higher while softening the cut position in energy bins with less leakage. As it will become clear as we move forward, this scheme maximizes the expected sensitivity.

The WIMP-search exposure is in general composed of two main components: the live time of the target mass and an energy-dependent signal efficiency associated with live time. The live time of the target mass is

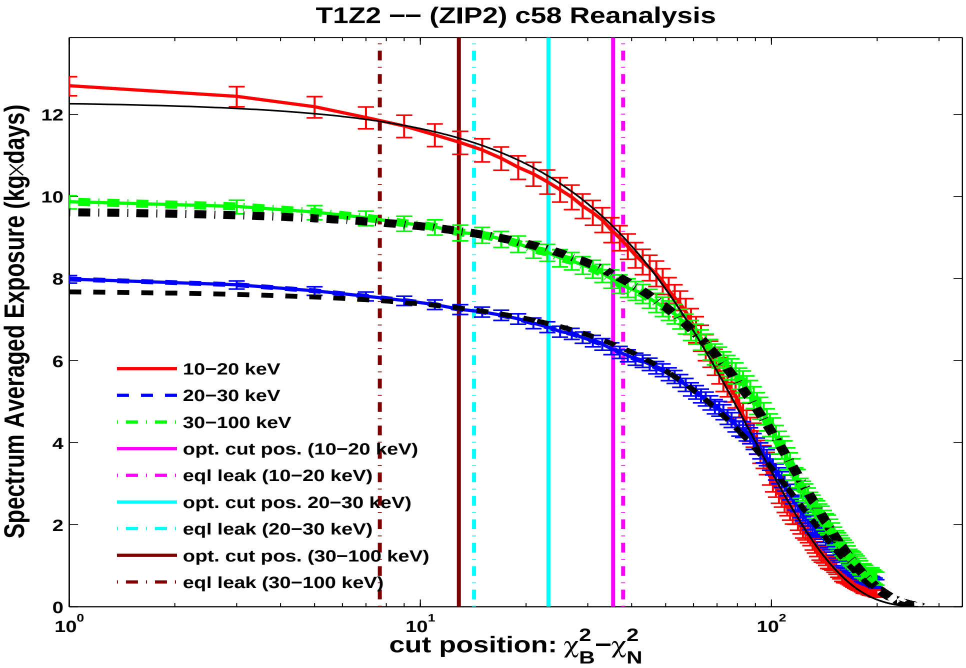

Figure 8.9: The spectrum-averaged exposure as functions of cut positions calculated using the ^{252}Cf calibration data for the c58 reanalysis. The black lines represent the fits to the data (shown in solid red for $10 - 20$ keV, dashed blue for $20 - 30$ keV and dotted green for $30 - 100$ keV). The vertical magenta, cyan and dark red lines represents the optimal cut positions while the dashed magenta, dashed cyan and dashed dark red lines are the cut positions for equal leakage in the three energy bins respectively. Plots for other detectors are shown in Appendix F.

simply the product of the live time with the detector's mass, where the live time indicates the number of the live days in the data after removing periods of elevated noise and abnormal running conditions. The power of a WIMP-search analysis is characterized by its sensitivity to observation of WIMP recoils and its expected background rate (which determines the significance of any observed events). This sensitivity can only be known if the exposure is accurately determined.

Live time

The live times (in days) for the runs 125 through 128 analyzes are shown in Table (8.2). They were calculated by imposing the cuts ∼ cBad_c58R&cQstd_c58R described in section (7.6.1). Values highlighted in red, in Table (8.2), indicate the Ge detectors that were deemed viable for the analysis featured in this thesis. A similar analysis using data from the Si detectors will be explored in Kevin McCarthy's dissertation (using a similar analysis technique) [461].

Target mass

The CDMS-II ZIP detectors are normally 240 g (105 g) for the Ge (Si) crystals respectively. Detectors whose sensors needed to be refurbished were repolished, therefore reducing their thickness below 1 cm. The actual ZIP

R125R						R126R					
	T1	T2	T3	T4	T5		T1	T2	T3	T4	T5
Z1	0	81.95	0	102.81	0	Z1	0	45.96	0	57.83	0
Z2	96.14	90.24	34.64	92.72	0	Z2	57.74	58.73	18.43	59.11	0
Z3	0	81.64	95.51	103.33	94.67	Z3	0	44	52.83	58.96	55.51
Z4	62.78	82.29	103.13	98.96	98.79	Z4	0	55.50	59.17	59.05	58.31
Z5	105.6	90.72	71.38	89.23	93.22	Z5	61.34	51.74	34.48	51.20	56.36
Z6	103.94	100.10	98.50	93.31	0	Z6	0	0	58.02	58.34	0
R127R						R128R					
	T1	T2	T3	T4	T5		T1	T2	T3	T4	T5
Z1	0	27.85	0	42.05	0	Z1	0	14.85	0	20.45	0
Z2	37.24	40.41	15.62	34.25	0	Z2	20.21	20.30	7.97	0	0
Z3	0	32.49	0	45.15	35.76	Z3	0	0	20.53	19.26	21.09
Z4	0	46.33	47.19	39.88	34.70	Z4	0	19.88	21.89	19.62	21.58
Z5	0	39.48	28.11	40.72	40.90	Z5	0	0	12.11	20.86	19.64
Z6	0	0	40.19	42.78	0	Z6	0	21.26	21.71	20.54	0

Table 8.2: Live Times for the c58 reanalysis (in days). Highlighted in red colors are the 14 detectors deemed viable for the c58 original analysis and during the reanalysis.

detector masses used in the c58 reanalysis and during the original c58 analysis are shown in Table(8.3). Although earlier analyses used the approximate 250 g (100 g) masses for all CDMS II Ge (Si) crystals, starting with the original c58 analysis, we have used more accurate values for the masses. The c58 analysis exposures are shown in Table (8.4).

	T1	T2	T3	T4	T5
Z1	230.5	101.4	104.6	101.4	224.5
Z2	227.6	104.6	231.2	238.9	229.5
Z3	219.3	219.3	104.6	101.4	101.4
Z4	104.6	104.6	238.9	234.6	224.5
Z5	0	0	12.11	20.86	19.64
Z6	219.3	238.9	238.9	231.9	234.8

Table 8.3: ZIP detector masses (in grams).

8.6.3 Exposure vs Expected Leakage

Given the expected leakage and the exposure as a function of cut position, it is possible to map the spectrum-averaged exposure as a function of the expected leakage. These curves are shown in Figure (8.10).

To compute the total exposure and total leakage, two different and independent approaches can been explored.

1. use the same cut positions ($\eta = \chi^2_B - \chi^2_N$) for all detectors to get their respective exposures and expected leakage and sum them up to get the total exposure and total expected leakage;
2. use different detector-dependent cut positions ($\eta = \chi^2_B - \chi^2_N$) for all detectors to get their respective exposures and expected leakage and sum them up to get the total exposure and total expected leakage.

R125R						R126R					
	T1	T2	T3	T4	T5		T1	T2	T3	T4	T5
Z1	0	8.31	0	10.43	0	Z1	0	4.66	0	5.86	0
Z2	21.88	9.44	8.01	22.15	0	Z2	13.14	6.14	4.26	14.12	0
Z3	0	17.90	9.99	10.48	9.60	Z3	0	9.65	5.53	5.98	5.63
Z4	6.57	8.61	24.64	20.69	22.18	Z4	0	5.80	14.14	13.85	13.09
Z5	23.04	21.67	17.05	20.69	21.89	Z5	13.45	12.36	8.24	11.87	13.23
Z6	10.87	10.47	22.82	22.29	0	Z6	0	0	13.44	13.94	0
R127R						R128R					
	T1	T2	T3	T4	T5		T1	T2	T3	T4	T5
Z1	0	2.82	0	4.26	0	Z1	0	1.51	0	2.07	0
Z2	8.48	4.23	3.61	8.18	0	Z2	4.60	2.12	1.84	0	0
Z3	0	7.13	0	4.56	3.61	Z3	0	0	2.15	1.95	2.14
Z4	0	4.85	11.27	9.36	7.79	Z4	0	2.08	5.23	4.60	4.84
Z5	0	9.43	6.72	9.44	9.60	Z5	0	0	2.89	4.84	4.61
Z6	0	0	9.31	10.22	0	Z6	0	2.22	5.03	4.91	0

Table 8.4: Exposures for the c58 reanalysis exposures (kg×days). Highlighted in red colors are the 14 detectors deemed viable for the c58 original analysis and during the reanalysis.

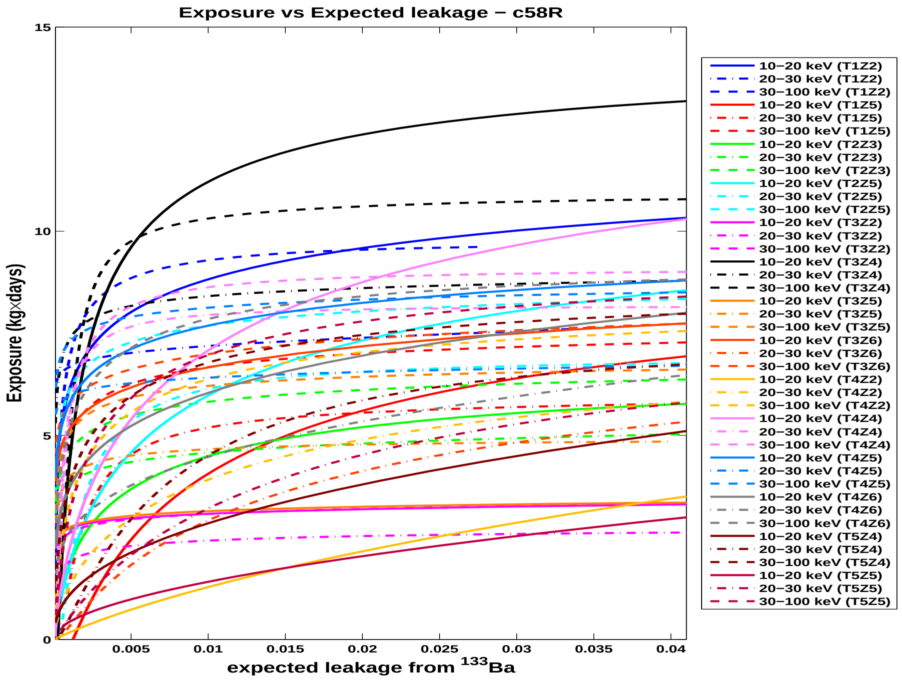

Figure 8.10: The spectrum-averaged exposure as function of the expected leakage (in terms of the number of leaked events) for the 14 Ge-ZIP detectors considered in the c58 reanalysis. Each color represents a single detector and different symbols for each color indicate the three energy bins of 10-20 keV, 20-30 keV and 30-100 keV.

In the subsequent development of the χ^2 timing cut, the second approach was used because it yields higher exposure for the same total expected leakage.

The total exposure and total expected leakage are obtained by summing individual detectors' exposures and expected leakages. Furthermore, the knowledge of the total exposure and total expected leakage is prerequisite to the simultaneous optimization of yield and timing cuts. The optimization was implemented as follows:

1. The cuts may be optimized for a given total expected leakage by requiring that the first derivatives of the spectrum-averaged exposure with respect to the expected leakage $\frac{d\mathcal{S}}{d\mathcal{L}}$ are equal for each detector and every energy bin (slopes of the curves in Figure (8.10)). The reason why we require the slopes to be equal is that we want the change in exposure over the change in leakage to be the same for all energy bins in every detector. If the slopes are not the same, we could increase the total exposure for the same leakage by tightening the cut with flatter slope while loosening the cut with the larger slope. So, choosing the same slope is equivalent to distributing the leakage in all these bins while we maximize the exposure.

2. Find the best total expected leakage (or equivalently the best slope) by choosing the exposure-leakage combination that yields smallest expected upper limit.

Figure (8.11) shows a cartoon that illustrates how the total exposure and total expected leakage were calculated. To determine the different cut positions, we use the slopes as a function of the expected leakage. The slopes are defined as the first derivative of the spectrum-averaged exposure with respect to the expected leakage. Since the exposure and the expected leakage are both functions of the cut position η, the above expression can also be written in the following form:

$$\mathbf{m} = \frac{d\mathcal{S}}{d\eta} \cdot \frac{d\eta}{d\mathcal{L}} = \frac{\left(\frac{d\mathcal{S}}{d\eta}\right)}{\left(\frac{d\mathcal{L}}{d\eta}\right)}, \tag{8.21}$$

where the chain rule has been applied to get the analytic form of the first derivative using the functional forms used to fit the exposure $\mathcal{S}$ and the expected leakage distribution tails $\mathcal{L}$. The illustration shown in Figure (8.11) is for a single detector with three energy bins employed to make the cut energy dependent. The curves of the slopes as a function of cut position, shown in Figure (8.12), were used to set the combinations of cuts.

To calculate the total exposure $\mathcal{S}$ and total expected leakage $\mathcal{L}$ for different detector-dependent cut positions, about 900 values of the slope, ranging from 10 to 100 in steps of 0.1, were used. For a selected slope, the expected leakage for each single energy bin was determined by a simple projection of the intersection points to the x-axis, call this $\mathcal{L}_e(z)$ (with $e = 1, 2, 3$ indicating the three energy bins and z refers to the ZIP detectors) as illustrated in the cartoon shown in Figure (8.11). Knowing the dependence of the expected leakage as a function of the cut position, the latter can be determined. Finally, using the exposure curves as a function of the cut position, the exposure $\mathcal{S}_e(z)$ can be calculated. The total exposure and total expected leakage for the chosen slope is given by $\sum_{\{e,z\}} \mathcal{S}_e(z)$ and $\sum_{\{e,z\}} \mathcal{L}_e(z)$, which is represented by a single dot shown in lower bottom-left plot of Figure (8.11).

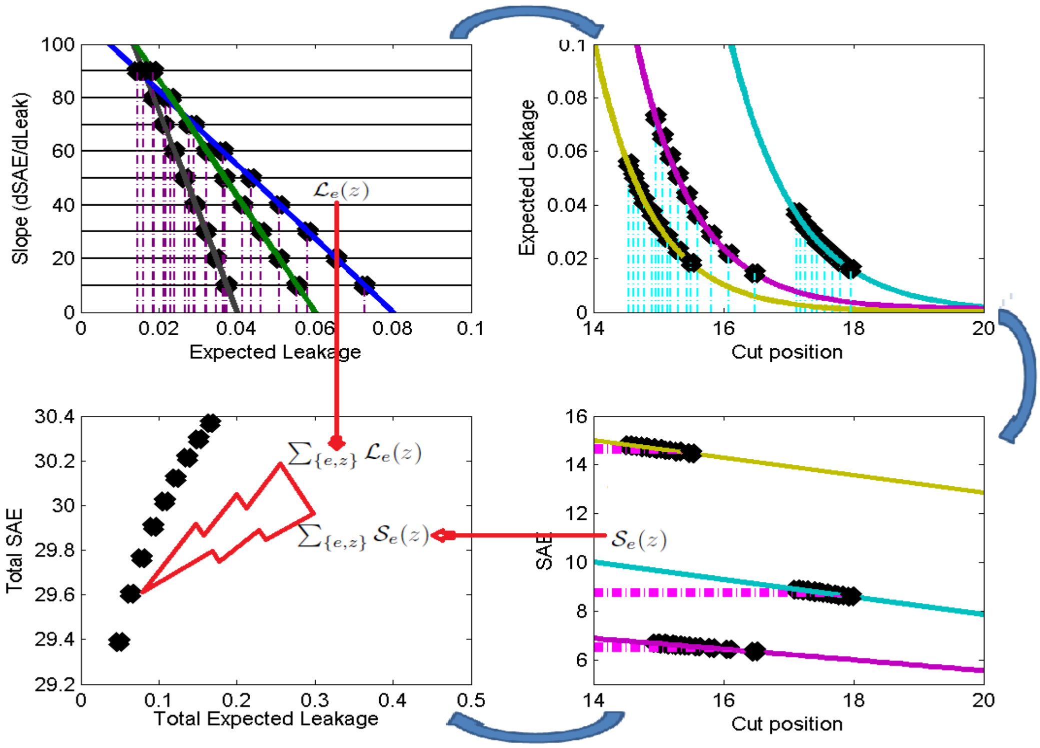

Figure 8.11: Cartoon illustrating the scheme used to calculate the total spectrum averaged exposure and the total expected leakage. The three colors used in the figure represents the three energy bins for a single detector. The scheme shown in the cartoon uses the slopes to compute the total exposure and total leakage. Starting from the top-left and proceeding to top right, bottom-left and bottom-right, this computation proceeds as follows: (1) pick a slope $\mathbf{m}$ and determine the expected leakage $\mathcal{L}_e(z)$ with e representing the three energy bins $10-20$ keV, $20-30$ keV, and $30-100$ keV. (2) use the expected leakages $\mathcal{L}_e(z)$ computed in step (1) to determine the cut positions $\eta_e(z)$. (3) knowing how the exposures vary as functions of the cut positions, one can determine the exposures $\mathcal{S}_e(z)$. Although illustrated only for one detector, steps (1)-(3) were carried out for the 14 detectors used in this analysis. Finally, (4) summing all the exposures $\sum_{\{e,z\}} \mathcal{S}_e(z)$ and leakages $\sum_{\{e,z\}} \mathcal{L}_e(z)$ to get the total exposure and total leakage represented by the black dot in the bottom-left plot. By repeating the steps (1)-(4), the curve of the total exposure as function of the total leakage can be determined.

8.6.4 Optimization

The values of the total expected leakage and the exposure as functions of cut position are used in this section to define an optimized χ^2 timing cut. At the same time, the nuclear-recoil (NR) acceptance band, in the ionization yield ($\mu_{NR} - 2\sigma_{NR} \leq \mu_{NR} \leq \mu_{NR} + 2\sigma_{NR}$), can be re-defined by simultaneously optimizing both the timing and yield cuts. The whole optimization recipe defines the timing and yield cuts that optimize the experiment's expected sensitivity.

8.6.5 Yield cut

The standard CDMS analysis uses a nuclear-recoil (NR) band to describe the expected WIMP-acceptance region. This signal region is typically defined by requiring the ionization yield to be within $\pm 2\sigma$ from the mean of the NR

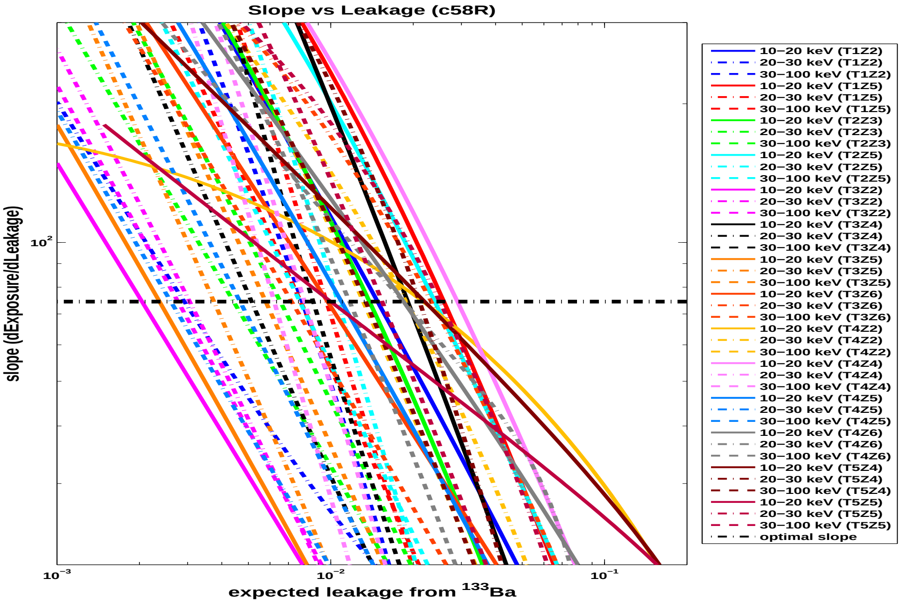

Figure 8.12: Slope as function of the expected leakage. The black dot-dashed horizontal line corresponds to the optimal set of timing-cut positions.

band. However, no prior study has been done to determine if this NR-band definition is optimal. The traditional NR band was designed to have high nuclear-recoil acceptance efficiency, about 95%. Moreover, this choice of $\pm 2\sigma$ was arbitrary.

During the original c58 analysis, I performed a study that indicated that $\pm 2\sigma$ NR-band is, in fact, not optimal. The optimized yield cut for this study was determined as $[-1.9, 1.5]\sigma$, with 90.45% NR band acceptance efficiency [448, 449]. This study, however, was not completed in time to be applied to the 2010 *Science* publication [425].

Optimizing the nuclear acceptance region is important in order to limit the low-yield surface events that droop into the NR-band as shown in Figure (8.13). The high-yield side of the NR band is more polluted from these low-yield background events than the low-yield side. Consequently, an asymmetric NR-band is optimal. In the past CDMS analyses, the width of the nuclear-recoil band was considered to be 2σ above and below the mean of the band, as already mentioned in the previous paragraph, this choice was somewhat arbitrary.The optimal band may not have the width that we have always used and may not necessarily be symmetric.

Figure (8.13) shows the cumulative distribution of the low-yield leakage as function of the $y*$ variable defined by

$$y* = \frac{yic - \mu_{NR}}{\sigma_{NR}}. \tag{8.22}$$

where yic is the ionization yield for events inside the inner charge electrode, μ_{NR} and σ_{NR} are the mean and standard deviation of the nuclear-recoil band. For the traditional $\pm 2\sigma$ NR-band, $y*$ is bounded between -2 and $+2$.

In the WIMP-search data, low-yield events come from betas (not present in Ba) and gamma interactions at the surface of the detectors, also giving rise to singles and multiples. The yield distribution of beta singles and multiples are roughly similar, so the WIMP-search multiples used in this study are appropriate to inform us about the yield distribution of WIMP-search singles.

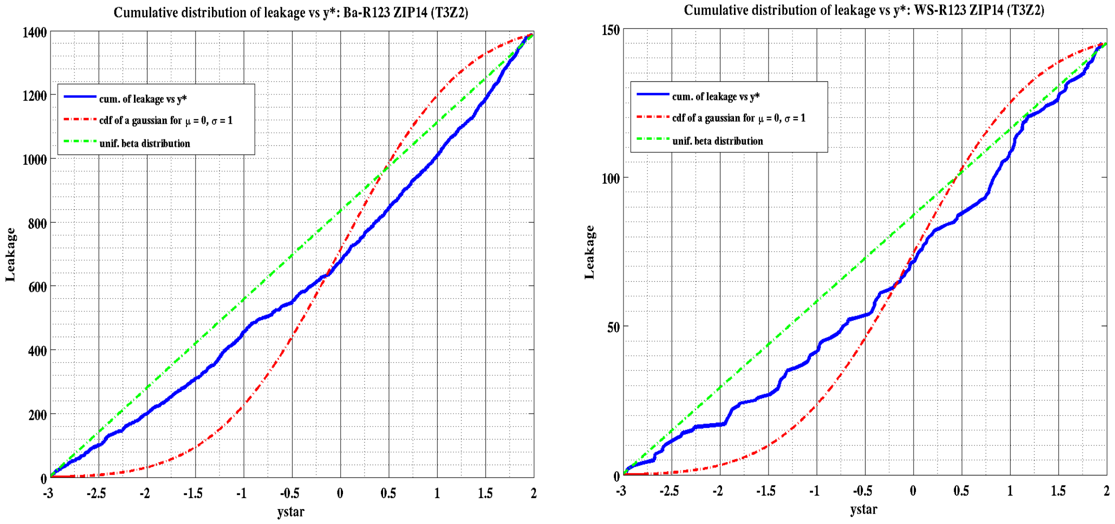

Figure 8.13: The cumulative distribution (CDF) of the leakage (blue) as function of the $y*$ variable introduced in equation (8.22) as observed using the R123-124 during the first study I conducted. On the left is the leakage estimated from the Ba calibration while on the right is the leakage calculated using WIMP-search data. Both distributions indicate that there are more leakage events at $y* > 0$ than expected for uniform distribution (green dotted) and more leakage events at $|y*| > 1$ than expected for nuclear recoils (red dotted CDF for a Gaussian distribution of mean 0 and standard deviation of 1), suggesting that the higher side of the nuclear-recoil band is exposed to more leakage events than the lower side.

For a given yield cut, defined by a lower and upper edge (running from 0.1 to 2.5 with a step size of 0.1 in order to account for a wide range of NR-band definitions (possibilities), the neutron efficiency and the number of leakage events (WIMP-search multiple scatters: WSMS) were calculated using the WIMP-search data. For each of these yield cuts, the neutron efficiency was calculate assuming the neutron data is gaussian distributed, i.e.

$$\epsilon(\zeta) = \frac{1}{\sqrt{2\pi}} \int_{-l}^{u} e^{-y^2/2} dy, \tag{8.23}$$

where $\zeta = (l, u)$ is the yield cut (i.e. $yic \in [-l, +u]\sigma$); l and u are the lower and upper edges of the nuclear-recoil band (which are allowed to vary between 0.1 to 2.5 for both in bins of 0.1).

Figure (8.14) shows the plot for the neutron efficiency ϵ as a function of the leakage l expressed in terms of the number of WIMP-search multiple scatters. The black dot indicates the efficiency ϵ and the leakage l for the traditional yield cut, i.e. the $\pm 2\sigma$ NR-band.

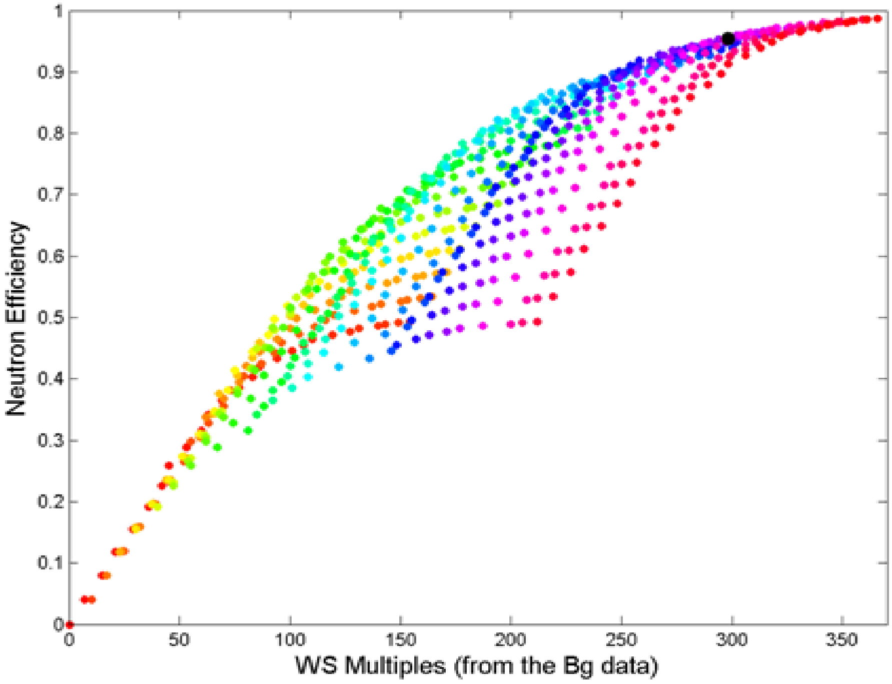

Figure 8.14: Neutron efficiency as function of WIMP-search multiple scatters. Each dot represents a yield cut. The traditional $\pm 2\sigma$ NR band with a neutron efficiency of 95.45%, shown in black dot, has a total WIMP-search multiple leakage of 298 events.

8.6.6 Simultaneous optimization

The simultaneous optimization scheme used in this analysis assumes that both the timing and the yield cuts are completely uncorrelated (or independent). Up to this point, the $\pm 2\sigma$ yield cut for the nuclear-recoil band is used. Moreover, this yield cut is not optimal. In order to find an optimal NR-band, a simultaneous optimization scheme that uses both the yield and the timing cuts is developed. In the definitions (8.24) and (8.25), the following terminology are used:

- $\mathcal{L}(\vec{\eta}, \zeta)$: the final expected leakage of the timing cut η and yield cut ζ.
- $\mathcal{L}_{tc}(\vec{\eta})$: the expected leakage of the timing cut η. This leakage was calculated according to the scheme described in the cartoon shown in Figure (8.11).
- $\mathcal{L}(\pm 2\sigma)$: the expected leakage of the traditional yield cut. This leakage is the number of WIMP-search multiple scatters inside the nuclear-recoil band.
- $\mathcal{L}(\zeta)$: the leakage of the yield cu, i.e. the number WIMP-search multiple scatters inside the $[-l, +u]\sigma$ NR-band calculated using the WIMP-search data.
- $\mathcal{S}(\vec{\eta}, \zeta)$: the final spectrum-averaged exposure of the timing cut η for a defined yield cut ζ.
- $\mathcal{S}_{tc}(\vec{\eta})$: the final spectrum-averaged exposure of the timing cut η only calculated according to the scheme

described in the cartoon shown in Figure (8.11).

- $\mathcal{S}(\zeta)$: the neutron efficiency for a given yield cut ζ calculated by assuming the neutron calibration data is Gaussian distributed. This is the efficiency of the $[-l, +u]\sigma$ NR-band, whose the nominal efficiency is given by Equation (8.23).
- $\mathcal{S}(\pm 2\sigma)$: the neutron efficiency for the standard yield cut definition of $\pm 2\sigma$, corresponding to 95.45%.

The final leakage and the final spectrum averaged exposure of the timing and yield cuts were then calculated using the following formulas:

$$\mathcal{L}(\eta, \zeta) = \mathcal{L}_{tc}(\eta) \cdot \frac{\mathcal{L}(\zeta)}{\mathcal{L}(\pm 2\sigma)}, \tag{8.24}$$

$$\mathcal{S}(\eta, \zeta) = \mathcal{S}_{tc}(\eta) \cdot \frac{\mathcal{S}(\zeta)}{\mathcal{S}(\pm 2\sigma)}, \tag{8.25}$$

where $\mathcal{L}(\pm 2\sigma) = 298$ events and $\mathcal{S}(\pm 2\sigma) = 95.45\%$ according to Figure (8.14).

Using the total exposure $\mathcal{S}_{tc}(\eta)$ and the total expected leakage $\mathcal{L}_{tc}(\eta)$ calculated using the procedure illustrated in Figure (8.11) and the relative efficiencies and the leakages of the yield cuts shown in Figure (8.14), the final leakage and exposure of both the timing and yield cuts were determined and used to compute the experimental sensitivity defined as

$$s = \frac{N90(\mathcal{L}(\eta, \zeta))}{\mathcal{S}(\eta, \zeta)}. \tag{8.26}$$

where N90 is an approximation of the 90% confidence level Poisson upper limit. This approximation was already discussed in chapter 3 and is given by Equation (3.57).

The result for the simultaneous optimization is shown in Figure (8.15), where each curve indicates a single yield cut while the timing cut is varied. The set of timing and yield cuts that optimizes the sensitivity is indicated by the blue solid curve overlaid with a thicker dashed black line, yielding an optimal NR-band defined as $-1.9 \leq y* \leq 1.8$.

The target leakage

The total leakage in a timing cut analysis is normally understood as the sum of the leakage contributions from all detectors considered in the analysis. As in a counting experiment, this total leakage, oftentimes referred to as target leakage, has to be defined in such way that the signal-to-background ratio ($\frac{S}{B}$) is high. Since the WIMP signal is determined by the spectrum averaged exposure, the choice of the target leakage has a direct impact on the total signal the experiment might measure. However, the total WIMP exposure cannot be the only criterion for choosing the target leakage since leakage necessarily increases with exposure. As Matt Fritts mentioned in his thesis "If the leakage is set very low, the exposure will be unacceptably small; if it is set too large, the presence of surface electrons recoils (SERs) in the WIMP signal region will weaken any conclusion that can be drawn from the result" [382], meaning that we really want a background free experiment. Since a background free experiment is extremely hard to achieve in practice, the only thing we can do is to keep these backgrounds extremely as low as we can while we maximize the sensitivity of the experiment. As shown in Figure (8.15), from our simultaneous

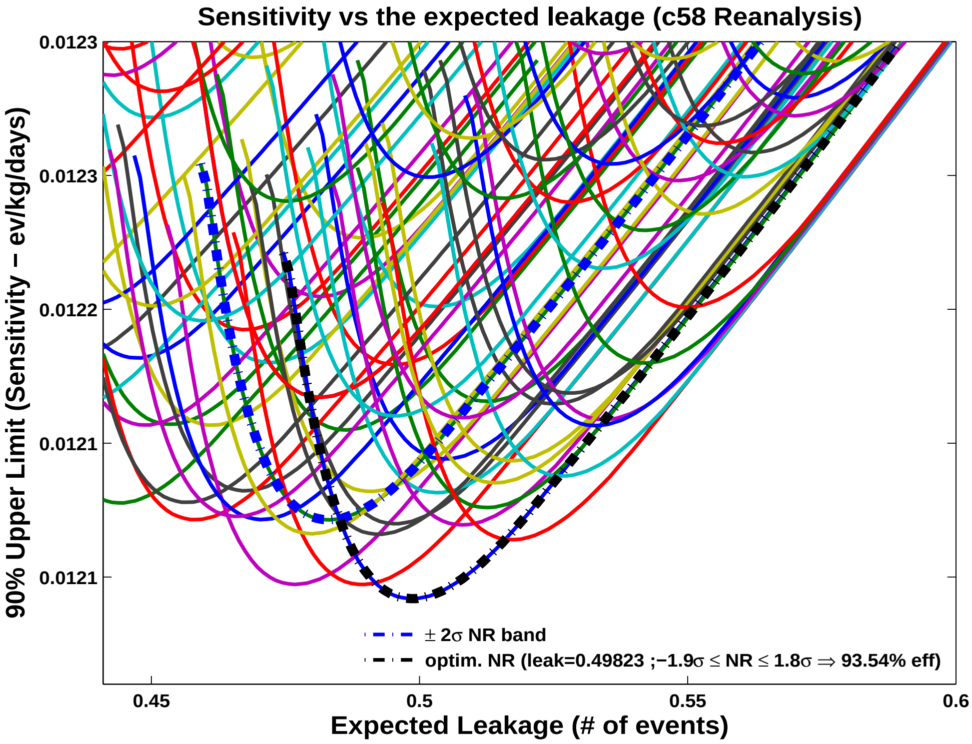

Figure 8.15: Sensitivity as function of the expected leakage. Each curve in this plot represents a fixed yield cut while the timing cut varies. The sensitivity for the standard yield cut is shown in green overlaid with a ticker dashed blue line, while the optimized sensitivity is the blue solid curve overlaid with a ticker dashed black line. This plot also shows that, as indicated in the legend, the optimal yield cut is given by $-1.9 \leq y* \leq 1.8$.

optimization scheme, the background dependent sensitivity curve has a minimum at an expected leakage of 0.499 events, the leakage at which the sensitivity is optimized. Consequently, the target leakage can be taken as the leakage for which the sensitivity is optimal.

This target leakage defines each detector's optimized timing cuts. In order to find these cuts, we use the slope calculated as a function of the expected leakage. The optimal slope is the slope at which the target leakage can be achieved (the black dash line in Figure (8.12) represents that optimal slope). The optimal slopes intersect each energy bin of each detector at a single point corresponding to the expected leakage. As a consistency check, the sum of these expected leakages add up to the target leakage of 0.499 events. Using the cartoon in Figure (8.11), the cut positions were determined as well as the exposure (after cuts) for each energy bin in each detector. This cut is named cChi2Edep_c58.

Figure (8.17) shows the total exposure as function of the total expected number of leakage events. The simultaneous optimization, as shown in the same figure, is better than the equal-leakage cut. The advantage of the optimized timing cut is that it uses the slope to determine the expected leakage for each energy bin in each detector, and so the cut positions. This optimization scheme chooses one (optimal) slope for all detectors and that results in tighter cut positions in some energy bins and detector, and looser cuts in others, so that the

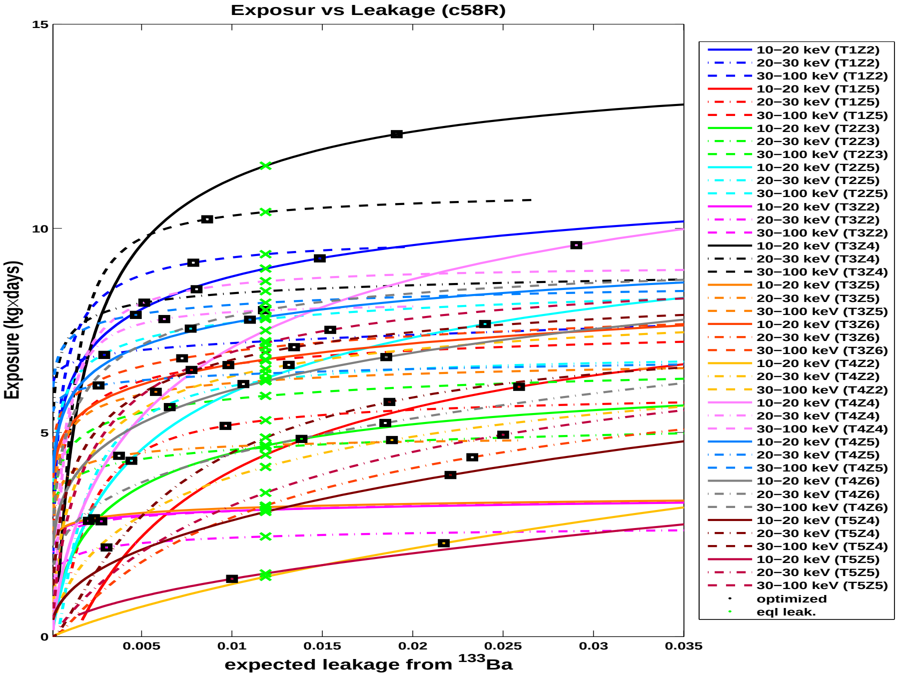

Figure 8.16: Exposure as function of the expected leakage for the 14 detectors (and 3 energy bins) used in this analysis. The black squares define the optimized timing-cut positions are and the green x's are the cut positions for equal-detector leakage.

expected sensitivity is optimized.

The energy dependence of the timing cut (cChi2Edep_c58) efficiency was calculated using five 5 keV bins from 5 to 30 keV, two 20 keV bins from 30 to 70 keV and one bin from 70 to 100 keV. The two lowest energy bins were added to determine the trend of the efficiency plot below our nominal recoil-energy threshold of 10 keV. Since this timing cut was binned into three energy bins of 10-20 keV, 20-30 keV and 30-100 keV, the energy bins for the efficiency estimates were carefully chosen in order not to mix data belonging to separate energy ranges. The data were fit using the following functional form:

$$g(E) = A_1 + \frac{A_2 E}{(E + A_3)^{A_4}} + A_5 e^{-A_6 E} + A_7 E. \tag{8.27}$$

T4Z2 was the exception, and is better modelled using

$$g(E) = B_1 \cdot (1 + \mathrm{erf}(B_2(E - B_3))) \cdot e^{-B_4 E}. \tag{8.28}$$

$A = [A_1, ..., A_7]$ and $B = [B_1, ..., B_4]$ are the fit parameters calculated using a MATLAB minimization routine. Figure (8.18) shows the timing-cut efficiency for a representative detector. For all the other detectors, the efficiency plots and fits are shown in Appendix C.

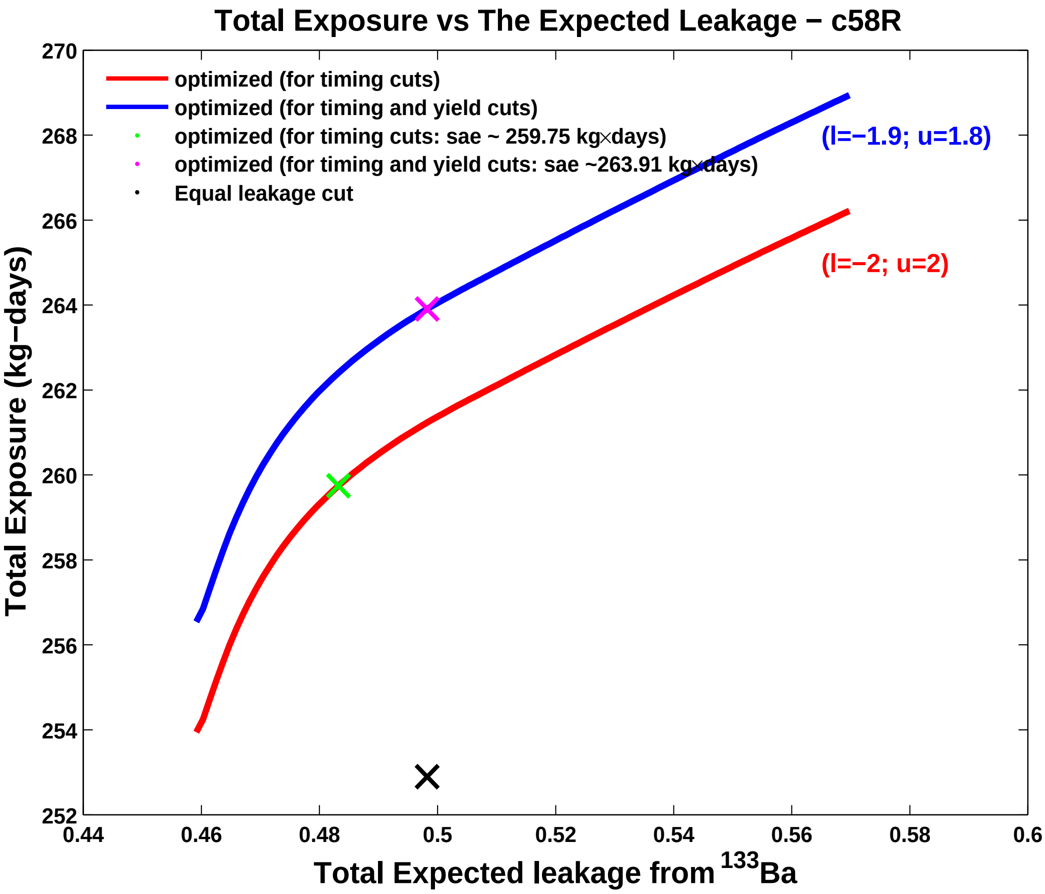

Figure 8.17: Total exposure as function of the total expected leakage. The blue curve is the exposure obtained for the optimized $l = -1.9$, $u = 1.8$ yield and timing cuts. The red curve is the exposure vs. the expected leakage for the traditional $\pm 2\sigma$ yield cut and optimized timing cut. The magenta x indicates the total exposure and the expected leakage that maximizes the expected sensitivity, and the black x shows the total exposure for the equal-leakage timing cut.

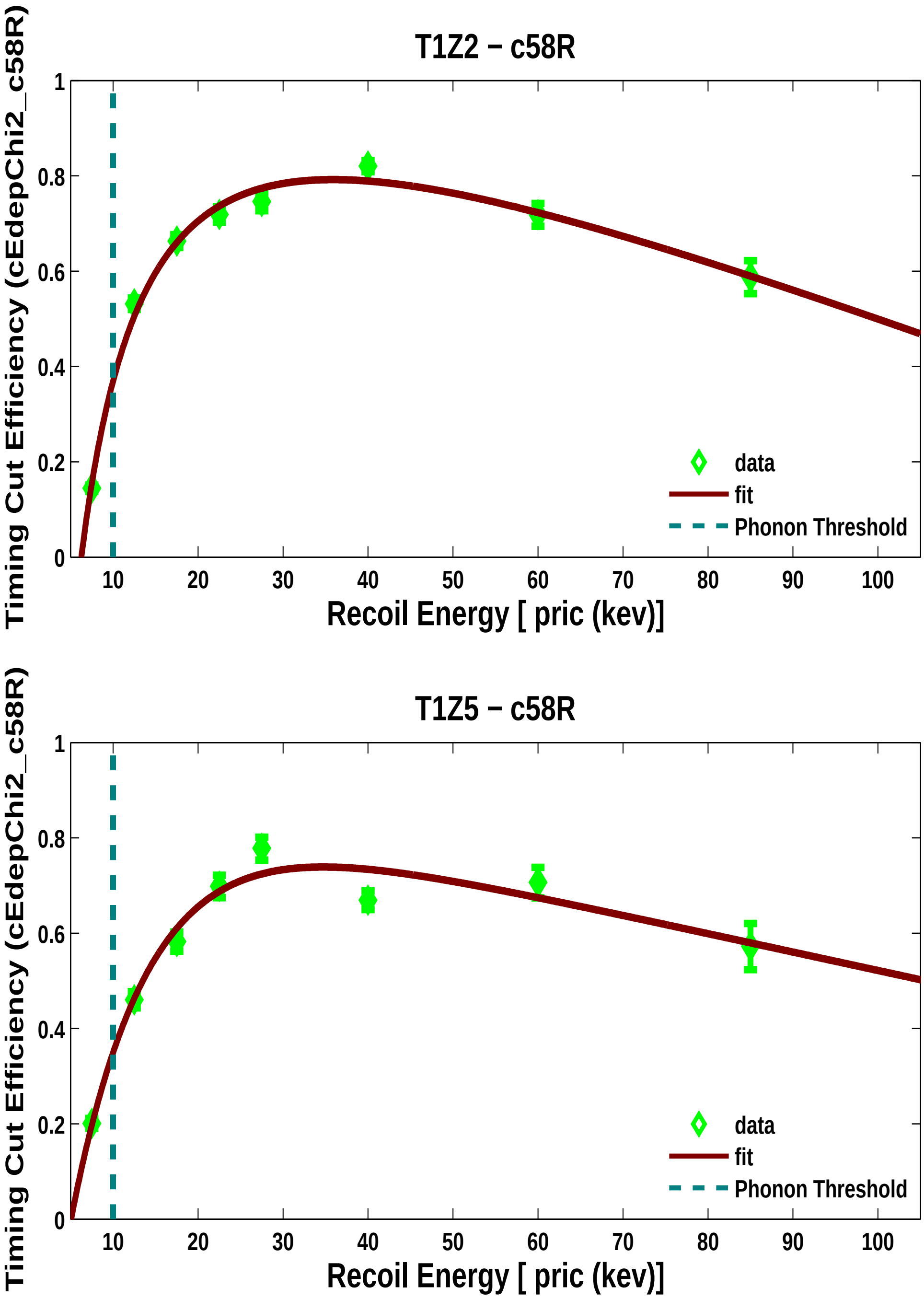

Figure 8.18: The optimized χ^2 timing-cut efficiency as function of energy for T1Z2 and T1Z5. The green error bars represent the fraction of ^{252}Cf neutrons data passing the cut while the dark red solid line is the fit to the data obtained using the function form given by Equation (8.27). The vertical dashed cyan line is the phonon energy threshold. The fits for other detectors are shown in Appendix C.

Combined Efficiency

The combined efficiency is calculated by the combination of the data-quality cut efficiencies and the timing-cut efficiency. A detector's overall efficiency is obtained by multiplying the respective efficiencies of each cut (energy dependent and energy independent alike).

Figure (8.19) show the efficiencies of the quality cuts, nuclear-recoil band (discussed in section 7.7.1), the fiducial volume (section 7.6.1) and the timing cut discussed in the next chapter (chapter 8). The efficiency of the quality cut includes the efficiencies of all the following energy independent-cuts: phonon standard deviation cut (section 7.5.2), phonon good start times (section 7.5.3), non negative phonon cut [318], the phonon saturation cut [318], the glitch cut [318], the veto cut (section 7.6.3), the MINOS neutrino beam cut and the singles cut (section 7.6.2), as well as the energy dependent cuts: the phonon trigger efficiency, the charge threshold (section 7.5.4), the surface events selection cut (cBelowER) [318] and the charge χ^2 cut (section 7.5.1).

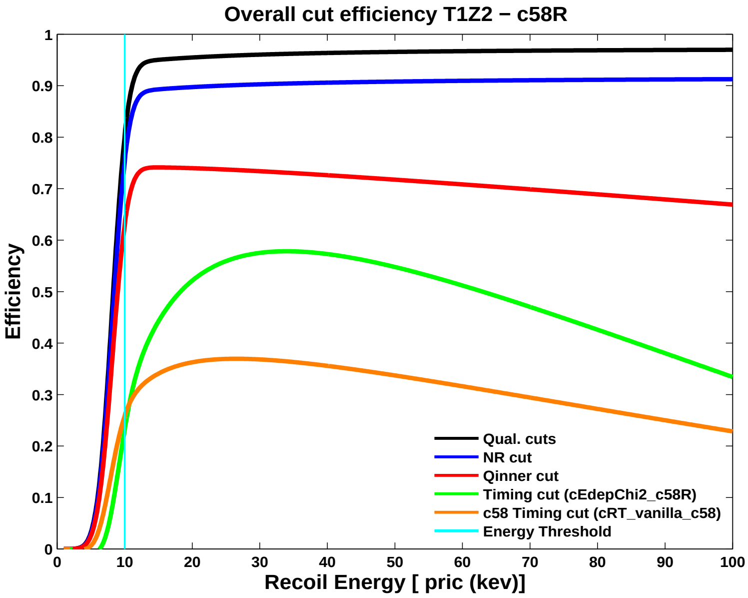

Figure 8.19: T1Z2 cut efficiencies for the c58 reanalysis. Shown in black is the efficiency all the basic data-quality cuts, the blue curve shows the nuclear recoil efficiency, in red is shown the the fiducial-volume cut efficiency and in green is plotted the efficiency of the χ^2 optimized timing cut analysis. Shown in color orange, is the c58 analysis timing cut efficiency. Plots for other detectors are shown in Appendix G

8.6.7 Signal efficiency

The total experimental efficiency is an average of the individual detector efficiencies, weighted by their relative exposure MT (product of masses and live times). Figure (8.20) plots this total efficiency as a function of recoil energy, indicating the cumulative contributions of various cuts. The net efficiency of the c58 analysis is also shown in Figure (8.20), orange color, while the net efficiency of the optimized timing cut of this analysis is shown in dark red color. The c58 timing cut is slightly higher than the optimized timing cut around the threshold energy, specifically in $10 - 14$ keV range. Outside this energy range, the χ^2 optimized timing cut efficiency (cChi2Edep_c58R) is higher than the c58 timing cut (cRT_vanilla_c58) It is worth mentioning that the largest costs in WIMP detection efficiency come from the fiducial-volume and surface-event rejection cuts.

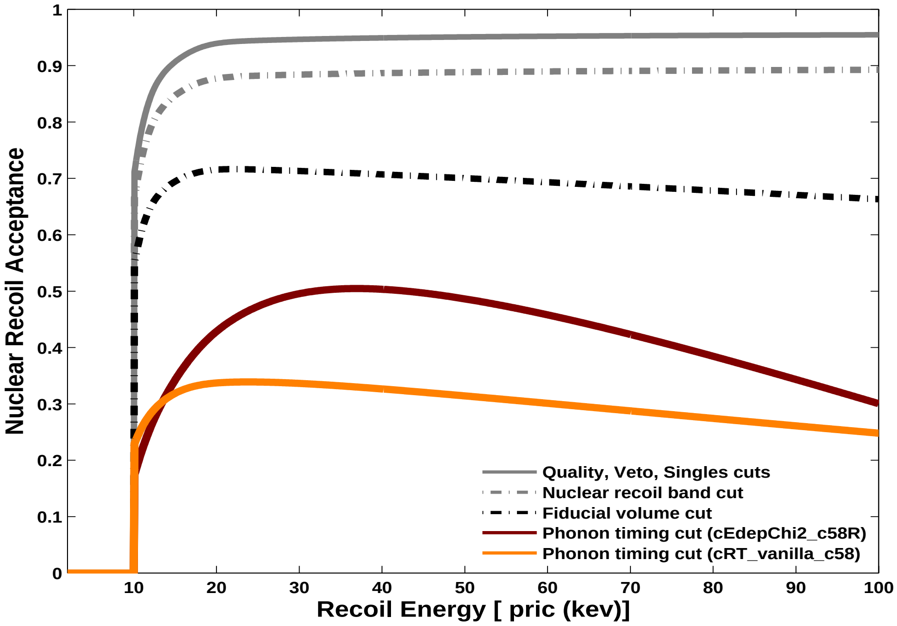

Figure 8.20: Overall analysis efficiency for the c58 reanalysis after all detectors are combined and weighted by their respective exposures. Shown in solid grey is the efficiency of all the basic data-quality cuts. The dashed grey curve shows the efficiency after adding the nuclear recoil band cut. The curve in dashed black color is the efficiency obtained after adding the fiducial-volume cut. Finally the efficiency curve shown in dark red is the overall efficiency of this analysis including the χ^2 timing cut analysis. The resulting overall efficiency of the χ^2 optimized timing cut is about 50% at 30 keV. Shown in color orange, is the original c58 analysis efficiency.

8.7 WIMP Search Results

The entire CDMS analysis procedure is carried out blindly, i.e. all the quality cuts, and more importantly the surface-event rejection cuts, are created and frozen before applying them to an independent data set, the WIMP-search data. The whole analysis streamline is blind in the sense that a blinding cut is created and applied to the WIMP-search data. This latter cut masks all signal events located inside the nuclear-recoil band (or simply the signal region). This procedure is strictly followed and applied by the collaboration in order to avoid bias.

In this section, I show and discuss the results of the blind analysis described in section (8.6). The expected surface-event background for the c58 reanalysis is described here as well. A detailed description of the cosmogenic neutron background for the current exposure is not considered, but is discussed extensively in the theses of Z. Ahmed [316] and T. Bruch [317]. This section starts with a description of the unblinding procedure, post-unblinding checks and then discuss the final results. Zero WIMP candidate events are observed in the signal region for the energy-dependent χ^2 analysis, and an upper limit on the WIMP-nucleon elastic cross section is determined as a function of WIMP mass. This limit on the spin-independent WIMP-nucleon cross section is $1.96 \times 10^{-44}\,\mathrm{cm}^2$ for a WIMP mass of 60 GeV/c^2 (which is $\sim 50\%$ lower than the original c58 analysis limit of $3.8 \times 10^{-44}\mathrm{cm}^2$ [425]).

8.7.1 Pre-unblinding checks

Before applying the surface-event rejection cut to the WIMP-search data and un-masking the nuclear-recoil band, it's important to perform few a sanity checks in order to ensure the performance of the surface-event rejection using an independent data set. One first check that was performed was to check that the number of nuclear-recoil single scatters N_z failing the timing cuts roughly matched the number that was predicted. The second check was to use WIMP-search data estimate number of the expected leakage surface events into the signal region. In addition to checking that estimate from the Barium calibration and WIMP-search data are consistent, the data are all combined to form our best estimate of the expected leakage. The leakage estimate is computed using multiple scatter events inside and outside the nuclear recoil-band in the WIMP-search data. Although the leakage may vary wildly from detector to detector, it is expected that WIMP-search multiples are likely distributed similarly to the WIMP-search singles. Therefore using this sample of events to estimate the leakage will give us a pretty good idea of how much leakage is expected for a particular surface-event rejection cut.

Three different methods were used to compute the leakage estimate. Although I will briefly discuss them below, these procedures were first applied during the original c58 analysis by Z. Ahmeed, D. Moore, M. Fritts and O. Kamaev [447] and are also discussed in the dissertations of Z. Ahmed [316] and M. Fritts [382]. This method uses beta multiples inside and outside the NR band and accounts also for face distribution systematics.

The starting formula for computing a leakage estimate is given by a revised form of equation (8.17), which can be simplified to

$$n = \sum_z N_z \cdot \left(\frac{b_z}{B_z}\right), \tag{8.29}$$

where where n is the expected number of WIMP-search nuclear-recoil single scatters passing a given timing-cut (summed over all detectors), N_z is now the number of nuclear-recoil single scatters *failing* the timing-cut (previously N_z stood for the total number passing or failing the timing cut) and the index z refers to a given ZIP detector. The ratio $\left(\frac{b_z}{B_z}\right)$ is an estimator for the cut performance in terms of a pass-fail ratio, b_z (B_z) is the number of surface events passing (failing) the timing cut. This formula statistically decouples the number of nuclear-recoil singles passing or failing surface-event rejection cut from the total number of WIMP-search singles. The methods exploited to determine the expected leakage are described below:

1. Method 1:

   The leakage can be estimated by calculating the pass-fail ratio of surface-event multiple scatters inside the nuclear-recoil band (NRMS) and multiply it by the expected number of nuclear-recoil single scatters (NRSS) for each detector, and finally summing over all detectors. This approach assumes that multiples and singles scatters are distributed identically. This method has the disadvantage of poor statistics and, additionally, it cannot properly account for the leakage estimate for the bottom, exterior detectors (such as T3Z6 and T4Z6) since all multiples on these detectors will be phonon side, which biases the leakage estimate low because charge-side betas have higher passage fractions. This method uses Equation (8.29) as is to get the leakage estimate.

2. Method 2:

   Given that events at low yield are more likely to be surface events on the phonon side rather than the charge side events, and that the phonon-side events are significantly less likely to leak past surface-event rejection cut, the leakage passage fractions can alternatively be estimated using the wide-beta-multiples sample located 5σ below the electron-recoil (ER) band but outside the nuclear-recoil band for the charge and phonon sides separately. These fractions are multiplied with the best estimates of the face distributed NRSS. For the bottom exterior detectors, since charge-side events cannot be tagged, it is assumed that all singles in the wide beta region are charge side. This is conservative since it slightly overestimates the number of charge-side events, which have higher passage fraction than phonon side events. Equation (8.29) is modified to reflect the extra input for this method:

   $$n_z = N_z \cdot \left(f_p \frac{p_z}{P_z} + f_q \frac{q_z}{Q_z} \right) \tag{8.30}$$

   where f_p and f_q (with $f_p + f_q = 1$) represent the phonon-side and charge-side scaling factors and reflect the face distributions measured using c34 NR multiples (and found to be consistent with c58) [453]. The values of f_p and f_q are listed in Table (8.5). The terms p_z (P_z) and q_z (Q_z) are the number of phonon-side and charge-side events passing (failing) the surface-event rejection cut.

   The advantages of method 2 are better statistics and the ability to use single scatters to estimate the passage fraction and accounts for the systematic difference in passage fraction between detector faces. The disadvantage of this method, however, is that the fraction of singles that are phonon-side vs charge-side is different at different yield and energy, therefore they must be corrected for. This approach fails to take into account the systematic differences between the wide-beta region and the signal region. Additionally, this method doesn't account for the energy dependence of the face distributions. Two extensions of this method that attempt to address shortcomings are discussed below.

3. Method 2+:

   Since there is a systematic difference in the energy spectra of wide betas and NRSS, the leakage passage fraction estimated using method 2 might be improved by incorporating energy dependence in a similar manner to the face distributions, by measuring the passage fraction in bins of energy. For method 2+, Two coarse energy bins are used: 10-30 keV and 30-100 keV, respectively referred to by low (l) and high

	Method 2	
Detector Name	f_q	f_p
T1Z2	0.3656	0.6344
T1Z5	0.3656	0.6344
T2Z3	0.3656	0.6344
T2Z5	0.3656	0.6344
T3Z2	0.1330	0.8670
T3Z4	0.1330	0.8670
T3Z5	0.1330	0.8670
T3Z6	0.8607	0.1394
T4Z2	0.1330	0.8670
T4Z4	0.1330	0.8670
T4Z5	0.1330	0.8670
T4Z6	0.8607	0.1394
T5Z4	0.1330	0.8670
T5Z5	0.1330	0.8670

Table 8.5: Scaling factors f_q and f_p used for the estimate of the expected leakage for Method 2 in the energy range of $10 - 100$ keV.

(h). Equation (8.29) is modified as follows:

$$n_z = N_z \cdot \sum_{e=(l,h)} \left(f_p^e \frac{p_i^e}{P_i^e} + f_q^e \frac{q_i^e}{Q_i^e} \right) = N_z \cdot \sum_{e=(l,h)} \sum_{f=(p,q)} S_{ef} \cdot B_{ef}. \tag{8.31}$$

N_z is the number of nuclear-recoil single scatters failing the timing cuts. This number is calculated using the number of expected NRSS failing the timing cuts scaled by the livetime ratio between c34 and c58. B_{ef} are the energy and face-dependent leakage passage fractions. Finally, S_{ef} are scaling factors that take into account the systematic difference in the energy and yield distributions between the calibration and WIMP search data [454]. This latter factor can be understood as the number which converts the barium leakage passage fraction B_{ef} into a WIMP-search expected leakage.

4. Method 2++:

A similar extension to method 2, an improvement to method 2+, uses three energy bins rather than two. For method 2++, the leakage estimates are divided into low (l), medium (m) and high (h) bins: 10 - 20 keV, 20 - 30 keV and 30 - 100 keV. Equation (8.31) is modified accordingly:

$$n_z = N_z \cdot \sum_{e=(l,m,h)} \left(f_p^e \frac{p_i^e}{P_i^e} + f_q^e \frac{q_i^e}{Q_i^e} \right) = N_z \cdot \sum_{e=(l,m,h)} \sum_{f=(p,q)} S_{ef} \cdot B_{ef}. \tag{8.32}$$

This method yields an estimate comparable to method 2++Ba, which is the leakage estimate obtained from the timing cut with the application of method 2++ using barium calibration data. The scaling factors for the three energy bins used for Method 2++ are shown in Table (8.6).

	Method 2++					
Detector Name	Ql	Qm	Qh	Pl	Pm	Ph
T1Z2	0.3060	0.0601	0.0929	0.1913	0.1148	0.2350
T1Z5	0.3060	0.0601	0.0929	0.1913	0.1148	0.2350
T2Z3	0.3060	0.0601	0.0929	0.1913	0.1148	0.2350
T2Z5	0.3060	0.0601	0.0929	0.1913	0.1148	0.2350
T3Z2	0.1313	0.0299	0.0119	0.2925	0.1463	0.3881
T3Z4	0.1313	0.0299	0.0119	0.2925	0.1463	0.3881
T3Z5	0.1313	0.0299	0.0119	0.2925	0.1463	0.3881
T3Z6	0.5110	0.0902	0.2104	0.0366	0.0314	0.1203
T4Z2	0.1313	0.0299	0.0119	0.2925	0.1463	0.3881
T4Z4	0.1313	0.0299	0.0119	0.2925	0.1463	0.3881
T4Z5	0.1313	0.0299	0.0119	0.2925	0.1463	0.3881
T4Z6	0.5110	0.0902	0.2104	0.0366	0.0314	0.1203
T5Z4	0.1313	0.0299	0.0119	0.2925	0.1463	0.3881
T5Z5	0.1313	0.0299	0.0119	0.2925	0.1463	0.3881

Table 8.6: Scaling factors used for the estimate of the expected leakage for Method 2++. Ql, Qm, Qh, Pl, Pm and Ph are the charge and phonon-side scaling factors for low, medium and high energy bins respectively of $10 - 20$ keV, $20 - 30$ keV and $30 - 100$ keV.

Leakage estimate results

The expected leakage was estimated using the events inside and outside the nuclear recoil band in the WIMP-search data according the recipes described by method 1, method 2, method 2+ and method 2++. These estimates were done for the interior and exterior detectors, then combined together to get the overall expected leakage. In order to get the uncertainties on the leakage estimates for various methods, an assumption that the data follow a binomial distribution was used. The two uncertainties represents the lower and upper bound uncertainties from the binomial distributions obtained from the various ratio of pass/faill leakage estimates (for phonon and charge-side events).

To test the performance of the timing cut, the leakage from method 2++Ba is compared against the leakage estimates obtained from the other methods. The leakage from method 2++Ba is the leakage estimate obtained from the timing cut using the ^{133}Ba calibration data. The leakage estimates calculated using $N_{z,2}$ were used as cross checks to the estimates obtained using $N_{z,1}$. Tables (8.7) and (8.8) show the results of the expected leakage for the various leakage estimate methods.

8.7.2 Results

Once the leakage estimate is calculated, the nuclear-recoil signal region is ready to be opened for the WIMP-search data. This step is called unblinding (or opening the box). The number of WIMP candidate events in the low-background data are the number of veto-anticoincident nuclear-recoil single scatters passing the timing cut together with the cut called cInsideNRChi2_c58. The latter cut is a version of the cut cWhatsInTheBox_c58R, with a tighter yield cut of $-1.9\sigma \leq y* \leq 1.8\sigma$ (as determined by the simultaneous optimization). After the

Interior Detectors		
	$N_{z,1}$	$N_{z,2}$
Metho1Ba	0.51+0.08 − 0.20	0.46+0.12 − 0.22
Metho1	1.21+0.08 − 0.20	0.95+0.40 − 1.16
Metho2	0.17+0.07 − 0.55	0.22+0.21 − 0.59
Metho2+	0.50+0.28 − 0.74	0.67+0.39 − 0.97
Metho2++	0.64+0.40 − 0.17	0.85+0.55 − 1.36
Metho2++Ba	0.42+0.10 − 0.10	0.47+0.10 − 0.10
Exterior Detectors		
Metho1Ba	0.15+0.07 − 0.20	0.17+0.12 − 0.2
Metho1	0.72+0.62 − 1.74	1.31+1.25 − 1.79
Metho2	0.28+0.15 − 0.31	0.36+0.52 − 0.77
Metho2+	0.15+0.06 − 1.06	0.17+0.08 − 1.27
Metho2++	0.18+0.11 − 1.98	0.18+0.12 − 2.04
Metho2++Ba	0.08+0.05 − 0.05	0.09+0.05 − 0.05

Table 8.7: Leakage estimates from various methods (Method 1, Method 2, Method 2+ and Method 2++). The leakage obtained by Method 2++Ba is the leakage of the timing cut using the ^{133}Ba calibration. $N_{z,1}$ and $N_{z,2}$ are the expected number of nuclear-recoil singles calculated according to two of the techniques described in section (8.6.1).

Combined expected leakage (Interior + Exterior Detectors)		
	N_1	N_2
Metho1Ba	0.325+0.05 − 0.14	0.32+0.08 − 0.14
Metho1	1.93+0.58 − 2.10	2.26+1.31 − 2.69
Metho2	0.45+0.17 − 0.63	0.58+0.56 − 0.97
Metho2+	0.65+0.29 − 1.29	0.84+0.38 − 1.60
Metho2++	0.82+0.41 − 2.30	1.03+0.56 − 2.45
Metho2++Ba	0.50+0.11 − 0.11	0.55+0.11 − 0.11
Best fit (1, 2++, 2++Ba)	0.501+0.090 − 0.108	0.567+0.106 − 0.109
chisq prob.	0.695 (0.706) (0.987)	0.568 (0.702)(0.981)

Table 8.8: The combine expected leakage for the χ^2 optimized timing cut. The best fits leakage is calculated from the leakage estimate from method1, method2++ and method2++Ba as well as the chi-square probabilities using $N_{z,1}$ and $N_{z,2}$.

application of these cuts, **no WIMP candidate events were observed**.

Two other timing cuts were also developed for the c58 reanalysis. The first is a traditional timing-cut analysis that uses only the phonon delay and rise time variables additively combining them to get a single discriminator (often referred to as the simple timing cut). This cut was developed during the original c58 analysis [447] and tuned for the reanalysis by Jianjie Zhang [451]. Tommy Hoffer used a neural network to develop the other timing cut [452]. Each alternative analyses resulted in two candidate events. One candidate (in T1Z5) was common to both analyses, while the neural network analysis resulted in a second event in T1Z5, and the simple timing analysis resulted in a candidate in T2Z3. My optimized timing cut developed in this analysis was chosen before the unblinding because of its better expected sensitivity. The events observed by the alternatives timing cut analyses are shown in the d_{χ^2} vs energy plane in Figure (8.22) and the optimized energy-dependent cut positions clearly demonstrate why these events are rejected by the energy-dependent χ^2.

As shown in Figures (8.22) and (8.23), the T1Z5 candidate event passing only the neural net cut has an ionization yield of $y = 0.204$ and a recoil energy of $E_R = 13.44$ keV and the candidate passing both the neural net and the simple timing cut has $y = 0.33$ with a recoil energy of $E_R = 12.30$ keV. This later candidate also passed the original timing cut, and it would have been a WIMP candidate event in my analysis if the energy dependence had not been taken into account because, as shown in Figure (8.22), at low energy, i.e. in the $10-20$ keV bin, significantly more leakage is expected for the same cut value. The advantage of the optimization is that it sets the cut position by minimizing the exposure in bins with worse expected leakage. The fact that the optimization distributes the total leakage in a such a way that the sensitivity is maximized, is equivalent to cutting hard in energy bins where leakage events are dominant.

An additional other WIMP candidate passed the simple timing-cut in detector T2Z3. This event, with an ionization yield $y = 0.332$ and a recoil energy $E_R = 10.81$ keV, is rejected by both the energy-dependent and independent χ^2 timing cuts due to its low $\chi^2_B - \chi^2_N = 17.405$ as can be noticed from the bottom plot in Figure (8.22).

Figure (8.21) illustrates the distribution of the WIMP-Search data in $\chi^2_B - \chi^2 N$ plan. In this plan, electron-recoil events are shown in dark cyan color while non-electron-recoils are shown in blues. Electron-recoils are considered to be events 3σ below the mean of the electron-recoil band to +Infinity. This definition is similar to selecting events above the **cBelowER_c58** cut which is defined as a selection of events laying 3σ below the mean of the electron-recoil band. Non-electron-recoils events, however, are a mixture of surface events and events that can potentially become event candidates if they pass both the timing cuts and the nuclear-recoil band cut (i.e. ionization yield cut). This plot is not very insightful due to lack of direct visible energy dependence. Figures (8.22) and (8.23) demarcates from Figure (8.21) due to such energy dependence which is also reflected by the way the optimized timing cut is implemented. A different version of the plot shown in Figure (8.22)is shown in ionization vs recoil energy plan and it is depicted in Figure (8.24). Events passing the rejection cut are shown in red dots and those failing the consistency cut are shown in black.

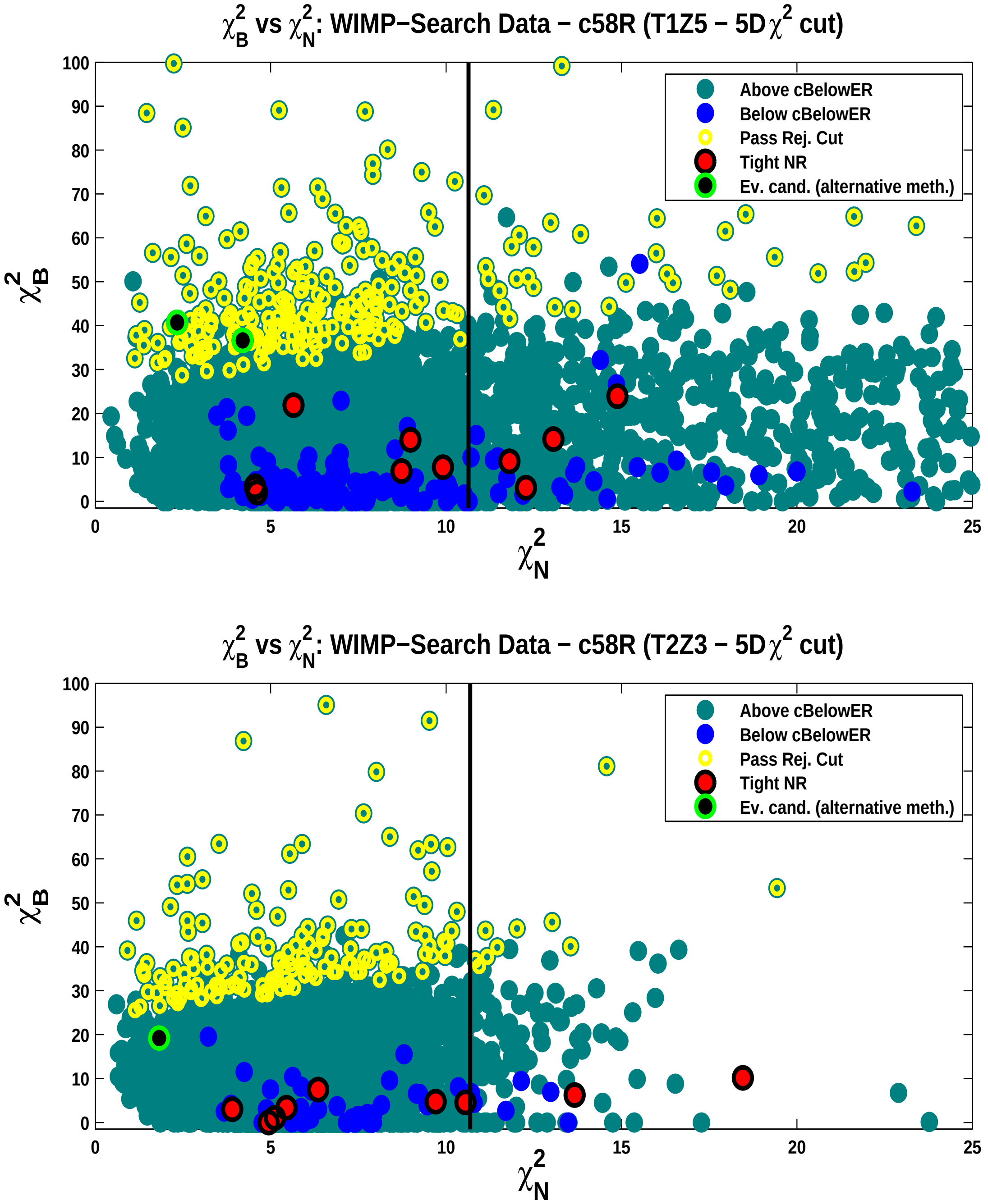

Figure 8.21: WIMP-Search distribution of χ^2_B as function of χ^2_N for T1Z5 (top) and T2Z3 (bottom). Events shown in dark cyan color represents events located above **cBelowER_c58** above the **cBelowER_c58** (representing mostly electron recoils events) while events in blue dots indicates non-electron-recoil events (which can either be surface events or event candidates for those laying inside the tight nuclear-recoil band). Events shown in red dots are WIMP-search events inside the tight nuclear-recoil band cut, i.e. the optimized nuclear-recoil band defined by a yield cut of $[l = -1.9; u = 1.8]$ while events in yellows dots are events shown passing the rejection cut. The green circle events with the black face represent events passing the alternative timing cuts developed during the reanalysis. The black vertical line show the consistency cut position. Plots for other detectors are shown in Appendix D.

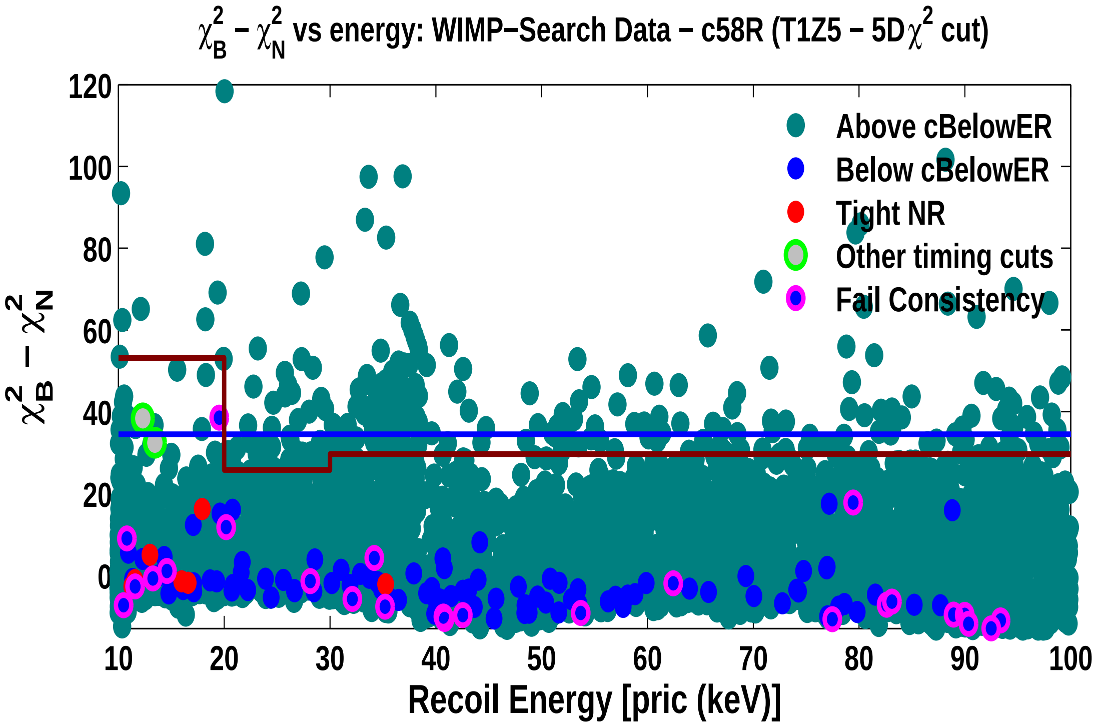

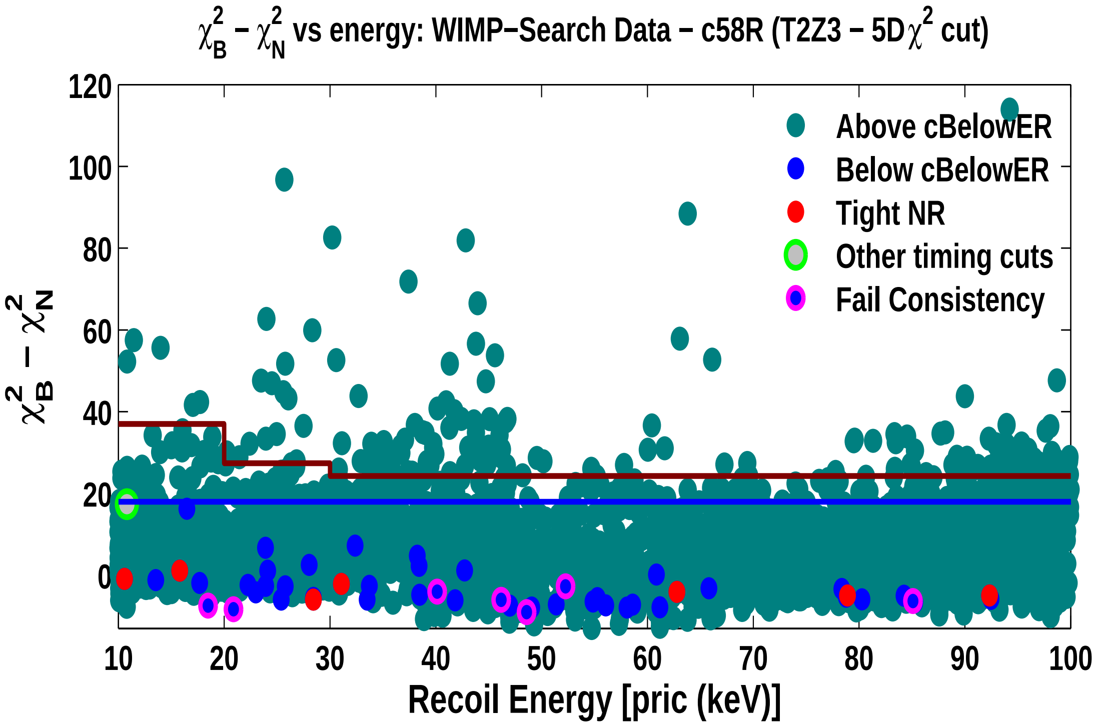

Figure 8.22: $\chi^2_B - \chi^2_N$ vs recoil energy for the low background data for T1Z5 (top) and T2Z3 (bottom). Events shown in dark cyan color represents events located 3σ above the **cBelowER_c58** (representing mostly electron-recoil events) while events in blue dots indicates non-electron-recoil events (which can either be surface events or event candidates for those laying inside the tight nuclear-recoil band). Red dots are WIMP-search events inside the tight nuclear-recoil band cut, i.e. the optimized nuclear-recoil band defined by a yield cut of $[l = -1.9; u = 1.8]$. Events shown in magenta circled with blue faces are events failing the consistency cut. The green circle events with the grey face represents events passing the alternative timing cuts developed during the reanalysis. The blue horizontal straight line is the energy independent cut while the dark red line represent the energy-dependent cut. Plots for other detectors are shown in Appendix D.

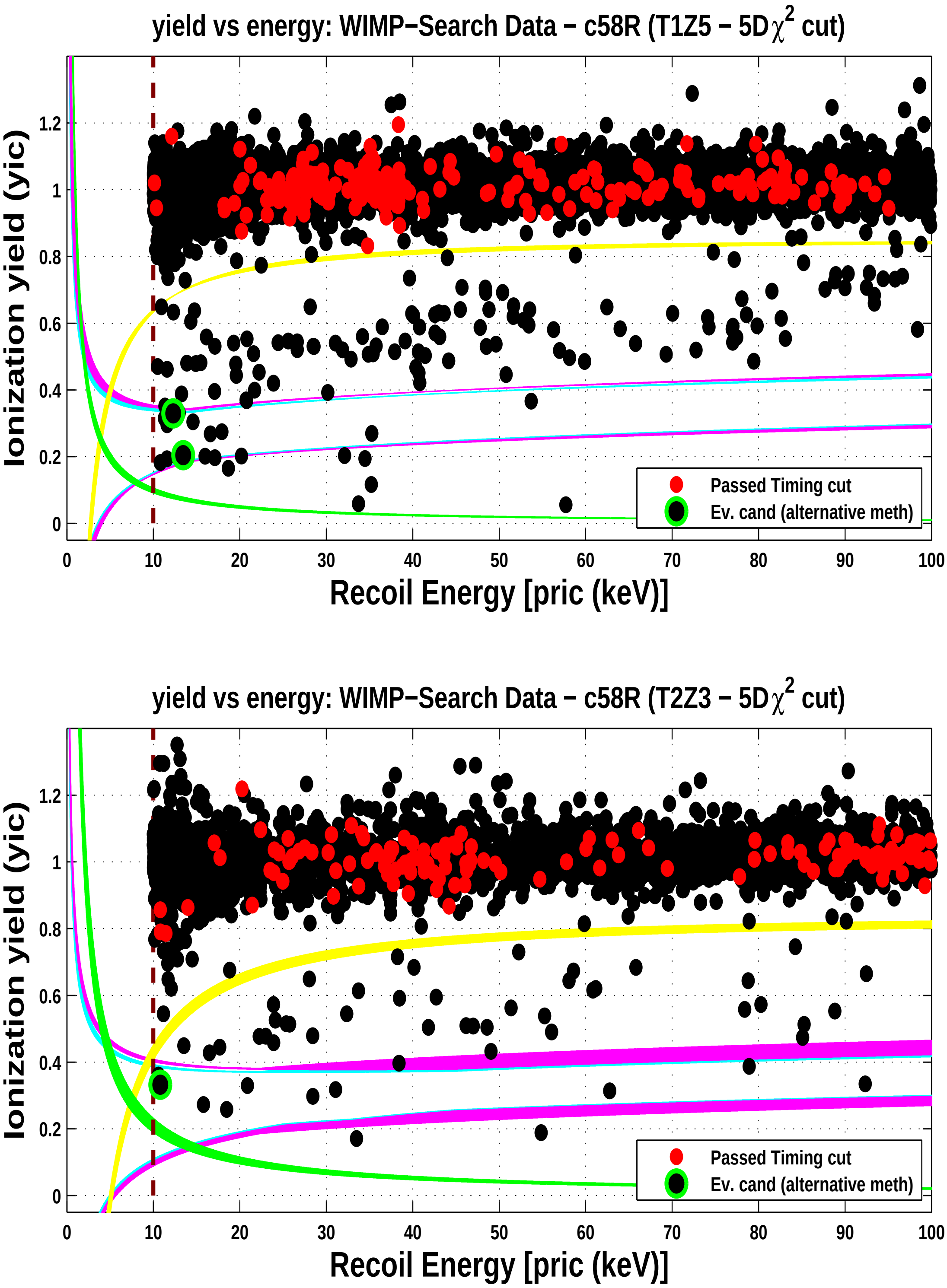

Figure 8.23: Ionization yield vs recoil energy showing the distribution of events in the WIMP-search (black dots) for T1Z5 (top) and T2Z3 (bottom). The events shown in red dots are the events passing the χ^2 optimized timing cuts above the 10 keV threshold. Note that all events passing the timing cut lie within 3σ of the electron-recoil band (yellow curve). The cyan and magenta curves indicate the tight and loose nuclear-recoil bands ($[l = -1.9; u = 1.8]$ and $[l = -2; u = 2]$, respectively), while the green circle with black face indicate the WIMP candidates identified by alternate timing-cut analyses. Plots for other detectors are shown in Appendix E.

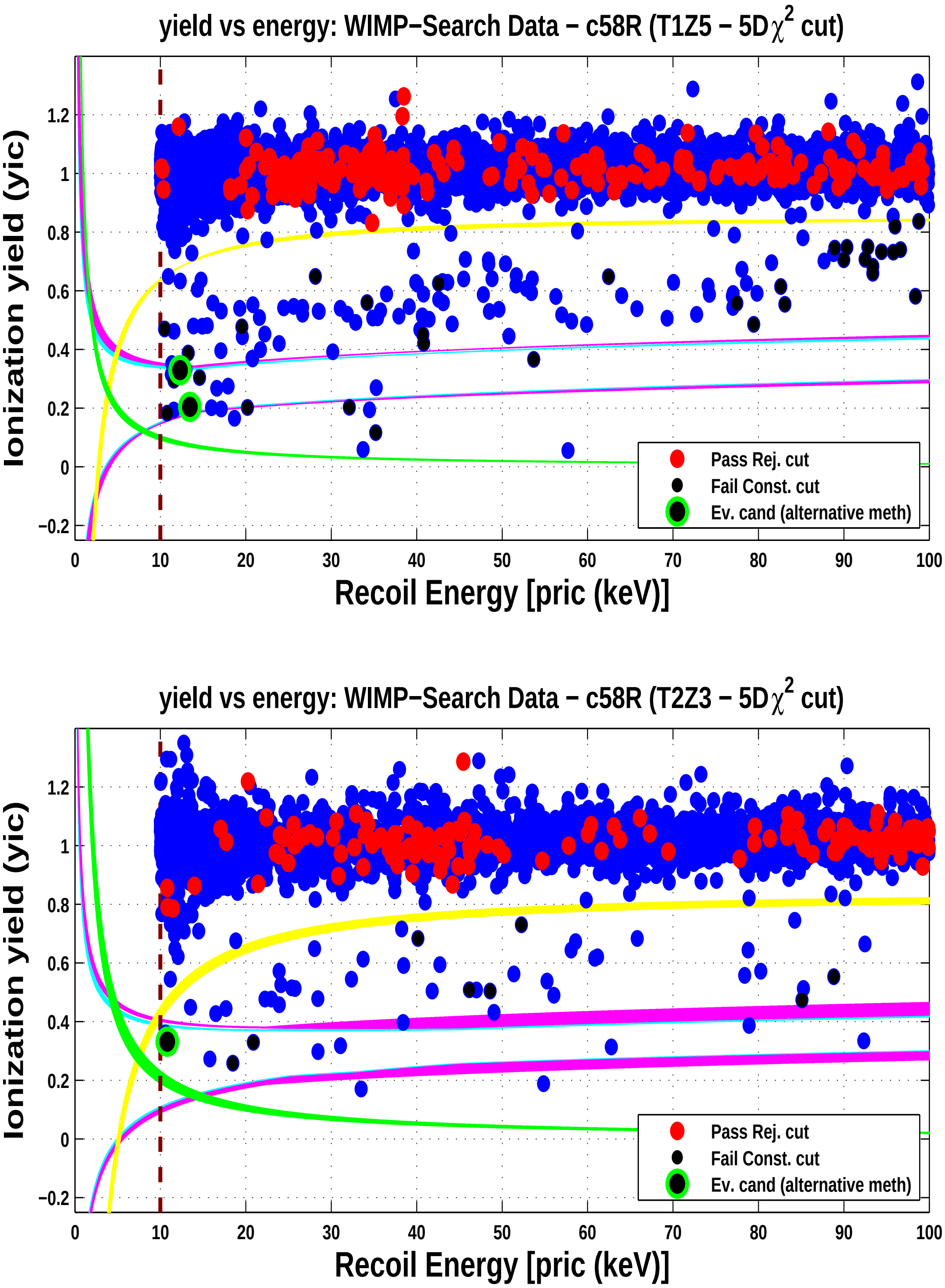

Figure 8.24: Another version of ionization yield vs recoil energy showing the distribution of events in the WIMP-search (blue dots) for T1Z5 (top) and T2Z3 (bottom). The events shown in red dots are the events passing the rejection cuts above the 10 keV threshold while the black dots are events failing the consistency cut. The yellow curve show the region of space of events laying within 3σ below the mean of the electron-recoil band. The cyan and magenta curves indicate the tight and loose nuclear-recoil bands ([$l = -1.9; u = 1.8$] and [$l = -2; u = 2$], respectively), while the green circle with black face indicate the WIMP candidates identified by alternate timing-cut analyses. Plots for other detectors are shown in Appendix E.

8.8 WIMP exclusion limit

Since no WIMP candidates were observed in this analysis, an upper limit on the WIMP-nucleon scattering cross section is set. An upper limit calculation typically depends on the experimental exposure, the energy-dependent detection efficiency, and (normally) the energies of any observed candidate events. Since, for the optimized χ^2 timing-cut analysis, no candidates are observed, the last of these can be ignored.

The upper limit is calculated using the statistical procedure called the **optimum interval method** [455, 456]. This method sets an upper limit based on the normalization of a signal of known spectral shape in presence of an unknown background. The optimum interval method generally sets a stronger upper limit than one obtained simply from Poisson statistics when there are candidate events, since the expected energy distribution of the events is taken into account. In the case of zero candidate events, the upper limit determined from the optimum interval method is identical to the usual Poisson-statistics upper limit [460].

Beside the optimum interval method, one might also consider the Feldman-Cousins technique. If the probability distributions of the expected backgrounds are known, the Feldman-Cousins technique [457] can be used to set a one or two-sided limit while the optimum interval method only sets a one-sided limit. There is a note by Richard W. Schnee detailing how the Feldman-Cousins ordering principle can be used [458] to set limits in the context of the CDMS experiment. During the c58 analysis, Tobias Bruch used this prescription to estimate the projected limit of the original c58 analysis [459]. This approach requires a full likelihood analysis of the expected backgrounds, and can be used to claim discovery if appropriate.

To compute the WIMP-nucleon cross-section limit, a standard halo-model WIMP distribution is assumed as discussed in (3.3.5). The WIMPs have a Maxwellian velocity distribution with a characteristic velocity of $v_0 = 220\,\mathrm{km/s}$, a local density of $\rho_0 = 0.3\,\mathrm{GeV/c^2}$ and an escape velocity of $v_{esc} = 545\,\mathrm{km/s}$, where the latter is taken from recent results from the RAVE survey [243]. These values are used as a conventional model in order to compare different experimental results. The expected recoil spectra for spin-independent interactions is calculated using equation (3.42), which requires the Helm nuclear form factor to be determined as function of the momentum transfer (Equation (3.11)) and is described in the Lewin and Smith paper [391].

The 90% confidence upper limit on the spin-independent WIMP-nucleon elastic-scattering cross section, determined by the procedure above, and is shown shown as the orange curve as orange curve in Figure (8.25). This limit is lower than those from the alternative analyses developed during the reanalysis by more than 60%. This analysis was chosen to be the primary timing cut for the reanalysis because its expected sensitivity was a factor of ~ 2 better than that of the other methods and the limit obtained with this analysis, as shown in Figure (8.25), will be quoted in a PRD paper in preparation [462].

The combined limit from this reanalysis including the exposure of all previous CDMS II data to the reanalysis is compared against the previous combined CDMS II limits in Figure (8.26) and the limit of this analysis is about a factor 2 lower than the original c58 analysis because its improved expected sensitivity. Also the optimized χ^2 timing cut has less total expected leakage of 0.5 event versus 0.9 events for the original analysis. The optimized timing cut optimizes the sensitivity while the timing cut developed during the original analysis maximized the exposure for a given total expected leakage. The total net exposure of the original c58 analysis was $\sim$ 191 kgdays while this analysis net exposure after cuts is 250.2 kgdays while the sensitivity is two improved during the reanalysis.

The upper limit from this analysis is also compared against the results of other leading experiments. Results from DAMA/LIBRA [463], CoGeNT [464], EDELWEISS [467], CREST II [465] and XENON100 [466] are shown. The combined CDMS upper limit reported with this analysis is second stringent limit in the field after XENON100. The dashed red line in the Figure (8.26) indicates the projected expected sensitivity for the SuperCDMS Soudan limit, and the XENON100 limit (solid back curveI is about the same than the projected SuperCDMS.

The timing cut analysis technique described in this dissertation has been applied to CDMS II silicon detectors by Kevin McCarthy [461] for the runs $125 - 128$. These detectors were not position corrected during the original c58 analysis. However, after the upgrade of charge optimal filter, the silicon detectors were processed and calibrated. The analysis results from the the optimized timing cut on these detectors will the central subject of Kevin McCarthy's dissertation and a central object of another publication.

To put our results in the context of supersymmetric framework based on the standards assumptions of the constrained minimal supersymmetric standard model (cMSSM), we overlaid our limit as well as limits from other WIMP-search experiments to the most recent SUSY parameter space obtained from a profile likelihood to the global fits of the cMSSM including the latest LHC SUSY and Higgs searches and XENON100 data as described in [468]. This new global fits of the cMSSM includes LHC 1 fb^{-1} integrated luminosity SUSY exclusion limits, recent LHC 5 fb^{-1} constraints on the mass for the Higgs boson and XENON100 direct detection data. The colored contour regions in the bottom of Figure (8.26) shows the current constrained minimal supersymmetric standard model (cMSSM) regions (with recent LHC and Higgs constraints) predicting where WIMPs may be found, assuming flat priors, at 68% (green), 95% (light green), and 99% (cyan) C.L. [468]. SuperCDMS Soudan and XENON100 will explore more of this regions in runs to come.

Current experiments are beginning to probe the most optimistic models of supersymmetry and future experiments will cut deep into the supersymmetric allowed parameter space. The future of the SuperCDMS experiment will focus to exploring these new regions where theoretical models predicts that WIMPs are likely to be found.

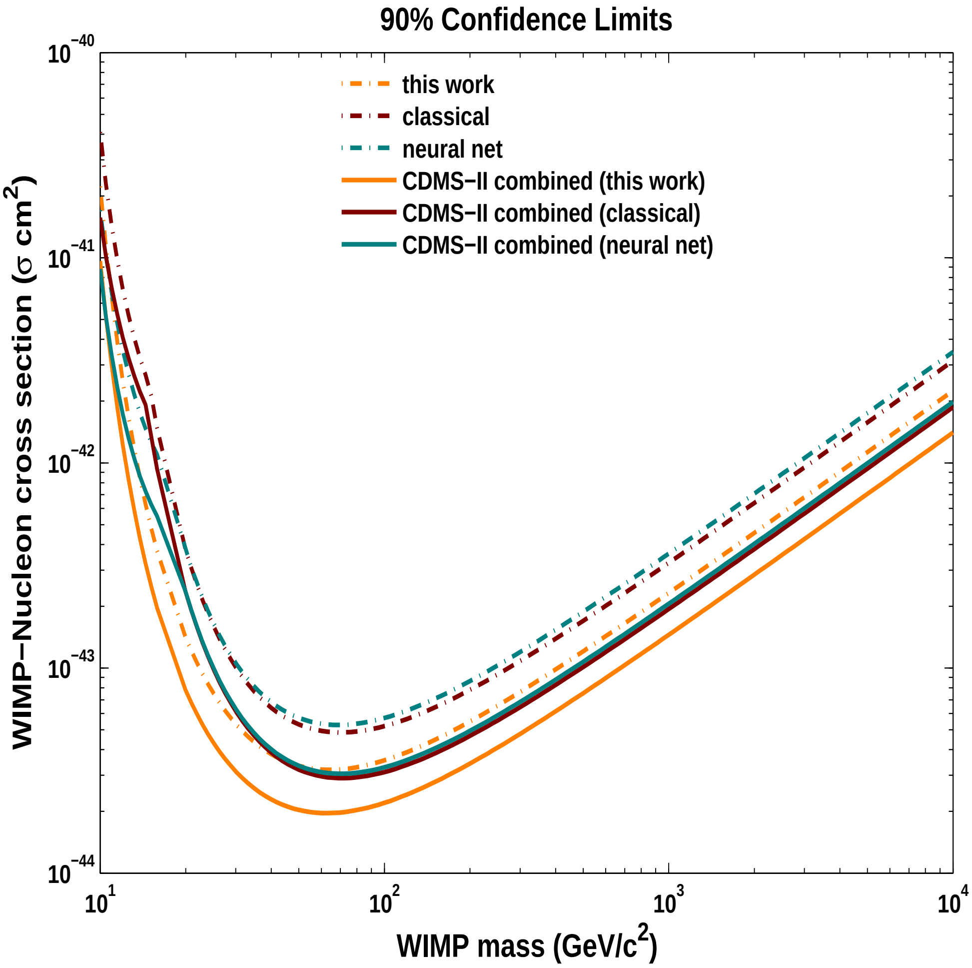

Figure 8.25: The calculated limit for this analysis as well the limits obtained with the traditional-classical-simple timing cut and the neural network timing cut. These limits are compared with a combined limits obtained using the respective timing cuts analyses developed during the c58 reanalysis with previous CDMS data. The limit achieved with previous CDMS-II and this analysis is sensitive to a spin-independent cross section of $\sigma_{SI} = 1.96 \times 10^{-44}\mathrm{cm}^2$ for a WIMP mass of 60 GeV/c^2. The combined CDMS+this analysis limit is at least 60% better than the limits obtained with the classical timing analysis (2.91×10^{-44} cm^2) and the neural net analysis (3.06×10^{-44} cm^2).

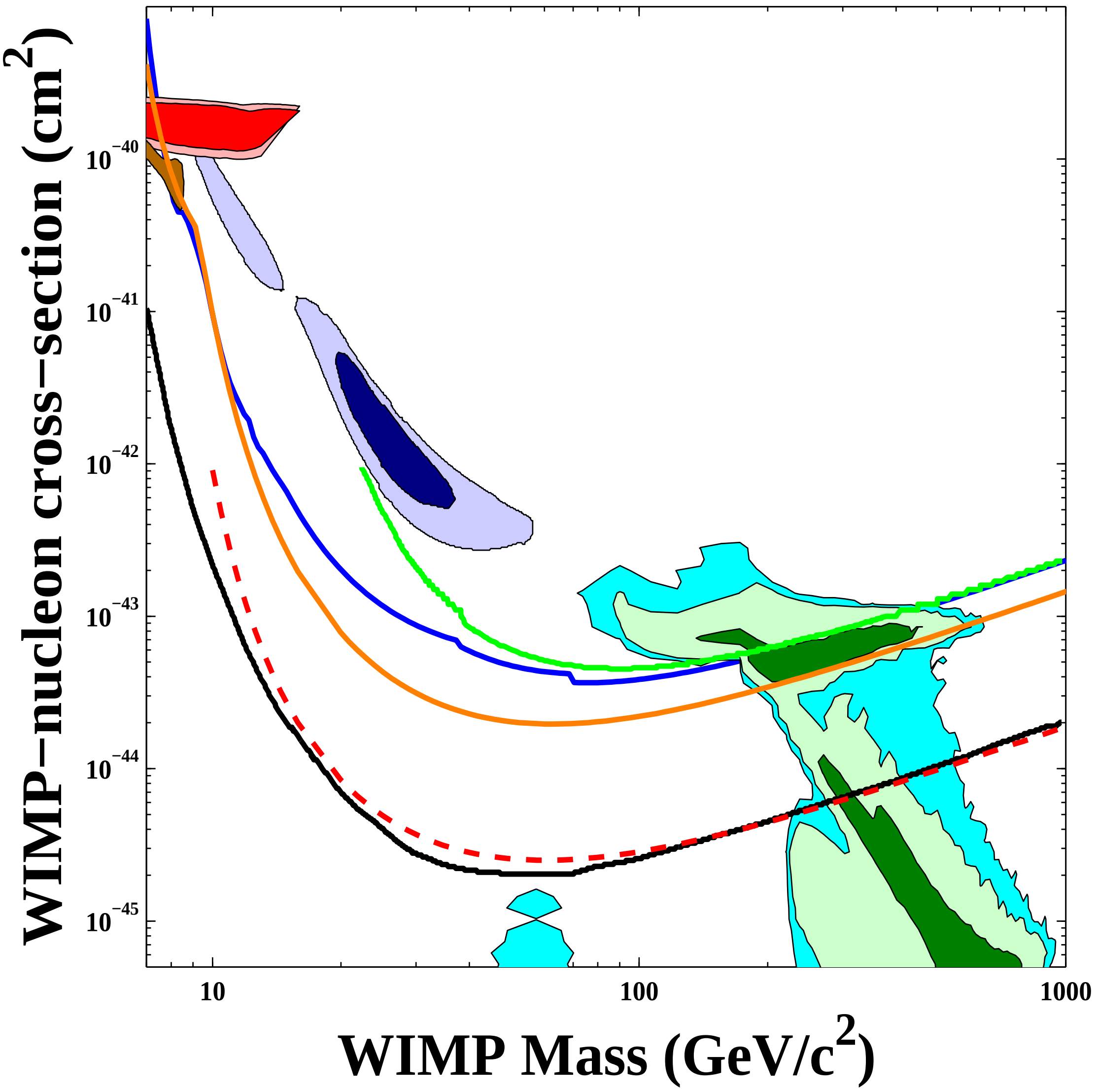

Figure 8.26: Plot of WIMP parameter space in the cross section vs WIMP mass plane. The calculated limit for this analysis (orange curve) [462] as well the limit from the previous CDMS II analysis (blue curve) [425]. On this plot is also shown other exclusion limit curves from other experiment and the constrained minimal supersymmetric standard (cMSSM) model theory region. The filled contours region shown in light purple and red represent the DAMA/LIBRA 90% and 99% confidence region for the recent excess of low energy events observed by the CoGeNT collaboration and the annual modulation reported by the DAMA/LIBRA collaboration [463]. The CoGeNT contour region for the annual modulation in the region of interest is the region shown with filled dark yellow color [464]. The WIMP parameter space compatible with the CRESST II results are shown in blue and light grey contour regions for 1σ and 2σ respectively [465]. The contour regions shown in cyan, light cyan and dark green represent the updated global fits of the cMSSM including the latest LHC SUSY and Higgs searches and XENON100 data [468]. The green cureve represents the final results of the EDELWEISS-II WIMP search using a 4-kg array of cryogenic germanium detectors with interleaved electrodes [467] while the black curve is the results from 225 Live Days of XENON100 Data [466]. The dashed red curve indicate the projected SuperCDMS Soudan limit. The limit from this analysis is $\sim$ 50% better than the 2009 CDMS II science result. Figure adapted from the SuperCDMS Soudan proposal, 2012 [469].

Conclusions

The last operations of CDMS II has concluded with the runs $125-128$. The analysis of these runs resulted in two candidate events and an upper limit on the WIMP-nucleon cross section of 3.8×10^{-44} cm^2, making the CDMS experiment sensitive to a WIMP mass of 60 GeV/c^2 and the most stringent limit at the time the results was published. The discovery that one of the candidate events suffered from pulse reconstruction led to the software upgrade, which has triggered a reanalysis. This dissertation has described the results of a WIMP-search using CDMS II reanalysis data accumulated at Soudan Underground Laboratory in Minnesota. No event candidates are observed using the analysis technique described in this dissertation. The results from the reanalysis of the five tower, among which only 14 viable detectors were used, has set an improved sensitivity and limit for Ge detectors due to the improved data processing and analysis techniques. The WIMP-nucleon limit set with the optimized χ^2 analysis two times lower than the previously published limit from the original c58 analysis [425].

The CDMS II experiment have now moved beyond, the SuperCDMS. The SuperCDMS collaboration is actively engaged in research and development programs to address their challenges and proceed to the design and fabrication of larger detector masses. In the SuperCDMS Soudan proposal [469], an extension of low-temperature WIMP detector technology to much larger masses and alternate bias and sensors in both face of the detectors has been proposed. These detectors are called the interleaved (or interdigitated) detectors, simply called the iZIPs. The aim of this proposal is to scale up (up to a ton-scale) the cryogenic experiment in order to make competitive and complementary to the large noble-liquid experiments and increase its detection potential. Although the identification of the nature of dark matter still remains an unanswered question of modern astrophysics, SuperCDMS Soudan projected and SuperCDMS SNOLAB limit will expore a large part of the SUSY parameter space and with a good control of the background, the discovery may just be at our corner.

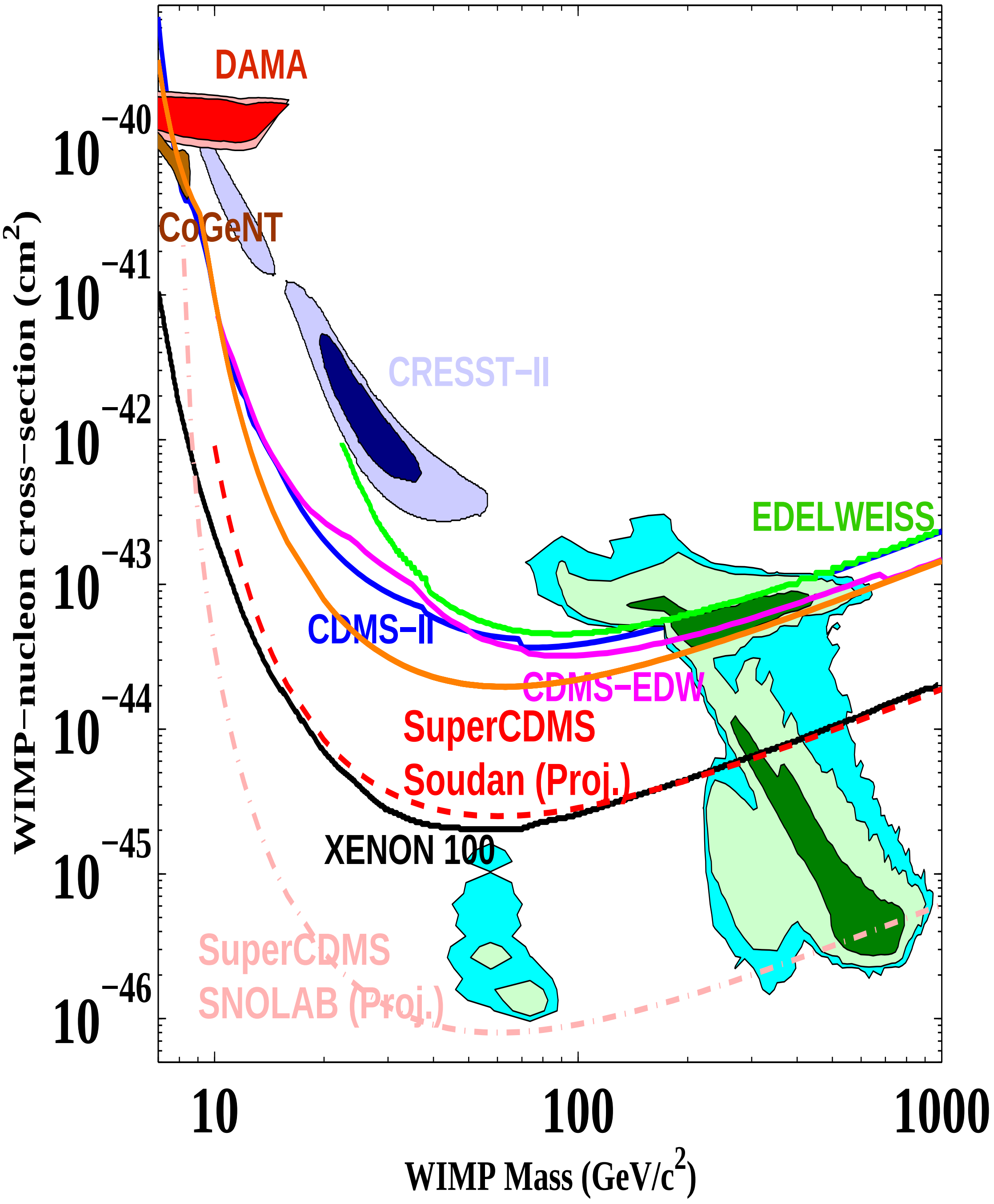

Figure 8.27: Current status for the recent upper limits (90% C.L.) on the WIMP-nucleon spin-independent cross section versus WIMP mass are shown for CDMS II Soudan (blue solid curve for previous limit and the limit shown in orange solid curve for this analysis), EDELWEISS II (green solid), combined CDMS-EDELWEISS II (magenta), and XENON100 (black solid). The purple filled region indicates the region where CRESST II reports a signal: 1σ allowed region (dark purple), 2σ allowed region (light purple). The red filled portions of the graph indicate the regions where DAMA reports a signal: 90% C.L. (red), and 99% C.L. (dark red). The orange colored region indicates where CoGeNT reports a signal. The other colored regions show the current cMSSM regions (with recent LHC and Higgs constraints) predicting where WIMPs may be found, assuming flat priors, at 68% (green), 95% (light green), and 99% (cyan) C.L. Also shown are projected sensitivities for the G1 SuperCDMS Soudan experiment for a three-year run (dashed red) and the proposed G2 SuperCDMS SNOLAB experiment with a 200 kg payload for four years running (dot- dashed light red); these assume no background subtraction. Figure adapted from the SuperCDMS Soudan proposal, 2012 [469].

Appendix A

Mean energy dependence

A.1 Multivariate distributions

In the treatment of our 5D χ^2 analysis, we have exploited the multivariate gaussian distribution using 5 timing variables. In one dimension, a gaussian distribution of a variable x with a mean μ_x and a standard deviation σ_x is given by

$$P(x) = \frac{1}{\sqrt{2\pi\sigma_x}} e^{-\frac{(x-\mu_x)^2}{2\sigma_x^2}}. \tag{A.1}$$

In order to grasp the intuition of the how to generalize the above distribution to a multivariate, let's illustrate it using a 2 dimensional system of the variables x and y. First, I am going to make the assumption that the two variables are not correlated. In addition to that, the two distributions are centered at zero. According to the rules of probability:

$$P(x, y) = P(x) \cdot P(y) = \frac{1}{2\pi\sigma_x\sigma_y} \exp\left[-\frac{1}{2}\left(\frac{x^2}{\sigma_x^2} + \frac{y^2}{\sigma_y^2}\right)\right]. \tag{A.2}$$

Now, we can rewrite the argument in the exponential (A.2) in matrix notation as:

$$P(x, y) = \frac{1}{2\pi\sigma_x\sigma_y} \exp\left[-\frac{1}{2}\begin{pmatrix} x & y \end{pmatrix} \cdot \begin{pmatrix} \frac{1}{\sigma_x^2} & 0 \\ 0 & \frac{1}{\sigma_y^2} \end{pmatrix} \cdot \begin{pmatrix} x \\ y \end{pmatrix}\right], \tag{A.3}$$

In which we can invert the 2×2 matrix in the above equation to obtain the matrix

$$\mathrm{M} = \begin{pmatrix} \sigma_x^2 & 0 \\ 0 & \sigma_y^2 \end{pmatrix}. \tag{A.4}$$

which is known as the error matrix for x and y. The diagonal terms σ_x^2 and σ_y^2 are respectively the variances of

x and of y, while the off-diagonal zeroes indicate that the errors of x and y are uncorrelated. The 2×2 matrix in (A.3) is known as the inverse error matrix. In general the element M_{ij} of an error matrix for a set of variables $x_l, x_2, \cdots, x_n$ is defined as the expectation value in case the distributions x and y are not gaussian. In such a situation, M_{ij} are calculated as

$$\mathrm{M}_{ij} = \langle (x_i - \overline{x}_i) \rangle \langle (x_j - \overline{x}_j) \rangle. \tag{A.5}$$

The above equation (A.5) lead to the property that the the covariance matrix is symmetric. The off-diagonal term is denoted as $cov(x, y)$. The probability (A.5) can be written the following compact for:

$$P(x,y) = \frac{1}{2\pi\sigma_x\sigma_y}\exp\left[-\frac{1}{2}\begin{pmatrix} x & y \end{pmatrix} \cdot M^{-1} \cdot \begin{pmatrix} x \\ y \end{pmatrix}\right]. \tag{A.6}$$

With this background introduction, we are now at the good standing to tackle the case where the variables are correlated. In such a case, the error matrix (A.4), takes the following form:

$$\mathrm{M} = \begin{pmatrix} \sigma_x^2 & cov(x,y) \\ cov(x,y) & \sigma_y^2 \end{pmatrix}. \tag{A.7}$$

Introducing (A.7) into (A.6), we get a 2 dimensional generalized multivariate gaussian distributions.

$$P(x,y) = \frac{1}{2\pi\sigma_x\sigma_y}\frac{1}{\sqrt{1-\rho^2}}\exp\left[-\frac{1}{2(1-\rho^2)}\left(\frac{x^2}{\sigma_x^2} + \frac{x^2}{\sigma_x^2} - \frac{2\rho xy}{\sigma_x\sigma_y}\right)\right], \tag{A.8}$$

with

$$\rho = \frac{cov(x,y)}{\sigma_x\sigma_y}. \tag{A.9}$$

In general, for N-dimension $X = (x_1, x_2, \cdots, x_N)$:

$$P(x,y) = \frac{1}{(2\pi)^{N/2}}\frac{1}{\det(\mathrm{M})}\exp\left(-\frac{1}{2}\widetilde{X}\cdot M^{-1}\cdot X\right) = \frac{1}{(2\pi)^{N/2}}\frac{1}{\det(\mathrm{M})}\exp\left(-\frac{1}{2}\chi^2\right), \tag{A.10}$$

where $\chi^2 = \widetilde{X} \cdot M^{-1} \cdot X$, is the N-dimensional χ^2 and det(M) is the determinant of the error matrix M, which can be generalized to the following form:

$$M = \begin{pmatrix} \sigma^2_{x_1x_1} & cov(x_1x_2) & \cdots & cov(x_1x_N) \\ cov(x_2x_1) & \sigma^2_{x_2x_2} & \cdots & cov(x_2x_N) \\ \vdots & \vdots & \ddots & \vdots \\ cov(x_Nx_1) & cov(x_Nx_2) & \cdots & \sigma^2_{x_Nx_N} \end{pmatrix}. \tag{A.11}$$

Note that $cov(x_ix_j) = cov(x_jx_i)$, so the covariance matrix M is symmetric. Any symmetric matrix has N diagonal elements and $\frac{N(N-1)}{2}$ off-diagonal elements, making a total of $\frac{N(N+1)}{2}$ matrix elements. The fit parameters for the means of the 5 variables are shown in the tables (A.1) to (A.5) listed in the subsequent pages of this appendix.

A.2 Implementation to the CDMS analysis

With 5 timing quantities used for the surface-event rejection, we created a 5-dimensional $\chi^2 = \widetilde{X} \cdot M^{-1} \cdot X$, with $X = \{\mathbf{pmintc}, \mathbf{pdelc}, \mathbf{pminrtCFc}, \mathbf{pdeCFc}, \mathbf{pminrtCF4070c}\}$. The means of each of the variables used in the χ^2 analysis were calculated and fitted to the functional form fit indicated by Equation $\mu_{k\alpha} = A_{k\alpha}(1) + A_{k\alpha}(2) \cdot E^2 + A_{k\alpha}(3)\sqrt{E}$. In order to get correct mean values, the distributions of these variables are assumed to be gaussian distributed and fitted to a gaussian in a preselected energy bin. These fits were performed for neutrons events as well as surface events making a clear distinction between face distribution (phonon and charge-side events) and betas. The fits obtained are shown in Tables (A.1) to (A.5). Figures (A.1) to (A.13) show the binned means as function of the recoil energy fron 10 to 100 keV. The black solid line overlaid to the data is the fit used to model the distributions of the means as a function of energy.

Table A.1: pdelc Fit parameters

	$\mu-$ pdelc								
	Neutron			Phonon - side			Charge - side		
Detector Name	$A_{kn}(1)$	$A_{kn}(2)$	$A_{kn}(3)$	$A_{kp}(1)$	$A_{kp}(2)$	$A_{kp}(3)$	$A_{kq}(1)$	$A_{kq}(2)$	$A_{kq}(3)$
T1Z2	11.502	-0.065	-0.0000	6.156	0.296	-0.0001	7.878	0.053	-0.0000
T1Z5	11.430	-0.051	-0.0000	5.508	0.476	-0.0002	7.376	0.238	-0.0001
T2Z3	11.971	-0.166	0.0000	4.251	0.674	-0.0003	5.859	0.463	-0.0003
T2Z5	11.689	-0.015	-0.0001	3.546	0.745	-0.0003	6.265	0.367	-0.0002
T3Z2	11.326	-0.022	-0.0001	4.515	0.583	-0.0002	8.074	0.049	-0.0000
T3Z4	12.418	-0.090	-0.0001	3.601	0.729	-0.0003	5.732	0.446	-0.0002
T3Z5	11.857	-0.106	-0.0000	5.107	0.495	-0.0002	6.619	0.292	-0.0001
T3Z6	12.158	-0.167	0.0000	6.934	0.249	-0.0001	7.950	0.085	-0.0000
T4Z2	9.382	0.330	-0.0002	0.097	1.203	-0.0005	3.606	0.720	-0.0003
T4Z4	11.019	0.148	-0.0002	1.447	0.980	-0.0004	2.916	0.841	-0.0004
T4Z5	11.295	0.091	-0.0002	2.392	0.848	-0.0003	5.439	0.411	-0.0002
T4Z6	7.919	0.735	-0.0005	-4.259	1.700	-0.0007	-2.042	1.505	-0.0006
T5Z4	9.870	0.312	-0.0002	0.419	1.104	-0.0004	6.249	0.196	-0.0001
T5Z5	7.072	0.791	-0.0005	-2.623	1.635	-0.0007	-0.651	1.369	-0.0006

Table A.2: pminrtc Fit parameters

	$\mu-$ pminrtc								
	Neutron			Phonon - side			Charge - side		
Detector Name	$A_{kn}(1)$	$A_{kn}(2)$	$A_{kn}(3)$	$A_{kp}(1)$	$A_{kp}(2)$	$A_{kp}(3)$	$A_{kq}(1)$	$A_{kq}(2)$	$A_{kq}(3)$
T1Z2	10.321	-0.136	0.0001	7.659	-0.155	0.0001	8.442	-0.275	0.0002
T1Z5	13.157	-0.533	0.0003	9.070	-0.332	0.0002	10.031	-0.598	0.0003
T2Z3	13.481	-0.637	0.0004	8.804	-0.311	0.0002	10.024	-0.642	0.0003
T2Z5	12.242	-0.464	0.0002	9.792	-0.552	0.0003	10.266	-0.661	0.0003
T3Z2	9.962	-0.057	-0.0000	7.928	-0.134	0.0001	8.711	-0.344	0.0002
T3Z4	14.520	-0.655	0.0004	10.091	-0.541	0.0003	10.679	-0.791	0.0003
T3Z5	13.198	-0.505	0.0002	9.728	-0.459	0.0003	9.974	-0.655	0.0003
T3Z6	11.292	-0.310	0.0002	8.884	-0.351	0.0002	8.696	-0.298	0.0002
T4Z2	15.781	-1.184	0.0007	12.339	-0.947	0.0005	11.355	-0.825	0.0004
T4Z4	15.336	-0.855	0.0004	11.497	-0.805	0.0005	13.074	-1.233	0.0006
T4Z5	13.942	-0.667	0.0003	11.225	-0.787	0.0004	10.648	-0.782	0.0003
T4Z6	14.386	-0.915	0.0005	11.564	-0.893	0.0004	11.399	-0.818	0.0004
T5Z4	14.098	-0.839	0.0004	11.571	-0.869	0.0004	11.879	-0.920	0.0004
T5Z5	15.214	-0.984	0.0005	12.305	-0.967	0.0005	14.082	-1.370	0.0006

Table A.3: pdelCFc Fit parameters

	$\mu-$ pdelCFc								
	Neutron			Phonon - side			Charge - side		
Detector Name	$A_{kn}(1)$	$A_{kn}(2)$	$A_{kn}(3)$	$A_{kp}(1)$	$A_{kp}(2)$	$A_{kp}(3)$	$A_{kq}(1)$	$A_{kq}(2)$	$A_{kq}(3)$
T1Z2	11.703	-0.110	0.0000	5.837	0.331	-0.0001	7.818	0.053	-0.0000
T1Z5	12.079	-0.086	-0.0000	5.841	0.361	-0.0001	8.139	0.032	-0.0000
T2Z3	12.625	-0.219	0.0001	4.593	0.541	-0.0002	6.751	0.207	-0.0001
T2Z5	12.204	-0.100	-0.0000	4.431	0.541	-0.0002	7.428	0.118	-0.0001
T3Z2	11.496	-0.039	-0.0001	4.599	0.534	-0.0002	8.290	-0.016	0.0000
T3Z4	13.567	-0.204	0.0000	4.209	0.549	-0.0002	7.030	0.107	-0.0001
T3Z5	12.443	-0.146	-0.0000	5.731	0.328	-0.0001	7.491	0.064	-0.0000
T3Z6	12.375	-0.203	0.0001	7.282	0.156	-0.0001	8.155	0.028	-0.0000
T4Z2	12.531	-0.258	0.0001	4.288	0.421	-0.0001	6.864	0.125	-0.0000
T4Z4	13.560	-0.229	0.0000	3.442	0.523	-0.0001	5.966	0.198	-0.0001
T4Z5	12.285	-0.036	-0.0001	4.373	0.422	-0.0001	6.991	0.063	0.0000
T4Z6	12.440	-0.100	-0.0000	2.268	0.554	-0.0002	3.492	0.536	-0.0002
T5Z4	12.696	-0.211	0.0000	3.979	0.449	-0.0001	8.911	-0.291	0.0002
T5Z5	11.618	-0.022	-0.0000	2.931	0.598	-0.0002	4.252	0.469	-0.0002

Table A.4: pminrtCFc Fit parameters

	$\mu-$ pminrtCFc								
	Neutron			Phonon - side			Charge - side		
Detector Name	$A_{kn}(1)$	$A_{kn}(2)$	$A_{kn}(3)$	$A_{kp}(1)$	$A_{kp}(2)$	$A_{kp}(3)$	$A_{kq}(1)$	$A_{kq}(2)$	$A_{kq}(3)$
T1Z2	9.689	0.056	-0.0000	6.853	0.137	-0.0001	7.645	0.004	0.0000
T1Z5	9.953	0.022	-0.0000	7.162	0.159	-0.0001	7.502	0.061	-0.0000
T2Z3	10.682	-0.150	0.0001	6.893	0.193	-0.0001	7.024	0.111	-0.0000
T2Z5	10.447	-0.065	0.0000	6.642	0.181	-0.0001	7.727	-0.036	0.0000
T3Z2	9.480	0.086	-0.0001	7.148	0.150	-0.0001	7.498	0.033	-0.0000
T3Z4	11.008	-0.084	0.0000	7.003	0.184	-0.0001	7.617	-0.030	0.0000
T3Z5	10.856	-0.101	0.0000	7.529	0.092	-0.0000	7.463	0.005	0.0000
T3Z6	10.344	-0.070	0.0000	7.553	0.050	-0.0000	7.602	0.045	-0.0000
T4Z2	11.648	-0.291	0.0002	6.513	0.226	-0.0001	6.890	0.066	-0.0000
T4Z4	10.572	-0.024	-0.0000	7.077	0.163	-0.0001	8.125	-0.141	0.0001
T4Z5	10.800	-0.085	0.0000	6.838	0.183	-0.0001	7.301	-0.012	0.0000
T4Z6	10.647	-0.082	0.0000	5.283	0.301	-0.0001	5.507	0.298	-0.0001
T5Z4	10.731	-0.111	0.0000	6.219	0.204	-0.0001	7.192	0.005	0.0000
T5Z5	9.288	0.169	-0.0001	5.939	0.297	-0.0001	7.964	-0.169	0.0001

Table A.5: pminrtCF4070c Fit parameters

	$\mu-$pminrtCF4070c								
	Neutron			Phonon - side			Charge - side		
Detector Name	$A_{kn}(1)$	$A_{kn}(2)$	$A_{kn}(3)$	$A_{kp}(1)$	$A_{kp}(2)$	$A_{kp}(3)$	$A_{kq}(1)$	$A_{kq}(2)$	$A_{kq}(3)$
T1Z2	9.948	0.165	-0.0001	7.183	0.254	-0.0001	9.916	-0.159	0.0001
T1Z5	11.203	0.083	-0.0001	7.603	0.255	-0.0001	8.254	0.085	-0.0000
T2Z3	11.611	-0.084	0.0001	7.043	0.320	-0.0002	7.590	0.164	-0.0001
T2Z5	10.289	0.101	-0.0001	6.557	0.347	-0.0001	8.717	-0.028	0.0000
T3Z2	10.132	0.137	-0.0001	7.443	0.281	-0.0001	8.168	0.141	-0.0001
T3Z4	12.029	-0.004	-0.0000	7.484	0.279	-0.0001	8.239	-0.011	0.0000
T3Z5	11.997	-0.026	-0.0000	8.213	0.149	-0.0001	8.558	-0.051	0.0001
T3Z6	10.424	0.084	-0.0000	8.011	0.152	-0.0001	8.457	0.107	-0.0000
T4Z2	14.384	-0.622	0.0004	7.106	0.270	-0.0001	6.997	0.208	-0.0001
T4Z4	12.200	-0.027	-0.0000	7.588	0.252	-0.0001	9.237	-0.223	0.0001
T4Z5	12.288	-0.156	0.0001	7.593	0.216	-0.0001	7.832	0.044	-0.0000
T4Z6	13.585	-0.528	0.0002	5.841	0.296	-0.0001	6.907	0.200	-0.0001
T5Z4	12.332	-0.309	0.0001	7.489	0.127	-0.0000	9.752	-0.193	0.0001
T5Z5	11.972	-0.152	0.0001	6.292	0.354	-0.0001	8.042	-0.050	0.0001

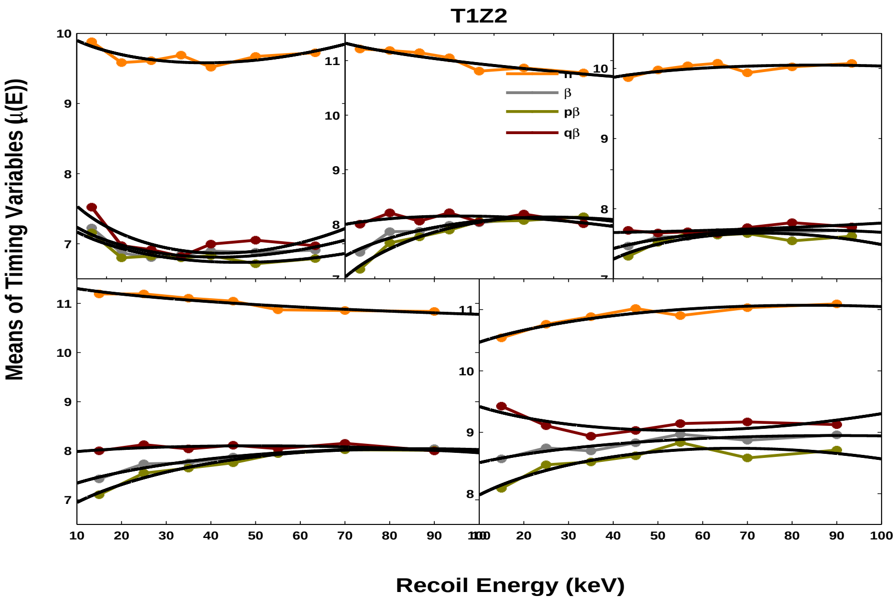

Figure A.1: Energy dependence of the means of the timing variables used in the χ^2 for T1Z2. In black is shown the fit to the data using the functional form fit in equation (8.5). Different colors indicate different event types: neutron (orange), phonon-side surface events (dark yellow) and charge-side surface events (dark red).

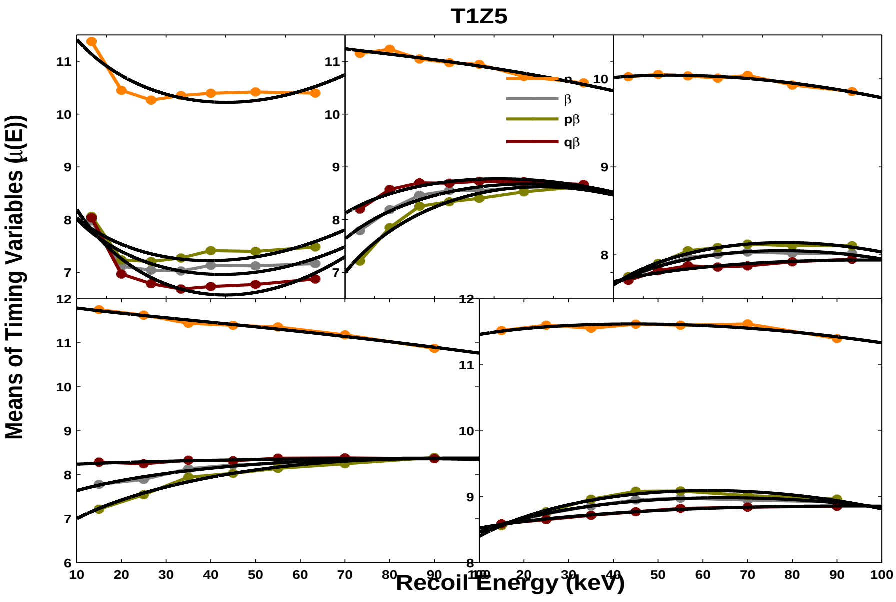

Figure A.2: Energy dependence of the means of the timing variables used in the χ^2 for T1Z5. In black is shown the fit to the data using the functional form fit in equation (8.5). Different colors indicate different event types: neutron (orange), phonon-side surface events (dark yellow) and charge-side surface events (dark red).

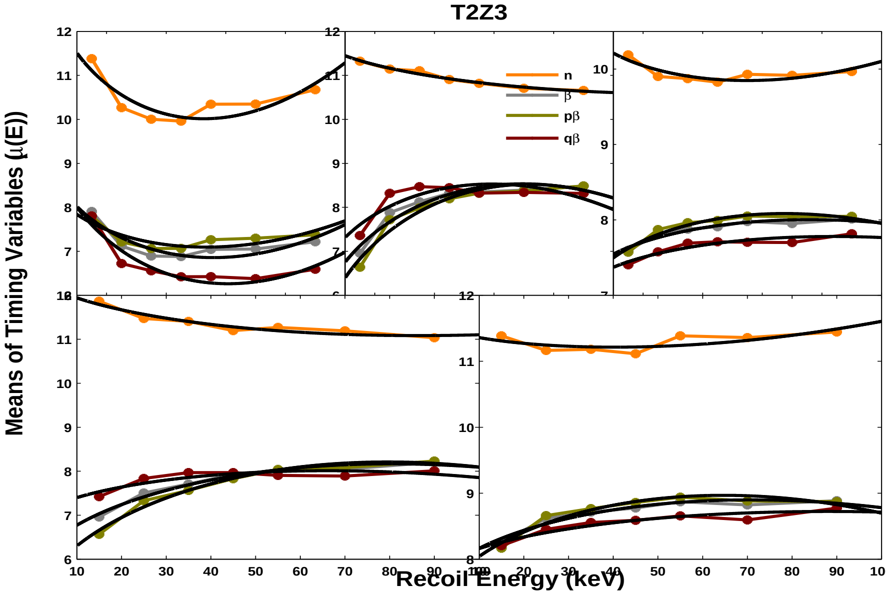

Figure A.3: Energy dependence of the means of the timing variables used in the χ^2 for T2Z3. In black is shown the fit to the data using the functional form fit in equation (8.5). Different colors indicate different event types: neutron (orange), phonon-side surface events (dark yellow) and charge-side surface events (dark red).

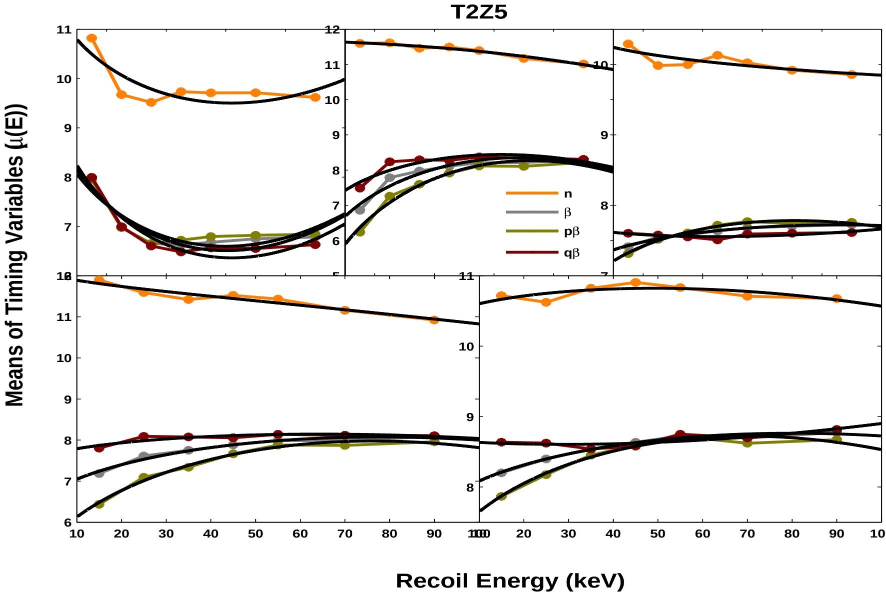

Figure A.4: Energy dependence of the means of the timing variables used in the χ^2 for T2Z5. In black is shown the fit to the data using the functional form fit in equation (8.5). Different colors indicate different event types: neutron (orange), phonon-side surface events (dark yellow) and charge-side surface events (dark red).

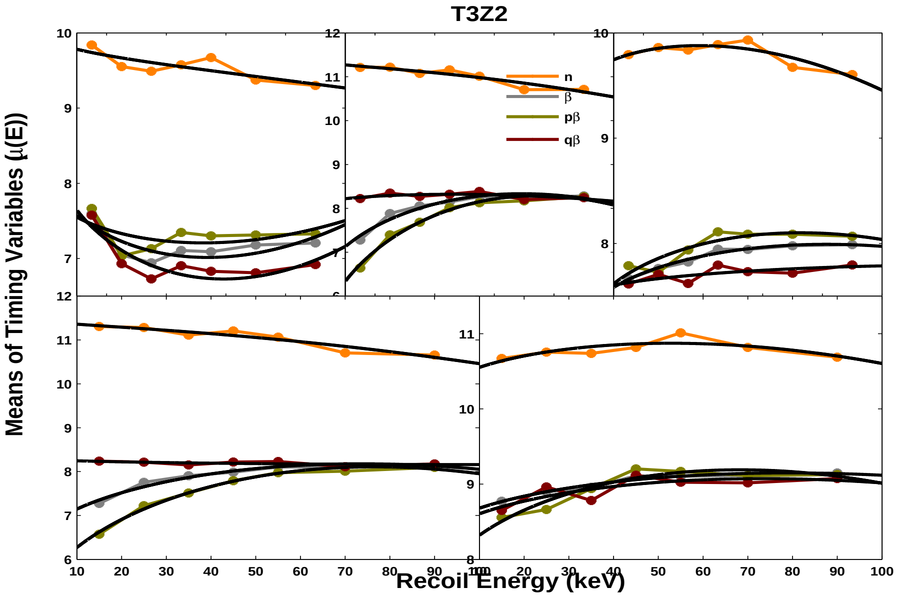

Figure A.5: Energy dependence of the means of the timing variables used in the χ^2 for T3Z2. In black is shown the fit to the data using the functional form fit in equation (8.5). Different colors indicate different event types: neutron (orange), phonon-side surface events (dark yellow) and charge-side surface events (dark red).

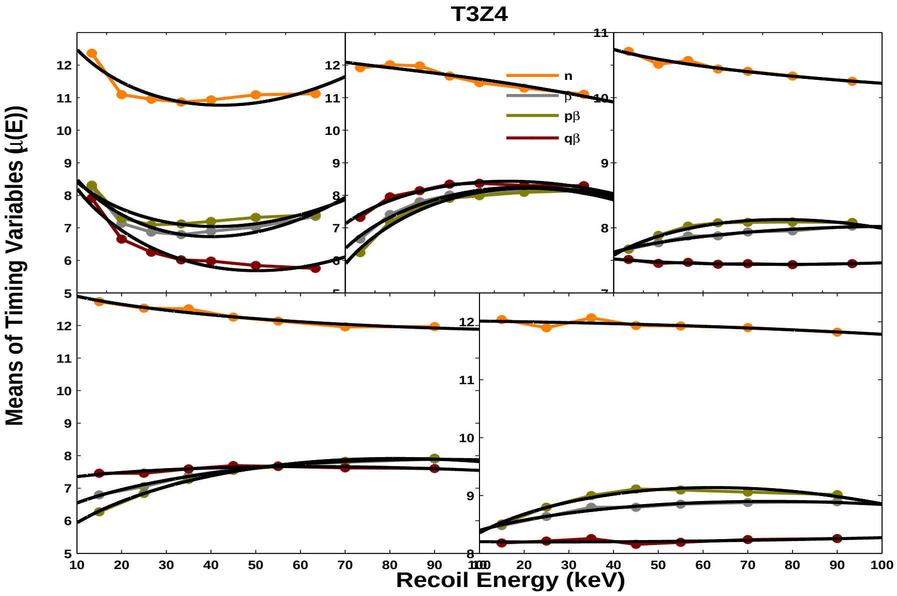

Figure A.6: Energy dependence of the means of the timing variables used in the χ^2 for T3Z4. In black is shown the fit to the data using the functional form fit in equation (8.5). Different colors indicate different event types: neutron (orange), phonon-side surface events (dark yellow) and charge-side surface events (dark red).

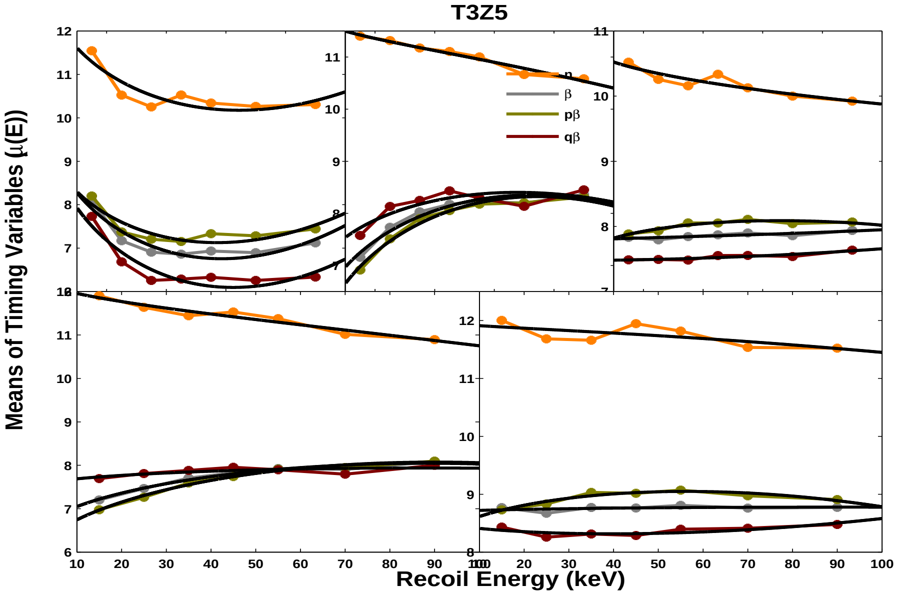

Figure A.7: Energy dependence of the means of the timing variables used in the χ^2 for T3Z5. In black is shown the fit to the data using the functional form fit in equation (8.5). Different colors indicate different event types: neutron (orange), phonon-side surface events (dark yellow) and charge-side surface events (dark red).

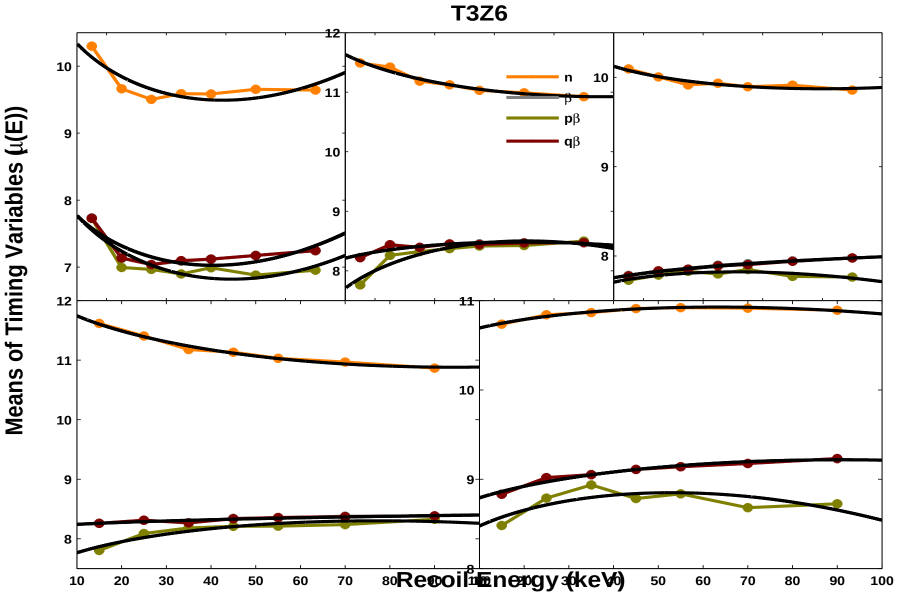

Figure A.8: Energy dependence of the means of the timing variables used in the χ^2 for T3Z6. In black is shown the fit to the data using the functional form fit in equation (8.5). Different colors indicate different event types: neutron (orange), phonon-side surface events (dark yellow) and charge-side surface events (dark red).

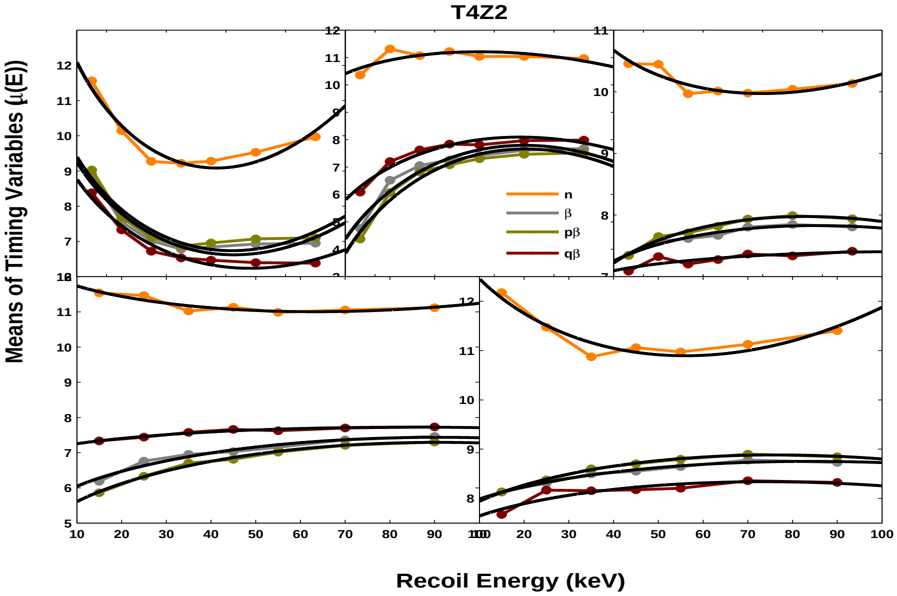

Figure A.9: Energy dependence of the means of the timing variables used in the χ^2 for T4Z2. In black is shown the fit to the data using the functional form fit in equation (8.5). Different colors indicate different event types: neutron (orange), phonon-side surface events (dark yellow) and charge-side surface events (dark red).

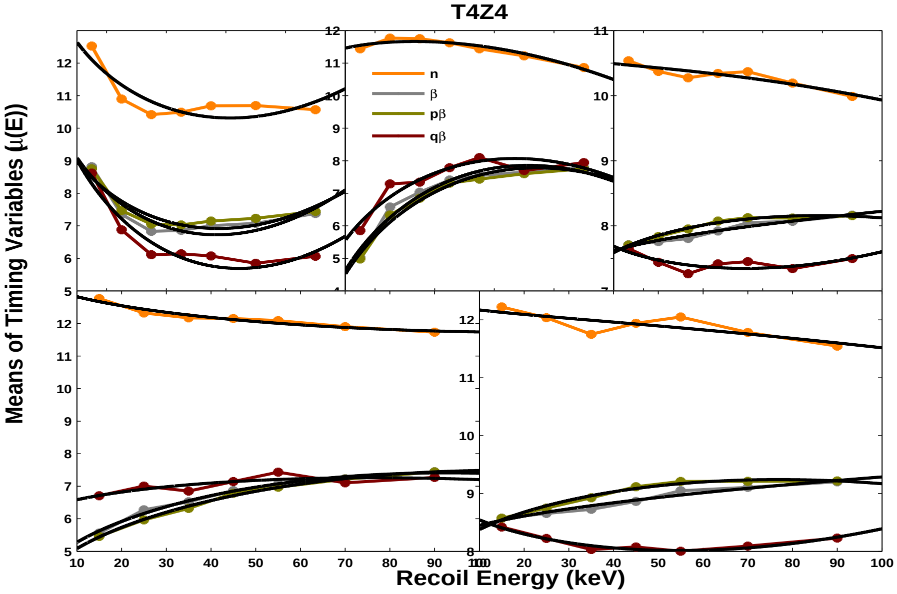

Figure A.10: Energy dependence of the means of the timing variables used in the χ^2 for T4Z4. In black is shown the fit to the data using the functional form fit in equation (8.5). Different colors indicate different event types: neutron (orange), phonon-side surface events (dark yellow) and charge-side surface events (dark red).

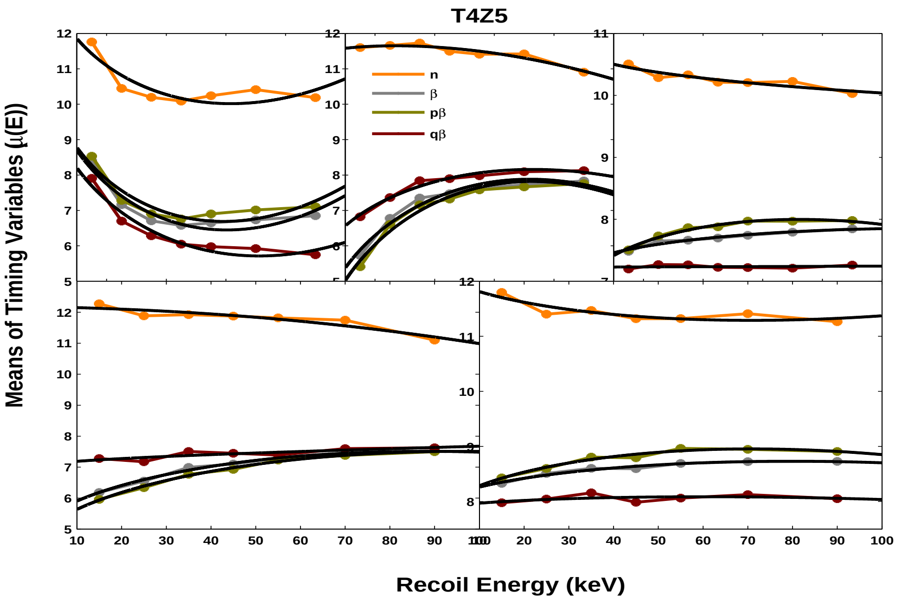

Figure A.11: Energy dependence of the means of the timing variables used in the χ^2 for T4Z5. In black is shown the fit to the data using the functional form fit in equation (8.5). Different colors indicate different event types: neutron (orange), phonon-side surface events (dark yellow) and charge-side surface events (dark red).

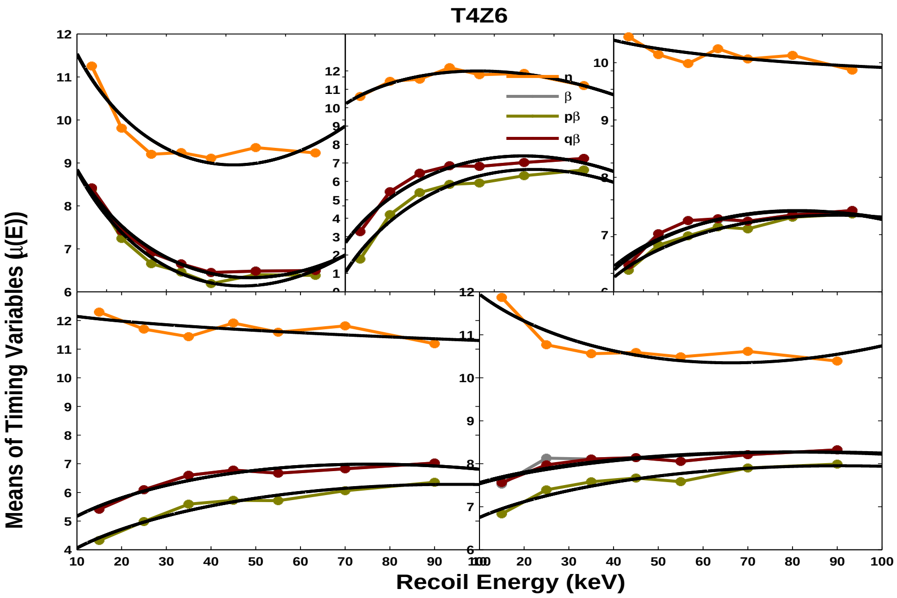

Figure A.12: Energy dependence of the means of the timing variables used in the χ^2 for T4Z6. In black is shown the fit to the data using the functional form fit in equation (8.5). Different colors indicate different event types: neutron (orange), phonon-side surface events (dark yellow) and charge-side surface events (dark red).

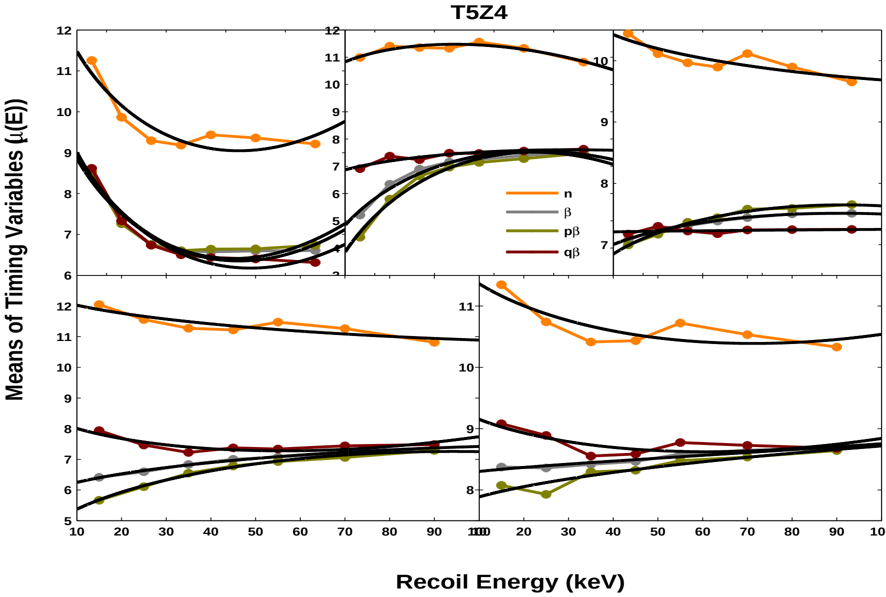

Figure A.13: Energy dependence of the means of the timing variables used in the χ^2 for T5Z4. In black is shown the fit to the data using the functional form fit in equation (8.5). Different colors indicate different event types: neutron (orange), surface events - betas(grey), phonon-side surface events (dark yellow) and charge-side surface events (dark red).

Appendix B

Energy dependence of covariance matrix elements

To form the matrix M (A.11) in 5 dimensions, we need to compute 15 matrix elements in total in which 5 are the diagonal elements and 10 are the off-diagonal (correlation terms). With the energy dependent χ^2, the means and the 15 elements of the covariance matrix (A.11) were calculated as function of the phonon recoil energy. The fit parameters for the elements of the covariance matrix are shown in Tables (B.1) to (B.15).

B.1 Covariance matrix fit parameters

Table B.1: Fit parameters used to compute the energy dependent covariance matrix elements (σ_{11}^2) for the energy dependent χ^2 timing cut analysis.

	σ_{11}^2											
	Neutron				Phonon - side				Charge - side			
Detector Name		$A_{kn(1)}$	$A_{kn}(2)$			$A_{kp(1)}$	$A_{kp}(2)$			$A_{kq(1)}$	$A_{kq}(2)$	
T1Z2	A=[	1.057	17.238	]	A=[	0.234	7.063	]	A=[	0.341	8.595	]
T1Z5	A=[	1.507	22.667	]	A=[	0.376	10.907	]	A=[	0.217	13.191	]
T2Z3	A=[	1.687	21.491	]	A=[	0.437	10.323	]	A=[	0.437	11.635	]
T2Z5	A=[	1.330	20.067	]	A=[	0.270	13.610	]	A=[	0.241	14.963	]
T3Z2	A=[	1.162	16.906	]	A=[	0.479	7.698	]	A=[	0.501	8.284	]
T3Z4	A=[	1.885	21.892	]	A=[	0.469	9.838	]	A=[	0.336	12.448	]
T3Z5	A=[	1.515	19.998	]	A=[	0.408	10.565	]	A=[	0.350	13.096	]
T3Z6	A=[	1.086	14.444	]	A=[	0.426	7.787	]	A=[	0.470	7.192	]
T4Z2	A=[	1.611	19.306	]	A=[	0.513	19.590	]	A=[	0.505	15.965	]
T4Z4	A=[	2.001	25.336	]	A=[	0.562	15.324	]	A=[	0.719	17.265	]
T4Z5	A=[	1.719	24.875	]	A=[	0.491	15.534	]	A=[	0.464	16.499	]
T4Z6	A=[	1.792	18.033	]	A=[	0.661	17.393	]	A=[	0.675	17.316	]
T5Z4	A=[	1.468	22.286	]	A=[	0.464	17.325	]	A=[	0.494	20.247	]
T5Z5	A=[	1.965	20.027	]	A=[	0.586	22.174	]	A=[	0.655	24.320	]

Table B.2: Fit parameters used to compute the energy dependent covariance matrix elements (σ_{12}^2) for the energy dependent χ^2 timing cut analysis.

	σ_{12}^2											
	Neutron				Phonon - side				Charge - side			
Detector Name		$A_{kn(1)}$	$A_{kn}(2)$			$A_{kp(1)}$	$A_{kp}(2)$			$A_{kq(1)}$	$A_{kq}(2)$	
T1Z2	A=[	0.833	16.144	]	A=[	0.136	0.454	]	A=[	0.246	1.099	]
T1Z5	A=[	1.070	16.222	]	A=[	-0.002	-0.131	]	A=[	0.119	0.002	]
T2Z3	A=[	1.141	20.510	]	A=[	0.200	0.003	]	A=[	0.184	0.004	]
T2Z5	A=[	1.171	18.179	]	A=[	-0.000	0.049	]	A=[	0.204	-0.037	]
T3Z2	A=[	0.979	14.207	]	A=[	0.206	0.001	]	A=[	0.208	0.012	]
T3Z4	A=[	1.167	22.512	]	A=[	0.002	-0.200	]	A=[	0.088	0.001	]
T3Z5	A=[	1.028	14.531	]	A=[	-0.000	0.002	]	A=[	0.216	-0.004	]
T3Z6	A=[	0.939	15.173	]	A=[	0.264	0.037	]	A=[	0.307	4.356	]
T4Z2	A=[	1.325	9.788	]	A=[	-0.002	-0.232	]	A=[	0.102	-0.002	]
T4Z4	A=[	1.328	21.572	]	A=[	0.001	0.183	]	A=[	0.398	0.003	]
T4Z5	A=[	1.137	22.367	]	A=[	-0.002	-0.257	]	A=[	0.228	0.003	]
T4Z6	A=[	1.653	0.001	]	A=[	0.309	-0.000	]	A=[	0.496	0.001	]
T5Z4	A=[	1.353	10.477	]	A=[	-0.002	0.143	]	A=[	0.397	-0.004	]
T5Z5	A=[	1.591	-0.001	]	A=[	0.057	-0.001	]	A=[	-0.004	0.111	]

Table B.3: Fit parameters used to compute the energy dependent covariance matrix elements (σ^2_{13}) for the energy dependent χ^2 timing cut analysis.

	σ^2_{13}											
	Neutron				Phonon - side				Charge - side			
Detector Name		$A_{kn(1)}$	$A_{kn}(2)$			$A_{kp(1)}$	$A_{kp}(2)$			$A_{kq(1)}$	$A_{kq}(2)$	
T1Z2	A=[	0.944	18.015	]	A=[	0.218	5.642	]	A=[	0.305	6.347	]
T1Z5	A=[	1.158	19.600	]	A=[	0.285	3.264	]	A=[	0.183	6.394	]
T2Z3	A=[	1.227	21.076	]	A=[	0.295	6.216	]	A=[	0.307	6.687	]
T2Z5	A=[	1.159	21.746	]	A=[	0.276	7.562	]	A=[	0.217	10.658	]
T3Z2	A=[	0.976	18.202	]	A=[	0.371	6.155	]	A=[	0.376	6.081	]
T3Z4	A=[	1.399	24.444	]	A=[	0.323	4.901	]	A=[	0.254	7.605	]
T3Z5	A=[	1.167	20.262	]	A=[	0.302	6.494	]	A=[	0.271	8.542	]
T3Z6	A=[	0.916	15.848	]	A=[	0.370	4.625	]	A=[	0.382	5.592	]
T4Z2	A=[	1.472	22.839	]	A=[	0.489	13.679	]	A=[	0.474	12.396	]
T4Z4	A=[	1.545	26.146	]	A=[	0.396	8.556	]	A=[	0.583	9.063	]
T4Z5	A=[	1.395	26.537	]	A=[	0.409	7.572	]	A=[	0.419	9.551	]
T4Z6	A=[	1.798	21.998	]	A=[	0.655	10.006	]	A=[	0.672	11.311	]
T5Z4	A=[	1.395	25.723	]	A=[	0.445	13.265	]	A=[	0.484	17.244	]
T5Z5	A=[	1.759	22.859	]	A=[	0.513	14.252	]	A=[	0.660	15.095	]

Table B.4: Fit parameters used to compute the energy dependent covariance matrix elements (σ^2_{14}) for the energy dependent χ^2 timing cut analysis.

	σ^2_{14}											
	Neutron				Phonon - side				Charge - side			
Detector Name		$A_{kn(1)}$	$A_{kn}(2)$			$A_{kp(1)}$	$A_{kp}(2)$			$A_{kq(1)}$	$A_{kq}(2)$	
T1Z2	A=[	0.852	16.227	]	A=[	0.133	2.499	]	A=[	0.257	3.525	]
T1Z5	A=[	1.231	18.199	]	A=[	0.218	0.002	]	A=[	0.151	6.615	]
T2Z3	A=[	1.372	20.853	]	A=[	0.316	-0.014	]	A=[	0.299	0.006	]
T2Z5	A=[	1.200	18.425	]	A=[	0.200	-0.008	]	A=[	0.210	7.087	]
T3Z2	A=[	1.000	14.579	]	A=[	0.263	-0.009	]	A=[	0.286	2.566	]
T3Z4	A=[	1.401	21.487	]	A=[	0.224	-0.003	]	A=[	0.251	0.032	]
T3Z5	A=[	1.183	14.647	]	A=[	0.215	0.002	]	A=[	0.292	3.107	]
T3Z6	A=[	0.960	15.253	]	A=[	0.306	3.256	]	A=[	0.345	5.338	]
T4Z2	A=[	1.379	11.534	]	A=[	0.296	0.001	]	A=[	0.345	-0.004	]
T4Z4	A=[	1.588	22.916	]	A=[	0.249	-0.002	]	A=[	0.484	9.714	]
T4Z5	A=[	1.269	22.693	]	A=[	0.267	0.000	]	A=[	0.295	7.373	]
T4Z6	A=[	1.688	0.000	]	A=[	0.506	3.412	]	A=[	0.626	3.060	]
T5Z4	A=[	1.363	12.246	]	A=[	0.284	-0.003	]	A=[	0.380	10.731	]
T5Z5	A=[	1.699	5.181	]	A=[	0.453	4.034	]	A=[	0.511	-0.001	]

Table B.5: Fit parameters used to compute the energy dependent covariance matrix elements (σ^2_{15}) for the energy dependent χ^2 timing cut analysis.

	σ^2_{15}											
	Neutron				Phonon - side				Charge - side			
Detector Name		$A_{kn(1)}$	$A_{kn}(2)$			$A_{kp(1)}$	$A_{kp}(2)$			$A_{kq(1)}$	$A_{kq}(2)$	
T1Z2	A=[	0.794	16.641	]	A=[	0.188	3.794	]	A=[	0.310	7.097	]
T1Z5	A=[	1.294	20.457	]	A=[	0.305	0.003	]	A=[	0.218	4.004	]
T2Z3	A=[	1.396	19.161	]	A=[	0.335	5.557	]	A=[	0.333	4.116	]
T2Z5	A=[	1.005	17.880	]	A=[	0.328	6.187	]	A=[	0.252	11.431	]
T3Z2	A=[	0.864	14.284	]	A=[	0.377	3.565	]	A=[	0.407	1.508	]
T3Z4	A=[	1.492	21.756	]	A=[	0.375	1.531	]	A=[	0.284	5.134	]
T3Z5	A=[	1.277	18.556	]	A=[	0.335	6.122	]	A=[	0.299	5.273	]
T3Z6	A=[	0.804	13.183	]	A=[	0.426	-0.005	]	A=[	0.427	4.691	]
T4Z2	A=[	1.365	19.733	]	A=[	0.526	14.339	]	A=[	0.561	8.046	]
T4Z4	A=[	1.722	22.851	]	A=[	0.453	7.980	]	A=[	0.637	6.664	]
T4Z5	A=[	1.403	23.467	]	A=[	0.472	8.341	]	A=[	0.417	9.378	]
T4Z6	A=[	1.449	20.445	]	A=[	0.762	9.245	]	A=[	0.746	12.450	]
T5Z4	A=[	1.115	21.317	]	A=[	0.518	10.032	]	A=[	0.426	15.854	]
T5Z5	A=[	1.633	21.627	]	A=[	0.576	15.267	]	A=[	0.649	13.301	]

Table B.6: Fit parameters used to compute the energy dependent covariance matrix elements (σ^2_{22}) for the energy dependent χ^2 timing cut analysis.

	σ^2_{22}											
	Neutron				Phonon - side				Charge - side			
Detector Name		$A_{kn(1)}$	$A_{kn}(2)$			$A_{kp(1)}$	$A_{kp}(2)$			$A_{kq(1)}$	$A_{kq}(2)$	
T1Z2	A=[	0.874	21.837	]	A=[	0.202	9.201	]	A=[	0.372	5.408	]
T1Z5	A=[	0.970	24.688	]	A=[	0.326	12.809	]	A=[	0.247	9.402	]
T2Z3	A=[	1.062	30.083	]	A=[	0.312	15.686	]	A=[	0.507	6.315	]
T2Z5	A=[	1.182	33.702	]	A=[	-0.000	20.391	]	A=[	0.196	14.440	]
T3Z2	A=[	1.094	23.463	]	A=[	0.481	9.314	]	A=[	0.390	7.835	]
T3Z4	A=[	1.005	36.748	]	A=[	0.355	15.752	]	A=[	0.392	13.114	]
T3Z5	A=[	0.986	23.700	]	A=[	0.418	8.931	]	A=[	0.429	11.534	]
T3Z6	A=[	1.022	24.861	]	A=[	0.352	12.087	]	A=[	0.336	12.498	]
T4Z2	A=[	1.358	49.402	]	A=[	0.285	30.156	]	A=[	0.118	27.536	]
T4Z4	A=[	1.188	50.485	]	A=[	0.414	23.144	]	A=[	0.817	18.894	]
T4Z5	A=[	0.962	41.396	]	A=[	0.204	23.123	]	A=[	0.380	20.372	]
T4Z6	A=[	1.875	66.830	]	A=[	0.793	37.825	]	A=[	0.994	48.461	]
T5Z4	A=[	1.415	52.922	]	A=[	0.266	34.461	]	A=[	0.462	31.384	]
T5Z5	A=[	1.723	61.335	]	A=[	0.278	40.960	]	A=[	0.417	41.901	]

Table B.7: Fit parameters used to compute the energy dependent covariance matrix elements (σ^2_{23}) for the energy dependent χ^2 timing cut analysis.

	σ^2_{23}											
	Neutron				Phonon - side				Charge - side			
Detector Name		$A_{kn(1)}$	$A_{kn}(2)$			$A_{kp(1)}$	$A_{kp}(2)$			$A_{kq(1)}$	$A_{kq}(2)$	
T1Z2	A=[	0.756	17.379	]	A=[	0.086	4.014	]	A=[	0.226	3.299	]
T1Z5	A=[	0.829	15.802	]	A=[	0.101	-0.037	]	A=[	0.114	2.720	]
T2Z3	A=[	0.873	20.181	]	A=[	0.164	5.232	]	A=[	0.264	-0.001	]
T2Z5	A=[	1.022	22.803	]	A=[	0.054	8.975	]	A=[	0.139	7.860	]
T3Z2	A=[	0.863	15.569	]	A=[	0.226	0.013	]	A=[	0.232	0.024	]
T3Z4	A=[	0.872	23.875	]	A=[	0.137	1.349	]	A=[	0.184	-0.001	]
T3Z5	A=[	0.802	16.854	]	A=[	0.141	-0.000	]	A=[	0.253	3.319	]
T3Z6	A=[	0.814	17.099	]	A=[	0.204	5.679	]	A=[	0.249	7.218	]
T4Z2	A=[	1.204	25.609	]	A=[	0.267	0.003	]	A=[	0.291	6.870	]
T4Z4	A=[	1.019	26.443	]	A=[	0.177	4.156	]	A=[	0.428	4.767	]
T4Z5	A=[	0.922	25.831	]	A=[	0.186	4.332	]	A=[	0.261	4.336	]
T4Z6	A=[	1.685	26.861	]	A=[	0.423	13.577	]	A=[	0.481	17.546	]
T5Z4	A=[	1.271	24.996	]	A=[	0.340	-0.003	]	A=[	0.370	10.434	]
T5Z5	A=[	1.428	25.963	]	A=[	0.268	12.729	]	A=[	0.476	0.001	]

Table B.8: Fit parameters used to compute the energy dependent covariance matrix elements (σ^2_{24}) for the energy dependent χ^2 timing cut analysis.

	σ^2_{24}											
	Neutron				Phonon - side				Charge - side			
Detector Name		$A_{kn(1)}$	$A_{kn}(2)$			$A_{kp(1)}$	$A_{kp}(2)$			$A_{kq(1)}$	$A_{kq}(2)$	
T1Z2	A=[	0.869	21.700	]	A=[	0.204	8.986	]	A=[	0.360	5.477	]
T1Z5	A=[	1.039	25.634	]	A=[	0.351	12.028	]	A=[	0.239	9.271	]
T2Z3	A=[	1.137	30.854	]	A=[	0.346	15.340	]	A=[	0.467	6.154	]
T2Z5	A=[	1.195	32.742	]	A=[	0.224	17.441	]	A=[	0.213	13.093	]
T3Z2	A=[	1.082	23.678	]	A=[	0.468	9.255	]	A=[	0.367	7.860	]
T3Z4	A=[	1.074	36.965	]	A=[	0.392	14.967	]	A=[	0.355	12.991	]
T3Z5	A=[	1.055	23.330	]	A=[	0.434	7.743	]	A=[	0.389	11.088	]
T3Z6	A=[	1.016	24.808	]	A=[	0.354	11.701	]	A=[	0.333	12.210	]
T4Z2	A=[	1.432	44.714	]	A=[	0.429	25.600	]	A=[	0.300	23.694	]
T4Z4	A=[	1.342	49.775	]	A=[	0.512	20.540	]	A=[	0.746	19.177	]
T4Z5	A=[	1.031	40.547	]	A=[	0.325	20.707	]	A=[	0.365	19.837	]
T4Z6	A=[	1.942	57.991	]	A=[	0.911	28.437	]	A=[	1.124	39.520	]
T5Z4	A=[	1.461	49.010	]	A=[	0.429	29.754	]	A=[	0.498	29.081	]
T5Z5	A=[	1.852	53.984	]	A=[	0.586	32.683	]	A=[	0.613	34.992	]

Table B.9: Fit parameters used to compute the energy dependent covariance matrix elements (σ^2_{25}) for the energy dependent χ^2 timing cut analysis.

	σ^2_{25}											
	Neutron				Phonon - side				Charge - side			
Detector Name		$A_{kn(1)}$	$A_{kn}(2)$			$A_{kp(1)}$	$A_{kp}(2)$			$A_{kq(1)}$	$A_{kq}(2)$	
T1Z2	A=[	0.522	16.953	]	A=[	0.026	4.279	]	A=[	0.067	4.413	]
T1Z5	A=[	0.865	18.007	]	A=[	-0.002	4.578	]	A=[	0.024	3.275	]
T2Z3	A=[	0.908	21.517	]	A=[	0.151	7.118	]	A=[	0.208	0.004	]
T2Z5	A=[	0.857	20.888	]	A=[	0.039	12.627	]	A=[	0.004	10.007	]
T3Z2	A=[	0.694	15.890	]	A=[	0.184	4.721	]	A=[	0.195	3.929	]
T3Z4	A=[	0.796	25.873	]	A=[	0.003	5.364	]	A=[	-0.003	3.772	]
T3Z5	A=[	0.820	17.611	]	A=[	0.086	-0.016	]	A=[	0.071	3.201	]
T3Z6	A=[	0.686	15.704	]	A=[	0.112	8.390	]	A=[	0.192	9.579	]
T4Z2	A=[	1.148	29.976	]	A=[	0.265	13.489	]	A=[	0.244	14.504	]
T4Z4	A=[	1.043	32.008	]	A=[	0.146	9.031	]	A=[	0.143	9.490	]
T4Z5	A=[	0.872	29.170	]	A=[	0.192	7.311	]	A=[	-0.002	8.535	]
T4Z6	A=[	1.476	38.406	]	A=[	0.521	23.490	]	A=[	0.726	27.670	]
T5Z4	A=[	1.050	29.982	]	A=[	0.332	17.658	]	A=[	-0.002	17.931	]
T5Z5	A=[	1.405	38.454	]	A=[	0.140	24.039	]	A=[	0.396	11.398	]

Table B.10: Fit parameters used to compute the energy dependent covariance matrix elements (σ^2_{33}) for the energy dependent χ^2 timing cut analysis.

	σ^2_{33}											
Detector Name	Neutron				Phonon - side				Charge - side			
T1Z2	A=[	0.842	19.591	]	A=[	0.198	6.345	]	A=[	0.260	7.204	]
T1Z5	A=[	0.906	18.941	]	A=[	0.198	5.978	]	A=[	0.132	6.606	]
T2Z3	A=[	0.928	21.241	]	A=[	0.226	6.961	]	A=[	0.230	7.852	]
T2Z5	A=[	0.999	26.148	]	A=[	0.205	9.929	]	A=[	0.152	11.617	]
T3Z2	A=[	0.840	19.941	]	A=[	0.319	6.179	]	A=[	0.310	6.451	]
T3Z4	A=[	1.052	26.528	]	A=[	0.242	6.428	]	A=[	0.206	7.419	]
T3Z5	A=[	0.921	21.450	]	A=[	0.247	6.990	]	A=[	0.231	7.729	]
T3Z6	A=[	0.783	17.928	]	A=[	0.322	5.698	]	A=[	0.306	7.453	]
T4Z2	A=[	1.274	40.563	]	A=[	0.451	16.490	]	A=[	0.412	16.775	]
T4Z4	A=[	1.198	31.548	]	A=[	0.302	9.656	]	A=[	0.476	10.617	]
T4Z5	A=[	1.123	31.525	]	A=[	0.337	9.488	]	A=[	0.375	9.260	]
T4Z6	A=[	1.672	51.909	]	A=[	0.611	17.862	]	A=[	0.627	19.408	]
T5Z4	A=[	1.231	41.687	]	A=[	0.421	16.784	]	A=[	0.393	22.570	]
T5Z5	A=[	1.507	42.822	]	A=[	0.449	17.507	]	A=[	0.630	15.917	]

Table B.11: Fit parameters used to compute the energy dependent covariance matrix elements (σ^2_{34}) for the energy dependent χ^2 timing cut analysis.

	σ^2_{34}											
	Neutron				Phonon - side				Charge - side			
Detector Name		$A_{kn(1)}$	$A_{kn}(2)$			$A_{kp(1)}$	$A_{kp}(2)$			$A_{kq(1)}$	$A_{kq}(2)$	
T1Z2	A=[	0.772	17.076	]	A=[	0.095	3.627	]	A=[	0.237	3.431	]
T1Z5	A=[	0.949	16.242	]	A=[	0.122	0.002	]	A=[	0.141	1.919	]
T2Z3	A=[	1.021	20.000	]	A=[	0.226	4.301	]	A=[	0.259	-0.003	]
T2Z5	A=[	1.054	21.454	]	A=[	0.166	6.850	]	A=[	0.179	6.880	]
T3Z2	A=[	0.876	15.532	]	A=[	0.243	-0.000	]	A=[	0.257	0.592	]
T3Z4	A=[	1.047	22.603	]	A=[	0.180	0.012	]	A=[	0.199	-0.009	]
T3Z5	A=[	0.916	16.161	]	A=[	0.164	0.002	]	A=[	0.243	4.457	]
T3Z6	A=[	0.828	16.757	]	A=[	0.239	5.305	]	A=[	0.281	6.782	]
T4Z2	A=[	1.287	18.038	]	A=[	0.234	0.000	]	A=[	0.308	6.342	]
T4Z4	A=[	1.235	23.706	]	A=[	0.234	0.003	]	A=[	0.442	3.063	]
T4Z5	A=[	1.040	24.116	]	A=[	0.238	-0.013	]	A=[	0.272	4.564	]
T4Z6	A=[	1.712	13.915	]	A=[	0.462	8.455	]	A=[	0.524	13.395	]
T5Z4	A=[	1.321	17.803	]	A=[	0.308	0.003	]	A=[	0.394	8.100	]
T5Z5	A=[	1.524	17.797	]	A=[	0.338	8.136	]	A=[	0.517	0.003	]

Table B.12: Fit parameters used to compute the energy dependent covariance matrix elements (σ^2_{35}) for the energy dependent χ^2 timing cut analysis.

	σ^2_{35}											
	Neutron				Phonon - side				Charge - side			
Detector Name		$A_{kn(1)}$	$A_{kn}(2)$			$A_{kp(1)}$	$A_{kp}(2)$			$A_{kq(1)}$	$A_{kq}(2)$	
T1Z2	A=[	0.699	17.289	]	A=[	0.159	6.159	]	A=[	0.277	6.382	]
T1Z5	A=[	1.023	18.801	]	A=[	0.232	6.171	]	A=[	0.165	5.525	]
T2Z3	A=[	1.048	19.398	]	A=[	0.284	6.755	]	A=[	0.252	6.491	]
T2Z5	A=[	0.885	19.475	]	A=[	0.251	10.843	]	A=[	0.143	12.664	]
T3Z2	A=[	0.753	14.321	]	A=[	0.337	4.794	]	A=[	0.323	4.369	]
T3Z4	A=[	1.133	23.268	]	A=[	0.308	5.637	]	A=[	0.225	6.209	]
T3Z5	A=[	1.017	18.681	]	A=[	0.309	5.731	]	A=[	0.229	5.614	]
T3Z6	A=[	0.686	14.026	]	A=[	0.367	4.901	]	A=[	0.330	7.497	]
T4Z2	A=[	1.263	20.577	]	A=[	0.515	14.887	]	A=[	0.508	10.368	]
T4Z4	A=[	1.389	24.006	]	A=[	0.360	9.853	]	A=[	0.499	9.781	]
T4Z5	A=[	1.166	24.542	]	A=[	0.406	10.427	]	A=[	0.356	9.264	]
T4Z6	A=[	1.495	15.576	]	A=[	0.731	15.500	]	A=[	0.685	17.553	]
T5Z4	A=[	1.104	19.541	]	A=[	0.505	13.258	]	A=[	0.424	12.296	]
T5Z5	A=[	1.504	23.639	]	A=[	0.540	16.632	]	A=[	0.593	14.095	]

Table B.13: Fit parameters used to compute the energy dependent covariance matrix elements (σ_{44}^2) for the energy dependent χ^2 timing cut analysis.

	σ_{44}^2											
	Neutron				Phonon - side				Charge - side			
Detector Name		$A_{kn(1)}$	$A_{kn}(2)$			$A_{kp(1)}$	$A_{kp}(2)$			$A_{kq(1)}$	$A_{kq}(2)$	
T1Z2	A=[	0.868	21.692	]	A=[	0.208	8.929	]	A=[	0.353	5.859	]
T1Z5	A=[	1.152	27.047	]	A=[	0.377	12.443	]	A=[	0.241	10.619	]
T2Z3	A=[	1.285	31.832	]	A=[	0.401	15.573	]	A=[	0.457	7.404	]
T2Z5	A=[	1.211	32.491	]	A=[	0.285	16.088	]	A=[	0.220	13.159	]
T3Z2	A=[	1.082	23.932	]	A=[	0.469	9.439	]	A=[	0.365	8.266	]
T3Z4	A=[	1.207	37.431	]	A=[	0.440	15.012	]	A=[	0.355	13.679	]
T3Z5	A=[	1.159	23.265	]	A=[	0.458	7.742	]	A=[	0.376	11.211	]
T3Z6	A=[	1.016	24.874	]	A=[	0.367	11.630	]	A=[	0.344	12.136	]
T4Z2	A=[	1.465	44.175	]	A=[	0.484	24.132	]	A=[	0.368	22.100	]
T4Z4	A=[	1.546	51.035	]	A=[	0.594	20.366	]	A=[	0.689	22.835	]
T4Z5	A=[	1.111	40.823	]	A=[	0.383	20.588	]	A=[	0.355	20.625	]
T4Z6	A=[	1.925	57.705	]	A=[	0.928	26.278	]	A=[	1.173	35.563	]
T5Z4	A=[	1.457	49.139	]	A=[	0.483	28.111	]	A=[	0.474	29.732	]
T5Z5	A=[	1.927	52.538	]	A=[	0.702	29.846	]	A=[	0.676	33.188	]

Table B.14: Fit parameters used to compute the energy dependent covariance matrix elements (σ_{45}^2) for the energy dependent χ^2 timing cut analysis.

	σ_{45}^2											
	Neutron				Phonon - side				Charge - side			
Detector Name		$A_{kn(1)}$	$A_{kn}(2)$			$A_{kp(1)}$	$A_{kp}(2)$			$A_{kq(1)}$	$A_{kq}(2)$	
T1Z2	A=[	0.567	16.626	]	A=[	0.122	2.892	]	A=[	0.160	3.576	]
T1Z5	A=[	1.048	18.702	]	A=[	0.109	1.965	]	A=[	0.160	2.067	]
T2Z3	A=[	1.135	21.237	]	A=[	0.268	6.273	]	A=[	0.272	0.013	]
T2Z5	A=[	0.907	19.557	]	A=[	0.236	9.787	]	A=[	0.199	8.107	]
T3Z2	A=[	0.722	15.962	]	A=[	0.245	3.812	]	A=[	0.260	3.628	]
T3Z4	A=[	1.058	24.351	]	A=[	0.206	2.646	]	A=[	0.184	1.987	]
T3Z5	A=[	0.992	17.140	]	A=[	0.194	-0.009	]	A=[	0.192	2.988	]
T3Z6	A=[	0.716	15.415	]	A=[	0.240	7.439	]	A=[	0.270	8.940	]
T4Z2	A=[	1.259	23.199	]	A=[	0.351	9.153	]	A=[	0.390	10.406	]
T4Z4	A=[	1.374	29.181	]	A=[	0.321	5.260	]	A=[	0.371	6.058	]
T4Z5	A=[	1.037	27.243	]	A=[	0.323	-0.006	]	A=[	0.177	7.490	]
T4Z6	A=[	1.508	31.550	]	A=[	0.652	12.005	]	A=[	0.834	18.109	]
T5Z4	A=[	1.108	25.346	]	A=[	0.449	11.329	]	A=[	0.233	15.702	]
T5Z5	A=[	1.569	28.450	]	A=[	0.398	17.860	]	A=[	0.514	7.622	]

Table B.15: Fit parameters used to compute the energy dependent covariance matrix elements (σ^2_{55}) for the energy dependent χ^2 timing cut analysis.

	σ^2_{55}											
	Neutron				Phonon - side				Charge - side			
Detector Name		$A_{kn(1)}$	$A_{kn}(2)$			$A_{kp(1)}$	$A_{kp}(2)$			$A_{kq(1)}$	$A_{kq}(2)$	
T1Z2	A=[	0.741	20.481	]	A=[	0.335	8.389	]	A=[	0.317	14.716	]
T1Z5	A=[	1.249	25.540	]	A=[	0.325	7.969	]	A=[	0.261	7.296	]
T2Z3	A=[	1.269	24.387	]	A=[	0.415	7.874	]	A=[	0.358	8.272	]
T2Z5	A=[	0.905	25.466	]	A=[	0.419	14.729	]	A=[	0.319	17.664	]
T3Z2	A=[	0.769	21.313	]	A=[	0.423	9.037	]	A=[	0.422	8.741	]
T3Z4	A=[	1.315	31.311	]	A=[	0.431	7.772	]	A=[	0.327	9.070	]
T3Z5	A=[	1.246	25.220	]	A=[	0.456	5.669	]	A=[	0.333	8.218	]
T3Z6	A=[	0.690	17.270	]	A=[	0.510	6.913	]	A=[	0.421	11.334	]
T4Z2	A=[	1.321	53.333	]	A=[	0.693	23.991	]	A=[	0.804	21.649	]
T4Z4	A=[	1.725	41.693	]	A=[	0.486	13.576	]	A=[	0.625	16.131	]
T4Z5	A=[	1.350	37.674	]	A=[	0.541	16.483	]	A=[	0.417	19.211	]
T4Z6	A=[	1.386	67.340	]	A=[	1.041	28.136	]	A=[	1.078	34.927	]
T5Z4	A=[	1.004	49.817	]	A=[	0.648	27.313	]	A=[	0.569	32.842	]
T5Z5	A=[	1.756	59.695	]	A=[	0.710	26.882	]	A=[	0.866	21.029	]

B.2 Covariance matrix elements

Figures (B.1) to (B.13) show the energy dependence of the covariance elements as a function of the recoil energy for the neutrons, betas, phonon and charge-side events. The black solid line represents the fit to the data.

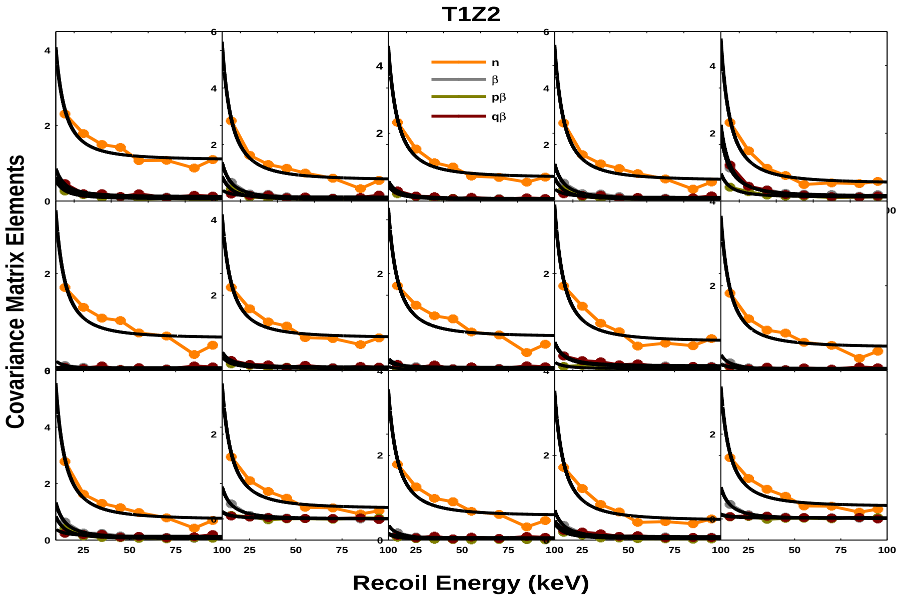

Figure B.1: Covariance matrix elements binned as function of energy for T1Z2. In black is shown the fit to the data using the functional form in equation (8.5). Different colors indicate events of different type: neutron (orange), surface events - betas(grey), phonon-side events (dark yellow) and charge-side events (dark red).

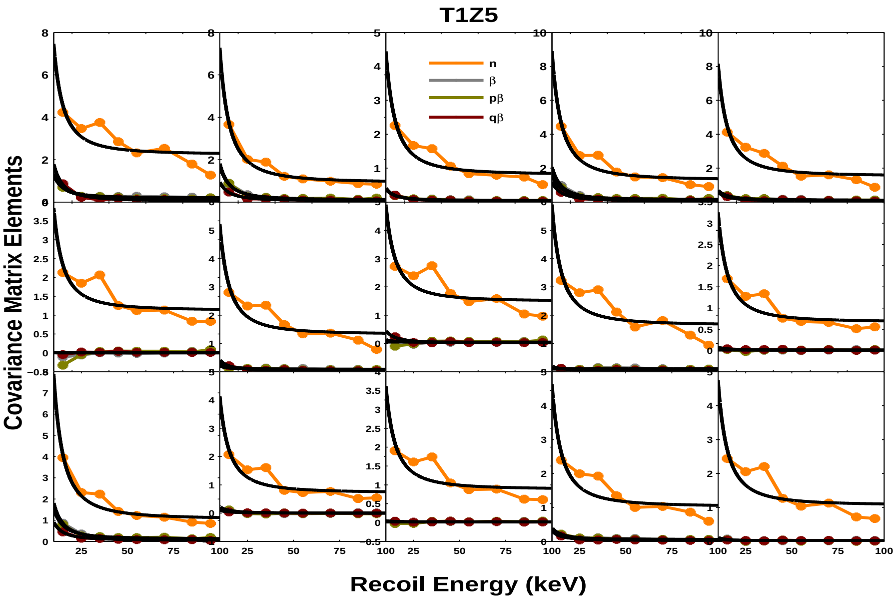

Figure B.2: Covariance matrix elements binned as function of energy for T1Z5. In black is shown the fit to the data using the functional form in equation (8.5). Different colors indicate events of different type: neutron (orange), surface events - betas(grey), phonon-side events (dark yellow) and charge-side events (dark red).

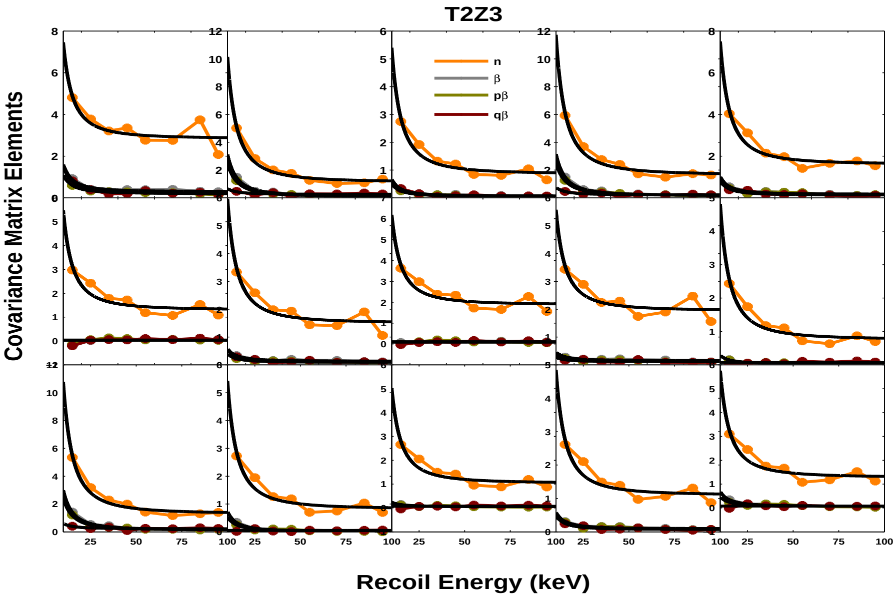

Figure B.3: Covariance matrix elements binned as function of energy for T2Z3. In black is shown the fit to the data using the functional form in equation (8.5). Different colors indicate events of different type: neutron (orange), surface events - betas(grey), phonon-side events (dark yellow) and charge-side events (dark red).

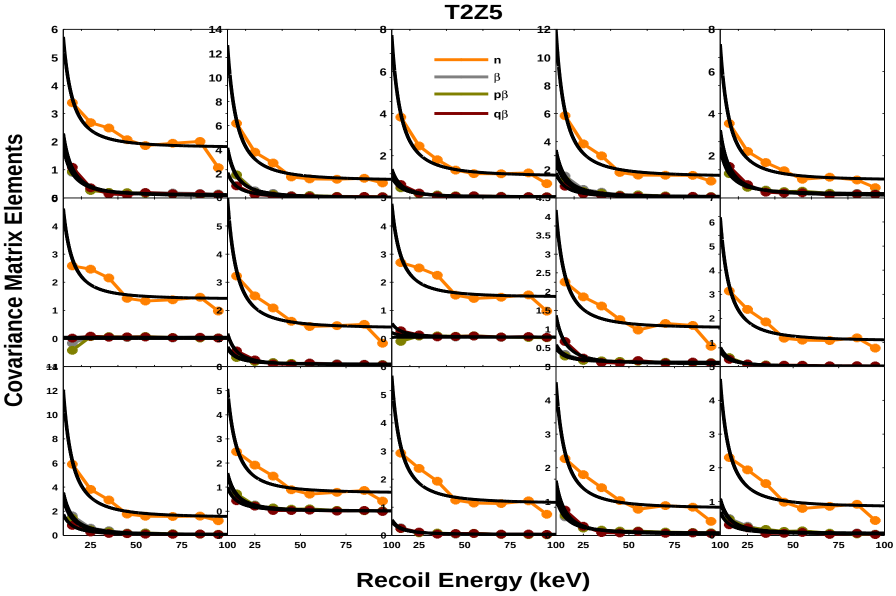

Figure B.4: Covariance matrix elements binned as function of energy for T2Z3. In black is shown the fit to the data using the functional form in equation (8.5). Different colors indicate events of different type: neutron (orange), surface events - betas(grey), phonon-side events (dark yellow) and charge-side events (dark red).

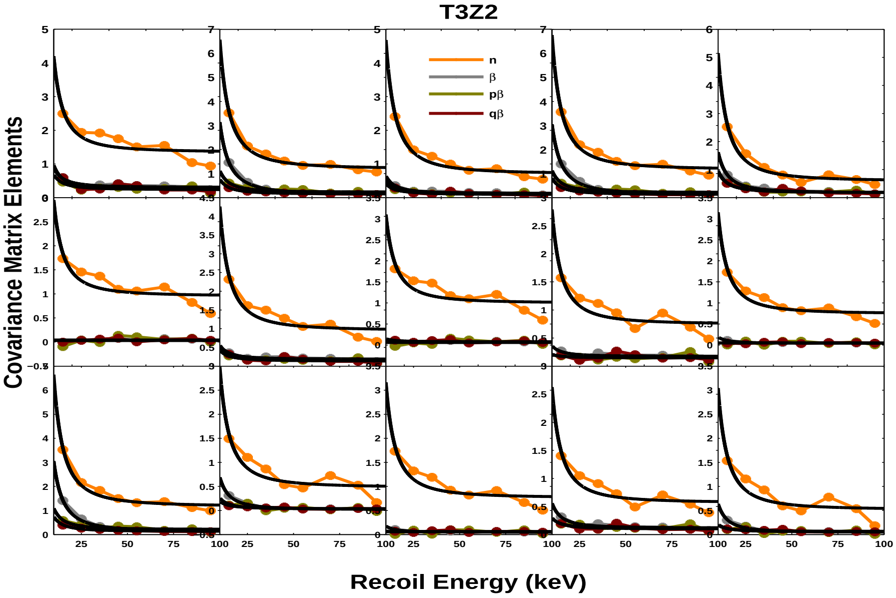

Figure B.5: Covariance matrix elements binned as function of energy for T2Z3. In black is shown the fit to the data using the functional form in equation (8.5). Different colors indicate events of different type: neutron (orange), surface events - betas(grey), phonon-side events (dark yellow) and charge-side events (dark red).

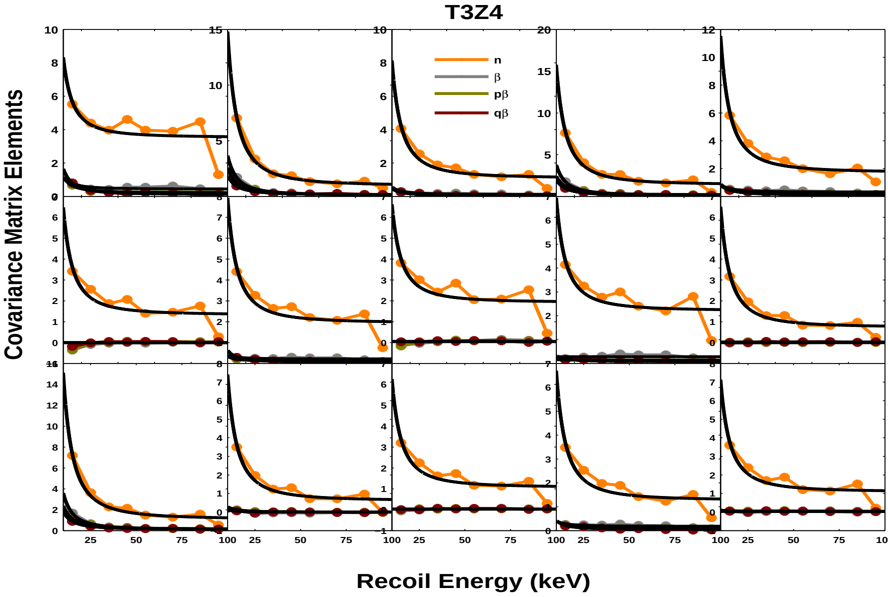

Figure B.6: Covariance matrix elements binned as function of energy for T2Z3. In black is shown the fit to the data using the functional form in equation (8.5). Different colors indicate events of different type: neutron (orange), surface events - betas(grey), phonon-side events (dark yellow) and charge-side events (dark red).

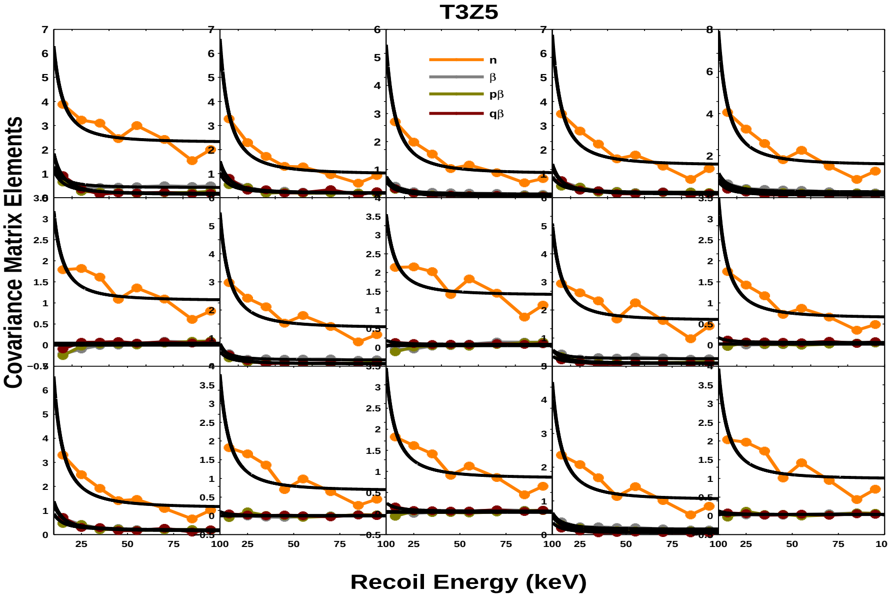

Figure B.7: Covariance matrix elements binned as function of energy for T2Z3. In black is shown the fit to the data using the functional form in equation (8.5). Different colors indicate events of different type: neutron (orange), surface events - betas(grey), phonon-side events (dark yellow) and charge-side events (dark red).

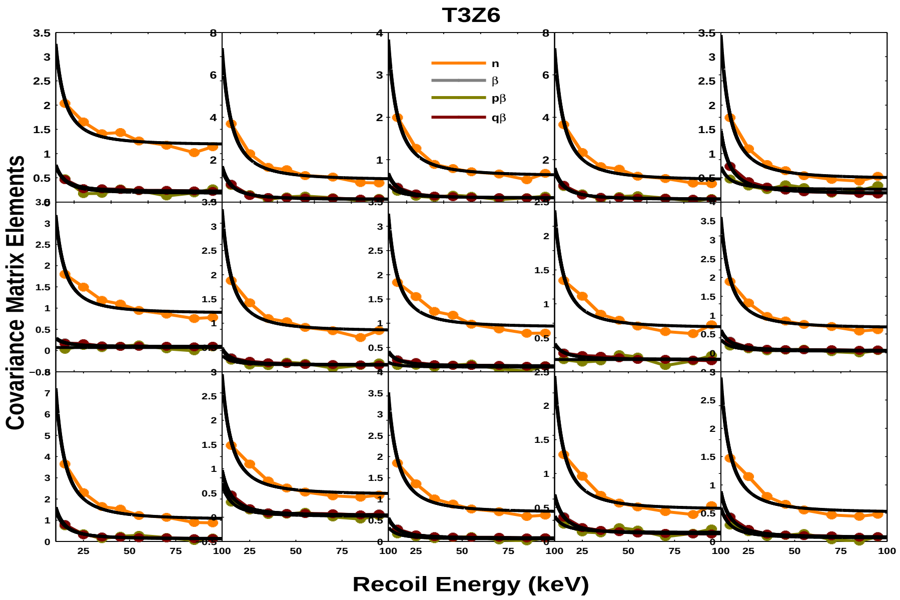

Figure B.8: Covariance matrix elements binned as function of energy for T2Z3. In black is shown the fit to the data using the functional form in equation (8.5). Different colors indicate events of different type: neutron (orange), surface events - betas(grey), phonon-side events (dark yellow) and charge-side events (dark red).

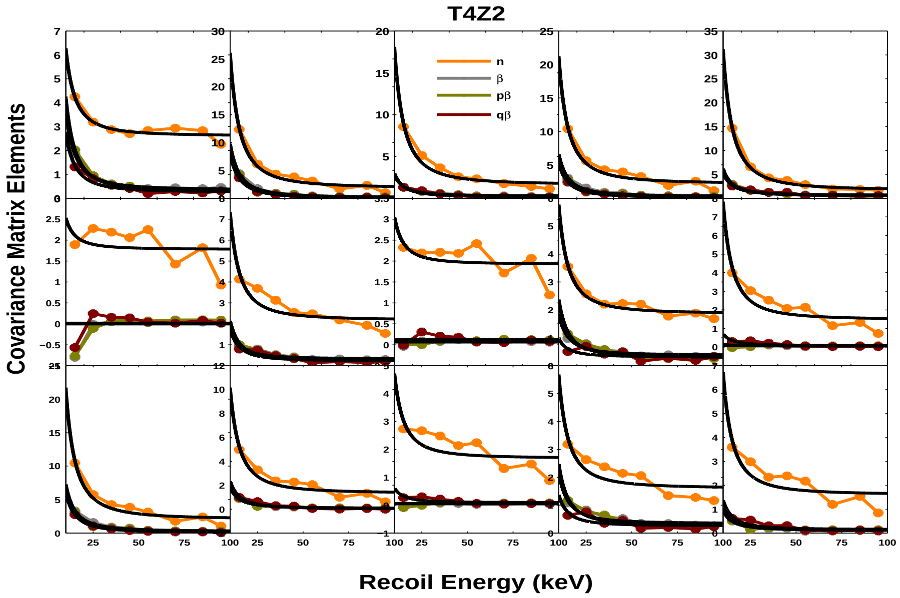

Figure B.9: Covariance matrix elements binned as function of energy for T2Z3. In black is shown the fit to the data using the functional form in equation (8.5). Different colors indicate events of different type: neutron (orange), surface events - betas(grey), phonon-side events (dark yellow) and charge-side events (dark red).

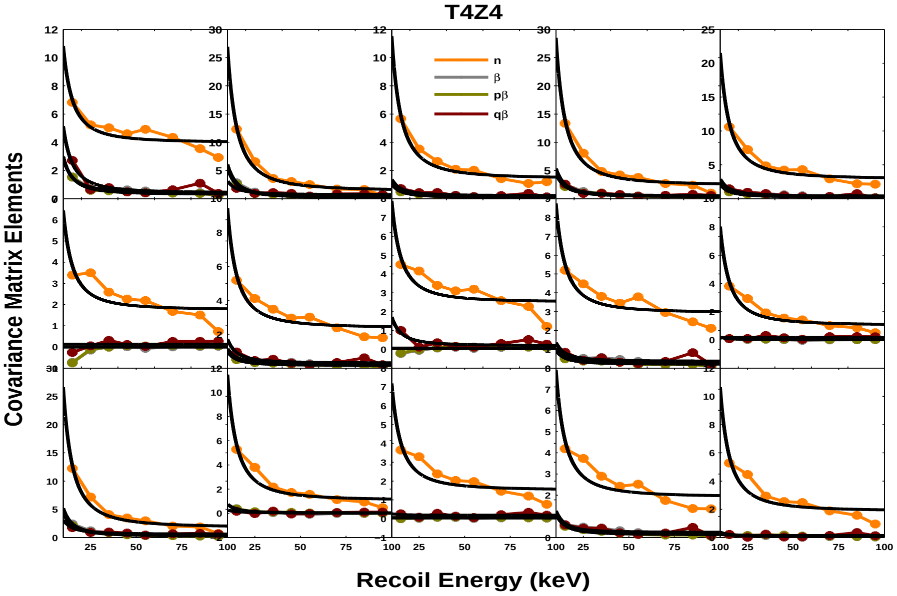

Figure B.10: Covariance matrix elements binned as function of energy for T2Z3. In black is shown the fit to the data using the functional form in equation (8.5). Different colors indicate events of different type: neutron (orange), surface events - betas(grey), phonon-side events (dark yellow) and charge-side events (dark red).

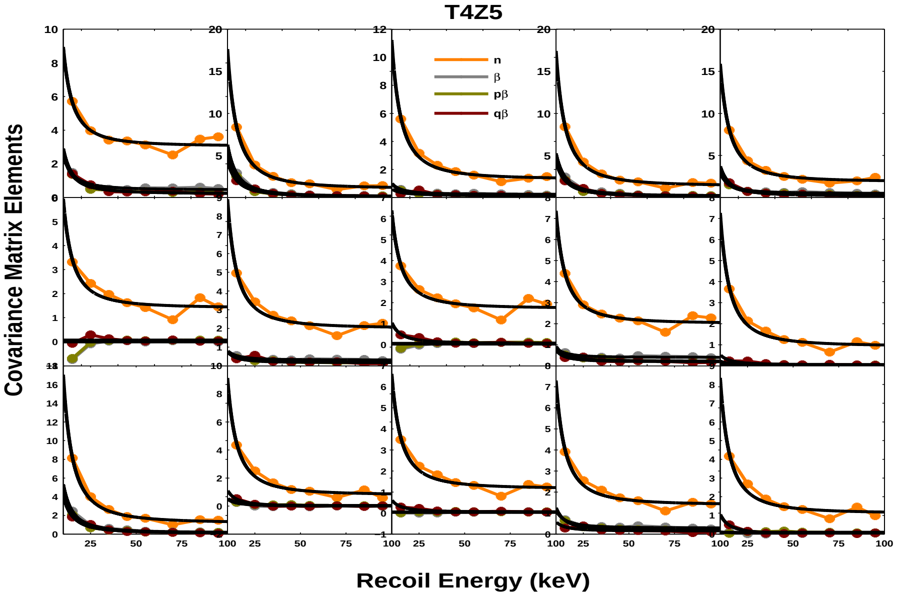

Figure B.11: Covariance matrix elements binned as function of energy for T2Z3. In black is shown the fit to the data using the functional form in equation (8.5). Different colors indicate events of different type: neutron (orange), surface events - betas(grey), phonon-side events (dark yellow) and charge-side events (dark red).

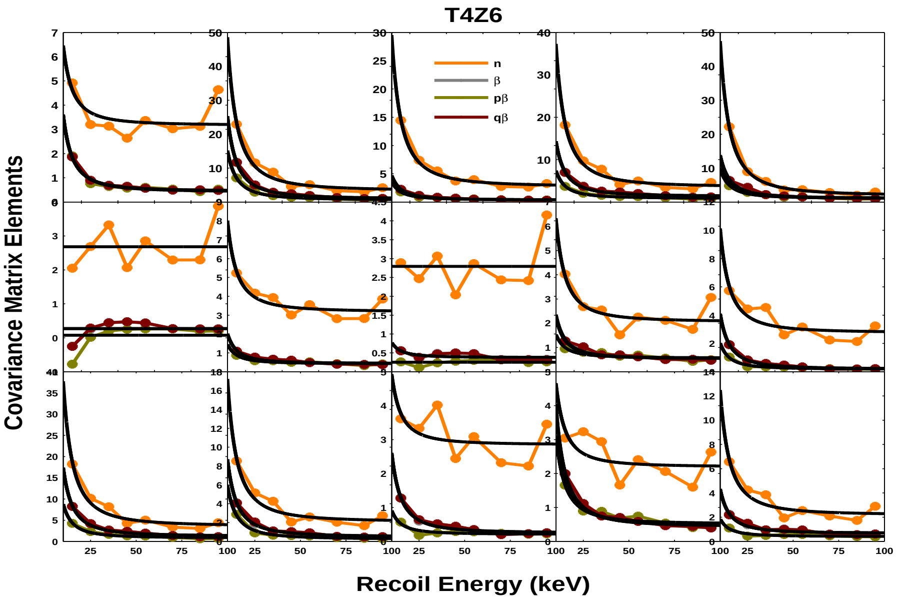

Figure B.12: Covariance matrix elements binned as function of energy for T2Z3. In black is shown the fit to the data using the functional form in equation (8.5). Different colors indicate events of different type: neutron (orange), surface events - betas(grey), phonon-side events (dark yellow) and charge-side events (dark red).

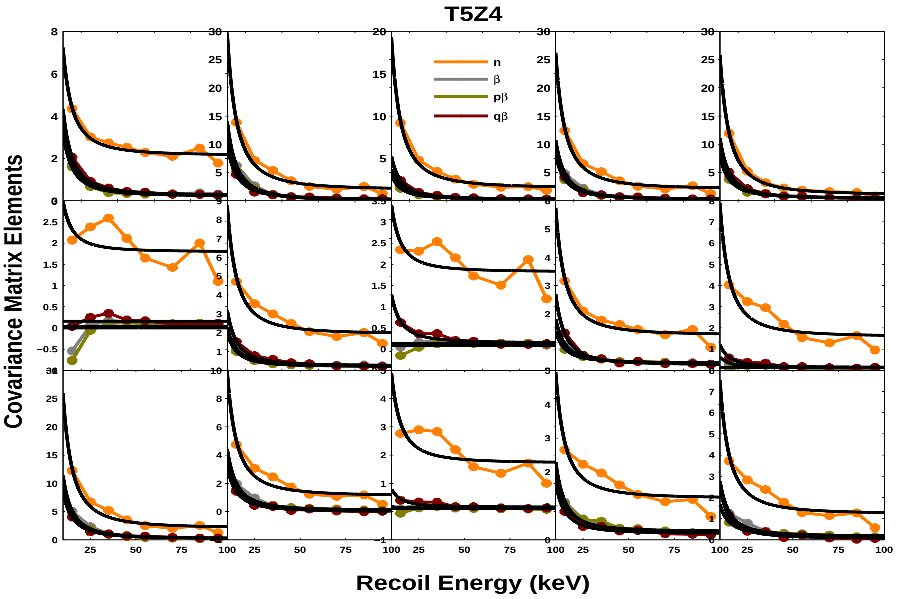

Figure B.13: Covariance matrix elements binned as function of energy for T2Z3. In black is shown the fit to the data using the functional form in equation (8.5). Different colors indicate events of different type: neutron (orange), surface events - betas(grey), phonon-side events (dark yellow) and charge-side events (dark red).

B.3 correlation coefficients

The correlation coefficients $\rho_{jk} = \frac{cov(x_j, x_k)}{\sigma_j \cdot \sigma_k}$ of the 5 variables used in the construction of the χ^2 are shown in Figures (B.14) to (B.23). These timing variables are taken in the following order {**pminrtc**, **pdelc**, **pminrtCFc**, **pdelCFc** and **pminrt4070CFc**}; they are indexed by {1, 2, 3, 4 and 5} as indicated in the plots below.

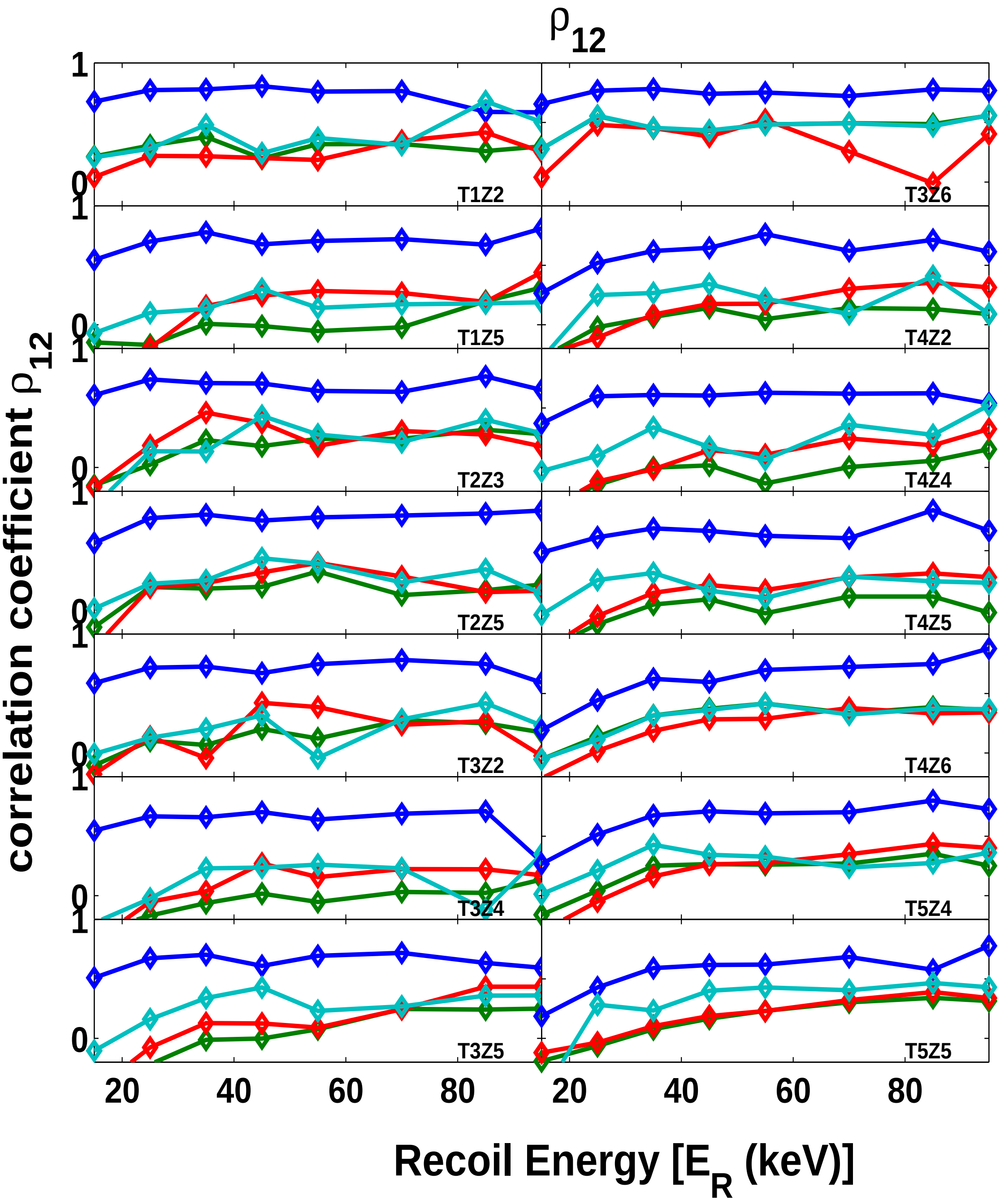

Figure B.14: The correlation coefficient ρ_{12}. The blue curve represents the energy dependence for the neutron sample while the green, the red and the cyan curves represents the energy dependence for the surface events betas, the phonon and the charge-side events respectively.

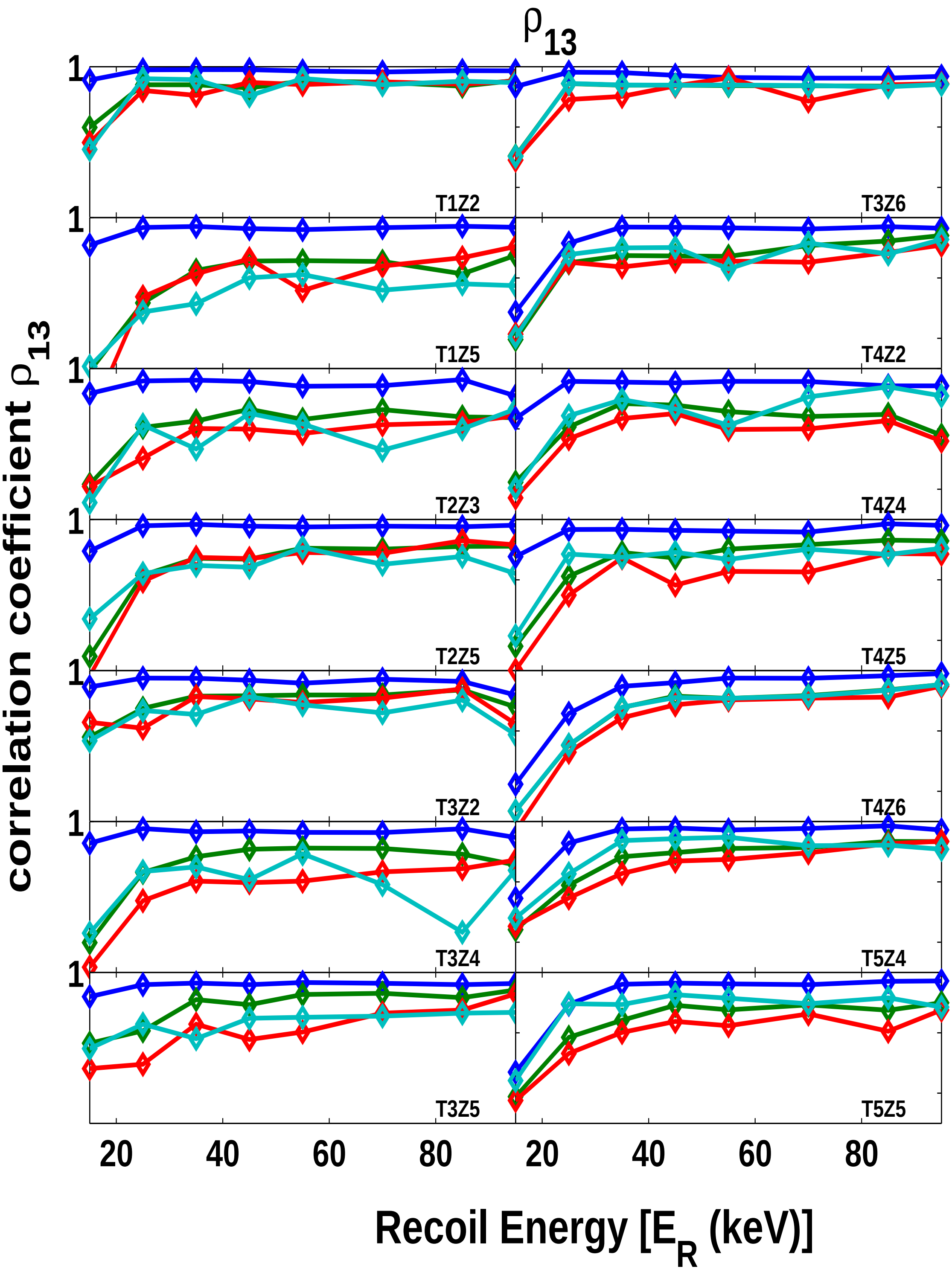

Figure B.15: The correlation coefficient ρ_{13}. The blue curve represents the energy dependence for the neutron sample while the green, the red and the cyan curves represents the energy dependence for the surface events betas, the phonon and the charge-side events respectively.

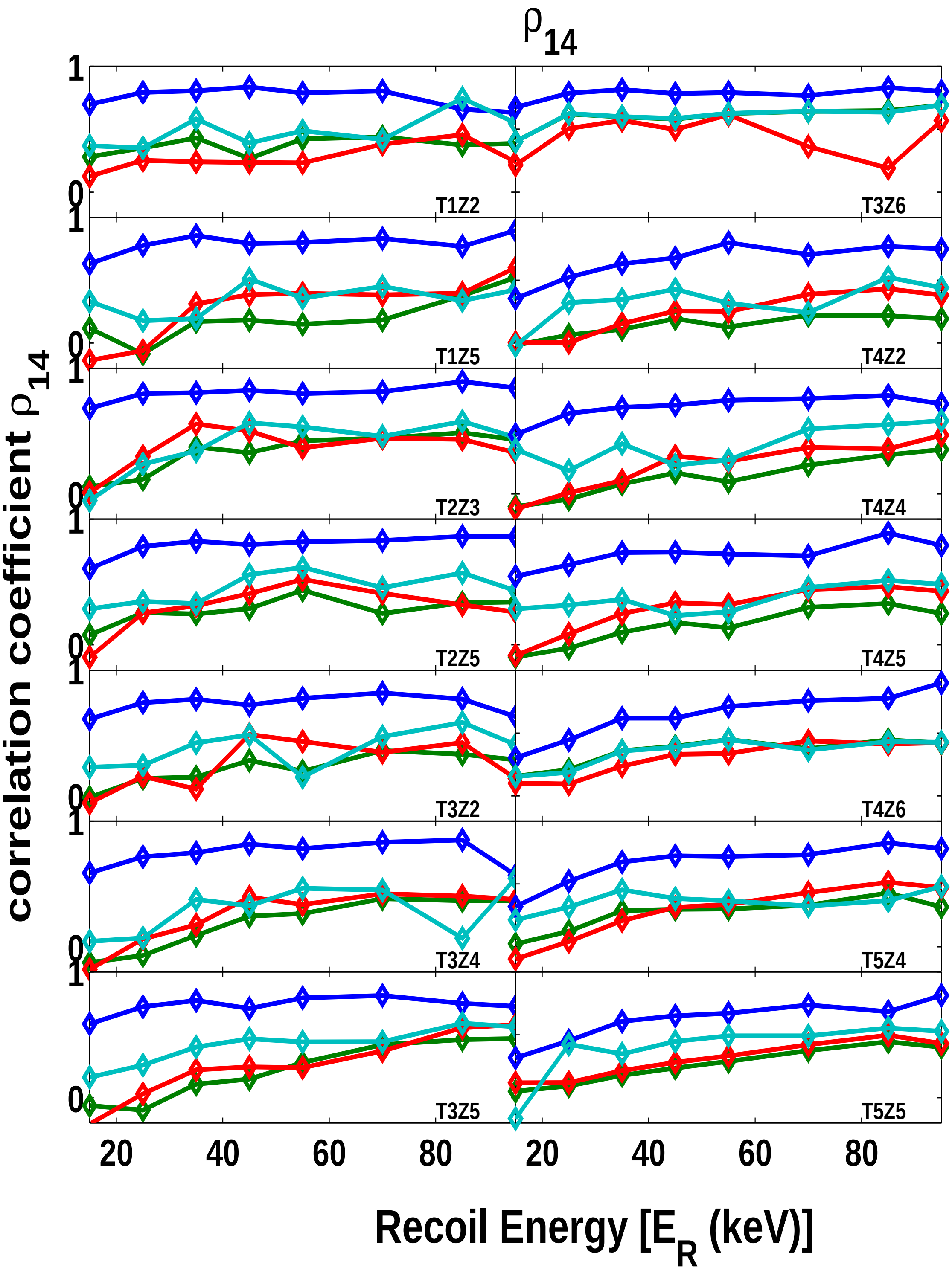

Figure B.16: The correlation coefficient ρ_{14}. The blue curve represents the energy dependence for the neutron sample while the green, the red and the cyan curves represents the energy dependence for the surface events betas, the phonon and the charge-side events respectively.

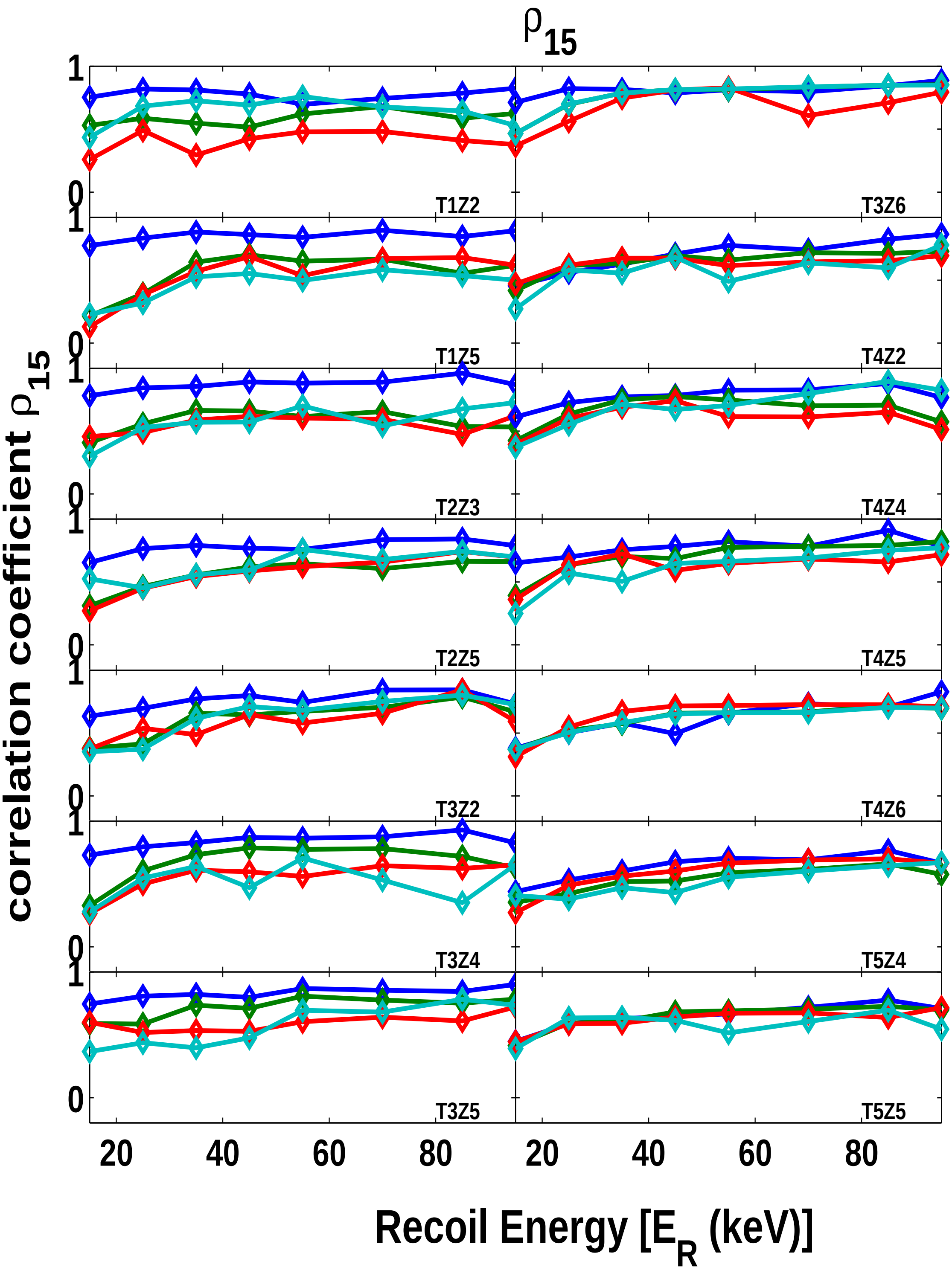

Figure B.17: The correlation coefficient ρ_{15}. The blue curve represents the energy dependence for the neutron sample while the green, the red and the cyan curves represents the energy dependence for the surface events betas, the phonon and the charge-side events respectively.

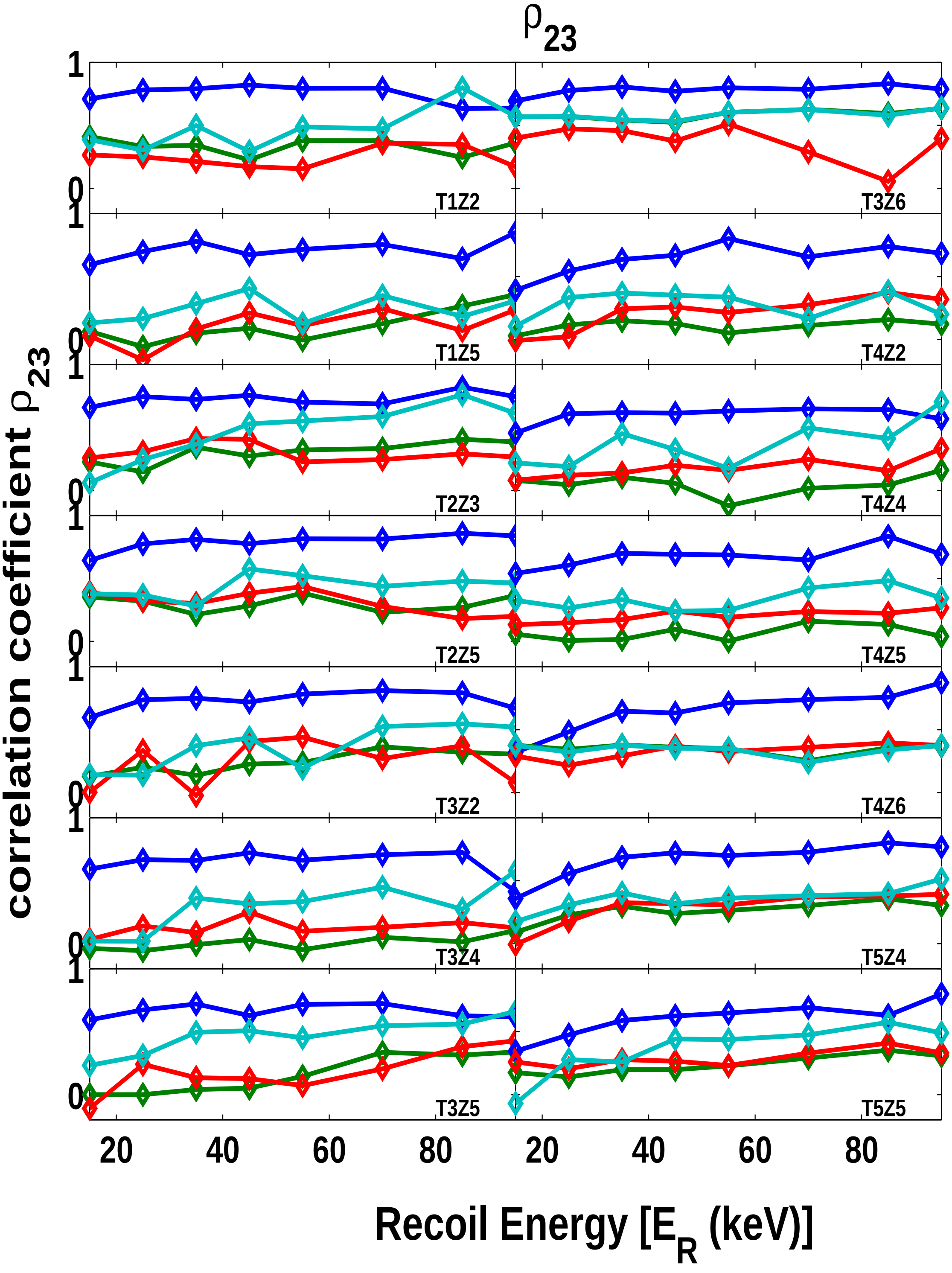

Figure B.18: The correlation coefficient ρ_{23}. The blue curve represents the energy dependence for the neutron sample while the green, the red and the cyan curves represents the energy dependence for the surface events betas, the phonon and the charge-side events respectively.

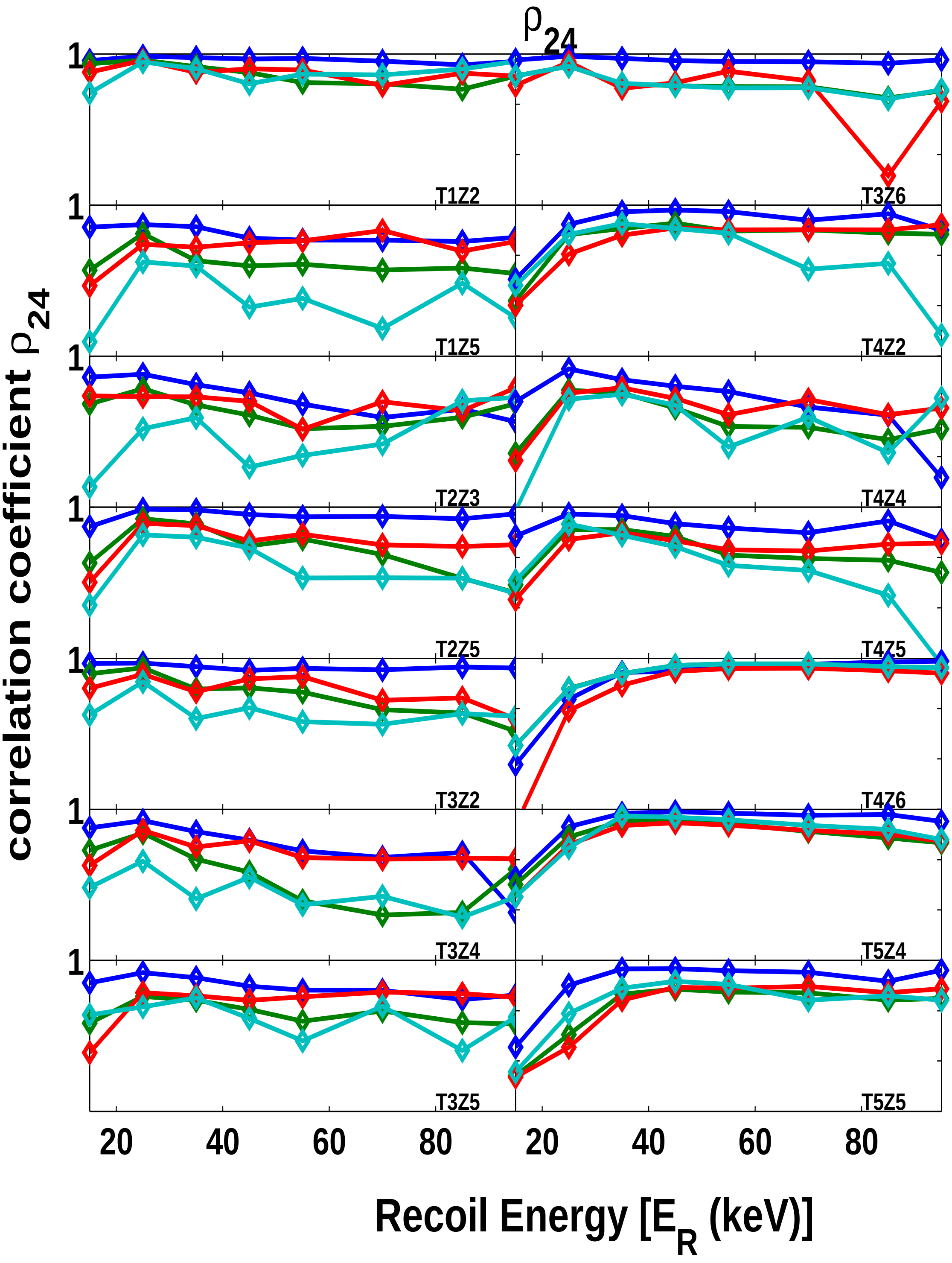

Figure B.19: The correlation coefficient ρ_{24}. The blue curve represents the energy dependence for the neutron sample while the green, the red and the cyan curves represents the energy dependence for the surface events betas, the phonon and the charge-side events respectively.

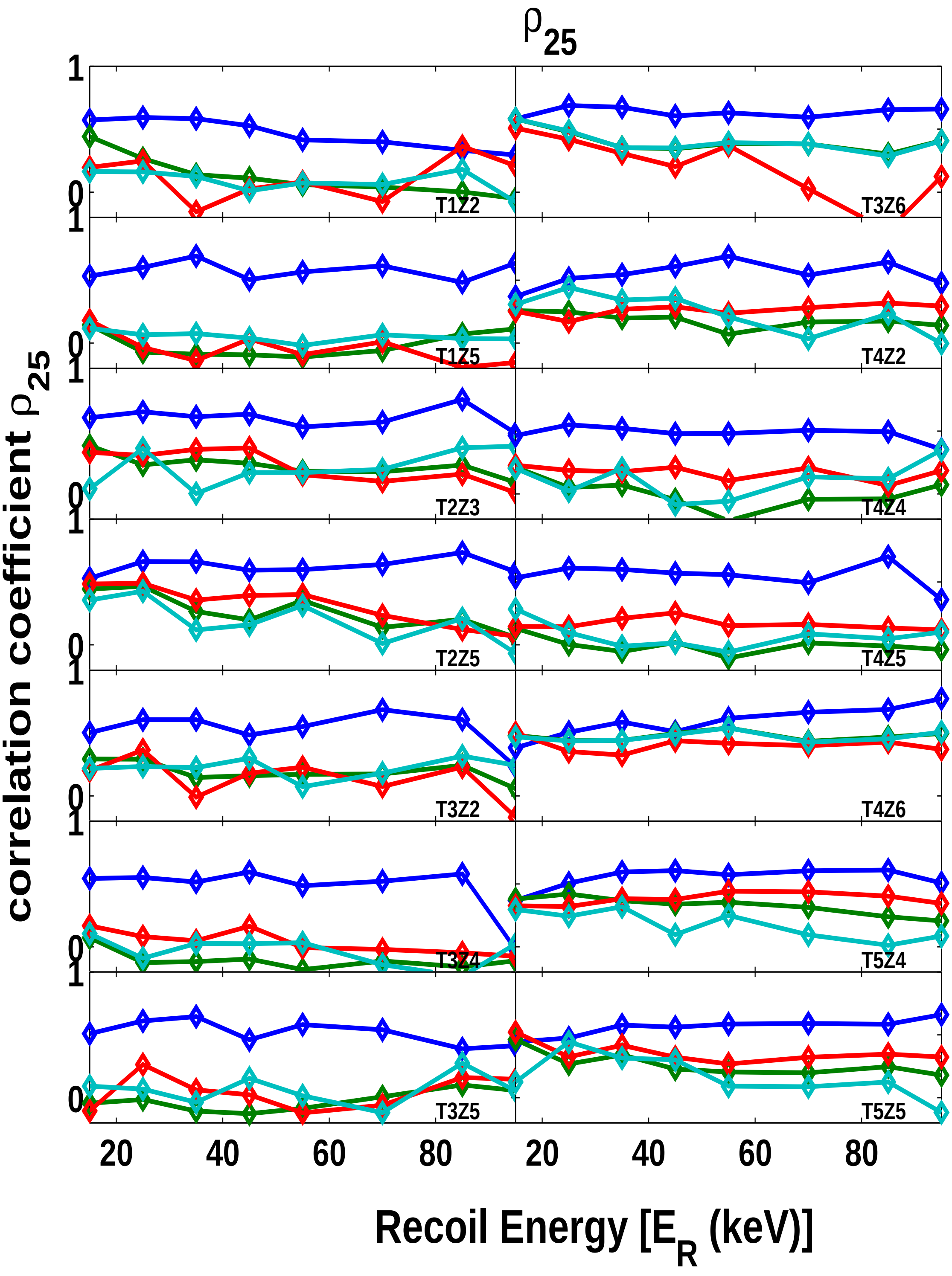

Figure B.20: The correlation coefficient ρ_{25}. The blue curve represents the energy dependence for the neutron sample while the green, the red and the cyan curves represents the energy dependence for the surface events betas, the phonon and the charge-side events respectively.

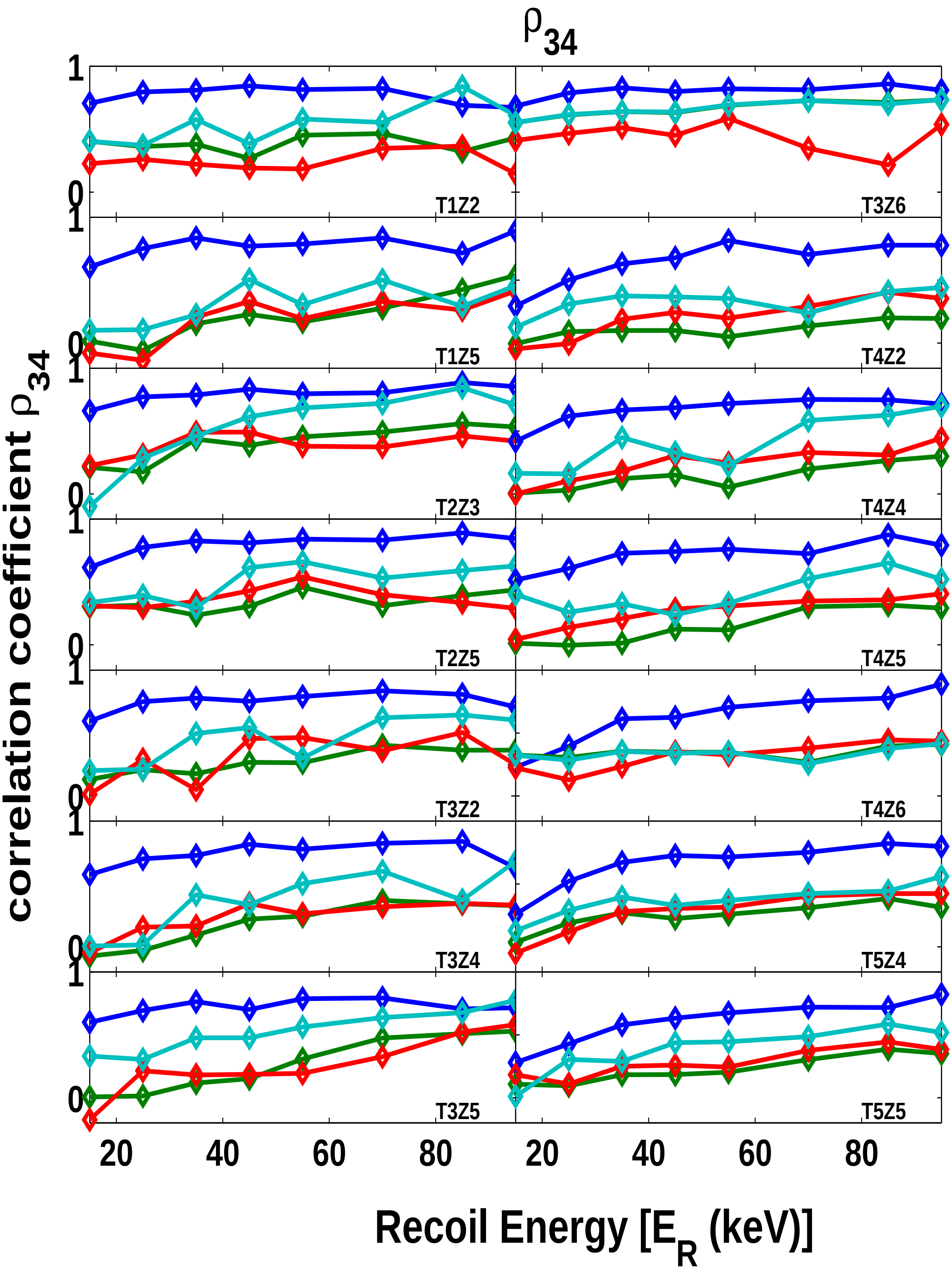

Figure B.21: The correlation coefficient ρ_{34}. The blue curve represents the energy dependence for the neutron sample while the green, the red and the cyan curves represents the energy dependence for the surface events betas, the phonon and the charge-side events respectively.

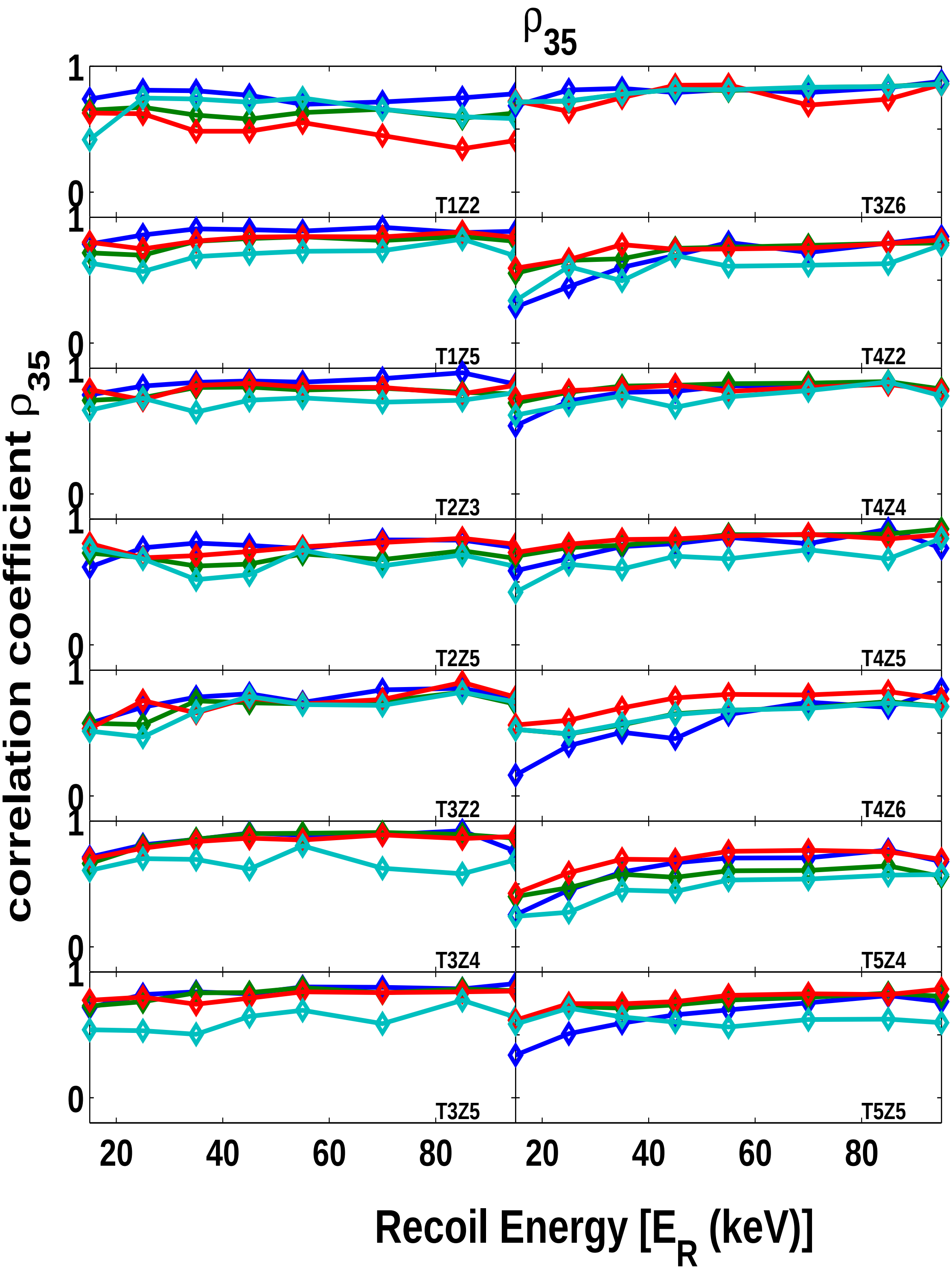

Figure B.22: The correlation coefficient ρ_{35}. The blue curve represents the energy dependence for the neutron sample while the green, the red and the cyan curves represents the energy dependence for the surface events betas, the phonon and the charge-side events respectively.

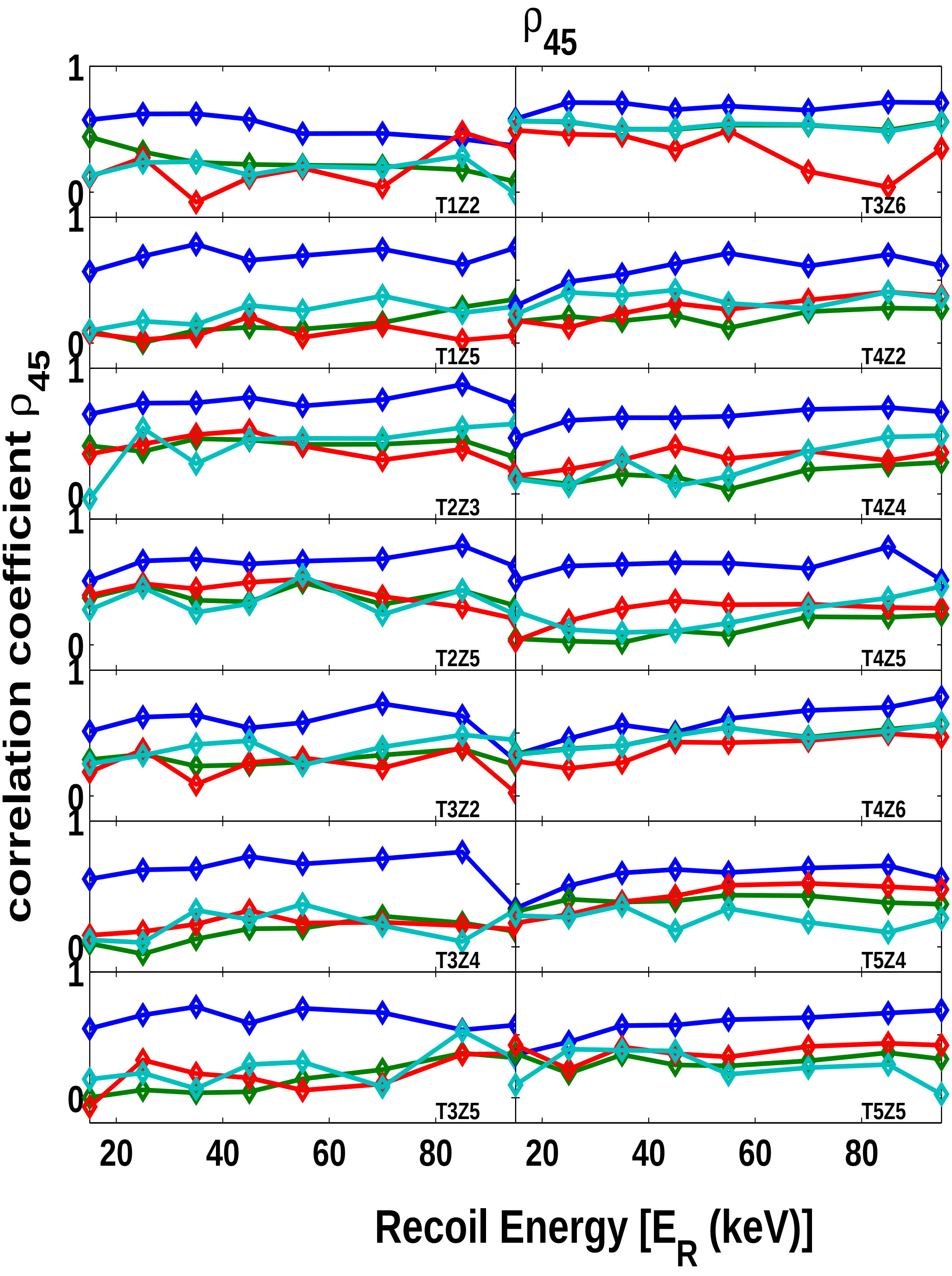

Figure B.23: The correlation coefficient ρ_{45}. The blue curve represents the energy dependence for the neutron sample while the green, the red and the cyan curves represents the energy dependence for the surface events betas, the phonon and the charge-side events respectively.

Appendix C

Energy-independent and energy-dependent efficiencies

C.1 Energy-Independent

Plots below show the χ^2 distributions and the energy dependence of the cut efficiencies for some detectors used in this analysis.

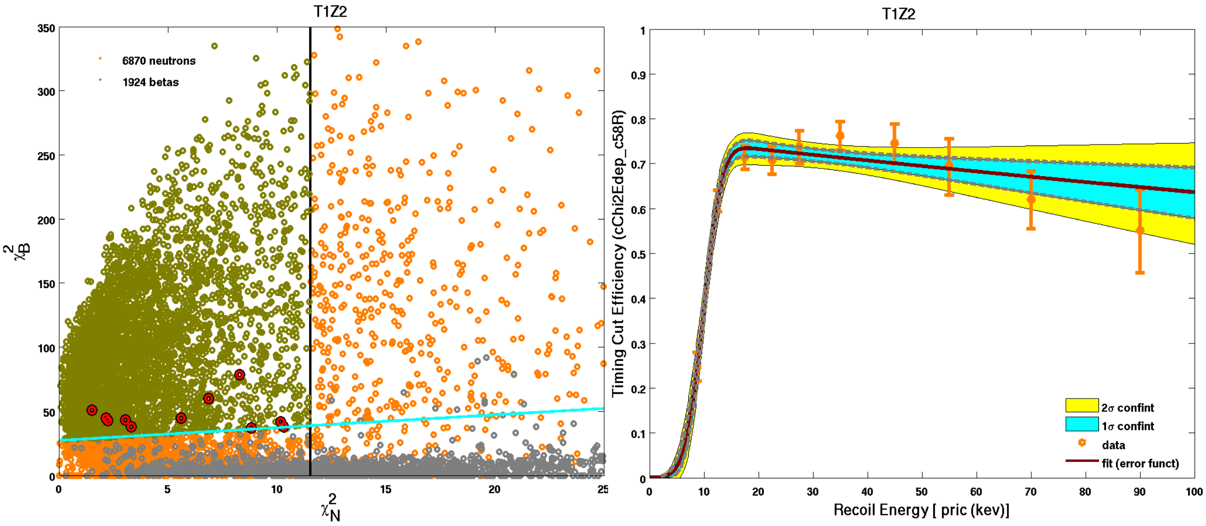

Figure C.1: Left:χ^2_B as function of χ^2_N where the neutrons distribution is shown in orange and the surface events in cyan for T1Z2. Dark yellow represents the events that pass the the energy-independent cuts indicated by a combination of the black vertical line and the cyan, slanting, line. The red black circled events represents the surface events leakage. Right is the neutron efficiency of the energy-independent cut as a function of energy. Orange error bars represents the data while the red solid line is the fit; the cyan and yellow regions are the $\pm 1\sigma$ and $\pm 2\sigma$ confidence intervals.

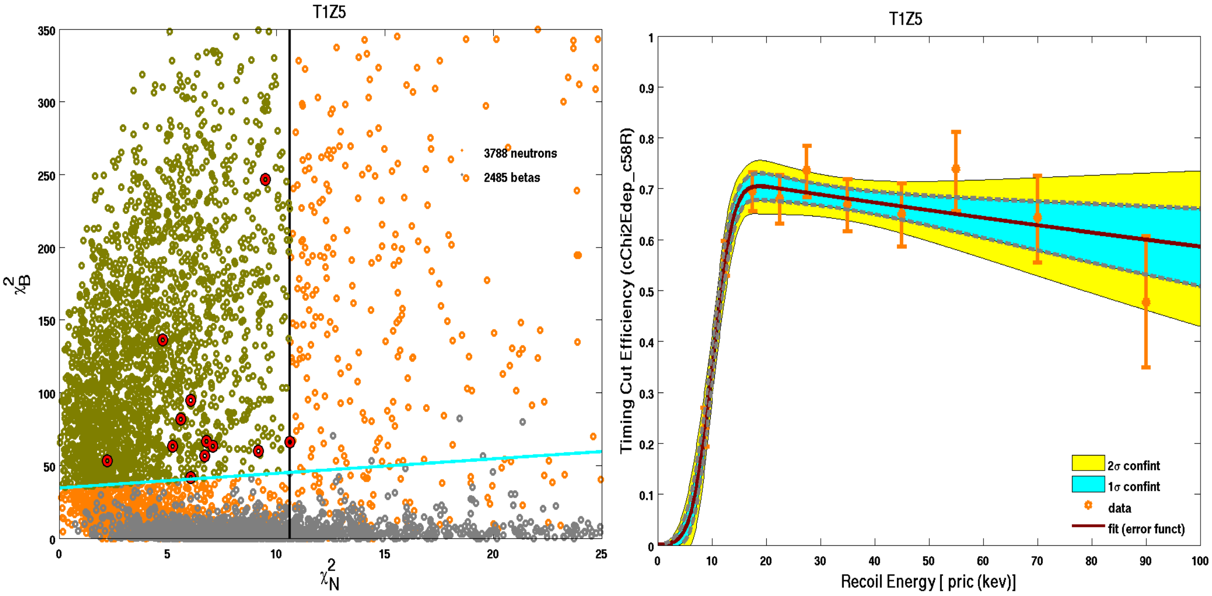

Figure C.2: Left:χ^2_B as function of χ^2_N where the neutrons distribution is shown in orange and the surface events in cyan for T1Z5. Dark yellow represents the events that pass the the energy-independent cuts indicated by a combination of the black vertical line and the cyan, slanting, line. The red black circled events represents the surface events leakage. Right is the neutron efficiency of the energy-independent cut as a function of energy. Orange error bars represents the data while the red solid line is the fit; the cyan and yellow regions are the $\pm 1\sigma$ and $\pm 2\sigma$ confidence intervals.

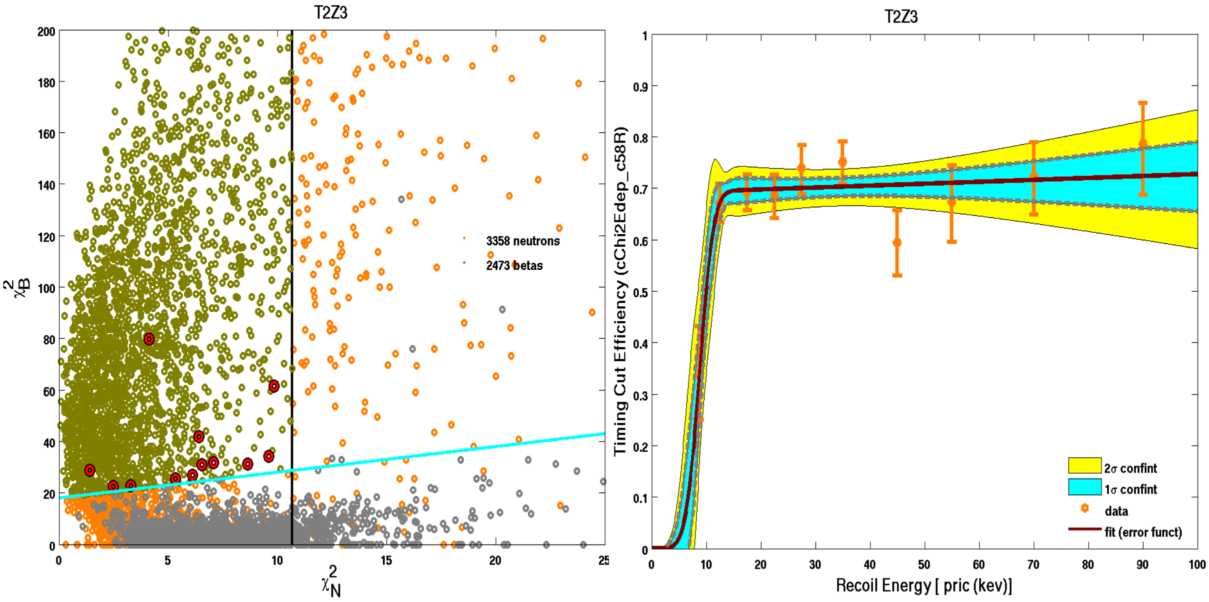

Figure C.3: Left:χ^2_B as function of χ^2_N where the neutrons distribution is shown in orange and the surface events in cyan for T2Z3. Dark yellow represents the events that pass the the energy-independent cuts indicated by a combination of the black vertical line and the cyan, slanting, line. The red black circled events represents the surface events leakage. Right is the neutron efficiency of the energy-independent cut as a function of energy. Orange error bars represents the data while the red solid line is the fit; the cyan and yellow regions are the $\pm 1\sigma$ and $\pm 2\sigma$ confidence intervals.

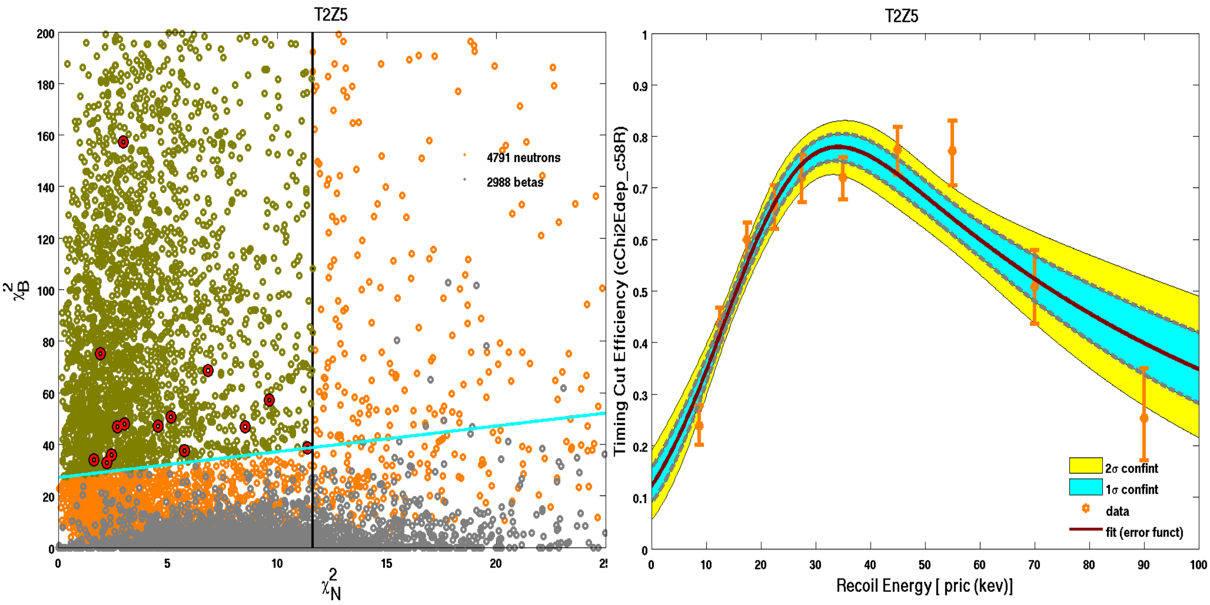

Figure C.4: Left:χ^2_B as function of χ^2_N where the neutrons distribution is shown in orange and the surface events in cyan for T2Z5. Dark yellow represents the events that pass the the energy-independent cuts indicated by a combination of the black vertical line and the cyan, slanting, line. The red black circled events represents the surface events leakage. Right is the neutron efficiency of the energy-independent cut as a function of energy. Orange error bars represents the data while the red solid line is the fit; the cyan and yellow regions are the $\pm 1\sigma$ and $\pm 2\sigma$ confidence intervals.

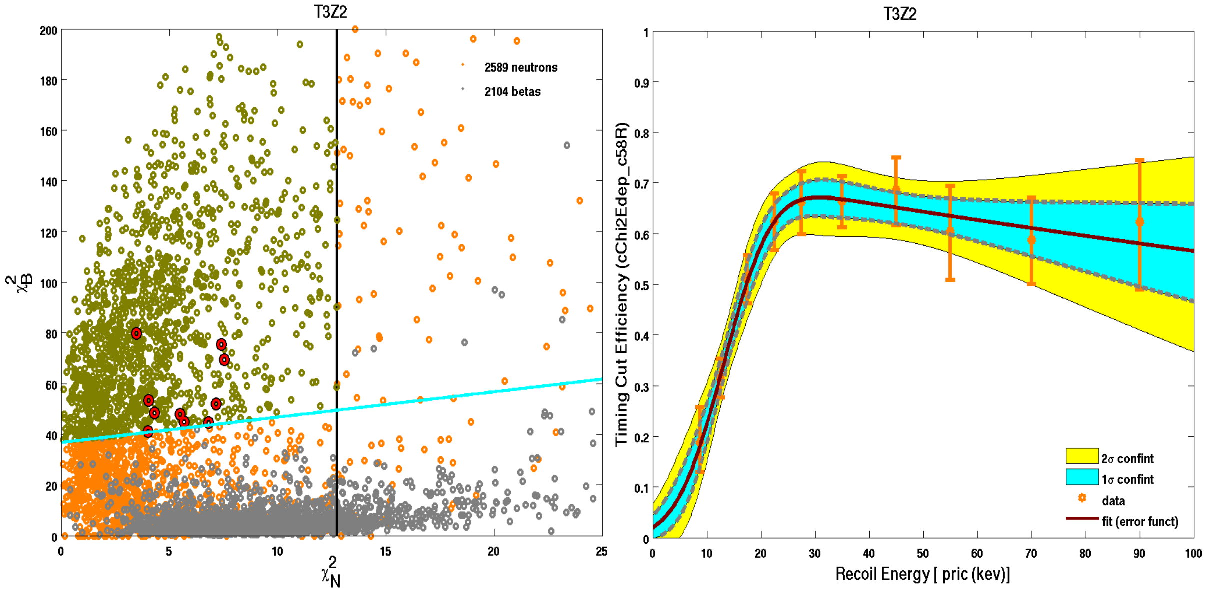

Figure C.5: Left:χ^2_B as function of χ^2_N where the neutrons distribution is shown in orange and the surface events in cyan for T3Z2. Dark yellow represents the events that pass the the energy-independent cuts indicated by a combination of the black vertical line and the cyan, slanting, line. The red black circled events represents the surface events leakage. Right is the neutron efficiency of the energy-independent cut as a function of energy. Orange error bars represents the data while the red solid line is the fit; the cyan and yellow regions are the $\pm 1\sigma$ and $\pm 2\sigma$ confidence intervals.

C.2 Energy dependence of the optimized χ^2 cut

The energy-dependent χ^2 timing cut (cEdepChi2_c58R) efficiency was calculated using the neutron calibration data. Figures (C.6) to (C.12) pictures the computed fitted efficiencies for the detectors used in this analysis.

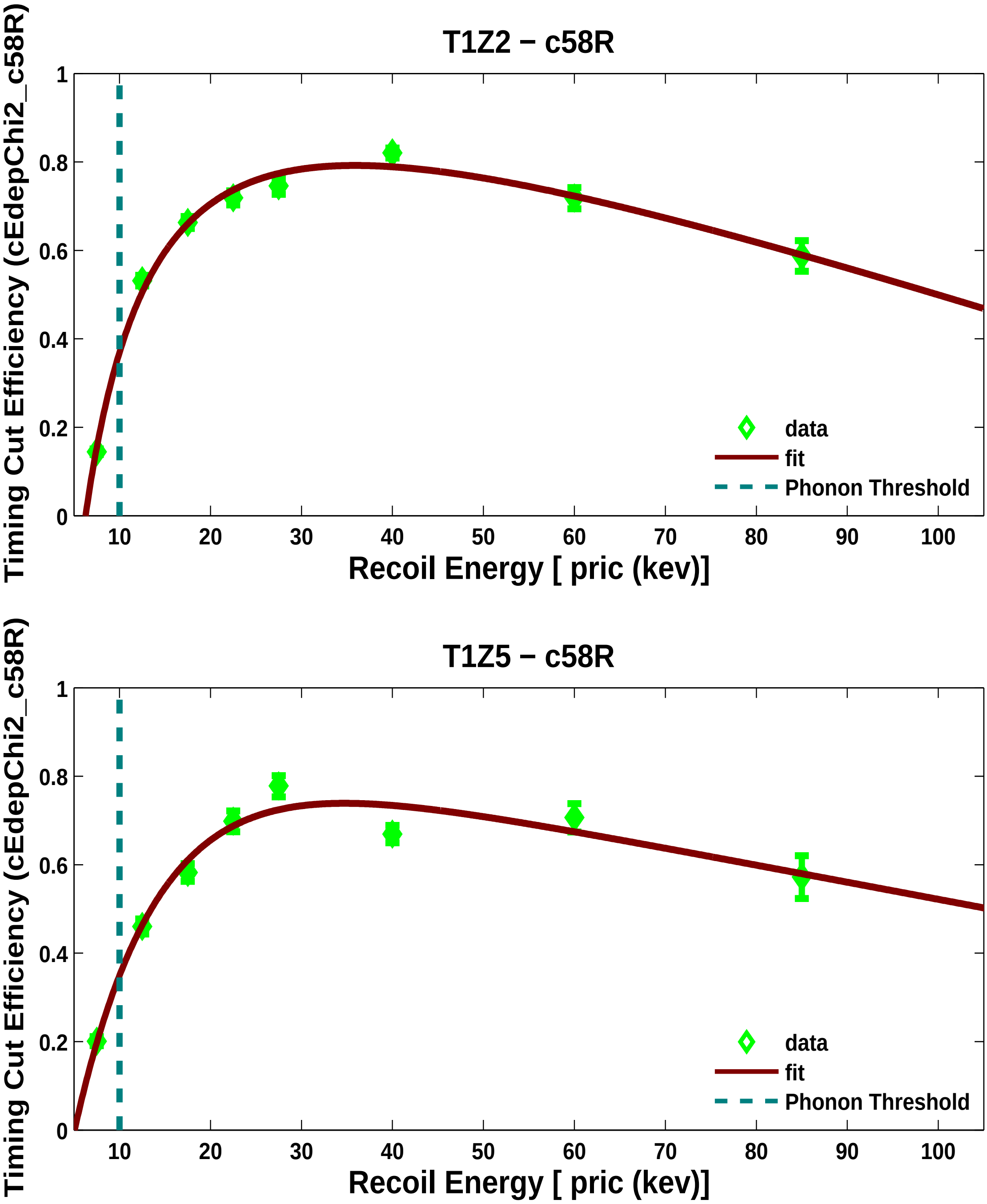

Figure C.6: The optimized χ^2 timing cut efficiency as function of energy for T1Z2 and T1Z5 (c58 reanalysis).

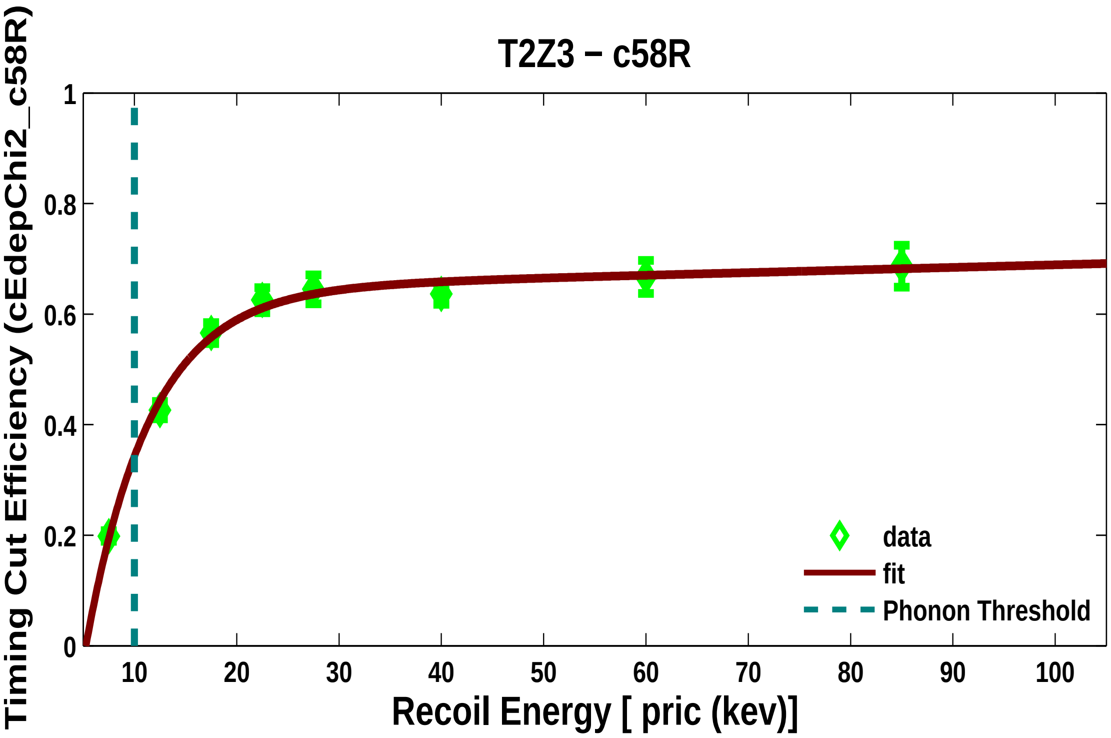

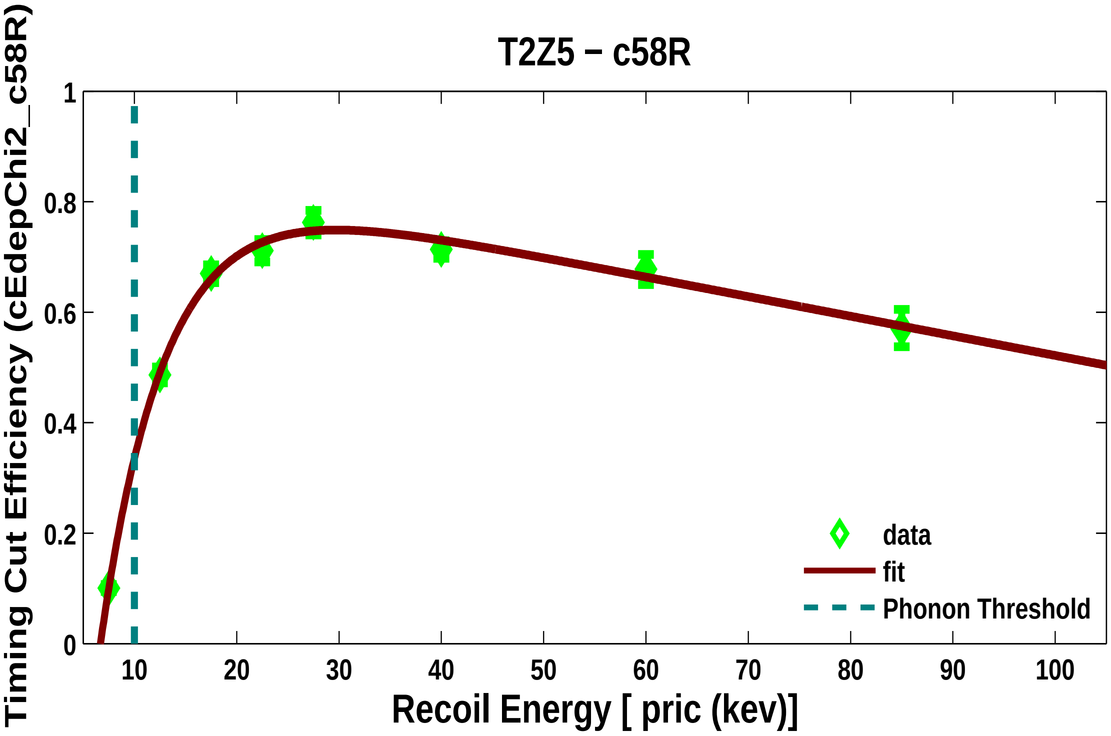

Figure C.7: The optimized χ^2 timing cut efficiency as function of energy for T2Z3 and T2Z5 (c58 reanalysis).

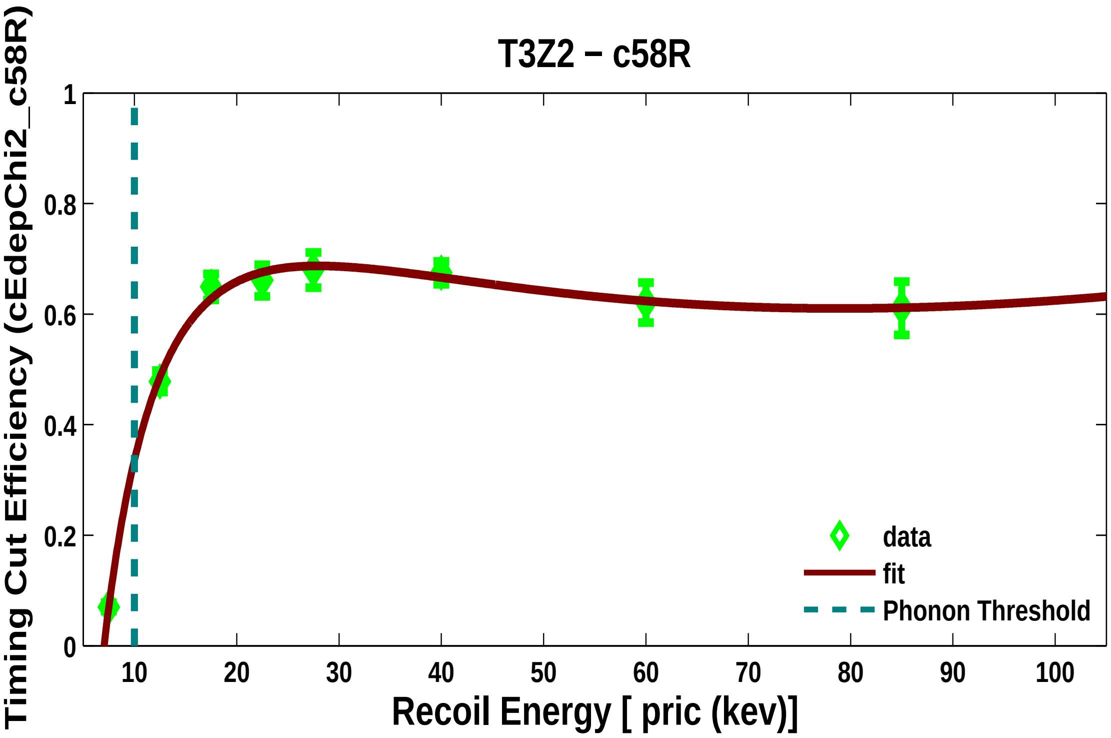

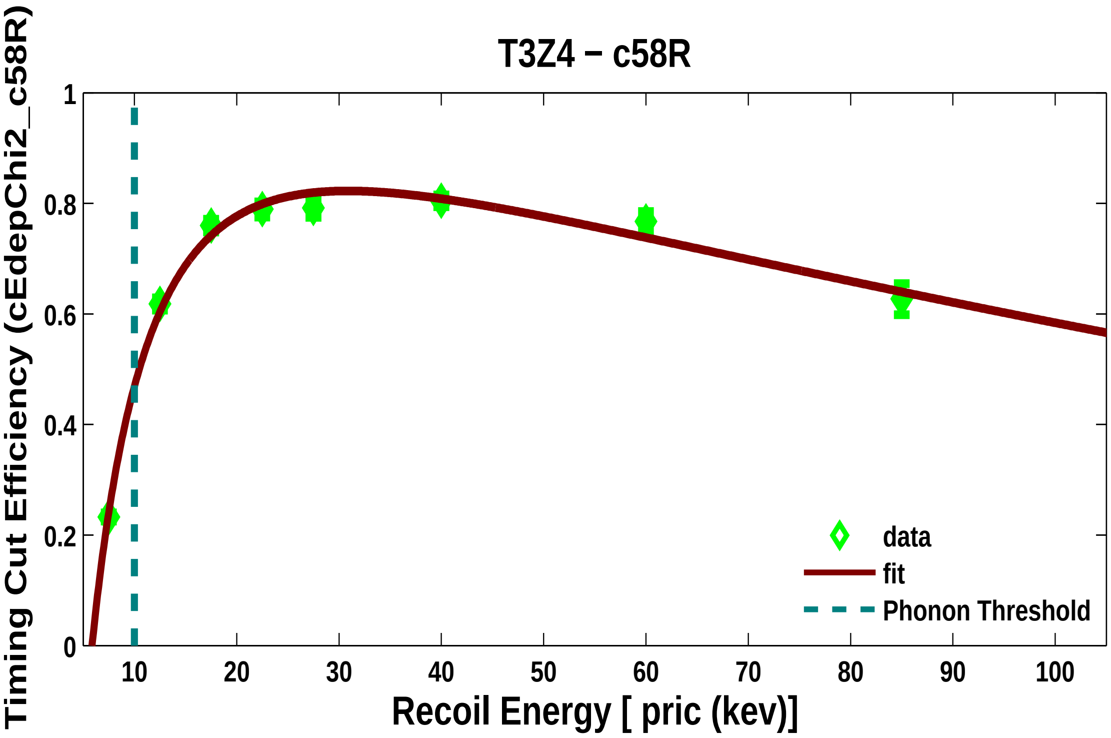

Figure C.8: The optimized χ^2 timing cut efficiency as function of energy for T3Z2 and T3Z4 (c58 reanalysis).

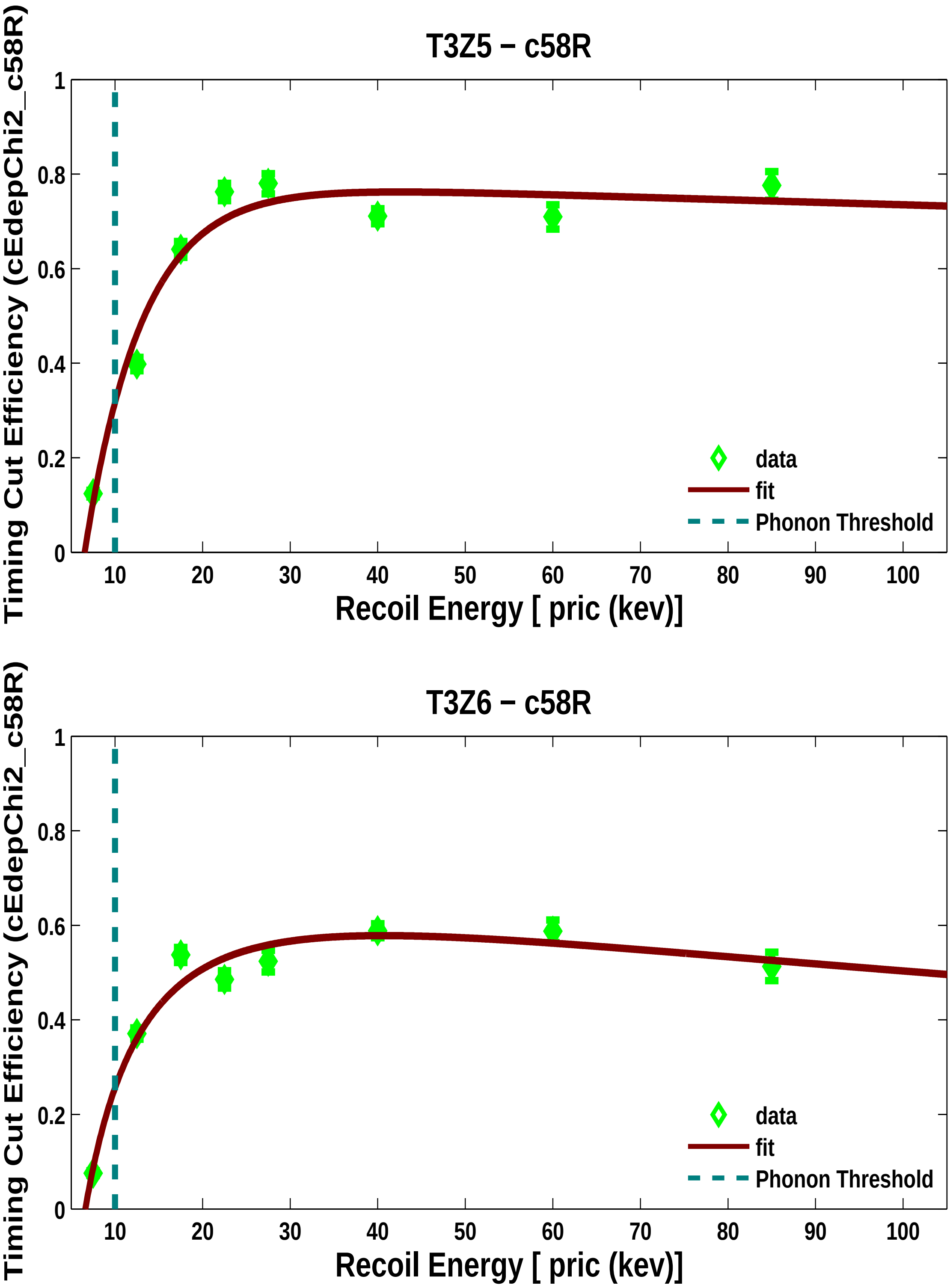

Figure C.9: The optimized χ^2 timing cut efficiency as function of energy for T3Z5 and T3Z6 (c58 reanalysis).

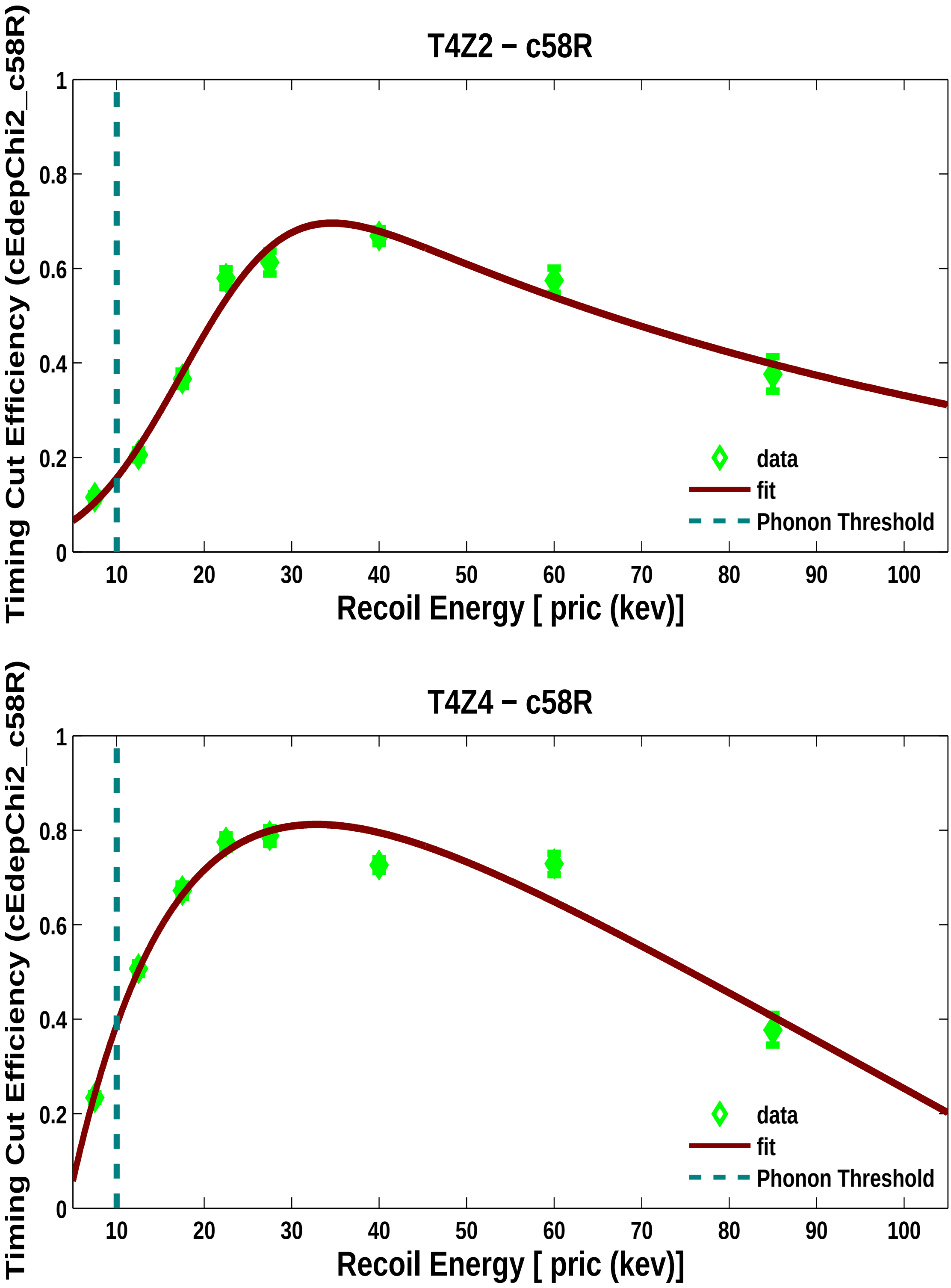

Figure C.10: The optimized χ^2 timing cut efficiency as function of energy for T4Z2 and T4Z4 (c58 reanalysis).

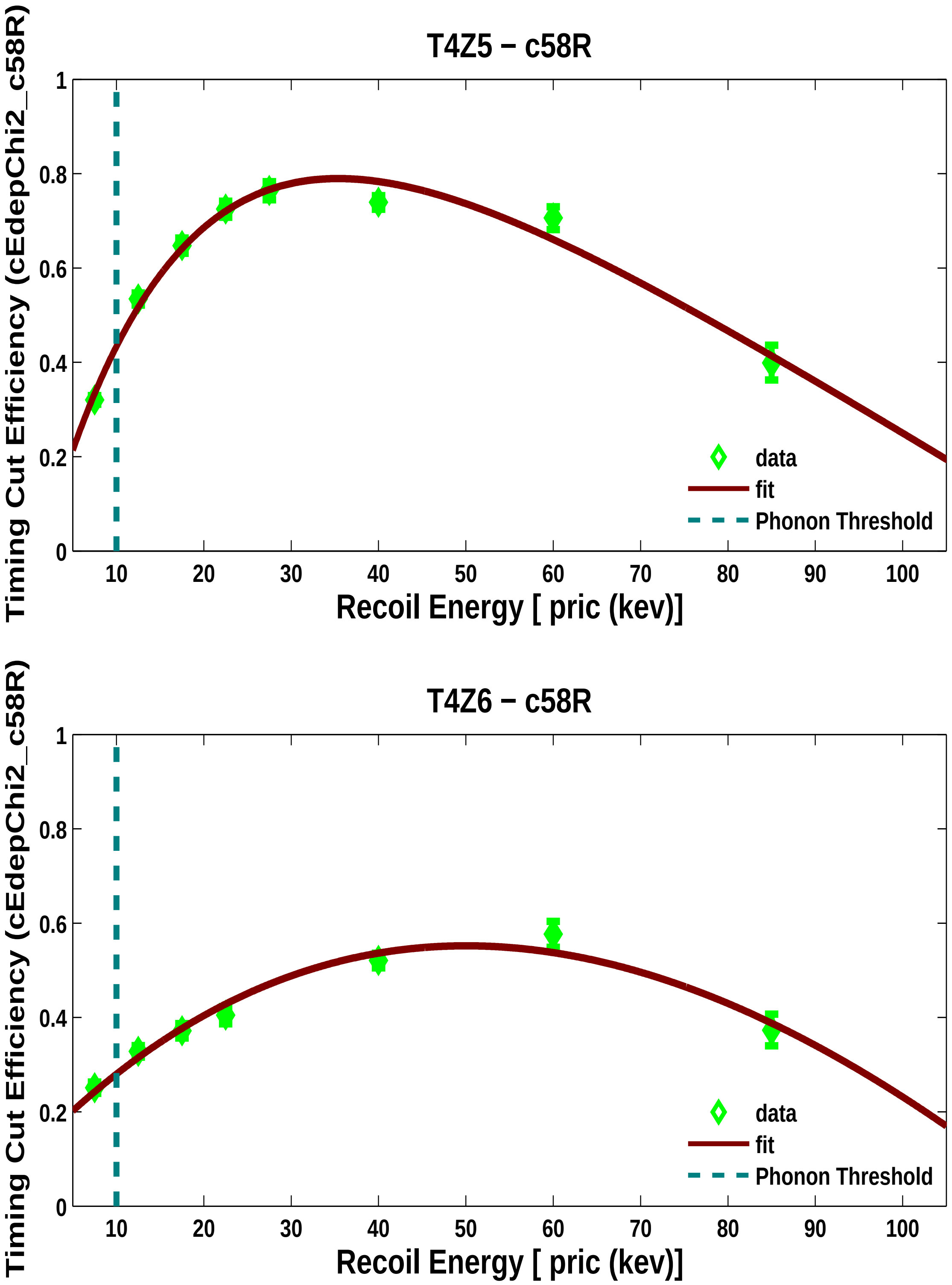

Figure C.11: The optimized χ^2 timing cut efficiency as function of energy for T4Z5 and T4Z6 (c58 reanalysis).

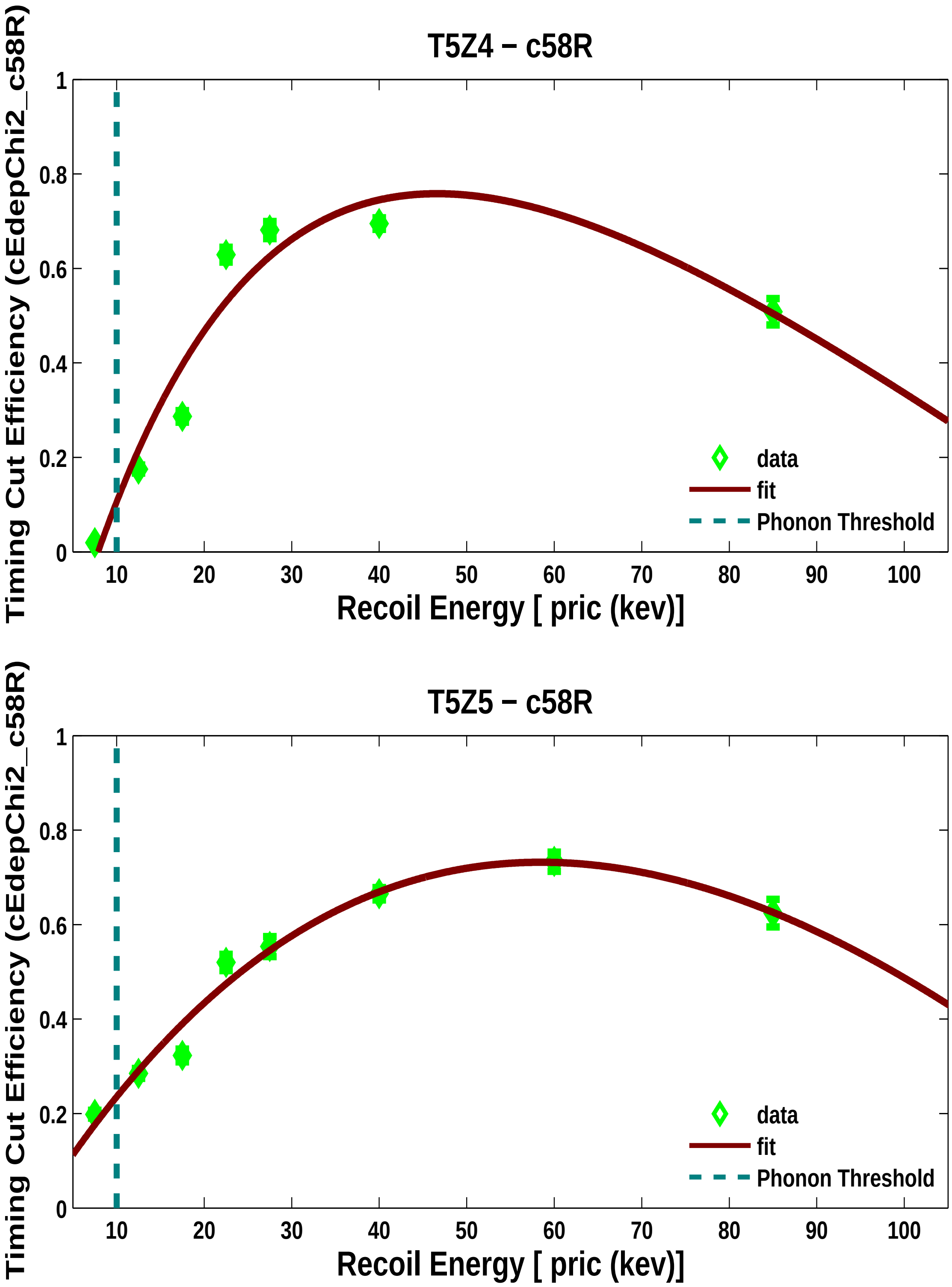

Figure C.12: The optimized χ^2 timing cut efficiency as function of energy for T5Z4 and T5Z5 (c58 reanalysis).

Appendix D

$\chi^2_B - \chi^2_N$ vs energy (WS data).

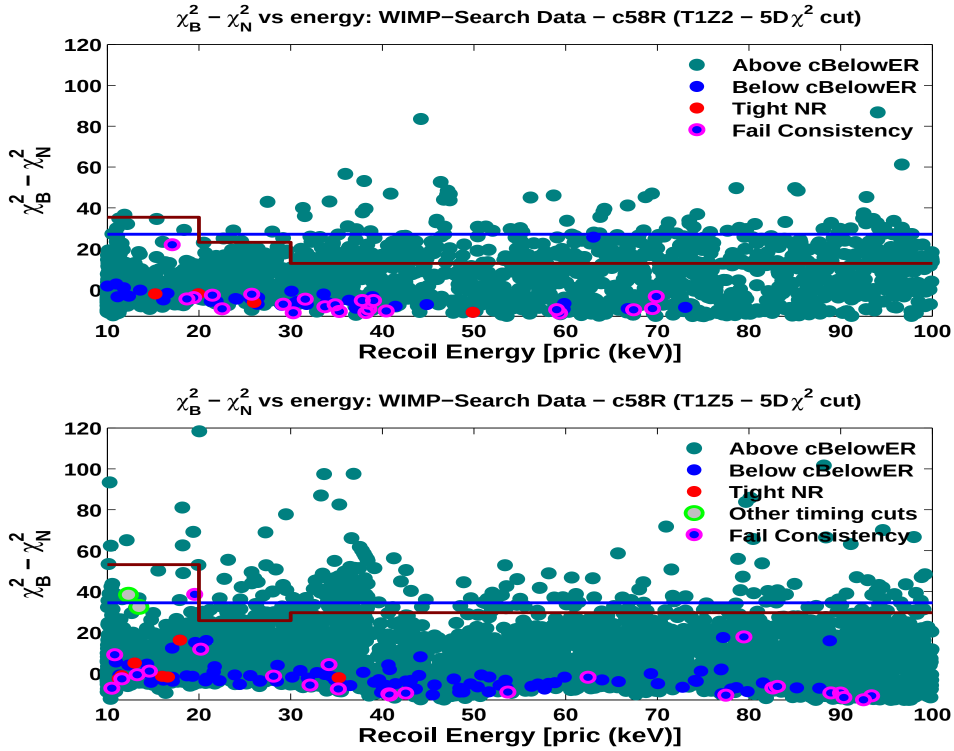

Figure D.1: $\chi^2_B - \chi^2_N$ vs recoil energy for the low background data for T1Z2 (top) and T1Z5 (bottom). Events shown in dark cyan color represents events located 3σ above the **cBelowER_c58** (representing mostly electron-recoil events) while events in blue dots indicates non-electron-recoil events (which can either be surface events or event candidates for those laying inside the tight nuclear-recoil band). Red dots are WIMP-search events inside the tight nuclear-recoil band cut, i.e. the optimized nuclear-recoil band defined by a yield cut of $[l = -1.9; u = 1.8]$. Events shown in magenta circled with blue faces are events failing the consistency cut. The green circle events with the grey face represents events passing the alternative timing cuts developed during the reanalysis. The blue horizontal straight line is the energy independent cut while the dark red line represent the energy-dependent cut.

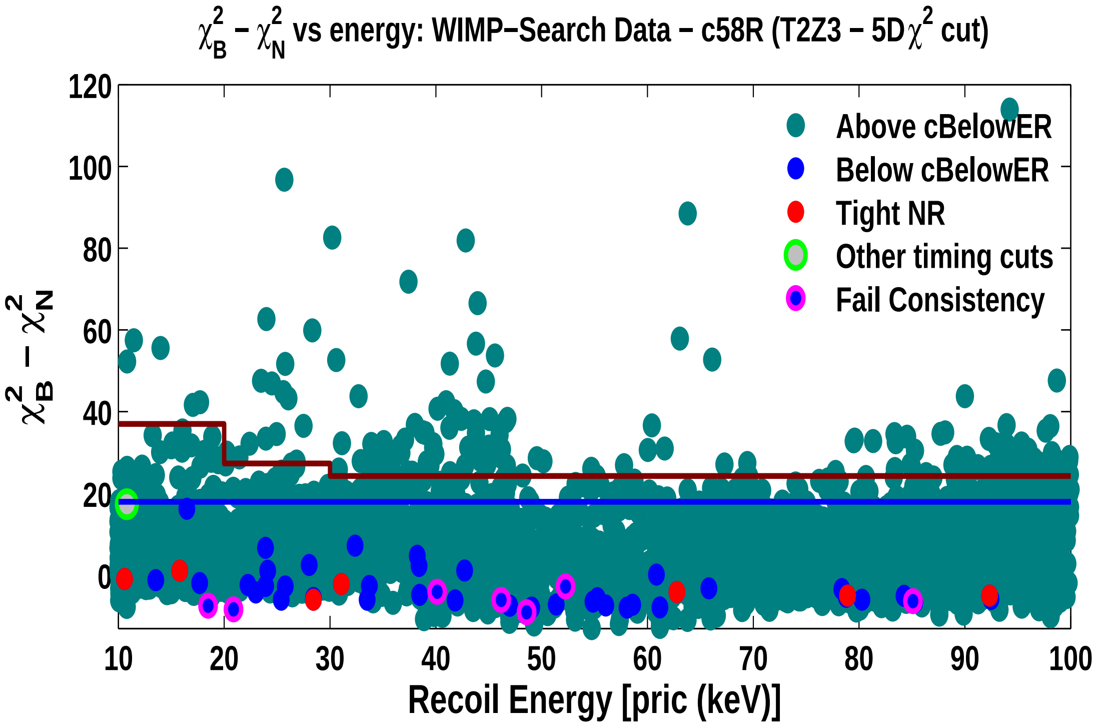

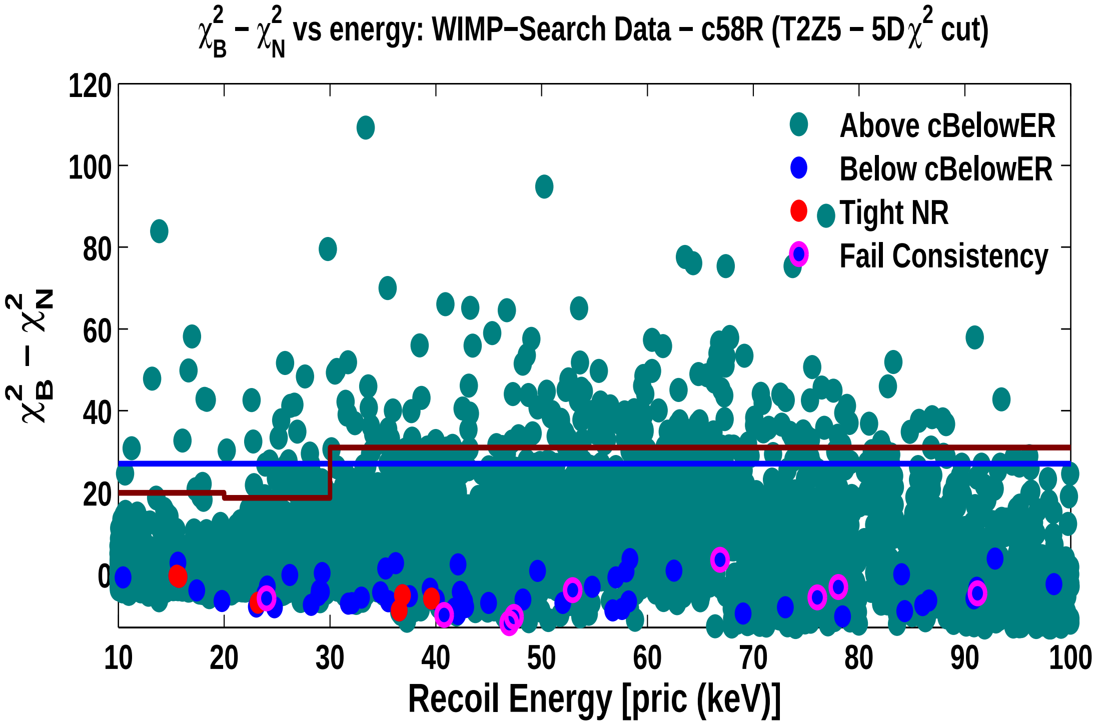

Figure D.2: $\chi_B^2 - \chi_N^2$ vs recoil energy for the low background data for T2Z3 (top) and T2Z5 (bottom). Events shown in dark cyan color represents events located 3σ above the **cBelowER_c58** (representing mostly electron-recoil events) while events in blue dots indicates non-electron-recoil events (which can either be surface events or event candidates for those laying inside the tight nuclear-recoil band). Red dots are WIMP-search events inside the tight nuclear-recoil band cut, i.e. the optimized nuclear-recoil band defined by a yield cut of $[l = -1.9; u = 1.8]$. Events shown in magenta circled with blue faces are events failing the consistency cut. The green circle events with the grey face represents events passing the alternative timing cuts developed during the reanalysis. The blue horizontal straight line is the energy independent cut while the dark red line represent the energy-dependent cut.

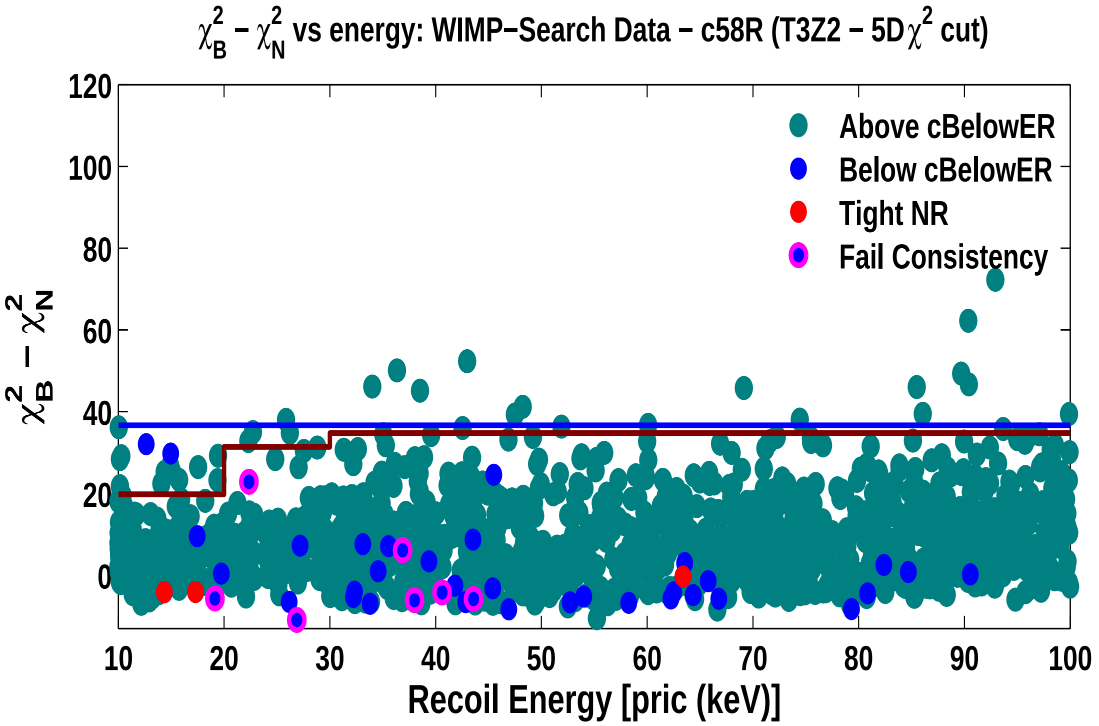

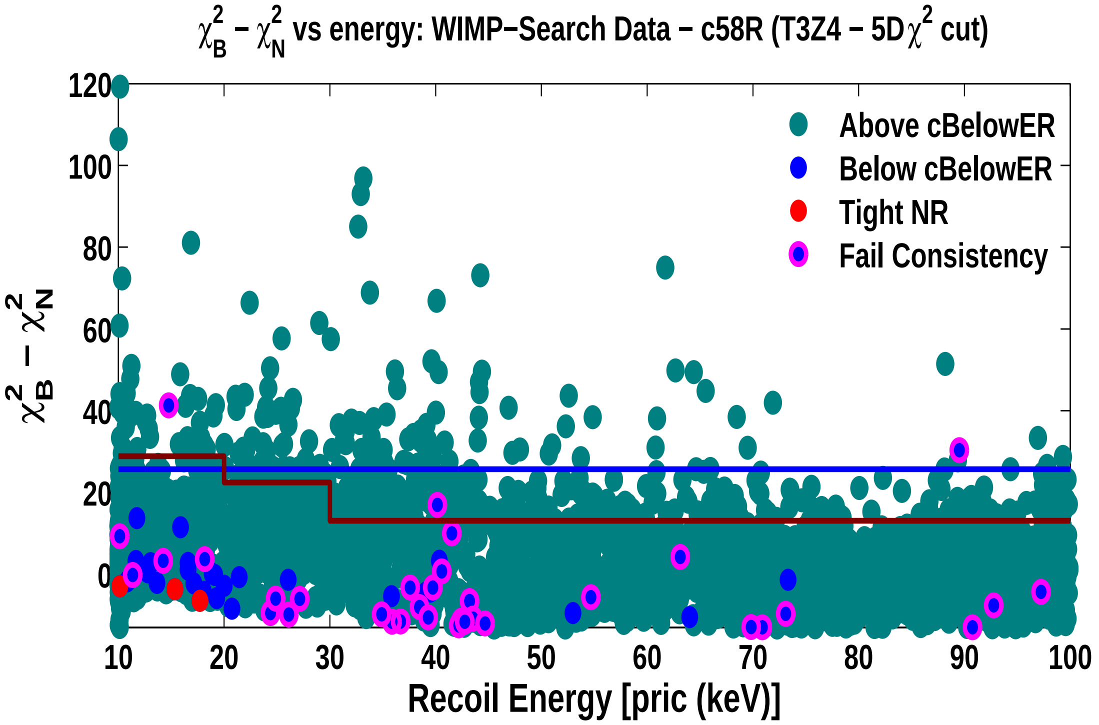

Figure D.3: $\chi^2_B - \chi^2_N$ vs recoil energy for the low background data for T3Z2 (top) and T3Z4 (bottom). Events shown in dark cyan color represents events located 3σ above the **cBelowER_c58** (representing mostly electron-recoil events) while events in blue dots indicates non-electron-recoil events (which can either be surface events or event candidates for those laying inside the tight nuclear-recoil band). Red dots are WIMP-search events inside the tight nuclear-recoil band cut, i.e. the optimized nuclear-recoil band defined by a yield cut of $[l = -1.9; u = 1.8]$. Events shown in magenta circled with blue faces are events failing the consistency cut. The green circle events with the grey face represents events passing the alternative timing cuts developed during the reanalysis. The blue horizontal straight line is the energy independent cut while the dark red line represent the energy-dependent cut.

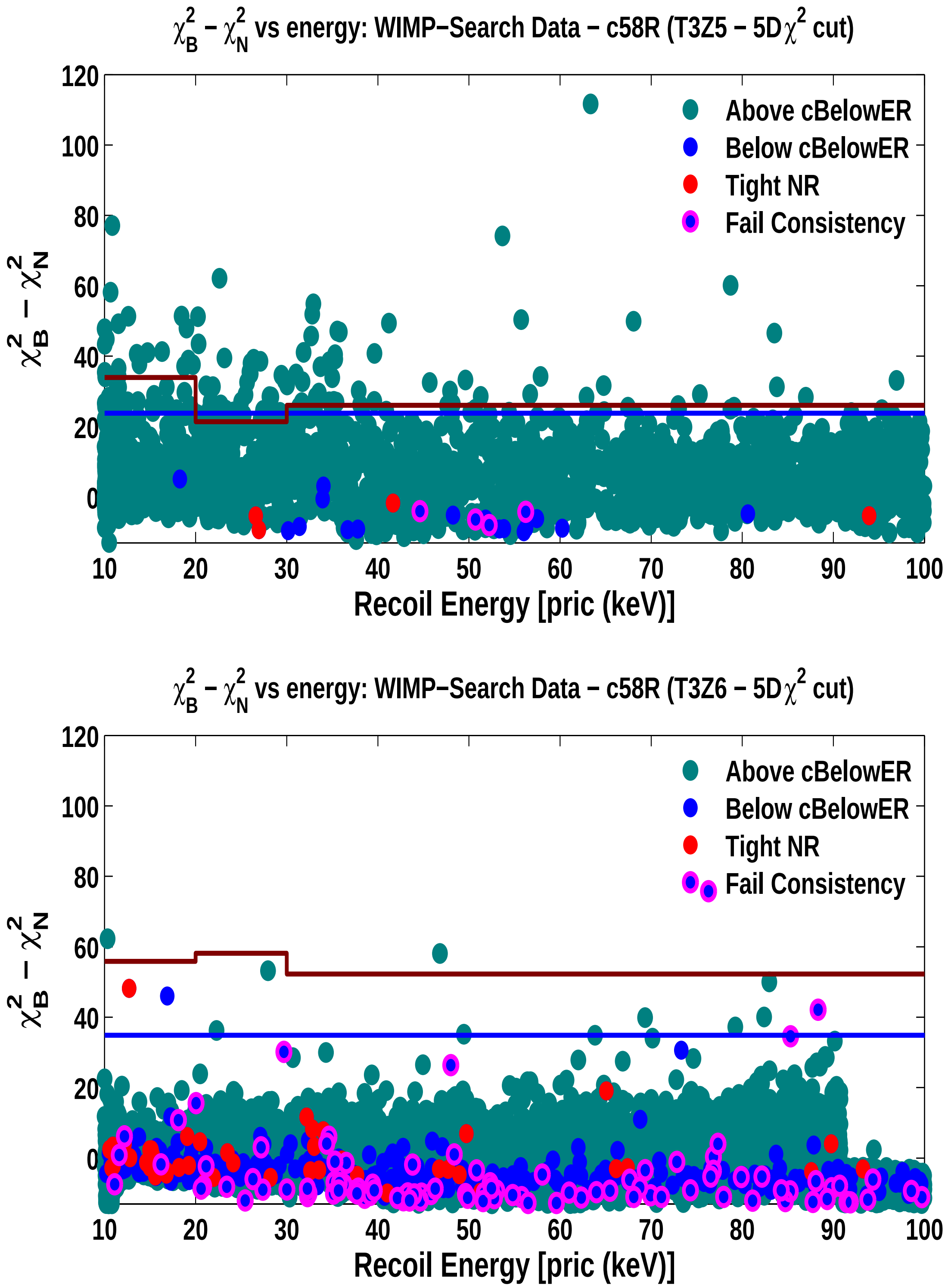

Figure D.4: $\chi^2_B - \chi^2_N$ vs recoil energy for the low background data for T3Z5 (top) and T3Z6 (bottom). Events shown in dark cyan color represents events located 3σ above the **cBelowER_c58** (representing mostly electron-recoil events) while events in blue dots indicates non-electron-recoil events (which can either be surface events or event candidates for those laying inside the tight nuclear-recoil band). Red dots are WIMP-search events inside the tight nuclear-recoil band cut, i.e. the optimized nuclear-recoil band defined by a yield cut of $[l = -1.9; u = 1.8]$. Events shown in magenta circled with blue faces are events failing the consistency cut. The green circle events with the grey face represents events passing the alternative timing cuts developed during the reanalysis. The blue horizontal straight line is the energy independent cut while the dark red line represent the energy-dependent cut.

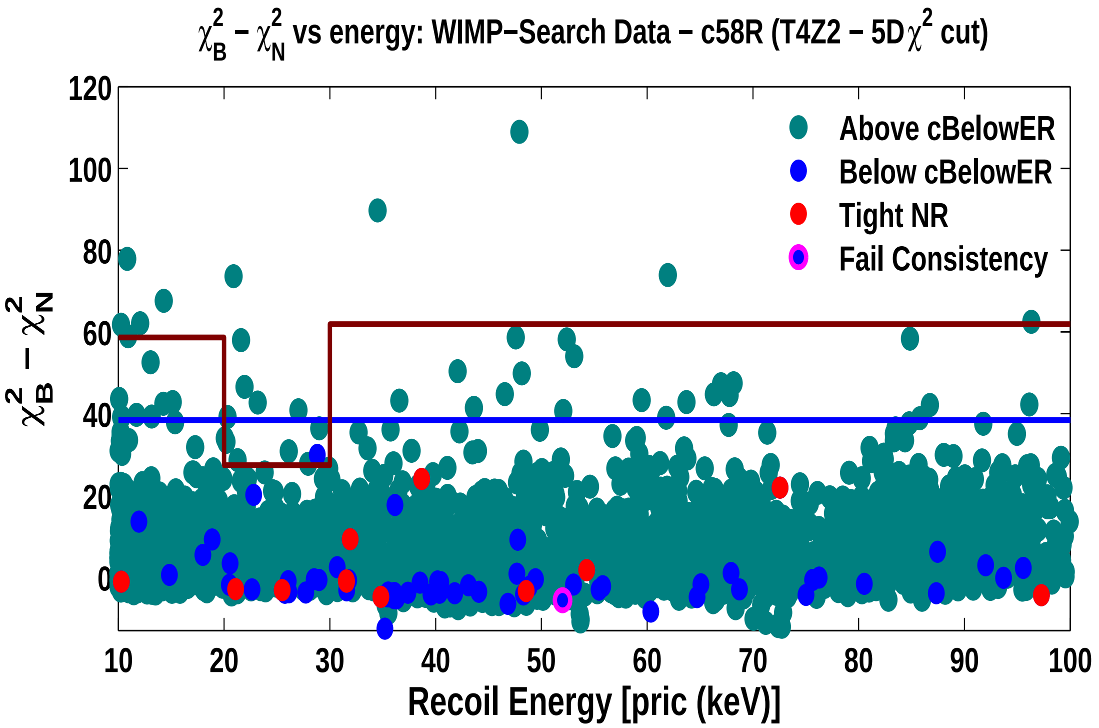

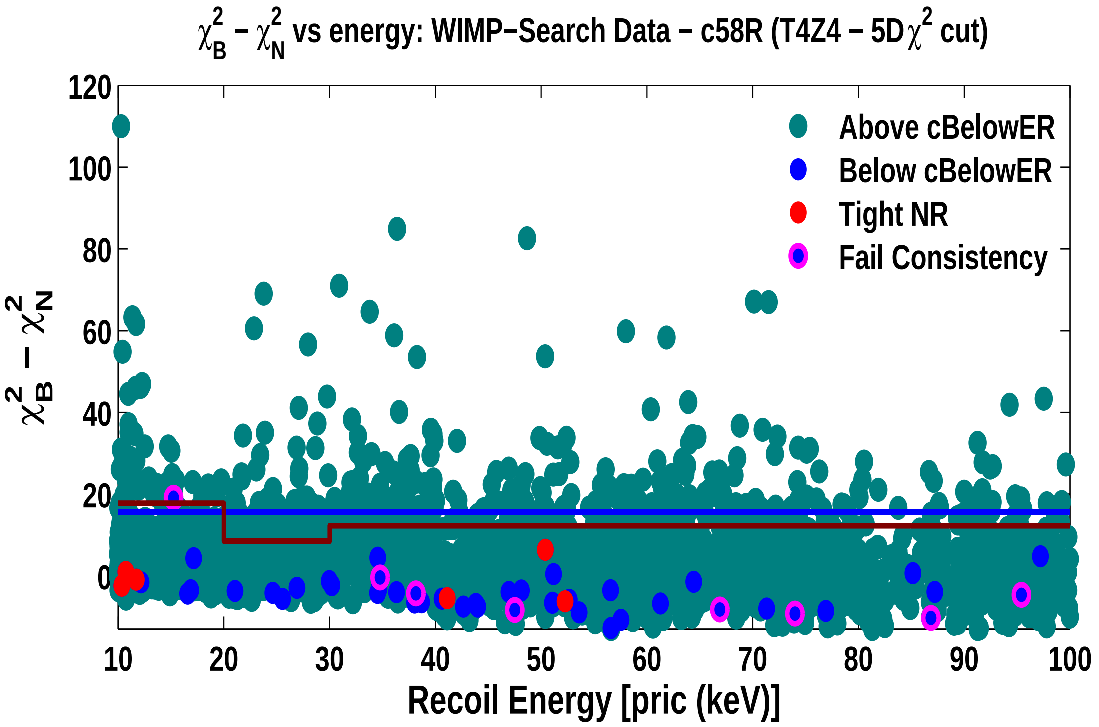

Figure D.5: $\chi^2_B - \chi^2_N$ vs recoil energy for the low background data for T4Z2 (top) and T4Z4 (bottom). Events shown in dark cyan color represents events located 3σ above the **cBelowER_c58** (representing mostly electron-recoil events) while events in blue dots indicates non-electron-recoil events (which can either be surface events or event candidates for those laying inside the tight nuclear-recoil band). Red dots are WIMP-search events inside the tight nuclear-recoil band cut, i.e. the optimized nuclear-recoil band defined by a yield cut of $[l = -1.9; u = 1.8]$. Events shown in magenta circled with blue faces are events failing the consistency cut. The green circle events with the grey face represents events passing the alternative timing cuts developed during the reanalysis. The blue horizontal straight line is the energy independent cut while the dark red line represent the energy-dependent cut.

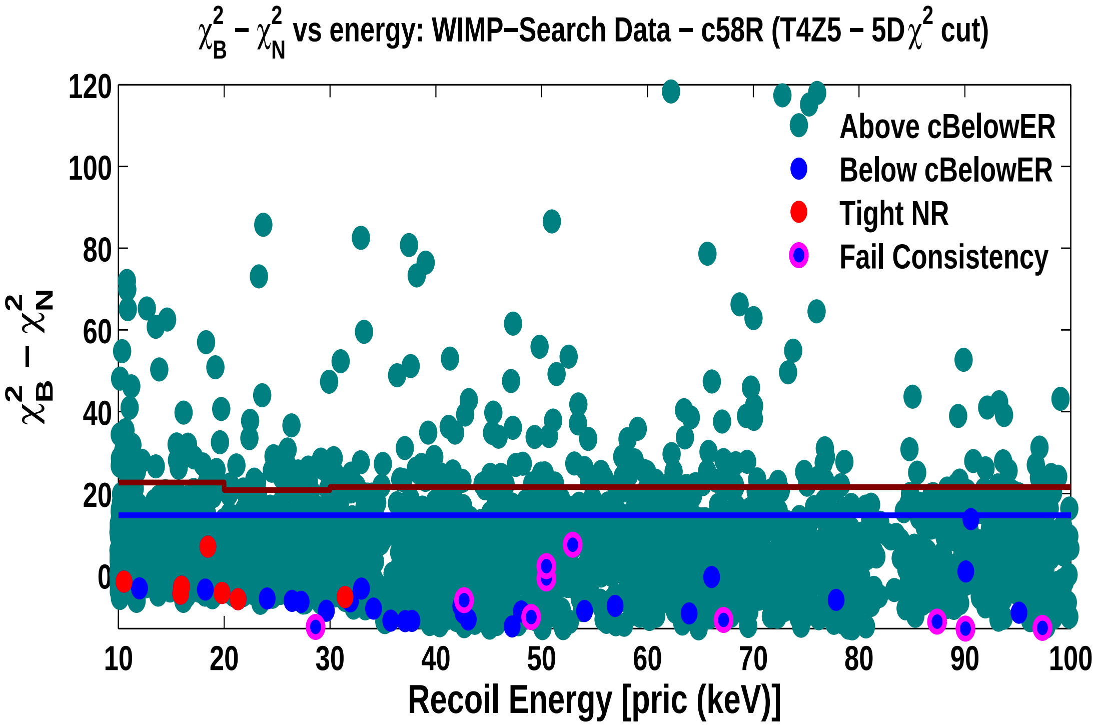

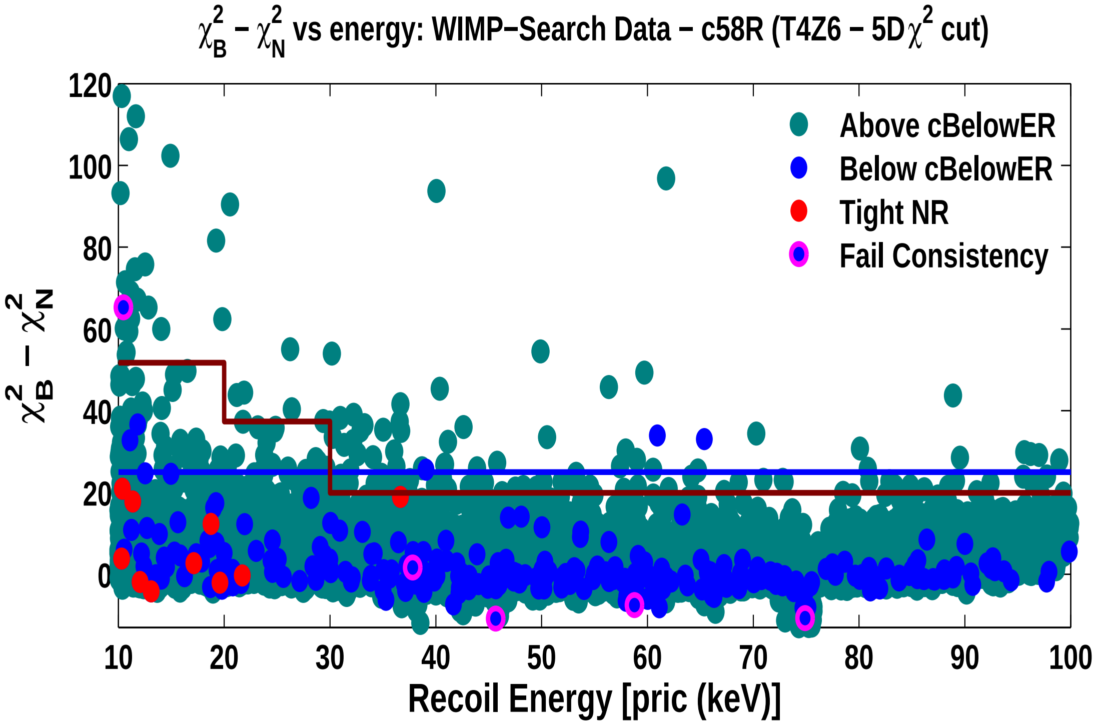

Figure D.6: $\chi^2_B - \chi^2_N$ vs recoil energy for the low background data for T4Z5 (top) and T4Z6 (bottom). Events shown in dark cyan color represents events located 3σ above the **cBelowER_c58** (representing mostly electron-recoil events) while events in blue dots indicates non-electron-recoil events (which can either be surface events or event candidates for those laying inside the tight nuclear-recoil band). Red dots are WIMP-search events inside the tight nuclear-recoil band cut, i.e. the optimized nuclear-recoil band defined by a yield cut of $[l = -1.9; u = 1.8]$. Events shown in magenta circled with blue faces are events failing the consistency cut. The green circle events with the grey face represents events passing the alternative timing cuts developed during the reanalysis. The blue horizontal straight line is the energy independent cut while the dark red line represent the energy-dependent cut.

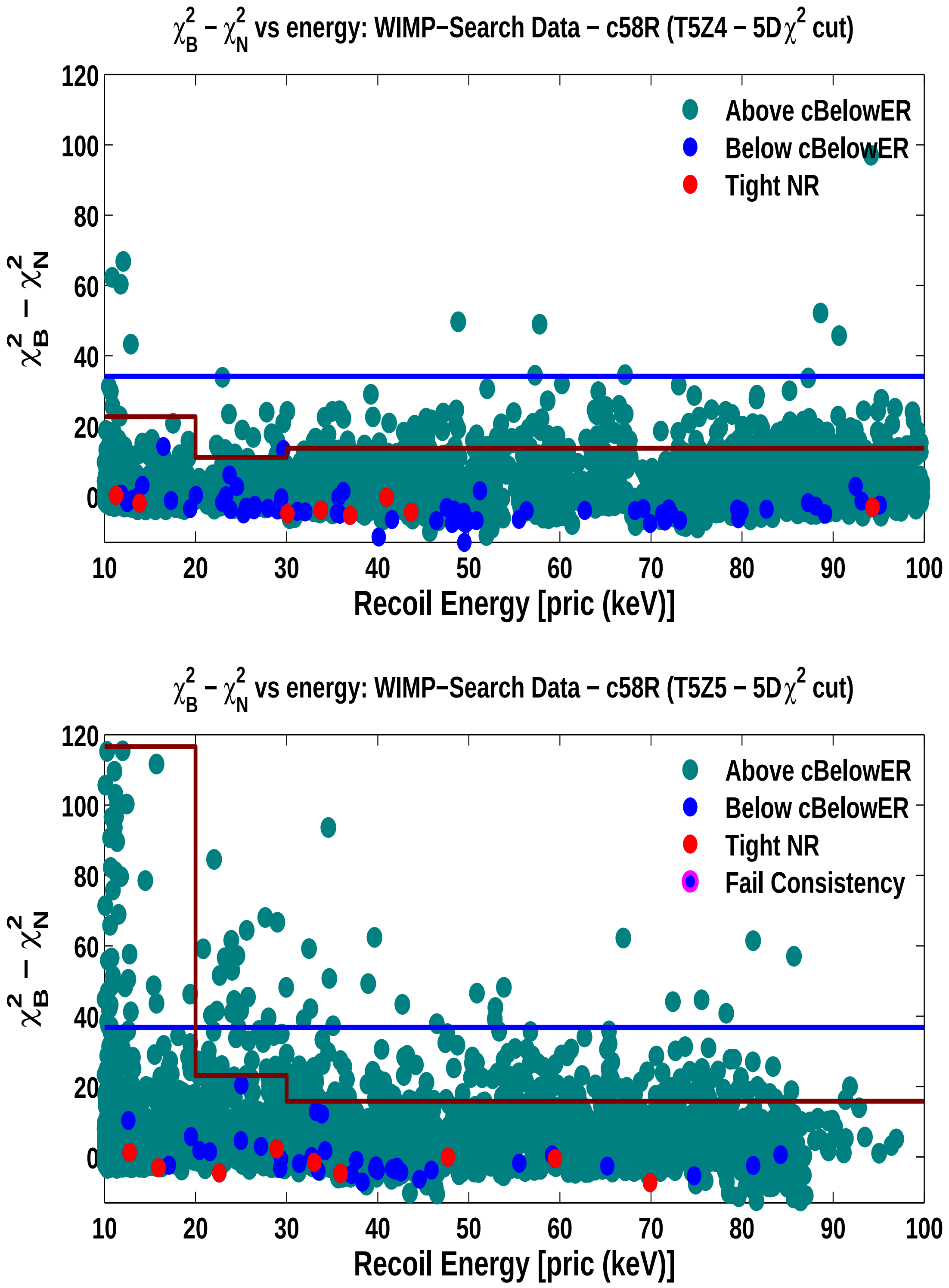

Figure D.7: $\chi^2_B - \chi^2_N$ vs recoil energy for the low background data for T5Z4 (top) and T5Z5 (bottom). Events shown in dark cyan color represents events located 3σ above the **cBelowER_c58** (representing mostly electron-recoil events) while events in blue dots indicates non-electron-recoil events (which can either be surface events or event candidates for those laying inside the tight nuclear-recoil band). Red dots are WIMP-search events inside the tight nuclear-recoil band cut, i.e. the optimized nuclear-recoil band defined by a yield cut of $[l = -1.9; u = 1.8]$. Events shown in magenta circled with blue faces are events failing the consistency cut. The green circle events with the grey face represents events passing the alternative timing cuts developed during the reanalysis. The blue horizontal straight line is the energy independent cut while the dark red line represent the energy-dependent cut.

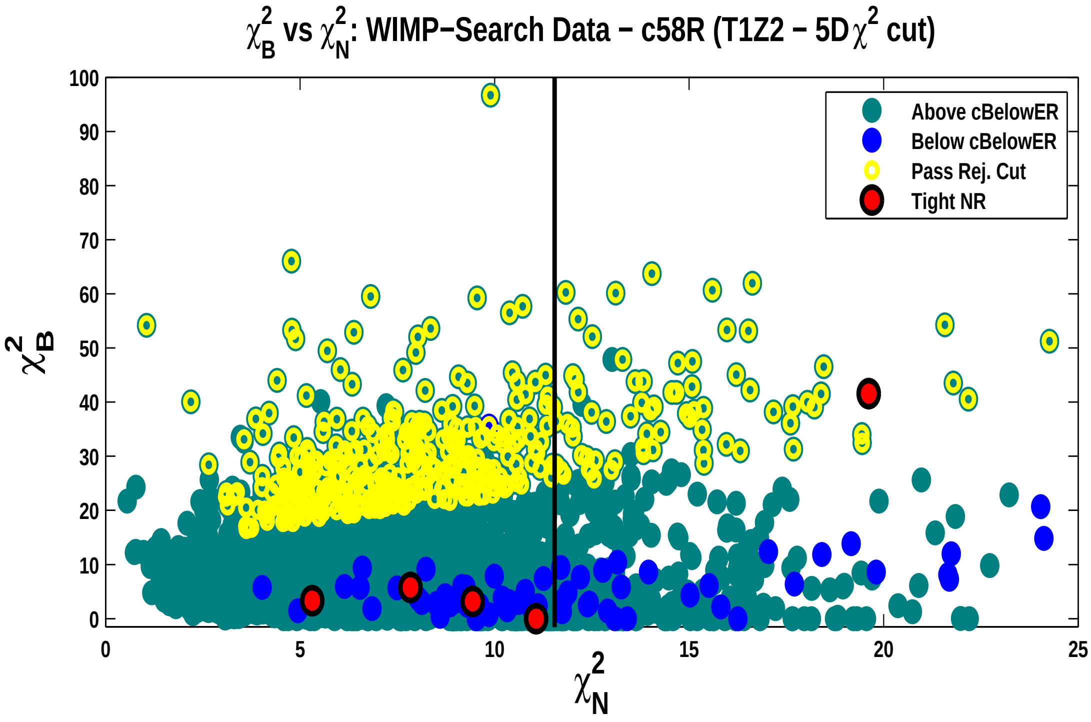

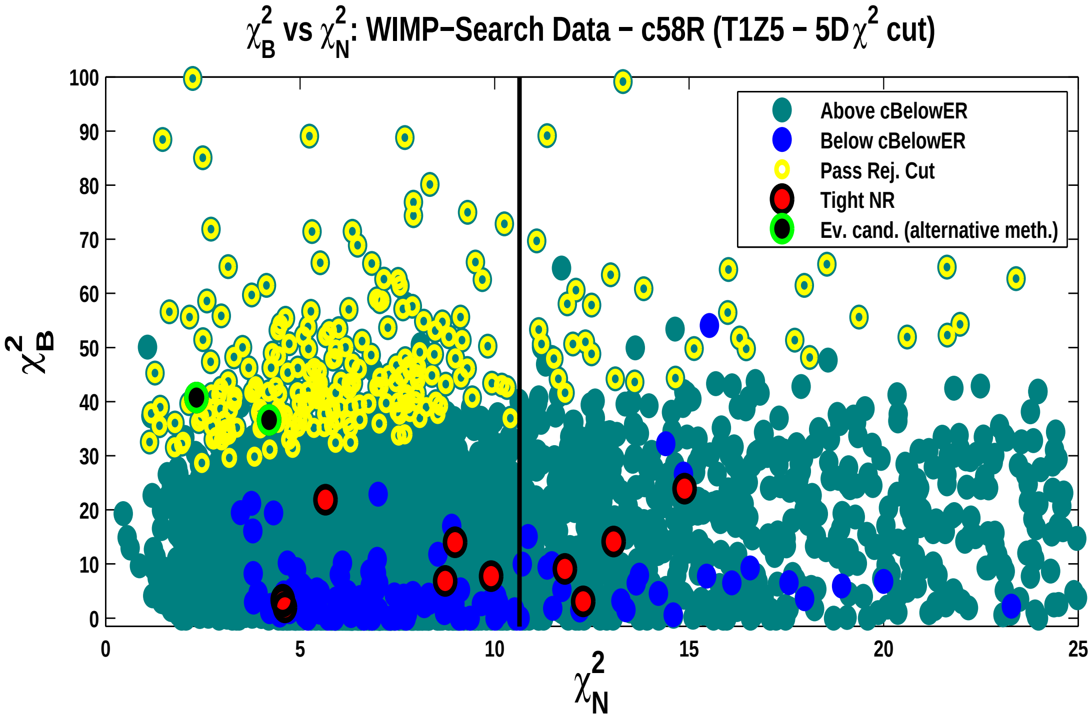

Figure D.8: WIMP-Search distribution of χ^2_B as function of χ^2_N for T1Z2 (top) and T1Z5 (bottom). Events shown in dark cyan color represents events located above **cBelowER_c58** above the **cBelowER_c58** (representing mostly electron recoils events) while events in blue dots indicates non-electron-recoil events (which can either be surface events or event candidates for those laying inside the tight nuclear-recoil band). Events shown in red dots are WIMP-search events inside the tight nuclear-recoil band cut, i.e. the optimized nuclear-recoil band defined by a yield cut of $[l = -1.9; u = 1.8]$ while events in yellows dots are events shown passing the rejection cut. The green circle events with the black face represent events passing the alternative timing cuts developed during the reanalysis. The black vertical line show the consistency cut position.

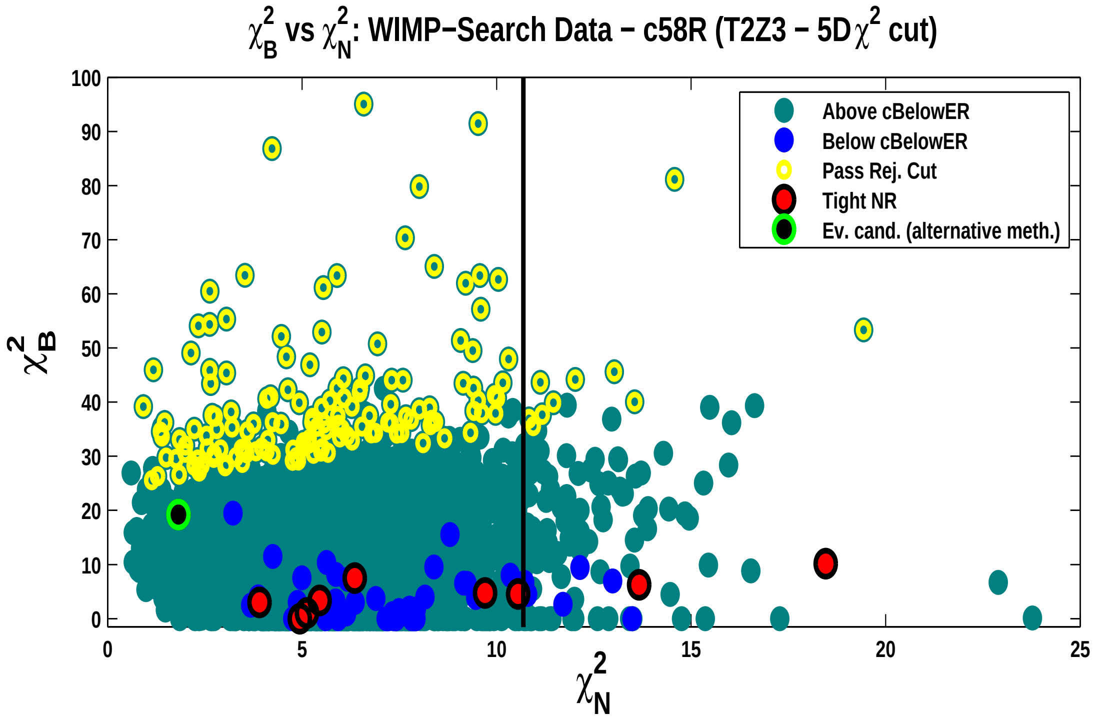

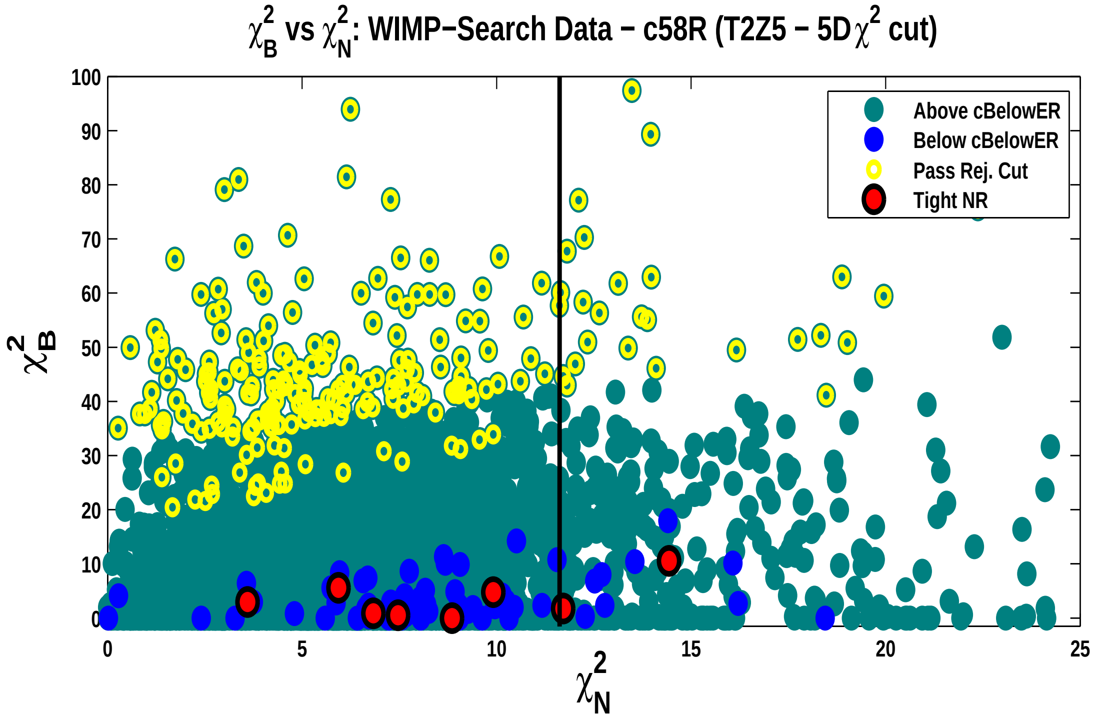

Figure D.9: WIMP-Search distribution of χ^2_B as function of χ^2_N for T2Z3 (top) and T2Z5 (bottom). Events shown in dark cyan color represents events located above **cBelowER_c58** above the **cBelowER_c58** (representing mostly electron recoils events) while events in blue dots indicates non-electron-recoil events (which can either be surface events or event candidates for those laying inside the tight nuclear-recoil band). Events shown in red dots are WIMP-search events inside the tight nuclear-recoil band cut, i.e. the optimized nuclear-recoil band defined by a yield cut of $[l = -1.9; u = 1.8]$ while events in yellows dots are events shown passing the rejection cut. The green circle events with the black face represent events passing the alternative timing cuts developed during the reanalysis. The black vertical line show the consistency cut position.

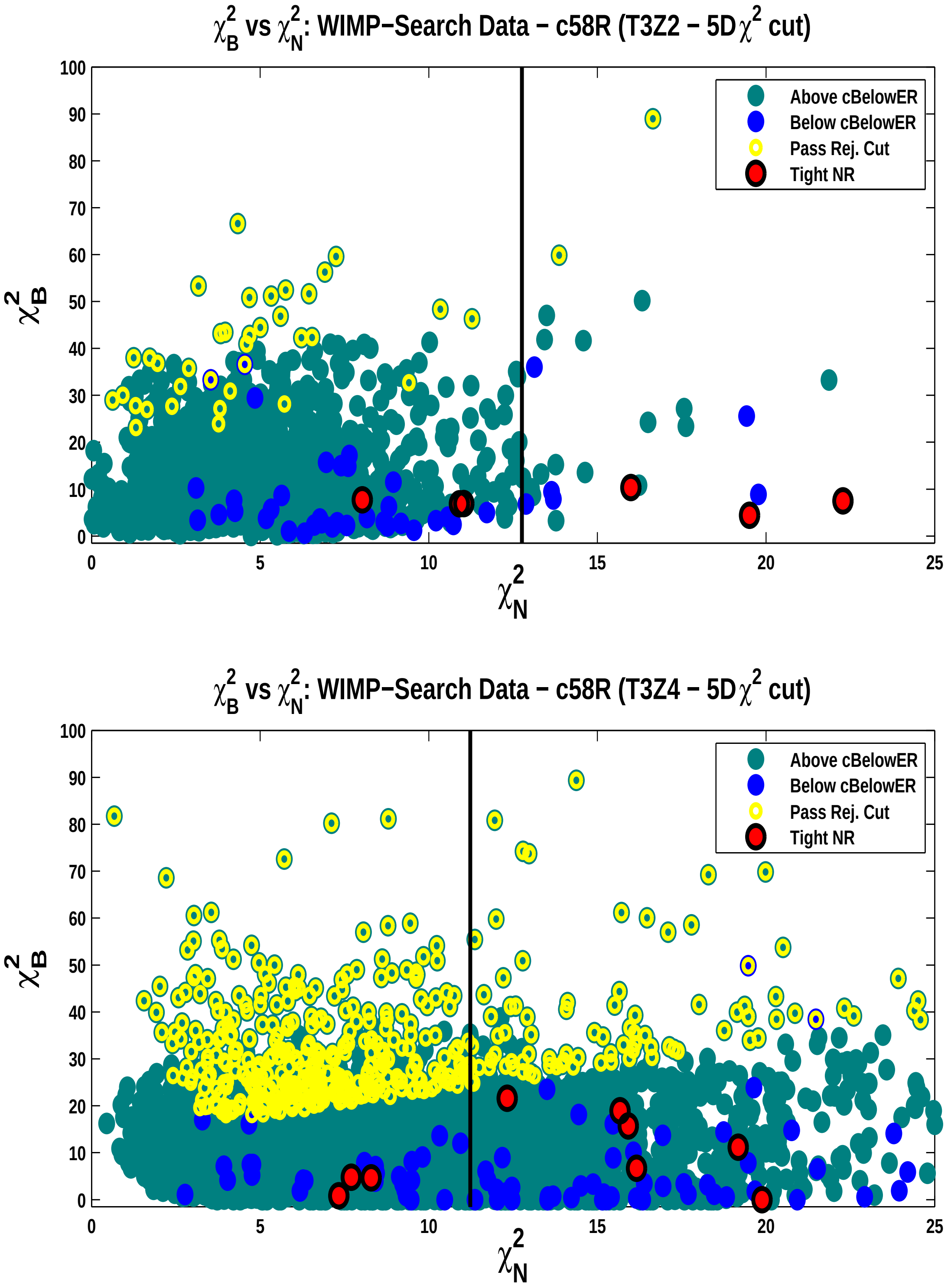

Figure D.10: WIMP-Search distribution of χ^2_B as function of χ^2_N for T3Z2 (top) and T3Z4 (bottom). Events shown in dark cyan color represents events located above **cBelowER_c58** above the **cBelowER_c58** (representing mostly electron recoils events) while events in blue dots indicates non-electron-recoil events (which can either be surface events or event candidates for those laying inside the tight nuclear-recoil band). Events shown in red dots are WIMP-search events inside the tight nuclear-recoil band cut, i.e. the optimized nuclear-recoil band defined by a yield cut of $[l = -1.9; u = 1.8]$ while events in yellows dots are events shown passing the rejection cut. The green circle events with the black face represent events passing the alternative timing cuts developed during the reanalysis. The black vertical line show the consistency cut position.

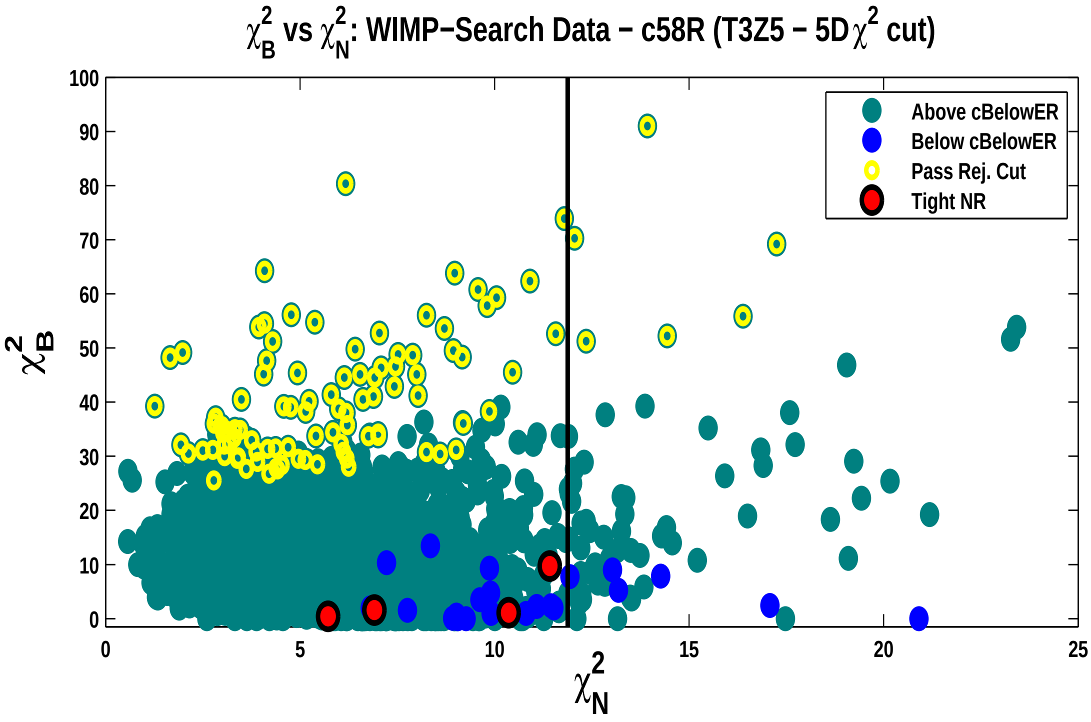

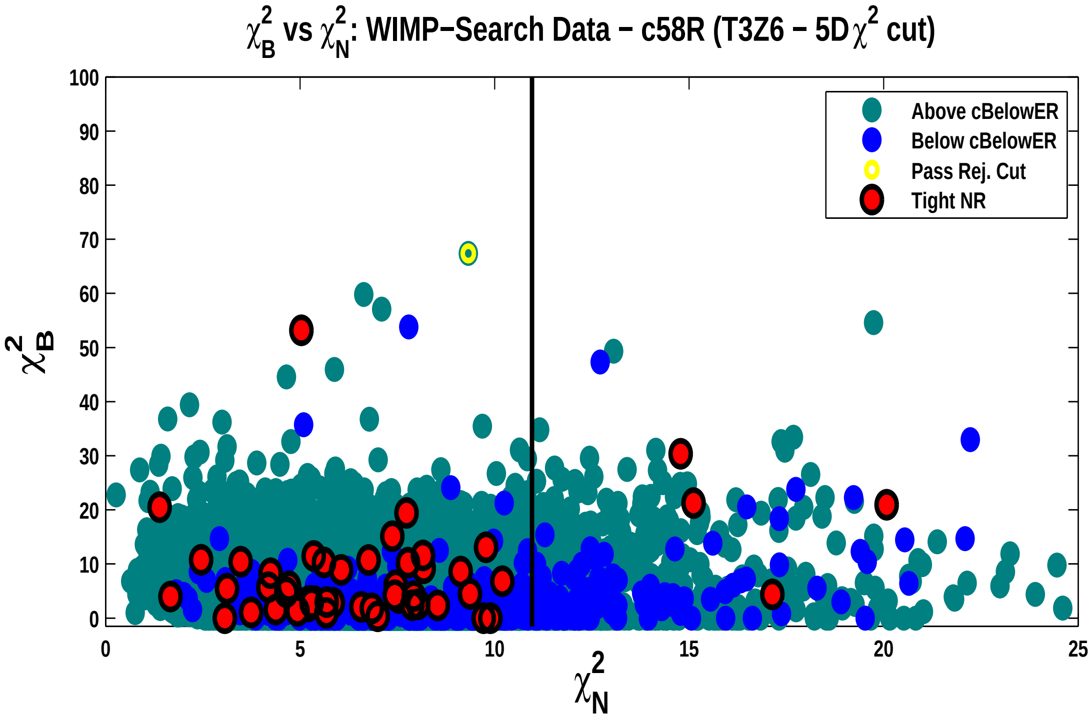

Figure D.11: WIMP-Search distribution of χ^2_B as function of χ^2_N for T3Z5 (top) and T3Z6 (bottom). Events shown in dark cyan color represents events located above **cBelowER_c58** above the **cBelowER_c58** (representing mostly electron recoils events) while events in blue dots indicates non-electron-recoil events (which can either be surface events or event candidates for those laying inside the tight nuclear-recoil band). Events shown in red dots are WIMP-search events inside the tight nuclear-recoil band cut, i.e. the optimized nuclear-recoil band defined by a yield cut of $[l = -1.9; u = 1.8]$ while events in yellows dots are events shown passing the rejection cut. The green circle events with the black face represent events passing the alternative timing cuts developed during the reanalysis. The black vertical line show the consistency cut position.

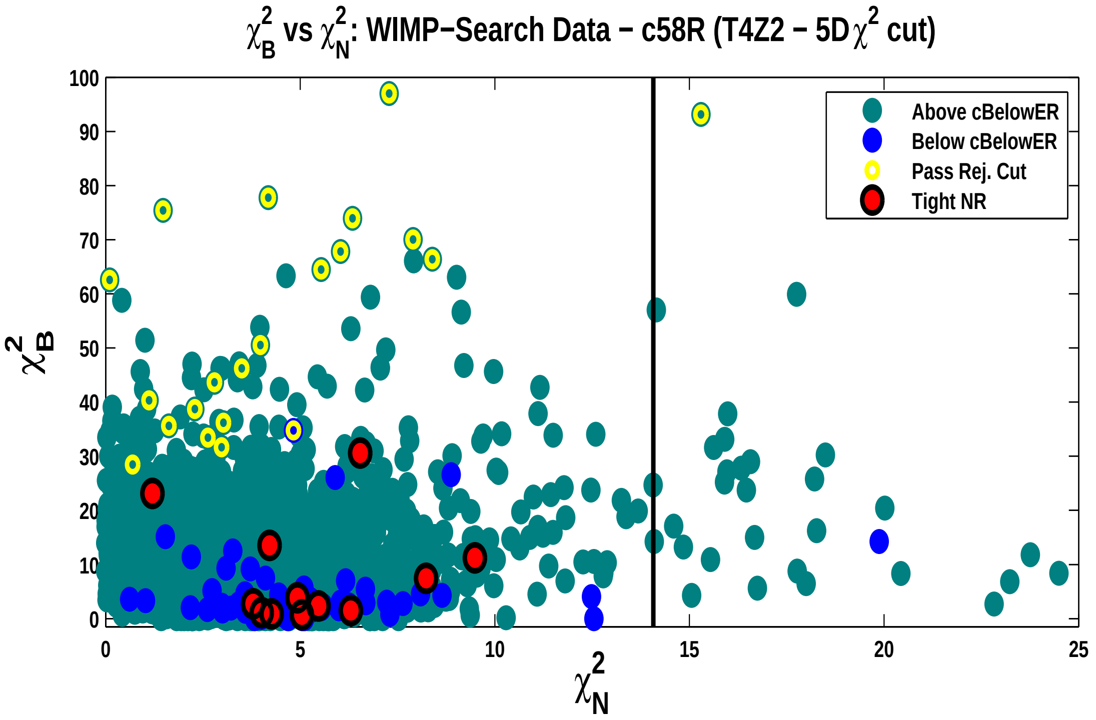

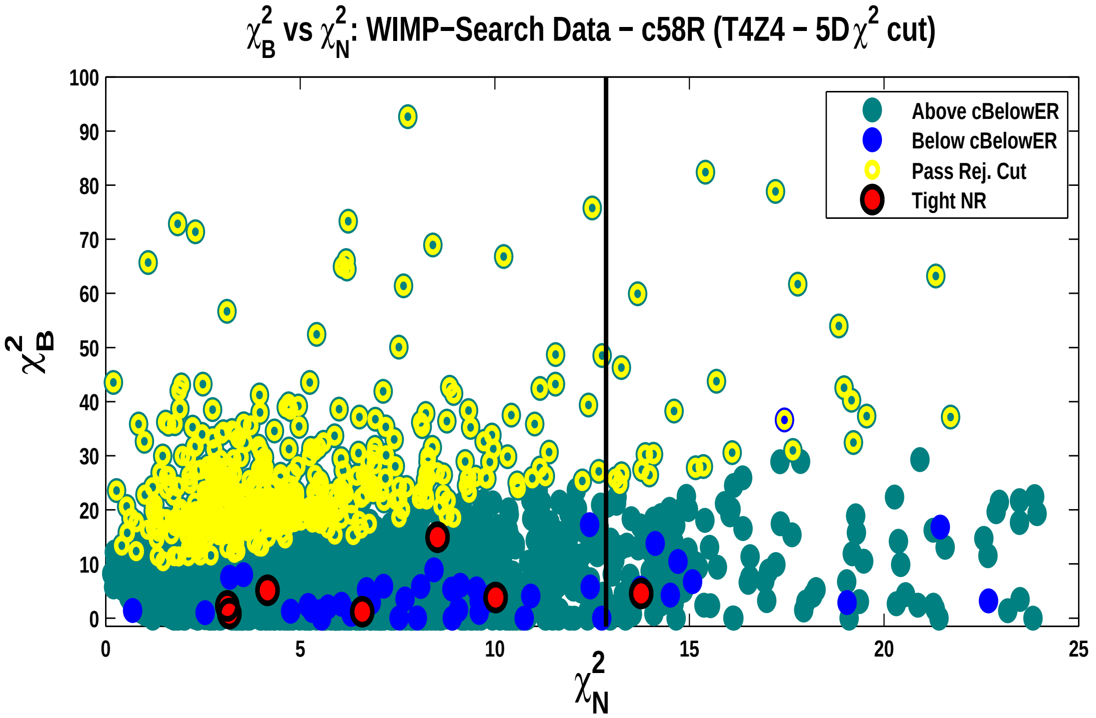

Figure D.12: WIMP-Search distribution of χ^2_B as function of χ^2_N for T4Z2 (top) and T4Z4 (bottom). Events shown in dark cyan color represents events located above **cBelowER_c58** above the **cBelowER_c58** (representing mostly electron recoils events) while events in blue dots indicates non-electron-recoil events (which can either be surface events or event candidates for those laying inside the tight nuclear-recoil band). Events shown in red dots are WIMP-search events inside the tight nuclear-recoil band cut, i.e. the optimized nuclear-recoil band defined by a yield cut of $[l = -1.9; u = 1.8]$ while events in yellows dots are events shown passing the rejection cut. The green circle events with the black face represent events passing the alternative timing cuts developed during the reanalysis. The black vertical line show the consistency cut position.

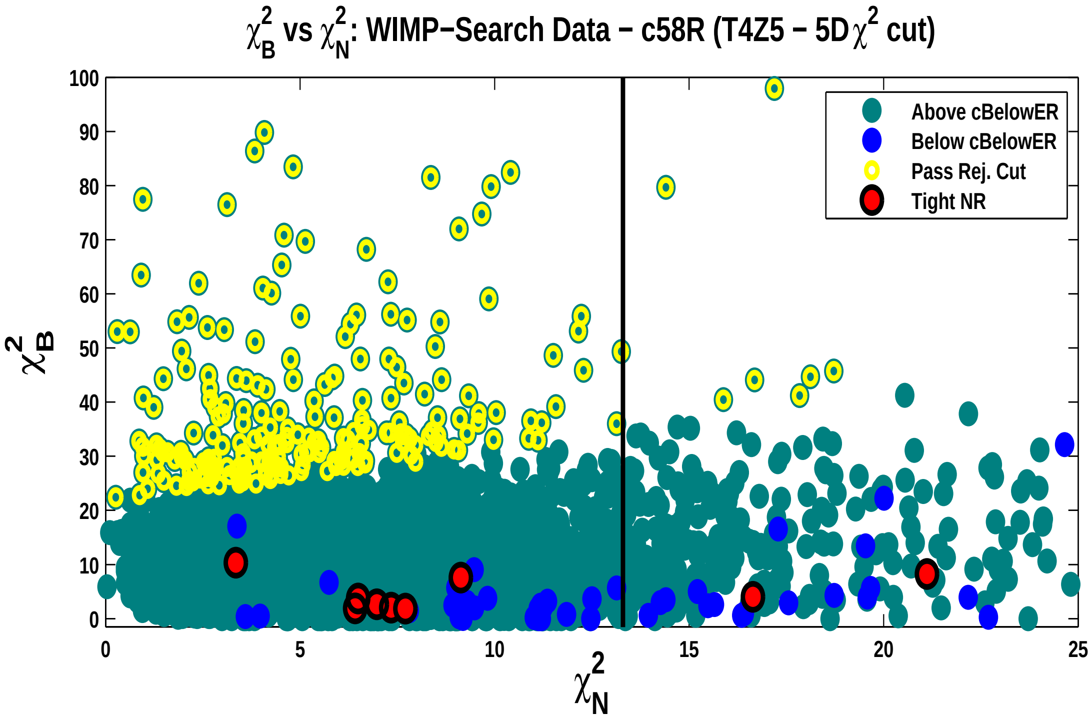

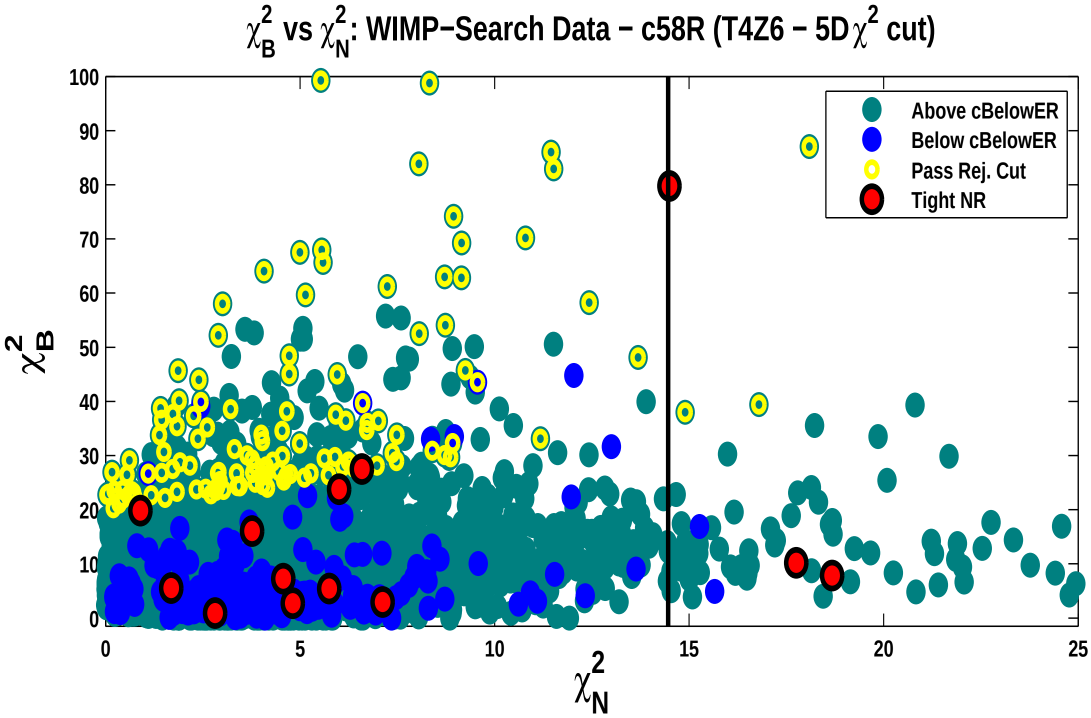

Figure D.13: WIMP-Search distribution of χ^2_B as function of χ^2_N for T4Z5 (top) and T4Z6 (bottom). Events shown in dark cyan color represents events located above **cBelowER_c58** above the **cBelowER_c58** (representing mostly electron recoils events) while events in blue dots indicates non-electron-recoil events (which can either be surface events or event candidates for those laying inside the tight nuclear-recoil band). Events shown in red dots are WIMP-search events inside the tight nuclear-recoil band cut, i.e. the optimized nuclear-recoil band defined by a yield cut of $[l = -1.9; u = 1.8]$ while events in yellows dots are events shown passing the rejection cut. The green circle events with the black face represent events passing the alternative timing cuts developed during the reanalysis. The black vertical line show the consistency cut position.

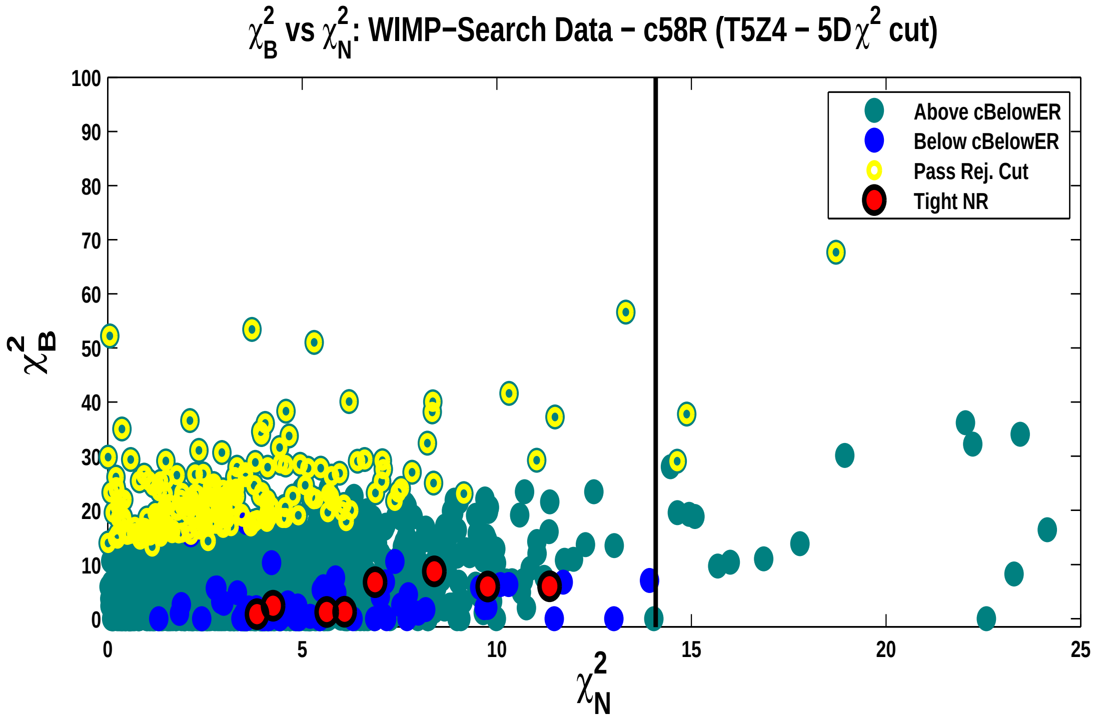

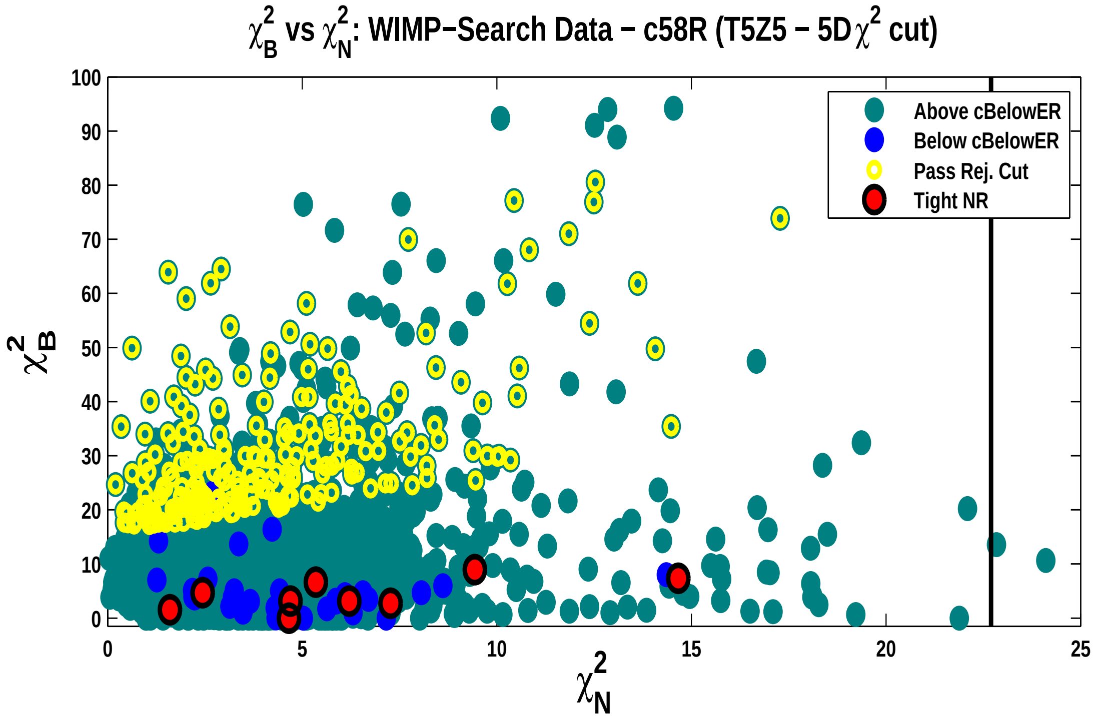

Figure D.14: WIMP-Search distribution of χ_B^2 as function of χ_N^2 for T5Z4 (top) and T5Z5 (bottom). Events shown in dark cyan color represents events located above **cBelowER_c58** above the **cBelowER_c58** (representing mostly electron recoils events) while events in blue dots indicates non-electron-recoil events (which can either be surface events or event candidates for those laying inside the tight nuclear-recoil band). Events shown in red dots are WIMP-search events inside the tight nuclear-recoil band cut, i.e. the optimized nuclear-recoil band defined by a yield cut of $[l = -1.9; u = 1.8]$ while events in yellows dots are events shown passing the rejection cut. The green circle events with the black face represent events passing the alternative timing cuts developed during the reanalysis. The black vertical line show the consistency cut position.

Appendix E

yield vs energy (WS data).

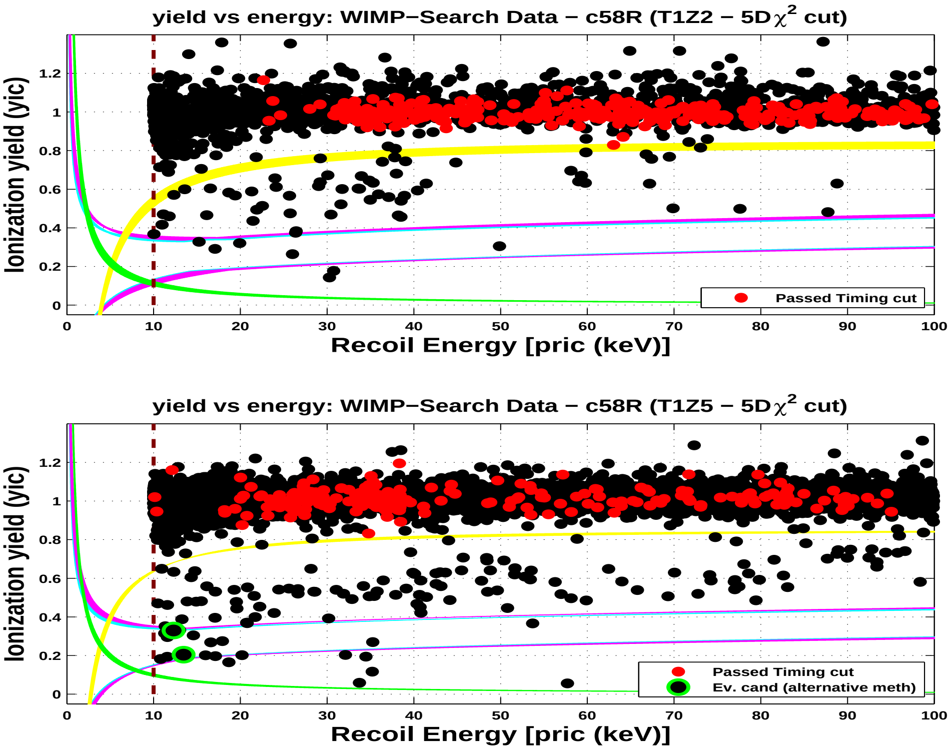

Figure E.1: Ionization yield vs recoil energy showing the distribution of events in the WIMP-search (black dots) for T1Z2 (top) and T1Z5 (bottom). The events shown in red dots are the events passing the χ^2 optimized timing cuts above the 10 keV threshold. Note that all events passing the timing cut lie within 3σ of the electron-recoil band (yellow curve). The cyan and magenta curves indicate the tight and loose nuclear-recoil bands ($[l = -1.9; u = 1.8]$ and $[l = -2; u = 2]$, respectively), while the green dots indicate the WIMP candidates identified by alternate timing-cut analyses.

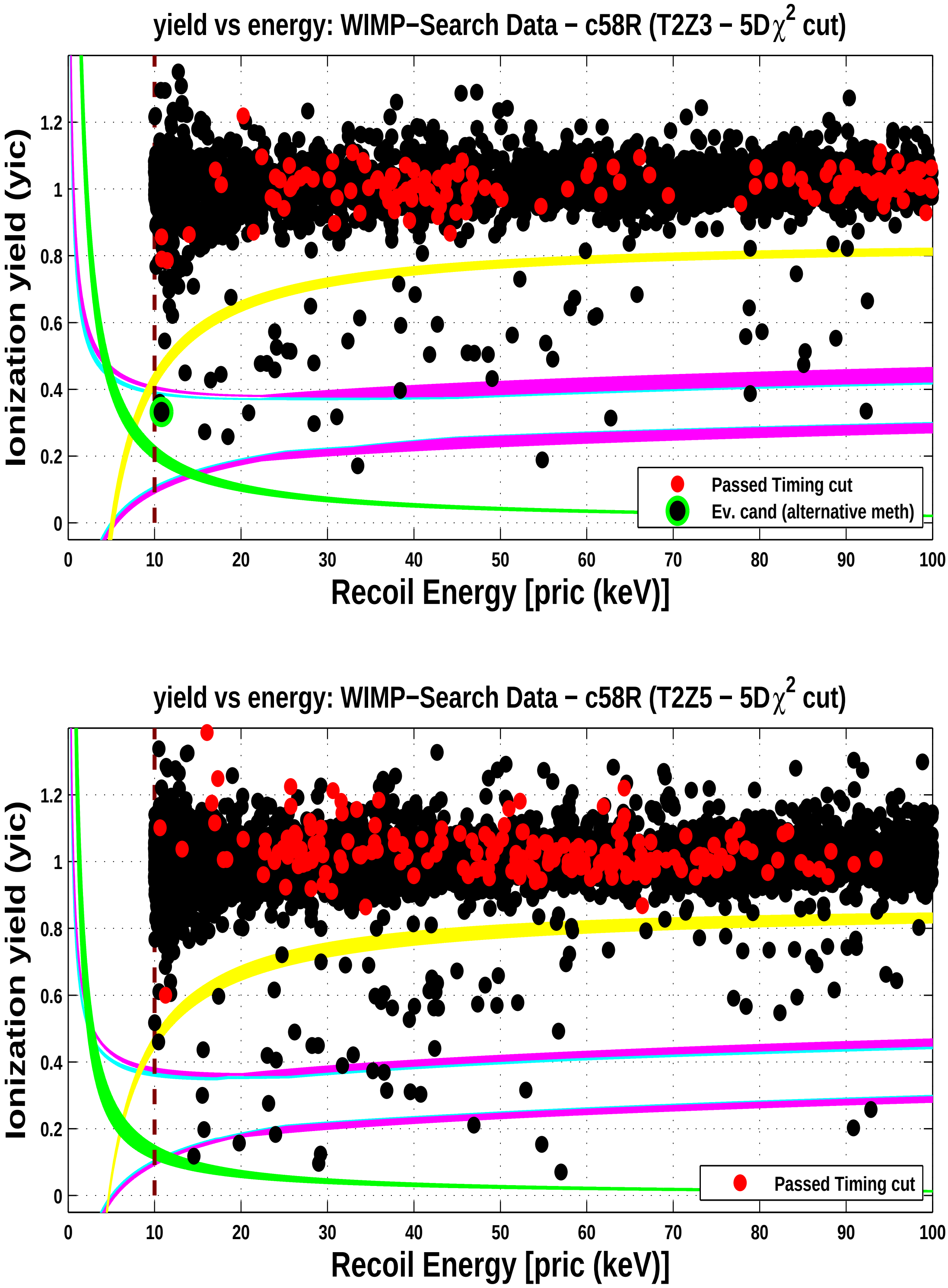

Figure E.2: Ionization yield vs recoil energy showing the distribution of events in the WIMP-search (black dots) for T2Z3 (top) and T2Z5 (bottom). The events shown in red dots are the events passing the χ^2 optimized timing cuts above the 10 keV threshold. Note that all events passing the timing cut lie within 3σ of the electron-recoil band (yellow curve). The cyan and magenta curves indicate the tight and loose nuclear-recoil bands ($[l = -1.9; u = 1.8]$ and $[l = -2; u = 2]$, respectively), while the green dots indicate the WIMP candidates identified by alternate timing-cut analyses.

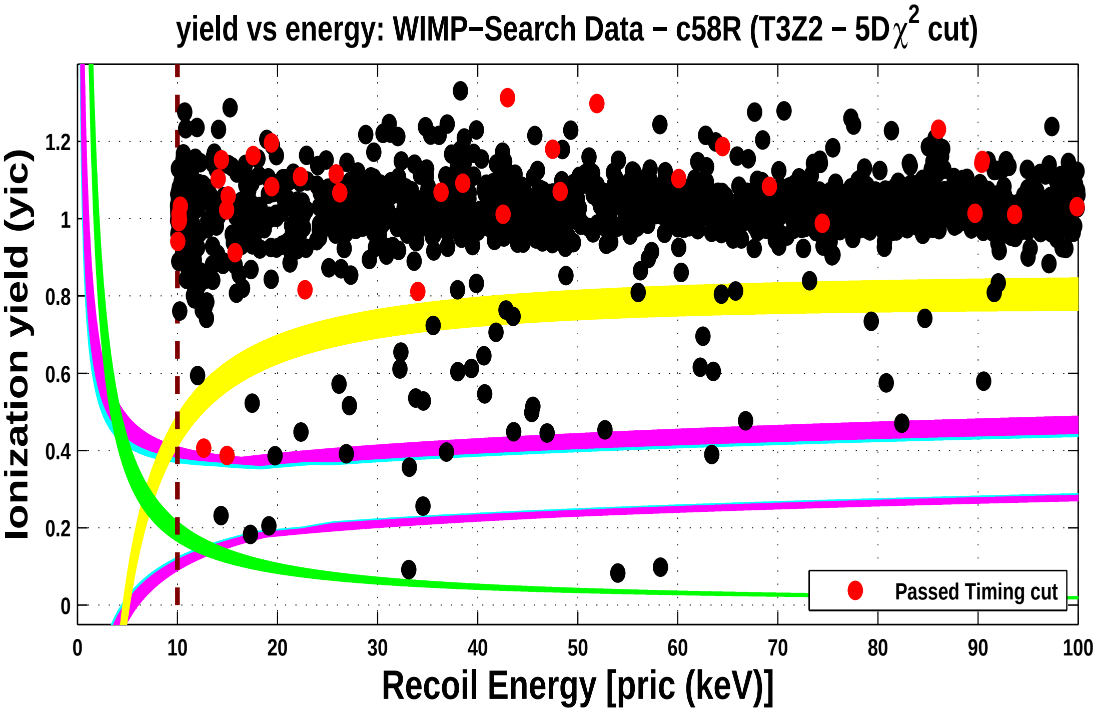

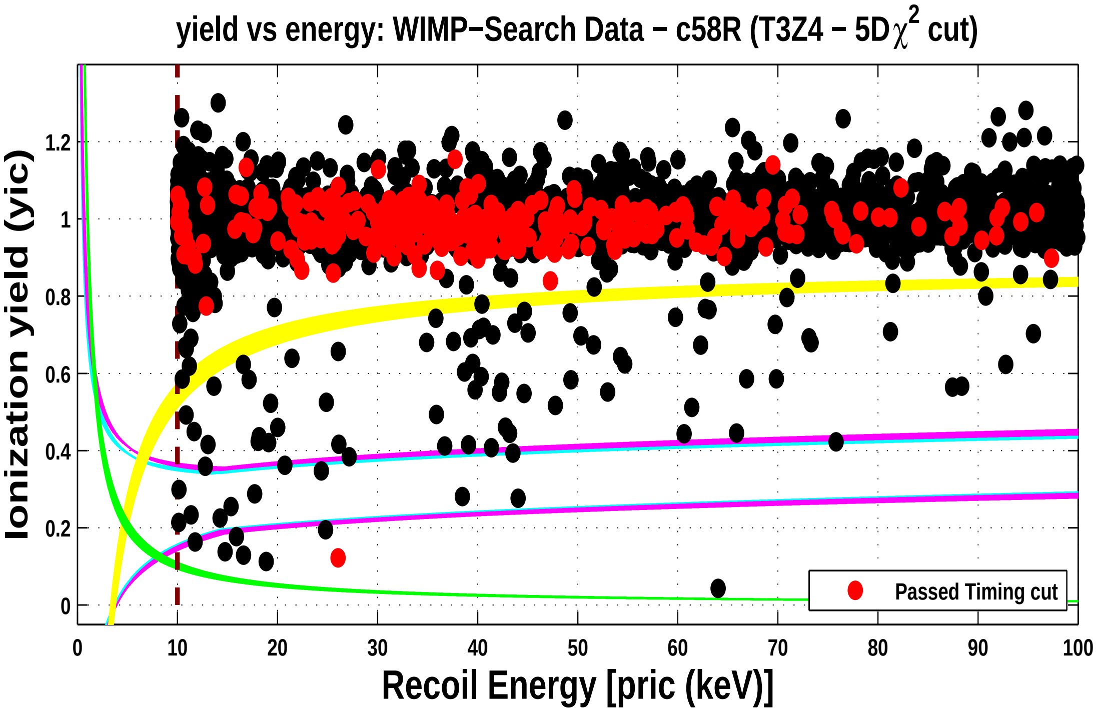

Figure E.3: Ionization yield vs recoil energy showing the distribution of events in the WIMP-search (black dots) for T3Z2 (top) and T3Z4 (bottom). The events shown in red dots are the events passing the χ^2 optimized timing cuts above the 10 keV threshold. Note that all events passing the timing cut lie within 3σ of the electron-recoil band (yellow curve). The cyan and magenta curves indicate the tight and loose nuclear-recoil bands ($[l = -1.9; u = 1.8]$ and $[l = -2; u = 2]$, respectively), while the green dots indicate the WIMP candidates identified by alternate timing-cut analyses.

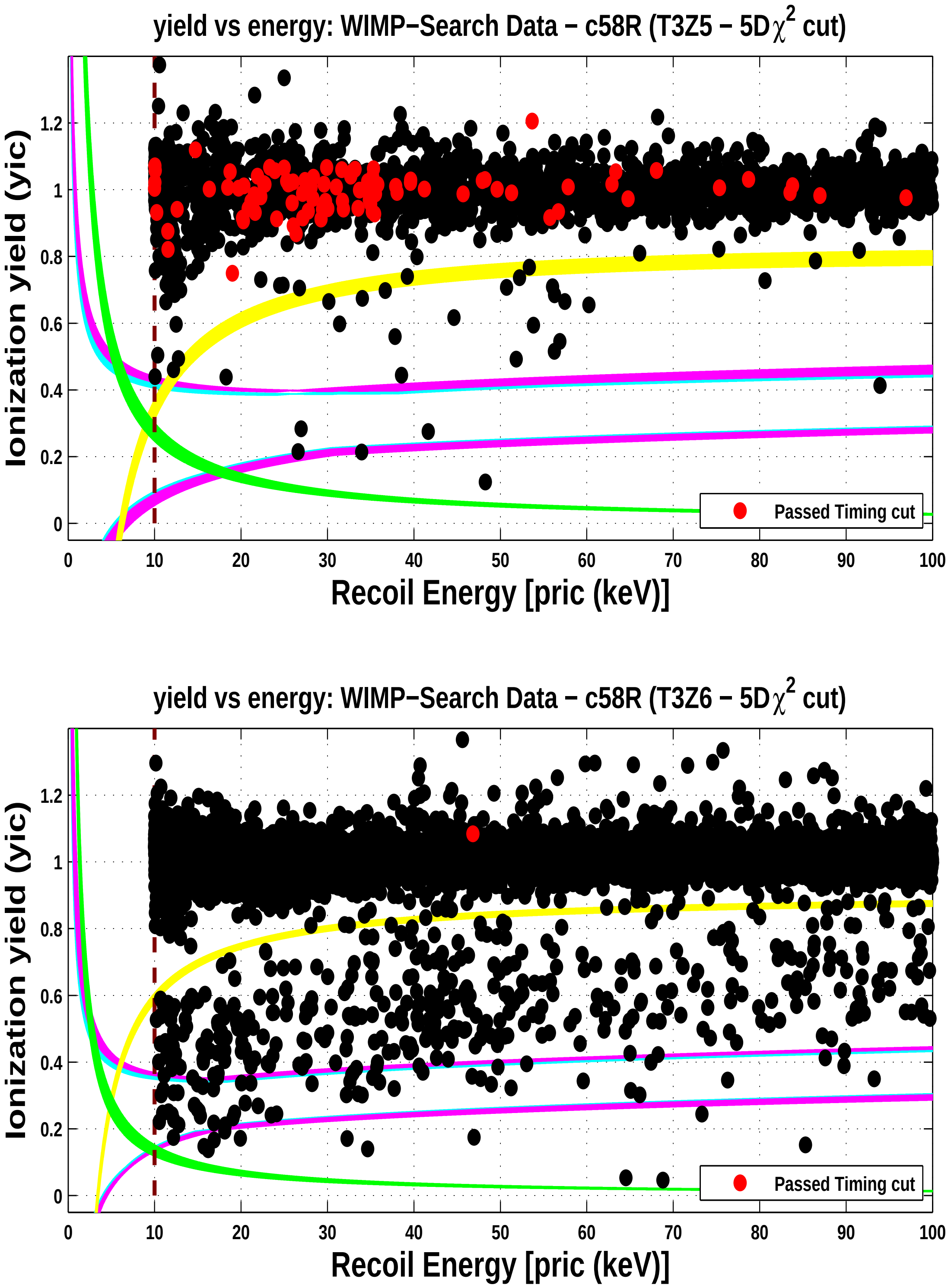

yield vs energy: WIMP−Search Data − c58R (T3Z5 − 5Dχ^2 cut)

yield vs energy: WIMP−Search Data − c58R (T3Z6 − 5Dχ^2 cut)

Figure E.4: Ionization yield vs recoil energy showing the distribution of events in the WIMP-search (black dots) for T3Z5 (top) and T3Z6 (bottom). The events shown in red dots are the events passing the χ^2 optimized timing cuts above the 10 keV threshold. Note that all events passing the timing cut lie within 3σ of the electron-recoil band (yellow curve). The cyan and magenta curves indicate the tight and loose nuclear-recoil bands ($[l = -1.9; u = 1.8]$ and $[l = -2; u = 2]$, respectively), while the green dots indicate the WIMP candidates identified by alternate timing-cut analyses.

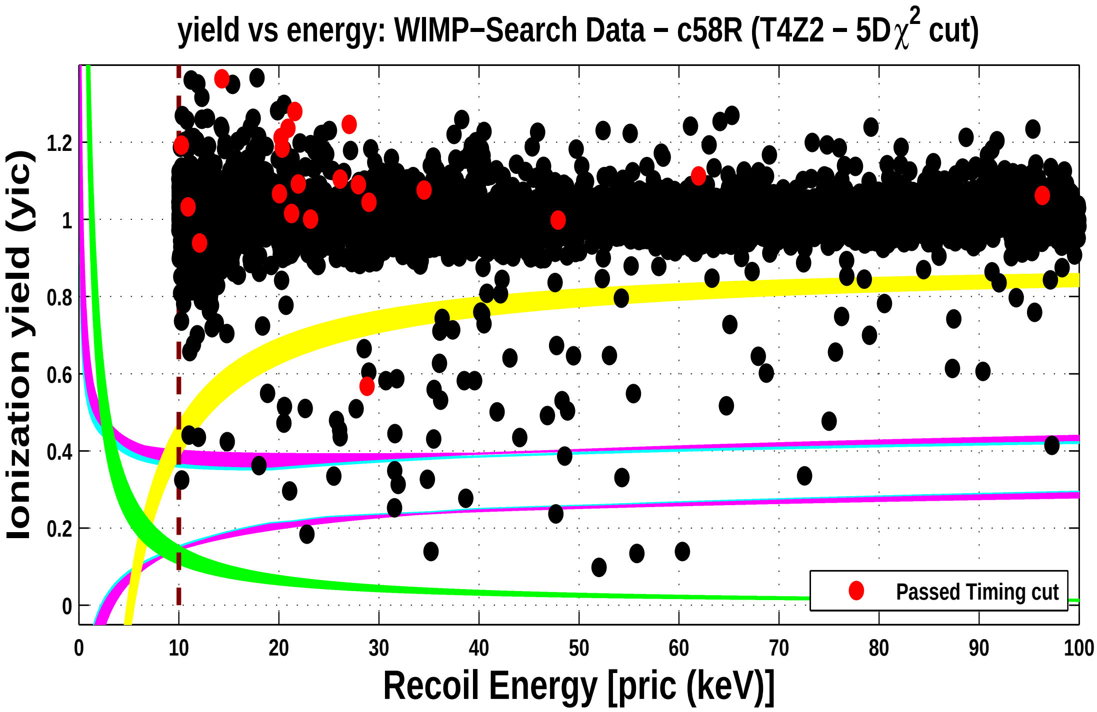

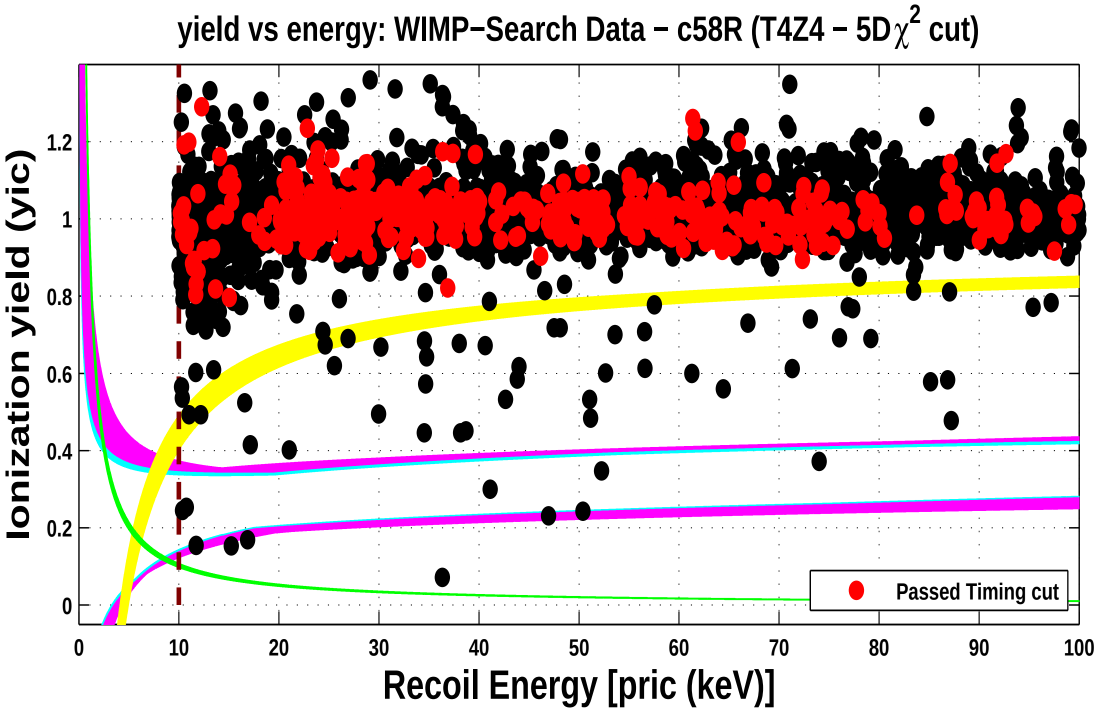

Figure E.5: Ionization yield vs recoil energy showing the distribution of events in the WIMP-search (black dots) for T4Z2 (top) and T4Z4 (bottom). The events shown in red dots are the events passing the χ^2 optimized timing cuts above the 10 keV threshold. Note that all events passing the timing cut lie within 3σ of the electron-recoil band (yellow curve). The cyan and magenta curves indicate the tight and loose nuclear-recoil bands ($[l = -1.9; u = 1.8]$ and $[l = -2; u = 2]$, respectively), while the green dots indicate the WIMP candidates identified by alternate timing-cut analyses.

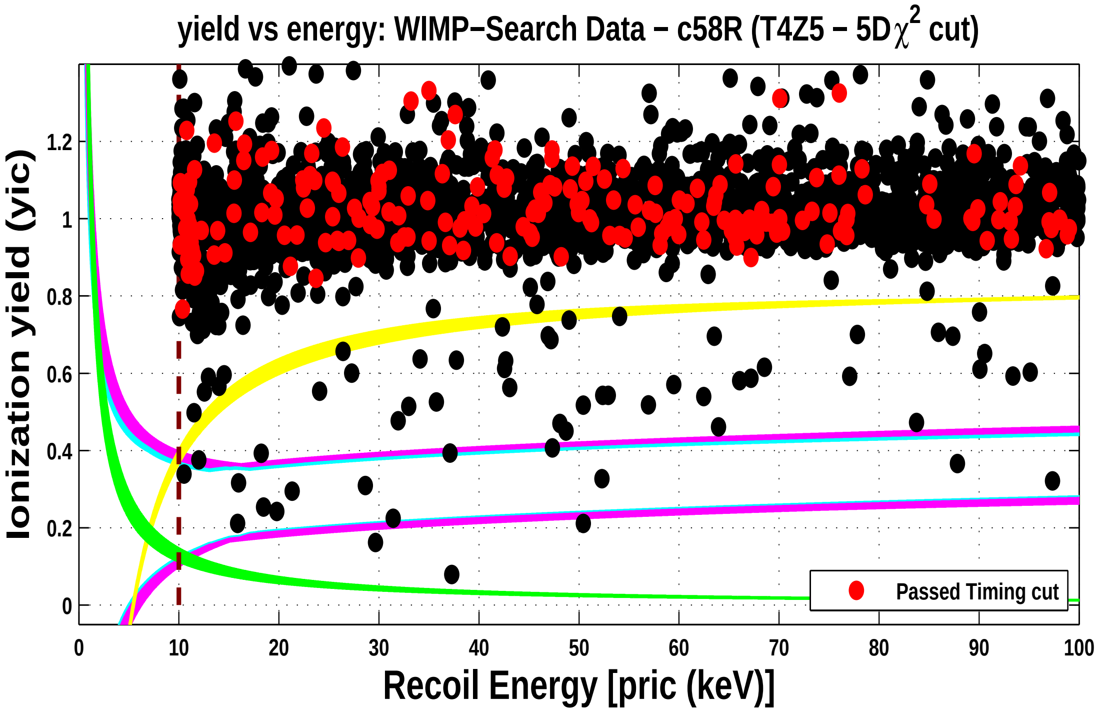

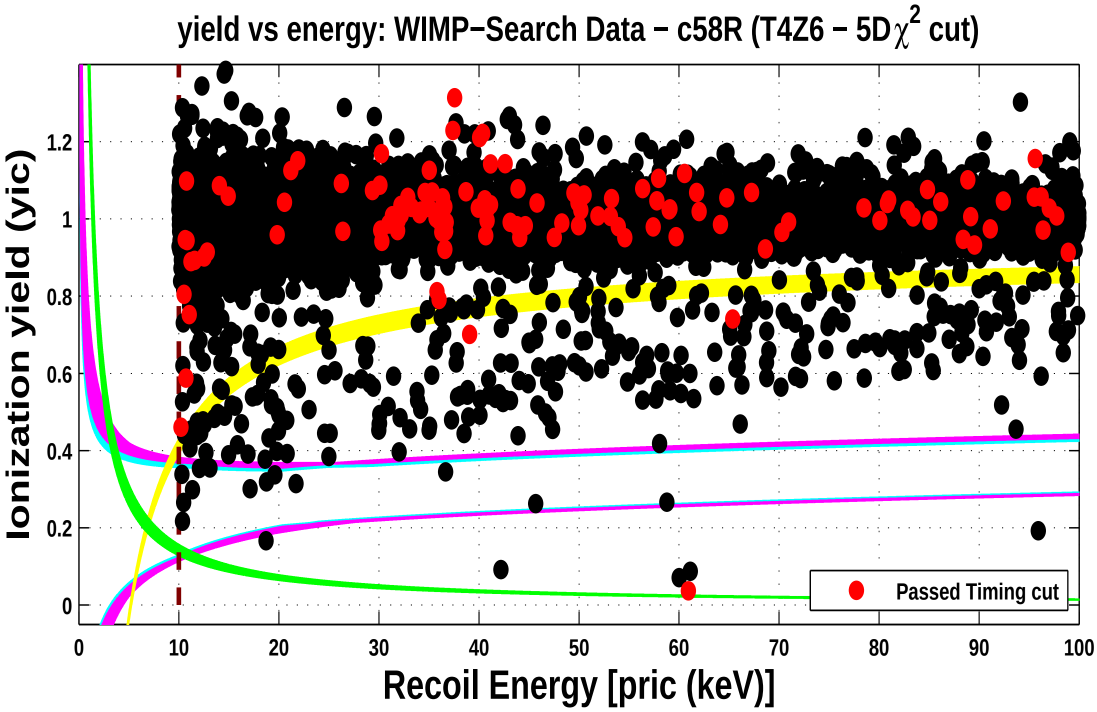

Figure E.6: Ionization yield vs recoil energy showing the distribution of events in the WIMP-search (black dots) for T4Z5 (top) and T4Z6 (bottom). The events shown in red dots are the events passing the χ^2 optimized timing cuts above the 10 keV threshold. Note that all events passing the timing cut lie within 3σ of the electron-recoil band (yellow curve). The cyan and magenta curves indicate the tight and loose nuclear-recoil bands ($[l = -1.9; u = 1.8]$ and $[l = -2; u = 2]$, respectively), while the green dots indicate the WIMP candidates identified by alternate timing-cut analyses.

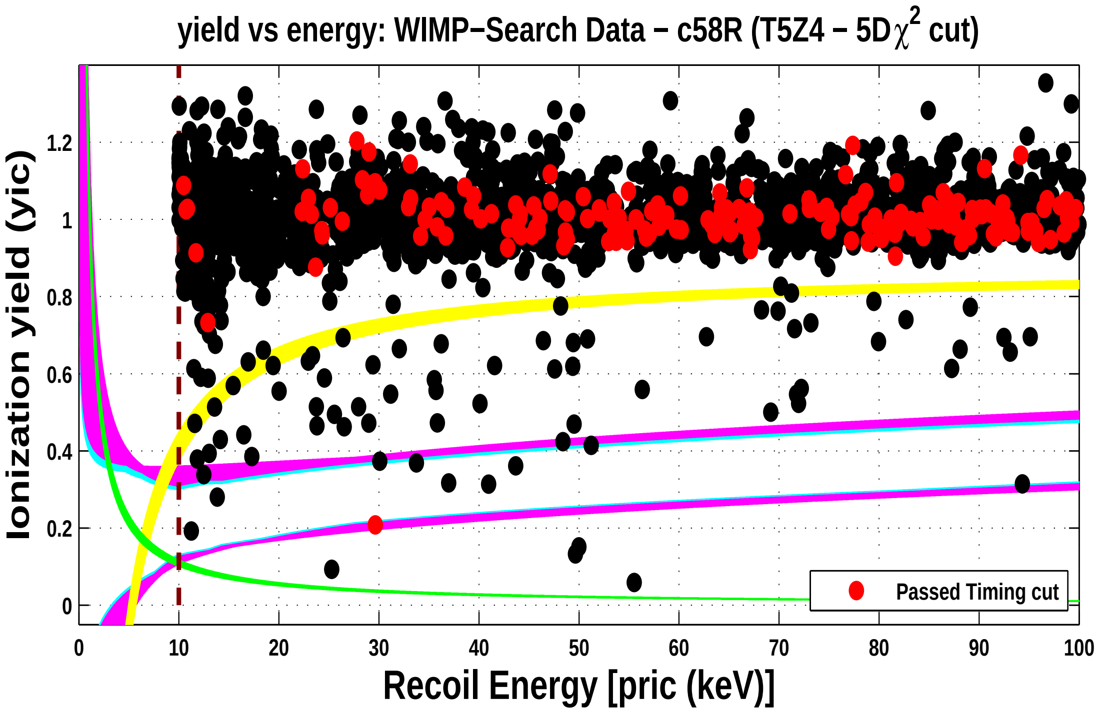

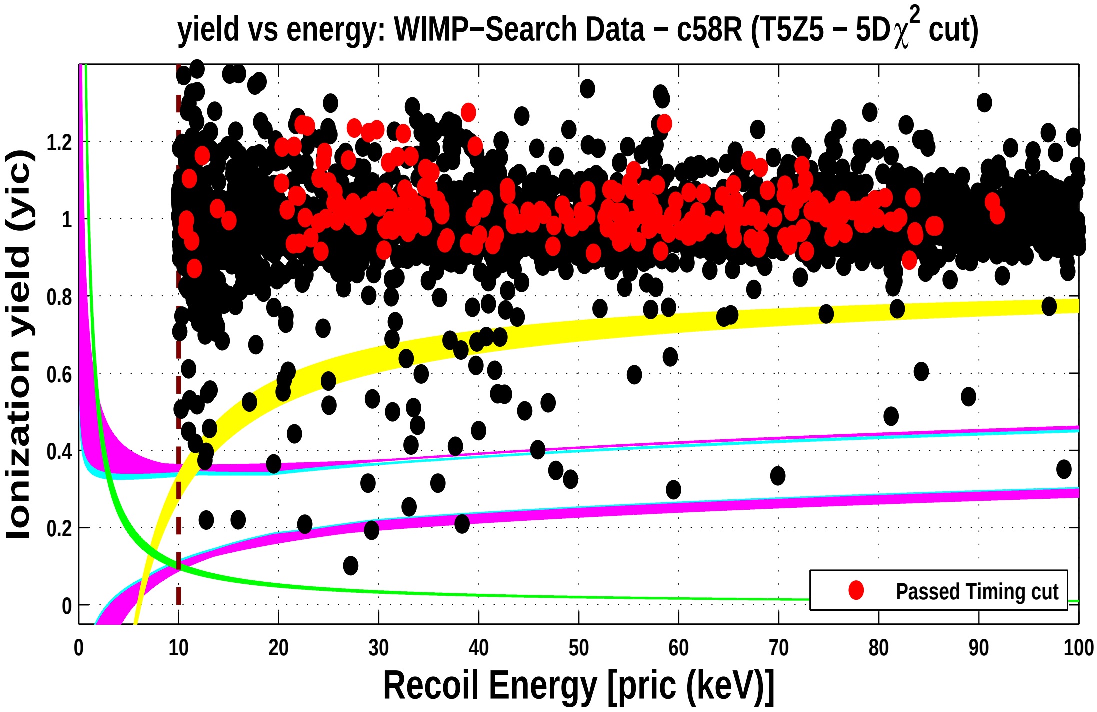

Figure E.7: Ionization yield vs recoil energy showing the distribution of events in the WIMP-search (black dots) for T5Z4 (top) and T5Z5 (bottom). The events shown in red dots are the events passing the χ^2 optimized timing cuts above the 10 keV threshold. Note that all events passing the timing cut lie within 3σ of the electron-recoil band (yellow curve). The cyan and magenta curves indicate the tight and loose nuclear-recoil bands ($[l = -1.9; u = 1.8]$ and $[l = -2; u = 2]$, respectively), while the green dots indicate the WIMP candidates identified by alternate timing-cut analyses.

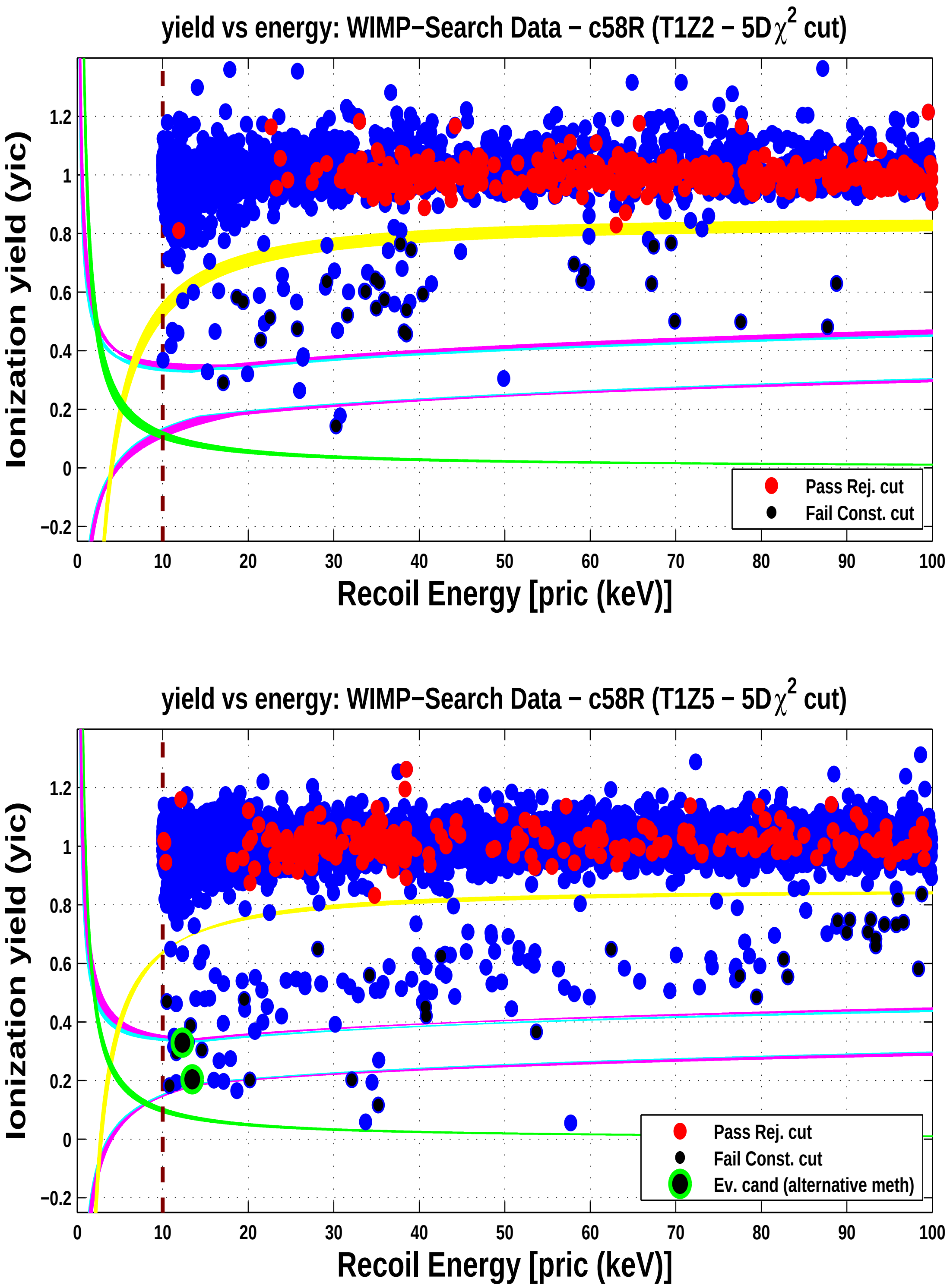

Figure E.8: Another version of ionization yield vs recoil energy showing the distribution of events in the WIMP-search (blue dots) for T1Z2 (top) and T1Z5 (bottom). The events shown in red dots are the events passing the rejection cuts above the 10 keV threshold while the black dots are events failing the consistency cut. The yellow curve show the region of space of events laying within 3σ below the mean of the electron-recoil band. The cyan and magenta curves indicate the tight and loose nuclear-recoil bands ($[l = -1.9; u = 1.8]$ and $[l = -2; u = 2]$, respectively), while the green circle with black face indicate the WIMP candidates identified by alternate timing-cut analyses.

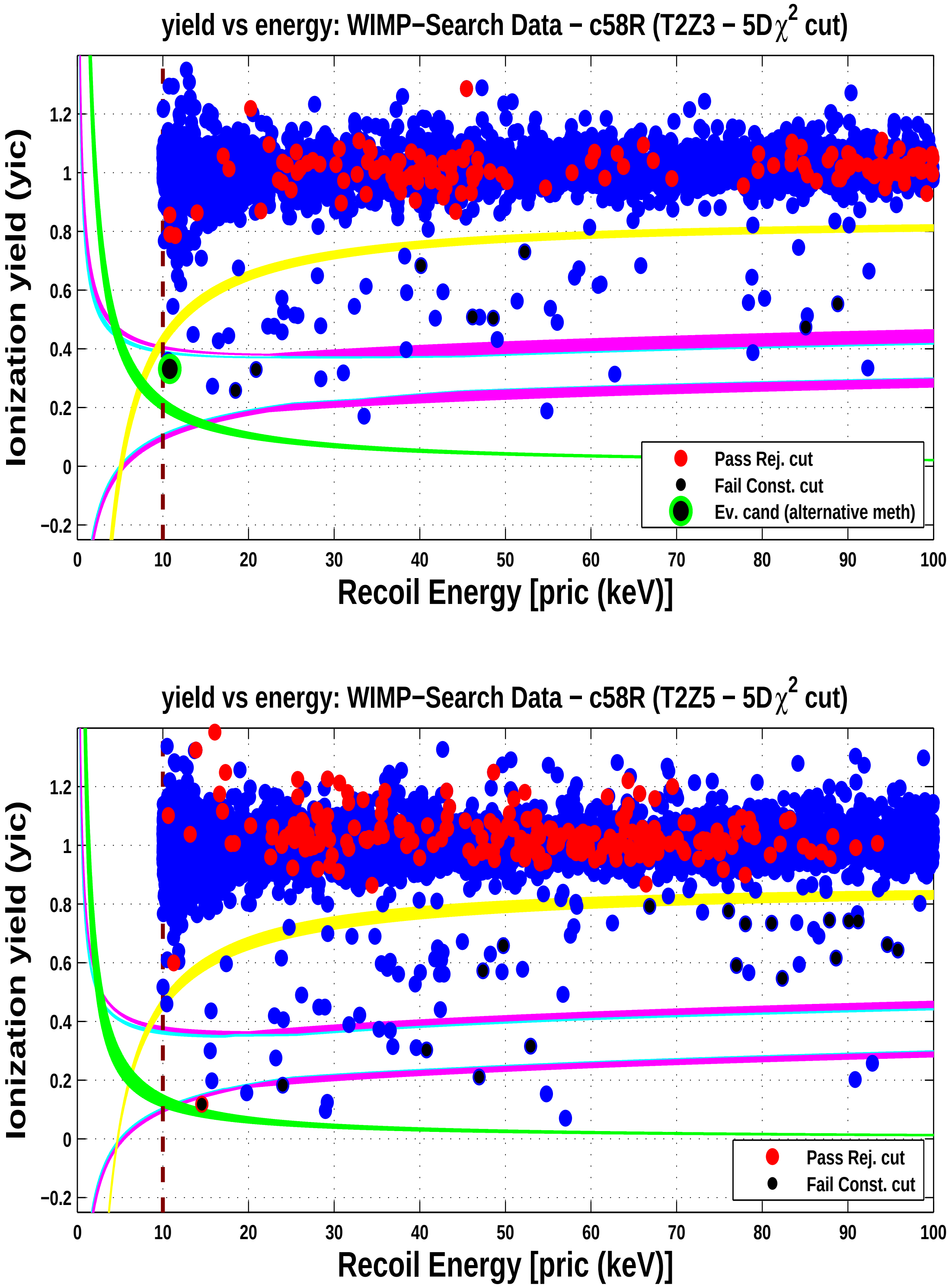
yield vs energy: WIMP−Search Data − c58R (T2Z3 − 5Dχ^2 cut)

yield vs energy: WIMP−Search Data − c58R (T2Z5 − 5Dχ^2 cut)

Figure E.9: Another version of ionization yield vs recoil energy showing the distribution of events in the WIMP-search (blue dots) for T2Z3 (top) and T2Z5 (bottom). The events shown in red dots are the events passing the rejection cuts above the 10 keV threshold while the black dots are events failing the consistency cut. The yellow curve show the region of space of events laying within 3σ below the mean of the electron-recoil band. The cyan and magenta curves indicate the tight and loose nuclear-recoil bands ($[l = -1.9; u = 1.8]$ and $[l = -2; u = 2]$, respectively), while the green circle with black face indicate the WIMP candidates identified by alternate timing-cut analyses.

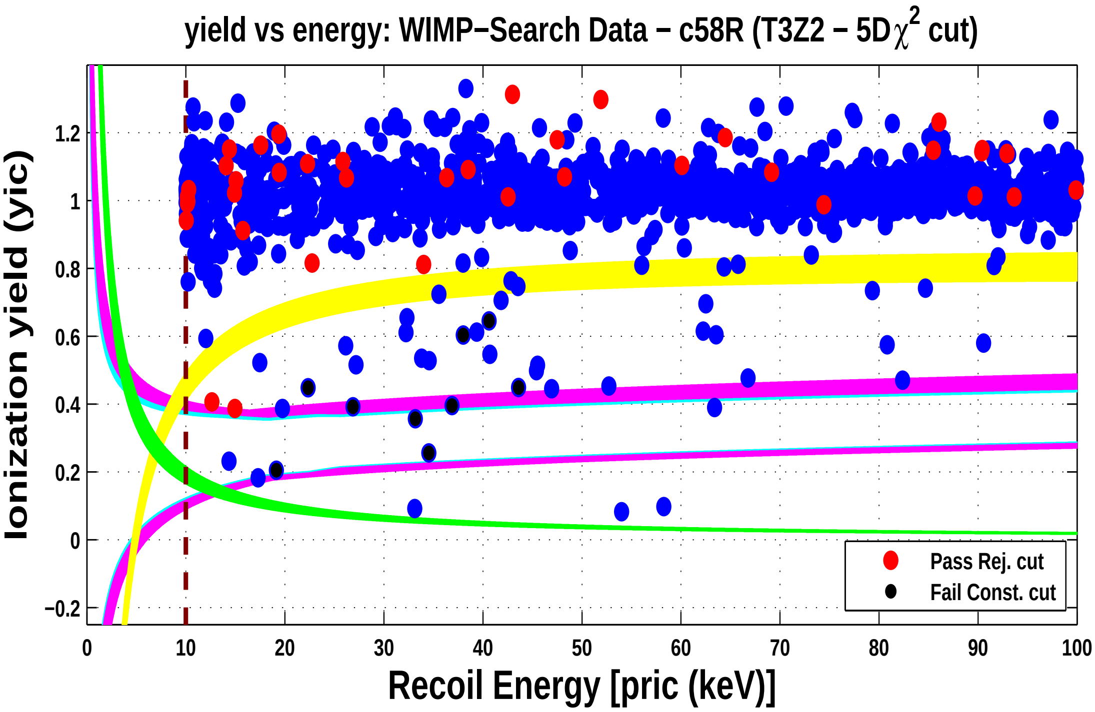

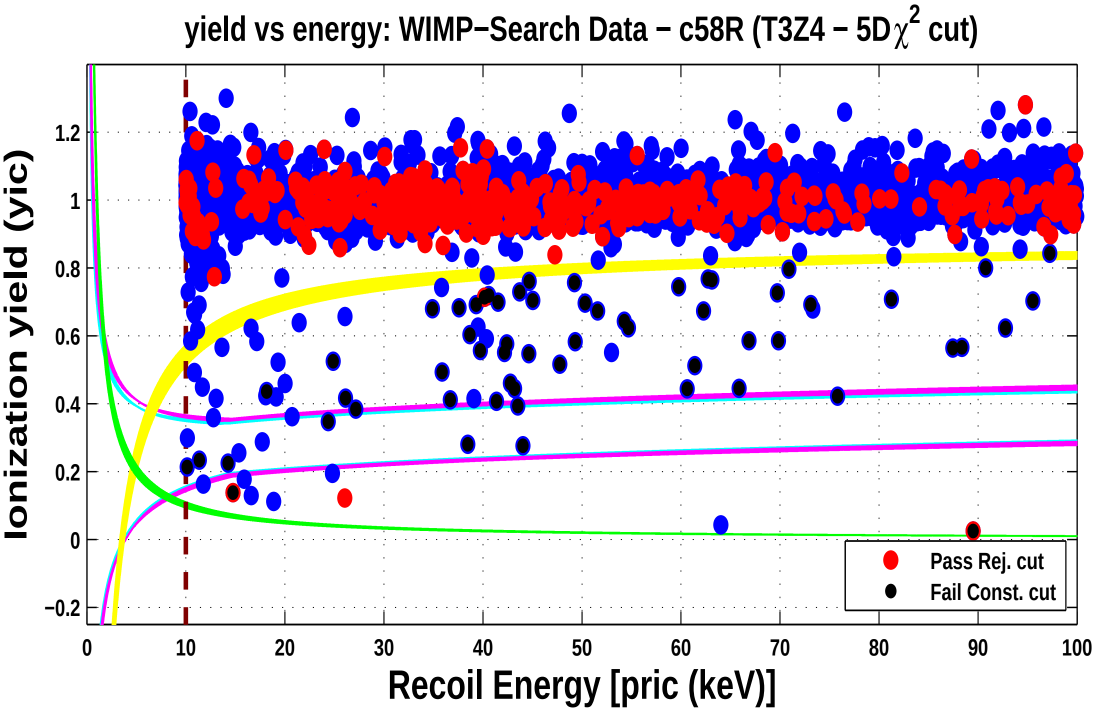

Figure E.10: Another version of ionization yield vs recoil energy showing the distribution of events in the WIMP-search (blue dots) for T3Z2 (top) and T3Z4 (bottom). The events shown in red dots are the events passing the rejection cuts above the 10 keV threshold while the black dots are events failing the consistency cut. The yellow curve show the region of space of events laying within 3σ below the mean of the electron-recoil band. The cyan and magenta curves indicate the tight and loose nuclear-recoil bands ($[l = -1.9; u = 1.8]$ and $[l = -2; u = 2]$, respectively), while the green circle with black face indicate the WIMP candidates identified by alternate timing-cut analyses.

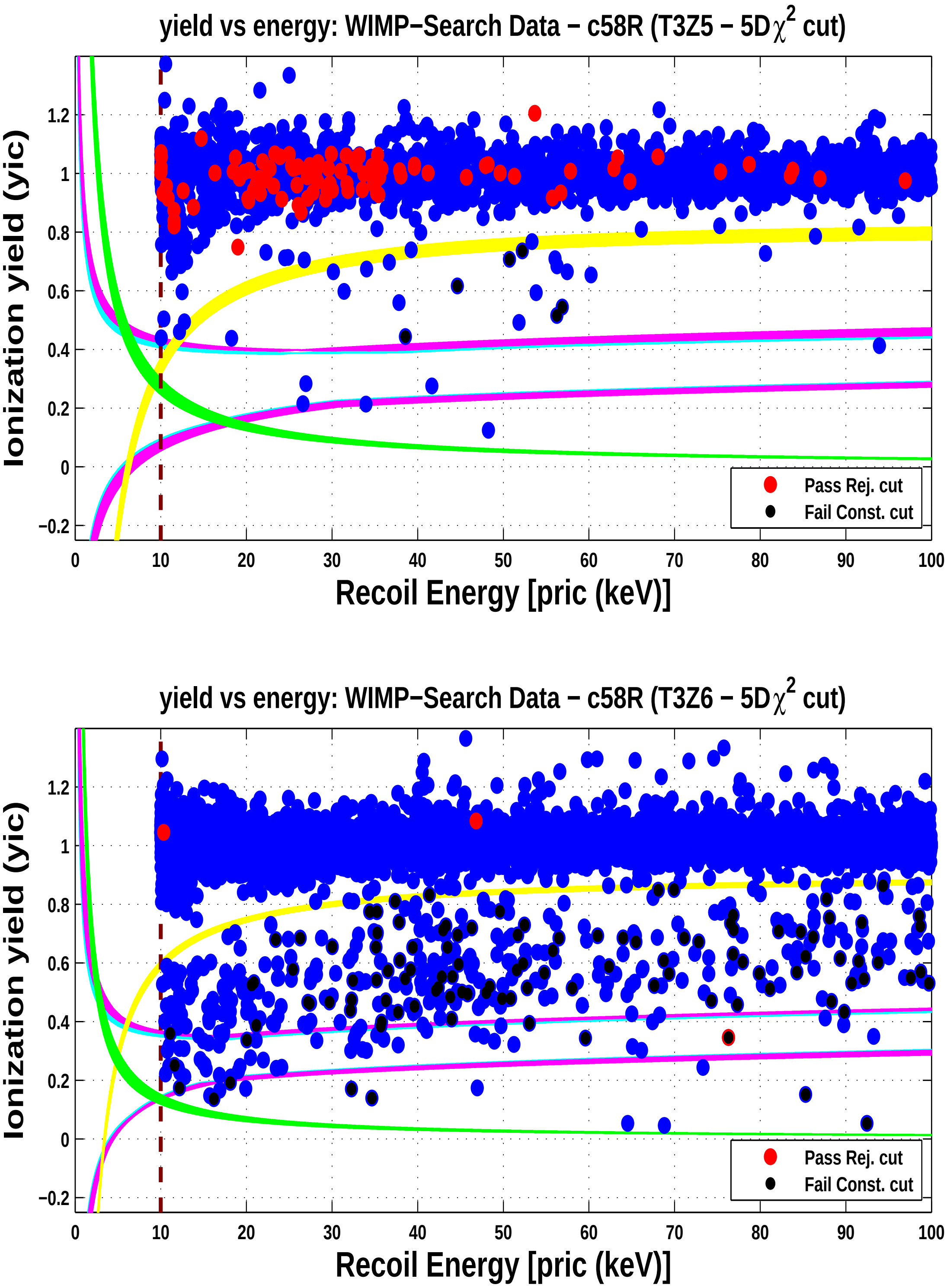

Figure E.11: Another version of ionization yield vs recoil energy showing the distribution of events in the WIMP-search (blue dots) for T3Z5 (top) and T3Z6 (bottom). The events shown in red dots are the events passing the rejection cuts above the 10 keV threshold while the black dots are events failing the consistency cut. The yellow curve show the region of space of events laying within 3σ below the mean of the electron-recoil band. The cyan and magenta curves indicate the tight and loose nuclear-recoil bands ($[l = -1.9; u = 1.8]$ and $[l = -2; u = 2]$, respectively), while the green circle with black face indicate the WIMP candidates identified by alternate timing-cut analyses.

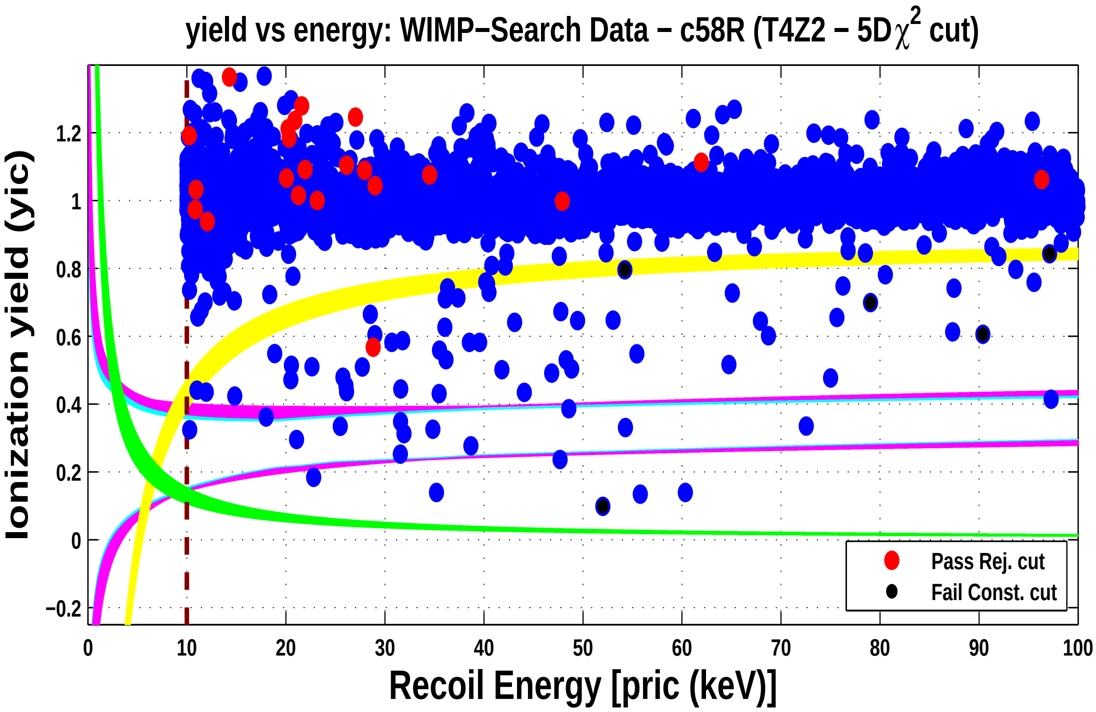

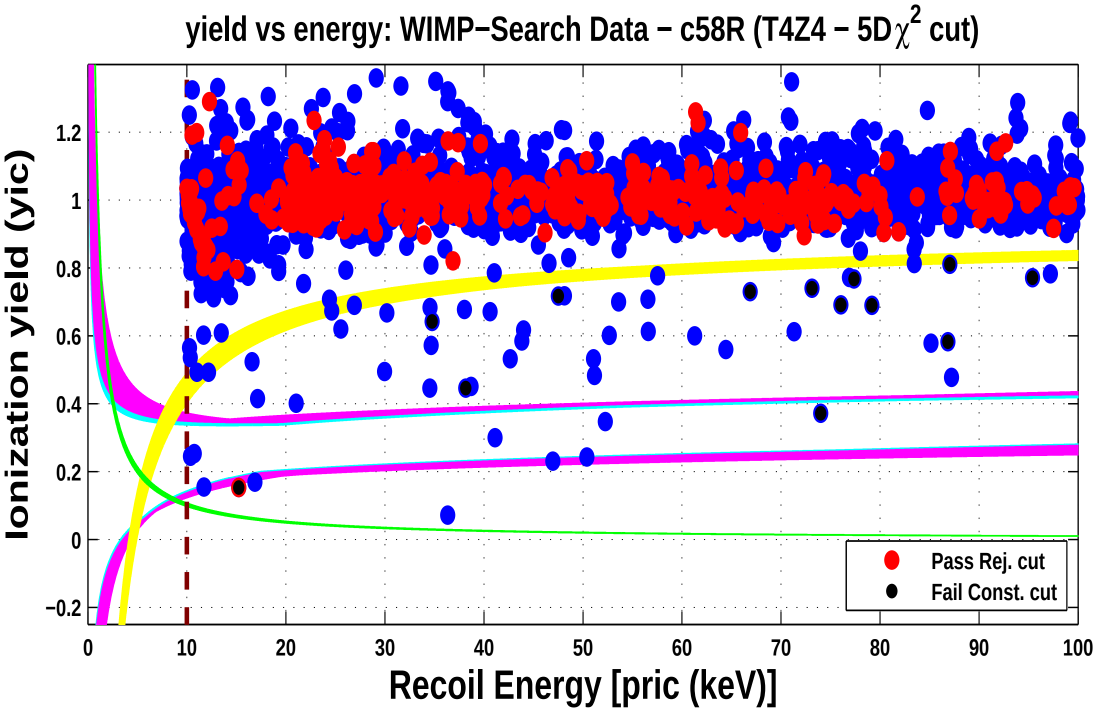

Figure E.12: Another version of ionization yield vs recoil energy showing the distribution of events in the WIMP-search (blue dots) for T4Z2 (top) and T4Z4 (bottom). The events shown in red dots are the events passing the rejection cuts above the 10 keV threshold while the black dots are events failing the consistency cut. The yellow curve show the region of space of events laying within 3σ below the mean of the electron-recoil band. The cyan and magenta curves indicate the tight and loose nuclear-recoil bands ($[l = -1.9; u = 1.8]$ and $[l = -2; u = 2]$, respectively), while the green circle with black face indicate the WIMP candidates identified by alternate timing-cut analyses.

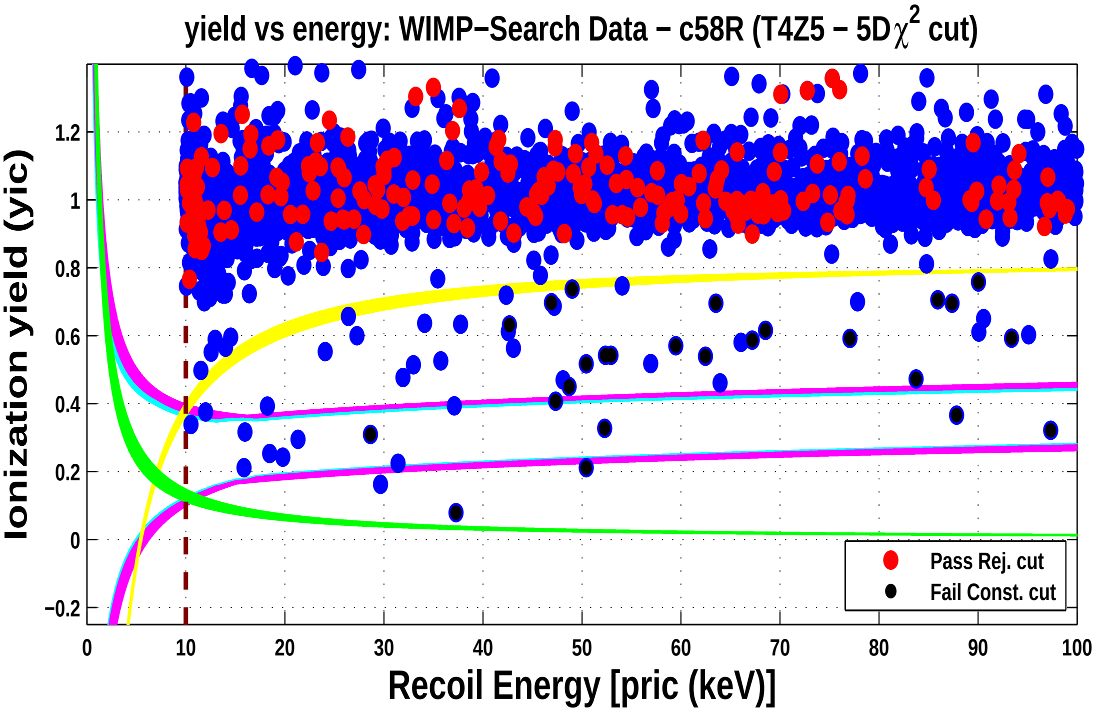

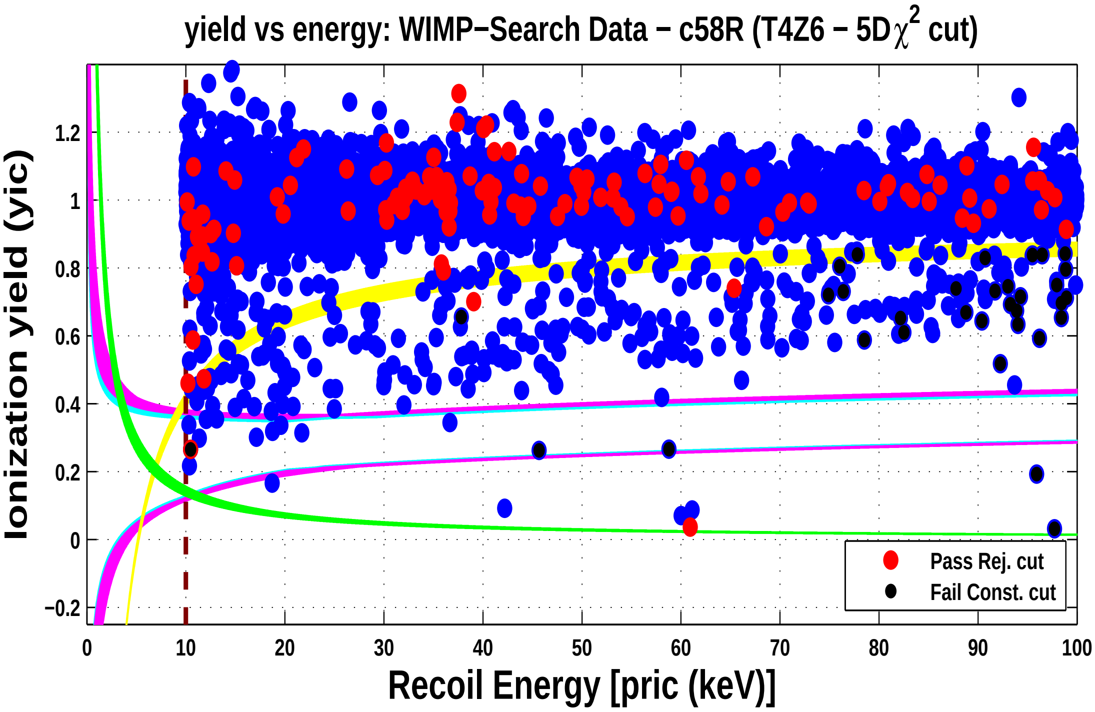

Figure E.13: Another version of ionization yield vs recoil energy showing the distribution of events in the WIMP-search (blue dots) for T4Z5 (top) and T4Z6 (bottom). The events shown in red dots are the events passing the rejection cuts above the 10 keV threshold while the black dots are events failing the consistency cut. The yellow curve show the region of space of events laying within 3σ below the mean of the electron-recoil band. The cyan and magenta curves indicate the tight and loose nuclear-recoil bands ($[l = -1.9; u = 1.8]$ and $[l = -2; u = 2]$, respectively), while the green circle with black face indicate the WIMP candidates identified by alternate timing-cut analyses.

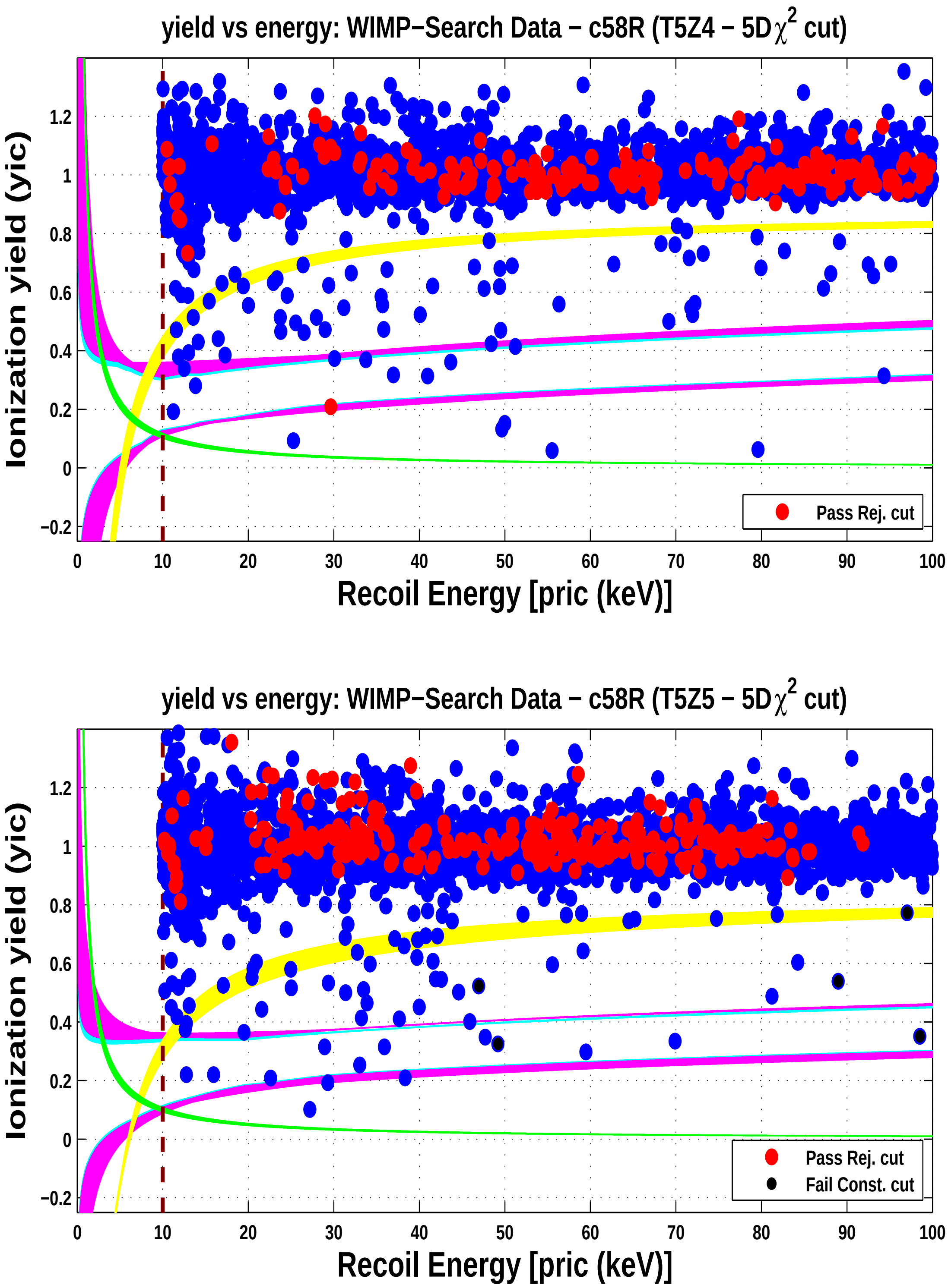

Figure E.14: Another version of ionization yield vs recoil energy showing the distribution of events in the WIMP-search (blue dots) for T5Z4 (top) and T5Z5 (bottom). The events shown in red dots are the events passing the rejection cuts above the 10 keV threshold while the black dots are events failing the consistency cut. The yellow curve show the region of space of events laying within 3σ below the mean of the electron-recoil band. The cyan and magenta curves indicate the tight and loose nuclear-recoil bands ($[l = -1.9; u = 1.8]$ and $[l = -2; u = 2]$, respectively), while the green circle with black face indicate the WIMP candidates identified by alternate timing-cut analyses.

Appendix F

SAE and leakage vs cut positions.

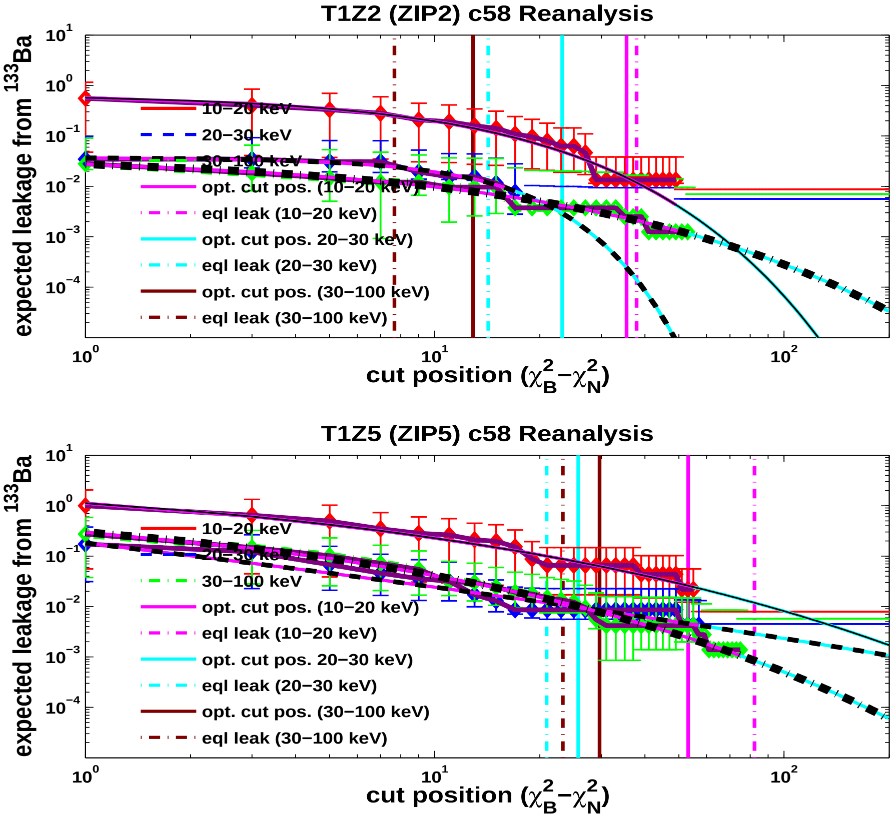

Figure F.1: The expected leakage as function of cut positions calculated from the ^{133}Ba calibration data for the c58 reanalysis for T1Z2 (top) and T1Z5 (bottom). The black solid lines represent fits to the data (shown in solid red for 10-20 keV, dashed blue for 20-30 keV and dotted green for 30-100 keV). The vertical magenta, cyan and dark red lines represents the optimal cut positions while the dashed magenta, dashed cyan and dashed dark red lines are the cut positions for equal leakage in the three energy bins respectively.

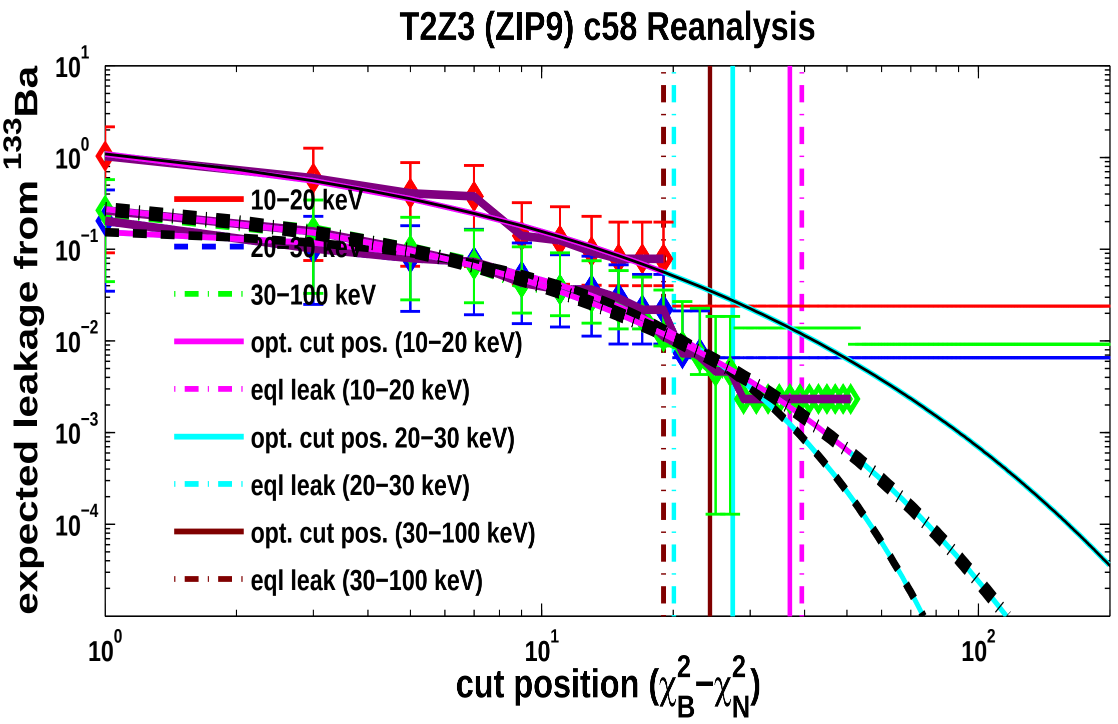

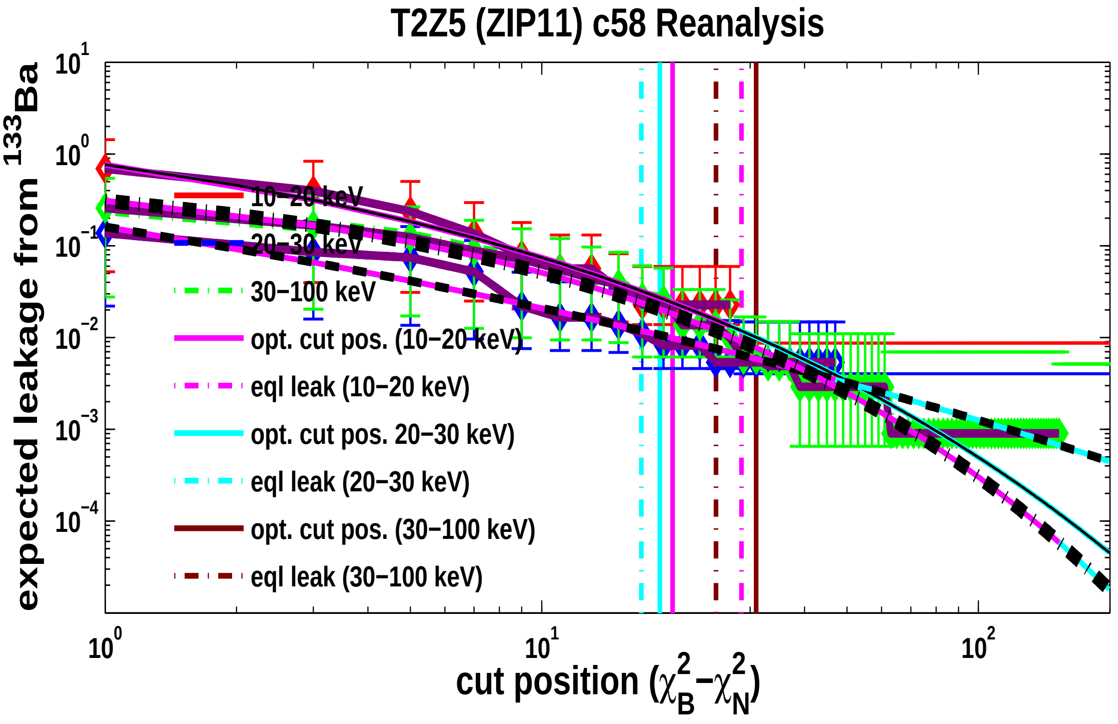

Figure F.2: The expected leakage as function of cut positions calculated from the ^{133}Ba calibration data for the c58 reanalysis for T2Z3 (top) and T2Z5 (bottom). The black solid lines represent fits to the data (shown in solid red for 10-20 keV, dashed blue for 20-30 keV and dotted green for 30-100 keV). The vertical magenta, cyan and dark red lines represents the optimal cut positions while the dashed magenta, dashed cyan and dashed dark red lines are the cut positions for equal leakage in the three energy bins respectively.

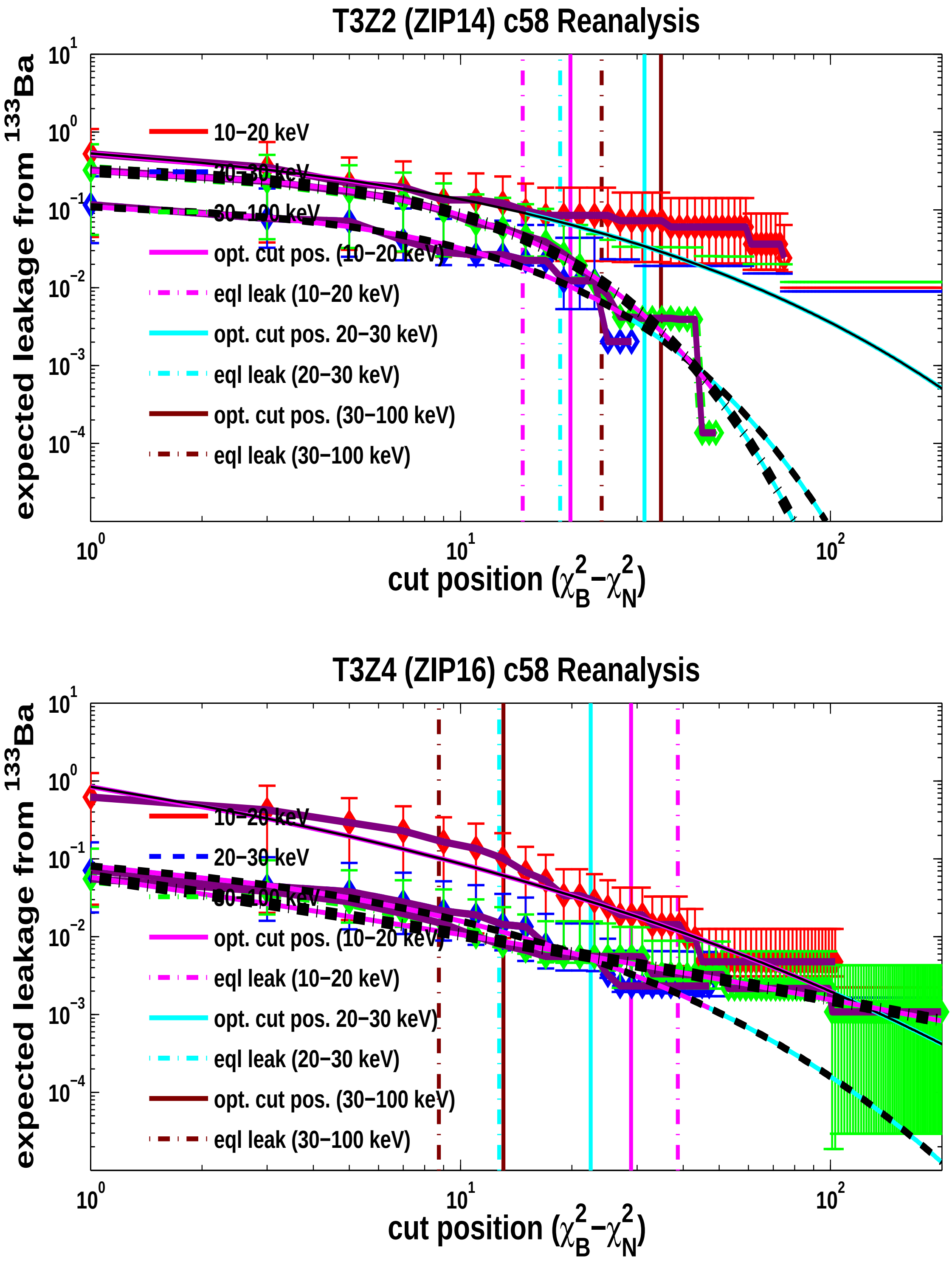

Figure F.3: The expected leakage as function of cut positions calculated from the ^{133}Ba calibration data for the c58 reanalysis for T3Z2 (top) and T3Z4 (bottom). The black solid lines represent fits to the data (shown in solid red for 10-20 keV, dashed blue for 20-30 keV and dotted green for 30-100 keV). The vertical magenta, cyan and dark red lines represents the optimal cut positions while the dashed magenta, dashed cyan and dashed dark red lines are the cut positions for equal leakage in the three energy bins respectively.

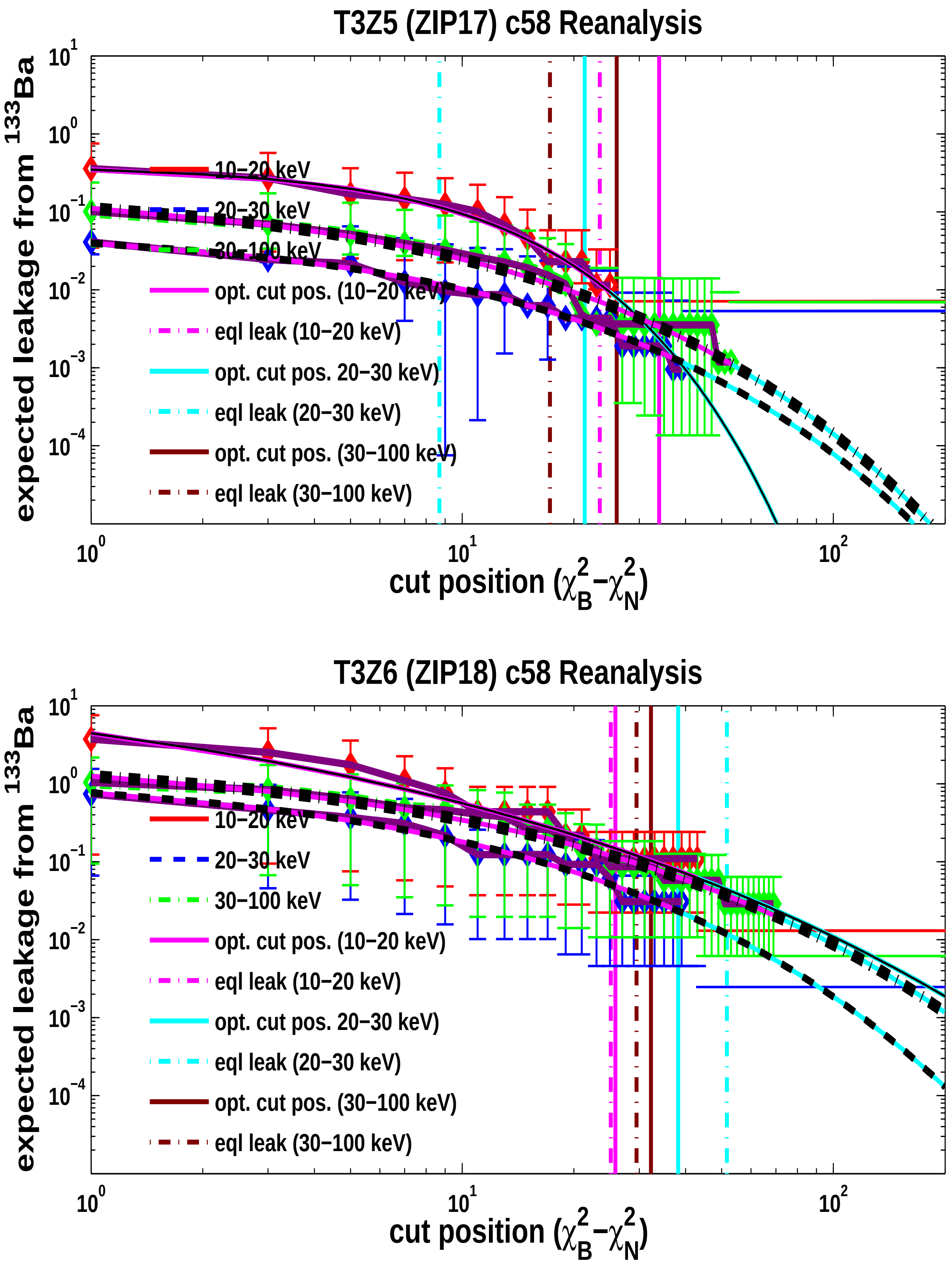

Figure F.4: The expected leakage as function of cut positions calculated from the ^{133}Ba calibration data for the c58 reanalysis for T3Z5 (top) and T3Z6 (bottom). The black solid lines represent fits to the data (shown in solid red for 10-20 keV, dashed blue for 20-30 keV and dotted green for 30-100 keV). The vertical magenta, cyan and dark red lines represents the optimal cut positions while the dashed magenta, dashed cyan and dashed dark red lines are the cut positions for equal leakage in the three energy bins respectively.

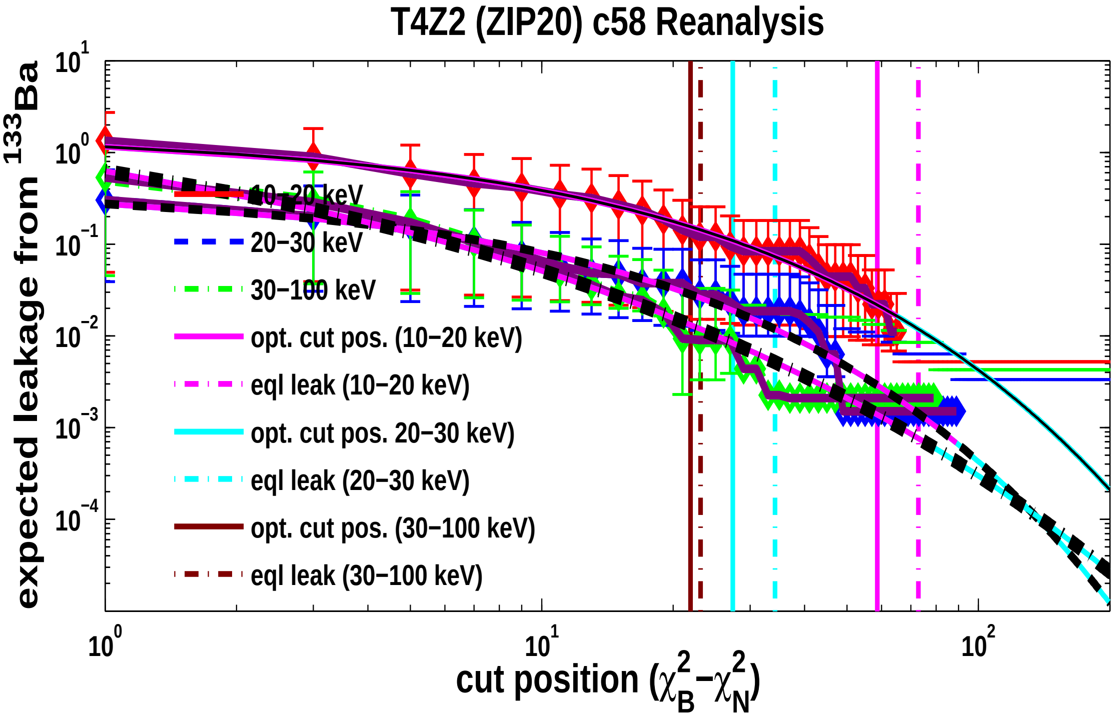

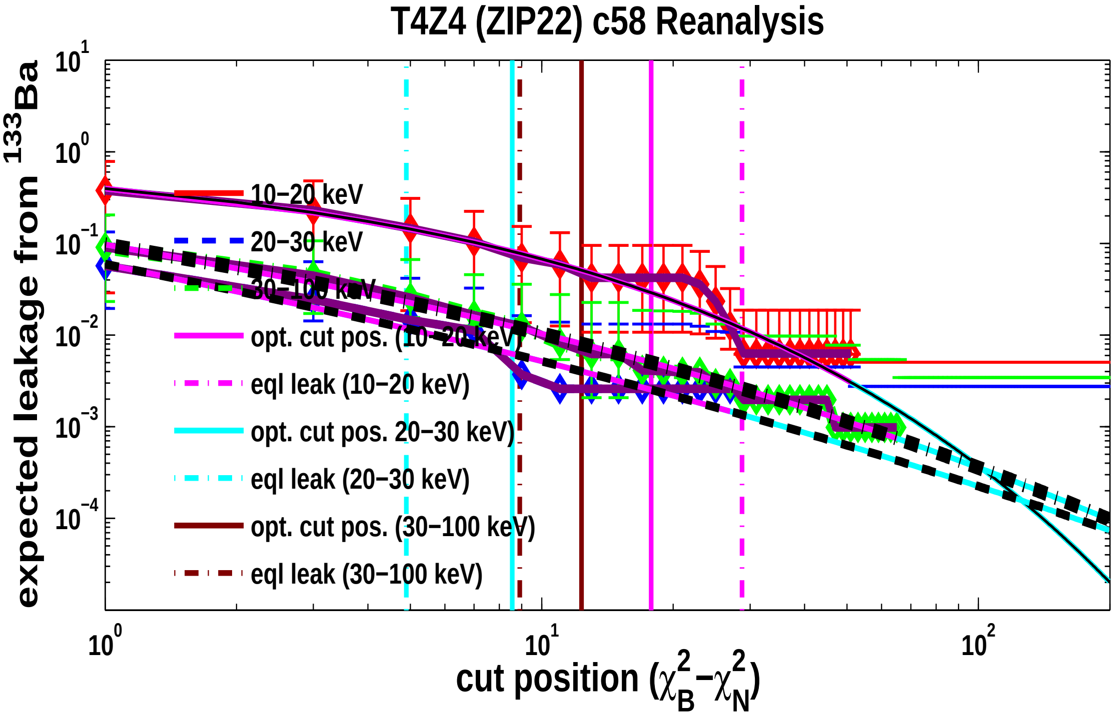

Figure F.5: The expected leakage as function of cut positions calculated from the ^{133}Ba calibration data for the c58 reanalysis for T4Z2 (top) and T4Z4 (bottom). The black solid lines represent fits to the data (shown in solid red for 10-20 keV, dashed blue for 20-30 keV and dotted green for 30-100 keV). The vertical magenta, cyan and dark red lines represents the optimal cut positions while the dashed magenta, dashed cyan and dashed dark red lines are the cut positions for equal leakage in the three energy bins respectively.

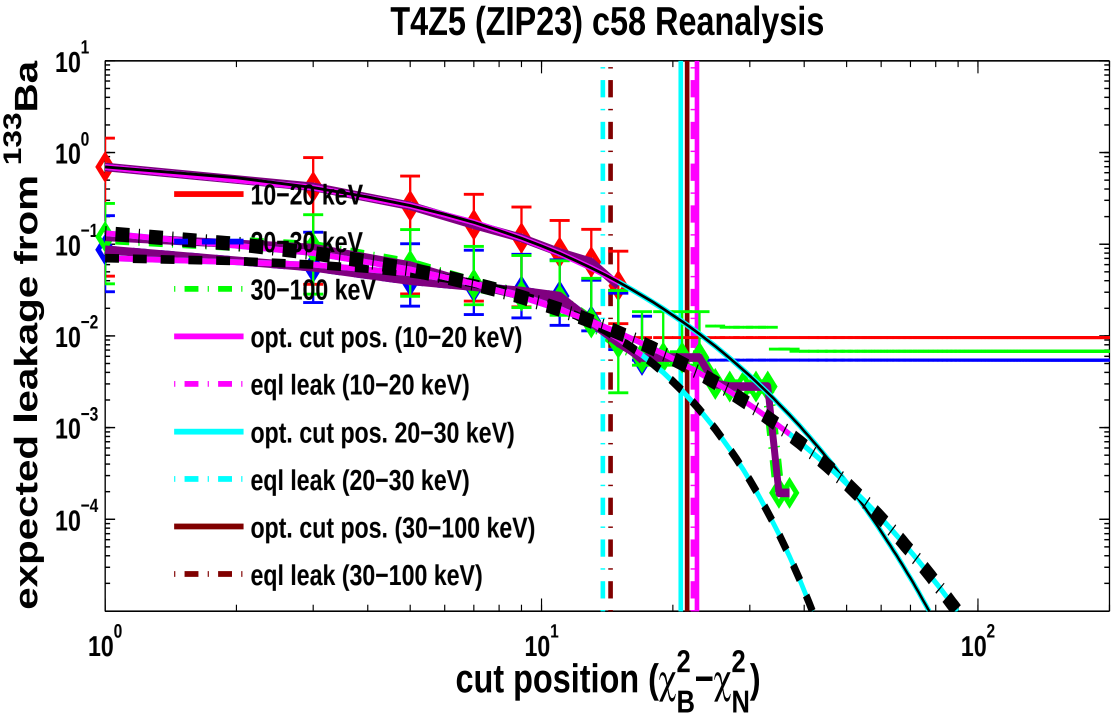

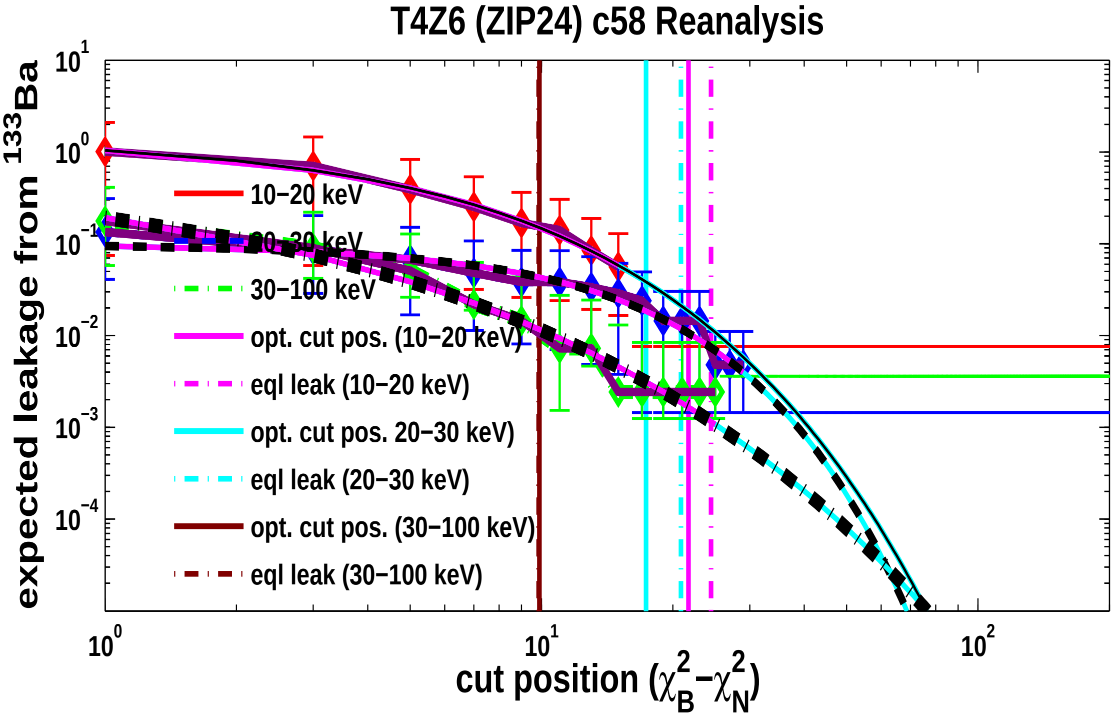

Figure F.6: The expected leakage as function of cut positions calculated from the ^{133}Ba calibration data for the c58 reanalysis for T4Z5 (top) and T4Z6 (bottom). The black solid lines represent fits to the data (shown in solid red for 10-20 keV, dashed blue for 20-30 keV and dotted green for 30-100 keV). The vertical magenta, cyan and dark red lines represents the optimal cut positions while the dashed magenta, dashed cyan and dashed dark red lines are the cut positions for equal leakage in the three energy bins respectively.

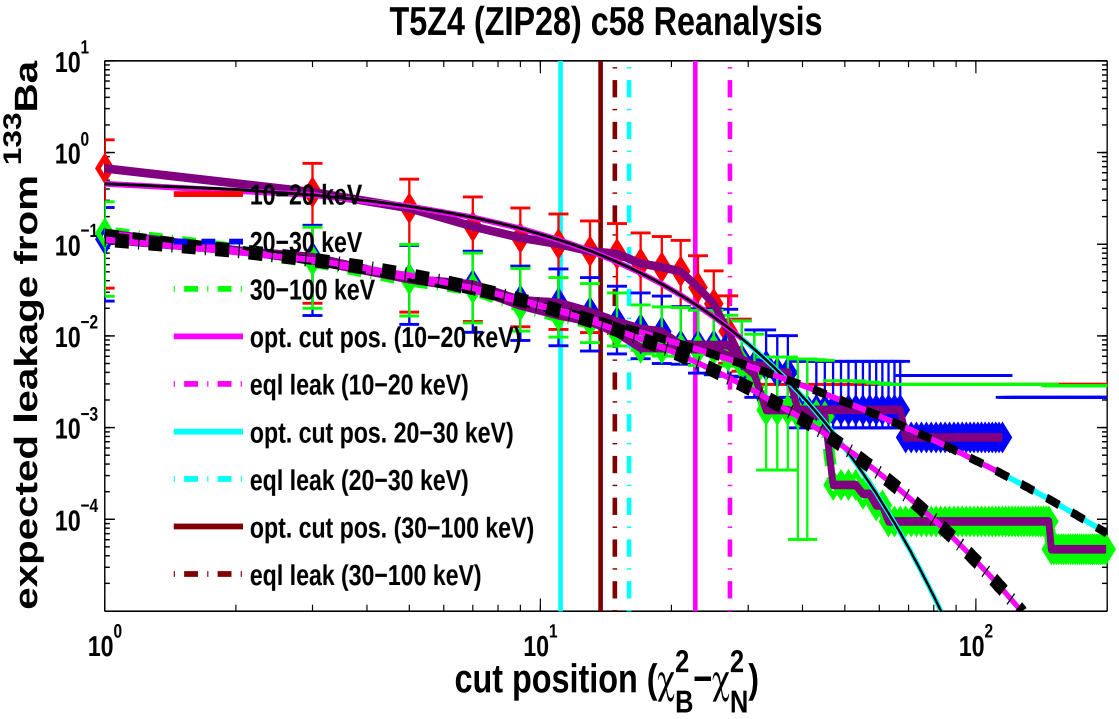

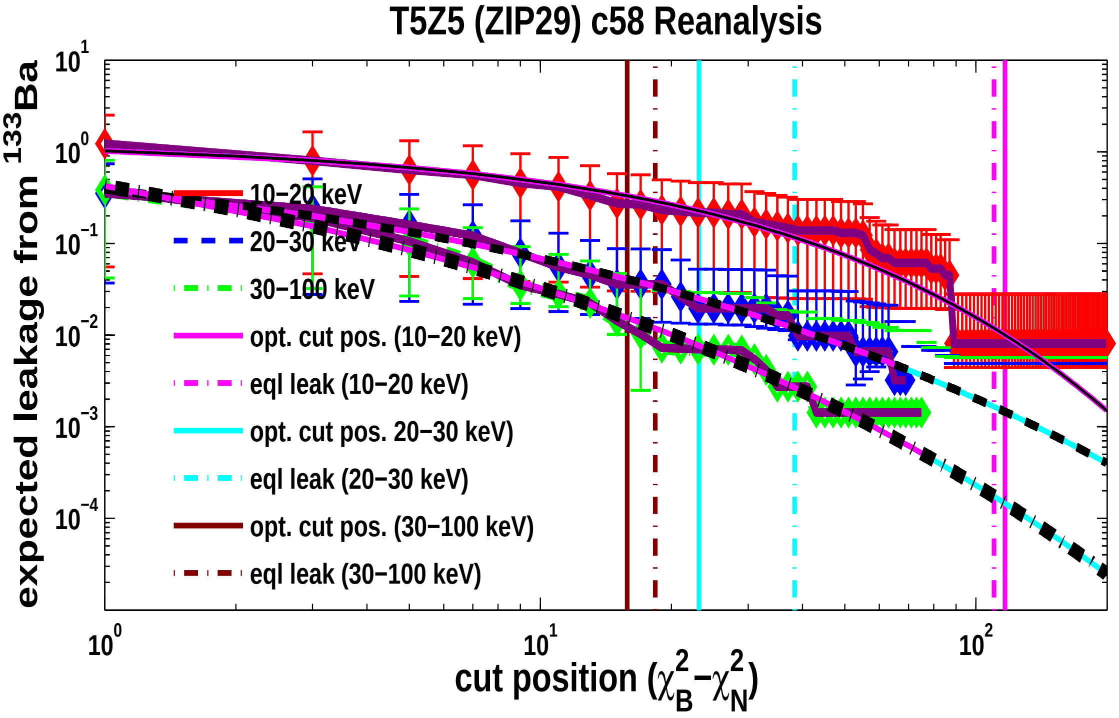

Figure F.7: The expected leakage as function of cut positions calculated from the ^{133}Ba calibration data for the c58 reanalysis for T5Z4 (top) and T5Z5 (bottom). The black solid lines represent fits to the data (shown in solid red for 10-20 keV, dashed blue for 20-30 keV and dotted green for 30-100 keV). The vertical magenta, cyan and dark red lines represents the optimal cut positions while the dashed magenta, dashed cyan and dashed dark red lines are the cut positions for equal leakage in the three energy bins respectively.

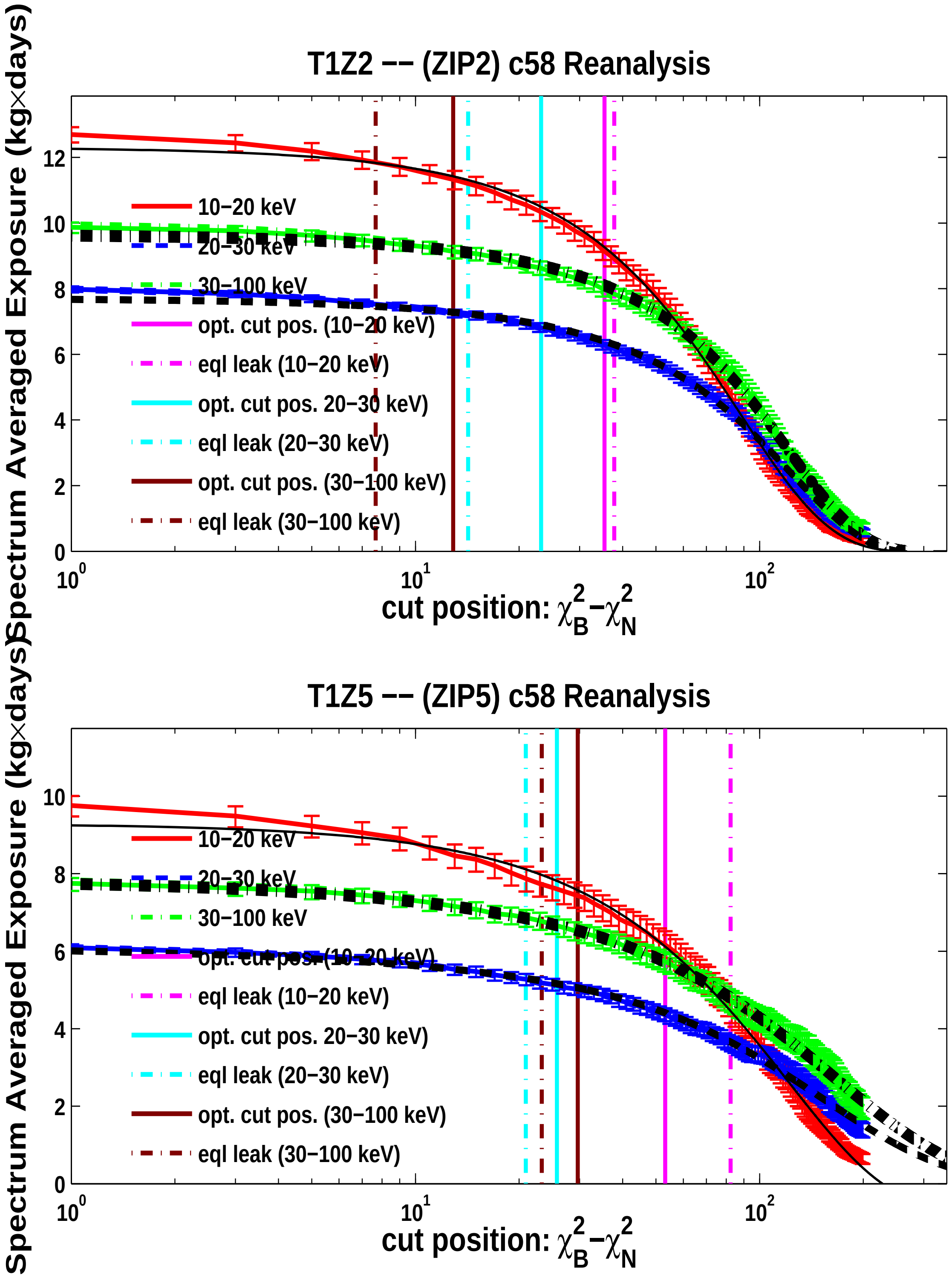

Figure F.8: The spectrum-averaged exposure as functions of cut positions calculated from the ^{252}Cf calibration data for the c58 reanalysis for T1Z2 and T1Z5. The black lines represent the fits to the data (shown in solid red for $10-20$ keV, dashed blue for $20-30$ keV and dotted green for $30-100$ keV). The vertical magenta, cyan and dark red lines represents the optimal cut positions while the dashed magenta, dashed cyan and dashed dark red lines are the cut positions for equal leakage in the three energy bins respectively.

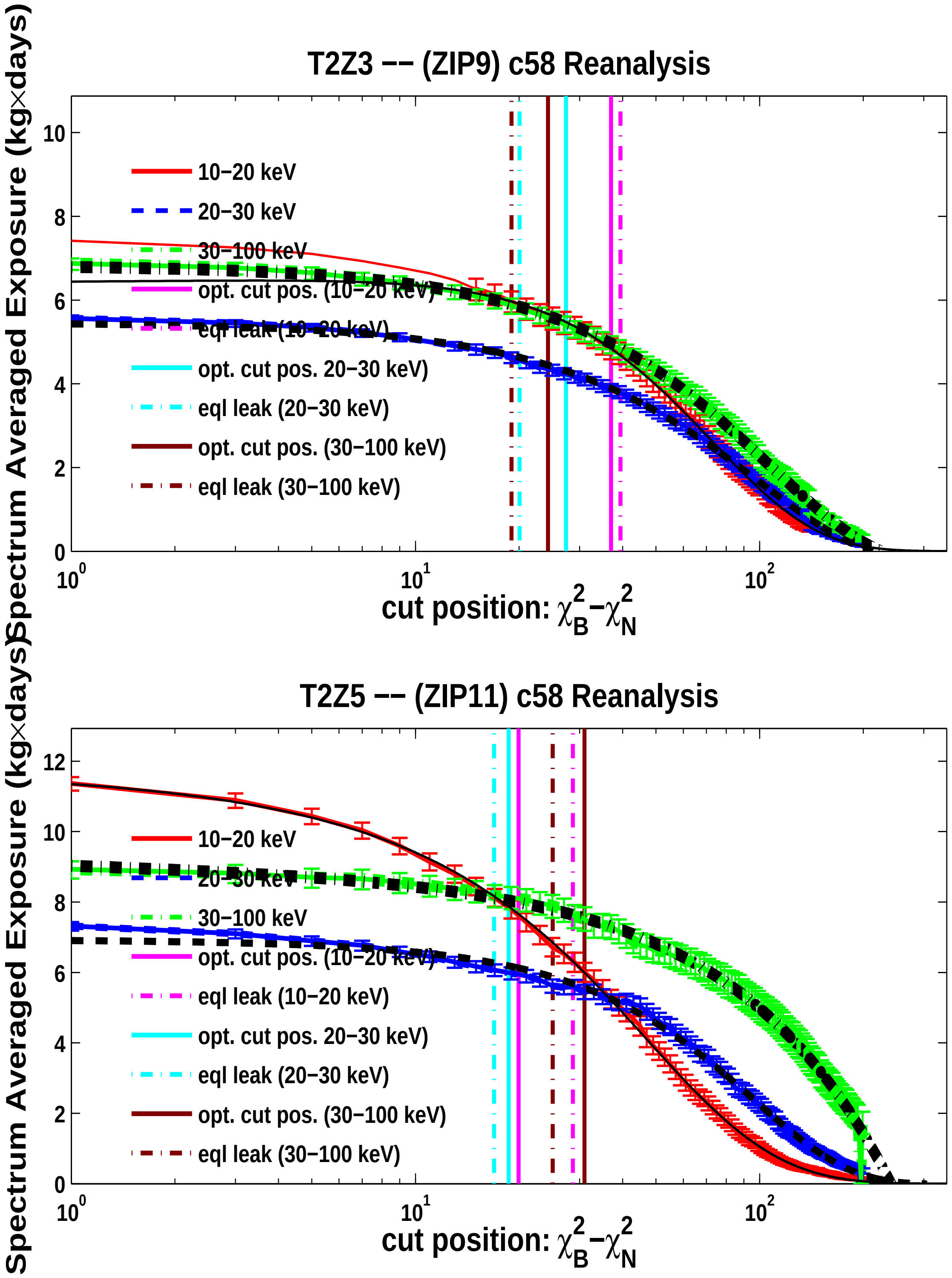

Figure F.9: The spectrum-averaged exposure as functions of cut positions calculated from the ^{252}Cf calibration data for the c58 reanalysis for T2Z3 and T2Z5. The black lines represent the fits to the data (shown in solid red for $10-20$ keV, dashed blue for $20-30$ keV and dotted green for $30-100$ keV). The vertical magenta, cyan and dark red lines represents the optimal cut positions while the dashed magenta, dashed cyan and dashed dark red lines are the cut positions for equal leakage in the three energy bins respectively.

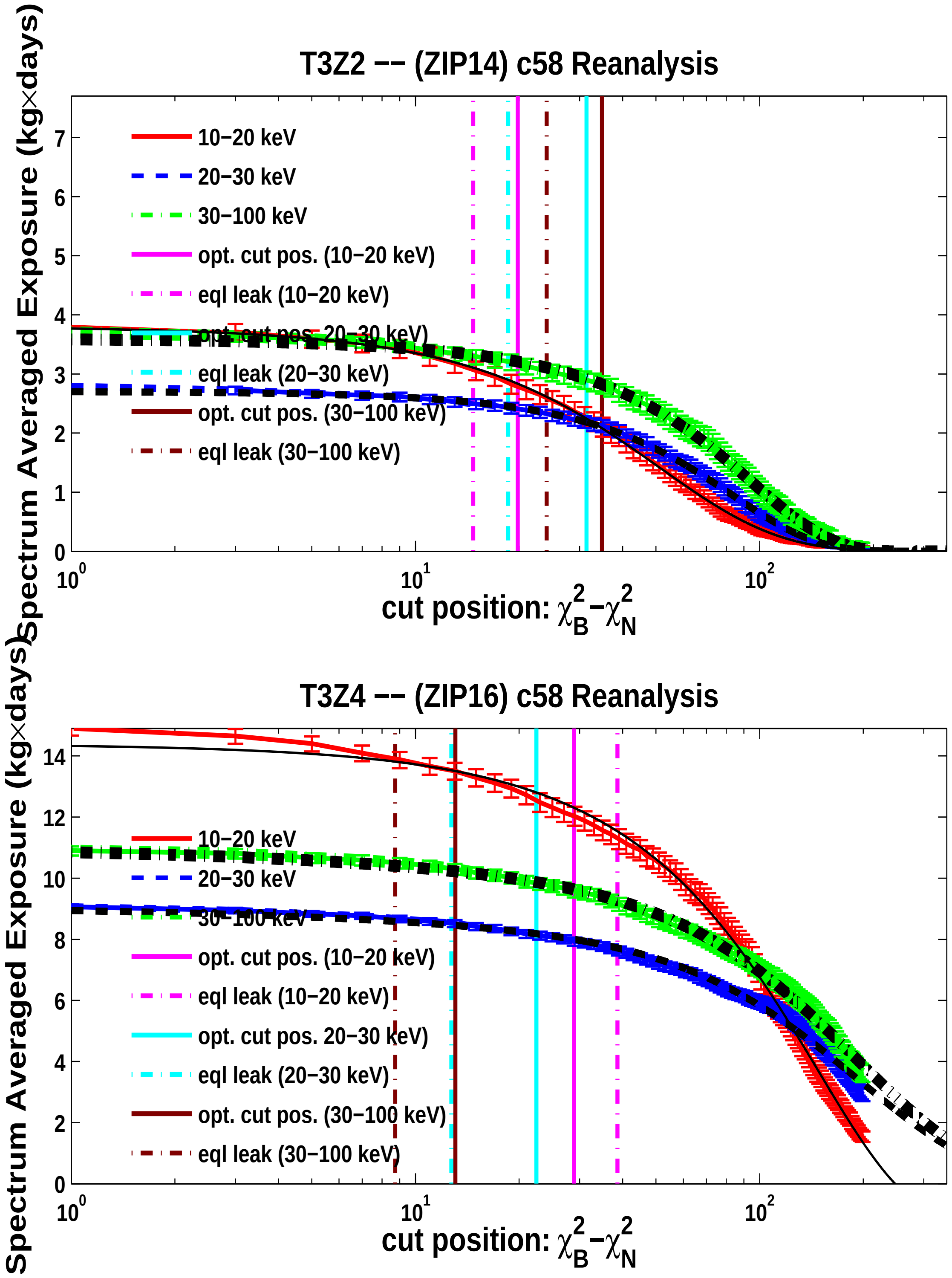

Figure F.10: The spectrum-averaged exposure as functions of cut positions calculated from the ^{252}Cf calibration data for the c58 reanalysis for T3Z2 and T3Z4. The black lines represent the fits to the data (shown in solid red for $10-20$ keV, dashed blue for $20-30$ keV and dotted green for $30-100$ keV). The vertical magenta, cyan and dark red lines represents the optimal cut positions while the dashed magenta, dashed cyan and dashed dark red lines are the cut positions for equal leakage in the three energy bins respectively.

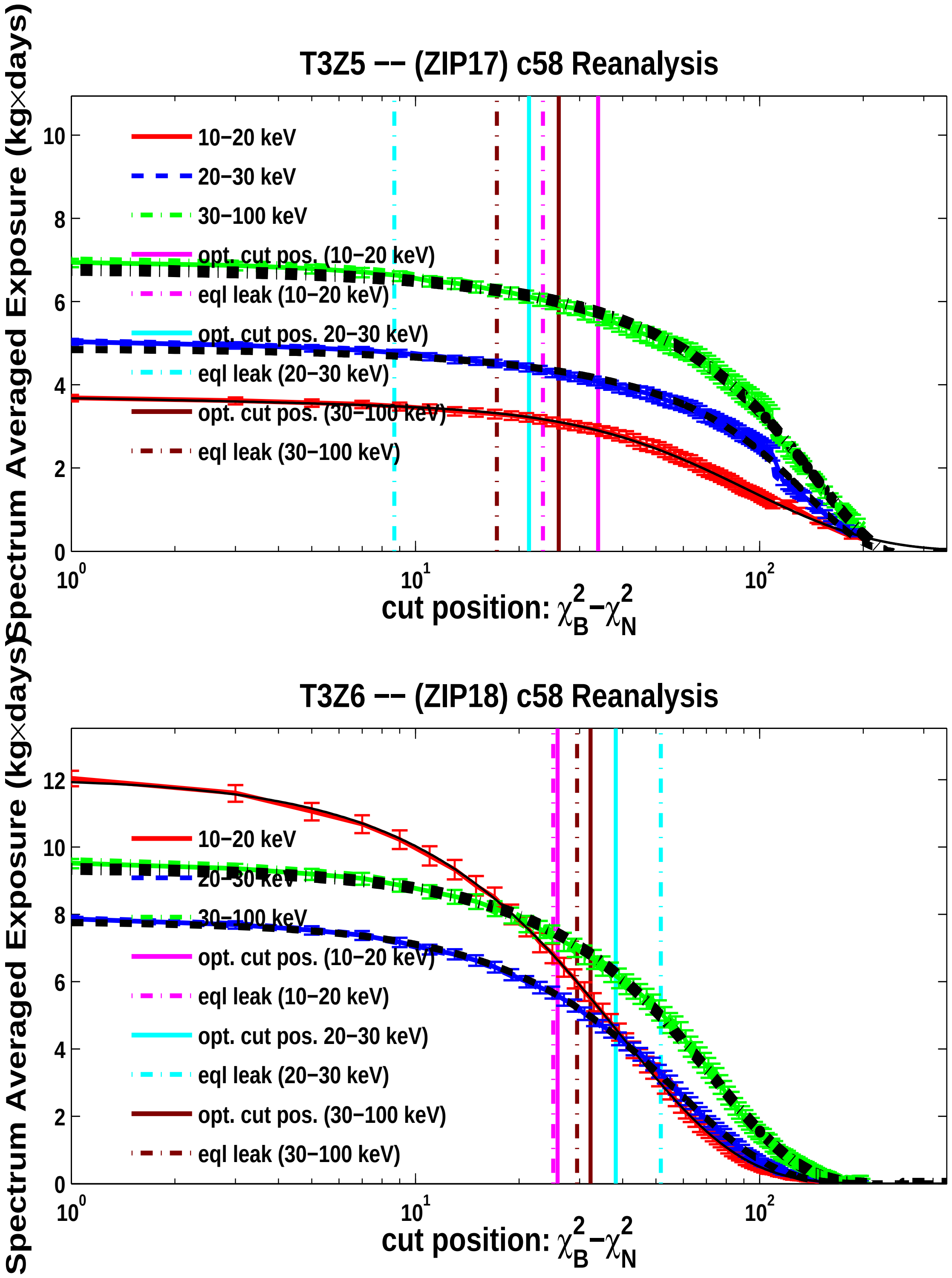

Figure F.11: The spectrum-averaged exposure as functions of cut positions calculated from the ^{252}Cf calibration data for the c58 reanalysis for T3Z5 and T3Z6. The black lines represent the fits to the data (shown in solid red for $10-20$ keV, dashed blue for $20-30$ keV and dotted green for $30-100$ keV). The vertical magenta, cyan and dark red lines represents the optimal cut positions while the dashed magenta, dashed cyan and dashed dark red lines are the cut positions for equal leakage in the three energy bins respectively.

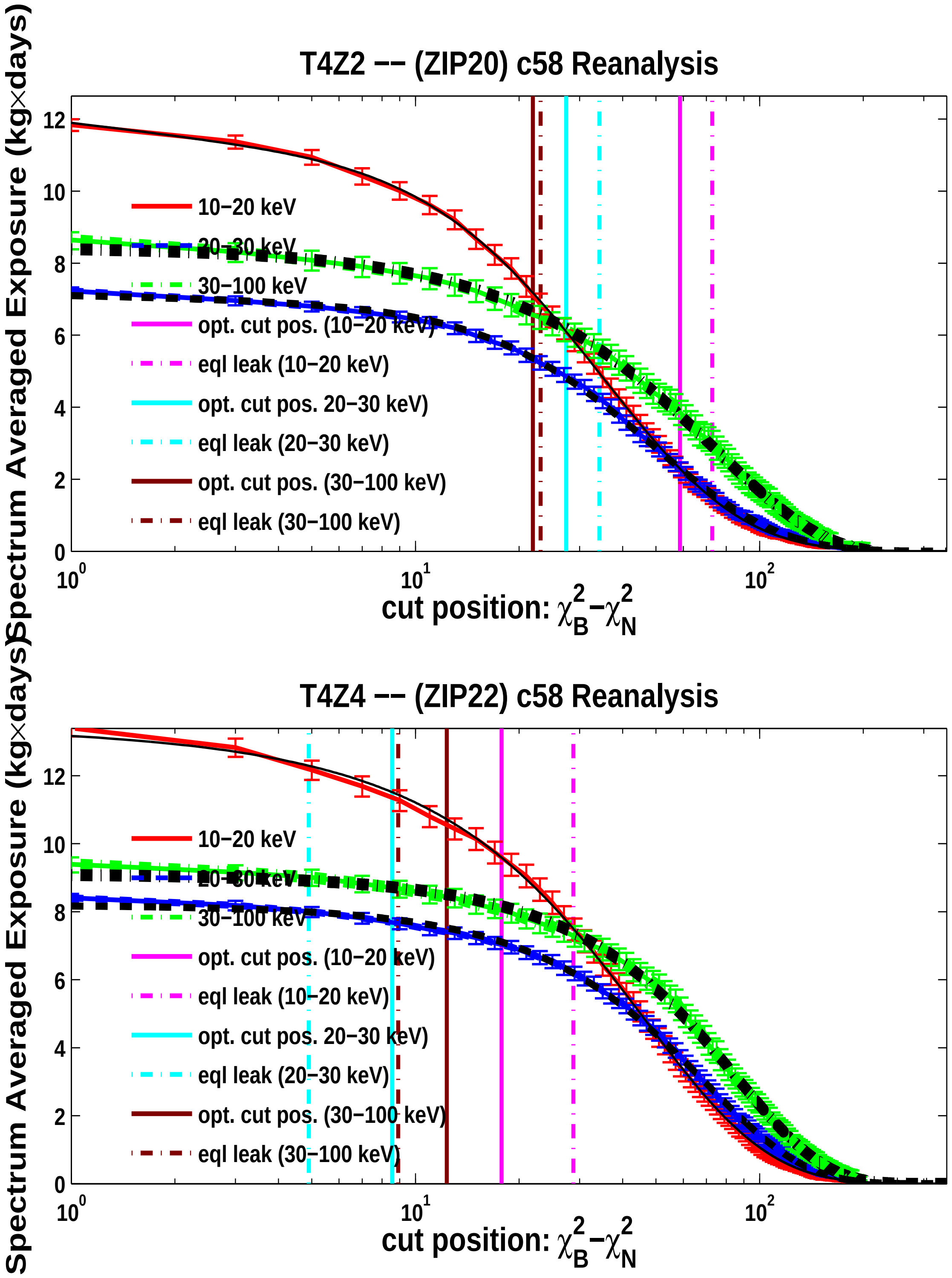

Figure F.12: The spectrum-averaged exposure as functions of cut positions calculated from the ^{252}Cf calibration data for the c58 reanalysis for T4Z2 and T4Z4. The black lines represent the fits to the data (shown in solid red for $10-20$ keV, dashed blue for $20-30$ keV and dotted green for $30-100$ keV). The vertical magenta, cyan and dark red lines represents the optimal cut positions while the dashed magenta, dashed cyan and dashed dark red lines are the cut positions for equal leakage in the three energy bins respectively.

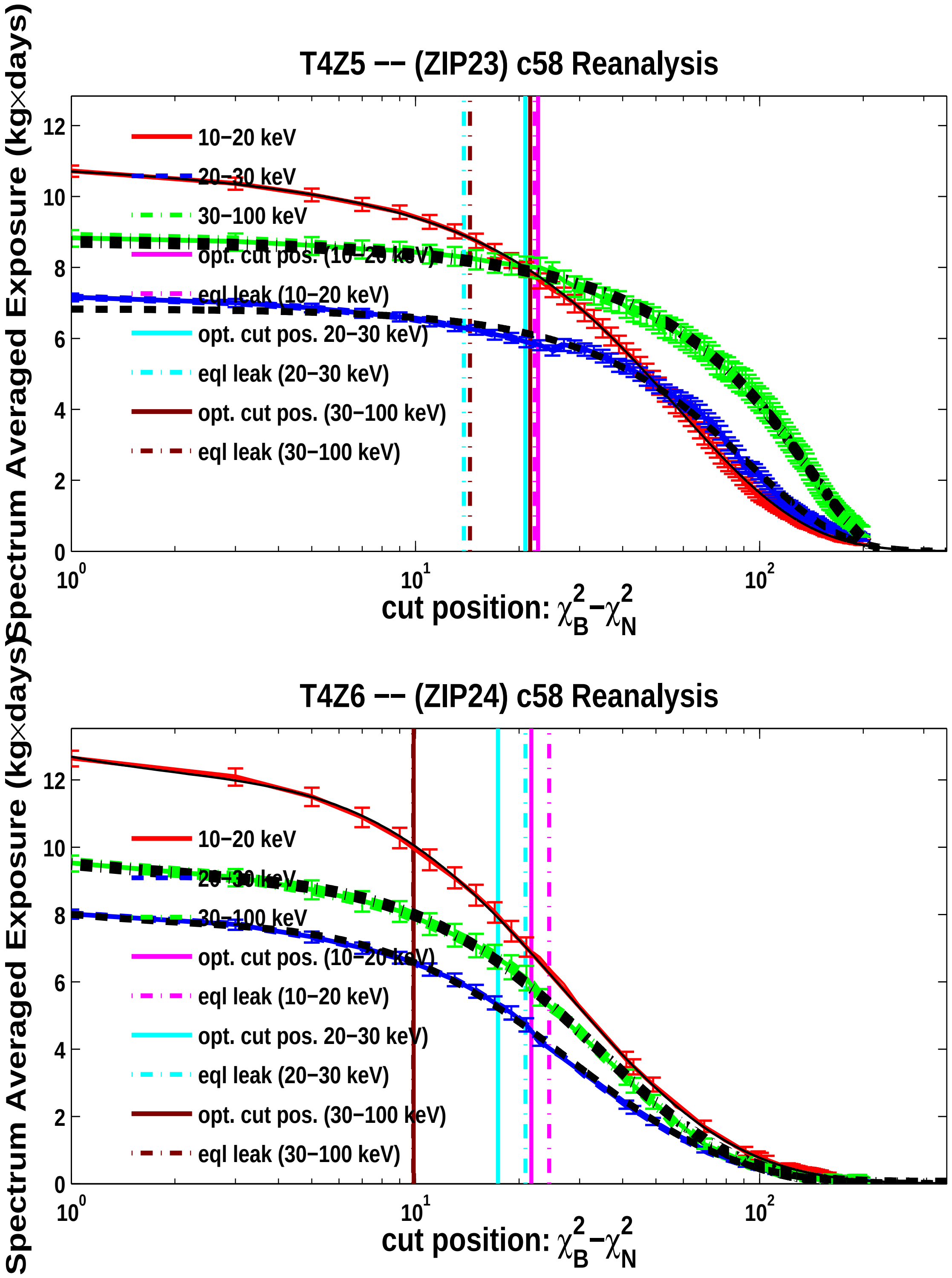

Figure F.13: The spectrum-averaged exposure as functions of cut positions calculated from the ^{252}Cf calibration data for the c58 reanalysis for T4Z5 and T4Z6. The black lines represent the fits to the data (shown in solid red for $10-20$ keV, dashed blue for $20-30$ keV and dotted green for $30-100$ keV). The vertical magenta, cyan and dark red lines represents the optimal cut positions while the dashed magenta, dashed cyan and dashed dark red lines are the cut positions for equal leakage in the three energy bins respectively.

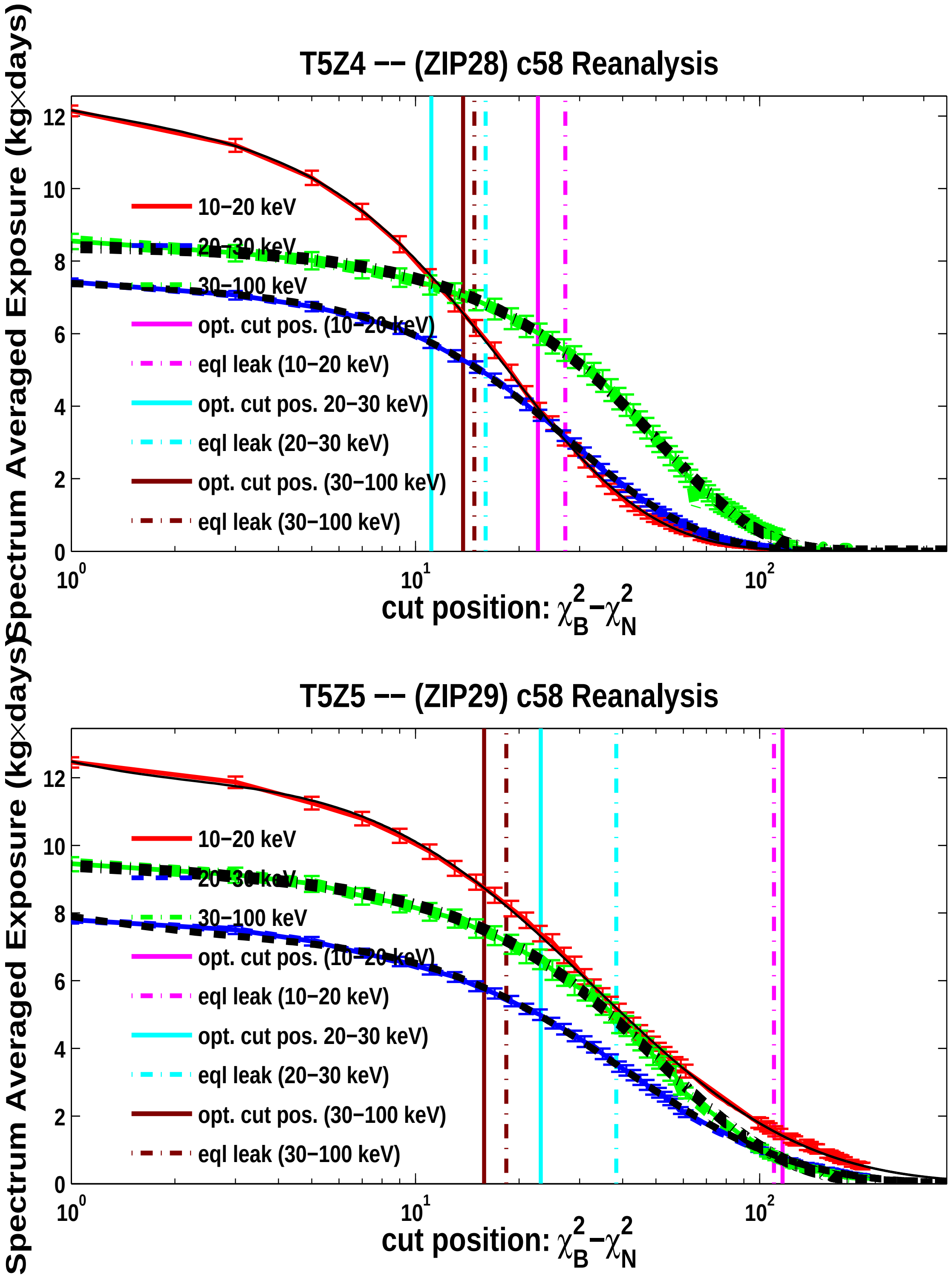

Figure F.14: The spectrum-averaged exposure as functions of cut positions calculated from the ^{252}Cf calibration data for the c58 reanalysis for T5Z4 and T5Z5. The black lines represent the fits to the data (shown in solid red for $10-20$ keV, dashed blue for $20-30$ keV and dotted green for $30-100$ keV). The vertical magenta, cyan and dark red lines represents the optimal cut positions while the dashed magenta, dashed cyan and dashed dark red lines are the cut positions for equal leakage in the three energy bins respectively.

Appendix G

Overall efficiencies vs energy.

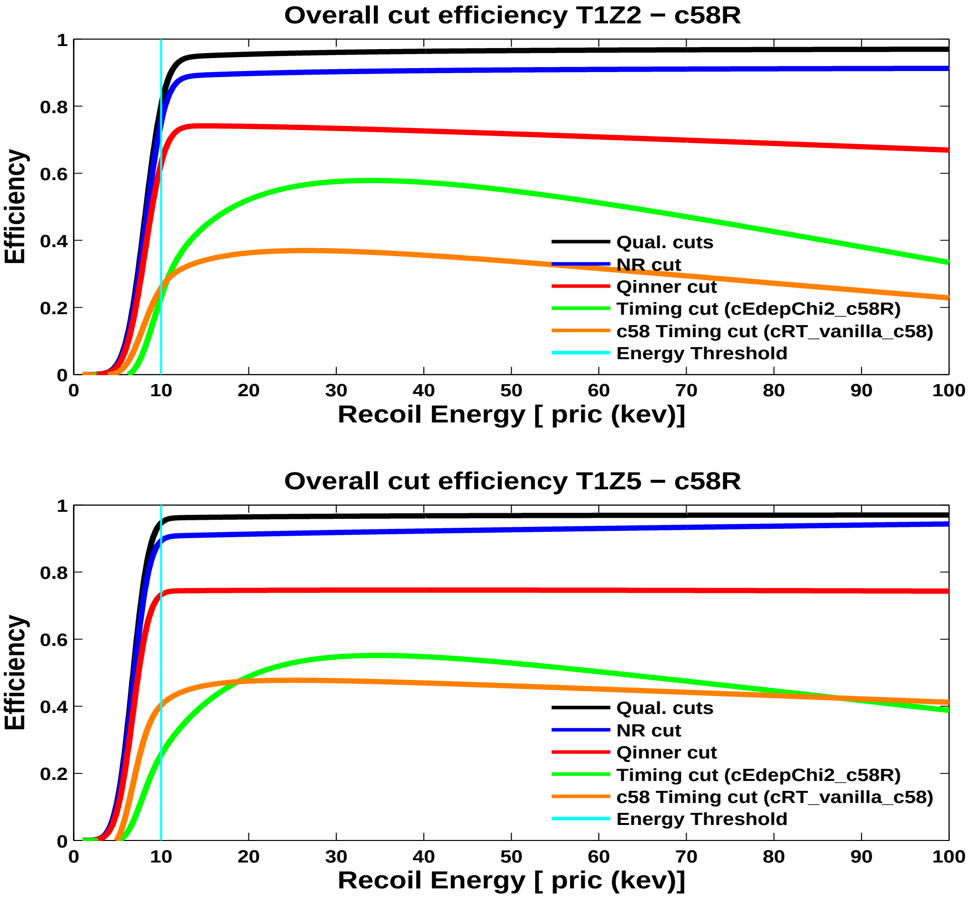

Figure G.1: Timing cut efficiencies for T1Z2 (top) and T1Z5 (bottom). Shown in black is the efficiency all the basic data-quality cuts, the blue curve shows the nuclear recoil efficiency, in red is shown the the fiducial-volume cut efficiency and in green is plotted the efficiency of the χ^2 optimized timing cut analysis. Shown in color orange, is the c58 analysis timing cut efficiency.

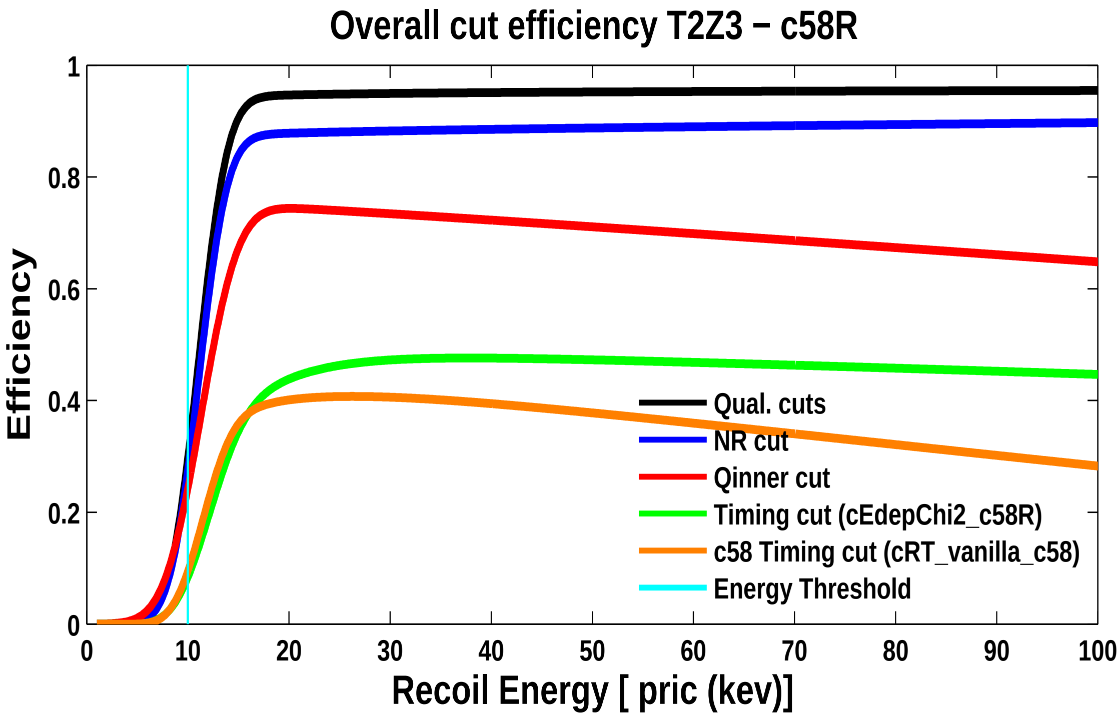

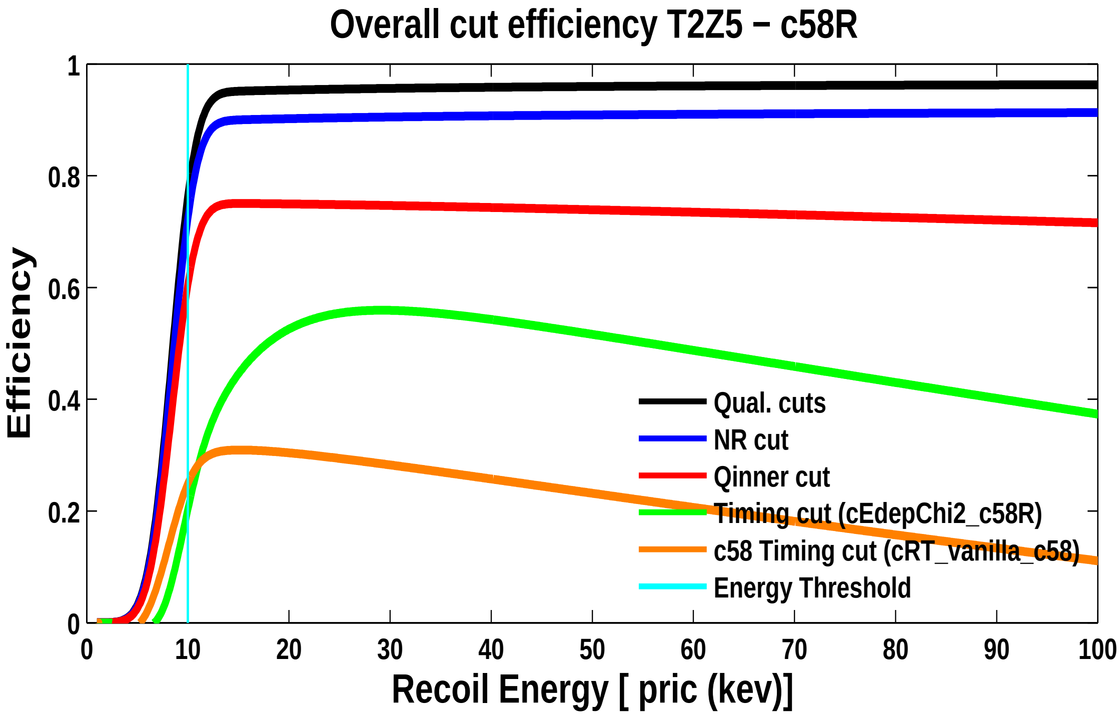

Figure G.2: Timing cut efficiencies for T2Z3 (top) and T2Z5 (bottom). Shown in black is the efficiency all the basic data-quality cuts, the blue curve shows the nuclear recoil efficiency, in red is shown the the fiducial-volume cut efficiency and in green is plotted the efficiency of the χ^2 optimized timing cut analysis. Shown in color orange, is the c58 analysis timing cut efficiency.

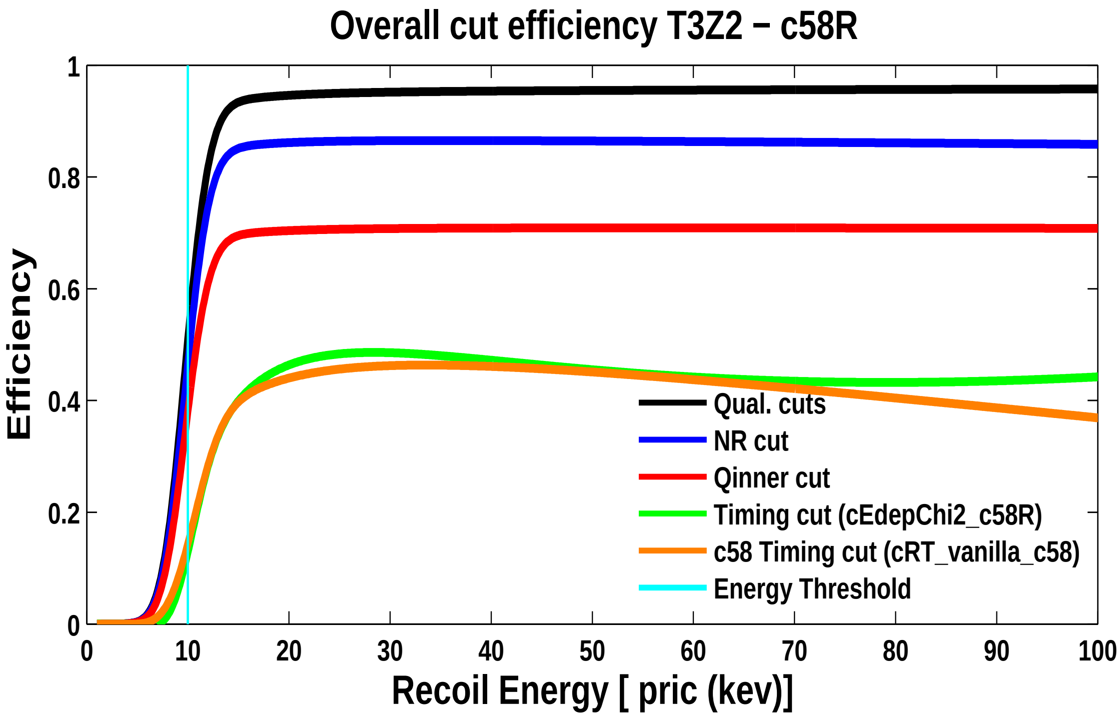

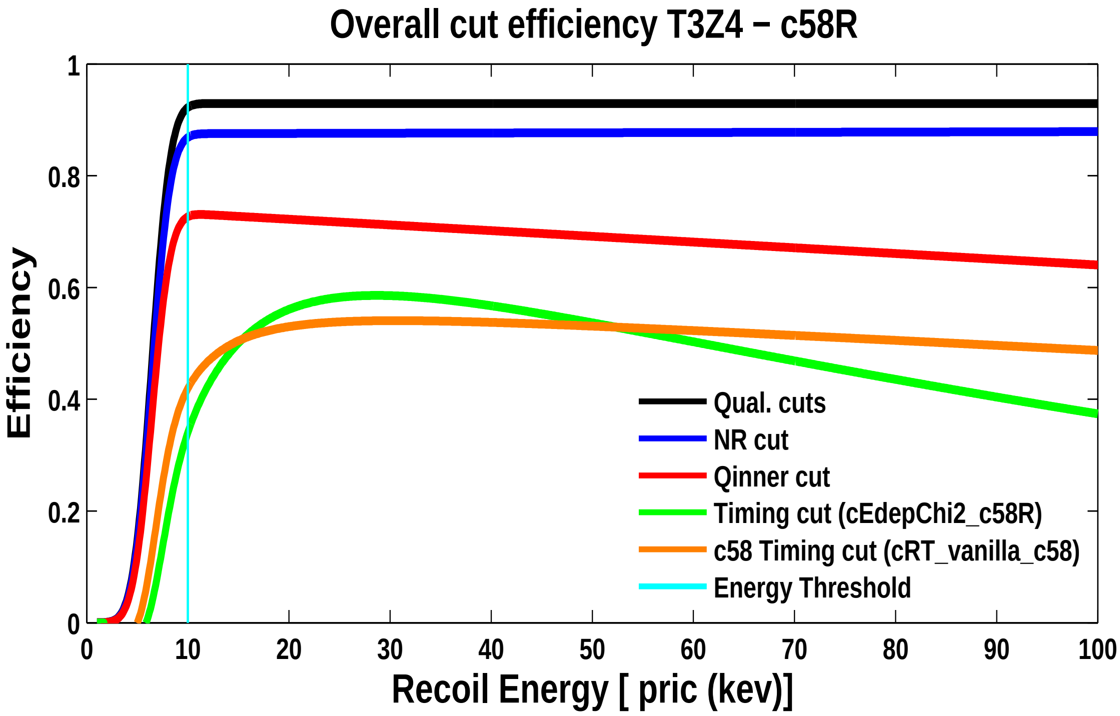

Figure G.3: Timing cut efficiencies for T3Z2 (top) and T3Z4 (bottom). Shown in black is the efficiency all the basic data-quality cuts, the blue curve shows the nuclear recoil efficiency, in red is shown the the fiducial-volume cut efficiency and in green is plotted the efficiency of the χ^2 optimized timing cut analysis. Shown in color orange, is the c58 analysis timing cut efficiency.

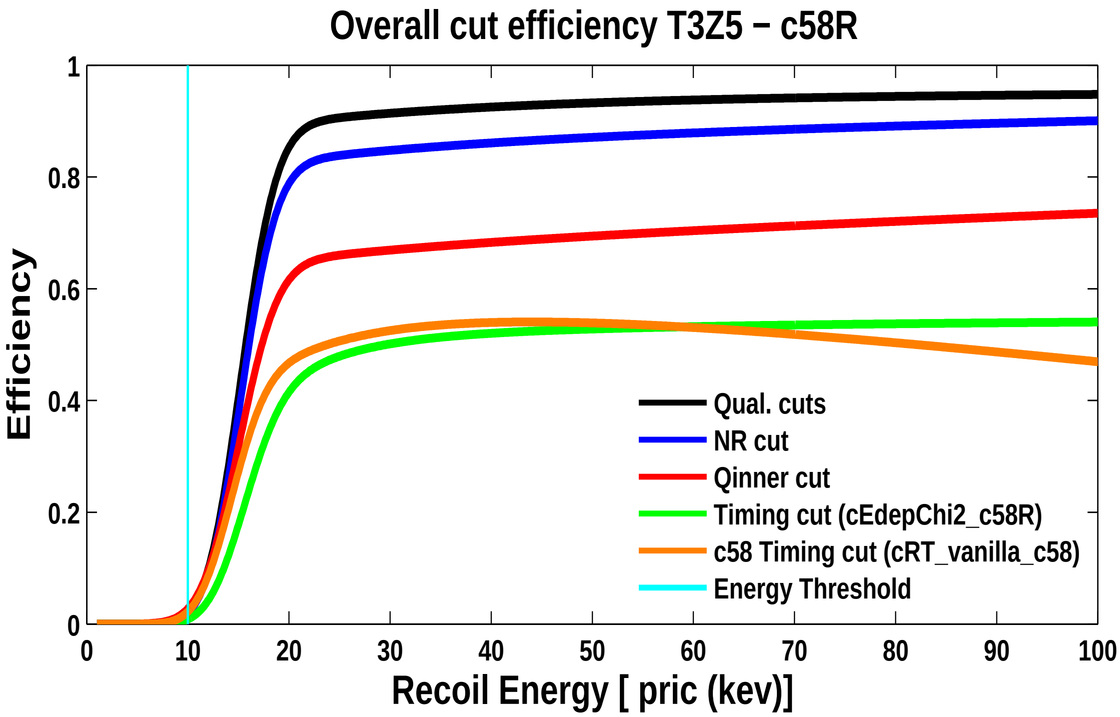

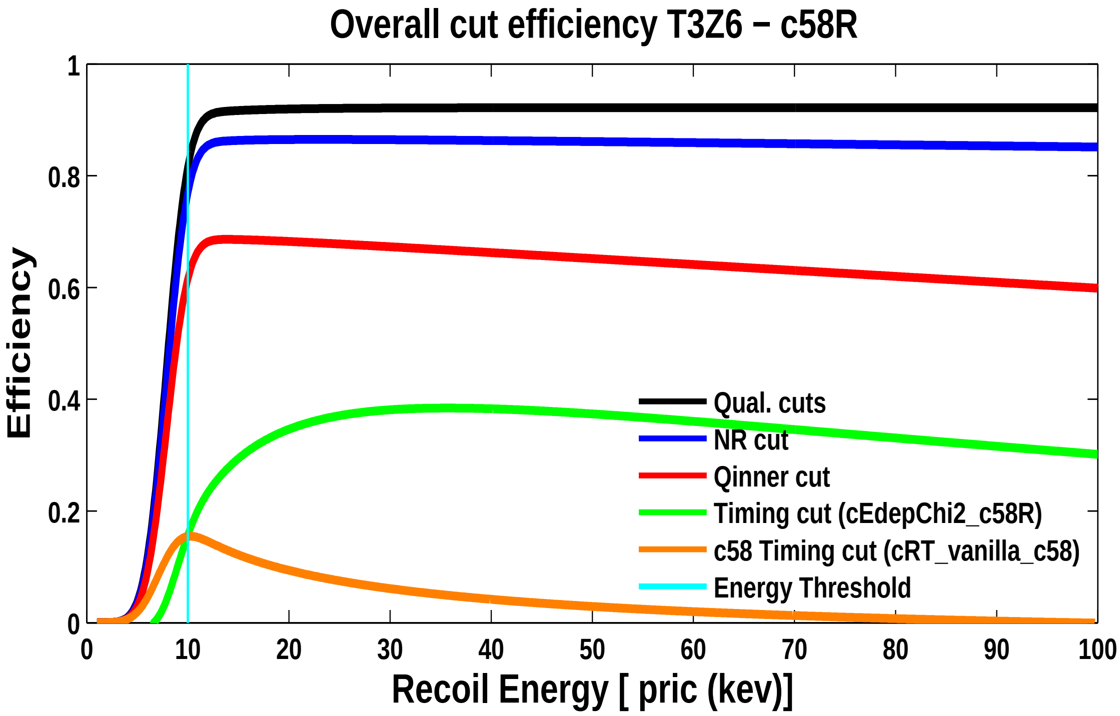

Figure G.4: Timing cut efficiencies for T3Z5 (top) and T3Z6 (bottom). Shown in black is the efficiency all the basic data-quality cuts, the blue curve shows the nuclear recoil efficiency, in red is shown the the fiducial-volume cut efficiency and in green is plotted the efficiency of the χ^2 optimized timing cut analysis. Shown in color orange, is the c58 analysis timing cut efficiency.

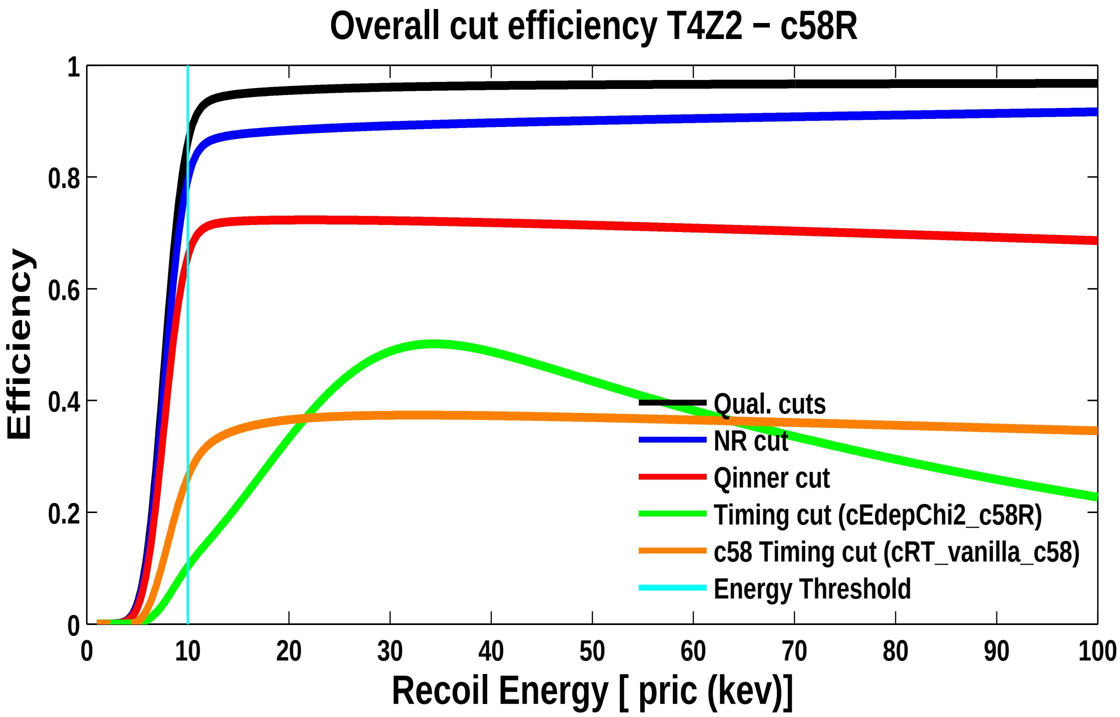

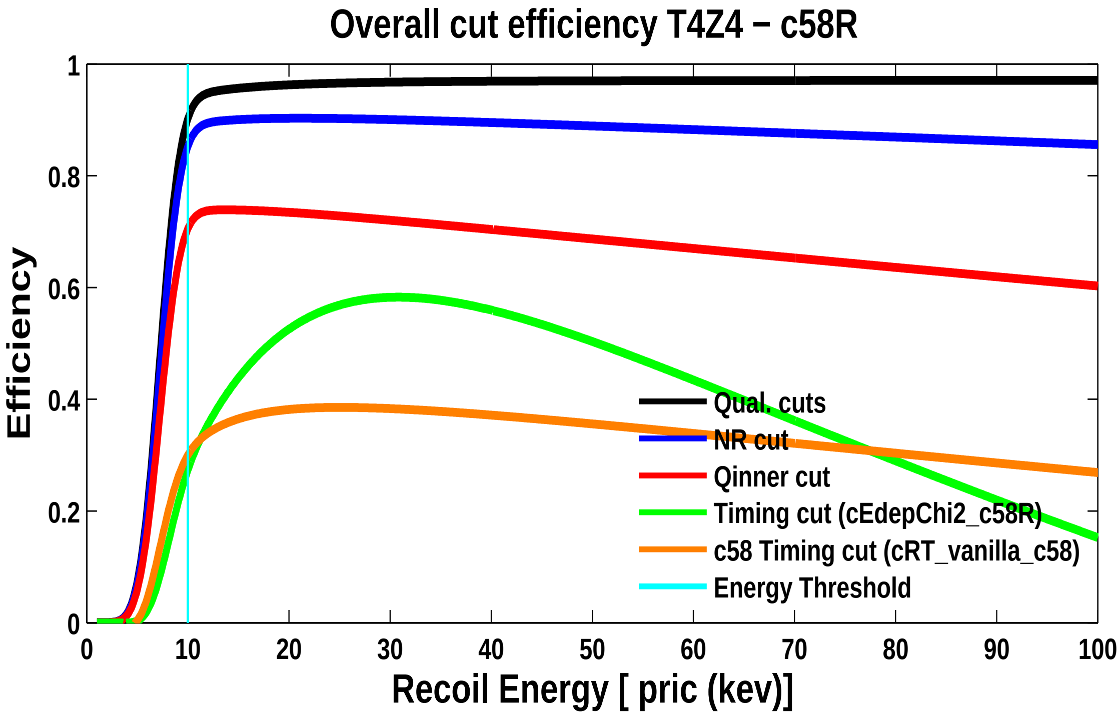

Figure G.5: Timing cut efficiencies for T4Z2 (top) and T4Z4 (bottom). Shown in black is the efficiency all the basic data-quality cuts, the blue curve shows the nuclear recoil efficiency, in red is shown the the fiducial-volume cut efficiency and in green is plotted the efficiency of the χ^2 optimized timing cut analysis. Shown in color orange, is the c58 analysis timing cut efficiency.

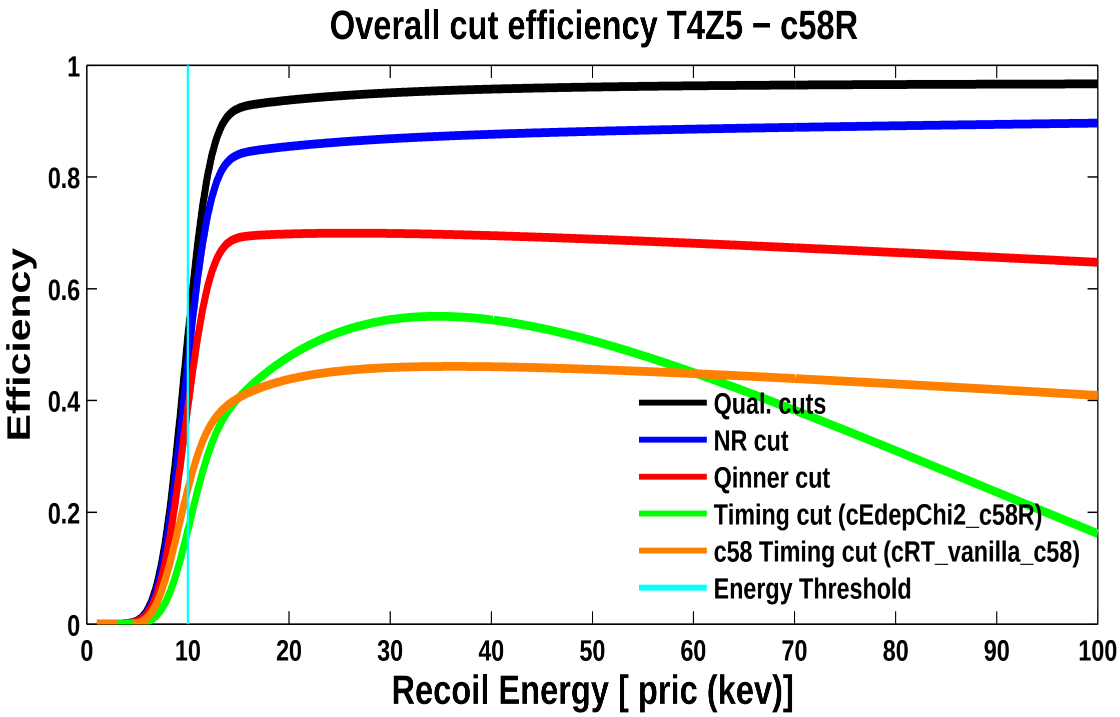

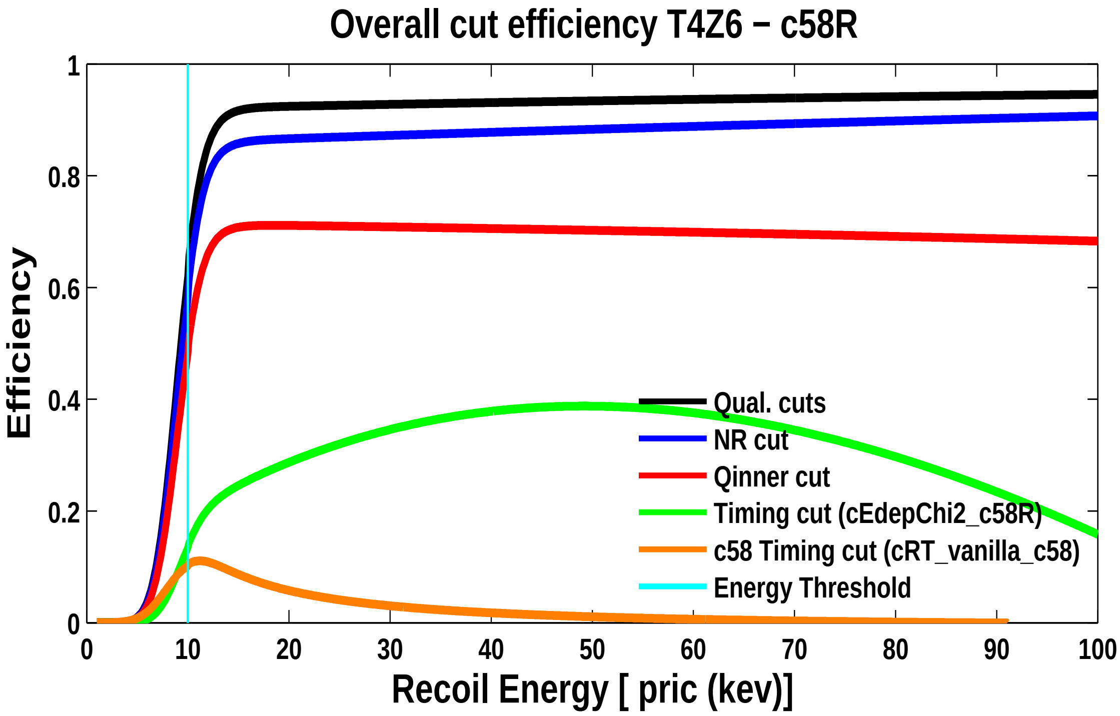

Figure G.6: Timing cut efficiencies for T4Z5 (top) and T4Z6 (bottom). Shown in black is the efficiency all the basic data-quality cuts, the blue curve shows the nuclear recoil efficiency, in red is shown the the fiducial-volume cut efficiency and in green is plotted the efficiency of the χ^2 optimized timing cut analysis. Shown in color orange, is the c58 analysis timing cut efficiency.

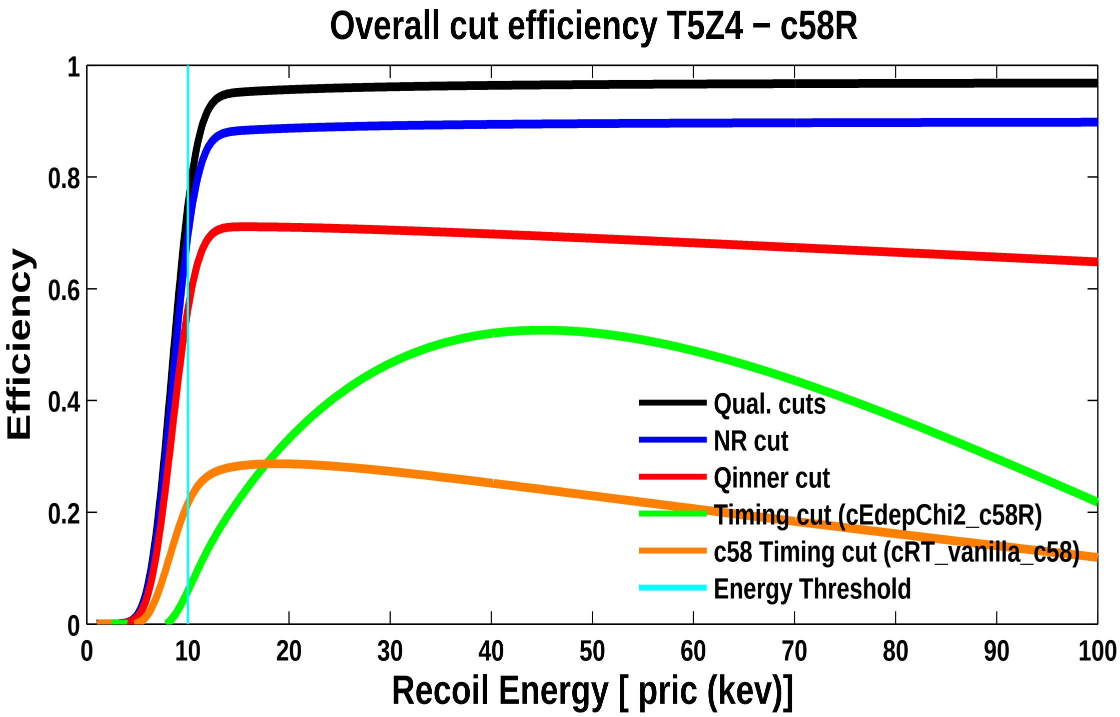

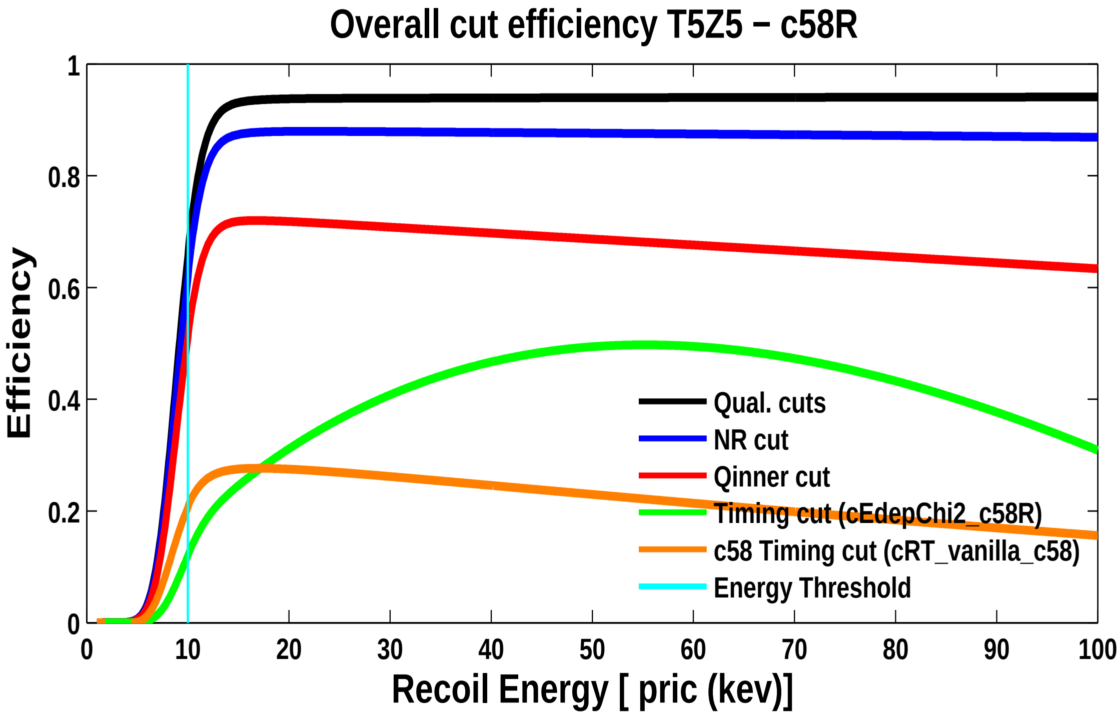

Figure G.7: Timing cut efficiencies for T5Z4 (top) and T5Z5 (bottom). Shown in black is the efficiency all the basic data-quality cuts, the blue curve shows the nuclear recoil efficiency, in red is shown the the fiducial-volume cut efficiency and in green is plotted the efficiency of the χ^2 optimized timing cut analysis. Shown in color orange, is the c58 analysis timing cut efficiency.

Bibliography

[1] F. Zwicky, 1993 Helv. Phys. Acta, 6, 1110.

[2] V. C. Rubin, Ford Jr W. K., Ap. J. 261:439, 1970.

[3] Milgrom, M. A: J. 270, 365, 1983.

[4] Bond, J. R., et al., In formation and Evolution of Galaxies and Large Structures (Reidel, Dodrecht).

[5] L. Bergstron and A. Goobar, Cosmology and Particle Astrophysics, 2nd edition, UK, 2006.

[6] Steven Weinberg: Cosmology, Oxford University Press Inc, Oxford University, New York (2008).

[7] Viatcheslav Mukhanov: Physical foundations of Cosmology, Cambridge University Press, Cambridge, UK (2005).

[8] E.W. Kolb and M. Turner: The early universe, Frontiers in Physics. Westview Press (1990).

[9] S. Dodelson: Modern Cosmology, Academic Press (2003).

[10] J.A. Peacock: Cosmological Physics, Cambridge University Press (1999).

[11] P. Peebles: Principles of Physical Cosmology, Princeton Universit Press (1993).

[12] T. Padmnabhan: Structure Formation in the Universe, Cambridge University Press (1993).

[13] David Bailin, Alexander Love: Cosmology in Gauge Field Theory and String Theory, Institute of Physics Publishng, Bristol (2004).

[14] David H. Lyth, Andrew Liddle: The Primordial Density Pertubation (Cosmology, Inflation and the Origine of the Universe), Cambridge University Press, Cambridge (2009).

[15] Adam G. Reiss and all.: Observational Evidence fromSupernovae for an Accelerated Universe and a Cosmological Constant, The American Astronomical Journal, 116, 1009 (1998).

[16] Perlmutter, S. et al.: Measurements of Ω and Λ from 42 high redshift supernovae, Astrophysical Journal, 517, 565 (1999)

[17] Riess, A. G., et al.: Type Ia Supernova Discoveries at $z > 1$ from the Hubble Space Telescope: Evidence for Past Deceleration and Constraints on Dark Energy Evolution, 2004, Astrophysical Journal, 607, 665

[18] http://www.darkenergysurvey.org/DECam/camera.shtml

[19] Ciardullo, The Planetary Nebula Luminosity Function at the Dawn of Gaia Robin, arXiv:1203.5551v1 (25 Mar 2012).

[20] Maximilian Stritzinger, Bruno Leibundgut, Stefanie Walch, Gertrud Contardo, Constraints on the Progenitor Systems of Type Ia Supernovae, arXiv:astro-ph/0506415v2 (5 Dec 2005).

[21] C. Badenes, K.J. Borkowski, E. Bravo, J.P. Hughes, U.Hwang, Exploring the Physics of Type Ia Supernovae Through the X-ray Spectra of their Remnants, arXiv:astro-ph/0506576.

[22] Xin Zhang, Feng-Quan Wu, Constraints on holographic dark energy from type Ia supernova observations, arXiv:astro-ph/0506310.

[23] Will Sutherland, On measuring the absolute scale of baryon acoustic oscillations, arXiv:1205.0715v1 (2012).

[24] Andrew Liddle: An Introduction To Modern Cosmology,University of Sussex, UK (2003).

[25] http://astro.uni-wuppertal.de/ kampert/Cosmology-WS0607.html.

[26] www.ualberta.ca/~pogosyan/teaching/ASTRO_122/lect30a/lecture30a.html.

[27] Albert Einstein, Sitz, Wiss. 1, 142 (1917).

[28] E. Wright et al., Astrophysics Journal 396 L13 (1992).

[29] G. Efstathiou, J.R. Bond, and White, M.N. of Royal Astronomical Society, 258 (1992).

[30] R.M. Wald, General relativity, University of Chicago Press, Chicago, IL, 1984.

[31] P.J.E Peebles, Principles of Physica Cosmology, Princeton University Press, New Jersey, 1993.

[32] A.G. Walker, Proc. London Math. Soc. 42, 90 (1936).

[33] A. Friedmann, Z. Phys. 10, 377 (1922).

[34] A. Friedmann, Z. Phys. 21, 326 (1924).

[35] A. Komatsu et al., Astrophysics J. Suppl. 192, 18

[36] Schneider, D.P., Schmidt, M., Gunn, J.E. 1991. Astron. J.102: 837, (2001).

[37] Peebles, P.J.E., Schramm, D.N., Turner, E.L., Kron, R.G. 1991. Nature 352: 769;

[38] Teitelboim, C. 1982. Phys. Rev. D 25: 3159

[39] Olive, K.A., Schramm, D.N., Steigman, G., Walker, T.P. 1990. Phys. Lett. B 236: 454

[40] Shkolvsky, J. 1967. Ap. J. Lett. 150: L1

[41] Peebles, P.J.E., Silk, J. 1990. Nature 346: 233

[42] Petrosian, V., Salpeter, E., Szekeres, P. 1967. Ap. J. 147: 1222
Tomboulis, E.T. 1990. Nucl. Phys. B 329: 410
Tonry, J.L. 1991. Ap. J. Lett. 373: L1

Toth, G., Ostriker, J.P. 1992. Ap. J. 389: 5

Traschen, J., Hill, C. 1986. Phys. Rev. D 33: 3519

Trimble, V. 1987. Annu. Rev. Astron. Astrophys. 25: 425

Turner, E.L. 1980. Ap. J. Lett. 242: L135

Turner, E.L. 1990. Ap. J. Lett. 365: L43

Turner, E.L. 1991. Astron. J. 101: 5

Turner, E.L., Ikeuchi, S. 1992. Ap. J. 389: 478

Turner, E.L., Ostriker, J.P., Gott, J.R. 1984. Ap. J. 284: 1

[43] E. Komatsu et al., Astrophy. J. Suppl. 192, 18 (2011).

[44] A.G. Riess et al., Astrophy. J. Suppl. 730, 119 (2011)

[45] A.G. Riess et al., Astrophys. J. 699, 539 (2009).

[46] W.L. Freedman et al., Astrophys. J. 553, 47 (2001).

[47] J. Friedman, M.S Turner, and D. Huterer, Ann. Rev. Astron. Astrophys. 46, 385 (2008).

[48] B. Gold et al., Astrophys. J. Suppl. 192, 15 (2011).

[49] G. Hinshaw et al., Astrophys. J. Suppl. 180, 225 (2009).

[50] Raymond Bunker, A Low-threshold Analysis of Data from the Cryogenic Dark Matter Search Experiment, PhD Thesis, UCSB, (2011).

[51] R.B. Tully and J.R. Fisher, Astron. Astrophys. 54, 661 (1977).

[52] D.G. York et al., Astron. J. 120, 1579 (2000).

[53] M. Girardi, G. Giuricin, F. Mardirossian, M. Mezzetti, and W. Boschin, Astrophys. J. 505, 74 (1998).

[54] J. Trumper, Adv. Space. Res. 2, 241 (1983).

[55] J. Trumper, Q. J. R. Astron. Soc. 33, 165 (1992).

[56] J. Trumper, Science 260, 1769 (1993).

[57] S. Borgani, in Lectures for 2005 Guillermo Haro Summer School on Clusters (Springer, Tonantzintla, Mexico, 2006).

[58] N. Kaiser, Mon. Not. Roy. Astron. Soc. 222, 323 (1986).

[59] G.L. Bryan and M.L. Norman, Astrophys. J. 495, 80 (1998).

[60] M. Colless et al. The 2df galaxy redshift survey: spectra and redshifts. Monthly Notices of the Royal Astronomical Society, 328:1039-1063, 2001.

[61] J.B. Peterson et al., Astrophys. J. 532, L83 (2000).

[62] A.D. Miller et al., Astrophys. J. Suppl. 140, 115 (2002).

[63] S. Padin et al., Astrophys. J. 549, L1 (2001).

[64] E.M. Leitch et al., Astrophys. J. 532, 37 (2000).

[65] S. Hanany et al., Astrophys. J. 545, L5 (2000).

[66] B.P. Crill et al., Astrophys. J. Suppl. 148, 527 (2002).

[67] C.L. Bennet et al., Astrophys. J. Suppl. 148, 1 (2003).

[68] N. Jarosik et al., Astrophys. J. Suppl. 192, 14 (2011).

[69] J.L. Weiland et al., Astrophys. J. Suppl. 192, 19 (2011).

[70] D. Larson et al., Astrophys. J. Suppl. 192, 16 (2011).

[71] B. Gold et al., Astrophys. J. Suppl. 192, 15 (2011).

[72] C. Bennet et al., Astrophys. J. Suppl. 192, 17 (2011).

[73] L. Page et al., Astrophys. J. 585, 566 (2003).

[74] G. Hinshaw et al., Astrophys. J. Suppl. 170, 288 (2007).

[75] G. Hinshaw et al., Astrophys. J. Suppl. 180, 225 (2009).

[76] E.L. Wright, G. Hinshaw, and C.L. Bennett, Astrophys. J. 458, L53 (1996).

[77] R.K. Sachs and A.M. Wolfe, Astrophys. J. 147, 73 (1967).

[78] J. Silk, Astrophys. J. 151, 459 (1968).

[79] K. Nakamura et al., J. Phys. G 37, 075021 (2012).

[80] LSND collaboration, Evidence for $\overline{\nu}_{mu} \to \overline{\nu}_e$ Oscillations from the LSND Experiment at LAMPF, arXiv:nucl-ex/9605003v1, 1996.

[81] Edward W. Kolb and Michael S. Turnera: On the relic abundance of stable neutrinos, Physics Letters B Volume 159, Issues 2 3, 19 September 1985, Pages 102106.

[82] K. N. Abazajian et al.: Light Sterile Neutrinos: A White Paper,arXiv:1204.5379v1 [hep-ph] 18 Apr 2012.

[83] Peter L. Biermann and Faustin Munyaneza: Dark Matter and Sterile Neutrinos, arXiv:astro-ph/0702173v1, 2007.

[84] S. J. Asztalos et al.: Improved rf cavity search for halo axions,Phys. Rev. D 69, 011101(R) (2004).

[85] C. Alcock et al. The MACHO project: Microlensing results from 5.7 years of LMC observations. Astrophys. J., 542:281-307, 2000.

[86] P. Tisserand et al. Limits on the Macho Content of the Galactic Halo from the EROS-2 Survey of the Magellanic Clouds. Astron. Astrophys., 469:387-404, 2007.

[87] Stephen P. Martin: A Supersymmetry Primer, arXiv:hep-ph/9709356v6 6 Sep 2011.

[88] S.P. Martin Phys. Rev. D 46, 2769 (1992)hep-ph/9207218.

[89] S.P. Martin Phys. Rev. D 54, 2340 (1996) hep-ph/9602349.

[90] R.N. Mohapatra, Phys. Rev. D 34, 3457 (1986).

[91] A. Font, L.E. Ibanez and F. Quevedo, Phys. Lett. B 228, 79(1989).

[92] P. Fayet, NucI. Phys. B90 (1975) 104.

[93] A. Salam and J. Strathdee, Nucl. Phys. B87 (1975) 85.

[94] G.R. Farrar and S. Weinberg, Phys. Rev. D27 (1983) 2732.

[95] P. Fayet, Phys. Lett. 69B (1977) 489.

[96] G. Farrar and P. Fayet, Phys. Lett. 76B (1978) 575.

[97] R.Barbier et al.: R-parity violating supersymmetry, hep-ph/0406039 (2005).

[98] Jacob D. Bekenstein, Relativistic gravitation theory for the modified Newtonian dynamics paradigm, Phys. Rev. D 70 (8): 083509, arXiv:astro-ph/0403694, Bibcode 2004PhRvD..70h3509B, doi:10.1103/PhysRevD.70.083509.

[99] Nelson D. Padilla and al., The 2dF Galaxy Redshift Survey: The clustering of galaxy groups,arXiv:astro-ph/0402577.

[100] E. Tago, J. Einasto, M. Einasto, E. Saar, Clusters and groups of galaxies in the 2dF galaxy redshift survey, arXiv:astro-ph/0501099.

[101] Scott C. Porter, Somak Raychaudhury, The Pisces-Cetus Supercluster: a remarkable filament of galaxies in the 2dF Galaxy Redshift Survey and Sloan Digital Sky surveys, arXiv:astro-ph/0511050.

[102] Ho Seong Hwang, Galaxy Orbits for Galaxy Clusters in Sloan Digital Sky Survey and 2dF Galaxy Redshift Survey,arXiv:0712.2301.

[103] https://www.cfa.harvard.edu/ dfabricant/huchra/zcat/

[104] Penzias, A. A. and Wilson, R. W., A Measurement of Excess Antenna Temperature at 4080 Mc/s. Astrophysical Journal, vol. 142, p.419421

[105] D. J. Fixsen and J. C. Mather, THE SPECTRAL RESULTS OF THE FAR-INFRARED ABSOLUTE SPECTROPHOTOMETER INSTRUMENT ON COBE,The Astrophysical Journal, 581:817822, 2002.

[106] Eiichiro Komatsu, Benjamin D. Wandelt, David N. Spergel, Anthony J. Banday, Krzysztof M. Gorski, Measurement of the cosmic microwave background bispectrum on the COBE DMR sky maps, arXiv:astro-ph/0107605.

[107] Gart Westerhout, The early history of radio astronomy. Ann. New York Acad. Sci. 189 Education in and History of Modern Astronomy (August 1972) 211-218 doi 10.1111/j.1749-6632.1972.tb12724.x

[108] Hendrik Christoffel van de Hulst, The Origin of Radio Waves From Space.

[109] History of High-Resolution Radio Astronomy. Annual Review of Astronomy and Astrophysics, September 2001.

[110] G. Neugebauer, Early Results from the Infrared Astronomical Satellite, Science 6 April 1984: Vol. 224 no. 4644 pp. 14-21 DOI: 10.1126/science.224.4644.14.

[111] Hiroshi Murakamia, Hideo Matsuhara, The Infrared Astronomical Satellite AKARI : Overview, Highlights of the Mission, Proc. of SPIE Vol. 7010 70100A-1.

[112] Charles W. Misner Kip S. Thorne, John Archibald Wheeler, John Wheeler, Kip Thorne, Gravitation (Physics Series), ISBN-13: 978-0716703440.

[113] Introducing Einstein's Relativity by Ray D'Inverno, ISBN-10: 0198596863 — ISBN-13: 978-0198596868.

[114] A First Course in General Relativity by Bernard F. Schutz, 0521277035 — ISBN-13: 978-0521277037.

[115] Relativity and Common Sense: A New Approach to Einstein by Hermann Bondi

[116] Spacetime Physics by John Archibald Wheeler, ISBN-10: 0716723271 — ISBN-13: 978-0716723271.

[117] Lorenzo Pareschi and Giovanni Russo, Numerical Solution of the Boltzmann Equation I: Spectrally Accurate Approximation of the Collision Operator, SIAM Journal on Numerical Analysis Vol. 37, No. 4 (2000), pp. 1217-1245.

[118] The Inflationary Universe by Alan H. Guth.

[119] Schaum's Outline of Tensor Calculus (Schaum's) by David C. Kay, ISBN-10: 0070334846 — ISBN-13: 978-0070334847.

[120] Introduction to Tensor Calculus, Relativity and Cosmology (Dover Books on Physics) by Derek F. Lawden, ISBN-10: 0486425401 — ISBN-13: 978-0486425405.

[121] Cosmology by Steven L. Weinberg, ISBN-10: 0198526822 — ISBN-13: 978-0198526827.

[122] Cosmology: A Very Short Introduction by Peter Coles, ISBN-10: 019285416X — ISBN-13: 978-0192854162.

[123] Cosmology in Gauge Field Theory and String Theory (Graduate Student Series in Physics) D. Bailin, Alexander Love, ISBN-10: 0750304928 — ISBN-13: 978-0750304924.

[124] The Universe Before the Big Bang: Cosmology and String Theory (Astronomers' Universe) by Maurizio Gasperini, ISBN-10: 3642093841 — ISBN-13: 978-3642093845.

[125] From the Universe to the Elementary Particles: A First Introduction to Cosmology and the Fundamental Interactions (Undergraduate Lecture Notes in Physics) by Ulrich Ellwanger, ISBN-10: 3642243746 — ISBN-13: 978-3642243745.

[126] Elements of String Cosmology by Maurizio Gasperini, ISBN-10: 0521187982 — ISBN-13: 978-0521187985. The Big

[127] The Big Bang, by Joseph Silk, ISBN-10: 080507256X — ISBN-13: 978-0805072563.

[128] Formation of Structure in the Universe by Avishai Dekel and Jeremiah P. Ostriker.

[129] E. Komatsu, et al. Five Year Wilkinson Microwave Anistropy Probe Observations: Cosmological Interpretation.The Astrophysical Journal Supplement Series, 180(2):330-376, 2009. ISSN 0067-0049.

[130] R. Amanullah, et al. Spectra and Hubble Space Telescope. Light curves of six Type Ia Supernovae at 0.511 and the Union2 Compilation. The Astrophysical Journal 716(1):712-738, 2010. ISSN 0004- 637X.

[131] V. Rubin and W. K. Ford Jr: Rotation of the Andromeda Nebula from a spectroscopic survey of emission regions. Astrophysical Journal 159, 379 (1970).

[132] V. Rubin, N. Thonnardand W. K. Ford Jr: Rotational properties of 21 SC galaxies with a large rangee of luminosities and radii from NGC 4605 (R=4 kpc) to UGC 2885 (R=122 kpc). Astroph. Journal 238, 471 (1980).

[133] Y. Sofue and V. Rubin, Rotation curves of spiral galaxies. Annual Rev. Astron. Astrophys. 39, 137 (2001).

[134] J. Binney and S. Tremaine, Galactic Dynamics (Princeton University Press, Princeton, NJ, 1987).

[135] J.F. Navarro, C.S. Frenk, and S.D.M. White, The structure of cold dark matter halos. The Astrophysical Journal 463, 563 (1996).

[136] C. Adami, A. Mazure, P. Katgert, and A. Biviano, The ESO Nearby Abell Cluster Survey. VII. Galaxy density profiles of rich clusters of galaxies. Astronomy and Astrophysics 336, 63-82 (1998).

[137] P. Katgert, A. Biviano, and A. Mazure, The ESO Abell Cluster Survey. XII. The mass and mass-to-light ratio profiles of rich clusters. The Astrophysics Journal 600, 657-669 (2004).

[138] M. Bartelmann. Gravitational lensing. 1010.3829, 2010. URL http://arxiv.org/abs/1010. 3829.

[139] P. Katgert, A. Biviano, and A. Mazure, The ESO Abell Cluster Survey. XII. The mass and mass-to-light ratio profiles of rich clusters. The Astrophysics Journal 600, 657-669 (2004).

[140] J. P. Kneib et al. Dynamics of Abell 2218 from optical and near-IR imagery of arc(let)s and the ROSAT/HRI X-ray map. Astron. Astrophys., 303:27-40, November 1995.

[141] J.-P. Kneib et al. Hubble Space Telescope Observations of the Lensing Cluster Abell 2218. Astrophys. J., 471:643, November 1996.

[142] D. E. Johnston et al. Cross-correlation Weak Lensing of SDSS galaxy Clusters II: Cluster Density Profiles and the Mass-Richness Relation. arXiv:0709.1159, 2007.

[143] D. Clowe et al. A direct empirical proof of the existence of dark matter. Astrophys. J.,648:L109-L113, 2006.

[144] D. Davis and R. W. III, Astroph. J. Lett. 470, 35 (1996).

[145] M.Loewenstein and R. W. III, Astroph. J. 518, 50 (1999).

[146] W. Hu and S. Dodelson. Cosmic Microwave Background Anisotropies. Ann. Rev. Astron. Astrophys., 40-171-216, 2002.

[147] W. Hu and M.J. White. A CMB Polarization Primer. New Astron., 2-323, 1997.

[148] M. R. Nolta et al. Five-Year Wilkinson Microwave Anisotropy Probe (WMAP) Observations: Angular Power Spectra. arXiv:0803.0593, 2008.

[149] D. Tytler, J. M. OMeara, N. Suzuki, and D. Lubin, astro-ph/0001318, to appear in Phys. Scr.

[150] D. Tytler et al., R. Swedish Acad. Sci. Physica Scripta T 85, 12 (2000).

[151] S. Burles and D. Tytler, Astroph. J. 507, 732 (1998).

[152] S. Burles et al., Phys. Rev. Lett. 82, 4176 (1999).

[153] J. O'Meara et al., Astroph. J. 552, 718 (2001).

[154] Y. Izotov and T. Thuan, Astroph. J. 500, 188 (1998).

[155] Y. Izotov et al., Astroph. J. 527, 757 (1999).

[156] D. Balser et al.,Astroph. J. 510, 759 (1999).

[157] S. Chandrasekhar, Mon. Not. Roy. Astron. Soc. 95, 207 (1935).

[158] M.M. Phillips, Astrophys. J. 413, L105 (1993).

[159] J. Frieman, M.S Turner, and D. Huterer, Ann. Rev. Astron. Astrophys. 46, 385 (2008).

[160] E. Hubble, Proc. N.A.S. 15, 168 (1929).

[161] S. Perlmutter et al., Astroph. J. 517, 565 (1999).

[162] A. Riess et al., Astron. J. 116, 1009 (1998).

[163] J. Tonry et al., Astroph. J. 594, 1 (2003).

[164] M. Hicken et al., Astrophys. J. 700, 1097 (2009).

[165] M. Kowalski et al., Astrophys. J. 686, 749 (2008).

[166] P. Astier, Astron. Astrophys. 447, 31 (2006).

[167] R.A. Knop et al., Astrophys. J. 598, 102 (2003).

[168] R. Kesler et al., Astrophys. J. Suppl. 185, 32 (2009).

[169] J. Guy et al., arXiv:1010.4743v1 (2010)

[170] N. Suzuki et al., arXiv:1105:3470v1 (2011), submitted to Astrophys. J.

[171] D.J. Eisenstein and M. White, Phys. Rev. D70, 103523 (2004).

[172] W.J. Percival et al., Mon. Not. Roy. Astron. Soc. 401, 2148 (2010).

[173] M. Colless et al., arXiv:astro-ph/0306581v1 (2003).

[174] Patric Labelle, Supersymmetry Demystified, a self teaching guide, McGraw Hill, NY; ISBN 978-0-07-163641-4.

[175] Sunil Golwala, PhD dissertation, Stanford University (1999).

[176] Vuk Mandic, PhD dissertation, Stanford University (1999).

[177] G. Belanger, A. Pukhov and G. Servant, Heavy Dirac Neutrino Dark Matter, LCWS/ILC (2007).

[178] Leanne D. Duffy and Karl van Bibber, Axions as Dark Matter Particles: arXiv:0904.3346v1 (2009).

[179] R. D. Peccei and H. R. Quinn. CP Conservation in the Presence of Instantons. Phys. Rev. Lett., 38:14401443, 1977.

[180] R. D. Peccei and H. R. Quinn. Constraints Imposed by CP Conservation in the Presence of Instantons. Phys. Rev., D16:17911797, 1977.

[181] S. Weinberg. A New Light Boson? Phys. Rev. Lett., 40:223226, 1978.

[182] F. Wilczek. Problem of Strong P and T Invariance in the Presence of Instantons. Phys. Rev. Lett., 40:279282, 1978.

[183] L. F. Abbott and P. Sikivie. A Cosmological Bound on the Invisible Axion. Phys. Lett., B120:133136, 1983.

J. Preskill, M. B. Wise, and F. Wilczek. Cosmology of the Invisible Axion. Phys. Lett., B120:127132, 1983.

M. Dine and W. Fischler. The Not-So-Harmless Axion. Phys. Lett., B120:137141, 1983.

[184] R. L. Davis. Goldstone Bosons in String Models of Galaxy Formation. Phys. Rev., D32:3172, 1985.

R. L. Davis. Cosmic Axions From Cosmic Strings. Phys. Lett., B180:225, 1986.

D. Harari and P. Sikivie. On the Evolution of Global Strings in the Early Universe. Phys. Lett., B195:361, 1987.

A. Vilenkin and T. Vachaspati. Radiation of Goldstone Bosons from Cosmic Strings. Phys. Rev., D35:1138, 1987.

R. L. Davis and E. P. S. Shellard. Do Axions Need Inflation? Nucl. Phys., B324:167, 1989.

A. Dabholkar and J. M. Quashnock. Pinning Down the Axion. Nucl. Phys., B333:815, 1990.

R. A. Battye and E. P. S. Shellard. Global String Radiation. Nucl. Phys., B423:260304, 1994.

R. A. Battye and E. P. S. Shellard. Axion String Constraints. Phys. Rev. Lett., 73:29542957, 1994.

M. Yamaguchi, M. Kawasaki, and J. Yokoyama. Evolution of Axionic Strings and Spectrum of Axions Radiated From Them. Phys. Rev. Lett., 82:45784581, 1999.

C. Hagmann, S. Chang, and P. Sikivie. Axion Radiation from Strings. Phys. Rev., D63:125018, 2001.

S. Chang, C. Hagmann, and P. Sikivie. Studies of the Motion and Decay of AxionWalls Bounded by Strings. Phys. Rev., D59:023505, 1999.

D. H. Lyth. Estimates of the Cosmological Axion Density. Phys. Lett., B275:279283, 1992.

M. Nagasawa and M. Kawasaki. Collapse of Axionic Domain Wall and Axion Emission. Phys. Rev., D50:48214826, 1994.

[185] S. L. Adler. Axial Vector Vertex in Spinor Electrodynamics. Phys. Rev., 177:24262438, 1969.

J. S. Bell and R. Jackiw. A PCAC Puzzle: $\pi^0 \to \gamma\gamma$ in the Sigma Model. Nuovo Cim., A60:4761, 1969.

[186] J. E. Kim. Light Pseudoscalars, Particle Physics and Cosmology. Phys. Rept., 150:1177, 1987.

H.-Y. Cheng. The Strong CP Problem Revisited. Phys. Rept., 158:1, 1988.

M. S. Turner. Windows on the Axion. Phys. Rept., 197:6797, 1990.

G. G. Raffelt. Astrophysical Methods to Constrain Axions and Other Novel Particle Phenomena. Phys. Rept., 198:1113, 1990. [25] Jihn E. Kim and Gianpaolo Carosi. Axions and the Strong CP Problem. [arXiv:0807.3125], 2008.

[187] R. Cameron et al. Search for nearly massless, weakly coupled particles by optical techniques. Phys. Rev., D47:37073725, 1993.

[188] C. Amsler et al. Review of particle physics. Phys. Lett., B667:1, 2008.

[189] P. Sikivie. Experimental tests of the *invisible* axion. Phys. Rev. Lett., 51:1415, 1983.

[190] R. Bradley et al. Microwave cavity searches for dark-matter axions. Rev. Mod. Phys., 75:777-817, 2003.

[191] L. D. Duffy et al. A high resolution search for dark-matter axions. Phys. Rev., D74:012006, 2006.

[192] Z. Ahmed et al., Search for Axions with the CDMS Experiment, arXiv:0902.4693v1 (2009).

[193] R.L.Davis, Cosmic Axions from Cosmic Strings, SLAC - PUB - 3895 (1986).

[194] Gianfranco Bertone, David G. Cerdeno, Mattia Fornasa, Roberto Ruiz de Austri, Charlotte Strege, Roberto Trotta, Global fits of the cMSSM including the first LHC and XENON100 data, arXiv:1107.1715v2 (2012).

[195] A. H. Chamseddine, R. L. Arnowitt and P. Nath, Phys. Rev. Lett. 49 (1982) 970.

G. L. Kane, C. F. Kolda, L. Roszkowski and J. D. Wells, Phys. Rev. D 49 (1994) 6173

Particle Dark Matter: Observations, Models and Searches, ed. G. Bertone, Cambridge University Press (2010)

L. Bergstrom, Rept. Prog. Phys. 63, 793 (2000).

[196] B. J. Carr and J. H. MacGibbon, Phys. Rep. 307, 141 (1998).

[197] Jonathan L. Feng, Arvind Rajaraman, and Fumihiro Takayama, SuperWIMP Dark Matter Signals from the Early Universe, arXiv:hep-ph/0306024v2 (2003).

J. L. Feng, A. Rajaraman and F. Takayama, Phys. Rev. Lett. 91, 011302 (2003) [hep-ph/0302215].

[198] H. Goldberg, Phys. Rev. Lett. 50, 1419 (1983).

[199] J. Ellis, J. S. Hagelin, D. V. Nanopoulos and M. Srednicki, Phys. Lett. B127, 233 (1983).

[200] A. H. Chamseddine, R. Arnowitt and P. Nath, Phys. Rev. Lett. 49, 970 (1982).

[201] R. Barbieri, S. Ferrara and C. A. Savoy, Phys. Lett. B 119, 343(1982).

[202] L. J. Hall, J. Lykken and S. Weinberg, Phys. Rev. D27, 2359 (1983).

[203] L. Alvarez-Gaume, J. Polchinski and M. B. Wise, Nucl. Phys. B 221, 495 (1983).

[204] T. Moroi, H. Murayama and M. Yamaguchi, Phys. Lett. B 303, 289 (1993);
M. Bolz, A. Brandenburg and W. Buchmuller, Nucl. Phys. B 606, 518 (2001)[hep-ph/0012052].

[205] D. N. Spergel et al., astro-ph/0302209.

[206] G. Servant and T. M. Tait, Nucl. Phys. B 650, 391 (2003) [hep-ph/0206071];
H. C. Cheng, J. L. Feng and K. T. Matchev, Phys. Rev. Lett. 89, 211301 (2002) [hep-ph/0207125];
G. Servant and T. M. Tait, New J. Phys. 4, 99 (2002) [hep-ph/0209262];
D. Hooper and G. D. Kribs, Phys. Rev. D 67, 055003 (2003) [hep-ph/0208261];
G. Bertone, G. Servant and G. Sigl, hep-ph/0211342.

[207] Clark, Stephen. Interactions of Q-balls and matter. 2006
Chung, D.J.H.; CrottyP.; Kolb E.W.; RiottoA.; Gravitational production of superheavy dark matter. Physical Review D Volume 64, Issue 4, August 15, 2001.
Gondolo, P.; Introduction to Non-Baryonic Dark Matter. Lectures delivered at the NATO Advanced Study Institute "Frontiers of the Universe", 8-20 Sept 2003, Cargese, France
Kusenko, A.; Steinhardt, P.J.; Q-Ball Candidates for Self-Interacting Dark Matter. Physical Review Letters, vol. 87, Issue 14 oKusenko, A.; Loveridge, L.C.; Shaposhnikov, M.; Supersymmetricdark-matter Q-balls and their interactions in matter. Physical Review D, vol. 72, Issue 2.
Roszkowski, L. Non-Baryonic Dark Matter-A Theoretical Perspective. COSMO-98. Second International Workshop on Particle Physics and the Early Universe. Edited by David O. Caldwell, AIP Conference Proceedings, vol. 478. American Institute of Physics, Woodbury, NY, 1999., p.316
Spergal, Dave.: http://www.astro.princeton.edu/ dns/MAP/Bahcall/ node8.html. (1996).

[208] Bekenstein, J., & Milgrom, M. 1984, ApJ, 286, 7
Bekenstein, J. D., & Sanders, R. H. 2006, EAS Publications Series, 20, 225
Bekenstein, J. D. 2004, Phys. Rev. D, 70, 083509
Bell, E. F., & de Jong, R. S. 2001, ApJ, 550, 212
Clowe, D.,Gonzalez, A., & Markevitch, M. 2004, ApJ, 604, 596
Milgrom, M. 1983, ApJ, 270, 365
Pointecouteau, E., & Silk, J. 2005, MNRAS, 364, 654
Sahni, V. 2005, The Physics of the Early Universe, 653, 141
Sanders, R. H., & McGaugh, S. S. 2002, ARA&A, 40, 263
Sanders, R. H., & Verheijen, M. A. W. 1998, ApJ, 503, 97

[209] M.W. Goodman and E. Witten, Detectability of certain dark-matter candidates. Phys. Rev. D 31, 3059 (1985).

[210] A. Kurylov and M. Kamionkowski. Generalized analysis of weakly-interacting massive particle searches. Phys. Rev., D69:063503, 2004.

[211] J. D Lewin and P.F Smith, Review of mathematic, numerical factors, and corrections for dark matter experiments based on elastic recoil, atroparticle physics 6 (1996).

[212] J. E. Gunn et al., ApJ 223, 1015 (1978).

[213] J. Silk and M. Srednicki, Phys. Rev. Lett. 53, 624 (1984).

[214] G. Lake, Nature 34, 39 (1990).

[215] M. Kuhlen, J. Diemand, P. Madau, ApJ 686, 262 (2008).

[216] V. Springel et al., Nature 456, 73 (2008).

[217] L. E. Strigari, ApJ 678, 614 (2008).

[218] K. Freese, Phys. Lett. B 167, 295 (1986).

[219] A. Gould, ApJ 321, 571 (1987).

[220] K. Griest, D. Seckel, Nucl. Phys. B 283, 681 (1987).

[221] L.M. Krauss, K. Freese, D.N. Spergel, W.H. Press , ApJ 299, 10001 (1985).

[222] J. Silk, K. Olive, M. Srednicki, Phys. Rev. Lett. 55, 257 (1985).

[223] CMS Collaboration, Phys. Lett. B698, 196 (2011).

[224] CMS Collaboration, CMS Physics Analysis Summary SUS-09-001, (2009).

[225] CMS Collaboration, CMS Physics Analysis Summary SUS-08-005, (2008).

[226] CMS Collaboration, CMS Physics Analysis Summary SUS-09-001, (2009).

[227] CMS Collaboration, Search for New Physics with Same-Sign Isolated Dilepton Events with Jets and Missing Transverse Energy, PRL 109, 071803 (2012).

[228] CMS Collaboration, Phys. Lett. B698, 196 (2011).

[229] CMS Collaboration, CMS Physics Analysis Summary SUS-08-005, (2008).

[230] D0 Collaboration, Phys. Lett. B660, 449 (2008).

[231] D0 Collaboration, Phys. Lett. B680, 34 (2009).

[232] CDF Collaboration, Phys. Rev. Lett. 102, 121801 (2009).

[233] D. Milstead, Nucl. Phys. B210211, 289 (2011).

[234] N. Bhattacharyya, A. Choudhury, and A. Datta, arXiv:1107.1997v3 (2011).

[235] S. Choi, S. Scopel, N. Fornengo, and A. Bottino, arXiv:1108.2190v1 (2011).

[236] CMS Collaboration, Search for supersymmetry in events with photons and low missing transverse energy in pp collisions at $\sqrt{s} = 7$ TeV, arXiv:1210.2052v1 [hep-ex] 7 Oct 2012

[237] G. Jungman, M. Kamionkowski, and K. Griest, Phys. Rep. 267, 195 (1996).

[238] D. R. Tovey, R. J. Gaitskell, P. Gondolo, Y. Ramachers and L. Roszkowski, Physics Letters B 488, arXiv:1101.5205v1 [astro-ph.CO] (2011).

[239] Richard W. Schnee, Introduction to Dark Matter Experiments, TASI lecture (2010).

[240] M. T. Ressell et al. Nuclear shell model calculations of neutralino - nucleus crosssections for Si-29 and Ge-73. Phys. Rev. D48:5519-5535, 1993.

[241] V. Dimitrov, J. Engel, and S. Pittel. Scattering of weakly interacting massive particles from Ge-73. Phys. Rev., D51:291-295, 1995.

[242] J. Engel. Nuclear form-factors for the scattering of weakly interacting massive particles. Phys. Lett., B264:114-119, 1991.

[243] Martin C. Smith and al, The RAVE Survey: Constraining the Local Galactic Escape Speed, arXiv:astro-ph/0611671v2 (2007).

[244] http://en.wikipedia.org/wiki/Compact_Muon_Solenoid.

[245] E. A. Baltz, et al. Determination of dark matter properties at highenergy colliders.
Physical Review D, 74(10):103521, 2006.doi:10.1103/PhysRevD.74.103521.
http://link.aps.org/doi/10.1103/PhysRevD.74.103521.

[246] K. Nakamura et al., J. Phys. G 37, 075021 (2010), with 2011 partial update for the 2012 edition.

[247] L. S. W. Group. Combined lower bound of the neutralino mass in a constrained MSSM model.
http://lepsusy.web.cern.ch/lepsusy/www/lsp cmssm summer04/cMSSM fnal.html, 2004. URL
http://lepsusy.web.cern.ch/lepsusy/www/lsp_cmssm_summer04/cMSSM_final.html.

[248] D. Collaboration and V. Abazov. Search for associated production of charginos and neutralinos in the trilepton fnal state using 2.3 fb^{-1} of data. Physics Letters B, 680(1):3443, 2009. ISSN 0370-2693. doi:DOI:10.1016/j.physletb.2009.08.011. URL http://www.sciencedirect.com/science/article/pii/S0370269309009460.

[249] C. Collaboration. Search for supersymmetry in $ppifmmode/barnelse/fi$ collisions at $s = 1.96TeV$ using the trilepton signature for Chargino-Neutralino production. Phys. Rev. Lett., 101(25):251801, 2008. doi:10.1103/PhysRevLett.101.251801.

[250] Bertone, Gianfranco; Hooper, Dan; Silk, Joseph: ”Particle dark matter: evidence, candidates and constraints”. Physics Reports 405: 279390. arXiv:hep-ph/0404175; Phys. Rep.405.279B. doi:10.1016/j.phys rep.2004.08.031 (2005).

[251] Bertone, G.; Merritt, D., ”Dark Matter Dynamics and Indirect Detection”. Modern Physics Letters A 20 (14): 10211036. arXiv:astro-ph/0504422. Bibcode 2005MPLA...20.1021B. doi:10.1142/S0217732305017391.

[252] HESS collaboration, Search for DarkMatter Annihilation Signals from the Fornax Galaxy Cluster with H.E.S.S., arXiv:1202.5494v1 [astro-ph.HE] 24 Feb 2012.

[253] PAMELA results on the cosmic-ray antiproton flux, arXiv:1007.0821v1 [astro-ph.HE] 6 Jul (2010).

[254] G. Jungman, M. Kamionkowski, and K. Griest, Phys. Rep. 267, 195 (1996).

[255] L. Bergstrom, Rep. Prog. Phys. 63, 793 (2000).

[256] G. Bertone, D. Hooper, and J. Silk, Phys. Rep. 405, 279 (2005).

[257] P. Kiraly et al., Nature 293, 120 (1981).

[258] S. Hawking, Nature 248, 30 (1974).

[259] M. Simon, A. Molnar, and S. Roesler, Astrophys. J. 499, 250 (1998).

[260] M. Boezio et al., Astrophys. J. 487, 415 (1997).

[261] M. Aguilar et al., Phys. Rep. 366, 331 (2002).

[262] F. Donato et al., Astrophys. J. 563, 172 (2001).

[263] V. S. Ptuskin et al., Astrophys. J. 642, 902 (2006).

[264] A. S. Beach et al., Phys. Rev. Lett. 87, 271101 (2001).

[265] L. J. Gleeson and W. I. Axford, Astrophys. J. 154, 1011 (1968).

[266] F. Donato, D. Maurin, P. Brun, T. Delahaye, and P. Salati, Phys. Rev. Lett. 102, 071301 (2009).90

[267] L. J. Gleeson and W. I. Axford, Astrophys. J. 154, 1011 (1968).

[268] J. W. Bieber et al., Phys. Rev. Lett. 83, 674 (1999).

[269] U. W.Langner and M. S. Potgieter, Adv. Sp. Res. 34, 144 (2004).

[270] M. Vogelsberger et al., arXiv:0812.0362v1 (2008).

[271] M. Zemp et al., Mon. Not. Roy. Astron. Soc.394, 641 (2009).

[272] S. Desai et al., Phys. Rev. D 70, 083523 (2004).

[273] T. DeYoung et al., Journal of Physics: Conference Series 136, 022046 (2008).

[274] R. Abbasi et al., Phys. Rev. Lett. 102, 201302 (2009).

[275] A. Gould, ApJ 321, 571 (1987).

[276] Sofia Sivertsson, Joakim Edsjo Accurate calculations of the WIMP halo around the Sun and prospects for its gamma-ray detection, arXiv:0910.0017

[277] K. Griest, D. Seckel, Nucl. Phys. B 283, 681 (1987).

[278] D. N. Spergel, W. H. Press, ApJ 294, 663 (1985).

[279] O. Adriani et al.: An anomalous positron abundance in cosmic rays with energies 1.5100 GeV, Vol 458—2 April 2009— doi:10.1038/nature07942.

[280] M. Boezio et al. PAMELA and indirect dark matter searches, New Journal of Physics 11 (2009) 105023.

[281] E. A. Baltz et al., Pre-launch estimates for GLAST sensitivity to Dark Matter annihilation signals, arXiv:0806.2911v2.

[282] W. B. Atwood, et al., The Large Area Telescope on the Fermi Gamma-ray Space Telescope Mission Fermi/LAT Collaboration, arXiv:0902.1089v1.

[283] A. A. Abdo, Measurement of the Cosmic Ray $e +^{+} e^{-}$ spectrum from 20 GeV to 1 TeV with the Fermi Large Area Telescope, arXiv:0905.0025v1 (2009).

[284] A. A. Abdo et al., Constraints on Cosmological Dark Matter Annihilation from the Fermi-LAT Isotropic Diffuse Gamma-Ray Measurement

[285] R. Abbasi et al., Limits on a muon flux from neutralino annihilations in the Sun with the IceCube 22-string detector, arXiv:0902.2460v3 (2009).

[286] R. Abbasi et al., An Absence of Neutrinos Associated with Cosmic Ray Acceleration in Gamma-Ray Bursts, arXiv:1204.4219v1 (2012).

[287] R. Abbasi et al., Multiyear search for dark matter annihilations in the Sun with the AMANDAII and IceCube detectors, arXiv:1112.1840v2 (2011).

[288] R. Abbasi et al., Searches for periodic neutrino emission from binary systems with 22 and 40 strings of IceCube, arXiv:1108.3023v2 (2012).

[289] R. Bernabei et al., Phys. Lett. B 389, 757 (1996).

[290] R. Bernabei, P. Belli, F. Cappella, R. Cerulli, C. J. Dai, A. d'Angelo, H. L. He, A. Incicchitti et al., AIP Conf. Proc. 1223, 50-59 (2010). [arXiv:0912.0660 [astro- ph.GA]].

[291] Marc Schumann, Dark MAtter Search with Liquid noble gases, arXiv:1206.2169v1 (2012).

[292] R. Bernabei, et al. New results from DAMA/LIBRA. The European Physical Journal C - Particles and Fields, 67(1):39−49, 2010. ISSN 1434-6044. 10.1140/epjc/s10052-010-1303-9, URL http://dx.doi.org/10.1140/epjc/s10052-010-1303-9.

[293] Chris Kelsoa, Dan Hoopera and Matthew R. Buckley: Toward A Consistent Picture For CRESST, CoGeNT and DAMA, arXiv:1110.5338v1 (2011).

[294] R. Bernabei et al.: The DAMA/LIBRA apparatus. Nuclear Instruments and Methods in Physics Research A592(3):297. arXiv:0804.2738.

[295] R. Bernabei et al.: results from DAMA/LIBRA and the combined results with DAMA/NaI. European Physical Journal C56:333. arXiv:0804.2741.

[296] E. Armengaud et al., arXiv:0912.0805v1 [astro-ph.CO] (2009).

[297] P. L. Brink et al., Nucl. Instrum. Meth. A 559, 414 (2006).

[298] A. Broniatowski et al., Journal of Low Temperature Physics 151, 830 (2008).

[299] G. Angloher et al., Astropart. Phys. 31, 270 (2009).

[300] C.E. Aalseth et al.: Results from a Search for Light-Mass Dark Matter with a P-type Point Contact Germanium Detector, arXiv:1002.4703v2 (2010).

[301] J. Angle et al., Phys. Rev. Lett. 100, 021303 (2008).

[302] V. N. Lebedenko et al., Phys. Lett. D 80, 052010 (2009).

[303] E. Aprile and L. Baudis, Proc. of Science (idm2008), 018 (2008).

[304] S. Fiorucci et al., arXiv:0912.0482v1 [astro-ph.CO] (2009).

[305] A. Minamino et al., arXiv:0912.2405 [astro-ph.CO] (2009).

[306] M.G. Boulay (DEAP-3600), arXiv:1203.0604.

[307] A. Hime (MiniCLEAN), arXiv:1110.1005.

[308] D.N. McKinsey, K.J. Coakley, Astropart. Phys. 22, 355 (2005).

[309] A. Marchionni et al. (ArDM), arXiv:1012.5967.

[310] D. Akimov et al. (DarkSide), arXiv:1204.6218.

[311] E. Behnke et al., Science 319, 933 (2008).

[312] S. Archambault et al.,Constraints on Low-Mass WIMP Interactions on 19F from PICASSO, arXiv:1202.1240v2 (2012).

[313] R. Essig, J. Mardon, T. Volansky: Direct Detection of Sub-GeV Dark Matter (arXiv:1108.5383v3).

[314] R. Essig, A. Manalaysay, J. Mardon, P. Sorensen, T. Volansky: XENON10 first results (arXiv:1206.2644v1).

[315] Jeff Filippini, A Search for WIMP Dark Matter Using the First Five-Tower Run of the Cryogenic Dark Matter Search, CDMS PhD Thesis, University of California at Berkeley (2008).

[316] Zeesh Ahmed, A DARK-MATTER SEARCH USING THE FINAL CDMS II DATASET AND A NOVEL DETECTOR OF SURFACE RADIOCONTAMINATION, CDMS PhD Thesis, California Institute of Technology (2012).

[317] Tobias Bruch, A Search for Weakly Interacting Particles with the Cryogenic Dark Matter Search Experiment, CDMS PhD Thesis (2010).

[318] Reuben Walter Ogburn, A SEARCH FOR PARTICLE DARK MATTER USING CRYOGENIC GERMANIUM AND SILICON DETECTORS IN THE ONE- AND TWO-TOWER RUNS OF CDMS-II AT SOUDAN, CDMS PhD Thesis, Stanford University (2008).

[319] D.S. Akerib et al., Exclusion Limits on the WIMP-Nucleon Cross-Section from the First Run of the Cryogenic Dark Matter Search in the Soudan Underground Lab, arXiv:astro-ph/0507190v1 8 Jul 2005.

[320] CDMS Internal note:http://cdms.berkeley.edu/wiki/lib/exe/detail.php?id=detectors%3Asoudan%3Ahome&media=analysis:r118r119:detectors:detector_tower_orientation.png

[321] CDMS Wiki page http://cdms.berkeley.edu/wiki/doku.php?id=detectors:soudan:home

[322] Glenn F. Knoll: Radiation Detection and Measurement, Third Edition (1999).

[323] Gerhard Lutz, Semiconductor Radiation Detectors, ISBN 978-3-540-71678-5 Springer Berlin Heidelberg New York.

[324] Y. P. Varshni, Physica 34, 149 (1967).

[325] C. D. Thurmond, J. Electrochem. Soc. 122, 1133 (1975).

[326] W. Shockley, Solid State Electronics 2, 35 (1961).

[327] X. F. Navick et al., Nucl. Instr. Meth. A444, 361 (2000).

[328] B.A. Young and K.M. Yu, Rev. Sci. Instrum. 66, 2625 (1995).

[329] C.A. Klein, IEEE Trans. Nucl. Sci. 15, 214 (1968).

[330] J. Lindhard et al., K. Dan. Vidensk. Selsk., Mat.-Fys. Medd. 33,No.10 (1963).

[331] J. Lindhard et al., K. Dan. Vidensk. Selsk., Mat.-Fys. Medd. 36, No.10 (1968).

[332] W. Sasaki and M. Shibuya, Experimental evidence of the anisotropy of hot electrons in n-type germanium. J. Phys. Soc. Japan 11, 1202-1203 (1956).

[333] K.M. Sundqvist and B. Sadoulet. Detectors of the Cryogenic Dark Matter Search: Charge transport and phonon emission in Ge h100i crystals at 40 mK. To appear in proceedings of Low Temperature Detectors 12 (2007).

[334] K.M. Sundqvist, Carrier Transport and Related Effects in Detectors of the Cryogenic Dark Matter Search, Ph.D. Thesis, Department of Physics, University of California, Berkeley (2012).

[335] K.D. Irwin, S.W. Nam, B. Cabrera, B. Chugg, and B.A. Young, Rev. Sci. Instrum. 66, 5322 (1995).

[336] R.M. Clarke et al., in Proceedings of the Second International Workshop on the Identification of Dark Matter, edited by N.J.C. Spooner and V. Kudryavtsev (World Scientific, Singapore, 1999), pp. 353358.

[337] T. Saab et al., in Ninth International Workshop on Low Temperature Detectors (AIP, New York, 2002), Vol. 605, pp. 497500.

[338] S.W. Nam, Ph.D. thesis, Stanford University, 1998.

[339] T. Saab, Ph.D. thesis, Stanford University, 2002.

[340] B. Cabrera, Nucl. Instr. Meth. A444, 304 (2000).

[341] T. Saab, R.M. Clarke, B. Cabrera, R.A. Abusaidi, and R. Gaitskell, Nucl. Instr. Meth. A444, 300 (2000).

[342] B. S. Neganov and V. N. Trofimov, J. Exp. Theor. Phys. 28, 328 (1978).

[343] P. N. Luke, Journal of Applied Physics 64(12), 6858 (1988).

[344] H. Maris, Phys. Rev. B, (1990).

[345] H. Maris and S. Tamura, Phys. Rev. B, (1993).

[346] S. Tamura, J.A. Shields, and J.P. Wolfe. Lattice dynamics and elastic phonon scattering in silicon. Phys. Rev. B 44, 3001 (1991).

[347] J.A. Shields, S. Tamura, and J.P. Wolfe. Elastic scattering of acoustic phonons in Si. Phys. Rev. B 43, 4966 (1991).

[348] S. Tamura. Isotope scattering of dispersive phonons in Ge. Phys. Rev. B 27, 858 (1983).

[349] S. Tamura and H.J. Maris. Spontaneous decay of TA phonons. Phys. Rev. B 31, 2595 (1985).

[350] S. Tamura. Spontaneous decay rates of LA phonons in quasi-isotropic solids. Phys. Rev. B 31, 2574 (1985).

[351] M. E. Huber, P. A. Neil, R. G. Benson, D. A. Burns, A. F. Corey, C. S. Flynn, Y. Kitaygorodskaya, O. Massihzadeh, J. M. Martinis, and G. C. Hilton. Dc squid series array amplifiers with 120 mhz bandwidth (corrected). IEEE Transactions on Applied Superconductivity, 11:40484053, June 2001.

[352] S.W. Nam, Ph.D. thesis, Stanford University, 1998.

[353] R.P. Welty and J.M. Martinis, IEEE Trans. Appl. Supercond. 3, 2605 (1993).

[354] M.E. Huber et al., IEEE Trans. Appl. Supercond. 11, 4048 (2001).

[355] K.D. Irwin, An application of electrothermal feedback for high resolution cryogenic particle detection. Appl. Phys. Lett. 66 (15), 1998 (1995).

[356] T. Minotani, K. Enpuku, and Y. Kuroki, J. Appl. Phys. 82, 457 (1997).

[357] Y.G. Shen and Y.W. Mai, Structure and properties of stacking faulted A15 tungsten thin films. Journal of Materials Science 36, 93-98 (2001).

[358] B.A. Young, S.W. Nam, P.L. Brink, B. Cabrera, B. Chugg, R.M. Clarke, A.K. Davies, and K.D. Irwin, Technique for fabricating tungsten thin film sensors with $T_c \ll 100$mK on germanium and silicon substrates. IEEE Trans. Appl. Supercond. 7, 3367 (1997).

[359] B. Young, T. Saab, B. Cabrera, J. J. Cross, and R. A. Abusaidi. Tc tuning of tungsten transition edge sensors using iron implantation. Journal of Applied Physics, 86(6975), 1999.

[360] A. A. Abrikosiv and L. P. Gorkov. Soviet Physics JETP, 12:1243, 1961.

[361] W. A. Roushen and J. Rouvalds. Susceptibility and order parameter for a superconductor with coupl ed magnetic impurities. Physical Review B, 3(5):2929, 1985.

[362] Blas Cabrera, Roland Clarke, Aaron Miller, Sae Woo Nam, Roger Romani, Tarek Saab, and Betty Young: Cryogenic Detectors Based on Superconducting Transition-Edge Sensors for Time-Energy Resolved Single-Photon Counters and for Dark Matter Searches, Preprint submitted to Physica B (1999).

[363] M. Kiveni, R.W. Schnee, M. Pyle and B. Serfass, http://titus.stanford.edu/cdms_restricted/detector_physics/iZIP/ebook/110220/saturation/LocalSaturation.html, CDMS internal note (2011).

[364] Matt Christopher Pyle, OPTIMIZING THE DESIGN AND ANALYSIS OF CRYOGENIC 2 SEMICONDUCTOR DARK MATTER DETECTORS FOR 3 MAXIMUM SENSITIVITY, PhD dissertation, Stanford University, CA (2012).

[365] F.E. Gray et al., Cosmic Ray Muon Flux at the Sanford Underground Laboratory at Homestake, arXiv:1007.1921v3 [nucl-ex] 8 Mar 2011.

[366] T. Enqvist et al., Measurements of muon flux in the Pyha salmi underground laboratory, Nuclear Instruments and Methods in Physics Research A 554 (2005).

[367] J.J. Beatty et al., COSMIC RAYS, particle data group, Revised August 2011.

[368] E.J. Weinberg, et.al., Physical Review D54, Particles and Fields, 1996 Particle Physics Booklet, 1994

[369] R. Clay and B. Dawson, Cosmic Bullets, High Energy Particles in Astrophysics, A-W 1997

[370] M. Shapiro, Cosmic Radiation in Contemporary Astrophysics, Reidel, 1986

[371] D. Montgomery, Cosmic Ray Physics, Princeton, 1949

[372] F. Delobeau, The Environment of the Earth, Reidel, 1971

[373] National Geophysical Data Center, NOAA, Cosmic Rays, http://web.ngdc.noaa.gov/stp/SOLAR/COSMIC_RAYS/cosmic.html

[374] Scott Fallows, Veto muon rejection efficiency c58, CDMS internal note: http://titus.stanford.edu/cdms_restricted/Soudan/R125-128/ebook/090824_3/.

[375] CDMS Cold hardware page maintained by Dennis Seitz, http://cdms.berkeley.edu/cdms_restricted/coldhardware/html/coldhardware.html.

[376] M. Pyle, Non Stationary Optimal Filter, CDMS internal note http://cdms.berkeley.edu/wiki/doku.php?id=software:cdmsbats_batroot_user_guide:ns_optimalfilter.

[377] M. Pyle, N-dimensional Optimal Filter, CDMS internal note http://cdms.berkeley.edu/wiki/doku.php?id=software:cdmsbats_batroot_user_guide:nd_optimalfilter.

[378] M. Pyle, N×M Optimal Filter, CDMS internal note http://cdms.berkeley.edu/wiki/doku.php?id=software:cdmsbats_batroot_user_guide:nxm_optimalfilter.

[379] Kyle Sundqvist, Charge crosstalk correction: http://titus.stanford.edu/cdms_restricted/Soudan /R125-128/ebook/090225/postprocessv3/R125_Charge_Calib.html.

[380] T. Shutt, et al. A solution to the dead-layer problem in ionization and phonon-based dark matter detectors. Nuclear Instruments and Methods in Physics Research Section A: Accelera- tors,

Spectrometers, Detectors and Associated Equipment, 444(1-2):pages 340-344, 2000. ISSN 0168-9002. doi:16/S0168-9002(99)01379-0. URL http://www.sciencedirect.com/science/article/pii/S0168900299013790.

[381] M. Fritts. PipeFitter. CDMS internal note, University of Minnesota, 2009. URL http://cdms.berkeley.edu/wiki/doku.php?id=analysis:r125:pipefitter.

[382] M. Fritts. Background Characterization and Discrimination in the Final Analysis of the CDMS II Phase of the Cryogenic Dark Matter Search. Ph.D. thesis, University of Minnesota, 2011. URL http://cdms.berkeley.edu/Dissertations/fritts.pdf.

[383] M. Pyle and P. Brooks. Impact of multiple χ^2 minima on PipeFitter energy and timing. CDMS internal note, Stanford University, 2008. URL http://titus.stanford.edu/cdms_restricted/Soudan/R123/ebook/080304/pf_degen.html.

[384] M. Pyle and B. Serfass. Preliminary comparison of yield resolution between PipeFitter and DarkPipe. CDMS internal note, 2007. URL http://titus.stanford.edu/cdms_restricted/Soudan/r118r119/ebook/070221/ebook_timing.html.

[385] R. W. Ogburn and L. Hsu. Pulse Integral. CDMS internal note, 2011. URL http://cdms.berkeley.edu/wiki/doku.php?id=software:cdmsbats_batroot_user_guide:pulseintegral.

[386] M. Pyle, et al. Comparing the energy resolution of optimal filter to integrals near threshold. CDMS internal note, 2006. URL http://titus.stanford.edu/cdms_restricted/Soudan/r118r119/ebook/060823/IntvsOF.html.

[387] Oleg Kamaev, Time-domain fit algorithms for phonon pulses, http://titus.stanford.edu/cdms_restricted/Soudan/R125-128/ebook/081118/phpulseTFits_R123.html

[388] Scott Fallows, Charge Calibration for T3-T5 for R130, http://titus.stanford.edu/cdms_restricted/Soudan/R130/ebook/091111/index.html

[389] Joseph M. Kiveni, Phonon Calibration for T3-T5 for R130, http://titus.stanford.edu/cdms_restricted/Soudan/R130/ebook/100126/phonon_calibration_t3_t5.html

[390] Kevin A. McCarthy, Phonon Calibration for R125-128,http://titus.stanford.edu/cdms_restricted/Soudan/R125-128/ebook/090226/phononcal/R58%20phonon%20calibration.html

[391] J. Lewin and P.F. Smith, Astropart. Phys. 6, 87 (1996).

[392] Jeter Hall, c58 Nuclear Recoil Bands, http://titus.stanford.edu/cdms_restricted/Soudan/R125-128/ebook/090624/c58_NR_bands.html

[393] Anthony Villano, Nuclear Recoil Bands in c58 Re-Analysis, http://www.hep.umn.edu/cdms/cdms_restricted/villaa/ebooks/111031_c58R_NRband/

[394] Scott Hertel, Improving the Walked Timing Parameters at Small Energy, http://titus.stanford.edu/cdms_restricted/Soudan/R125-128/ebook/081119_1/webpage1/variablebutterworth.html

[395] C. Chang. The Cryogenic Dark Matter Search (CDMS-II) - frstresults from the Soudan Mine. PhD thesis, Stanford University, 2004.

[396] Joseph M. Kiveni, Trigger rate Analysis, CDMS internal note: http://titus.stanford.edu/cdms_restricted/Soudan/R125-128/ebook/090701/cTrigBurst_c58/cTrigBurst.html

[397] Joseph M. Kiveni, Analysis of Trigger Efficiencies for c58, CDMS internal note: http://titus.stanford.edu/cdms_restricted/Soudan/R123/ebook/091508/code.html

[398] Joseph M. Kiveni, Update on the Trigger Efficiencies for r123, CDMS internal note: http://titus.stanford.edu/cdms_restricted/Soudan/R123/ebook/091508/index.html

[399] Rupak Mahapatra, First Look at Phonon Trigger Efficiency, CDMS Internal note: http://titus.stanford.edu/cdms_restricted/Soudan/R123/ebook/071127_2/index.html.

[400] Jeff FIlippini: R123 Trigger Efficiencies Aren't So Bad!, CDMS Internal note: http://titus.stanford.edu/cdms_restricted/Soudan/R123/ebook/071204_4/trigeff.html.

[401] Kolmogorov-Smirnov Test, http://www.physics.csbsju.edu/stats/KS-test.html

[402] S. A. Hertel. KS tests for WIMP-search data for c58. CDMS internal note,http://titus.stanford.edu/cdms_restricted/Soudan/R125-128/ebook/ 090520/c58BgKS.html.

[403] S. A. Hertel. KS tests for Ba data for c58. CDMS internal note, http:// titus.stanford.edu/cdms_restricted/Soudan/R125-128/ebook/090429/c58BaKS.html.

[404] Joseph M. Kiveni, Ba KS TEST R130 for ST1, CDMS internal note: http://titus.stanford.edu/cdms_restricted/Soudan/R130/ebook/100420/r130_kstest_ba.html

[405] Joseph M. Kiveni, WS KS TEST R130 for ST1, CDMS internal note: http://titus.stanford.edu/cdms_restricted/Soudan/R130/ebook/100420/r130_kstest_bg.html

[406] Joseph M. Kiveni, Helium Fils Studies, CDMS internal note: http://titus.stanford.edu/cdms_restricted/Soudan/R125-128/ebook/090721/heFilmStudies.html

[407] Cathy N. Bailey, PhD dissertation, Physics Department of Case Wester Reserve University THE CRYOGENIC DARK MATTER SEARCH: FIRST 5-TOWER DATA AND IMPROVED UNDERSTANDING OF IONIZATION COLLECTION, January 2010.

[408] O. Kamaev, S. Hertel, Low Yield Fraction (Neutralization) in Wimp-Search Data c58 , CDMS internal note: http://titus.stanford.edu/cdms_restricted/Soudan/R125-128/ebook/090713/neutralization_bg_c58.html

[409] O. Kamaev, K. McCarthy, J. Zhang, Neutralization for Ba in Run 125-128, CDMS internal note: http://titus.stanford.edu/cdms_restricted/Soudan/R125-128/ebook/090414_neut/neut58.html

[410] Anthony N. Villano, Ba Neutralization cut for silicon detectors pre position correction, CDMS internal note: http://titus.stanford.edu/cdms_restricted/Soudan/R125-128/ebook/110920/

[411] Lauren Hsu, Study of Charge Optimal Filter Delay Resolution, CDMS internal note: http://titus.stanford.edu/cdms_restricted/Soudan/R125-128/ebook/091124_3/index.html

[412] Jianjie Zhang, Charge χ^2 Cut and Efficiencies for the Reprocessed Run 125-128 Data, CDMS internal note: http://www.hep.umn.edu/cdms/cdms_restricted/misc/110524/cChiSq.html

[413] J. Sander and R. Mahapatra, A Measurement of the Efficiency of the Qinner Cut, CDMS internal note: http://titus.stanford.edu/cdms_restricted/Soudan/R119/ebook/050321_2/qi_efficiency2.html

[414] Allan , Detailed Study of cQin_c58 Efficiency, CDMS internal note: http://titus.stanford.edu/cdms_restricted/Soudan/R125-128/ebook/090730/CQinC58/DetailedCQinC58EfficiencyStudy.php

[415] D. Moore. cPstd and cQstd cuts for c58. CDMS internal note, http:// titus.stanford.edu/cdms_restricted/Soudan/R125-128/ebook/090317_2/index.html.

[416] D. Moore. Updates to cPstd c58 and cQstd c58. CDMS internal note, http://titus.stanford.edu/cdms_restricted/Soudan/R125-128/ebook/090622_4/.

[417] Danielle Speller, cSingle_c58R Definition and Efficiencies. CDMS internal note, http://titus.stanford.edu/cdms_restricted/Soudan/R125-128/ebook/120130/cSingle_c58Reff_final.html

[418] M. Fritts and S. Fallows. Veto Cut for c58. CDMS internal note, http://titus.stanford.edu/cdms_restricted/Soudan/R125-128/ ebook/090622_3/.

[419] Joseph M. Kiveni and Richard W. Schnee, Looking at cGoodPstartTime, CDMS internal note: http://titus.stanford.edu/cdms_restricted/Soudan/R130/ebook/100820/cgoogpstarttime.html

[420] Joseph M. Kiveni, Follw up on the Trigger Efficiency for the run c58, CDMS internal note: http://titus.stanford.edu/cdms_restricted/Soudan/R125-128/ebook/090929/FollowUp.html

[421] Denis Seitz,Substrate thicknesses for CDMS-II 1-cm thick detectors at Soudan - Nov 2008, CDMS elog boob: http://cdms.berkeley.edu/cdms_restricted/detectors/detsubsysnotes/0811/0811001/Detector-Thickness.html

[422] V. Mandic et al.,Study ofthe dead layer in germanium for the CDMS detectors, Nuclear Instruments and Methods in Physics Research A 520 (2004) 171174.

[423] Robert H. Nelson, The Veto System Pulser and Studies of Deep Underground Muons for the CDMS-II Experiment, A dissertation submitted in partial satisfaction of the requirements for the degree of Bachelors of Science, UCSB-2003.

[424] Raymond Bunker, private communication.

[425] Z. Ahmed et al.: Results from the Final Exposure of the CDMS II Experiment, arXiv:0912.3592v1, Science 327, 1619 (2010).

[426] William H., Saul A. Teukolsky, William T. Vetterling, Brian P. Flannery: Numerical Recipes in C, The Art of Scientific Computing Second Edition.

[427] Scott A. Hertel, Advancing the Search for Dark Matter: from CDMS II to SuperCDMS, PhD dissertation, MIT, 2012.

[428] Giovanni Bianchi and Roberto Sorrentino (2007). Electronic filter simulation & design. McGraw-Hill Professional. pp. 1720. ISBN 978-0-07-149467-0.

[429] J. Sander, Results from the Crogenic Dark Matter Search Using a χ^2 Squared Analysis, Ph.D. Thesis, Department of Physics, University of California at Santa Barbara (2007).

[430] J. Sander and R. Mahapatra: R119 3D χ^2 Timing Cut Applied to the Closed ^{133}Ba Data; CDMS internal note: http://titus.stanford.edu/cdms_restricted/Soudan/R119/ebook/050307_2/timing_closedba.html

[431] J. Sander and R. Mahapatra: Final 3-D Chi2 Timing Cut; CDMS internal note: http://titus.stanford.edu/cdms_restricted/Soudan/R119/ebook/050221/index.html

[432] J. Sander and R. Mahapatra: 3D χ^2 Optimized Timing Cut Based on pfracc, pminrtc and pdelc with Correlations; CDMS internal note: http://titus.stanford.edu/cdms_restricted/Soudan/R119/ebook/050215/index.html

[433] J. Sander and R. Mahapatra: χ^2 Optimized 4D Timing cut based on y, pfracc, pminrtc and pdelc; CDMS internal note: http://titus.stanford.edu/cdms_restricted/Soudan/R119/ebook/050208_3/index.html

[434] J. Filippini: χ^2 Cuts at Low Energies; CDMS internal note: http://titus.stanford.edu/cdms_restricted/Soudan/R119/ebook/050421/index.html

[435] J. Filippini: Energy dependent χ^2 cut; CDMS internal note: http://titus.stanford.edu/cdms_restricted/Soudan/R119/ebook/050402/index.html

[436] J. Filippini: What Shape Should Our Timing Cuts Have; CDMS internal note: http://titus.stanford.edu/cdms_restricted/Soudan/R119/ebook/050313/index.html

[437] J. Filippini: χ^2 timing cut using pminrtc and pdelc with Fitted Covariance Matrix; CDMS internal note: http://titus.stanford.edu/cdms_restricted/Soudan/R119/ebook/050220/index.html

[438] J. Filippini: First Look at Chi2 Timing cut using pminrtc and pdelc; CDMS internal note: http://titus.stanford.edu/cdms_restricted/Soudan/R119/ebook/050215_3/index.html

[439] Walter R. Ogburn: Simple χ^2 timing cut; CDMS internal note: http://titus.stanford.edu/cdms_restricted/Soudan/r118r119/ebook/070817/

[440] Walter R. Ogburn: 4D χ^2 timing cut with radius; CDMS internal note:
http://titus.stanford.edu/cdms_restricted/Soudan/r118r119/ebook/070822/

[441] Walter R. Ogburn: 3D χ^2 timing cut with radius- & energy-correction; CDMS internal note:
http://titus.stanford.edu/cdms_restricted/Soudan/r118r119/ebook/070822_2/

[442] Kunj Prassad: χ^2 timing cut; CDMS internal note:
http://titus.stanford.edu/cdms_restricted/Soudan/R130/ebook/100613/

[443] Joseph M. Kiveni: Using χ^2 for surface events rejection in R130; CDMS internal note:
http://titus.stanford.edu/cdms_restricted/Soudan/R130/ebook/100520/index.html

[444] Joseph M. Kiveni, c58R Timing Cuts Analaysis using a 5D Optimized Energy Dependent χ^2, CDMS internal note:
http://titus.stanford.edu/cdms_restricted/Soudan/R125−128/ebook/120731/chisqanalysis_new.html

[445] J.Filippini, Form of Fit to Parameter Variances; CDMS internal notes:
http://titus.stanford.edu/cdms_restricted/Soudan/R119/ebook/050220/fitform.html

[446] Xinjie Qiu, 2D gaussian density model and χ^2 timing cut; CDMS internal notes:
http://titus.stanford.edu/cdms_restricted/Soudan/r118r119/ebook/070531/

[447] Zeesh Ahmed, Dave Moore, Oleg Kamaev, Matt Fritts: Automated Tuning of Timing Cuts
http://titus.stanford.edu/cdms_restricted/Soudan/R125-128/ebook/090914_1/

[448] Joseph M. Kiveni, Richard W. Schnee: Neutron Band Asymmetry Study,CDMS internal note,
http://titus.stanford.edu/cdms_restricted/Soudan/R125-128/ebook/090818/BandAsymetry.html

[449] Joseph M. Kiveni, Richard W. Schnee: Asymmetric Nuclear Band,CDMS internal note,
http://titus.stanford.edu/cdms_restricted/Soudan/R125-128/ebook/091124_1/NR_band_study.html

[450] Richard W. Schnee: Calculating Estimated Leakage and Uncertainties for R123, CDMS internal note,
http://titus.stanford.edu/cdms_restricted/Soudan/R123/ebook/080215/LeakageMethod123.pdf

[451] Jianjie Zhang: C58 Ge Reanalysis Timing Cuts, CDMS internal note,
http://www.hep.umn.edu/cdms/cdms_restricted/zhang/120729/

[452] Jianjie Zhang: C58 reanalysis neural network timing analysis, CDMS internal note,
http://titus.stanford.edu/cdms_restricted/Soudan/R125-128/ebook/120815_2/nnet_final.html

[453] David Moore, Systematic differences between Ba and low background beta distributions, CDMS internal note: http://titus.stanford.edu/cdms_restricted/Soudan/R125-128/ebook/090720_2/.

[454] Matt Fritts, Zeesh Ahmed and David Moore, Draft of Plan for Timing Cut Initial Leakage Estimation and Optimization, CDMS internal note:
http://titus.stanford.edu/cdms_restricted/Soudan/R125-128/ebook/090811/OLDindex.html.

[455] S. Yellin, Phys. Rev. D 66, 032005 (2002).

[456] S. Yellin, arXiv:0709.2701v1 [physics.data-an] (2007).

[457] G. J. Feldman and R. D. Cousins, Phys. Rev. D 57, 3873 (1998).

[458] Richard W. Schnee, CDMS Internal note:
http://cdms.berkeley.edu/cdms_restricted/cdmsnotes/0105/0105006/fcmemo.pdf

[459] Tobias Bruch, Detection thresholds and upper limits for CDMS, CDMS Internal note of University of Zurich:
http://www.physik.unizh.ch/groups/groupbaudis/cdms/restricted/internet_notes/090629/detuplimr123.pdf.

[460] Thomas Hebbeker, CwalictuhlaPtoinisgsoUnpSpteartiLsitmicis, Humboldt University (Berlin), February23,2001.

[461] Kevin Mc Carthy, Livetime of c58 Si data, CDMS internal notes:
http://titus.stanford.edu/cdms_restricted/Soudan/R125-128/ebook/120828_4/20120828_LiveTime.html

[462] CDMS collaboration, Results of the reanalysis of the CDMS II Soudan data, PRD in preparation.

[463] Dan Hooper, J.I. Collar, Jeter Hall, Dan McKinsey, Chris Kelso: A Consistent Dark Matter Interpretation For CoGeNT and DAMA/LIBRA, 10.1103/PhysRevD.82.123509 (arXiv:1007.1005v3).

[464] CoGeNT collaboration: Search for an Annual Modulation in a p-Type Point Contact Germanium Dark Matter Detector http://prl.aps.org/pdf/PRL/v107/i14/e141301 (2011).

[465] G. Angloher, et, al.: Results from 730 kg days of the CRESST-II Dark Matter Search, arXiv:1109.0702v1.

[466] XENON100 Collaboration, Dark Matter Results from 225 Live Days of XENON100 Data, arXiv:1207.5988v1.

[467] EDELWEISS Collaboration: Final results of the EDELWEISS-II WIMP search using a $4-$ kg array of cryogenic germanium detectors with interleaved electrodes, arXiv:1103.4070v3.

[468] C. Strege, et. al: Updated global fits of the cMSSM including the latest LHC SUSY and Higgs searches and XENON100 data, arXiv:1112.4192v2.

[469] SuperCDMS Collaboration, SuperCDMS Soudan proposal, 2012.

Curriculum Vitae

Author Name: Joseph Manungu Kiveni

Place of birth: Lukolela, Democratic Republic of The Congo

Date of birth: May 9, 1978

Education:

1. PhD Candidate, Physics Department, Syracuse University, Syracuse, New-York, (2008 to 2012).
2. M.S., Physics Department, Syracuse University, Syracuse, New-York, (2009).
3. Diploma program in Theoretical high energy physics, International Center for Theoretical Physics (ICTP), Trieste, Italy, (2005).
4. B.Sc.(cum laude.), Physics, University of Kinshasa (UNIKIN), Kinshasa - Dem. Rep. of Congo (2004).

Professional experience:

Syracuse University, Department of Physics, Graduate Student Instructor/Assistant & Graduate Student Researcher (2008-2011)

Honors and Awards:

Recipient of the Marie Curie Cryogenic Program held in Kosice, Slovakia, 2010.

Future professorial fellow, Syracuse University, Syracuse New York (2009).

Inductee member of the Phi Beta Delta chapter honorary society of the Syracuse University, Syracuse New York (2009).

Diploma Program fellowships recipient, International Center for Theoretical Physics (ICTP), Trieste - Italy, 2004-2005.

Invited Junior-young Scientist researcher (under the guidance of Alexei Yu Smirnov), International Center for Theoretical Physics (ICTP), Trieste - Italy, 2006.

Scientific Training:

Excellence In Detector Instrumentation and Technology held at Fermi National Laboratory, Batavia, IL, USA, Feb. 2012.

Marie Curie Advanced Cryogenics course and applications, Kosice, Slovakia, 2010.